

**Analytical Investigation of the Dynamics  
of Tethered Constellations in Earth Orbit (Phase II)**

**Final Report**

Contract NAS8-36606

For the period 22 February 1985 through 31 March 1994

Principal Investigators

Enrico C. Lorenzini

Gordon E. Gullahorn

Mario L. Cosmo

Robert D. Estes

May 1994

Prepared for

National Aeronautics and Space Administration

Marshall Space Flight Center, Alabama 35812

Smithsonian Institution

Astrophysical Observatory

Cambridge, Massachusetts 02138

The Smithsonian Astrophysical Observatory

is a member of the

Harvard-Smithsonian Center for Astrophysics



## TABLE OF CONTENTS

SUMMARY .....	1
INTRODUCTION .....	4
1.0 COMPUTER CODES FOR THE DYNAMICS OF TETHERED SYSTEMS .....	5
1.1 Tether Dynamics Simulators .....	5
1.2 Data Analysis Software .....	6
2.0 COMPARISON OF VARIOUS TETHERED SYSTEM SIMULATORS .....	10
2.1 Test Cases Comparison of Results .....	10
2.2 Comparison Plots and Discussion .....	11
2.3 Time Series Plots .....	15
2.4 Power Spectral Density of Simulator Results .....	28
2.5 PSD Plots .....	30
2.6 Conclusions .....	35
2.7 References .....	36
3.0 VARIABLE-G/MICRO-G LABORATORY TETHERED TO THE SPACE STATION .....	37
4.0 TETHERED SPACE CENTRIFUGE .....	39
5.0 TWO-DIMENSIONAL STRUCTURES WITH TETHERS .....	40
6.0 TETHERED HIGH-GAIN ANTENNAS .....	41
7.0 PROPAGATION OF ELF WAVES INTO THE IONOSPHERE .....	42
8.0 REENTRY OF TETHERED CAPSULES .....	43
9.0 DEPLOYMENT DYNAMICS OF SEDS-I .....	44
Figure Captions .....	44
9.1 SEDS-I deployer .....	45
9.2 Simulation of SEDS-1 Deployment Dynamics .....	46
9.2 Off-Nominal Deployment Cases .....	57
9.3 Conclusions on the simulation of SEDS-1 deployment .....	62
9.4 References .....	62

10.0 ANALYSIS OF SEDS-I FLIGHT DATA .....	63
Figure Captions.....	63
10.1 Introduction.....	64
10.2 Data Check and Validation .....	65
10.3 Covariance Analysis .....	67
10.4 End-mass Orientation.....	67
10.5 Data Analysis and Validation An Example .....	68
10.6 Conclusions.....	69
10.7 Pulse Propagation Analysis.....	69
10.8 Fit of Simulation to Flight Data.....	70
11.0 DYNAMICS AND CONTROL OF SEDS-II.....	94
Figure Captions.....	94
11.1 SEDS-2 Closed-loop Control Law.....	97
11.1.1 Control Scheme.....	97
11.1.2 Implementation of Control Law.....	98
11.1.3 Robustness of Control Law .....	116
11.1.4 Validation of SEDS-2 Control Law .....	135
11.1.5 Simulation of latest baseline deployments .....	137
11.2 Control law performance during the flight .....	149
11.2.1 Estimate of the maximum libration at the end of deployment.....	149
11.2.2 More on the performance of the control law.....	156
11.3 Conclusions on SEDS-2 control law .....	157
11.4 References .....	159
ACKNOWLEDGMENTS.....	160



## **SUMMARY**

This final report covers the 9-year research on future tether applications and on the actual flights of the Small Expendable Deployment System (SEDS) as described briefly in the following.

In order to keep the size of the report at a manageable level, the highlights of the research are presented here while the interested reader can obtain all the necessary details from the 34 quarterly reports that have covered systematically our research activity throughout this contract.

This final report is subdivided according to the major topics of investigation as follows:

### **(1) Computer codes for the dynamics of tethered systems**

(a) Description of numerical codes MASTER20 and MASTERDEPO to simulate the orbital and attitude dynamics of tethered systems during station keeping and deployment maneuvers; (b) algorithms to estimate orientation, angular rates and angular accelerations of SEDS-1 endmass from instruments' data; (c) algorithms to validate SEDS-1 endmass data.

### **(2) Comparison of various tethered system simulators**

Design of test case situations; simulation by various groups; comparison of results.

### **(3) Variable-g/micro-g laboratory tethered to the Space Station**

(a) Dynamics analysis; (b) Conceptual design; (c) Investigation of potential applications; and (d) Propagation of disturbances and isolation from noise of a variable-gravity/micro-gravity laboratory tethered to the Space Station. A single tether and a dual tether configuration are analyzed.

### **(4) Tethered space centrifuge**

Investigation of the stability, the acceleration noise, and the suitability of the acceleration levels for human habitation of a 1-km-long tethered centrifuge in low Earth orbit. Analysis of the dynamics of the centrifuge during the spin-up and spin-down phases.

### **(5) Two-dimensional structures with tethers**

Various two-dimensional tethered structures for low Earth orbit are proposed for use as planar array antennas. The stability of the structures is investigated and the system parameters for specific mechanisms of stabilization are computed.

### **(6) Tethered high-gain antennas**

Conceptual design of a travelling wave antenna for transmission from space of ELF/VLF waves to the ground. Analysis of a V-shaped antenna, which consists of two long tethers in the same orbit separated by a distance, for the reception of HF emissions from outer space.

### **(7) Propagation of ELF waves into the ionosphere**

Development of a method for the numerical calculation of the electromagnetic wave field on the Earth's surface associated with the operation of an electrodynamic tethered satellite system of constant or slowly varying current orbiting in the ionosphere.

### **(8) Reentry of tethered capsules**

Dynamical and thermal analysis of the reentry of a capsule with an attached heat-resistant tether which slows down the reentry at high altitudes and reduces drastically the maximum temperature experienced by the capsule. The results of these type of reentry are then compared to a reentry without tether and to a reentry with a low-melting-point tether (i.e., reentry of SEDS-I).

### **(9) Deployment dynamics of SEDS-I**

Simulation of the position and satellite attitude dynamics of SEDS-1. Deployment simulations for different values of the tension model parameters. Identification of the upper limits of the minimum friction in the deployer for a successful deployment.

### **(10) Analysis of SEDS-I flight data**

(1) Analysis of magnetometer data; (2) Estimation of attitude determination accuracy from instrument data; (3) Computation of attitude rates; (4) Validation of load cells and magnetometer data with accelerometer readings; (5) Post-flight simulation of SEDS-I

deployment by using the Carroll tension model and adjusting the parameters to fit the flight data.

### **(11) Dynamics and Control of SEDS-II**

(1) Development of a closed-loop control law for SEDS-2 for providing a small libration amplitude and a low tether exit velocity at the end of deployment; (2) Analysis of the robustness of the closed-loop deployment control law with respect to tension model errors and actuator errors.

## INTRODUCTION

This is the Final Report submitted by the Smithsonian Astrophysical Observatory (SAO) under NASA/MSFC contract NAS8-36606, "Analytical Investigation of Tethered Constellations in Earth Orbit (Phase II)." This report covers the period of activity from 22 February 1985 through 31 March 1994. The Principal Investigators (PIs) for this contract have been E.C. Lorenzini, M.L. Cosmo, G.E. Gullahorn, and Robert D. Estes.

This final report presents the highlights of the research conducted through the 9-year-long activity while the interested reader is referred to the 34 quarterly reports of this contract for a much more detailed description of the project. Whenever possible, the papers published under this contract have been incorporated into this report. The papers have the advantage of providing a more concise description than the quarterly reports. Moreover, the refereed papers have the added advantage of having been formally reviewed.

## 1.0 COMPUTER CODES FOR THE DYNAMICS OF TETHERED SYSTEMS

The development of software has been a major effort throughout the whole course of the study. The purpose of the software developed can be divided in two main areas:

- 1 ) Simulation of the dynamics of orbiting tethers.
- 2 ) Data analysis of tether flight conditions from instrumentation data

### 1.1 Tether Dynamics Simulators

Two codes have been written to simulate the dynamics of spaceborne tethers: MASTER20 and MASTERDEP0. MASTER20 was originally written to simulate the three-dimensional dynamics of the microgravity/variable gravity laboratory.

MASTER20 has been extensively used afterwards to simulate various other applications like artificial gravity and tether-initiated reentry. MASTERDEP0 is a further refinement of MASTER20. It can simulate tether deployment as it was originally developed to simulate SEDS deployments and the attitude dynamics of the end-mass. The numerical integration of SEDS-1 flight provided a very good fit of the flight data as shown in Section 10.

Moreover, we used MASTERDEP0 to analyze the complicated attitude dynamics of SEDS' end-mass. The results of this analysis have been included in a paper submitted for publication to *Acta Astronautica*. In the same paper, a passive device for reducing the amplitudes of attitude oscillations is also presented and its effectiveness assessed. A copy of the paper is shown in Section 9.

Both codes model the tether as well as the platforms as lumped masses connected by massless spring-dashpot systems to simulate tether elasticity and structural damping.

Each lump is acted upon by tensional, aerodynamic and gravitational forces. MASTER20 drag force adopts a dynamic Jacchia 1977 neutral density model and MASTERDEP0 adopts the Mass Spectrometer Incoherent-Scatter-1986 (MSIS-86) model. The gravitational forces include the second zonal harmonic of the gravity field ( $J_2$  term).

MASTER20 and MASTERDEP0 also simulate the thermal effects on the tension due mainly to the terminator crossings, as well as the Earth's albedo and IR radiation. An improved version of MASTER20 includes aerodynamic heating to simulate low orbiting probes and tether reentry conditions.

The code's integrator routine is a fourth-order Runge-Kutta with adjustable stepsize. This routine has proven to be reliable, even if not fast, under very demanding numerical situations such as deployment with many lumps and tension discontinuity due to thermal shocks.

In MASTERDEP0 the deployment maneuver is simulated by placing a new lump close to the deployer along the unit vector connecting the deployer to the closest old lump with the same deployer velocity plus a term that takes into account the relative motion between the last two lumps. The integration is then stopped, the new system state vector is updated for the new lump and the integration is started again until the final length is reached.

The platform attitude dynamics is computed by integrating the kinematics and the Euler equations. The kinematics equations express the time evolution of the Euler angles with respect to the inertial frame (3-1-3 rotation sequence). The Euler equations relate the time derivative of the angular rates to the external torques.

The torques considered are related to the tether visco-elastic force, the gravity gradient, the aerodynamic drag and attitude control.

The codes run on a VAX-780, MicroVax, Apple Macintosh and Sun Sparc Station-2.

## **1.2 Data Analysis Software**

Several programs were written to analyze and validate SEDS flight data. Additional software was written to compare the flight data to theoretical models.

### **QUEST Program**

One of the main objective in SEDS data analysis was the estimation of the end-mass orientation. To this end we wrote the program QUEST that adopts QUEST (QUaternion ESTimation) and Triad (algebraic method) algorithms to estimate the attitude matrix  $A$ . Quest algorithm uses a set of  $N$  observations at each time to compute the attitude matrix  $A$

given a quaternions set  $q$  that minimizes in a least square sense the cost function  $L(A)$  (Wahba's function):

$$L(A) = \sum_k^N a_k |\underline{w}_k - A \underline{v}_k|^2$$

where:

$N$  = number of sets of unit vector observations

$a_k$  = weights =  $1/\sigma_k^2$  ( $\sigma$ = measurement standard deviation)

$\underline{w}_k$  = k-th set of unit vector observation in the body reference frame)

$\underline{v}_k$  = k-th set of unit vector representation with respect to the reference frame.

The Triad algorithm instead uses only two reference vectors to determine the three Euler angles. Even though this is not an optimal method it can be easily implemented to check Quest results.

Both algorithms have been extensively used in the past to estimate spacecraft orientation. On the other hand the definition of the vector observations has posed a challenging problem. In order to estimate the orientation of a rigid body two reference vectors are needed. In SEDS case only the magnetometer was dedicated to such measurements using the geomagnetic field as the reference. As a second vector, we have adopted the "tether" direction vector. Specifically, the direction of the line connecting the end-mass to the deployer has been compared to the load cell unit vector.

A thorough analysis of the errors affecting the vector measurements was needed to characterize the attitude covariance.

The vector measurement error  $\sigma_{vec}$  can be written as

$$\sigma_{vec}^2 = \sigma_{mod}^2 + \sigma_{meas}^2$$

where

$\sigma_{mod}$  = modeling error

$\sigma_{meas}$  = instrument's measurement error

The magnetometer modeling error takes into account:

- a) the error in the knowledge of the strength and orientation of the Earth's magnetic field
- b) the error in the computation of the reference magnetic field due to the knowledge of the end-mass orbital position

The load cells modeling error takes into account that:

- a) the line connecting the two end-platforms does not coincide with the direction of the tensiometer because of the bowing of the tether
- b) the direction of the unit vector connecting the two end-platforms is affected by the knowledge of the end-platforms positions.

The magnetometer and load cells instrument error is 9.3 mGauss and 10 mN, respectively.

The expressions of the covariance matrices for TRIAD and QUEST algorithms are not reported here for the sake of brevity.

### Other Software

During the course of the analysis we also wrote software to validate and check the end-mass instrumentation's data.

Namely we developed:

- 1) Least-square estimator of the magnetometer bias
- 2) Estimation of the end-mass angular rates.
- 3) Comparison of the estimated angular acceleration with the accelerometer's data:

$$\underline{\Delta} = \underline{A} - (\underline{T}/M) = d\underline{\omega}/dt \times \underline{\rho} + \underline{\omega} \times (\underline{\omega} \times \underline{\rho})$$

where  $\underline{A}$  and  $\underline{T}$  are the accelerometer and load cells signal, respectively,  $M$  the satellite mass,  $\underline{\omega}$  the angular rates and  $\underline{\rho}$  the accelerometers' body coordinates.

The results of the estimation of SEDS-1 end-mass orientation and data validation are presented in Section 10.



4) FFT routine to analyze instruments' data

5) Computation of theoretical oscillations modes from tension and length data, namely:

- a) First three lateral ("string") modes
- b) Spring-mass mode
- c) Pitch (e.g. end-mass attitude) mode.

## 2.0 COMPARISON OF VARIOUS TETHERED SYSTEM SIMULATORS

Several tasks were performed to support the Tether Applications Simulation Working Group (TASWG). Only the second task (the test case comparison) is discussed here. The other two tasks, and more detail on the test cases, are given in an Interim Report included in Quarterly Report #16.

First, a questionnaire soliciting information on current or planned tether simulation programs was widely circulated. The responses were summarized in a table.

Second, a set of "test cases" was defined to allow comparison of the attempts of various programs to simulate the same physical situations. These cases were simulated by a number of program authors, including SAO with the program SKYHOOK. An extensive set of plots is presented showing the agreements and differences among the results. Spectral analyses are and differences among the results. Spectral analyses are also given.

Third, "analytic" results were discussed which a simulator author might wish to use for validating a program. A bibliography was given. Only the second task (the test case comparison) is discussed here. The other two tasks, and more detail on the test cases, are given in an Interim Report included in Quarterly Report #16.

### 2.1 Test Cases: Comparison of Results

Four test cases were designed. The salient features are described in the following section, while more detailed specifications are given in Quarterly Report #16. The physical characteristics of the system are similar to those of TSS-1. A 20 km deployed length (TSS-1 nominal) is used in three cases, while one case uses a 100 km deployed length. None of the cases employ tether reel motion, i.e. the tether natural length remains fixed.

The tether is assumed to be idealized viscoelastic -- i.e. obeying a Hooke's law for tension due to stretching, and having a damping force proportional to the velocity of deformation. This assumption, particularly on the damping force, may not be very realistic (Carroll, private communication; Xe and Powell, 1988), but it does allow an unambiguous and simply treated internal force model. As far as is known, no simulator uses a different elasticity model.

Results were obtained from six simulators. GTOSS results were provided by David Lang of Lang Associates. STOCS results were provided by Roger Wacker of Lockheed Engineering and Management Services Company, Inc. SKYHOOK simulations were

performed at SAO by Gordon Gullahorn. Peter Bainum of Howard University provided results from an unnamed simulator which we refer to as HOWARD U. Arun Banerjee of Lockheed Missiles and Space Company provided results from a simulator "Tether", which are referred to as LOCKHEED. Arun Misra of McGill University provided results which we refer to by MCGILL U. (John Glaese of Control Dynamics Company provided results for one case; unfortunately, resources did not permit translation from the format provided.)

A preliminary report of the test case findings was made at a workshop associated with the Second International Conference on Tethers in Space ("Space Tethers for Science in the Space Station Era") in Venice, October 1987. Additional and corrected results are included here.

## 2.2 Comparison Plots and Discussion

The results for the four test cases are plotted in the next section. The plots consist of time series of the variables: radial, in-plane and out-of-plane position of the satellite with respect to the Shuttle; the respective velocities; and in cases A and C, the direction cosines of the satellite axes with respect to the radial/in-plane/out-of-plane axes. Plots of variables which do not vary (e.g. out-of-plane motion where not excited) or which reproduce other variables (some angular variables) are omitted to save space.

Because all the cases except B remain essentially in a vertical (radial) configuration, the radial position for these cases is "normalized" by subtracting the first value for each simulator from the successive values. This makes the labels on the left margin easier to interpret. Also, the different simulators had different mean values for the radial component, which could overwhelm the more interesting time variations if plotted on an absolute scale.

Note that the in-plane velocity has an offset due to the way in which velocities were specified: as the difference of absolute spatial velocities of the satellite and shuttle, projected onto the in/out/radial axes. A more intuitively meaningful velocity would have been to project the relative positions onto the axes, and take the time derivatives of these. The other velocities are also not the same as the more intuitive definition would provide; the difference is less pronounced because of the vertical configuration of the tether in three of four cases.

Most of the plots follow a common format: results from all simulators which participated in a given case are given on a separate plot for each applicable variable, with

the simulators distinguished by line type. (A key to the line types is at the beginning of the plots.) The case and variable are at the top of the plot. The plots are given in the order they are discussed below.

#### CASE A:

The satellite is deployed at 20 km in hanging equilibrium, and has attitude dynamics. It is given an initial impulse orthogonal to the tether in the orbital plane, to produce an initial center of mass velocity of 0.2 m/s. Output was requested every second for the first 1000 s, and every 5 s for 5000 s. Possible phenomena which might be exhibited: in-plane libration, transverse tether oscillations, and coupling of these transverse oscillations with rigid body motions.

Three simulators -- SKYHOOK, GTOSS and STOCS -- provided results including satellite attitude. SKYHOOK, due to run time restrictions, only simulated the first 763 s. McGill University provided results, although their simulator does not include satellite attitude.

First, plots for the full 5000 seconds are shown. Selected plots restricted to 1000 seconds are shown following these to more clearly show the SKYHOOK behavior.

The situation specified should restrict the system to motion in the orbital plane. All four simulators successfully passed this "null test" and out-of-plane plots are not shown. Rigid body motion was also restricted to one angle. The cosine of the angle  $\alpha_y$  between the satellite "radial" axis (originally in the radial or vertical direction) and the in-plane axis of the orbital coordinate system, is plotted: this is nominally 90°, and small departures of the cosine from zero are proportional to the angle between the satellite and reference vertical axes.

Agreement among the various simulators is seen to be quite reasonable for a case of this complexity, except for the radial component of the McGill results, which is plotted separately. The McGill radial oscillations are much larger (about 10 m) than those for the other simulators (about 0.3 m for SKYHOOK, and 0.05 m superposed on a slow 0.5 m baseline variation for STOCS and GTOSS). This might be due, for instance, to starting the simulation with a tether stretched beyond equilibrium.

The similarity between the STOCS/GTOSS results (which used the same basic engine) and SKYHOOK on the angular variation are encouraging. To achieve this agreement,

however, the SKYHOOK input had to be adjusted: the first trial had used output generated by a program which in the case with a finite satellite (as opposed to point mass satellite) left the tether overstretched, resulting in a pronounced excitation of radial (longitudinal, axial) modes. This coupled with the attitude oscillations, leading to a gradual but substantial buildup of their magnitude.

#### **CASE B:**

A point mass satellite at the end of a 20 km tether is initially at rest in the system rotating with the Shuttle, with the tether in a linear configuration,  $45^\circ$  out of plane, under zero tension. The system is "released" and allowed to swing freely. This case may be expected to demonstrate tether longitudinal modes, particularly bobbing, and coupling of in-plane and out-of-plane librations.

Results were provided by all simulators except McGill University. The substantial out-of-plane libration indeed coupled to provide significant in-plane libration. On the plots showing the full motion, the different simulations are so close as to be almost indistinguishable. The scale is so large, however, that moderate disagreement could exist. One set of results (GTOSS) was arbitrarily chosen and the other results were different with respect to GTOSS and plotted; i.e., at each time, the value plotted is that from a given simulation minus that from GTOSS. Three plots showing the difference position variables follow the standard plots for case B. As can be seen, the various results begin in close agreement and gradually drift away from the GTOSS results with an overall slow oscillation, reaching magnitudes of 10's to 100 or so meters by the finish of the simulation (about 1 orbit).

#### **CASE C:**

The system has a 20 km tether and a satellite with attitude dynamics. Starting from hanging equilibrium, the initial conditions are obtained by (a) tilting the satellite about the tether attachment point by  $45^\circ$  in the positive out-of-plane direction, and (b) imparting an initial velocity parallel to the tether. This case might be expected to demonstrate coupling of (large) satellite attitude oscillations with tether tension variations (spring-mass and longitudinal modes).

Results were obtained from STOCS and GTOSS for 1000 s, and from SKYHOOK for about 500 s (restricted due to long run times). The radial components show similar oscillations, with SKYHOOK about two to three times as large as GTOSS/STOCS results.

GTOSS and STOCS show some out-of-plane motion, about a satellite radius; the period is much longer than expected attitude oscillations, and its source is not clear. GTOSS and SKYHOOK show similar trends of in-plane motion, but different magnitudes; STOCS shows a different trend, of similar magnitude. Lang (private communication) reports that the differences between STOCS and GTOSS have been resolved.

All nine direction cosines of the satellite attitude are plotted. STOCS and GTOSS generally show similar character, though they differ in details and sometimes in the long term trend. SKYHOOK results show a different overall character from the other two. In particular, the SKYHOOK results generally show an increase in the short period oscillation magnitude toward the end of the run, while the other results show a generally constant oscillation superposed on a baseline trend. This could be a result of coupling between the attitude oscillations and the higher modes of longitudinal tether oscillation. This difference will be further commented on in the section on power spectral densities. It is interesting to note the variety of distinctive behaviors of the attitude variables.

#### **CASE D:**

The system has a point mass satellite and deployed tether length of 100 km. An impulse is applied to the satellite to generate a  $\Delta V$  of 0.5 m/s in a direction perpendicular to the tether and  $45^\circ$  out-of-plane. Phenomena of interest might include in-plane and out-of-plane libration, transverse tether oscillations, and the different frequencies of in-plane and out-of-plane transverse modes due to a restoring force toward the orbital plane (this effect becomes significant only when tether mass is substantial compared to satellite mass).

All six programs ran the simulation, making this case interesting for the completeness of its response. (Only four provided velocity information, SKYHOOK and LOCKHEED lacking this output.)

There is a general differentiation of the simulators into two classes, also apparent in the less well represented cases. Notice that although the overall variations in the in-plane component are comparable, three simulators show smooth variation (GTOSS, STOCS and HOWARD U) while three have a superposed rapid oscillation (SKYHOOK, LOCKHEED and MCGILL U). This same distinction is apparent in the two plots of normalized radial component: the first, smooth, class shows variations of only a meter or two, and rapid oscillations of only about 0.2 m (GTOSS and STOCS) or 1 m (HOWARD U); the second, rougher, class must be plotted separately, since they show oscillations of hundreds of meters amplitude. The out-of-plane component shows similar results, only now MCGILL

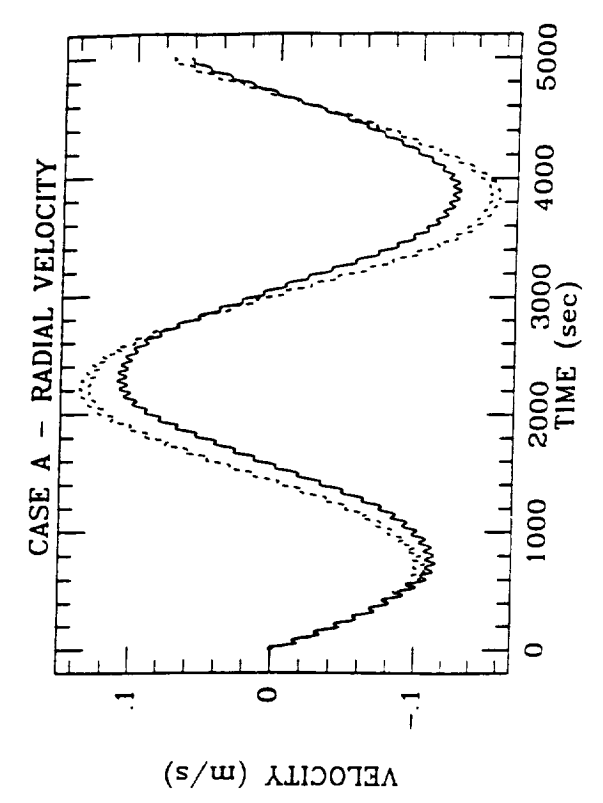
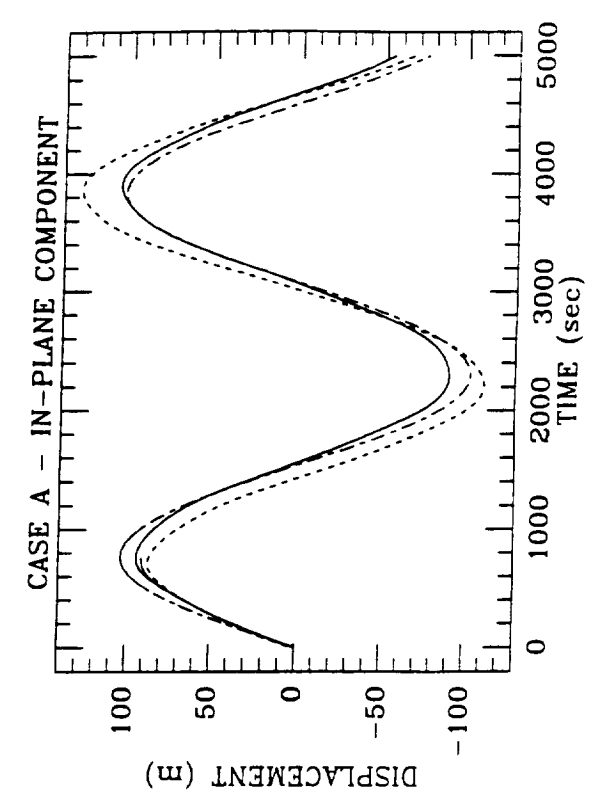
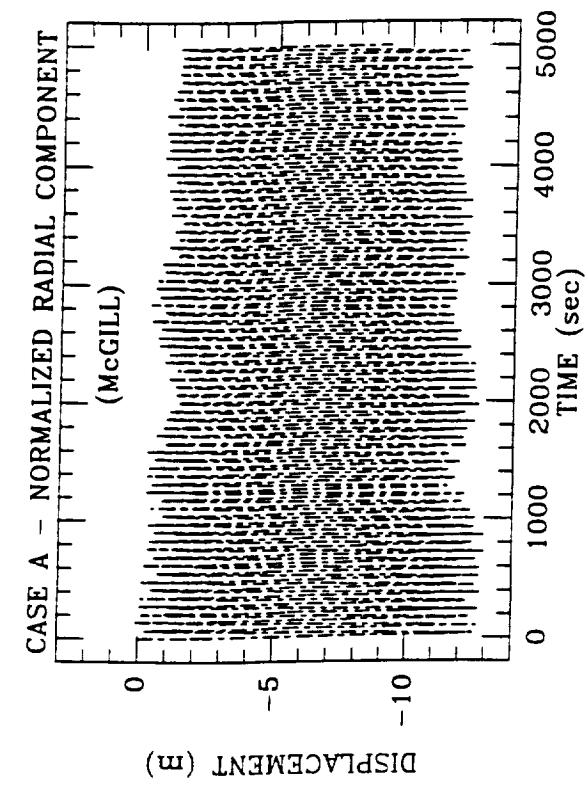
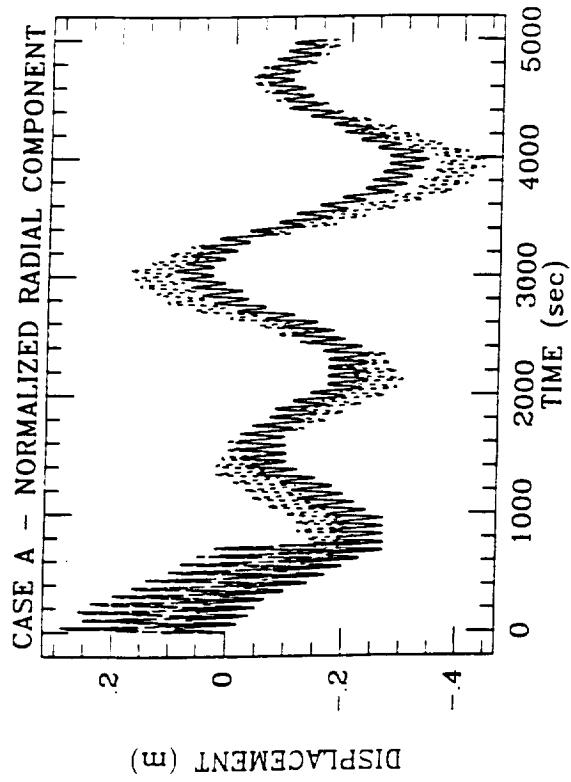
U joins the "smooth" class. Note that on the out-of-plane plot, GTOSS and STOCS are indistinguishable.

One final set of plots is shown displaying the differences between two different uses of the same program to attempt simulation of the same cases. For cases A and D (which involved an "impulse" to the satellite), McGILL U performed simulations (a) by having a thruster modelled in the satellite fire briefly, and (b) by giving the satellite an equivalent initial velocity ( $\Delta V$ ), as if the thruster firing were brief but powerful. The moderate, but still noticeable, differences are displayed without further comment; the dotted lines represent the results where thrusters are used.

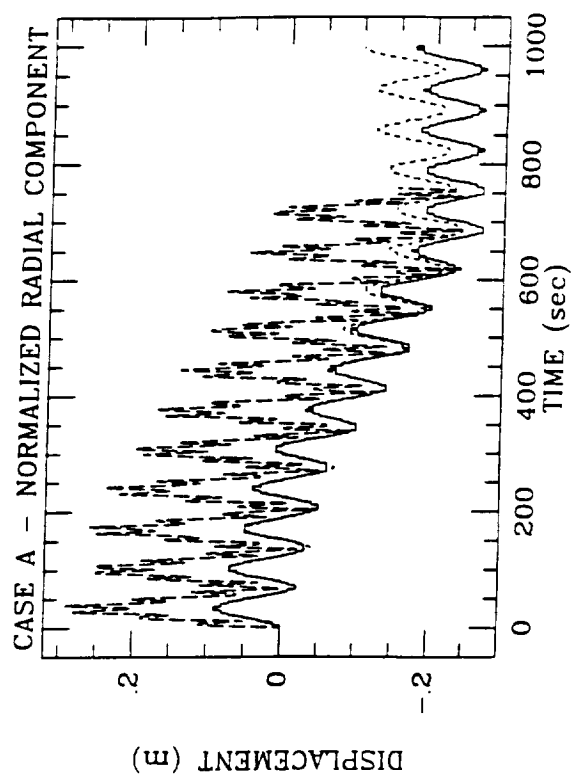
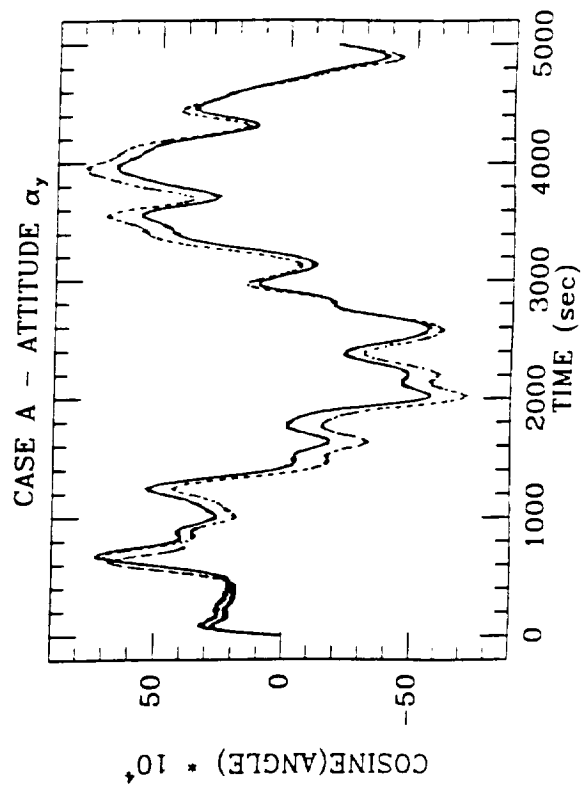
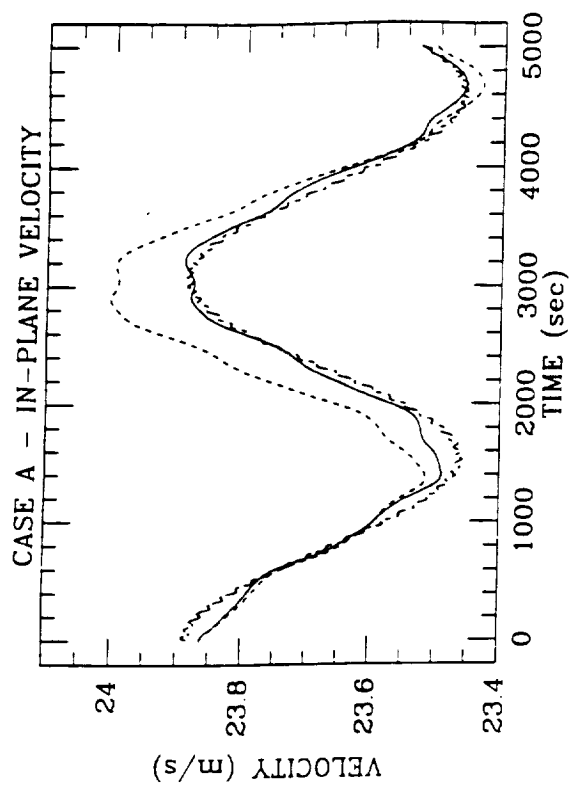
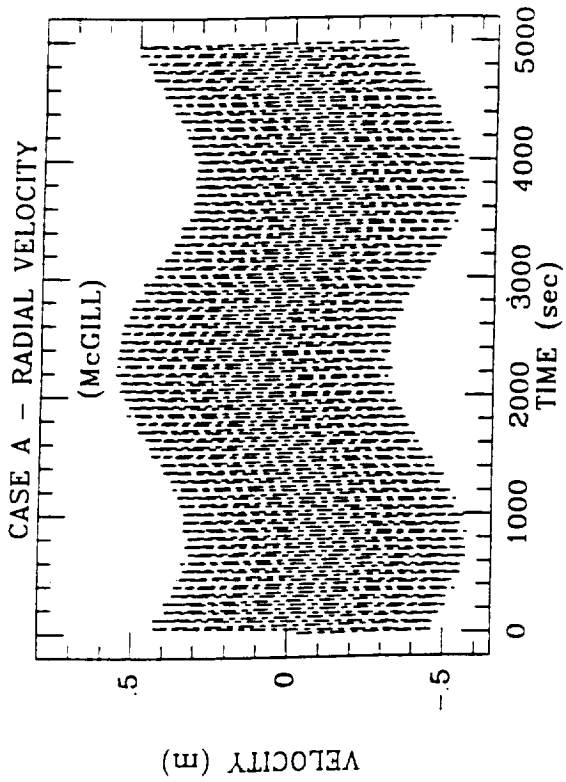
### 2.3 Time Series Plots

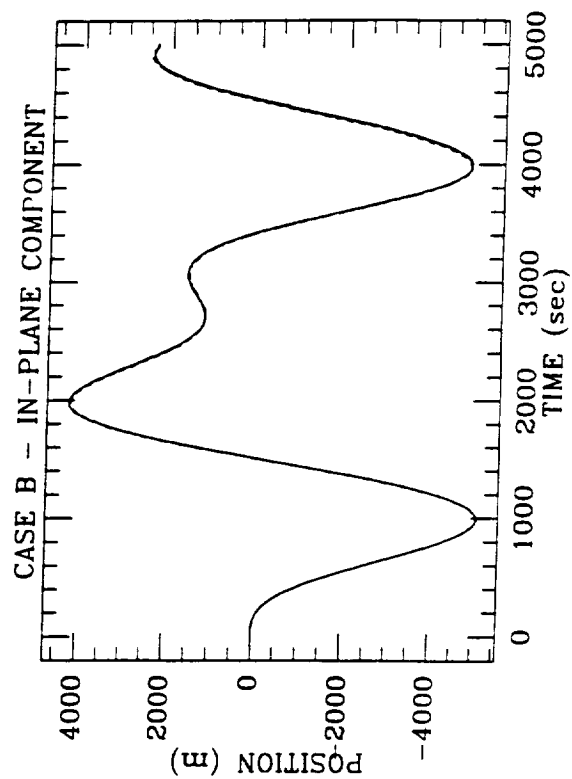
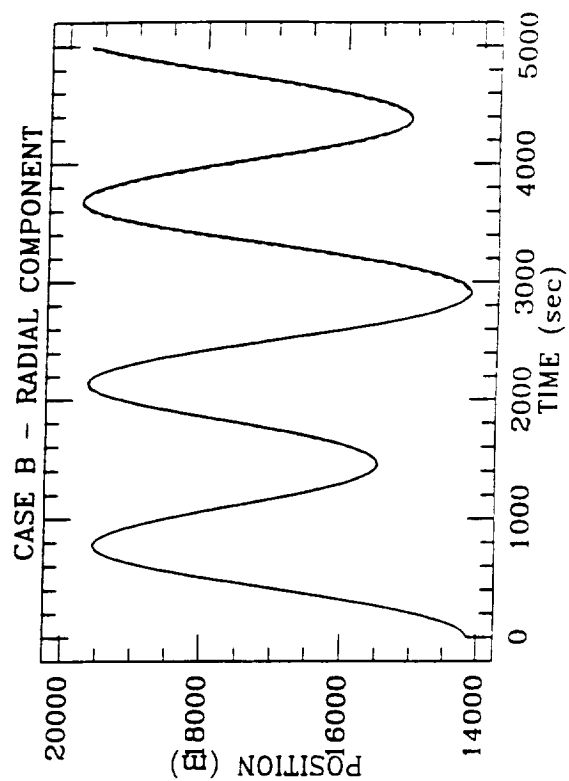
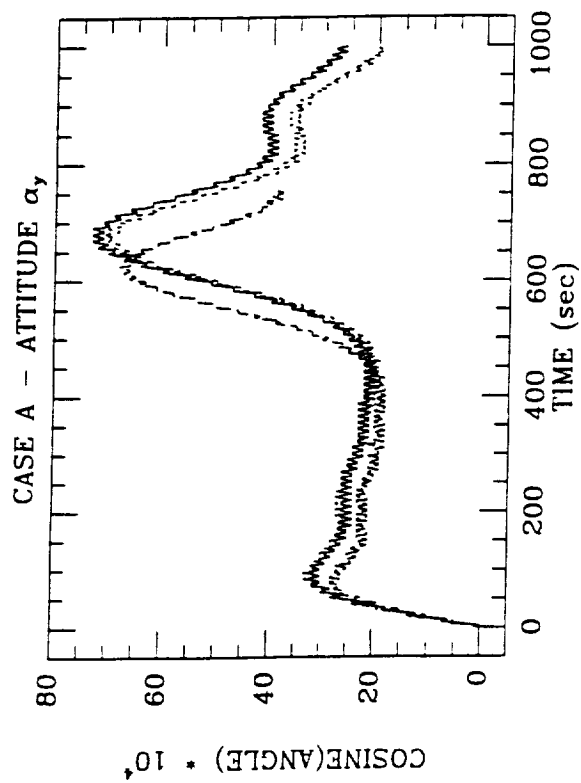
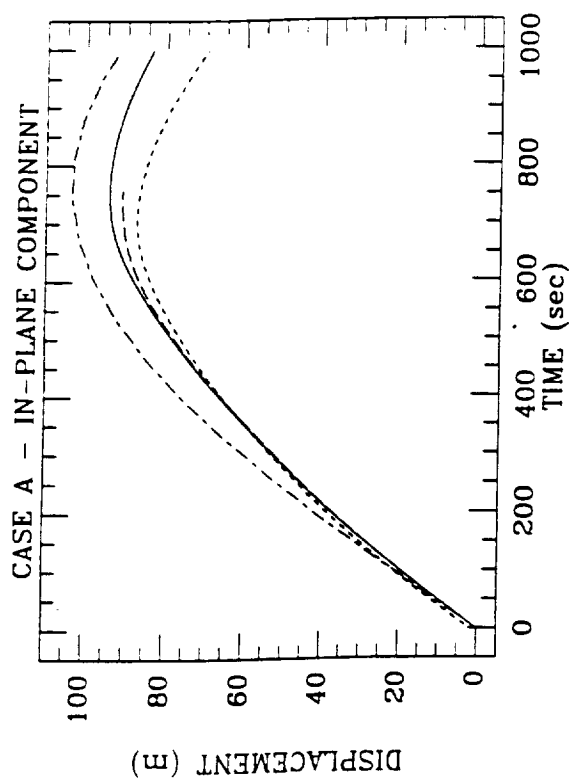
This section contains the time series plots discussed above. As feasible, the results from several simulators are presented on one plot, with a universal line-type key given by:

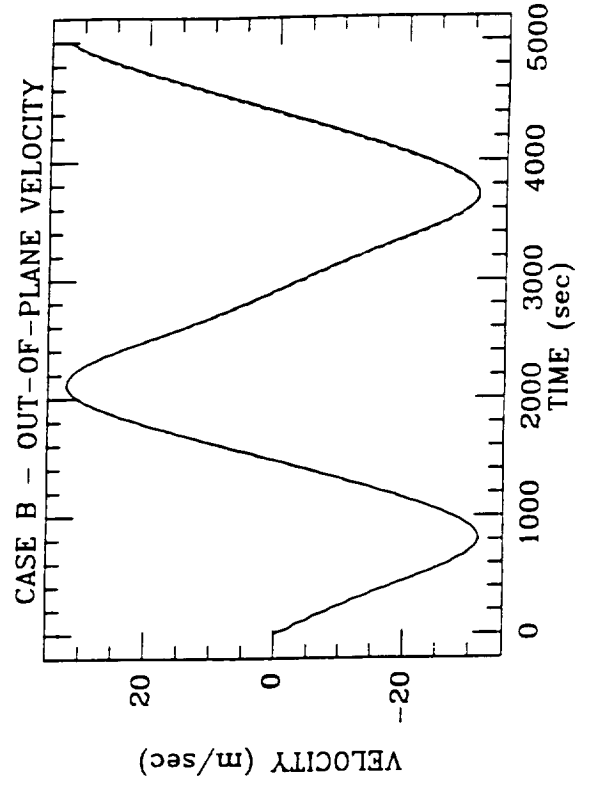
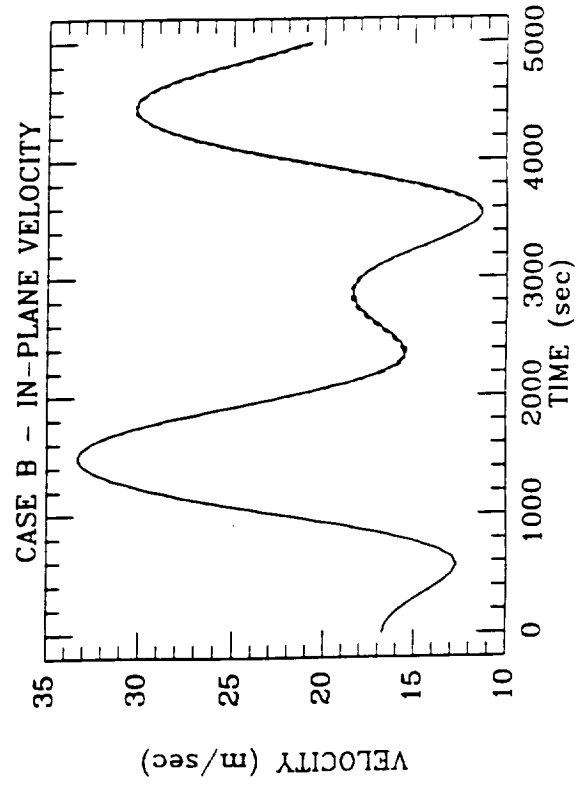
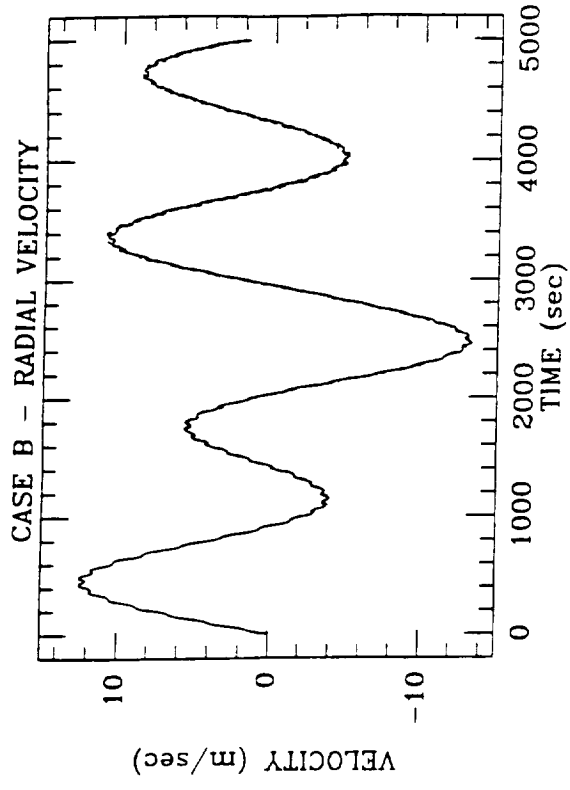
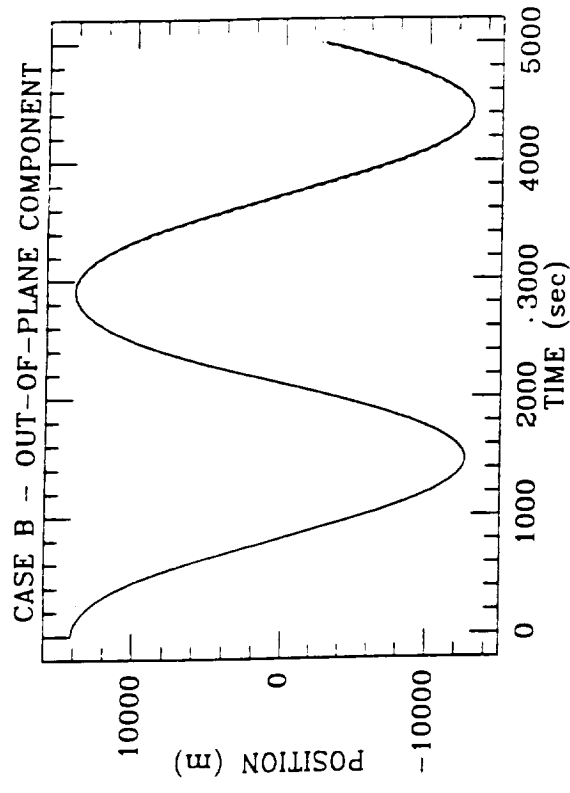
SIMULATOR / LINE TYPE KEY	
—————	GTOSS
-----	STOCS
-----	SKYHOOK
-----	HOWARD U
-----	LOCKHEED
-----	McGILL U

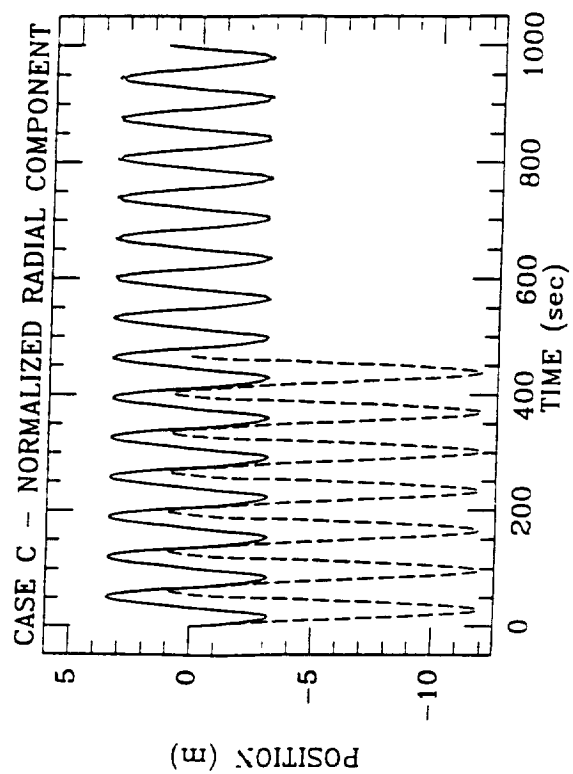
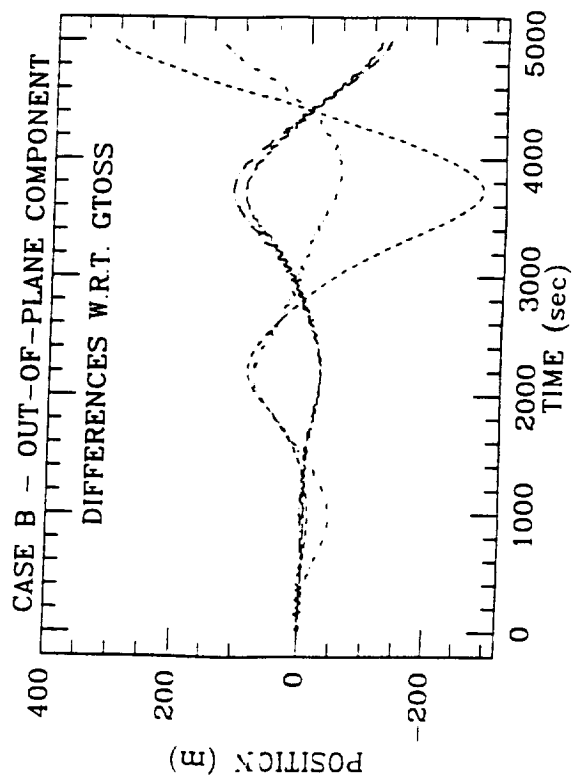
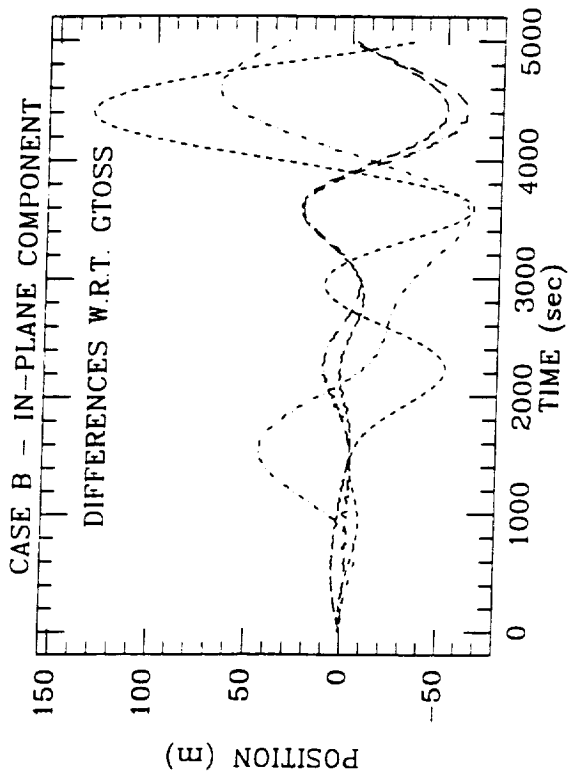
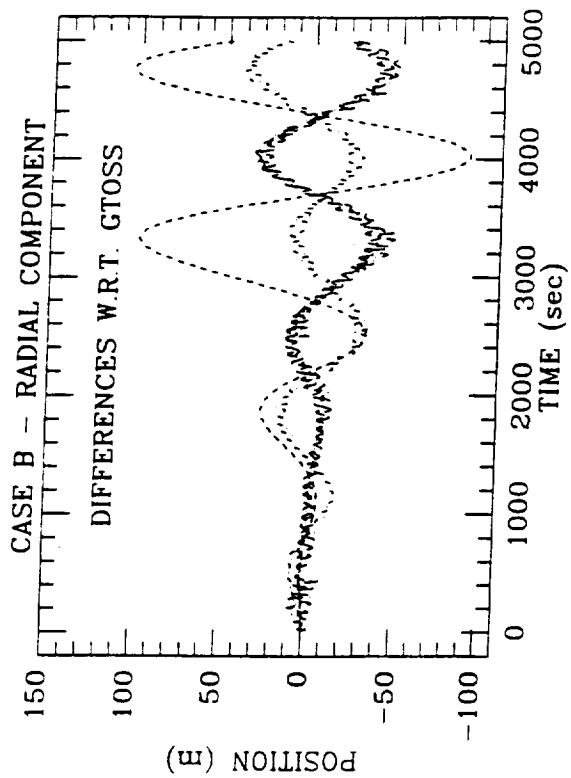


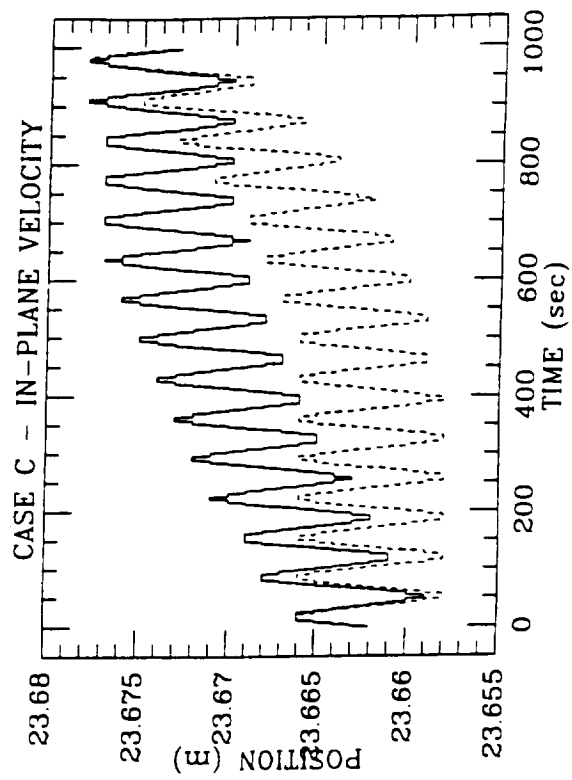
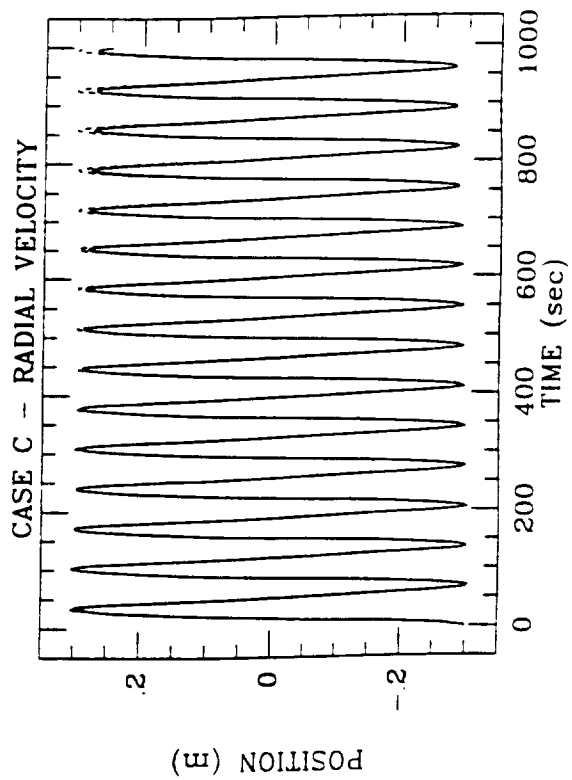
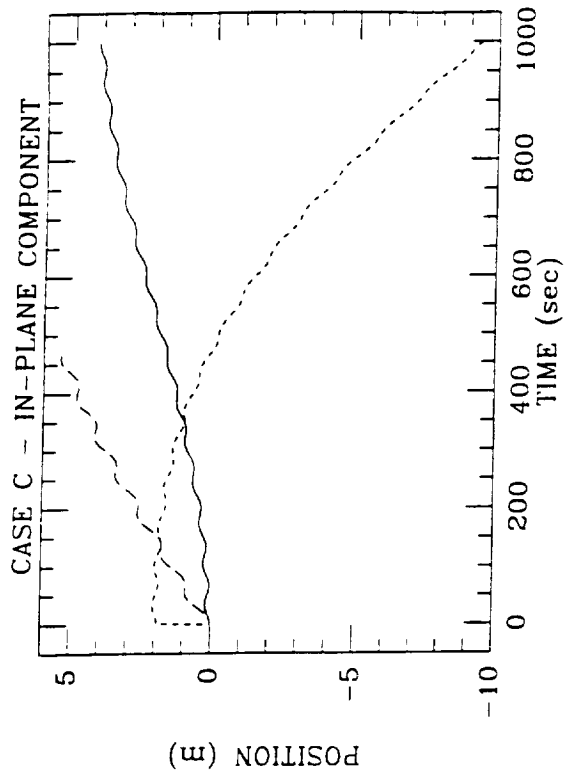
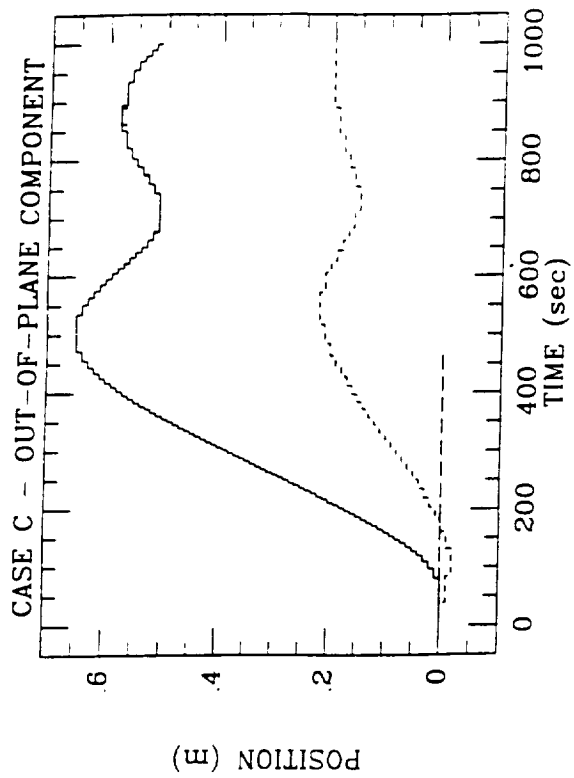


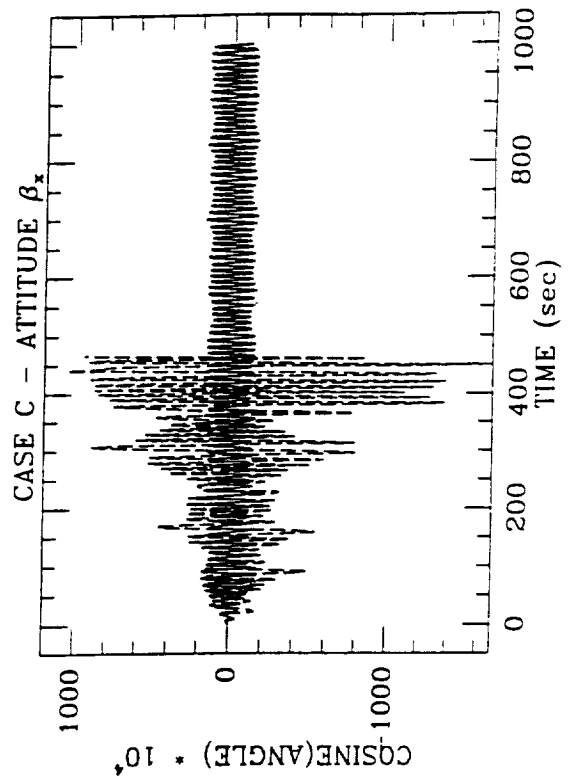
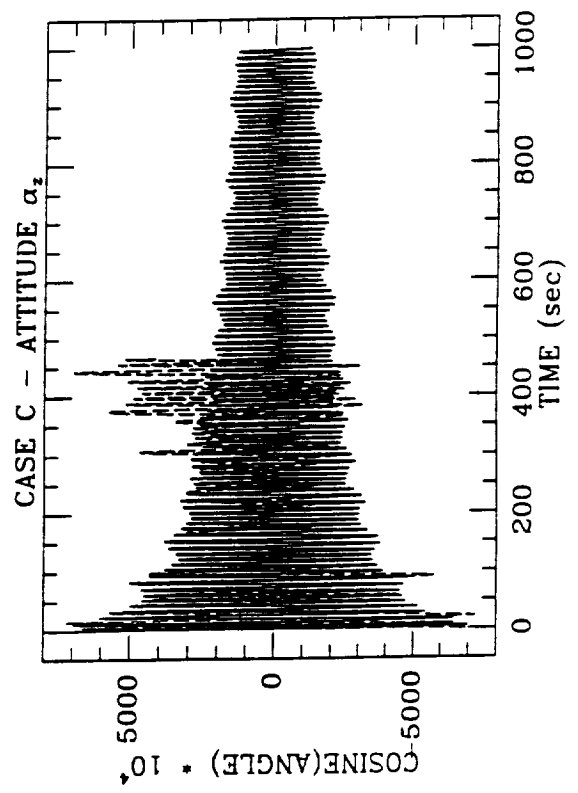
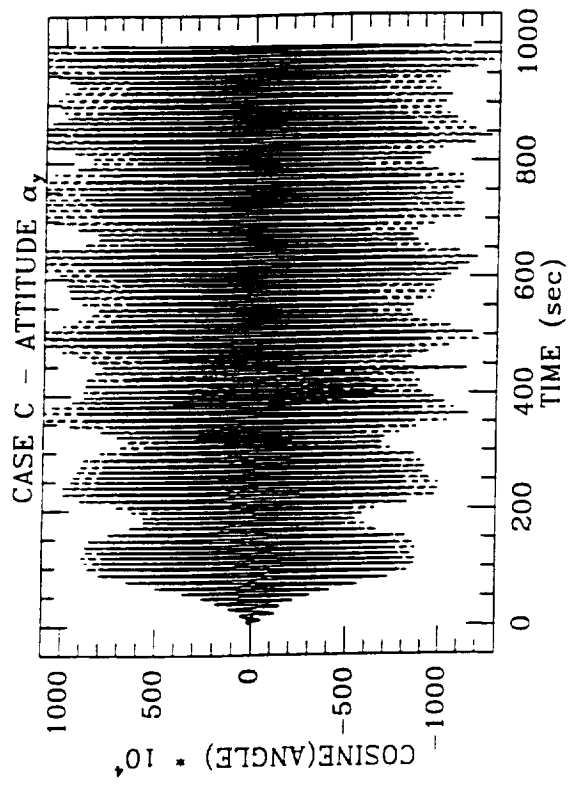
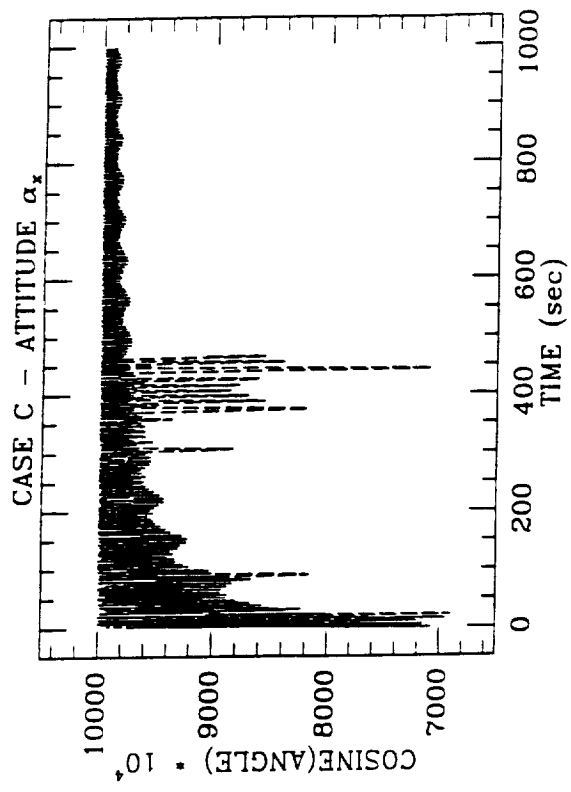


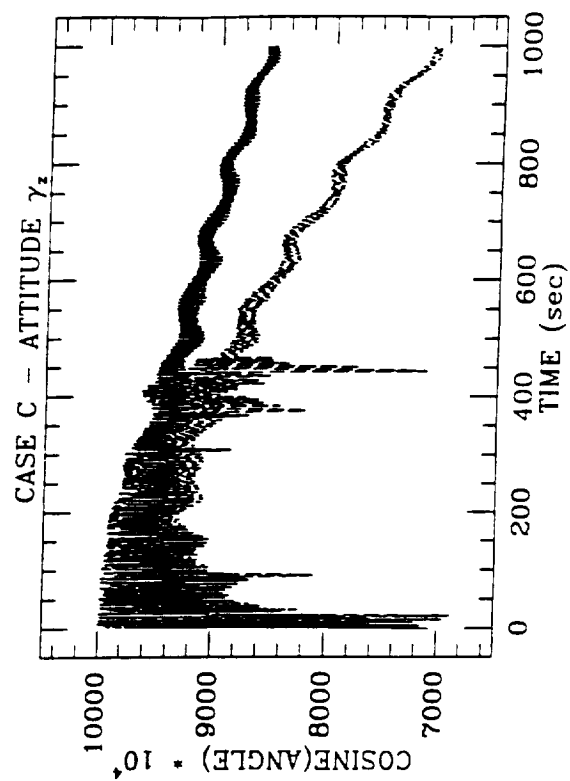
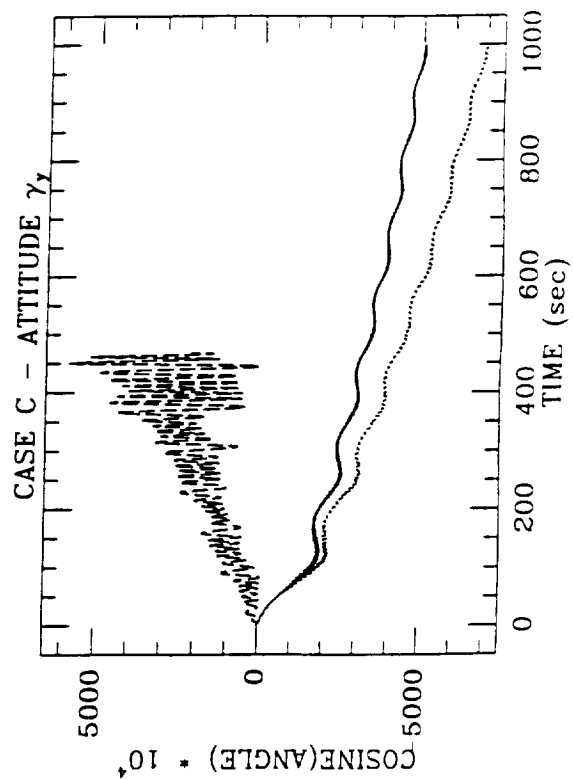
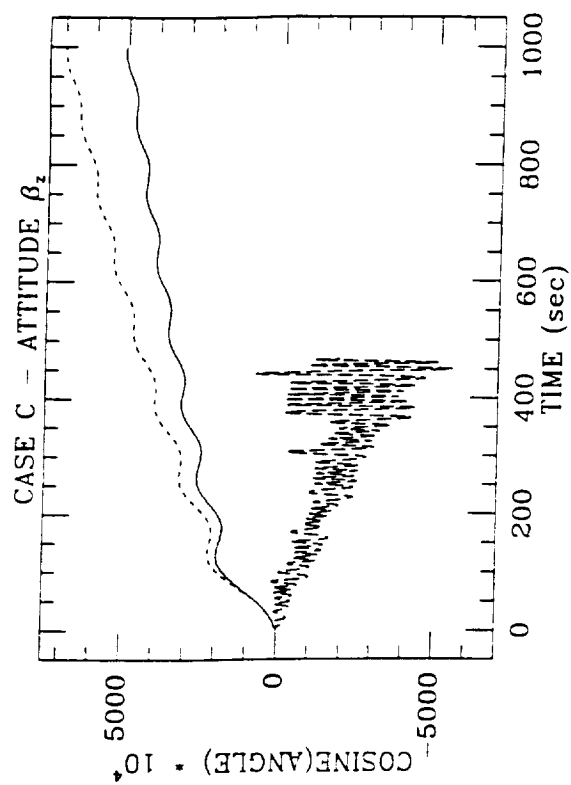
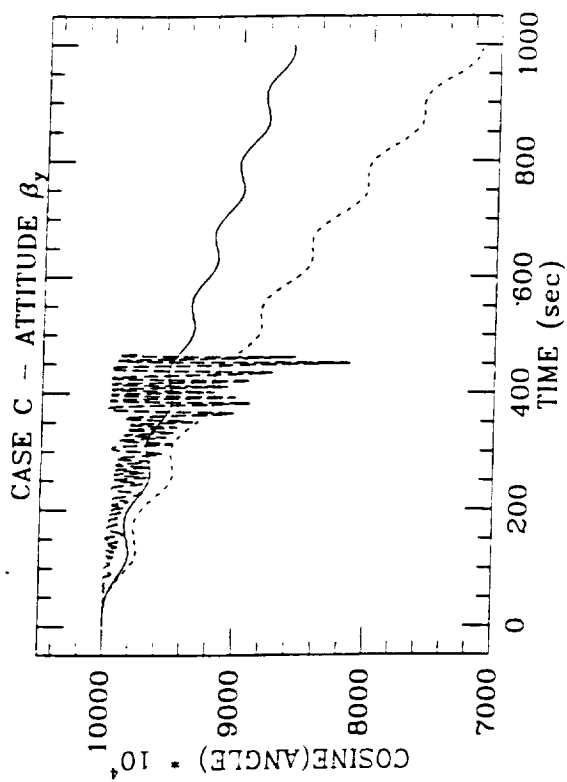


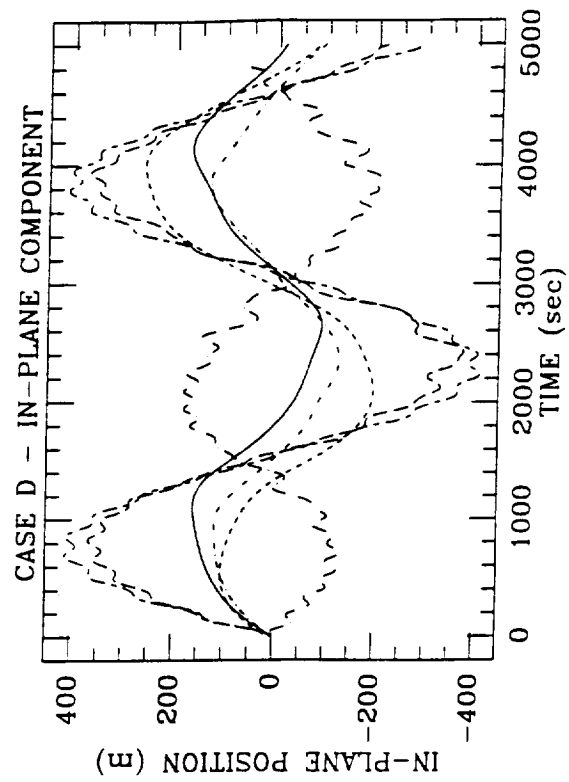
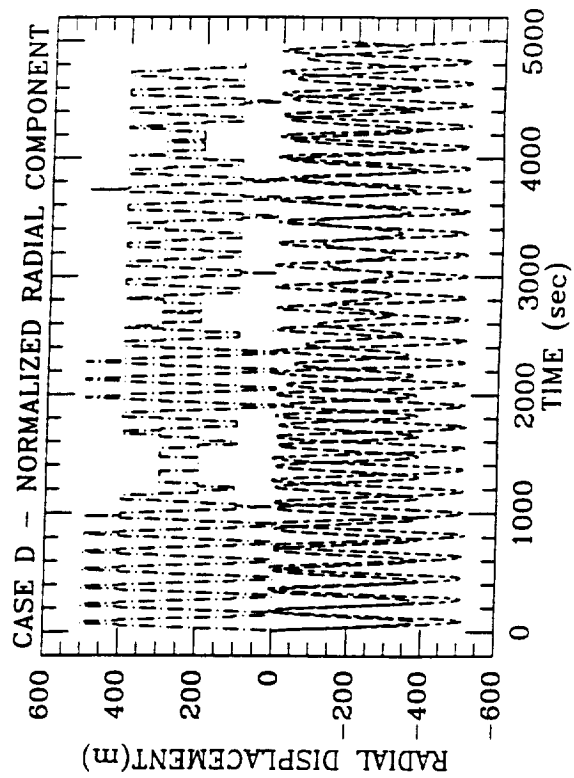
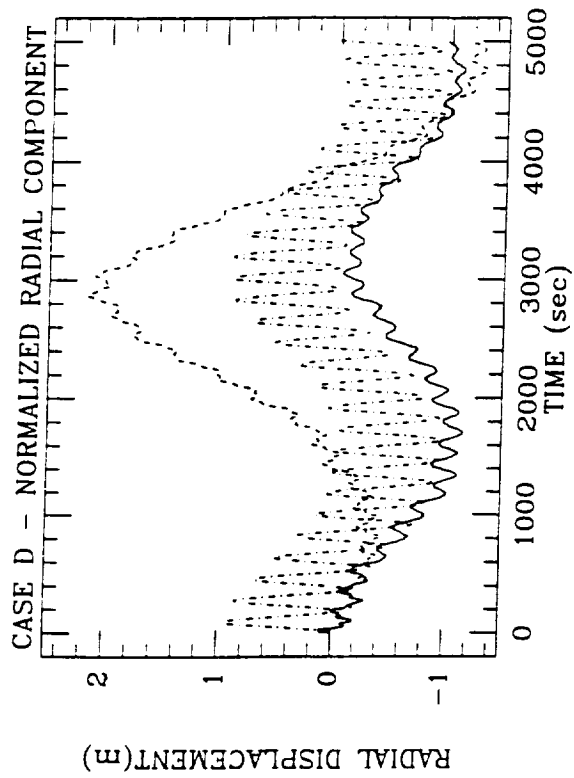
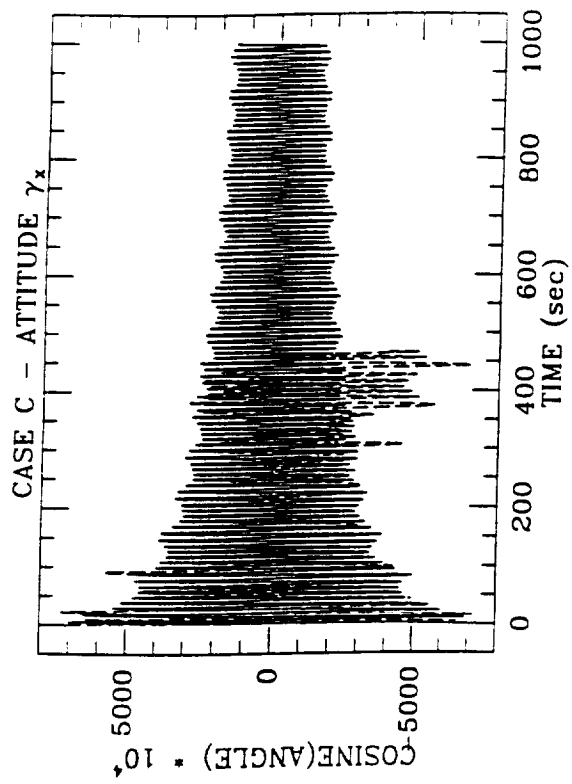




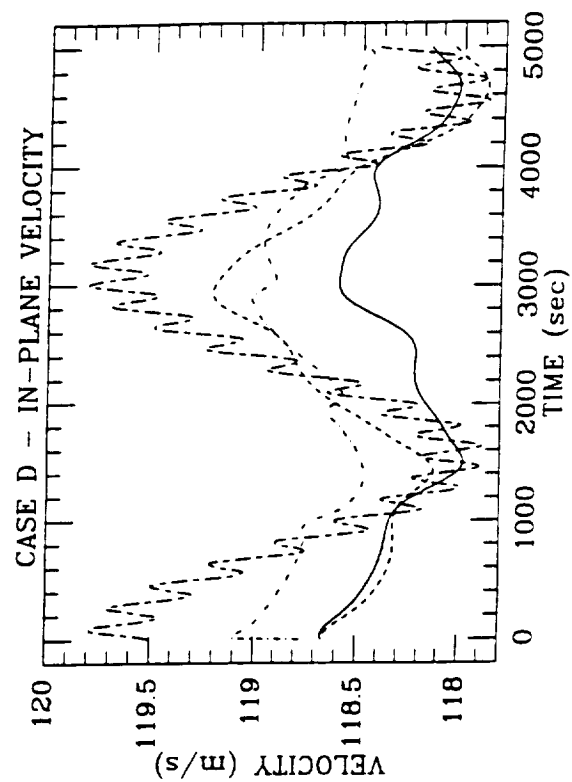
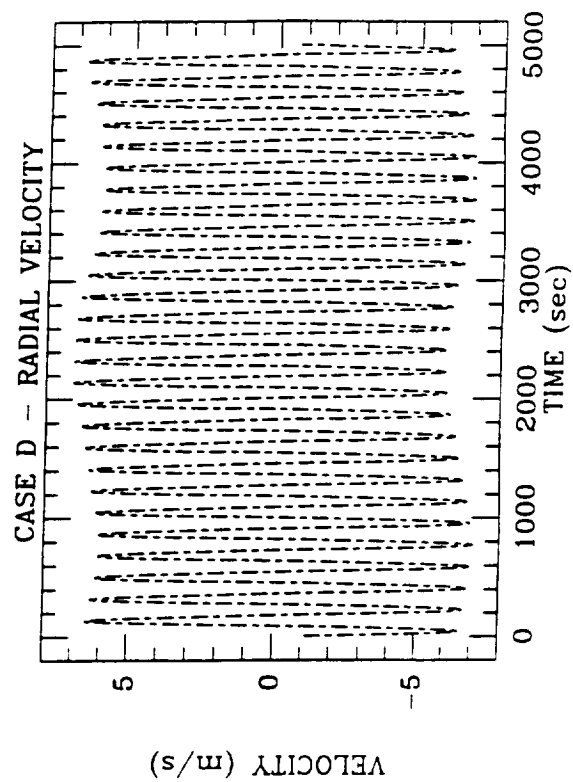
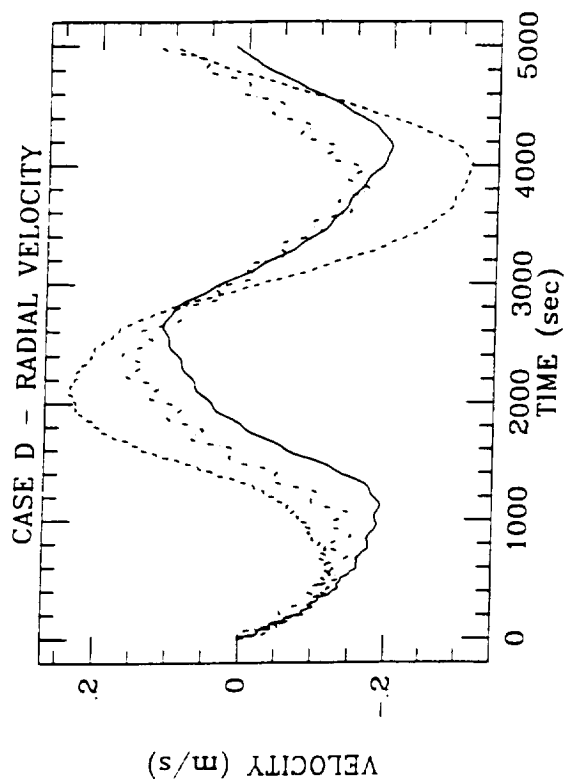
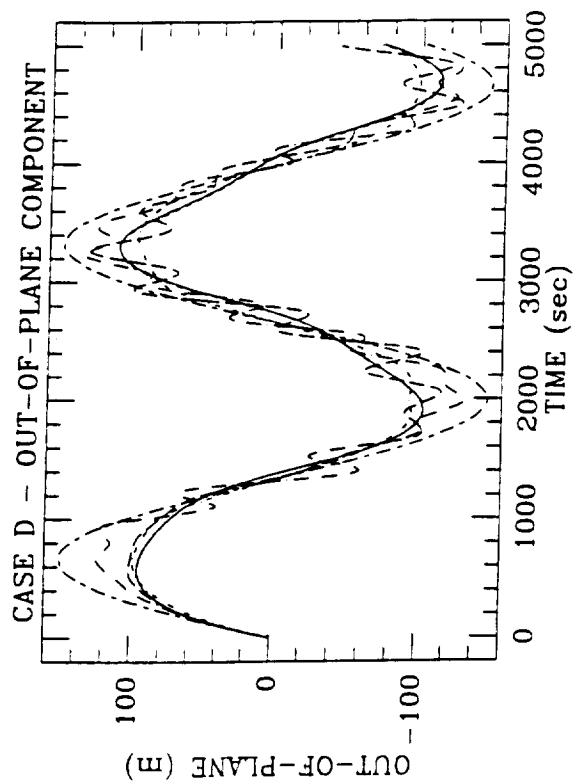


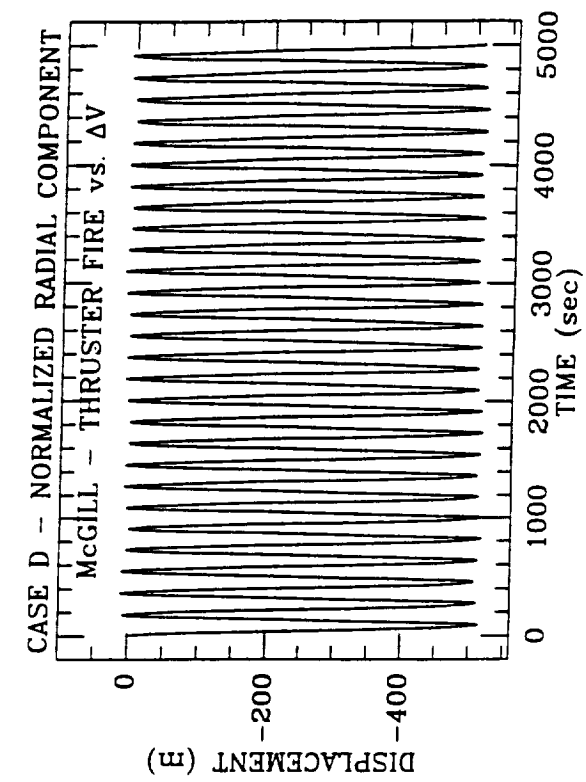
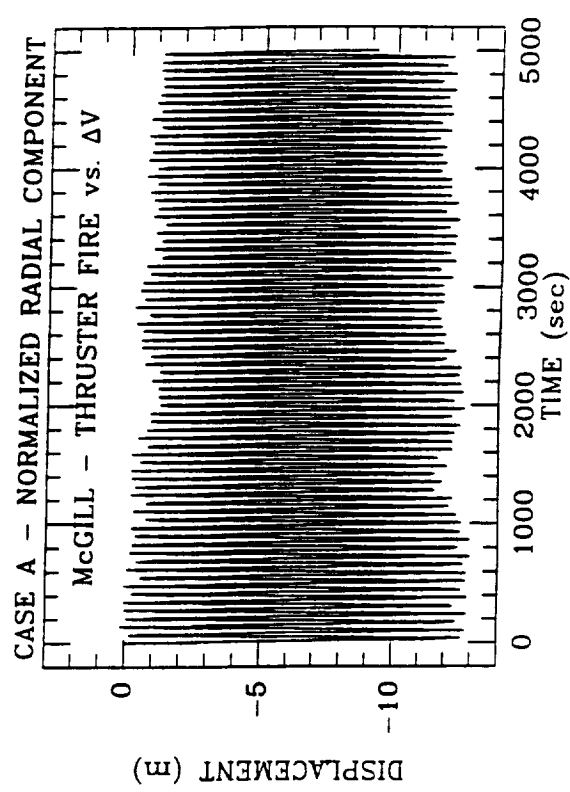
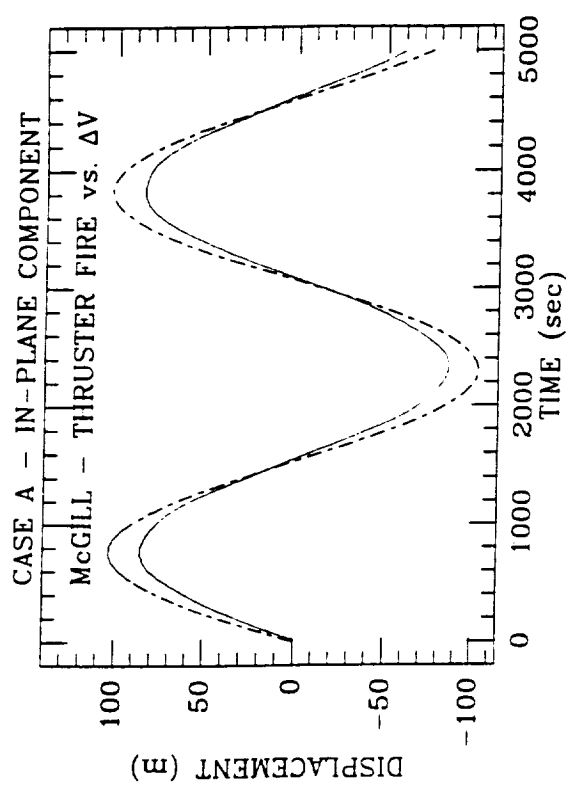
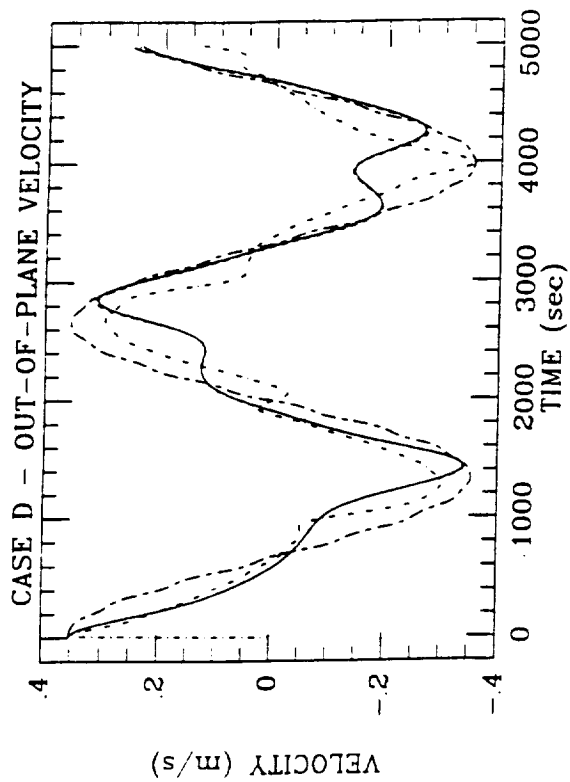




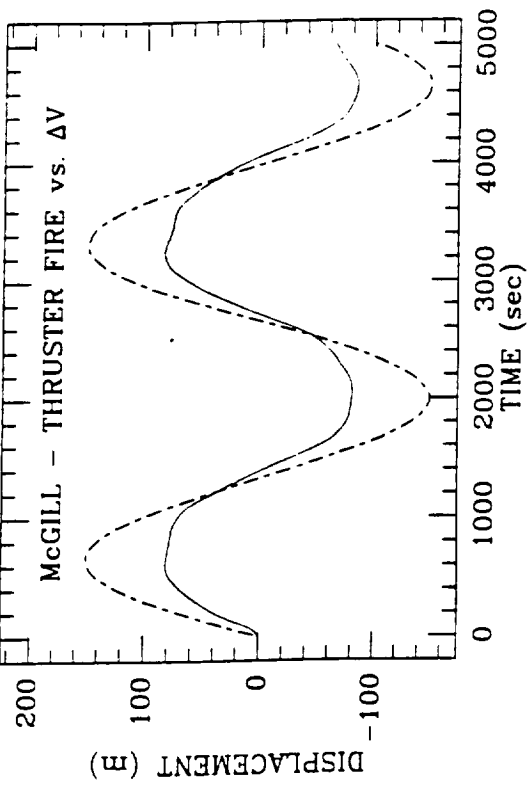




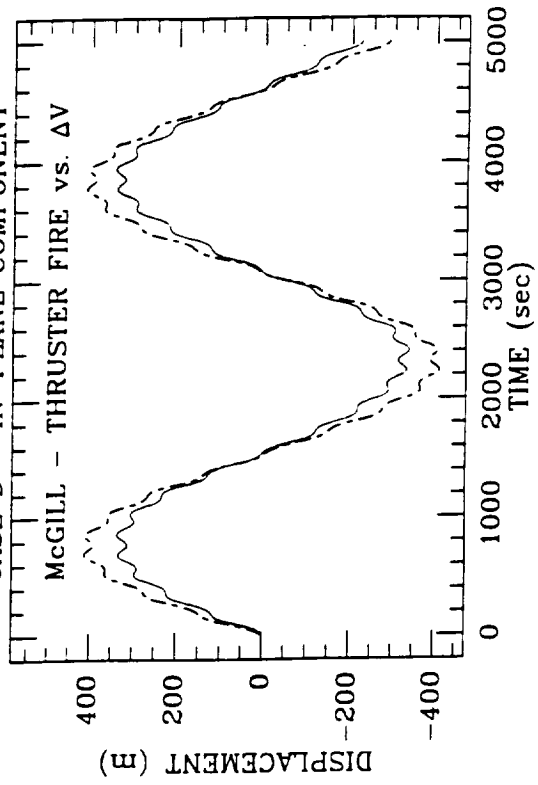




CASE D - OUT-OF-PLANE COMPONENT



CASE D - IN-PLANE COMPONENT



## 2.4 Power Spectral Density of Simulator Results

Direct plots of time series of selected aspects (e.g. satellite position) of simulator results (or any other "data") are one of the most obvious ways to examine the system behavior. Another window into this behavior is provided by spectral analysis of these time series. Spectral methods provide at least two insights:

Tethered systems, as most mechanical systems, can be largely considered as a linear system. (Non-linearities, for instance the interaction of the satellite attitude with the tether tension variations, are generally dominated by the linear aspects and form small perturbations to linearity.) Linear systems possess distinct frequencies of natural vibration (modal frequencies, or eigen-frequencies) and associated modal shapes; any unforced vibration will be a superposition of these shapes/frequencies. Spectral analysis of simulator results will show sharp peaks at a set of frequencies which can be compared to those expected on theoretical bases, either generally (e.g., we expect a satellite oscillation, a spring-mass longitudinal frequency, and a series of column-mode longitudinal frequencies) or by comparing to numerically predicted modal frequencies. Lack of expected modes can point out limitations or restrictions of the simulator's model, while reproduction of predicted frequencies could provide a numerical measure of one aspect of a simulator's accuracy (unless the simulator is more accurate than the idealized theoretical model!).

A second aspect which spectral analysis can highlight is the more general behavior of a simulator's results. Often one looks at the time series plot and makes a comment along the lines of "simulator A appears smoother than B, i.e. B looks like it has more short time scale variability." This may be more directly, and less vaguely, seen by looking at the power spectral density (PSD) plots and noting that B is stronger at higher frequencies. The PSD also allows some analysis of the source: if the high frequency strength of B is primarily at a few spectral "lines" (narrow peaks), this is probably due to B successfully modeling (presumably) physical modes of vibration that A misses; while if it is a fairly level high "baseline", then the high frequency behavior is likely due to some "noise", such as roundoff or truncation error in the program or output digitization.

An appropriate means of looking at strength vs. frequency in the "data" (simulator output) is to compute a power spectral density (PSD). In broad outline, the discrete Fourier transform (DFT) of the data sequence is computed (usually with a fast Fourier transform, or FFT, algorithm); this gives a set of complex values at a discrete set of points in

frequency space. The magnitude squared of this spectrum is then the PSD. More details are given in Quarterly #14 of this contract, and can also be found in Press, et al., (1986, Sec. 12.7).

A number of sample PSD plots are shown in the next section for cases A, C and D. Brief discussion of a few of these is below.

#### **CASE A:**

First, plots are shown of PSDs of the radial component and the single distinct direction cosine comparing SKYHOOK and GTOSS results (the line type key is the same as for the time series plots). The angular variable shows only one "line", corresponding to the satellites mode of oscillation about its center of mass, and the two simulators agree closely in this frequency domain just as they did in the time domain. For the radial component, both show a sharp line at low frequency, at very nearly the same frequency; SKYHOOK, however, displays a series of lines at progressively higher frequencies, corresponding to internal "bar mode" oscillations of the tether. The baseline behavior of the two is close, so the differences apparent in the time series plots are due primarily to the extra modes modeled by SKYHOOK. The absence of higher modes in the GTOSS results implies that the simulation was made without any nodes along the tether, nor with higher modes if the modal model was used. Note also that the first internal mode, at about 0.1 Hz, is very close to the satellite attitude oscillation in frequency; this is probably the vehicle for the coupling noted when SKYHOOK was accidentally run with a large initial longitudinal oscillation.

Due to the limited SKYHOOK run, only 256 points could be used in the above PSDs. GTOSS results allowed 512 point PSDs with correspondingly higher resolution; plots are given, comparing the first and last 512 points, which agree closely.

#### **CASE C:**

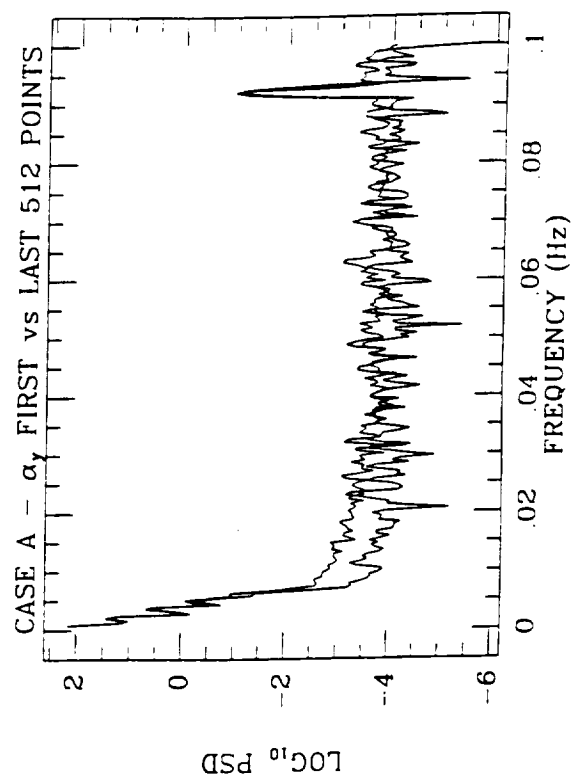
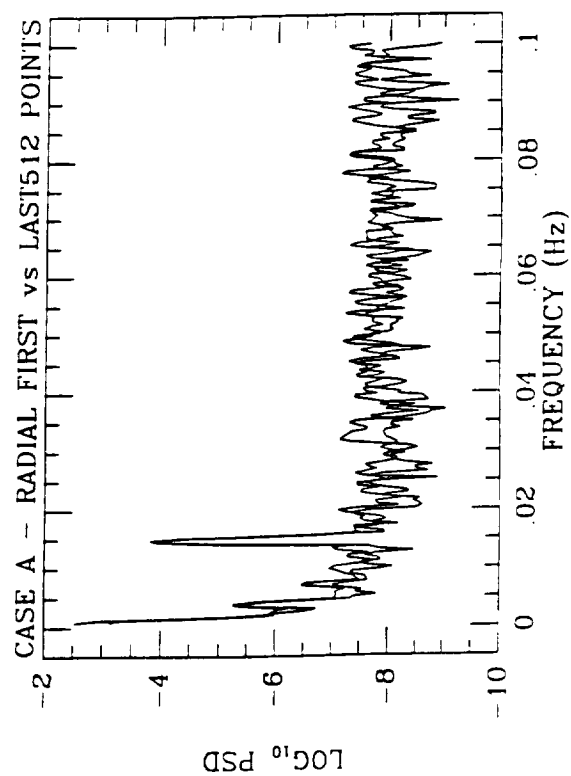
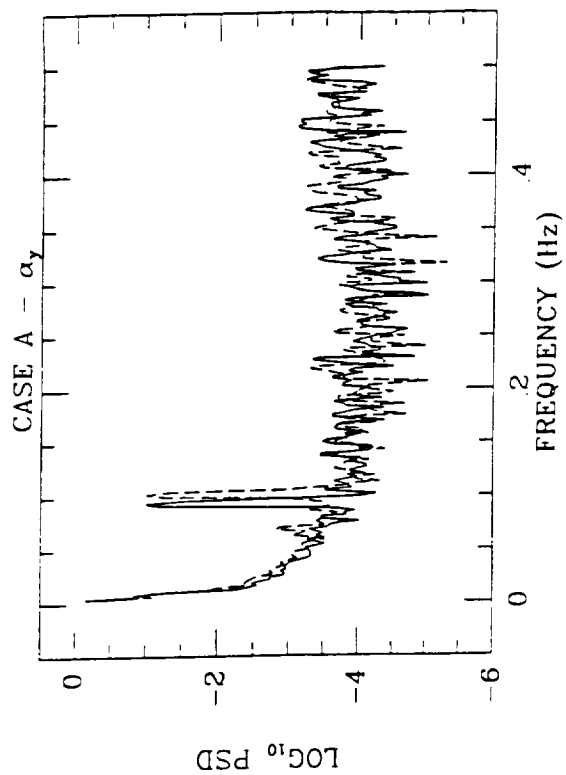
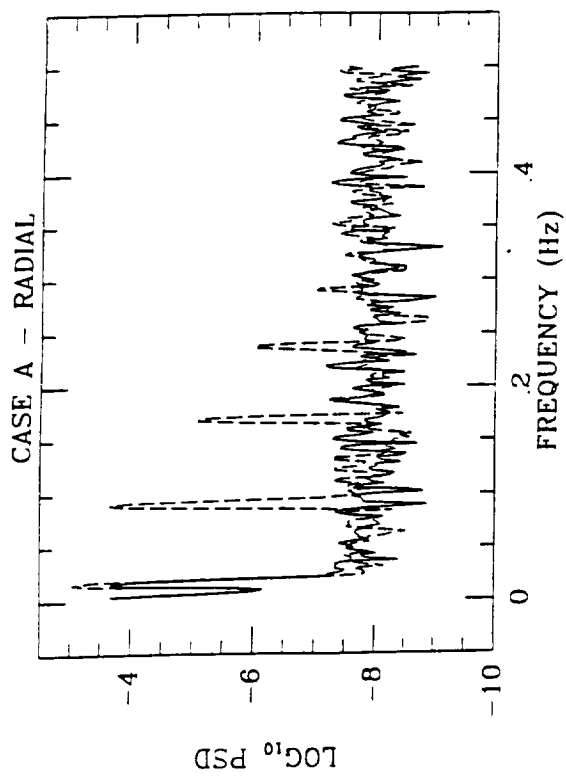
Recall that the time series plots of angular variables in case C showed widely differing character. Without comment, 512 point PSDs of GTOSS results for a number of these variables are shown, and obviously differ widely. Comparisons of SKYHOOK and GTOSS are also shown.

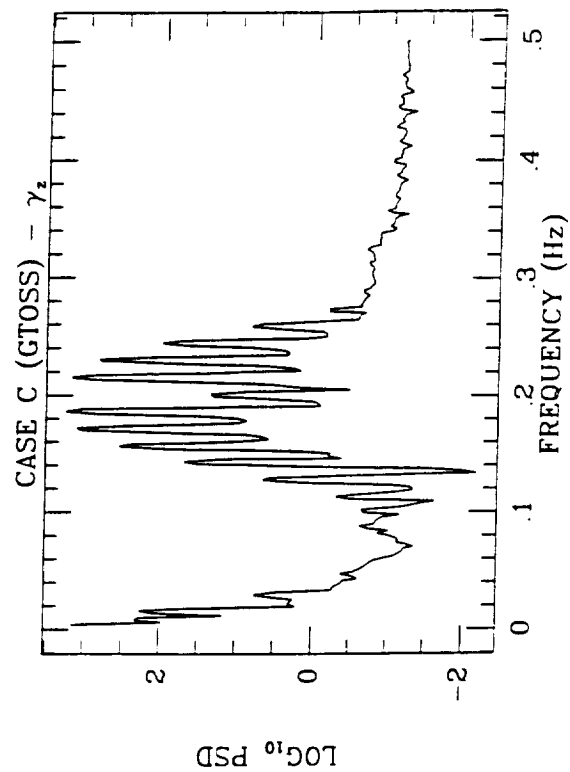
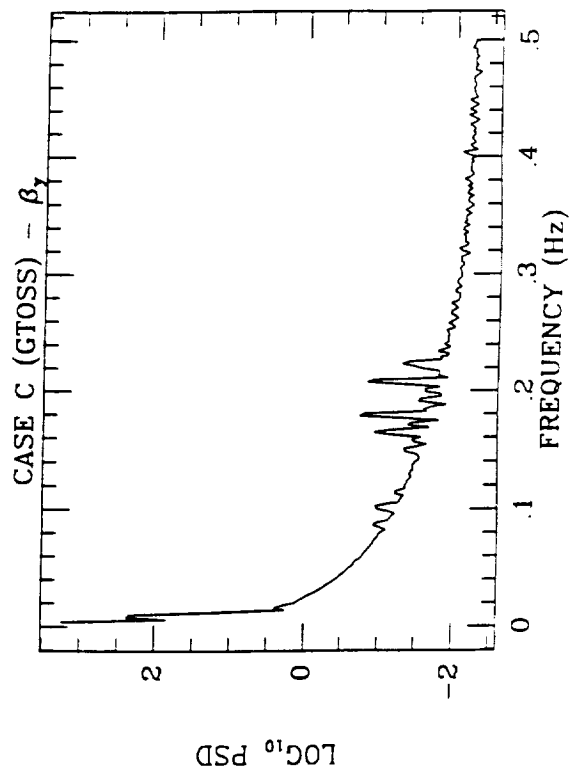
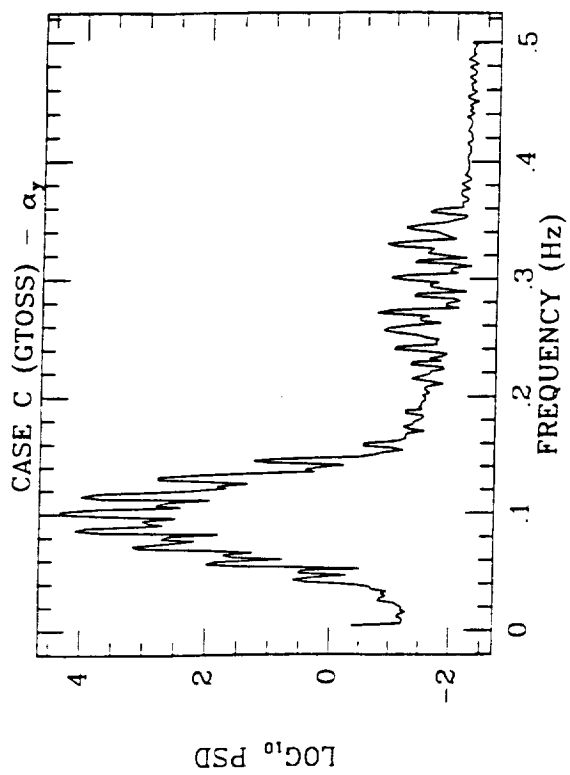
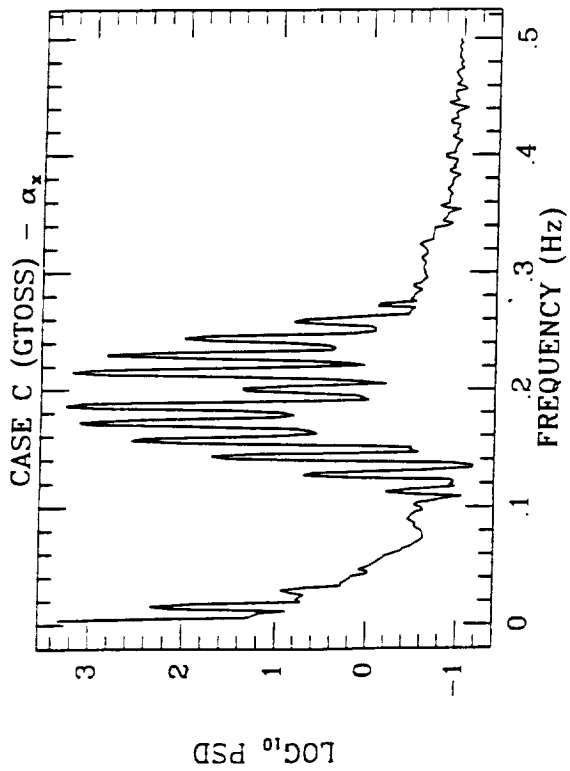
## **CASE D:**

This case had all six simulators respond. Comparison PSD plots are shown. Note the variety of spectral lines shown, and the differing high frequency baselines, particularly for the radial component.

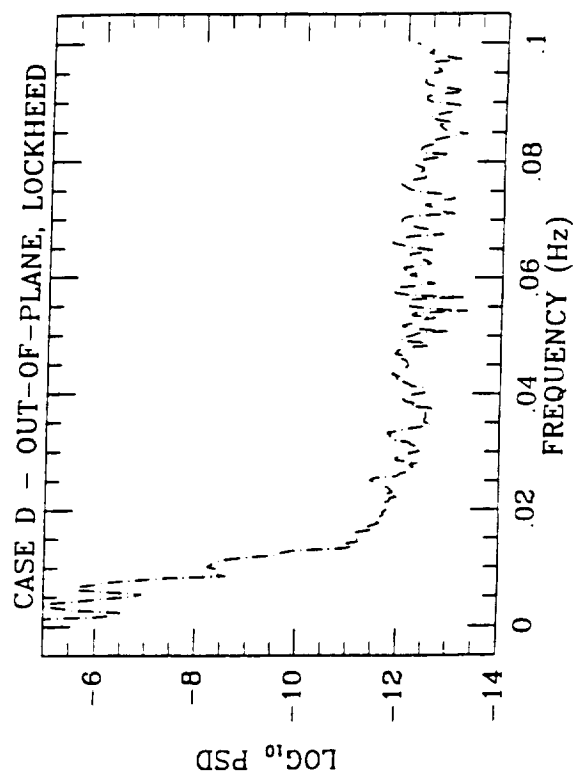
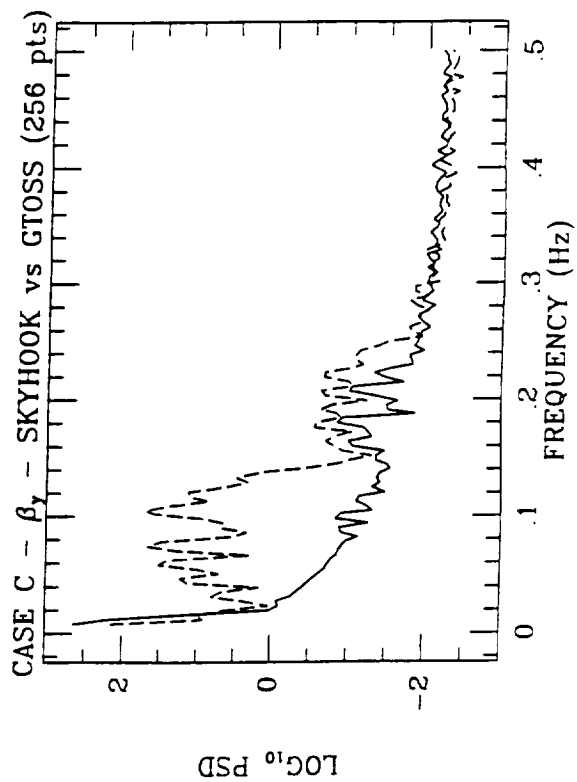
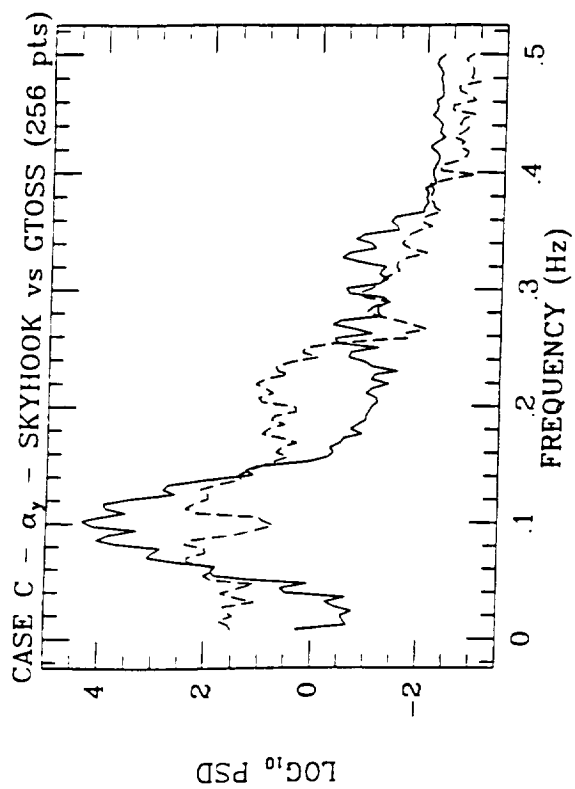
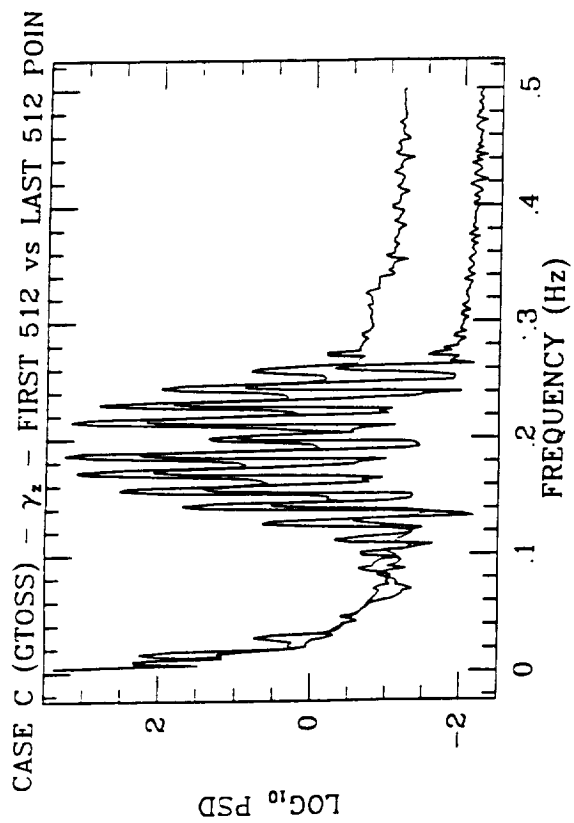
### **2.5 PSD Plots**

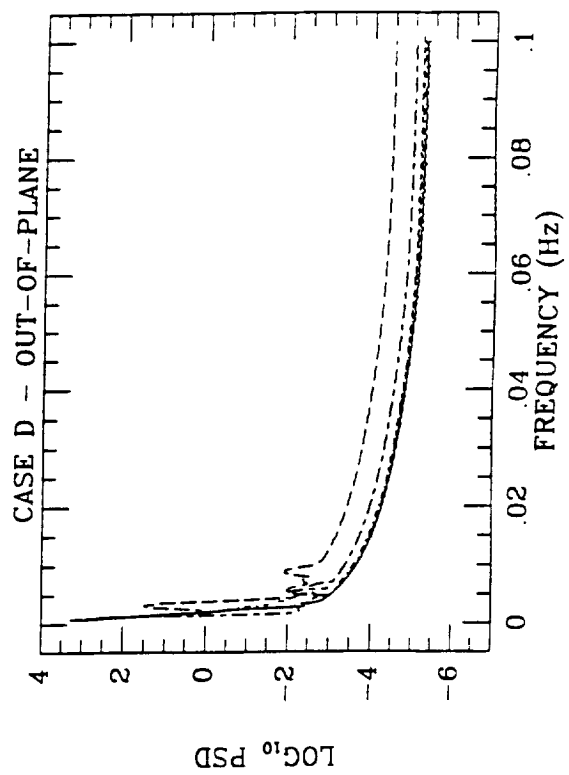
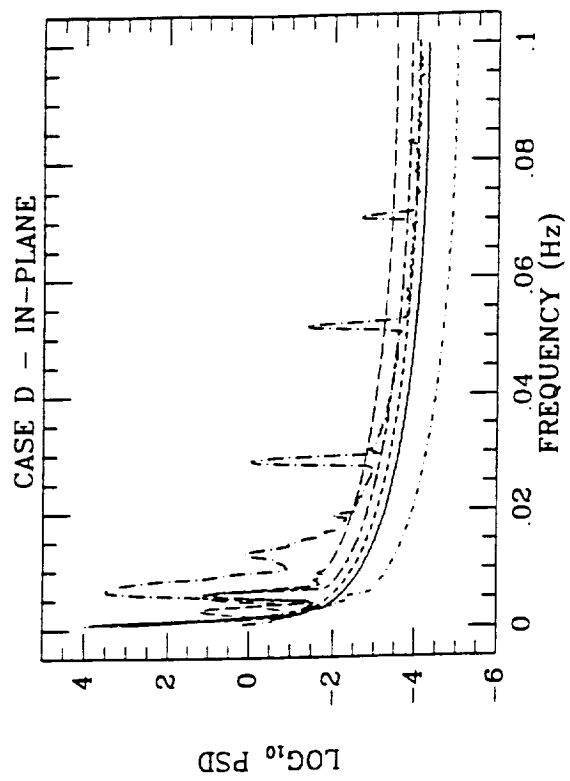
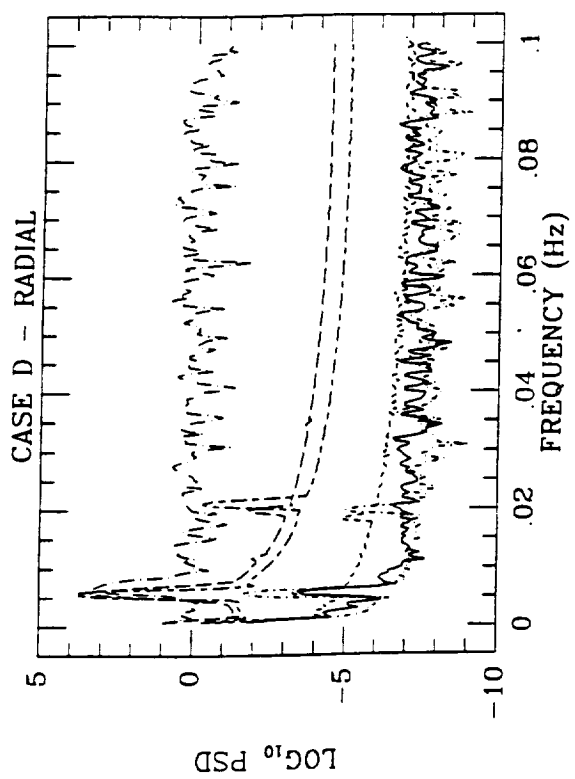
The PSD plots are on the next four pages.











## 2.6 Conclusions

The results from the various simulators when applied to a set of test cases showed both encouraging agreement and disheartening and sometimes puzzling disagreement. The disagreement generally appears to be due to failure to unambiguously specify and implement the physical situation intended, or due to predictable limitations of the model used, rather than to "error". Display in the spectral domain via PSD helps understand the sources of disagreement.

Several comments should be made with regard to the test cases chosen and their use.

First, on the complexity of the cases chosen. On the basis of several teleconferences and material supplied by the test case subcommittee, two factors were deemed of prime importance: (a) a small number of cases so that the comparison runs might actually be made, and (b) inclusion of simulations that would depend on a wide variety of non-trivial phenomena. Additionally, cases were chosen on the basis of being, typically, capable of being set up as small changes from simulations which could be routinely run, e.g. starting from a hanging equilibrium state.

In retrospect, this philosophy is seen to have two pitfalls. First, since several phenomena often interact in one simulation and since some of the phenomena have no readily available theoretical results (e.g., coupling of in-plane and out-of-plane libration for large angles), the "expected" results are known only vaguely if at all. Second, again because of the complexity of the cases, when (as was the case for all except case B) the simulations do not agree it becomes difficult to determine the causes of the disagreement and which simulation is more "correct".

A more practical philosophy for the choice of test cases would have a larger number of cases, each isolating one single phenomena, considering simpler, linearized effects before complex interactions. This is typically the way in which a developing simulator should be verified, though all too often it appears not to be carried out rigorously. These would often involve theoretically expected results, and be more in the line of validation against analytic solutions as discussed in Quarterly Report #16. What would be of interest, though not feasible in the current effort, would be to obtain results from various simulators to observe the effort (CPU hours?) required to simulate a certain effect with given accuracy.

The second point is that disagreement in simulator results can come about in several ways: (a) the program or model may be faulty, leading to incorrect computation, (b) the

situation simulated may not be what was requested or intended, due to either poor specification, faulty input, or exceeding the range of the simulator, (c) the output may be misinterpreted. In the ultimate goal of obtaining answers to posed questions, problems with setup or interpretation are just as incorrect (though less fundamental) as problems with computation. One must consider success of the whole system (user + operator + program) in predicting the evolution of a physically specified situation.

Related to this, and apparent from our experience with the test case exercise, is the difficulty in specifying and implementing unambiguously a physical situation to be simulated. There is a sign difference in the angle variable output between SKYHOOK and GTOSS (and the similar STOCS).

One disturbing aspect of the whole subject of tether simulation, programs for which have been written for a decade now, is the apparent lack of any validation by comparison to physical experiment. Although the space environment is certainly different from the Earth based laboratory, the task of modifying simulators to include the laboratory gravity field (constant) should not be insuperable; neither should performing quantitative experiments. The cost would certainly be less than that of a space mission, and the opportunities for repetition and more detailed observation greater.

## 2.7 References

Xe, X., and J.D. Powell, 1988. "Tether Damping in Space," in Space Tethers for Science in the Space Station Era, ed. by L. Guerriero and I. Bekey (Bologna: Societa Italiana di Fisica), pp. 153-162.

Press, W.H., B. Flannery, S.A. Teukolsky and W.T. Vetterline, 1986. Numerical Recipes: The Art of Scientific Computing, Cambridge: Cambridge University Press.

### 3.0 VARIABLE-G/MICRO-G LABORATORY TETHERED TO THE SPACE STATION

Tethers offers the possibility of varying the level of the apparent acceleration on board a laboratory by exploiting the gravity gradient. By moving the laboratory along a vertical tether attached to a mother station (e.g., the Space Station) or by placing the laboratory at various distances from the mother station, the laboratory will experience an apparent acceleration level which increases with the distance from the mother station.

In low Earth orbit, with a tether length of 10 km, the static acceleration on board the laboratory, owing to the gravity gradient, can vary between zero at the system's center of mass (CM) and  $4 \times 10^{-3}$  g at the tip of the tether. The external perturbations acting on the system at the Space Station altitude of 450 km (a value that was valid at the time of our study) causes fluctuations of the accelerations  $a$ . The magnitudes of the acceleration was estimated as follows:  $a \leq 10^{-6}$  g for frequency  $\leq 10^{-3}$  Hz;  $a \leq 10^{-7}$  g for  $10^{-3}$  Hz < frequency <  $10^{-2}$  Hz; and  $a < 10^{-7}$  g for frequency  $\geq 10^{-2}$  Hz.

Two configurations were investigated during our study: (A) a single-tether system whereby the Space Station is at a non-null acceleration level; and (B) a dual tethered system whereby the gravity laboratory moves along the upper tether and the lower tether was added to nullify the acceleration on board the Station and to provide a pollution-free platform for the study of the Earth.

The propagation of disturbances from the Station, through the tether, to the gravity laboratory and to the outer platform at the tether tip was also investigated. In conclusion, it was found that a small material damping (of a few percents) is enough to abate dramatically the longitudinal waves at frequency above 1-2 Hz. The transverse waves, instead, are only slightly affected by material damping because transverse waves have only a non-linear coupling to the tether stretch.

Four papers are included in the following which summarizes the highlights of our research on this topic as follows:

Paper 1 presents the deployment strategy for the single-tether system and the techniques to damp the vibration modes excited during deployment.

Paper 2 deals with the acceleration noise levels on board the gravity laboratory of the dual-tether system. The influence of external perturbations is analyzed in detail for two

distinct cases: (a) for a laboratory fixed on the tether; and (b) for a laboratory crawling along the tether. Moreover, the acceleration noise levels caused by external perturbations are compared to those required by a number of microgravity processes proposed for the low-gravity environment of the Space Station.

Paper 3 focuses on the attitude dynamics of the gravity laboratory placed at 1-km distance from the Space Station and investigates the noise component related to the attitude degrees of freedom.

Paper 4 investigates the propagation of longitudinal and transverse waves along the tether from the Station to the gravity laboratory and to the platform at the tether tip. The model treats the tether as a continuum and takes into account the effect of gravity gradients, material damping, and the inertia of the masses at the end of the tether or attached along the tether.

See also Quarterly Reports No. 1 through No. 15 of this contract for more details.

# **A Three-Mass Tethered System for Micro-*g*/Variable-*g* Applications**

E.C. Lorenzini

Reprinted from



## **Journal of Guidance, Control, and Dynamics**

Volume 10, Number 3, May-June 1987, Page 242

AMERICAN INSTITUTE OF AERONAUTICS AND ASTRONAUTICS • 1633 BROADWAY • NEW YORK, N.Y. 10019

# A Three-Mass Tethered System for Micro-g/Variable-g Applications

Enrico C. Lorenzini\*

Harvard-Smithsonian Center for Astrophysics, Cambridge, Massachusetts

This paper describes a Space-Station-attached tethered system for micro-g/variable-g applications. The system consists of three platforms: the Space Station, an end mass anchored at the end of a 10-km-long kevlar tether, and a micro-g/variable-g laboratory with the capability of crawling along the tether. Control strategies are devised for performing both the deployment and the stationkeeping maneuvers of the system. Effective algorithms are identified for damping out the major oscillations of the system.

## Nomenclature

$a$	= semimajor axis
$A_i$	= $i$ th tether cross section
$E_i$	= $i$ th tether Young's modulus
$F_i$	= force acting upon the $i$ th mass
$g$	= gravity acceleration at the Earth's surface
$k_{ii}$	= $i$ th-tether stiffness
$l_i$	= distance between mass $m_i$ and mass $m_{i+1}$
$m_i$	= $i$ th mass
$r_i$	= radius vector from the Earth's center to the $i$ th mass
$T_i$	= tension in the $i$ th tether
$x, z$	= orbiting axes
$x_B, z_B$	= body axes
$x_I, z_I$	= inertial axes
$\Omega$	= orbital rate
$\rho_i$	= radius vector from the system center of mass to the $i$ th mass

## Introduction

THE ongoing development of the Space Station program has vitalized research in microgravity related experiments. Material processing, pharmaceutical production, and life sciences are the disciplines that will benefit the most from an orbiting laboratory capable of providing a microgravity acceleration level (or better) at frequency  $< 0.1$  Hz for 1 day to 1 month duration.<sup>1,2</sup> The current requirements for the microgravity laboratory on board the Space Station specify a  $10^{-5}$  g acceleration level at all frequencies.<sup>3</sup> This acceleration level is marginally satisfactory for most of the envisioned microgravity experiments. Furthermore, the microgravity experiments severely restrict the scheduling of other "noisy" activities onboard the Space Station. The reasons above prompted us to conceive an alternative configuration for the microgravity laboratory that makes use of a tethered system attached to the Space Station.<sup>4,5</sup> As shown in Fig. 1 the system consists of a 10-km-long, 2-mm-diameter kevlar tether attached to the Station at one end. Another platform (e.g., a scientific platform) with a presently estimated mass of 9.06 metric tons is attached to the other end of the tether. The micro-g/variable-g laboratory (in short, "g-laboratory" or "g-platform") with an estimated mass of 5 metric tons is also attached to the tether in between the two

end platforms. The g-laboratory is equipped with a mechanism for "crawling" along the tether from one end to the other. The stable configuration of the system, as thoroughly dealt with in other papers,<sup>6,7</sup> is along the local vertical while the tether is stretched by opposite forces resulting from the balance of gravitational and centrifugal forces acting upon the system. The point where the above-mentioned forces balance out is often called "orbit center" and its distance from the Earth's center, when the tether mass is neglected, is given by

$$r_0 = \left( \sum_{i=1}^3 m_i r_i / \sum_{i=1}^3 m_i / r_i^2 \right)^{1/2} \quad (1)$$

where  $r_i$  is the length of the radius vector from the  $i$ th mass to the Earth's center and the summation is extended to the three masses which constitute the system. For moderately long systems the orbit center coincides with the center of gravity and with the center of mass (C.M.). In our case, assuming a Space Station mass of 90.6 metric tons (as foreseen for the initial phase of the Space Station program), the offset between the center of mass and the orbit center is 1.2 m when the g-laboratory is located at the orbit center and the Space Station is flying at 500 km altitude. If the laboratory is displaced from the orbit center it will experience a steady-state acceleration, linearly dependent upon the distance from the orbit center  $l_{oc}$ , the modulus of which is given by

$$A_g = 3\Omega^2 l_{oc} \quad (2)$$

This acceleration is usually called gravity gradient acceleration but actually two thirds of it originates from gravitational forces and one third from centrifugal forces.

It follows from the description above that by placing the g-platform at various distances from the orbit center, the g-laboratory will experience correspondingly different accelerations ranging from zero-g at the orbit center to approximately  $10^{-2}$  g at the tether end opposite the Station.

Once the system is deployed from the Space Station the residual oscillations (e.g., vibrations excited during the deployment phase) must be damped out by active and/or passive dampers. Both the deployment maneuver and the damping algorithms activated during the stationkeeping phase are described in the next sections.

## Mathematical Models

Two reference frames are erected (see Fig. 1). The orbiting reference frame  $[x, z]$  rotates at constant orbital rate  $\Omega$ . Its origin coincides with the system (C.M.) at time  $t = 0$  with the  $z$  axis along the local vertical toward the Earth's center, and the

Received June 11, 1986; presented as Paper 86-1990 at the AIAA/AAS Guidance, Navigation and Control Conference, Williamsburg, VA, Aug. 18-20, 1986; revision received Dec. 16, 1986. This paper is declared a work of the U.S. Government and is not subject to copyright protection in the United States.

\*Scientist, Radio and Geoastronomy Division.



$x$  axis along the local horizon on the orbital plane toward the direction of flight.

The body reference frame  $[x_B, z_B]$  has its origin at the system C.M., with the  $z_B$  axis parallel to the line through the end masses ( $m_1$  and  $m_3$ ) of the system and pointing toward  $m_1$ , and the  $x_B$  axis on the orbital plane toward the direction of flight.

Two different mathematical models have been derived for the dynamics of the system based on different choices for the integration variables. Both models describe the two-dimensional dynamics (in the orbital plane) with respect to the orbiting reference frame. The assumptions are the same for the two models: point masses, spherical Earth, second-order expansion of the gravity potential, elastic but massless tethers. In the first model, moreover, the orbit of the system C.M. is assumed to be circular.

Mathematical model 1 makes use of the Lagrangian coordinates  $\theta, l_1, l_2, \epsilon$  (see Fig. 1). The kinetic energy of the system is given by

$$T = \frac{1}{2} \sum_{i=1}^3 m_i |v_{H_i}|^2 \quad (3)$$

where the inertial velocity  $v_n$  can be expressed in the orbiting reference frame as follows:

$$v_{H_i} = v_{H_i} + \Omega \times a + (\dot{\theta} + \Omega) \times \rho_{H_i} \quad (4)$$

In Eq. (4) the subscript  $B$  identifies the body reference frame. By developing Eq. (4) and by substituting in Eq. (3) we get:

$$T = \frac{1}{2} \sum_{i=1}^3 m_i \left\{ \dot{x}_{H_i}^2 + \dot{z}_{H_i}^2 + (\dot{\theta} - \Omega)^2 (x_{H_i}^2 + z_{H_i}^2) + 2(\dot{\theta} - \Omega)(\dot{x}_{H_i} z_{H_i} - x_{H_i} \dot{z}_{H_i}) \right\} + \frac{1}{2} m_{tot} \Omega^2 a^2 \quad (5)$$

where  $m_{tot} = m_1 + m_2 + m_3$  expresses the total mass of the system.

$$V = -\mu \sum_{i=1}^3 \frac{m_i}{|r_i|} \quad (6)$$

The potential energy expansion, with respect to the body axes, truncated to the second order gives

$$V = -\frac{1}{2} \sum_{i=1}^3 m_i \Omega^2 \left\{ (3\cos^2\theta - 1)z_{B_i}^2 + (3\sin^2\theta - 1)x_{B_i}^2 - 6\sin\theta\cos\theta x_{B_i} z_{B_i} \right\} - m_{tot} \Omega^2 a^2 \quad (7)$$

Since  $\epsilon \ll l$ , we can express  $x_{B_i}, z_{B_i}$  in terms of  $l_i$  and  $\epsilon$  as follows:

$$\begin{aligned} z_{B1} &= R_3 l_2 + (1 - R_1) l_1 \\ z_{B2} &= R_3 l_2 - R_1 l_1 \\ z_{B3} &= (R_3 - 1) l_2 - R_1 l_1 \\ x_{B1} &= -R_2 \epsilon \\ x_{B2} &= (1 - R_2) \epsilon \\ x_{B3} &= -R_2 \epsilon \end{aligned} \quad (8)$$

where  $R_i = m_i/m_{tot}$ .

The Lagrangian function  $L$  is readily obtained by subtracting the potential energy from the kinetic energy, while the equations of motion are given by

$$\frac{d}{dt} \left( \frac{\partial L}{\partial \dot{q}_i} \right) - \frac{\partial L}{\partial q_i} = Q_{q_i}, \quad i = 1, \dots, 4 \quad (9)$$

where the Lagrangian coordinates are

$$q_1 = \theta; q_2 = \epsilon; q_3 = l_1; q_4 = l_2 \quad (10)$$

Substitution of Eqs. (8) into Eqs. (5) and (7) gives the Lagrangian as a function of the variables  $l_1, l_2, \epsilon, \theta$ . After lengthy derivatives we get the following equations of motion:

$$\begin{aligned} & \ddot{\theta} [R_1 l_1 (l_1 + u) + R_3 l_2 (l_2 - u) + R_2 (1 - R_2) \epsilon^2] \\ & + 2(\dot{\theta} - \Omega) [R_1 l_1 (\dot{l}_1 + \dot{u}) + R_3 l_2 (\dot{l}_2 - \dot{u}) \\ & + R_2 (1 - R_2) \epsilon \dot{\epsilon}] + 3\Omega^2 \sin\theta \cos\theta [R_1 l_1 (l_1 + u) \\ & + R_3 l_2 (l_2 - u) - R_2 (1 - R_2) \epsilon^2] + 3\Omega^2 (\sin^2\theta \\ & - \cos^2\theta) R_2 u \dot{\epsilon} - R_2 \epsilon [R_1 \ddot{l}_1 - R_3 \ddot{l}_2] - R_2 \ddot{\epsilon} u = Q_{\theta}/m_{tot} \\ & R_2 (1 - R_2) [\ddot{\epsilon} + g \epsilon] - 2(\dot{\theta} - \Omega) R_2 \dot{u} \\ & - (\ddot{\theta} + d) R_2 u = Q_{\epsilon}/m_{tot} \\ & R_1 (1 - R_1) [\ddot{l}_1 + b \dot{l}_1] + R_1 R_3 [\ddot{l}_2 + b \dot{l}_2] \\ & - 2(\dot{\theta} - \Omega) R_1 R_2 \dot{\epsilon} - (\ddot{\theta} - d) R_1 R_2 \epsilon = Q_{l_1}/m_{tot} \\ & R_3 (1 - R_3) [\ddot{l}_2 + b \dot{l}_2] + R_1 R_3 [\ddot{l}_1 + b \dot{l}_1] \\ & + 2(\dot{\theta} - \Omega) R_2 R_1 \dot{\epsilon} + (\ddot{\theta} - d) R_2 R_1 \epsilon = Q_{l_2}/m_{tot} \end{aligned} \quad (11)$$

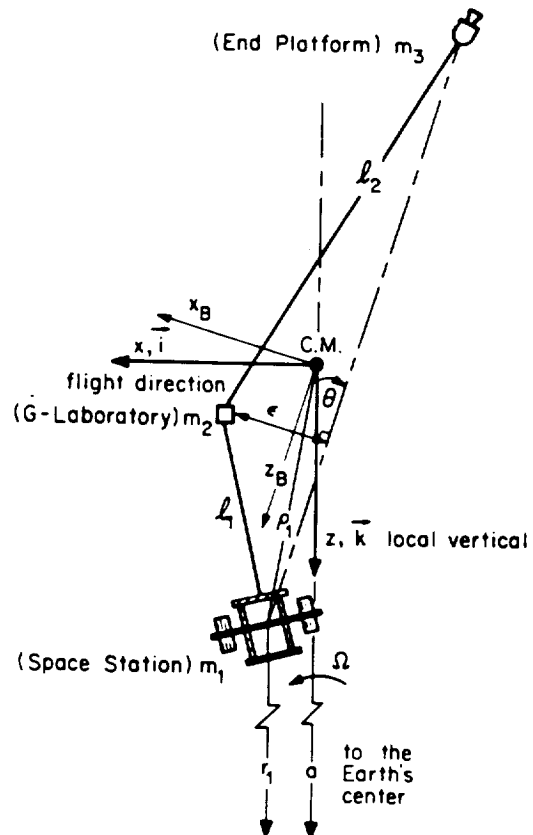


Fig. 1 Schematic of three-mass tethered system.

where

$$\begin{aligned} b &= \Omega^2 (1 - 3\cos^2\theta) - (\dot{\theta} - \Omega)^2 \\ d &= 3\Omega^2 \sin\theta \cos\theta \\ g &= \Omega^2 (1 - 3\sin^2\theta) - (\dot{\theta} - \Omega)^2 \end{aligned} \quad (12)$$

while  $u$  is the distance of  $m_2$  from the system C.M. and  $\dot{u}$  is the associated rate of change given respectively by

$$\begin{aligned} u &= R_3 l_2 - R_1 l_1 \\ \dot{u} &= R_3 \dot{l}_2 - R_1 \dot{l}_1 \end{aligned} \quad (13)$$

The generalized forces in Eqs. (11) are given by

$$Q_j = \sum_{i=1}^3 F_i \frac{\partial r_i}{\partial q_j}, \quad j=1, \dots, 4 \quad (14)$$

where  $F_i$  are the forces acting upon the three masses. Since  $\epsilon \ll l_i$ , we have that  $\sin(\epsilon/l_i) \approx \epsilon/l_i$  and  $\cos(\epsilon/l_i) \approx 1$ . The forces  $F_i$  are therefore given by:

$$\begin{aligned} F_1 &= -T_1 (\cos\theta + \epsilon/l_1 \sin\theta) \mathbf{k} \\ &\quad - T_1 (\sin\theta - \epsilon/l_1 \cos\theta) \mathbf{i} \\ F_2 &= [(T_1 - T_2) \cos\theta + (T_1/l_1 + T_2/l_2) \epsilon \sin\theta] \mathbf{k} \\ &\quad + [(T_1 - T_2) \sin\theta - (T_1/l_1 + T_2/l_2) \epsilon \cos\theta] \mathbf{i} \\ F_3 &= T_2 (\cos\theta - \epsilon/l_2 \sin\theta) \mathbf{k} \\ &\quad + T_2 (\sin\theta + \epsilon/l_2 \cos\theta) \mathbf{i} \end{aligned} \quad (15)$$

where  $T_1$  and  $T_2$  are the tensions in tethers 1 and 2, respectively. The radius vectors  $r_i$  are given by

$$\begin{aligned} r_i &= x_i \mathbf{i} + z_i \mathbf{k} \\ &= (z_{Bi} \sin\theta + x_{Bi} \cos\theta) \mathbf{i} \\ &\quad + (z_{Bi} \cos\theta - x_{Bi} \sin\theta) \mathbf{k}, \quad i=1, 2, 3 \end{aligned} \quad (16)$$

By using Eqs. (8) and by substituting Eqs. (15) and (16) into Eq. (14) we finally get

$$\begin{aligned} Q_\theta &= 0 \\ Q_\epsilon &= -\epsilon (T_1/l_1 + T_2/l_2) \\ Q_{l_1} &= -T_1 \\ Q_{l_2} &= -T_2 \end{aligned} \quad (17)$$

Since Eqs. (11) are of the form  $A\ddot{x} = b(x, \dot{x})$  the coefficient matrix  $A$  must be inverted in order to integrate numerically the equations of motion.

In mathematical model 2 the integration variables are the Cartesian coordinates of the masses with respect to the above-mentioned orbiting reference frame. The variables  $l_1, l_2, \epsilon, \theta$  are then obtained from the Cartesian coordinates. The assumptions for model 2 are the same as those of model 1 except for the circularity of the orbit. With reference to Fig. 1, the inertial acceleration of the  $i$ th mass with respect to the rotating orbiting frame is given by

$$\ddot{r}_i = \ddot{p}_i + 2\Omega \times \dot{p}_i + \Omega \times (\Omega \times r_i), \quad i=1, 2, 3 \quad (18)$$

The equations of motion in functional form are given by

$$m_i \ddot{r}_{i1} = F_{Ri} + F_{Ti}, \quad i=1, 2, 3 \quad (19)$$

where  $F_{Ri}$  is the gravity force acting upon the  $i$ th mass given by

$$\begin{aligned} F_{Ri} &= -\nabla V_i = -\nabla \left\{ \frac{1}{2} m_i [2\Omega^2 a^2 \right. \\ &\quad \left. + 2\Omega^2 a z_i - \Omega^2 (x_i^2 + z_i^2) + 3\Omega^2 z_i^2] \right\} \end{aligned} \quad (20)$$

while  $F_{Ti}$  is the total tension acting upon the  $i$ th mass. By developing Eqs. (18-20) we obtain the well-known Hill's equations as follows:

$$\begin{aligned} \ddot{x}_i - 2\Omega \dot{z}_i &= F_{Tx_i}/m_i, \quad i=1, 2, 3 \\ \ddot{z}_i - 3\Omega^2 z_i + 2\Omega \dot{x}_i &= F_{Tz_i}/m_i, \quad i=1, 2, 3 \end{aligned} \quad (21)$$

With reference to Fig. 2 we derive the force  $F_{Ti}$  as follows:

$$F_{Ti} = [T_{xi} + T_{xi-1}] \mathbf{i} + [T_{zi} - T_{zi-1}] \mathbf{k}, \quad i=1, 2, 3 \quad (22)$$

where  $T_{xi}, T_{zi}$  are the components of the tension  $T_i$  in the tether connecting the  $i$ th mass to the  $i+1$ th mass, given by

$$\begin{aligned} T_{xi} &= T_i \cos\beta_i = T_i (x_{i+1} - x_i)/l_i, \quad i=1, 2 \\ T_{zi} &= T_i \sin\beta_i = T_i (z_{i+1} - z_i)/l_i, \quad i=1, 2 \end{aligned} \quad (23)$$

while  $T_{x3} = T_{z3} = 0$ . The relations between  $l_1, l_2, \theta, \epsilon$  and the integration variables can be easily computed as follows:

$$\begin{aligned} \theta &= \tan^{-1} \left\{ \frac{x_1 - x_3}{z_1 - z_3} \right\} \\ l_i &= [(x_{i+1} - x_i)^2 + (z_{i+1} - z_i)^2]^{1/2}, \quad i=1, 2 \end{aligned} \quad (24)$$

The lateral displacement  $\epsilon$  is derived by computing the coordinates of the point of intersection  $(x_c, z_c)$  between the straight line through  $m_1$  and  $m_3$  and its perpendicular through  $m_2$ . The result is as follows:

$$\epsilon = [(x_2 - x_c)^2 + (z_2 - z_c)^2]^{1/2} \text{sign}(x_2 - x_c) \quad (25)$$

where

$$\begin{aligned} x_c &= [x_1 - x_2 \tan^2\theta + (z_2 - z_1) \tan\theta] / (1 - \tan^2\theta) \\ z_c &= [x_c - x_2] \tan\theta - z_2 \end{aligned} \quad (26)$$

In both models 1 and 2 the tension in each tether is computed from the tether stretch. A longitudinal oscillation damper (along the tether) with stiffness  $k_i$  and damping  $b_i$  has been added to each tether segment. In Fig. 2,  $l_{ci}$  is the commanded length of the  $i$ th tether that can follow a prescribed control law if the associated tether is actually controlled by a reel system or if not, it is the natural tether length,  $l_{di}$  is the length of the associated longitudinal damper and  $l_{ti}$  the  $i$ th tether stretch. Tether tensions and stretches of the longitudinal dampers for the three-mass system are therefore as follows:

$$\begin{aligned} T_i &= k_i l_{ti} = \frac{E_i A_i}{l_{ci}} (l_i - l_{di} - l_{ci}), \quad i=1, 2 \\ l_{di} &= \frac{k_{ti}}{b_i} l_{ti} - \frac{k_i}{b_i} l_{di}, \quad i=1, 2 \end{aligned} \quad (27)$$

Both models 1 and 2 have been numerically integrated by using a fourth-order Runge-Kutta integrator with variable step

size. Results for test cases with circular orbit of the system C.M. have been identical, demonstrating the reliability of the models.

Model 1 is suitable for analytical simplifications which provide direct insights into the dynamics of the system. Model 2 does not have this feature but can be more efficiently integrated than model 1 (especially with more than three masses) because it does not require any matrix inversion. The equations of motion of model 2 are summarized below:

$$\begin{aligned}\ddot{x}_1 &= 2\Omega\dot{z}_1 + T_1(x_2 - x_1)/(m_1 l_1) \\ \ddot{x}_2 &= 2\Omega\dot{z}_2 + T_2(x_3 - x_2)/(m_2 l_2) \\ &\quad + T_1(x_1 - x_2)/(m_2 l_1) \\ \ddot{x}_3 &= 2\Omega\dot{z}_3 + T_2(x_2 - x_3)/(m_3 l_2) \\ \ddot{z}_1 &= 3\Omega^2 z_1 - 2\Omega\dot{x}_1 + T_1(z_2 - z_1)/(m_1 l_1) \\ \ddot{z}_2 &= 3\Omega^2 z_2 - 2\Omega\dot{x}_2 + T_2(z_3 - z_2)/(m_2 l_2) \\ &\quad + T_1(z_1 - z_2)/(m_2 l_1) \\ \ddot{z}_3 &= 3\Omega^2 z_3 - 2\Omega\dot{x}_3 + T_2(z_2 - z_3)/(m_3 l_2)\end{aligned}\quad (28)$$

where, for equal cross sections and Young's moduli of the two tethers, we have

$$\begin{aligned}T_1 &= EA l_{11}/l_{c1} \\ T_2 &= EA l_{12}/l_{c2} \\ l_{11} &= l_1 - l_{d1} - l_{c1} \\ l_{12} &= l_2 - l_{d2} - l_{c2} \\ l_{d1} &= k_{11} l_{11}/b_1 - k_{11} l_{d1}/b_1 \\ l_{d2} &= k_{12} l_{12}/b_2 - k_{12} l_{d2}/b_2\end{aligned}\quad (29)$$

Equations (28) and (29) together with Eqs. (24-26) describe the two-dimensional dynamics of the three-mass tethered system.

### Damping Algorithms

Before dealing with the deployment maneuvers of the three-mass system we must conceive effective algorithms for damping out the oscillations associated with the various degrees of freedom of the system; namely, the libration  $\theta$ , the lateral oscillation  $\epsilon$ , and the longitudinal oscillations  $l_1, l_2$ .

#### Libration/Lateral Dampers

From Eq. (11) we can infer that the libration of the system, when the  $g$ -laboratory  $m_2$  is placed at the system C.M. ( $m_1 l_1 = m_3 l_2$ ), is described in first approximation, for small oscillations, by the following simplified equation

$$\ddot{\theta} + 2(\dot{\theta} - \Omega)l + 3\Omega^2 l^2 \theta = 0 \quad (30)$$

where  $l = l_1 + l_2$ . We assume, moreover, that the tether is unstretchable; hence  $l = l_c$ .

In Eq. (30) the second is the dissipative term. The energy dissipated for each libration cycle is therefore given by

$$\begin{aligned}E_d &= 2 \int_0^\tau l l'(\dot{\theta} - \Omega)\dot{\theta} dt \\ &= 2l_0 \int_0^\tau l'(\dot{\theta} - \Omega)\dot{\theta} dt\end{aligned}\quad (31)$$

where  $\tau = 2\pi/(\sqrt{3}\Omega)$  is the period of the libration and  $l_0$  is the tether length for  $\theta = 0$ . Our goal is to implement a tether control law (for the two tethers) that maximizes  $E_d$ . Let us adopt the following control law:

$$l_c = l_0(1 - K_\theta \theta) \quad (32)$$

with the gain  $K_\theta$  greater than zero. The length control law expressed by Eq. (32) can be readily transformed into a rate control law. Here we adopt the length control formulation because it gives a more immediate insight into the dynamics of the system, as explained later.

Since  $d\theta^2/dt = 2\theta\dot{\theta}$  and, for small values of  $\theta$ ,  $l = l_0$ , by multiplying Eq. (30) by  $\theta$  and integrating from 0 to  $\tau$  we obtain

$$l_0^2 \int_0^\tau d\theta^2 + 2l_0 \int_0^\tau l'(\dot{\theta} - \Omega)\dot{\theta} dt + 3\Omega^2 l_0^2 \int_0^\tau \theta d\theta = 0 \quad (33)$$

For light damping the approximate solution of Eq. (30), over one cycle, is as follows:

$$\theta = \hat{\theta} \sin(\sqrt{3}\Omega t) \quad (34)$$

where  $\hat{\theta}$  is the libration amplitude and  $\sqrt{3}\Omega$  the frequency. By substituting Eq. (34), its derivative, and Eq. (32) into equation (33), and after computing the integrals [the third integral in Eq. (33) is equal zero] we finally get

$$\frac{\Delta\theta}{\hat{\theta}} = \frac{\pi}{\sqrt{3}\hat{\theta}} \frac{\delta l}{l_0} \quad (35)$$

where  $\delta l = 2l_0 K_\theta \hat{\theta}$  is the peak-to-peak tether length variation as derived from Eq. (32), while  $\Delta\theta$  is the decrease of libration amplitude per libration cycle. In the case of light damping Eq. (35) expresses the logarithmic decrement of the libration angle. The most important and unique feature of the control law (S-type) expressed in Eq. (35) is that the logarithmic decrement increases inversely with the libration amplitude  $\hat{\theta}$ . The trajectory followed by the end masses is readily obtained by substituting Eq. (34) into Eq. (32) and solving for the  $x$  and  $z$  components. It is interesting to note that the trajectory fol-

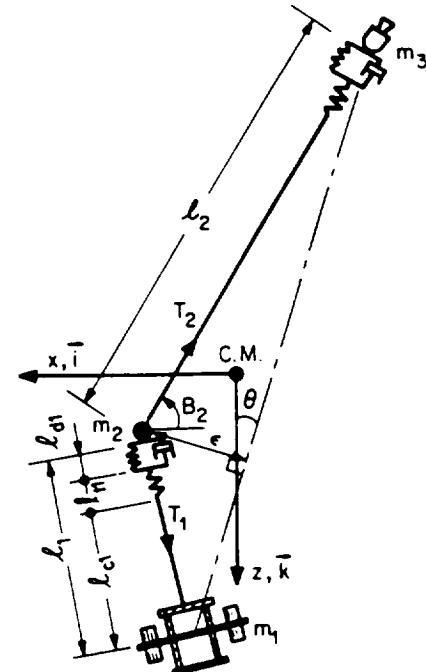


Fig. 2 Schematic of longitudinal dampers.

lowed by the end masses in a damping cycle is not an eight-shaped yo-yo cycle<sup>6,7</sup> but an S-shaped cycle. In other words, the tether is shortened during the retrograde part of the libration and is lengthened during the prograde part as shown in Fig. 3. The control law expressed by Eq. (32) can be adapted to a three-mass system by modifying and generalizing Eq. (32) as follows:

$$\begin{aligned} l_{c1} &= l_{01}[1 - (K_\theta\theta - K_\epsilon\epsilon/l_1)] \\ l_{c2} &= l_{02}[1 - (K_\theta\theta + K_\epsilon\epsilon/l_2)] \end{aligned} \quad (36)$$

Both  $\theta$  and  $\epsilon$  are fed back into the tether reel control. Because of the last terms in Eq. (36) the mass  $m_2$  is moved along the wire in such a way as to produce Coriolis forces which are opposed to the lateral displacement  $\epsilon$  in order to detract energy from the oscillation associated to that degree of freedom. A simplified version of Eq. (36) can be obtained by assuming  $K_\epsilon = K_\theta$ , consequently we obtain (see Fig. 3)

$$\begin{aligned} l_{c1} &= l_{01}[1 - K_\theta(\theta - \epsilon/l_1)] = l_{01}(1 - K_\theta\theta_1) \\ l_{c2} &= l_{02}[1 - K_\theta(\theta + \epsilon/l_2)] = l_{02}(1 - K_\theta\theta_2) \end{aligned} \quad (37)$$

This simplified version, where  $\theta_1$  and  $\theta_2$  are fed back into the reel control system, is the one adopted in the following simulations. The value of the gain  $K_\theta$  has been determined by imposing a maximum tether length variation, during a libration damping cycle, of 1% of the fully deployed tether length per degree of libration  $\theta$ . The lateral oscillation  $\epsilon$  actually gives a smaller contribution than the libration  $\theta$ . The resulting value for the gain is  $K_\theta = 0.55$ .

#### Longitudinal Dampers

Two passive dampers (spring-dashpot), mounted in series to their respective tethers, have been added to the system for damping the longitudinal tether oscillations. The passive solution has been chosen in order to simplify the design of the three-mass system. According to our design philosophy the reel system (unavoidably massive) controls the low frequency oscillations (librational and lateral) of the system while the passive dampers damp the higher frequency, longitudinal oscillations.

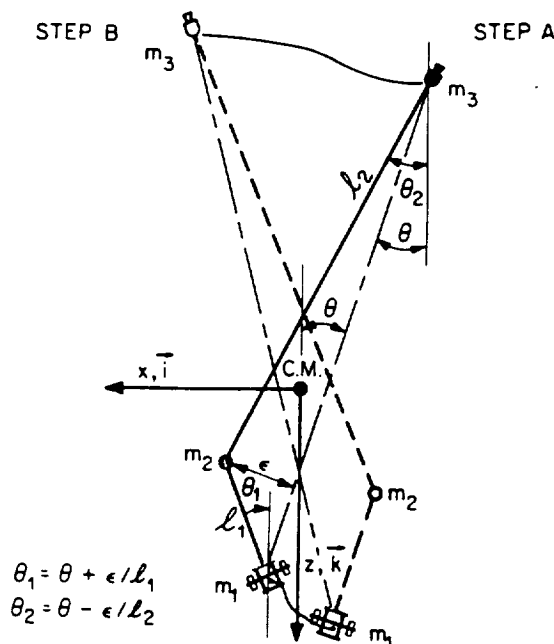


Fig. 3 Pictorial representation of system's dynamics during a libration cycle with librational/lateral dampers switched on.

In order to maximize the energy transfer between the longitudinal vibrations of the tethers and of the respective longitudinal dampers, the natural frequency of each damper must be equal to the natural frequency of the associated tether. Since the longitudinal oscillation frequency changes with tether length the passive dampers perform best for a specific tether length only. An adaptive system could be implemented instead but it has not been included in the present analysis. In the present design each passive damper is tuned to the frequency of the associated 2-mm-diam kevlar tether at the natural tether length during stationkeeping:  $l_{sk1}$  and  $l_{sk2}$ , respectively. The damping coefficient  $\xi$  has been set at 0.9 for both dampers. From numerical simulations  $\xi = 0.9$  has proved to maximize the damping of the longitudinal vibrations in the two tether segments. Since mass  $m_2$  is placed at the system C.M.,  $l_{sk1}m_1 = l_{sk2}m_3$  and the angular frequency of tether 1 is equal to the angular frequency of tether 2, as indicated by

$$\begin{aligned} \omega_{l1} &= \omega_{l2} = [EA/(l_{sk1}m_1)]^{1/2} = 2.74 \times 10^{-2} \text{ rad/s} \\ &= 4.4 \times 10^{-3} \text{ Hz} \end{aligned} \quad (38)$$

where  $EA = 61645 \text{ N}$  for a 2-mm-diam kevlar tether,  $l_{sk1} = 909 \text{ m}$ , and  $m_1 = 90.6 \text{ metric tons}$ . Consequently the gains of the longitudinal dampers in Eq. (29) are as follows:

$$\begin{aligned} k_1 &= EA/l_{sk1} = 67.81 \text{ N/m} \\ k_2 &= EA/l_{sk2} = 6.781 \text{ N/m} \\ b_1 &= 2\xi\omega_{l1}m_1 = 4460.24 \text{ N/(m/s)} \\ b_2 &= 2\xi\omega_{l2}m_2 = 446.024 \text{ N/(m/s)} \end{aligned} \quad (39)$$

where  $l_{sk1}/l_{sk2} = m_3/m_1 = 1/10$ . Equation (38) also indicates that the tethers provide a very effective isolation of the laboratory from any oscillation of the Space Station or the end platform with a frequency greater than 0.1 Hz.

#### Deployment Strategy

Deployment of the system is obtained by unwinding the two tethers from two reel systems that control independently tether 1 and tether 2. Equation (30) refers to a two-mass system but it also describes approximately the dynamic of a three-mass system as long as mass  $m_2$  is located at the system C.M. From Eq. (30) we infer that in order to have a deployment with constant  $\theta$  (deployment along a straight line) the reeled out tether length must be an exponential function of time.<sup>6</sup> Generalizing this to a three-mass system, each tether length must increase exponentially with time and  $l_1/l_2 = l_{sk1}/l_{sk2}$  (fully deployed tether lengths) in order to maintain the mass  $m_2$  at the C.M. The exponentially increasing phase (acceleration phase) is followed by an exponential deceleration phase and subsequently by a transition phase to stationkeeping conditions. All the transitions between sequential phases are simultaneous for the two tethers. In the following formulas  $l_{l1}$  is the initial tether length of tether 1,  $l_{E1}$  is the tether length at the beginning of the deceleration phase,  $l_{T1}$  is the length at the beginning of the transition phase (as later explained),  $l_{f1}$  is the final length, and  $l_{c1}$  is the controlled tether length. In formulas the first two phases are summarized as follows:

Phase I (acceleration)  $l_{l1} \leq l_{c1} < l_{E1}$

$$\begin{aligned} l_{c1} &= l_{l1}e^{at} \\ l_{c2} &= l_{l2}e^{at} \end{aligned} \quad (40)$$

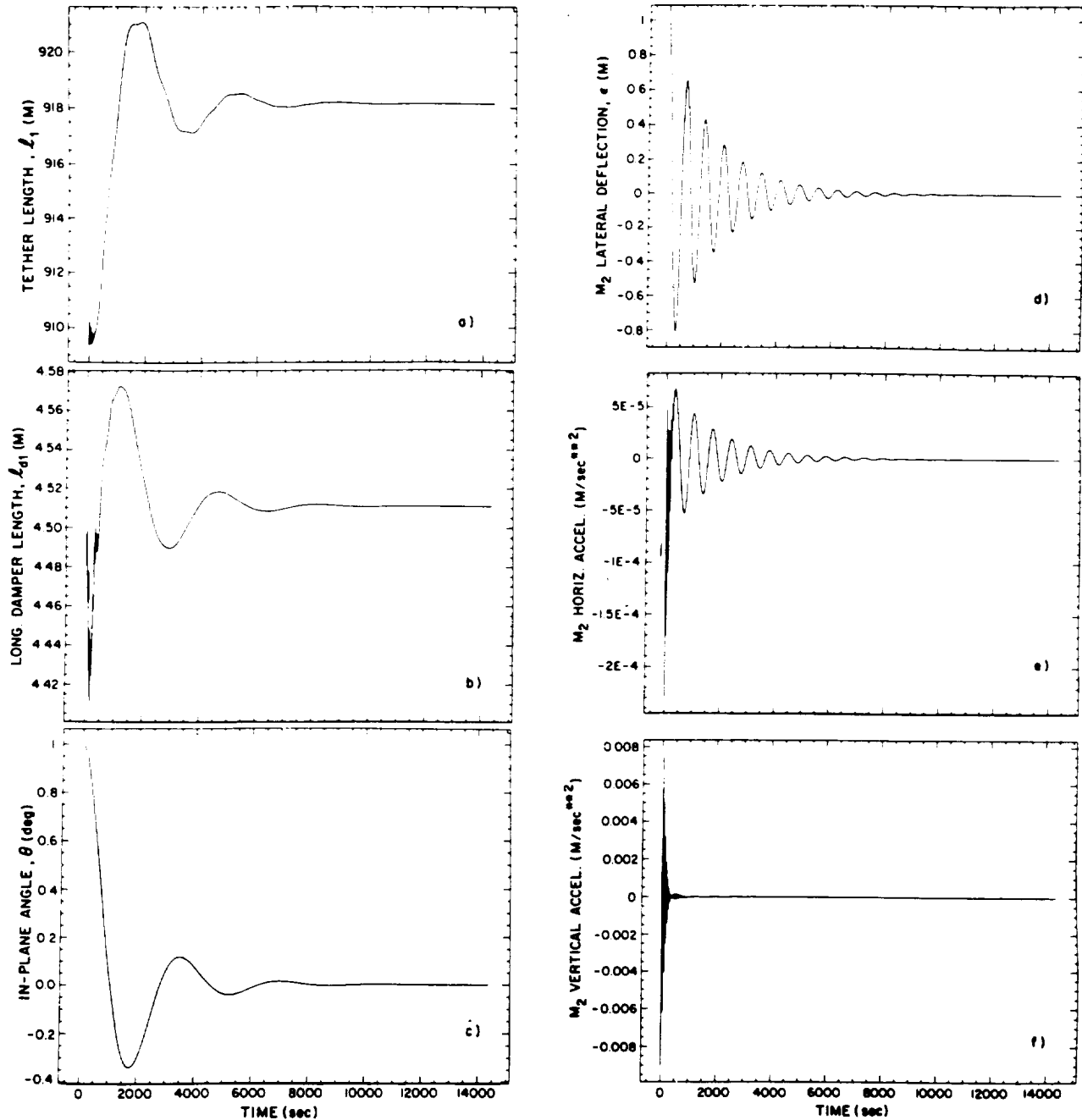


Fig. 4 Dynamics of three-mass tethered system during stationkeeping. 1 orbit = 5677 s.

Phase II (deceleration)  $l_{E1} \leq l_{c1} < l_T$

$$\begin{aligned} l_{c1} &= (l_T - l_{l1})e^{-\beta t} + l_{l1} \\ l_{c2} &= (l_T - l_{l2})e^{-\beta t} + l_{l2} \end{aligned} \quad (41)$$

where  $\beta = \alpha / (l_T / l_{l1} - 1)$  and  $\alpha = \frac{3}{4} \Omega \sin(2\theta_c)$ . In Eqs. (39),  $\theta_c$  is the constant value of  $\theta$  during the acceleration phase.

The final tether lengths  $l_{l1}$  and  $l_{l2}$  are the tether lengths at which the tether speed would be reduced to zero if the deceleration phase were continued indefinitely. In order to speed up the deceleration phase,  $l_{l1} > l_{sk1}$  and  $l_{l2} > l_{sk2}$ .

The transition control law is activated when the actual speed of tether 1 during the deceleration phase equals the tether speed imposed by the stationkeeping control law with a libration angular rate  $\dot{\theta}_T$  at the time of transition between the two

phases, as set forth in the formula

$$-\beta(l_{c1} - l_{l1}) = l_{sk1} k_\theta \dot{\theta}_T \quad (42)$$

and similarly for tether 2. However, tether speed continuity does not imply tether length continuity. The mismatch is corrected by the transition control law and by a choice of control parameters that minimizes such mismatch. The transition control law is a semicycle of a cosinusoidal function of duration  $\Delta T$  activated at the transition time. In formulas

Phase III (transition)  $l_T \leq l_{c1}$

$$\begin{aligned} l_{c1} &= l_{sk1} (1 - f_T - k_\theta \theta) \\ f_T &= f_{0T} \cos\left(\frac{\pi}{2} \frac{t}{\Delta T}\right) \end{aligned} \quad (43)$$

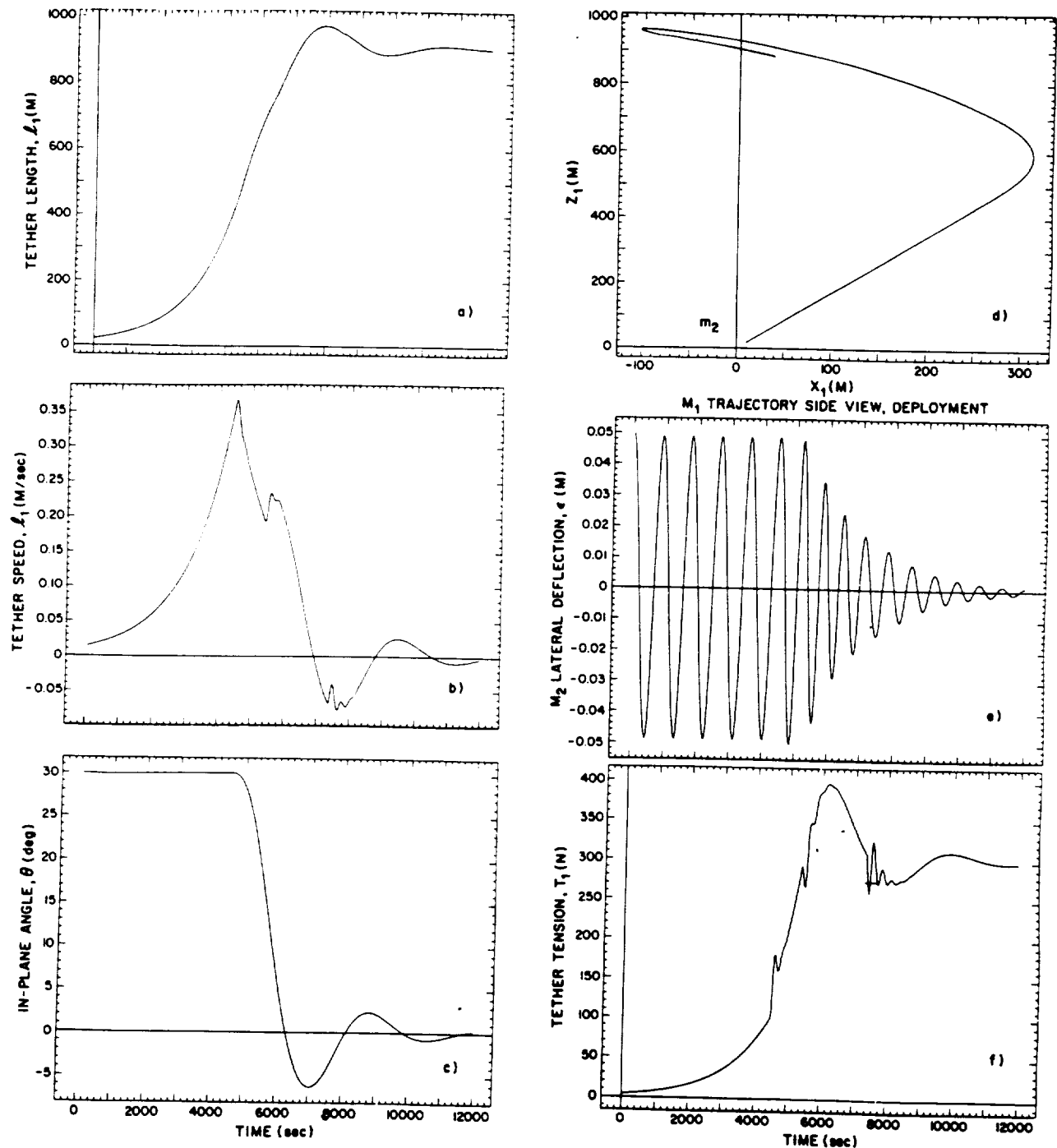


Fig. 5 Dynamics of three-mass tethered system during deployment. 1 orbit = 5677 s.

where  $f_{0T} = \Delta/l_{sk1}$  is the tether length mismatch at transition divided by the stationkeeping tether length. Similar formulas apply to tether 2.

This deployment strategy is similar to the one formulated by Misra and Modi.<sup>8</sup> Unlike the deployment strategy of that paper, the measurement of the libration angle  $\theta$  is not required during the acceleration phase of our deployment maneuver. Consequently radar tracking is not necessary at short distances where the radar is blind. Secondly, the librational damper is activated before the end of deployment and remains active during the following stationkeeping phase when damping of librations is also necessary. In the above-mentioned reference, on the contrary, the damping of librations is proportional to

the deployment speed and it tends to zero at the end of the deployment maneuver.

### Numerical Simulation

#### Stationkeeping Phase

The effectiveness of the dampers during stationkeeping is shown in the following set of plots. These plots have been obtained by simulating the dynamic response of the constellation for 14,000 s during the stationkeeping phase under the following initial conditions: the initial tether lengths are  $l_{11} = 909$  m and  $l_{12} = 9090$  m, the initial libration angle is  $\theta_1 = 1$  deg, and the initial lateral deflection of mass  $m_2$  is  $\epsilon_1 = 0.10$  m. Figures 4a and 4b show the tether length and the longitudinal damper

length, respectively, for tether 1. The same quantities for tether 2 have a similar time dependence but are scaled up a factor of 10. Figures 4c and 4d show the libration angle  $\theta$  and the lateral deflection  $\epsilon$ , respectively. Finally, Figs. 4e and 4f show the horizontal and vertical acceleration components measured on board the *g*-laboratory. Initial transients are effectively abated and, at the end of the simulation, the acceleration level at the *g*-laboratory (*in the absence of external forcing terms*) is well below  $10^{-8}$  g.

#### Deployment Phase

The parameters for the deployment maneuver adopted in this study have been obtained by trial and error after several deployment simulation runs. The following set of parameters provides a stable, fast maneuver and minimizes the mismatch at the transition between the deployment and stationkeeping phases. The parameters are as follows:

$$\begin{aligned} l_{E1} &= 500 \text{ m} \\ l_{J1} &= l_{sk1} + \sigma = 909 + 100 = 1009 \text{ m} \\ \theta_c &= 30 \text{ deg} \\ \Delta T &= 2000 \text{ s} \end{aligned} \quad (44)$$

In the deployment maneuver simulation shown here the initial tether lengths are  $l_{11} = 20$  m,  $l_{12} = 200$  m. Although these values are greater than in actuality, they allow a deployment without tether slackenings. The system shows a tendency to go temporarily slack at the very beginning of the deployment maneuver because of small errors in the initial conditions. An in-line thruster, as also proposed by Banerjee and Kane<sup>9</sup> and adaptive longitudinal dampers can help considerably in relieving the slack tether problem but were not included in this study. An initial libration angle  $\theta_i = 30$  deg and an alignment error of the three masses  $\epsilon_i = 0.05$  m complete the set of initial conditions. The dynamic response, however, is fairly insensitive to these parameters. Figures 5a and 5b show the tether length and tether speed respectively of tether 1 vs time. The corresponding quantities for tether 2 are like those of tether 1 scaled up by a factor of 10 (they are not shown here for brevity's sake). The deployment is completed in approximately 3 h. This value, however, is affected by the initial tether length and is therefore ultimately affected by the position of the reeling system on the Space Station with respect to the Station C.M. More important are the initial tether speeds which must be as close as possible to the initial design speeds, according to the law  $\dot{l}_i = \alpha \dot{l}_{i0}$ , in order to avoid slackening of the tethers. In Fig. 5b the different phases of the deployment control law are evident: the activation of the rotational damper results in the ripple at approximately 5500 s, while the disactivation results in the second ripple at 7500 s. The time history of the libration angle  $\theta$  is plotted in Fig. 5c, where the  $\theta$  angle is constantly equal to  $\theta_c$ , as expected, during the deployment acceleration phase. Figure 5d shows the side view of the trajectory of mass 1 (Space Station) with respect to the system center of mass. Mass 3 (the end platform) follows a mirrorlike trajectory scaled up by a factor of 10. Mass 2 (the *g*-laboratory) remains very close to the system C.M. throughout the deployment maneuver. Figure 5e is the lateral displacement  $\epsilon$  of mass 2 vs time. When the librational/lateral damper

is switched on at 5500 s this oscillation begins to be damped out. The damping of  $\epsilon$  is less effective than that of the angle  $\theta$  because the librational/lateral damper is tuned to the librational frequency. By using a multifrequency damping technique, as formulated in Eqs. (36), the damping of the lateral oscillation can be further improved. Figure 5f shows the time history of the tension in tether 1 which is very close to that of tether 2 throughout the entire deployment maneuver.

#### Conclusions

The proposed tethered system is an advisable alternative to the presently contemplated micro-*g* laboratory installed near the Space Station C.M. The low frequencies of the long tethers and associated dampers provide a good isolation from Space Station and/or end platform oscillations at a frequency higher than 0.1 Hz (it is possible to improve even further on this score). The tether system has the additional capability of controlling the position of the *g*-laboratory along the tether in order to nullify the gravity gradient or to vary it according to a prescribed profile. The proposed deployment strategy allows the system to reach its final configuration in approximately 3 h. The initial part of deployment, however, requires a more detailed analysis. The active and passive dampers added to the system provide an effective abatement of the longitudinal, librational, and lateral oscillations, as demonstrated by the simulations of the deployment and stationkeeping phase. A thorough analysis of the perturbations acting upon the system is yet required. It will be a topic of investigation in our future studies.

#### Acknowledgments

Acknowledgment is made to Dr. Georg von Tiesenhausen, NASA/MSFC and Mr. William O. Nobles, Martin Marietta Aerospace, who participated in originating the idea of a three-mass tethered *g*-laboratory. Dr. Georg von Tiesenhausen also supported the dynamics analysis of the system, NASA/MSFC Contract NAS8-36606.

#### References

- <sup>1</sup>Sharpe, A. (Ed). "Low Acceleration Characterization of Space Station Environment," Teledyne Brown Engineering, Final Report for NASA/MSFC Contract NAS8-36122, Mod. 6, Oct. 1985.
- <sup>2</sup>Baughner, C.R. (Ed). "Micro-g Requirements Analysis, Space Station RUR-2," EMS Product, Report for NASA/MSFC, WP01, EMS R5.1.4, Aug. 1985.
- <sup>3</sup>Carruthers, J. R., "Acceleration Level Requirements for Microgravity Science on the Space Station," INTEL, Report for NASA/MSFC, May 1985.
- <sup>4</sup>Lorenzini, E. C., "Analytical Investigation of the Dynamics of Tethered Constellations in Earth Orbit," SAO, Final Report for NASA/MSFC under Contract NAS8-35497, Dec. 1984.
- <sup>5</sup>Bekey, I., "Tethers Open New Space Options," *Astronautics and Aeronautics*, April 1983.
- <sup>6</sup>Baker, W. P. et al., "Tethered Subsatellite Study," NASA TMX-73314, March 1976.
- <sup>7</sup>Spencer, T. M., "Atmospheric Perturbation and Control of a Shuttle/Tethered Satellite," Proceeding of the 8th IFAC Symposium on "Automatic Control in Space," Sept. 1980.
- <sup>8</sup>Misra, A. K. and Modi, V. J., "Deployment and Retrieval of Shuttle Supported Tethered Satellites," *Journal of Guidance, Control and Dynamics*, Vol. 5, No. 3, May-June 1982, pp. 278-285.
- <sup>9</sup>Banerjee, A. K. and Kane, T. R., "Tethered Satellite Retrieval with Thruster Augmented Control," *Journal of Guidance, Control and Dynamics*, Vol. 7, No. 1, Jan.-Feb. 1984, pp. 45-50.





# **Dynamics and Control of the Tether Elevator/Crawler System**

E. C. Lorenzini, M. Cosmo, S. Vetrella,  
A. Moccia

Reprinted from



## **Journal of Guidance, Control, and Dynamics**

Volume 12, Number 3, May-June 1989, Pages 404-411  
AMERICAN INSTITUTE OF AERONAUTICS AND ASTRONAUTICS, INC.  
370 L'ENFANT PROMENADE, SW • WASHINGTON, DC 20024

PRECEDING PAGE BLANK NOT FILMED

# Dynamics and Control of the Tether Elevator/Crawler System

E. C. Lorenzini\* and M. Cosmo†

*Harvard-Smithsonian Center for Astrophysics, Cambridge, Massachusetts*  
and

S. Vetrella‡ and A. Moccia‡

*Universita' di Napoli, Naples, Italy*

This paper investigates the dynamics and acceleration levels of a new tethered system for micro- and variable-gravity applications. The system consists of two platforms tethered on opposite sides to the Space Station. A fourth platform, the elevator, is placed in between the Space Station and the upper platform. Variable- $g$  levels on board the elevator are obtained by moving this facility along the upper tether, while microgravity experiments are carried out on board the Space Station. By controlling the length of the lower tether the position of the system center of mass can be maintained on board the Space Station despite variations of the system's distribution of mass. The paper illustrates the mathematical model, the environmental perturbations and the control techniques which have been adopted for the simulation and control of the system dynamics. Two sets of results from two different simulation runs are shown. The first set shows the system dynamics and the acceleration spectra on board the Space Station and the elevator during station-keeping. The second set of results demonstrates the capability of the elevator to attain a preselected  $g$ -level.

## Introduction

CURRENT studies of microgravity experiments onboard the Space Station point out several requirements of such experiments that cannot be met by the microgravity laboratory presently designed for the Space Station. A variety of experiments, encompassing among others life sciences, material processes, and pharmaceutical research, have been proposed for the Space Station's microgravity laboratory. The threshold levels of acceleration noise for such experiments range from  $10^{-2}$  to  $10^{-8}$   $g$ . A facility capable of exploring all or part of the range specified above would greatly enhance the capability of the Space Station in the area of microgravity. On the other hand such a system should not alter the acceleration level onboard the Space Station above the present requirement of  $10^{-5}$   $g$  (at all frequencies) in order to not interfere with the experiments to be carried out on the station.

The system that we propose consists of two end platforms (See Fig. 1), tethered to opposite sides of the Space Station. The upper and lower tethers have a diameter of 2 mm and a length of approximately 10 km. Since the upper and lower platforms are in a pollution-free environment (far from the station), they can be used for observation of the sky and the Earth respectively. The controlled gravity laboratory is located onboard a "space elevator" that can crawl along the upper tether between the Space Station and the upper platform. Microgravity experiments are carried out onboard a stationary laboratory (SML) that is attached to the transverse boom of the station. In order to minimize the gravity gradient acceleration onboard this laboratory, the center of mass (CM) of the system must be as close as possible to the stationary microgravity laboratory.<sup>1</sup> Consequently, the steady-state acceleration level onboard the elevator ranges from  $1.5 \times 10^{-5}$  to  $4 \times 10^{-3}$   $g$  as the elevator moves from the upper boom of

the station to the tether tip, while the length of the lower tether is controlled in order to maintain the system CM at the SML.

This system has been called TECS, which stands for Tether Elevator/Crawler System.

The capability provided by the elevator will allow scientists to solve such major unresolved issues of microgravity science as experimental measurement of threshold values, the influence of  $g$ -jitters and hysteresis problems. Since TECS can maintain the system CM at the appropriate location by controlling the tether lengths, the elevator can maneuver along the tether without interfering with the microgravity experiments carried out on the station.

## Description of the System

The system is formed by the Space Station with a mass of 306 metric tons and a frontal area of  $2.7 \times 10^3$   $m^2$ , by the elevator with a mass of 5 metric tons and a frontal area of 10  $m^2$ , and by two end-platforms  $m_1$  and  $m_4$  with a mass of 10 metric tons and a frontal area of 10  $m^2$  each. The platforms are connected by 2-mm-diam Kevlar tethers with the thermal and mechanical characteristics listed in Table 1.

The distance between the SS and the upper platform is 10 km. The length of the lower tether is adjusted from 10 km to 15 km as a function of the position of EL along the upper tether in order to control the position of the system CM.

Several microgravity processes<sup>1-3</sup> require minimum acceleration levels ranging from  $10^{-2}$  to  $10^{-8}$   $g$  at low frequencies. According to Refs. 1 and 2, the threshold levels of the acceleration for most of the proposed microgravity experiments exhibit a linear dependence upon the frequency for frequencies between  $10^{-1}$  and 1 Hz; and a quadratic dependence above 1 Hz (see Fig. 2 derived from Ref. 1). As shown in Fig. 2, microgravity processes are mostly sensitive to disturbances with frequency smaller than  $10^{-3}$  Hz. Consequently, external perturbations with a frequency content comparable to the orbital frequency, such as acceleration terms generated by aerodynamic forces and  $J_2$  gravity components, strongly affect the microgravity experiments.

On the other hand, the noise arising from among others, structural vibrations, crew motion, vernier thrusters for atti-

Paper presented at the PSN/NASA/ESA/AIDAA/AIAA/AAS Second International Conference on Tethers in Space, Venice, Italy, Oct. 4-8, 1987. Received Nov. 10, 1987; revision received March 14, 1988. Copyright © American Institute of Aeronautics and Astronautics, Inc., 1988. All rights reserved.

\*Staff Scientist, Radio and Geoastronomy Division.

†Visiting Scientist, Radio and Geoastronomy Division.

‡Chair of Aerospace Systems Engineering.

tude control and spacecraft dockings, usually called *g*-jitters, have frequencies greater than  $10^{-3}$  Hz, and are less of a problem according to Fig. 2.

In addition, longitudinal vibrations of the tethers are excited by thermal shocks, which take place at the crossing of the terminator. Given the actual mechanical characteristics and lengths of the tethers of our system, these oscillations, also called thermal *g*-jitters, have a frequency range from  $10^{-3}$  to  $10^{-2}$  Hz. According to Fig. 2, those are of intermediate importance to the microgravity experiments.

In the next sections we will address the impact of TECS on the acceleration level onboard the Space Station. We will also

evaluate the acceleration fluctuations, onboard the elevator, caused by environmental perturbations with respect to scientific requirements.

## Mathematical Model

### Equations of Motion

The motion of this tethered system is described with respect to an orbiting reference frame (ORF) that rotates at constant orbital rate  $\Omega$  and radius  $R_0$ . The origin of this frame coincides with the initial position of the system CM (see Fig. 3). The  $x$  axis is along the ORF velocity vector, the  $z$  axis is along the local vertical toward the Earth, and the  $y$  axis completes the right-handed reference frame.

An Earth-centered inertial reference frame (IRF) is also erected. The  $X$  axis points toward the vernal equinox, the  $Z$  axis points toward the North Pole and the  $Y$  axis completes the right-handed reference frame.

The three-dimensional mathematical model, adopted for our analysis, has been developed according to the following assumptions: lumped masses, elastic tethers and generic orbit of the system.<sup>4,5</sup>

If we denote  $r_i$  as the position vector of the  $i$ th mass  $m_i$  with respect to ORF,  $F_{g,i}$ ,  $F_{d,i}$  and  $F_{T,i}$  as the gravity, drag, and tensional forces acting respectively upon the  $i$ th mass, the equations of motion of the  $N$  masses of the system in vectorial form are

$$\ddot{r}_i = -\ddot{R}_0 - 2\Omega \times \dot{r}_i - \Omega \times (\Omega \times r_i) + (1/m_i)(F_{g,i} + F_{d,i} + F_{T,i}), \quad i = 1, \dots, N \quad (1)$$

where the prime denotes derivation with respect to time. Equations (1) are a set of  $N$  vectorial equations or correspondingly a set of  $3 \times N$  scalar equations that have to be integrated numerically in order to obtain the motion of the system.

### Environmental Models

Because of the very low acceleration levels in which we are interested, an accurate model of external forces is necessary in order to simulate with high enough fidelity the effects of the environment on the system dynamics. The external perturbations considered in the present analysis are the gravitational forces  $F_g$ , the aerodynamic forces  $F_d$ , and the thermal effects on the tensional forces  $F_T$ .

Unlike other tether simulation models,<sup>6,7</sup> our gravity model is not linearized and takes into account the second zonal harmonic of the gravity field ( $J_2$  term). The  $J_2$  term has a secular effect on such orbital parameters of the system as mean anomaly, argument of perigee, and right ascension of the ascending node. The  $J_2$  term also affects the librations and lateral oscillations (see next section) of a long multimass tethered system such as the one under analysis.

The drag model is an analytical fit of Jacchia's 1977 density model.<sup>8,9</sup> The atmospheric density varies as a function of the altitude (the Earth's oblateness is also considered) and the local exospheric temperature. The latter takes into account the diurnal variation, which is a function of local solar time, latitude, and solar activity.

The thermal inputs on the tether segments are the solar illumination, the Earth's albedo, and the infrared Earth radiation. The only cooling process is the emitted radiation. The position of the terminator is computed as a function of the Sun's position along the ecliptic. As the system crosses the terminator, the tether temperature varies abruptly; consequently, the tether segments expand or contract and the tethers' tensions exhibit steep variations. The  $N - 1$  equations of the thermal balance of the tether segments are added to

Table 1 Characteristics of Kevlar tether

Young's modulus	$1.96 \times 10^{10}$ N/m <sup>2</sup>
Absorptivity, $\alpha$	0.75
Emissivity, $\epsilon$	0.5
Specific heat	2500 J/Kg-K
Linear density	$4.85 \times 10^{-3}$ Kg/m
Coefficient of thermal expansion	$-2 \times 10^{-6}$ K <sup>-1</sup>

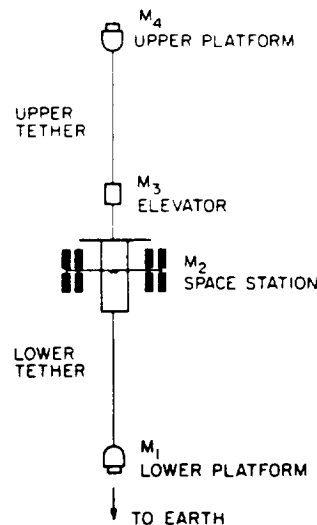


Fig. 1 Schematic of tether elevator/crawler system.

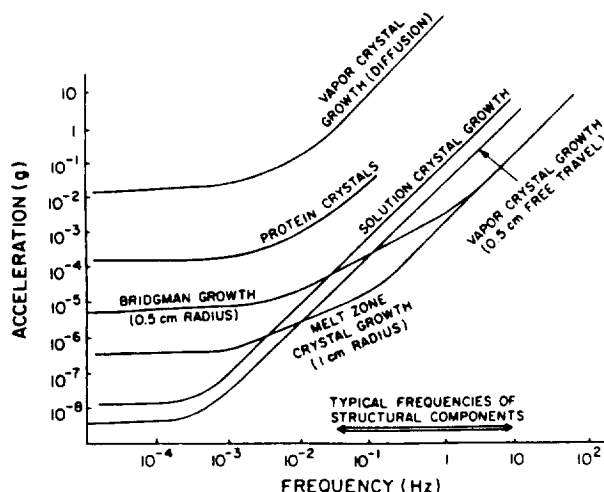


Fig. 2 Acceleration sensitivity of material processes.<sup>1</sup>

Eqs. (1). The thermal equation of the  $j$ th tether segment is given by

$$\dot{T}_j = \frac{2r_j \alpha_j I_{\text{sun,inc}} + a I_{\text{sun}} \alpha_j r_j f_j \cos \gamma_j + 2\pi r_j \sigma \tilde{\alpha}_j f_j T_{\oplus}^4 - 2\pi r_j \sigma \epsilon_j T_j^4}{\rho_j c_j \pi r_j^2}$$

$$j = 1, \dots, N-1 \quad (2)$$

where

- $a$  = Earth albedo (annual average)
- $c_j$  = specific heat of  $j$ th tether
- $f_j$  = view factor of  $j$ th tether
- $I_{\text{sun}}$  = solar flux
- $I_{\text{sun,inc}}$  = solar flux incident on tether
- $I_{\text{sun}}$  and  $I_{\text{sun,inc}}$  are equal to zero during the eclipses
- $r_j$  = radius of  $j$ th tether
- $T_j$  = temperature of  $j$ th tether
- $T_{\oplus}$  = Earth temperature
- $\alpha_j$  = absorptivity of  $j$ th tether
- $\tilde{\alpha}_j$  = infrared absorptivity of  $j$ th tether
- $\epsilon_j$  = emissivity of  $j$ th tether
- $\gamma_j$  = sun zenith angle of  $j$ th tether
- $\sigma$  = Stefan-Boltzmann constant
- $\rho_j$  = volume density of  $j$ th tether

### System Dynamics

#### Degrees of Freedom

The coordinates  $x, y, z$ , of the point masses with respect to the ORF are numerically integrated by the computer code with a fourth-order Runge-Kutta or a predictor-corrector integration routine.

A second set of coordinates has also been selected in order to provide a more direct description of the system dynamics. This set of coordinates is formed by (see Fig. 3): the in-plane (in the orbital plane)  $\theta$  and out-of-plane (orthogonal to the orbital plane)  $\phi$  angles of libration between the line connecting the end-masses and the local vertical through the system CM; the  $N-1$  lengths of tether segments  $\ell_j$ , where  $N$  is the number of the lumped masses and the  $N-2$  lateral deflections  $\epsilon_j$  of the inner masses with respect to the line through the end-masses. The coordinates  $\epsilon_j$  are further projected onto the in-plane  $\epsilon_{ji}$  and out-of-plane components  $\epsilon_{oj}$ .

This set of parameters identifies such characteristic oscillations of the system as the low frequency  $f$  librations ( $f \approx 10^{-4}$  Hz), the medium frequency lateral oscillations ( $f \approx 10^{-3}$  Hz), and the higher frequency longitudinal oscillations ( $10^{-3} \text{ Hz} < f < 10^{-2} \text{ Hz}$ ).

#### Accelerations

The acceleration measured by an accelerometer package onboard any platform of the system is the sum of the external, excluding the gravitational, and internal forces (e.g., tensions) acting upon a platform divided by the mass of that platform. Since the platforms librate approximately like the overall tethered system, an accelerometer package onboard a platform (e.g., the elevator) does not measure the orthogonal components of the acceleration caused by the librations (as an accelerometer package on a pendulum measures zero along the axes orthogonal to the pendulum).

First we erect the orbiting reference frame  $x_{CM}y_{CM}z_{CM}$  (CMRF) that is like the previously defined ORF except for the origin of CMRF which coincides with the instantaneous CM of the system. Since the attitude dynamics of the individual platforms are not modeled in the present code, the best approximation to a body reference frame is the system-body reference frame (SBRF). This frame of coordinates is rotated by the two angles  $\theta$  and  $\phi$  with respect to the CMRF (see Fig. 3). The accelerations measured onboard the Space Station and the space elevator are projected onto the SBRF whose compo-

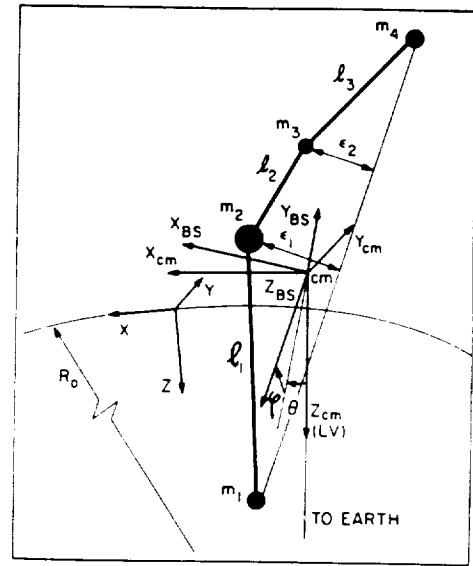


Fig. 3 Reference frames.

nents are the most meaningful for the experimenter. The acceleration components of the SBRF are as follows: the front component along the  $x_{SB}$  axis, the side component along the  $y_{SB}$  axis, and the longitudinal component along the  $z_{SB}$  axis.

#### Damping of Oscillations

The system has several oscillations, associated with some of its degrees of freedom, that can affect the "quality" of the accelerations measured on board the Space Station and the space elevator.

As pointed out in previous papers,<sup>10,11</sup> the tethers introduce a "noise" at the longitudinal vibration frequencies that may impair the performance of the system. Lateral deflections and longitudinal oscillations also have a nonnegligible effect on the accelerations on board the elevator.

At the orbital inclination of 28.5 deg the in-plane perturbations are much stronger than the out-of-plane perturbations. In-plane oscillations, furthermore, are excited by Coriolis forces during transient maneuvers of the system (e.g., deployment and crawling maneuvers), while out-of-plane oscillations are not. Luckily the in-plane oscillations are much easier to damp out by means of tether control than the out-of-plane oscillations.

This section explains briefly the strategy that we adopt for damping the in-plane oscillations by controlling the lengths of the tethers. A more thorough treatment of this rather complex topic, which is beyond the scope of this paper, will be presented in a future paper.

Damping of longitudinal tether vibrations is provided by passive (spring-dashpot systems in series with each tether segment) or active (reel control) dampers. The latter is the most likely mechanization of the longitudinal dampers because a passive damper would be required to stretch tenths of meters. In the active case, the  $i$ th reel controls the tension of the associated tether segment with a proportional-derivative control law. The  $i$ th control law is tuned to the frequency of the longitudinal oscillations of the  $i$ th tether segment. The derivative term is such as to provide a damping ratio of 90% of the critical value which provides an effective damping of the longitudinal (spring-mass mode) oscillations.

The in-plane libration and the in-plane lateral oscillations are damped out by exploiting the Coriolis forces. The reels control the tether lengths with terms proportional to the libration angle  $\theta$  and the in-plane components of the lateral deflections  $\epsilon_{ji}$  in such a way as to extract energy from the above mentioned oscillations. In-plane Coriolis forces have a

strong coupling with the displacements of the platforms in the orbital plane. An effective damping of the libration and of the lateral oscillations can be obtained by controlling the tether lengths in opposition to the oscillations to be damped out.

As a conclusion to this section we wish to point out that the longitudinal dampers must be activated throughout the mission in order to damp out the oscillations arising from the thermal shocks. The in-plane dampers, on the contrary, are only necessary during transient phases (e.g., deployment and crawling maneuvers). The in-plane dampers, however, can be conservatively activated during steady-state phases (e.g., station-keeping) in order to improve (slightly) the performance during such phases. Out-of-plane dampers are not necessary under normal conditions. Active thrusters could be used sporadically under emergency conditions.

#### Elevator's Control

The most peculiar feature of TECS is the capability of the elevator to crawl along the upper tether in order to produce an assigned  $g$  profile vs time onboard the elevator. One of these maneuvers consists of moving the elevator from its initial location, and consequently initial  $g$  level, to a final position with a different  $g$  level. This maneuver is usually called  $g$  tuning and it is designed for exploring acceleration thresholds of microgravity experiments.

A control law, suitable for this maneuver, must meet the following requirements: 1) acceleration and deceleration phases as smooth as possible, 2) small perturbations of the system dynamics, and 3) capability of maintaining the acceleration level onboard the Space Station below  $10^{-5} g$ .

Toward this end we derived a modified hyperbolic tangent control law<sup>11</sup> (MHT) with the addition of a constant velocity phase.<sup>12</sup> The constant velocity phase starts at the end of the acceleration phase when the maximum velocity is reached, and the acceleration is equal to zero. The hyperbolic tangent is resumed at the end of the constant velocity phase to decelerate the elevator. Since the hyperbolic tangent is asymptotic, a cut-off distance  $\sigma$  from the target point on the tether has been adopted in order to limit the total travel time. In terms of the variation of the traveled tether length  $\Delta\ell$  vs time, the control law for the elevator's motion can be expressed as follows:

Acceleration

$$t < t_A$$

$$\Delta\ell_c = \Delta\ell'_c [\tanh(\alpha t)]^\gamma \quad (3a)$$

Constant Velocity

$$t_A \leq t < t_B$$

$$\Delta\ell_c = \Delta\ell'_c [\tanh(\alpha t_A)]^\gamma + \Delta\ell''_c \frac{t - t_A}{t_B - t_A} \quad (3b)$$

Deceleration

$$t_B \leq t \leq t_\sigma$$

$$\Delta\ell_c = \Delta\ell'_c \{\tanh\alpha[t - (t_B - t_A)]\}^\gamma + \Delta\ell''_c \quad (3c)$$

where

$\Delta\ell'_c$  = tether length traveled during acceleration plus tether length traveled during deceleration

$\Delta\ell''_c$  = tether length traveled during the constant-velocity phase

$t_A$  = time at which the maximum velocity is reached

$t_B$  = time at the end of the constant-velocity phase

$t_\sigma$  = time at the cut-off distance  $\sigma$  from the target point

$\alpha$  = rate parameter

$\gamma$  = shape parameter

The ratio of the tether length traveled during acceleration plus deceleration to the total length traveled is the dimensionless parameter  $\chi$ . Calling the total length traveled  $\Delta\ell_{cT}$ , we have

$$\Delta\ell_{cT} = \Delta\ell'_c + \Delta\ell''_c \quad (4a)$$

$$\Delta\ell'_c = \chi \Delta\ell_{cT} \quad (4b)$$

$$\Delta\ell''_c (1 - \chi) \Delta\ell_{cT} \quad (4c)$$

By using the three control parameters  $\alpha$ ,  $\gamma$ , and  $\chi$ , the total travel time, the maximum crawling velocity, and the acceleration profile vs time can be conveniently adjusted to meet the first two requirements. The transition between two sequential segments of the control law is smooth since the acceleration has no discontinuity (specifically the acceleration is equal to zero at transition). Consequently, the elevator crawls along the tether according to three sequential and smoothly continuous phases.

In order to meet the third requirement, the lower reel controls the lower tether according to Eq. (3), where the length variations  $\Delta\ell'_c$  and  $\Delta\ell''_c$  have been scaled down by the factor  $m_3/m_1$ . Because of this compensatory control, the system CM is maintained very close to its initial position during the elevator's maneuver.

Since a long Kevlar tether is highly deformable, the total traveled length  $\Delta\ell_{cT}$  must be corrected for the elastic deformation of the tether if the desired final distance between the Space Station and the elevator is to be attained with good accuracy. This corrective term is easily computed before starting the maneuver.

As a result of a parametric analysis of the MHT control law, we found that for a typical long-distance-maneuver (e.g.,  $\Delta\ell_{cT} = 4$  km) an appropriate choice of the control parameter is  $\alpha = 10^{-3} s^{-1}$ ,  $\gamma = 4$ , and  $\chi = 0.2$ . The cut-off distance  $\sigma$  was assumed equal to 1 m. The results of a simulation run, in which the elevator maneuvers according to Eqs. (3) and the previously selected control parameters, is shown later on in this paper.

## Numerical Results

### Station-Keeping

The first set of numerical results are relevant to a station-keeping simulation run. The system is initially at rest and aligned with LV. The elevator is at 1 km from the Space Station and the lower tether is 10.5 km long. The sun is at the summer solstice and the initial tether temperature is 290 K for all tether segments. All the environmental perturbations modeled in our code are acting upon the system. The longitudinal and in-plane lateral/librational dampers are activated during the entire simulation run. The duration of the simulation run is 20 orbits in order to show the very long frequency beating phenomena. The Space Shuttle orbits at an initial altitude of 450 km and an inclination of 28.5 deg. The orbital period is equal to 5615 s.

The acceleration components measured onboard the Space Station and the relative spectra are depicted in the following figures: the front component and its spectrum in Figs. 4a and 4d; the side component and its spectrum in Figs. 4b and 4e; the longitudinal component and its spectrum in Figs. 4c and 4f. None of the spectra of this section show the dc components that have been removed from the acceleration components before computing the fast Fourier transforms.

The amplitudes of the front and side accelerations are of the order of  $10^{-8} g$ . The amplitudes are influenced by the librations and their coupling with the lateral oscillations. In particular, the side component shows a beating phenomenon between the out-of-plane libration and the out-of-plane lateral oscillations. The spectrum of the front acceleration component (Fig. 4d) shows a main harmonic at the orbital frequency

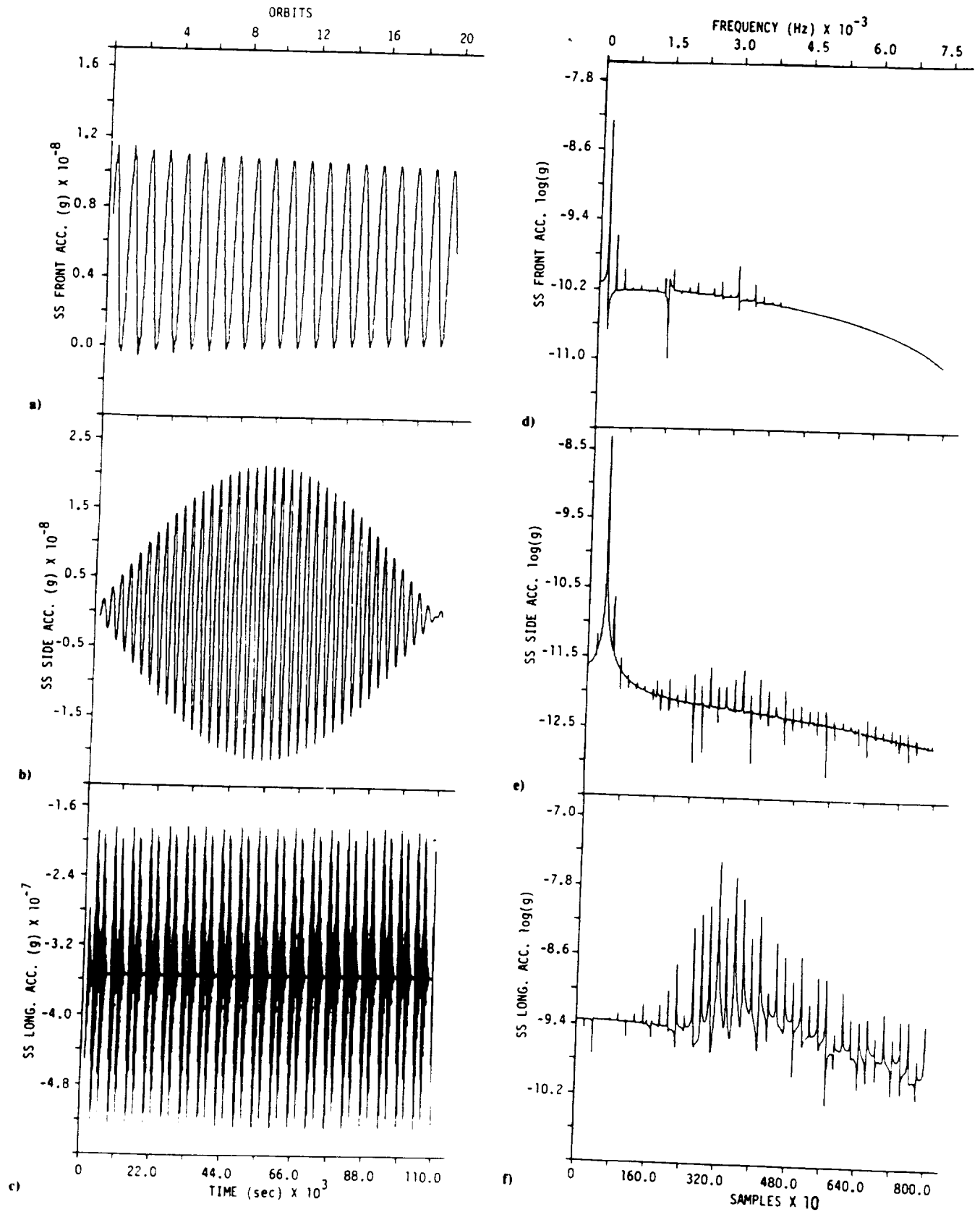


Fig. 4 Space Station acceleration components: a) front, b) side, and c) longitudinal. Space Station acceleration spectra: d) front, e) side, and f) longitudinal.

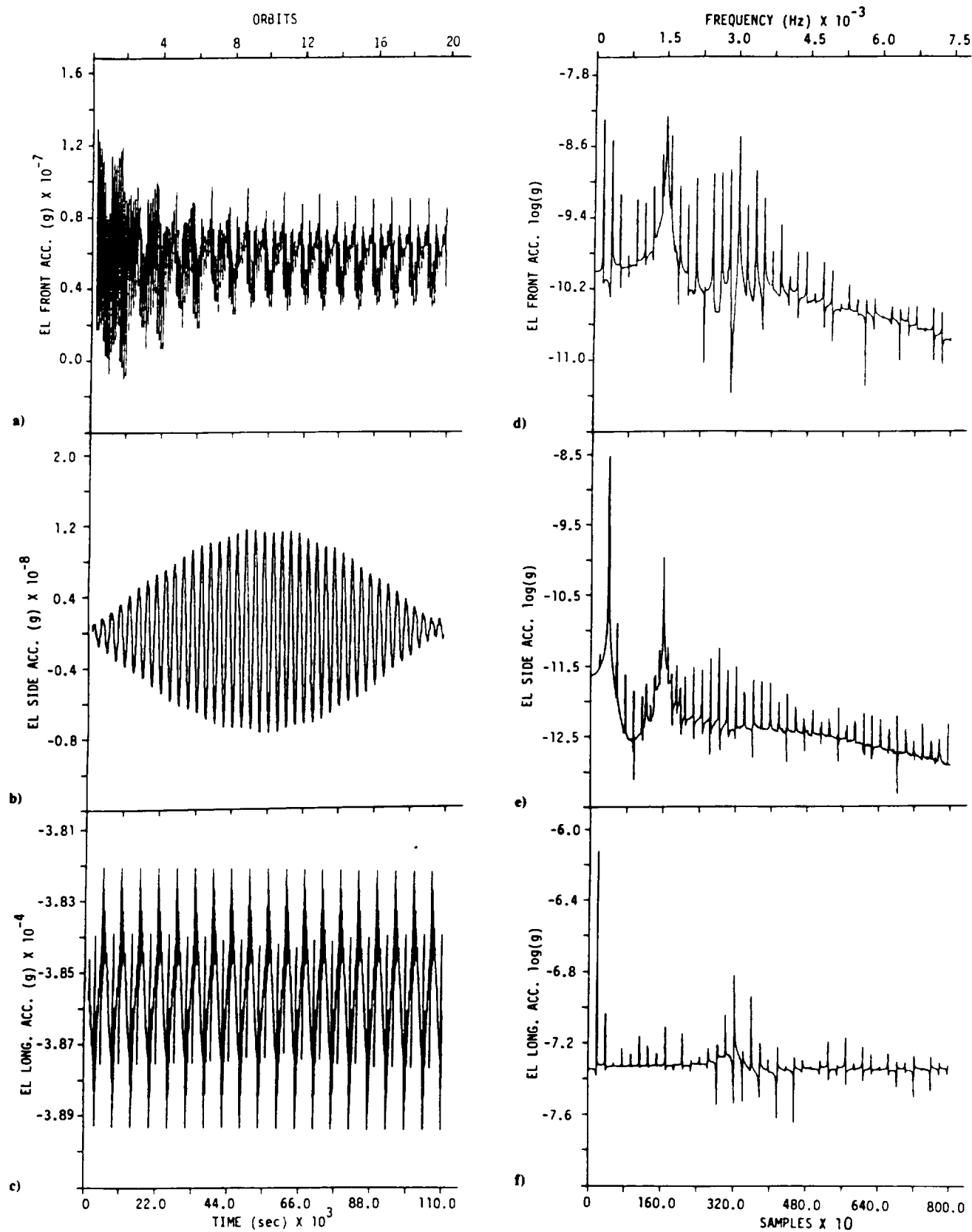


Fig. 5 Elevator acceleration components: a) front, b) side, and c) longitudinal. Elevator acceleration spectra: d) front, e) side, and f) longitudinal.

( $f = 1.8 \times 10^{-4}$  Hz) and a smaller harmonic at twice the orbital frequency, both caused by the  $J_2$  gravity term and the drag. In particular the Space Station accounts for the major contribution to the drag. The spectrum of the lateral acceleration component (Fig. 4e) shows two harmonics at the same frequencies as the previous case but with inverted amplitudes.

The longitudinal acceleration exhibits a dc component of  $3.6 \times 10^{-7}$  g arising from the offset between the system CM and the orbital center (the zero acceleration point of the system). This dc component can be eliminated by adjusting the length of the lower tether in order to place the orbital center at the SML onboard the Space Station where the acceleration is measured. In this simulation run, however, we have decided to show the effect of the above-mentioned offset upon the acceleration level onboard the SML. The longitudinal acceleration component exhibits relatively strong thermal jitters, which are caused by the crossing of the terminator and are subsequently abated by the in-line dampers (Fig. 4c). The spectrum of the longitudinal acceleration component in Fig. 4f shows frequencies, higher than the orbital frequency, of approximately  $3 \times 10^{-3}$  Hz, which are typical of longitudinal oscillations (excited by thermal shocks).

This analysis demonstrates, within the assumptions of our model, that TECS provides a negligible contribution to the acceleration noise onboard the Space Station.

The acceleration components measured onboard the elevator and the relative spectra are depicted in the following set of figures: the front component and its spectrum in Figs. 5a and 5d; the side component and its spectrum in Figs. 5b and 5e; and the longitudinal component and its spectrum in Figs. 5c and 5f. The front and side components show harmonics at the orbital frequency and at twice the orbital frequency that are caused by the  $J_2$  term and by the drag. The drag also accounts for the dc component of the front acceleration. The higher frequency harmonics in the spectra are generated by thermal shocks. The orders of magnitude of the fluctuations of the front and side components are  $10^{-7}$  and  $10^{-8}$  g, respectively.

The longitudinal acceleration component is shown in Fig. 5c. The longitudinal acceleration has a dc component of  $-3.86 \times 10^{-4}$  g, which is provided by the gravity gradient caused by the offset between the EL and the orbital center. The harmonic at the orbital frequency (see Fig. 5f), with an amplitude of the order of  $10^{-6}$  g, is caused by the  $J_2$  gravity term. The  $J_2$  component forces the system to librate, hence

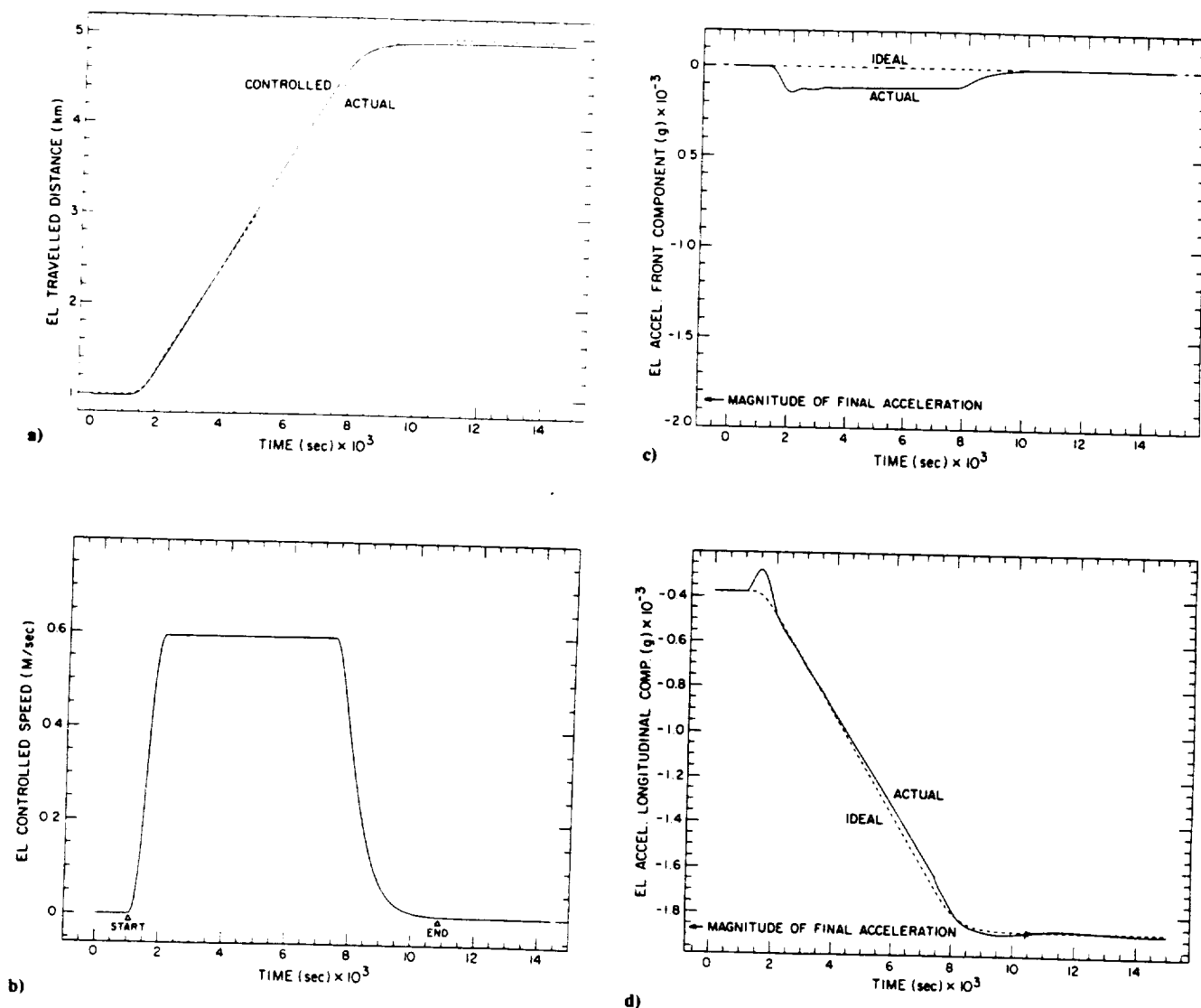


Fig. 6 Dynamics properties of elevator during a crawling maneuver: a) distance, b) speed, c) front acceleration, and d) longitudinal acceleration.



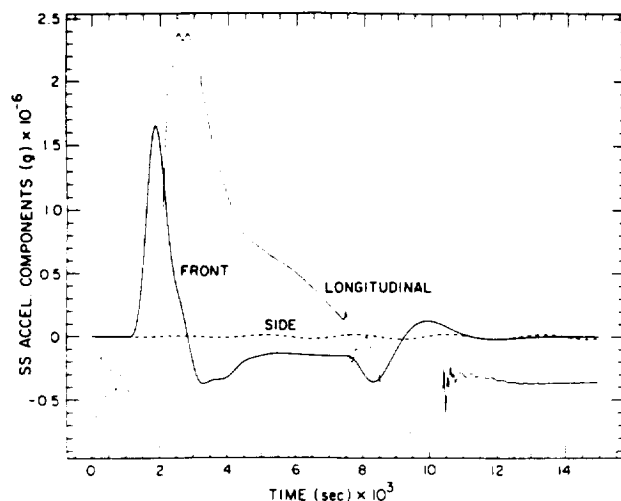


Fig. 7 Acceleration components onboard the Space Station.

stretching the tethers with the libration frequency. The tether tensions produced by this mechanism balance out at the system CM. Since the elevator is offset from the CM, the  $J_2$ -induced tether tensions apply a differential force to the elevator, which accounts for the spectral line at the orbital frequency. The higher-frequency harmonics of the longitudinal acceleration component are centered around the longitudinal natural frequency of the upper tether system. These higher-frequency components are generated by thermal shocks.

#### Crawling Maneuvers

We show in this section the results of a typical crawling maneuver. The system is initially at rest and aligned with LV. At time  $t = 1000$  s the elevator starts moving, according to Eqs. (3), from the initial distance of 1 km from the Space Station to the final distance of 5 km from the Space Station. The control parameters are those selected in the previous section. At the same time, the length of the lower tether is controlled in order to compensate for the elevator's displacement. In this case the thermal perturbations are negligible with respect to the variations of the acceleration level and therefore have been neglected.

The actual distance from the Space Station and the controlled distance traveled by the elevator are depicted in Fig. 6a. The elevator-controlled velocity is shown in Fig. 6b. The front and longitudinal acceleration components onboard the elevator are shown in Figs. 6c and 6d. Both the acceleration components onboard the elevator are compared to the respective unperturbed components (ideal case of an elevator that moves without perturbing the system). The front component during the maneuver is affected by the Coriolis force, while the longitudinal component is mostly affected by the elasticity of the system. The side acceleration component is not shown, because it is negligible with respect to the other components.

The acceleration components onboard the elevator, of which the longitudinal component is the greatest, have a behavior close to the ideal and achieve smoothly the steady-state values at the end of the crawling, as required by a g-tuning type of maneuver.

The acceleration components onboard the Space Station, along the SBRF, are depicted in Fig. 7. Since the lower platform is controlled in such a way as to balance the elevator's motion, the acceleration level onboard the Space Station are well within the requirement for microgravity experiments.

#### Conclusions

The proposed tethered system supplements the Space Station with a facility for carrying out experiments in a con-

trolled gravity environment. The acceleration level onboard the elevator can be tuned between  $1.5 \times 10^{-5}$  and  $4 \times 10^{-3}$  g, making possible the exploration of threshold acceleration levels for several experiments proposed by the microgravity scientific community.

The "quality" of the acceleration onboard the elevator is as follows: the longitudinal component is the most critical, with harmonic components of  $10^{-6}$  g at frequencies lower than  $10^{-3}$  Hz and of  $10^{-7}$  g for frequencies between  $10^{-3}$  and  $10^{-2}$  Hz. The front component of the acceleration depends primarily on the drag of the Space Station and ultimately on its configuration. The side component of the acceleration is negligible. The quality of the acceleration onboard the elevator is therefore better than onboard the stationary microgravity laboratory of the Space Station.

This tethered system moreover, can control the vertical position of the system center of mass despite a modification of the system's configuration. In particular, we have demonstrated the system's capability of maintaining the acceleration level on the station within the microgravity requirements, notwithstanding the elevator's maneuvers along the upper tether in performing g-tuning experiments.

The proposed system does not have an appreciable impact on the acceleration level onboard the Space Station. The tethered-system-related noise is a few orders of magnitude less than the  $10^{-5}$  g acceleration level specified for the station.

#### Acknowledgments

This paper has been supported in the United States by NASA/MSFC Contract NAS8-36606, with James Harrison and Chris Rupp as Program Directors, and in Italy by PSN/CNR Contract. The authors would also like to thank Ms. Catherine Mannick for the help provided in editing the paper.

#### References

- <sup>1</sup>Sharpe, A. (ed), "Low Acceleration Characterization of Space Station Environment," Teledyne Brown Engineering, Final Rept. for NASA/MSFC Contract NAS8-36122, Mod. 6, Oct. 1985.
- <sup>2</sup>Baughner, C. R. (ed), "Micro-g Requirements Analysis, Space Station RUR-2," EMS Product, Rept. for NASA/MSFC, WPO1, EMS R5.1.4, Aug. 1985.
- <sup>3</sup>Carruthers, J. R., "Acceleration Level Requirements for Microgravity Science on the Space Station," INTEL, Rept. for NASA/MSFC, May 1985.
- <sup>4</sup>Kalaghan, P. M., Arnold, D. A., Colombo, G., Grossi, M. D., Kirshner, L. R., and Orringer, O., "Study of the Dynamics of a Tethered Satellite System (SKYHOOK)," Smithsonian Astrophysical Observatory Final Rept. for NASA/MSFC, Contract NAS8-32199, March 1978.
- <sup>5</sup>Lang, D. D., "TOSS Reference Manual," NASA NAG9-16715, Vol. 1, May 1985.
- <sup>6</sup>Baker, P. W., Dunkin, J. A., Galabott, Z. J., Johnston, K. D., Kissel, R. R., Rheinfurt, M. H., and Siebel, M. P. L., "Tethered Subsatellite Study," NASA TMX-73314, March 1976.
- <sup>7</sup>Spencer, T. M., "Atmospheric Perturbation and Control of a Shuttle/Tethered Satellite," *Proceedings of the Eighth IFAC Symposium*, edited by C. W. Munsay, Pergamon, New York, 1980.
- <sup>8</sup>Roberts, C. E., "An Analytical Model for Upper Atmosphere Densities Based Upon Jacchia's 1970 Models," *Celestial Mechanics*, Vol. 4, 1971, pp. 368-377.
- <sup>9</sup>Jacchia, L. G., "Thermospheric Temperature, Density and Composition: New Models," Smithsonian Astrophysical Observatory, Cambridge, MA, Rept. SR375, March 1975.
- <sup>10</sup>Lorenzini, E. C., "A Three-Mass Tethered System for Micro-g/Variable-g Applications," *Journal of Guidance, Control, and Dynamics*, Vol. 10, May-June 1987, pp. 242-249.
- <sup>11</sup>Lorenzini, E. C., "Artificial Gravity Laboratory," *Tether Dynamics Simulation*, NASA CP 2458, pp. 141-160, 1987.
- <sup>12</sup>Swenson, F. R., "Tether Crawler System," Tri-State Univ., Angola, IN, Rept. for NASA-MSFC, Contract NGT 01-002-099, Aug. 1986.



## WAVE PROPAGATION IN THE TETHER ELEVATOR/ CRAWLER SYSTEM†

ENRICO C. LORENZINI and MARIO COSMO

Harvard-Smithsonian Center for Astrophysics, 60 Garden Street, Cambridge, MA 02138, U.S.A.

(Received 31 August 1989; revised version received 18 April 1990)

**Abstract**—This paper analyzes the propagation of disturbances along the upper-tether of the Tether Elevator-Crawler System. Both longitudinal and transverse waves are investigated as the waves propagate from the station to the elevator, and beyond to the upper-platform. The model takes into account the effects of gravity gradient and material damping. An estimate of the various damping mechanisms affecting transverse waves is also provided in the paper. The frequency response functions at the elevator and at the upper-platform are computed for either a longitudinal or a transverse perturbation of the tether attachment point to the station.

### 1. INTRODUCTION

The Tether Elevator-Crawler System [1] (TECS) is designed for carrying out experiments in a controlled gravity environment. A schematic of TECS is shown in Fig. 1. An elevator (EL) is attached to a 10-km-long tether which connects the station to the upper-platform (UP). On the other side of the station the lower-tether system is deployed. The length of the lower-tether is adjusted in order to keep the orbital center (the point of zero apparent acceleration) of the whole system at the desired location on the station during the elevator's maneuvers.

By moving the elevator along the tether, the level of apparent acceleration on-board the elevator can be varied according to a pre-set profile. The quality of the acceleration level is an important requirement for those conducting experiments in the microgravity laboratory. Suitable control laws for the elevator motion have been devised [1,2] whereby the acceleration fluctuations during the elevator motion are smaller than 10% of the maximum value of the steady-state acceleration.

Another important source of acceleration noise, however, is the space station itself. Any perturbation that reaches the attachment point of the tether to the station propagates along the tether and eventually perturbs the gravity laboratory on the elevator. An analysis of how the perturbation propagates along the upper-tether of TECS is therefore of primary importance for assessing the actual quality of the acceleration on the elevator.

The space station (SS) is a source of non-negligible disturbances at a wide range of frequencies. In general, the low frequency (around  $10^{-3}$  Hz) disturbances are associated with aerodynamic and orbital

perturbations, the medium frequency (from  $10^{-2}$  to 10 Hz) disturbances with the structural vibrations of the station; and the high frequency ( $> 10$  Hz) disturbances with rotating machinery and human activity on-board the station.

The wave propagation along the tether is influenced by the tether material damping and to some extent by the dissipative medium surrounding the tether and the platforms. The tether is a complex non-isotropic continuum and the damping varies with the tether length according to a function which depends on the damping model adopted. Furthermore, material damping of kevlar™ tethers is significantly affected by temperature.

Recent investigations [3,4] have shown that the damping of a kevlar tether is best represented by a combination of viscous and structural damping. This conclusion, however, is based upon a few experimental results obtained from short tether samples. Given the level of uncertainty of the test results, the most accredited value of material damping ranges between 1 and 5% for the first longitudinal mode of a 10-km tether.

The material damping affects primarily the propagation of longitudinal waves, while it has a much smaller effect on transverse waves [3]. Transverse waves are also influenced by the interaction with the surrounding atmosphere more than longitudinal waves. A preliminary estimate of the damping provided by these mechanisms with respect to transverse waves is given later on in the paper.

### 2. MATHEMATICAL MODEL

Figure 2 shows the upper portion of TECS and the reference frames. If we assume the realistic case of small perturbations, we can treat the longitudinal and the transverse waves independently [5]. For each set of waves we will compute the dynamic response to a

†Paper presented at the *Tether Dynamics Workshop*, San Francisco, Calif., U.S.A., 16 May 1989.

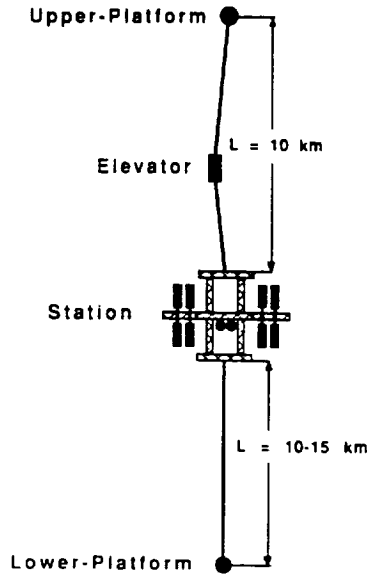


Fig. 1. Schematic of Tether Elevator/Crawler System (TECS).

sinusoidal excitation of the tether attachment point to the space station, that is the frequency response function (FRF). The perturbation acts along the tether axis for the longitudinal waves while it acts transversely to the tether axis for the transverse waves. We also assume that the elevator and the upper-platform are point masses. We start by analyzing the longitudinal waves.

### 2.1. Longitudinal waves

With reference to Fig. 2 the equations of motion and the boundary conditions are as follows [6]:

$$\begin{aligned} \mu \frac{\partial^2 u_j}{\partial t^2} &= \left\{ EA + E'A \frac{\partial}{\partial t} \right\} \frac{\partial^2 u_j}{\partial z_j^2} + 3\Omega^2 \mu u_j, \quad j = 1, 2 \\ m_2 \frac{\partial^2 u_2}{\partial t^2} &= - \left\{ EA + E'A \frac{\partial}{\partial t} \right\} \frac{\partial u_2}{\partial z_2} + 3\Omega^2 m_2 u_2, \quad z_2 = L_2 \end{aligned} \quad (1)$$

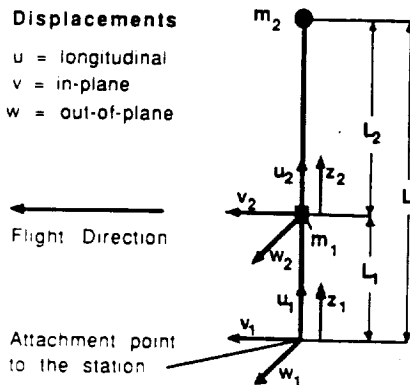


Fig. 2. Schematic of upper-tether of TECS and reference frames.

$$\begin{aligned} m_1 \frac{\partial^2 u_1}{\partial t^2} &= - \left\{ EA + E'A \frac{\partial}{\partial t} \right\} \frac{\partial u_1}{\partial z_1} - \left\{ EA \right. \\ &\quad \left. + E'A \frac{\partial}{\partial t} \right\} \frac{\partial u_2}{\partial z_2} + 3\Omega^2 m_1 u_1, \quad z_1 = L_1; \quad z_2 = 0 \\ u_2(0, t) &= u_1(L_1, t) \\ u_1 &= \exp(i\omega t), \quad z_1 = 0 \end{aligned}$$

where  $z_1$  and  $z_2$  are the vertical coordinates for tether segments 1 and 2,  $u_1$  and  $u_2$  the longitudinal tether stretches,  $\mu$  the tether linear density,  $\Omega$  the orbital rate,  $m_1$  and  $m_2$  the masses of the elevator and the upper-platform respectively,  $EA$  the tether stiffness, and  $E'A$  the tether axial viscosity. In eqns (1) we have adopted a viscous damping model for the tether. This is a reasonable approximation given the uncertainties regarding material damping of long kevlar tethers. Results obtained with a viscous damping model can be applied to a different damping model in the neighborhood of a given frequency for which an equivalent viscous damping coefficient has been computed. The boundary conditions express the balance of the forces on masses  $m_1$  and  $m_2$ , and the tether continuity at the elevator.

After defining  $u_1 = u_1/L_1$ ,  $u_2 = u_2/L_2$ ,  $z_1 = z_1/L_1$ ,  $z_2 = z_2/L_2$ ,  $t = t\Omega$  and  $\omega = \omega/\Omega$  we obtain non-dimensional equations as follows:

$$\begin{aligned} \frac{\partial^2 u_j}{\partial t^2} &= \epsilon_j^2 \left\{ 1 + b \frac{\partial}{\partial t} \right\} \frac{\partial^2 u_j}{\partial z_j^2} + \gamma u_j, \quad j = 1, 2 \\ \frac{\partial^2 u_2}{\partial t^2} &= -\epsilon_2^2 a_2 \lambda_2 \left\{ 1 + b \frac{\partial}{\partial t} \right\} \frac{\partial u_2}{\partial z_2} + \gamma u_2, \quad z_2 = 1 \\ \frac{\partial^2 u_1}{\partial t^2} &= -\epsilon_1^2 a_1 \gamma_1 \left\{ 1 + b \frac{\partial}{\partial t} \right\} \frac{\partial u_1}{\partial z_1} \\ &\quad - \epsilon_2^2 a_1 \lambda_2 \left\{ 1 + b \frac{\partial}{\partial t} \right\} \frac{\partial u_2}{\partial z_2} + \gamma u_1, \quad (2) \\ z_1 &= 1; \quad z_2 = 0 \\ u_2(0, t) &= u_1(1, t) \\ u_1 &= \exp(i\omega t), \quad z_1 = 0. \end{aligned}$$

The non-dimensional coefficients in eqns (2) are given by:  $\epsilon_1 = c/\Omega L_1$ ;  $\epsilon_2 = c/\Omega L_2$ ;  $a_1 = L\mu/m_1$ ;  $a_2 = L\mu/m_2$ ;  $\lambda_1 = L_1/L$ ;  $\lambda_2 = L_2/L = 1 - \lambda_1$ ;  $b = E'A\Omega/EA$  and  $\gamma = 3$ , where  $c = (EA/\mu)^{1/2}$  is the longitudinal wave speed,  $L_1$  and  $L_2$  are the lengths of the two tether segments, and  $L$  is the overall length of the upper-tether.

Equations (2) are a set of linear, partial differential equations with separable variables. Substitution of  $u_1 = R_1(z_1) \exp(i\omega t)$  and  $u_2 = R_2(z_2) \exp(i\omega t)$ , where  $R_1$  and  $R_2$  are complex numbers, into eqns (2) leads to the following ordinary differential equations:

$$\frac{\partial^2 R_j}{\partial z_j^2} + \beta_j^2 R_j = 0, \quad j = 1, 2 \quad (3a)$$

$$-\omega^2 R_2 = -\epsilon_2^2 a_2 \lambda_2 \{ 1 + i\omega b \} \frac{\partial R_2}{\partial z_2} + \gamma R_2, \quad z_2 = 1 \quad (3b)$$

$$\begin{aligned}
-\omega^2 R_1 &= -\epsilon_1^2 a_1 \lambda_1 \{1 + i\omega b\} \frac{\partial R_1}{\partial z_1} - \epsilon_2^2 a_1 \lambda_2 \\
&\times \{1 + i\omega b\} \frac{\partial R_2}{\partial z_2} + \gamma R_1 \quad z_1 = 1; \quad z_2 = 0 \quad (3c) \\
R_2(0) &= R_1(1) \quad (3d) \\
R_1(0) &= 1 \quad (3e)
\end{aligned}$$

where

$$\begin{aligned}
\beta &= \sqrt{\frac{\omega^2 + \gamma}{1 + i\omega b}} \\
\beta_1 &= \beta/\epsilon_1 \\
\beta_2 &= \beta/\epsilon_2 \quad (4)
\end{aligned}$$

The solutions of eqns (3a) are  $R_1 = A_1 \sin(\beta_1 z_1) + B_1 \cos(\beta_1 z_1)$  and  $R_2 = A_2 \sin(\beta_2 z_2) + B_2 \cos(\beta_2 z_2)$ . After substitution of the above expressions into the boundary conditions (3b)–(3e) we finally obtain the FRFs at the elevator  $R_1(1)$  and at the upper-platform  $R_2(1)$  as follows:

$$\begin{aligned}
R_1(1) &= \left[ \cos \beta_1 - \delta_1 \sin \beta_1 \right. \\
&\quad \left. - \frac{\sin \beta_1 \sin \beta_2 + \delta_2 \sin \beta_1 \cos \beta_2}{\cos \beta_2 - \delta_2 \sin \beta_2} \right]^{-1} \\
R_2(1) &= R_1(1) \Theta_L \quad (5)
\end{aligned}$$

where

$$\delta_1 = \beta_1/a_1 \gamma_1; \quad \delta_2 = \beta_2/a_2 \lambda_2$$

and

$$\Theta_L = [\cos \beta_2 - \delta_2 \sin \beta_2]^{-1} \quad (6)$$

is an attenuation function which expresses how much the longitudinal waves are abated when they propagate from the elevator to the upper-platform.

Since the equations of motion are linear the FRF represents the displacement or acceleration at the elevator or at the upper-platform for a unit displacement or acceleration, respectively, at the station.

## 2.2. Transverse waves

For thin and long tethers (i.e.  $h/L \ll 1$  where  $h$  is the tether diameter) like those under consideration, the bending stiffness can be neglected and the tethers treated as perfectly flexible strings.

For  $\mu L \ll m_1$  and  $m_2$ , as in TECS, the tensions in the two tether segments are approximately constant along the tethers. Consequently, the equations of motion for the transverse waves have the same structure as those for the longitudinal waves. Furthermore, since the horizontal gravity gradient is null in the orbital plane (in-plane) and different from zero in the transverse plane (out-of-plane), the equations of motion in the two planes are slightly different. The out-of-plane equations are as follows [5]:

$$\mu \frac{\partial^2 w_j}{\partial t^2} = \left\{ T_j + d \frac{\partial}{\partial t} \right\} \frac{\partial^2 w_j}{\partial z_j^2} - \Omega^2 \mu w_j \quad j = 1, 2 \quad (7)$$

where  $w_1$  and  $w_2$  are the out-of-plane displacements of tether segments 1 and 2 respectively,  $T_1$  and  $T_2$  are the average tensions in tethers 1 and 2, and  $d$  is the viscous damping coefficient expressed in N-s (equivalent to  $E'A$  of longitudinal waves). In eqns (7) we have adopted a viscous damping model for the transverse waves. This is only a first order approximation as explained later, which, however, leads to a simple analytical solution of the equations of motion. This simplification is acceptable in light of the numerous unknowns involved in estimating the damping of long kevlar tethers.

The in-plane equations of motion are readily obtained by simply setting the gravity gradient term (i.e. the  $\Omega^2$ -term) in eqns (7) equal to zero and by substituting the in-plane displacements  $v_j$  for  $w_j$ . The average tether tensions in eqns (7) are given by:

$$\begin{aligned}
T_2 &= 3\Omega^2 m_2 L \\
T_1 &= T_2 + 3\Omega^2 m_1 L_1 \quad (8)
\end{aligned}$$

After defining non-dimensional variables as  $w_1 = w_1/L_1$ ,  $w_2 = w_2/L_2$ ,  $\omega = \omega/\Omega$  and  $t = t\Omega$  we obtain non-dimensional equations and boundary conditions as follows:

$$\begin{aligned}
\frac{\partial^2 w_j}{\partial t^2} &= v_j^2 \left\{ 1 + d_j \frac{\partial}{\partial t} \right\} \frac{\partial^2 w_j}{\partial z_j^2} + \gamma w_j \quad j = 1, 2 \\
\frac{\partial^2 w_2}{\partial t^2} &= -v_2^2 a_2 \lambda_2 \left\{ 1 + d_2 \frac{\partial}{\partial t} \right\} \frac{\partial w_2}{\partial z_2} + \gamma w_2 \quad z_2 = 1 \quad (9) \\
\frac{\partial^2 w_1}{\partial t^2} &= -v_1^2 a_1 \lambda_1 \left\{ 1 + d_1 \frac{\partial}{\partial t} \right\} \frac{\partial w_1}{\partial z_1} - v_2^2 a_1 \lambda_2 \\
&\times \left\{ 1 + d_2 \frac{\partial}{\partial t} \right\} \frac{\partial w_2}{\partial z_2} + \gamma w_1 \quad z_1 = 1; \quad z_2 = 0 \\
w_2(0, t) &= w_1(1, t) \\
w_1 &= \exp(i\omega t) \quad z_1 = 0
\end{aligned}$$

where  $v_1 = c_1/\Omega L_1$ ,  $v_2 = c_2/\Omega L_2$ ,  $d_1 = d\Omega/T_1$ ,  $d_2 = d\Omega/T_2$ ,  $\gamma = -1$  for the out-of-plane waves and  $\gamma = 0$  for the in-plane waves,  $c_1 = (T_1/\mu)^{1/2}$  and  $c_2 = (T_2/\mu)^{1/2}$  are the transverse wave speeds in tethers 1 and 2, while the other symbols have been previously defined. By a procedure similar to that followed for the longitudinal waves, we obtain the FRF for transverse waves at the elevator  $TR_1(1)$  and at the upper-platform  $TR_2(1)$  as follows:

$$\begin{aligned}
TR_1(1) &= \left[ \cos \phi_1 - \sigma_1 \sin \phi_1 \right. \\
&\quad \left. - \tau \frac{\sin \phi_1 \sin \phi_2 + \sigma_2 \sin \phi_1 \cos \phi_2}{\cos \phi_2 - \sigma_2 \sin \phi_2} \right]^{-1} \\
TR_2(1) &= TR_1(1) \Theta_T \quad (10)
\end{aligned}$$

where  $\Theta_T$  is the transverse wave attenuation function given by:

$$\Theta_T = [\cos \phi_2 - \sigma_2 \sin \phi_2]^{-1} \quad (11)$$

and

$$\begin{aligned}\phi_1 &= \frac{1}{v_1} \sqrt{\frac{\omega^2 + \gamma}{1 + i\omega d_1}} \\ \phi_2 &= \frac{1}{v_2} \sqrt{\frac{\omega^2 + \gamma}{1 + i\omega d_2}} \\ \sigma_1 &= \phi_1 / a_1 \lambda_1 \\ \sigma_2 &= \phi_2 / a_2 \lambda_2 \\ \tau &= (T_1 / T_2)^{1/2}\end{aligned}\quad (12)$$

By setting  $\gamma = 0$  in eqns (9)–(12), we obtain the corresponding expressions for the in-plane transverse waves.

### 3. DAMPING OF TRANSVERSE WAVES

The damping of transverse waves is much smaller than that of longitudinal waves. Since no bending stiffness is considered, there is negligible linear damping of lateral oscillations in free space. Light damping, however, is provided by three different mechanisms: (1) through orbital coupling (in-plane only); (2) through non-linear coupling with the tether stretch; and (3) through interaction with the atmosphere.

Mechanism (1) operates in-plane only: the orbital coupling between the in-plane transverse displacement and the longitudinal modes (through Coriolis forces) produces a small linear damping of the in-plane transverse oscillations. In Ref. [3] the modal damping ratio is computed for linear oscillations of a perfectly flexible, long tether with constant tension, orbiting in space. With the parameters of TECS we obtain a damping ratio for the first mode of  $\approx 10^{-7}\%$  which is negligible.

Mechanism (2) provides damping through the non-linear coupling of transverse displacements (in-plane and out-of-plane) and longitudinal stretch. A first approximation of the non-linear damping ratio due to non-linear coupling is computed in Ref. [3] by equating the energy dissipated in lateral oscillations to the energy loss associated with the elongation engaged in a given lateral vibration mode. Furthermore, the longitudinal strain associated with the lateral deformation is assumed to be uniformly distributed along the tether. Consequently, the non-linear modal damping ratio for a tether segment of length  $L$ , with an end-platform of mass  $M$  is given by [3]:

$$\xi_k \approx 2 \left( \frac{\pi}{4} \right)^3 \frac{E'A}{\Omega L M \sqrt{\eta} \sqrt{3 + \eta}} k^2 (B_k L)^2 \quad (13)$$

where  $k$  is the mode number,  $\eta = \mu L / M$  the ratio of the tether mass to the platform mass, and  $B_k$  the amplitude of the  $k$ th mode. After assuming a ratio  $B_1 / L = 0.01$  for the first mode,  $E'A = 1100$  N-s, which is consistent with a damping ratio of 1% for the first longitudinal mode,  $L = 10$  km, and  $M = 10$

tons, we obtain a damping ratio for the first transverse mode of about  $10^{-3}\%$ .

The adoption of this value of damping ratio for interpreting the numerical results for transverse waves (obtained with a viscous model) should be done with full awareness of the limitations involved. The viscous model, in fact, provides increasing damping for an increasing value of frequency, while the non-linear damping is proportional to the product  $k^2 B_k^2$  and hence to the energy stored in the mode. Furthermore, unlike the viscous model, the non-linear damping depends upon the modal amplitude.

Mechanism (3) provides a negligible contribution to damping of transverse waves at the orbital altitude of TECS for the frequencies of interest.

In conclusion, even if the non-linear damping ratio is three orders of magnitude smaller than that of longitudinal waves, mechanism (2) provides the most significant damping for transverse waves with non-negligible modal amplitudes.

### 4. NUMERICAL RESULTS

Numerical results are based on the following parameters for TECS:  $m_1(\text{EL}) = 5$  tons,  $m_2(\text{UP}) = 10$  tons,  $\mu = 4.9 \times 10^{-3}$  kg/m,  $L = 10$  km,  $\Omega = 1.119 \times 10^{-3}$  rad/s (i.e. an orbital altitude of 450 km) and  $EA = 61,645$  N.

#### 4.1. Longitudinal waves

Figure 3(a)–(c) show the magnitude of the FRF at the elevator vs the dimensional frequency for  $\lambda_1 = 0.1$ , 0.5 and 0.9, which correspond to distances between SS and EL of 1, 5 and 9 km. The three plots in each figure are for a damping ratio of the first mode of a 10-km tether of 0, 1 and 5% respectively. The resonance peaks for zero damping are, of course, infinite and are shown in dashed lines in the figures. Figure 3(d) is a 3-D plot of the FRF magnitude at the elevator, for  $\lambda_1 = 0.1$ , vs frequency and vs damping ratio. Figure 3(e) is a 3-D plot of the FRF magnitude, for a 1% damping ratio, vs frequency and vs fractional distance  $\lambda_1$ .

It is clear from these figures that a light material damping is sufficient to provide a strong attenuation, for frequencies  $> 2$  Hz, of the longitudinal waves which propagate from the station to a 1-km-distant elevator. The attenuation increases dramatically as the elevator moves further away from the station and the cut-off frequency decreases to about 1 Hz.

Figure 4 is a 3-D plot of the magnitude of the attenuation function  $\Theta_L$  for a damping ratio of 1%, vs frequency and vs fractional distance  $\lambda_1$ . It is evident from the figure that a small material damping is sufficient to provide a strong attenuation of the longitudinal waves propagating beyond the elevator. The elevator acts as an effective attenuator for the upper-platform of longitudinal perturbations generated at the station.

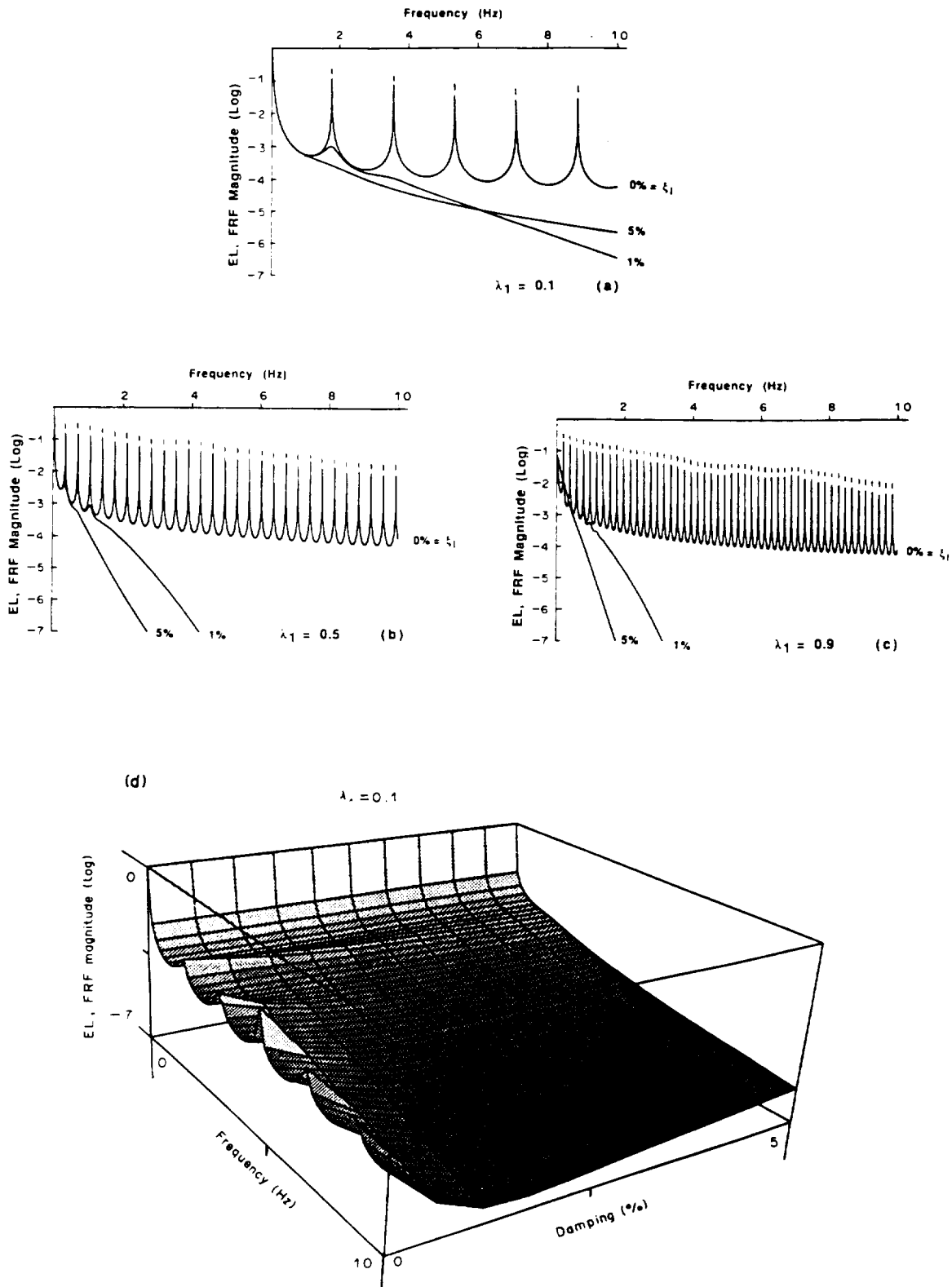


Fig. 3. (a)-(d) Caption overleaf

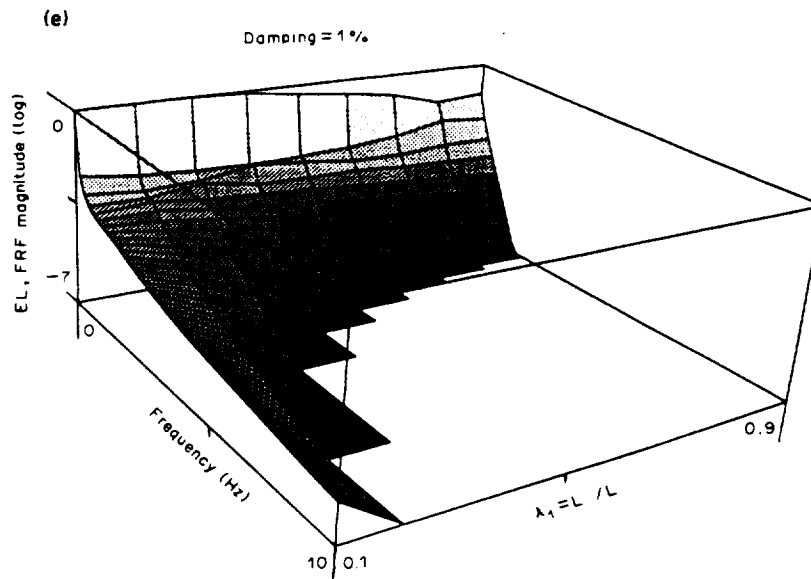


Fig. 3. (e)

Fig. 3. Magnitude of frequency response function (FRF) at elevator for longitudinal waves vs frequency, fractional distance  $\lambda_1 = L_1/L$ , and tether material damping.

#### 4.2. Transverse waves

Figure 5(a)–(c) show the magnitude of the FRF at the elevator for out-of-plane transverse waves vs the dimensional frequency for fractional distances  $\lambda_1 = 0.1, 0.5$  and  $0.9$ . The three plots in each figure are for a viscous damping ratio for the first mode of a 10-km tether of  $10^{-3}$ ,  $10^{-2}$  and  $10^{-1}\%$  respectively. For zero damping the resonance peaks would be infinite.

The results for in-plane transverse waves do not differ appreciably from those of out-of-plane waves

because the gravity gradient term plays a minor role in the transverse wave dynamics.

By assuming a viscous damping ratio of  $10^{-3}\%$  for transverse waves (see previous section for the limitations involved in this assumption), the transverse perturbations in TECS are only moderately attenuated as they propagate from the station to the elevator. Additional damping devices may be added to the system in order to improve the attenuation.

Figure 6 shows the magnitude of the attenuation function  $\Theta_T$  for a damping ratio of  $10^{-3}\%$ , vs frequency and vs fractional distance  $\lambda_1$ . The elevator

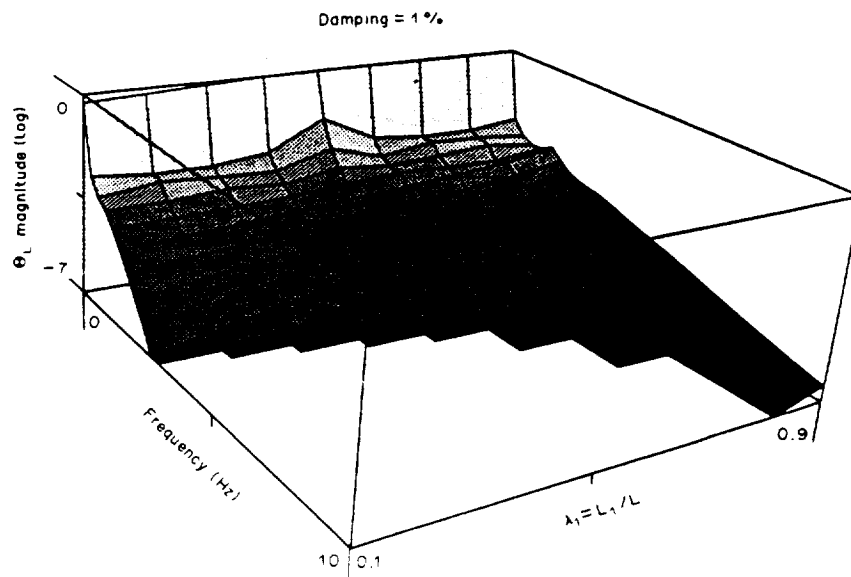


Fig. 4. Magnitude of longitudinal waves attenuation function (see text) vs frequency and fractional distance for 1% material damping.



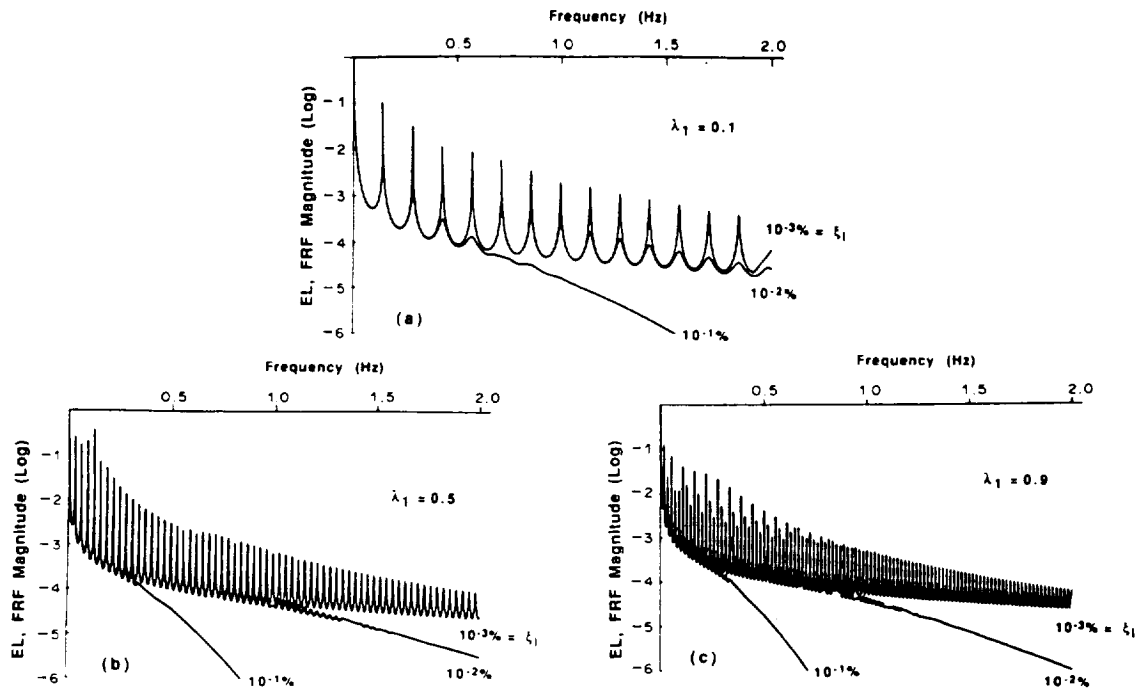


Fig. 5. Magnitude of FRF at elevator for transverse waves vs frequency, fractional distance  $\lambda_1 = L_1/L$ , and tether material damping.

acts as an attenuator for the upper-platform of transverse perturbations generated at the station. This may suggest a way to design a passive damper to be placed between the station and the elevator for increasing the attenuation of transverse waves.

##### 5. CONCLUSIONS

Perturbations propagate along the tether of TECS from the station to the elevator and beyond, to the upper-platform. However, a small value of viscous

material damping (1–5% damping is estimated for kevlar tethers) is sufficient to abate dramatically the longitudinal waves with a frequency above 1–2 Hz. The attenuation of the longitudinal waves increases with the distance of the elevator from the station.

Transverse waves, on the contrary, are much less attenuated because the only significant damping is through non-linear coupling with the longitudinal tether stretch. The damping provided by this mechanism depends upon the transverse modal amplitude and is about three orders of magnitude smaller, even

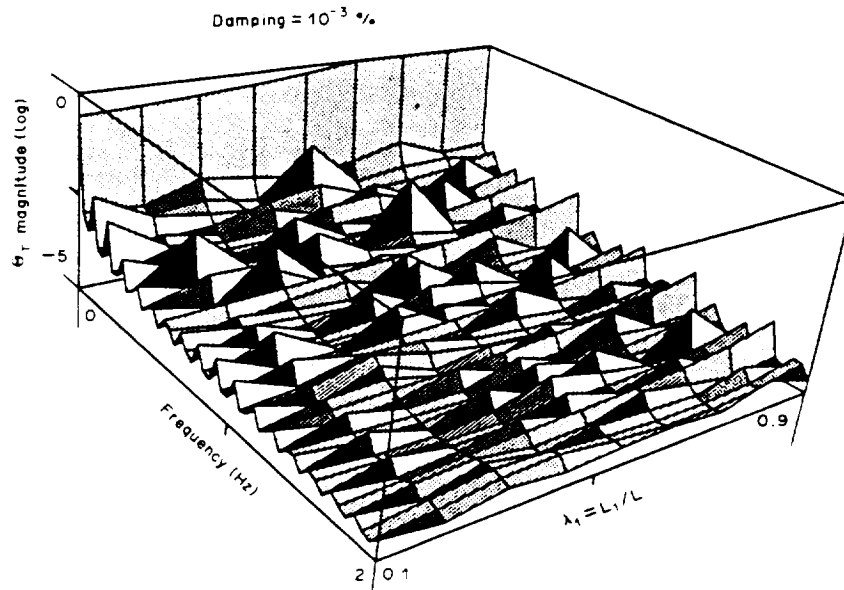


Fig. 6. Magnitude of transverse waves attenuation function (see text) vs frequency and fractional distance for  $10^{-3}\%$  viscous damping.

for non-negligible modal amplitudes (e.g. amplitude of the first transverse mode  $\approx 1\%$  of the tether segment length), than the longitudinal damping.

For both longitudinal and transverse waves, the elevator attenuates the perturbations propagating from the station to the upper-platform. This conclusion may suggest a way of designing a passive attenuator for transverse waves to be placed between the elevator and the station.

*Acknowledgements*—Support for this paper was provided by contract NAS8-36606 from NASA Marshall Space Flight Center with Charles Rupp and James Harrison as program directors.

#### REFERENCES

1. E. C. Lorenzini, M. Cosmo, S. Vetrella and A. Moccia, Dynamics and control of the Tether Elevator/Crawler System. *J. Guidance Control Dynam.* **12**, 404–411 (1989).
2. M. Cosmo, E. C. Lorenzini, S. Vetrella and A. Moccia, Transient dynamics of the Tether Elevator/Crawler System. *Proceedings of the AIAA/AAS Astrodynamics Conference*, Minneapolis, Minn., pp. 480–489 (1988).
3. X. He and D. Powell, Tether damping in space. *J. Guidance Control Dynam.* **13**, 104–112 (1990).
4. F. Angrilli, G. Bianchini, M. Da Lio and G. Fanti, Modelling the mechanical properties and dynamics of the tethers for TSS-1 and TSS-2. *ESA J.* **12**, 353–368 (1988).
5. F. Graziani, S. Sgubini and A. Agneni, Disturbance propagation in orbiting tethers. *Advances in the Astronautical Sciences* (Edited by M. Bainum, I. Bekey, L. Guerriero and P. A. Penzo), Vol. 26, pp. 301–315 (1987).
6. G. E. Gullahorn and R. G. Holfeld, Tether as a dynamic transmission line. *Space Tethers for Science in the Space Station Era* (Edited by L. Guerriero and I. Bekey), Società Italiana di Fisica, Conference Proceedings, Vol. 14, pp. 163–168 (1988).

S. Vetrella & A. Moccia

*Università di Napoli, Naples, Italy*

E.C. Lorenzini & M. Cosmo

*Harvard-Smithsonian Center for Astrophysics, Cambridge, USA*

## **Attitude Dynamics of the Tether Elevator/Crawler System for Microgravity Applications\***

### **Abstract**

The Tether Elevator/Crawler System (TECS) consists of two end platforms tethered to opposite sides of the Space Station. A variable-gravity laboratory is located onboard an elevator which can crawl along the upper tether. This paper analyses the elevator's attitude dynamics in order to evaluate its effect on microgravity applications. To this end, a simulation model is described and numerical results are given for a steady-state case. It is shown that the elevator attitude dynamics, without attitude control, contribute additional spectral lines to the acceleration noise.

---

\* Based on a paper presented at the  
AIAA/NASA/ASI/ESA Third International  
Conference on Tethers in Space, San Francisco,  
USA, 17-19 May 1989.

**PRECEDING PAGE BLANK NOT FILMED**

# 1. Introduction

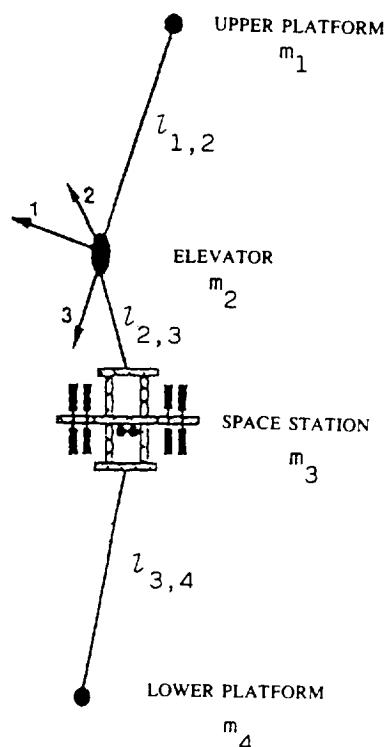


Figure 1. Schematic of the Tether Elevator/Crawler System (TECS)

The Tether Elevator/Crawler System (TECS) is designed for conducting experiments in a controlled gravity environment. Two 10 km-long tethers are deployed on opposite sides of the Space Station (SS). The variable-gravity laboratory is placed onboard an elevator (EL), which can crawl along the upper tether (Fig. 1). Because of the dual-tether configuration, variable gravity profiles can be generated onboard the elevator while the acceleration level on board the stationary microgravity laboratory of the Space Station is maintained below  $10^{-5}$  g.

The analysis carried out in Reference 1 demonstrates that TECS makes a negligible contribution to the acceleration noise level onboard the Space Station. The tether-related acceleration noise is, in fact, a few orders of magnitude smaller than the required  $10^{-5}$  g. On the other hand, by moving the elevator along the upper tether, the variable-gravity laboratory on the elevator experiences an acceleration level that varies with the distance between the elevator and the system's centre of mass (CM). From the upper boom to the tether's tip, the acceleration level ranges from  $1.5 \times 10^{-5}$  g to  $4 \times 10^{-3}$  g, making it possible to explore thresholds and hysteresis phenomena.

Onboard an elevator positioned 1 km from the Station, the acceleration fluctuations

## Nomenclature

$d$	= distance defined in Figure 3
$E$	= Young's modulus
$F$	= force
$I_1, I_2, I_3$	= principal moments of inertia
$l$	= tether length
$m$	= mass
$M_1, M_2, M_3$	= torque components
$M_b$	= matrix defined by Equation (4)
$M_{\gamma\alpha\beta}$	= rotation matrix
$M_{\psi\vartheta\varphi}$	= rotation matrix
$r$	= tether radius
$\mathbf{R}$	= position vector with respect to the inertial reference frame
$T$	= temperature
$\mathbf{u}_{k,k+1}$	= unit vector from the $k$ -th to the $(k+1)$ -th mass
$\mathbf{V}$	= velocity with respect to the atmosphere
$x, y, z$	= reference frame defined in Figure 3
$X, Y, Z$	= inertial reference frame
$\alpha, \beta, \gamma$	= pitch, roll, yaw angles
$\epsilon$	= thermal expansion coefficient
$\zeta$	= damping coefficient
$\rho$	= position vector with respect to the body reference frame
$\psi, \vartheta, \varphi$	= Euler's angles of the body reference frame
$\omega$	= body frame angular velocity
$\Omega_{\oplus}$	= Earth's angular velocity

## Subscripts

1,2,3	= body reference frame
$a$	= aerodynamic
$CM$	= centre of mass
$d$	= damping
$e$	= elastic
$g$	= gravitational
$k$	= $k$ -th lumped mass
$l$	= lower tether
0	= initial
$u$	= upper tether

(g-quality) are about  $10^{-6}$  g at frequencies lower than  $10^{-3}$  Hz, and about  $10^{-7}$  g for frequencies of between  $10^{-3}$  Hz and  $10^{-2}$  Hz. Algorithms to control the motion of the elevator have also been derived in Reference 1. These control laws allow the elevator to travel over long distances without inducing a significant acceleration noise.

The analysis carried out thus far on the dynamics of TECS has treated the platforms of the system (e.g. the Station and the elevator) as point masses. The influence of the rigid-body dynamics of a particular platform upon the acceleration levels has been neglected so far. This paper, on the other hand, evaluates the contribution of the rigid-body dynamics of the elevator to the acceleration noise level onboard the elevator itself. To this end, in addition to the model described in Reference 1, a different numerical simulation program has been developed. A description of this model will be presented in the first part of the paper.

Numerical results show that the rotational dynamics of the elevator contribute additional spectral lines to the acceleration noise. Because of the quasi-symmetrical external forces, the centre of rotation (CR) of the elevator is very close to its centre of mass. Consequently, the effects of the rigid-body dynamics are minimised when the microgravity experiments are placed at the elevator's centre of mass.

The rotation-related spectral lines are also evaluated by applying Fast Fourier Transforms (FFTs) to the acceleration components onboard the elevator. The frequencies of the new spectral lines, obtained from the dynamic simulation, are then compared to the theoretical values of the attitude frequencies. Finally, the new acceleration spectra are examined in the light of acceptable threshold levels for proposed microgravity experiments versus the frequency of disturbances.

The three-dimensional model is based on the discretisation of the system by means of lumped masses, connected by massless springs and dashpots<sup>2</sup> (a lumped mass is a point mass where the forces are applied and to which an area is assigned to take into account the atmospheric drag). To the area and mass of each lumped mass, those of the half-tether connecting them to the adjacent lumped masses are added. Depending on the trade-off between computing time and accuracy of the model, the tether too can be simulated by lumped masses. In this case, up to 12 masses can be lumped at different positions along the tether (Fig. 2).

## 2. Mathematical model

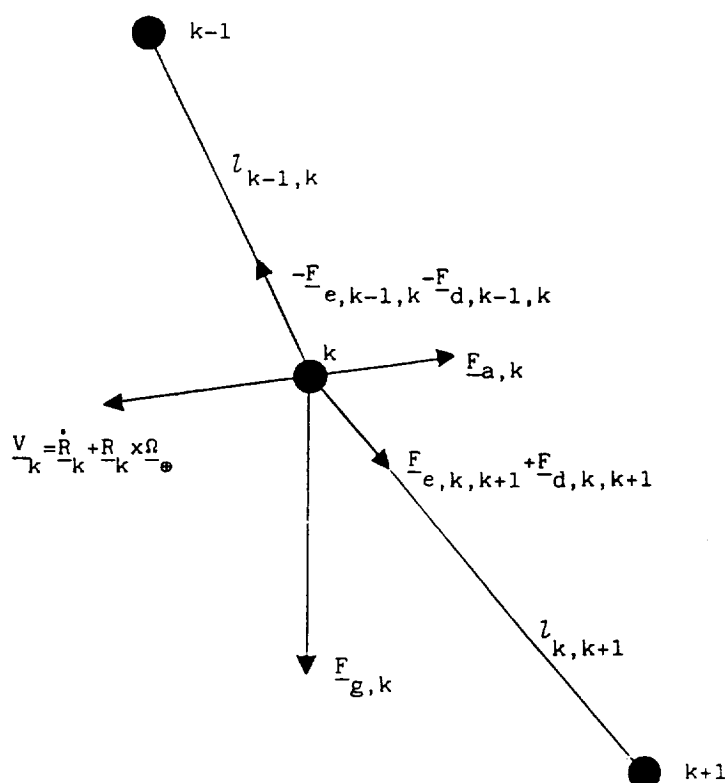


Figure 2. Forces acting on a lumped mass

The system motion is described by force- and energy-equilibrium differential equations, the unknown quantities in which are the temperature and the components of the position and velocity vectors, in the right-handed inertial reference frame (origin at the centre of the Earth, X-axis directed along the first point of Aries, X-Y equatorial plane)<sup>3</sup>.

The environmental perturbations considered in the present analysis are: the gravitational force, including the second zonal harmonic of the gravity field, the aerodynamic forces and the thermal effects on the tensional forces.

The atmosphere is assumed to rotate with the Earth's ellipsoid and its density is computed using the US Standard Atmosphere<sup>4</sup>. For each lumped mass, the aerodynamic drag is evaluated considering the velocity of its centre of mass relative to the atmosphere.

The tether thermal inputs are: the solar illumination and the flux due to the atmospheric drag. The only cooling process is the emitted radiation. Since the tether length variation strongly affects the attitude dynamics of the platform, particular attention is devoted to the evaluation of the partial and total eclipse conditions of each lumped mass<sup>5</sup>, in order to improve the accuracy of the modelling of the tether's stretching due to thermal effects.

In the following, the attitude of the elevator is simulated by means of kinematics and Euler's moment differential equations:

$$\begin{bmatrix} \dot{\psi} \\ \dot{\vartheta} \\ \dot{\varphi} \end{bmatrix} = \frac{1}{\sin \vartheta} \begin{bmatrix} \sin \varphi & \cos \varphi & 0 \\ \cos \varphi \sin \vartheta & -\sin \varphi \sin \vartheta & 0 \\ -\sin \varphi \cos \vartheta & -\cos \varphi \cos \vartheta & \sin \vartheta \end{bmatrix} \begin{bmatrix} \omega_1 \\ \omega_2 \\ \omega_3 \end{bmatrix} \quad (1)$$

$$\dot{\omega}_1 = [M_1 + \omega_2 \omega_3 (I_2 - I_3)] / I_1$$

$$\dot{\omega}_2 = [M_2 + \omega_1 \omega_3 (I_3 - I_1)] / I_2 \quad (2)$$

$$\dot{\omega}_3 = [M_3 + \omega_1 \omega_2 (I_1 - I_2)] / I_3$$

The unknowns in the above equations are the Euler's angles of the body reference frame (whose axes coincide with the principal axes) with respect to the inertial reference frame, and the body-frame components of the inertial angular velocity vector.

The platform is assumed to be a rigid body, approximated by simple geometrical elements (Fig. 3).

The torques are computed taking into account the aerodynamic drag and the tether visco-elastic force, without the gravity gradient and attitude control.

The total aerodynamic torque is computed by adding the contribution of each geometrical element (spheres, fins, cylinders), and neglecting the spin effect<sup>5</sup>.

The tether tension is computed as follows:

$$\begin{aligned} \mathbf{F}_{e,k,k+1} &= \frac{E\pi r^2}{l_{0,k,k+1}} \left\{ l_{k,k+1} - l_{0,k,k+1} [1 + \epsilon(T_k - T_{0,k})] \right\} \mathbf{u}_{k,k+1} \\ \mathbf{F}_{d,k,k+1} &= 2\zeta \left[ \frac{E\pi r^2 m_k m_{k+1}}{l_{0,k,k+1} (m_k + m_{k+1})} \right]^{1/2} [(\dot{\mathbf{R}}_{k+1} - \dot{\mathbf{R}}_k) \cdot \mathbf{u}_{k,k+1}] \mathbf{u}_{k,k+1} \end{aligned} \quad (3)$$

The transformation between the inertial reference frame and the body frame is given by a 3-1-3 rotation matrix ( $M_{\varphi\vartheta\omega}$ ).

The attitude angles are defined with respect to a right-handed reference frame, with origin in the centre of mass, and unit vector components, given by the rows of the following matrix:

[illegible]

where  $\mathbf{W} = \mathbf{R} \times \dot{\mathbf{R}}$ .

$$\alpha = \sin^{-1}(-a_{3,1})$$

$$\gamma = \sin^{-1} \left( \frac{a_{2,1}}{\cos \alpha} \right)$$

$$M_{\gamma\alpha\beta} = M_b M_{\gamma\beta c}^T \quad (6)$$

Gear's algorithm adjusts the step size in order to achieve fast integration and model the high-frequency oscillations. The foregoing requires a preliminary analysis of these

207

frequencies and an accurate selection of the maximum allowed step size in order to obtain a constant sampling step.

Particular attention must be devoted to initial conditions and physical parameters characterising the system. An orbit-generator program is used to compute the initial position and velocity vectors of each lumped mass: in addition to the Keplerian orbit, a perturbed orbit is described by the first-order Kozai theory<sup>8</sup>. The unstretched lengths of the tethers and the initial conditions for longitudinal oscillation dampers are computed by means of the equilibrium equation for each tether segment.

### 3. Acceleration levels

The acceleration measured by an accelerometer package located at the centre of mass of the elevator is the sum of the external, excluding the gravitational, and internal forces (e.g. tensions) acting upon the platform divided by its mass.

By solving the differential equations, we compute the acceleration of the centre of mass with respect to the inertial reference frame.

The acceleration of a point off the centre of mass with respect to the inertial reference frame, is computed by using the relative-motion equation for a rigid body.

$$\ddot{\mathbf{R}} = \ddot{\mathbf{R}}_{CM} + \dot{\boldsymbol{\omega}} \times \boldsymbol{\rho} + \boldsymbol{\omega} \times (\boldsymbol{\omega} \times \boldsymbol{\rho}) \quad (7)$$

### 4. Numerical results

Table 1 shows the system configuration and Table 2 the thermal and mechanical characteristics of the Kevlar tether adopted. In order to compare the present simulation model with the model described in References 1 and 7, the tether mass has been neglected. Consequently, the longitudinal tether vibrations are not modelled in these particular simulation runs.

The duration of the simulation run is 1.5 orbits, which includes three crossings of the terminator. The simulation starts with the system at the ascending node, on the X-axis of the inertial reference frame, at an altitude of 450 km and an inclination of 28.5°. The system is aligned along the local vertical and the Sun is at the vernal equinox. The initial tether temperature is 290 K. All environmental perturbations are acting upon the system. Only the longitudinal dampers are activated during the simulation, because the in-plane and out-of-plane libration dampers make no significant contribution to the acceleration during steady-state phases<sup>1</sup>.

The elevator, approximated by a right circular cylinder, has principal moments of inertia  $I_1 = I_2 = 8619.8 \text{ kg m}^2$ ,  $I_3 = 3906.3 \text{ kg m}^2$  about the longitudinal, transverse and vertical axes, respectively. We assume zero initial attitude angles in order to study the steady-state attitude dynamics.

The analysis is further simplified by positioning the attachment points on the vertical axis of the cylinder which, together with the previous assumptions, gives  $\omega_3 = \text{constant}$ .

Figures 4 – 6 show the elevator attitude angles: the low-frequency oscillations are due to in-plane and out-of-plane natural oscillations, temperature, and gravitational-

Table 1. Discretisation of the system

Symbols in Fig. 1	Steady-state tether length (m)	Platform mass (kg)	Tether mass (kg)	Platform cross-sectional area (m <sup>2</sup> )	Tether cross-sectional area (m <sup>2</sup> )
$m_1$	8998	10 000	21.8	10	9.0
$I_{1,2}$					
$m_2$	998	5000	24.2	10	10.0
$I_{2,3}$					
$m_3$	10 500	306 752	27.9	2790	11.5
$I_{3,4}$					
$m_4$		10 000	25.5	10	10.5

Table 2. Kevlar tether characteristics

Radius	$1 \times 10^{-3}$
Linear density	$4.85 \times 10^{-3} \text{ kg m}^{-1}$
Solar radiation absorptivity	0.75
Thermal emissivity	0.5
Specific heat	$2500 \text{ J kg}^{-1} \text{ K}^{-1}$
Young's modulus	$1.96 \times 10^{10} \text{ N m}^{-2}$
Thermal expansion coefficient	$-2 \times 10^{-6} \text{ K}^{-1}$
Damping coefficient	0.10
Drag coefficient	2



force variations. The effects of damped longitudinal oscillations are negligible and, in addition, the plot scale does not reflect the natural frequency of the pitch and roll.

The acceleration and its spectrum for the elevator centre of mass and for a test point P are plotted in Figures 7 and 8 and Figures 9 and 10, respectively. Note that the DC component is omitted in the spectra shown in this paper.

The acceleration levels are mainly due to the contributions at low frequencies and at the pitch natural frequency ( $6.7 \times 10^{-2}$  Hz), which provides an acceleration of about  $10^{-7}$  g.

The elevator dynamics do not appreciably influence the acceleration level of the Space Station centre of mass, as shown in Figures 11 and 12.

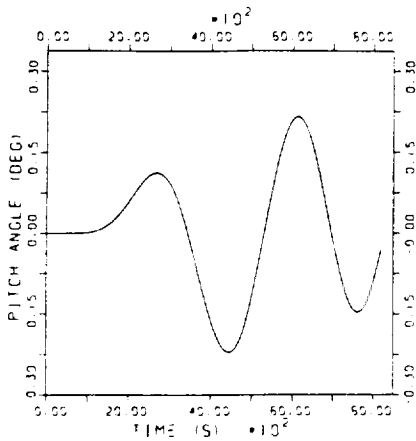


Figure 4. Elevator pitch angle

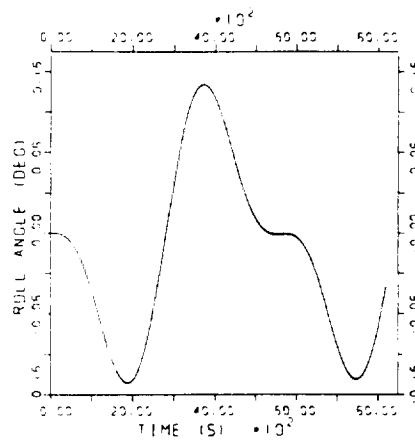


Figure 5. Elevator roll angle

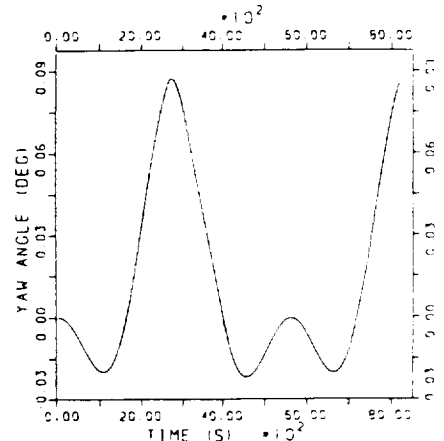


Figure 6. Elevator yaw angle

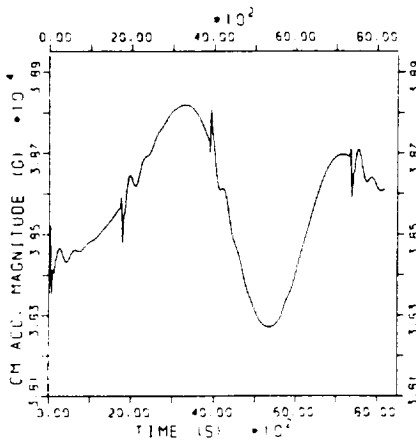


Figure 7. Elevator centre-of-mass acceleration

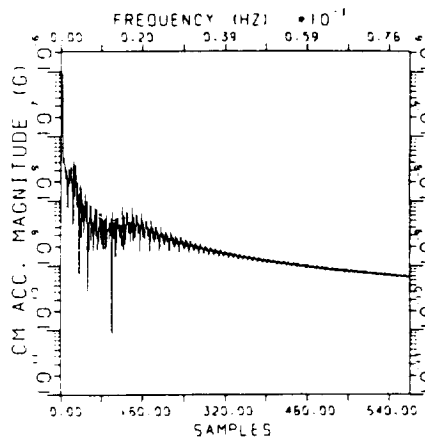


Figure 8. Elevator centre-of-mass acceleration spectrum

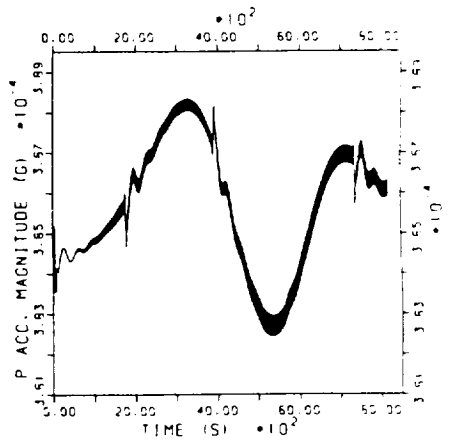


Figure 9. Test point P(1,0,0) acceleration

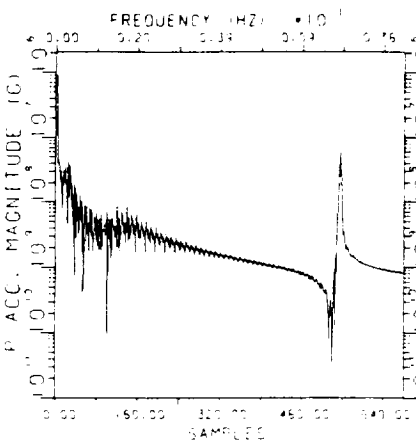


Figure 10. Test point P(1,0,0) acceleration spectrum

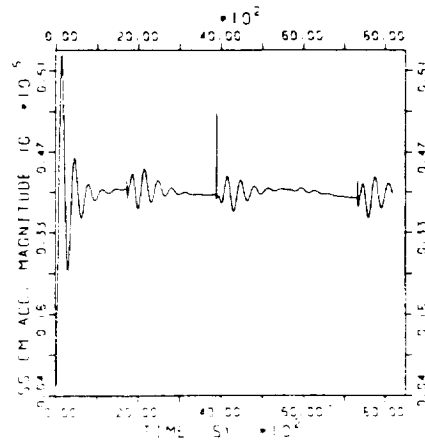


Figure 11. Space Station centre-of-mass acceleration

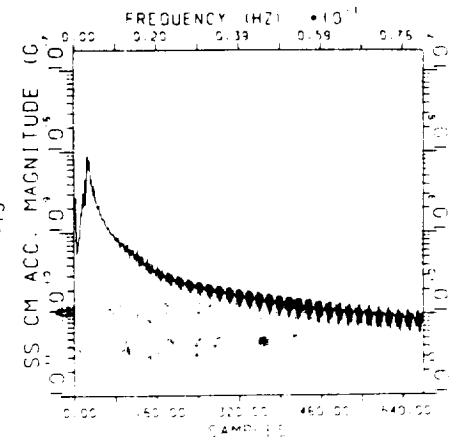
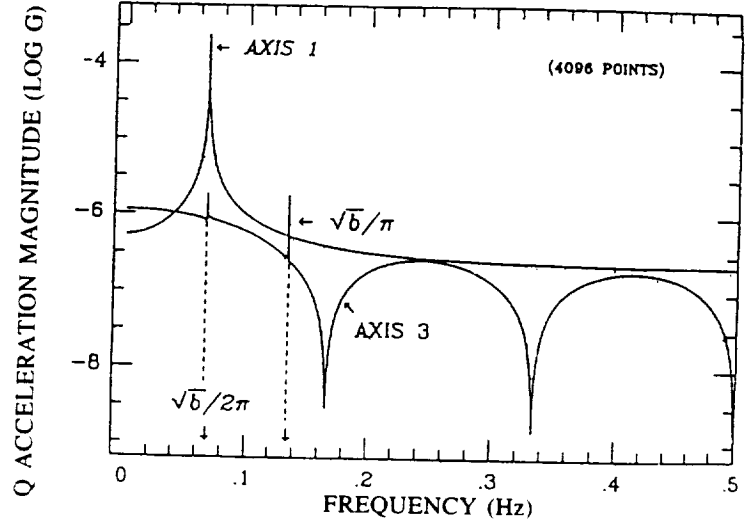


Figure 12. Space Station centre-of-mass acceleration spectrum

A second simulation was run in order to investigate the effect of an initial pitch angle of  $10^{-2}$  rad upon the 1 and 3 acceleration components at a test point Q. Only two harmonic components, at the pitch natural frequency and twice the pitch natural frequency, were present in the axis-3 component (Fig. 13).

A simplified analysis of the attitude oscillations is given below to validate the numerical results.

Figure 13. Test point Q(0,0,2) longitudinal and vertical acceleration component spectrum



## 5. Simplified attitude model

With reference to Figure 3, the equations that describe the attitude dynamics of the elevator orbiting the Earth at constant rate  $\omega$ , under the assumption of small angles, are<sup>9</sup>:

$$\text{Roll} \quad \ddot{\beta} + (q\omega^2 + b)\beta = (1-q)\omega\dot{\gamma}$$

$$\text{Yaw} \quad \ddot{\gamma} = -\psi\dot{\beta} \quad (8)$$

$$\text{Pitch} \quad \ddot{\alpha} + b\alpha = 0$$

where

$$q = 1 - I_3/I_1$$

$$b = (F_{e,d,u} + F_{e,d,l}) \frac{d}{I_1}$$

Note that the yaw dynamics are coupled to the roll dynamics. The influence of the yaw upon the roll, however, is attenuated by the factor  $(1-q)$ . Furthermore, the roll motion has a frequency very close to that of the pitch motion, which is equal to  $\sqrt{b}/2\pi$ .

Let us consider, for instance, the effects on the acceleration levels due to a small pitch perturbation  $\alpha$ . Since the pitch motion is decoupled, as shown in Equation (8), from the yaw and roll motions, we can write the in-plane components of the acceleration at a point  $(\rho_1, 0, \rho_3)$  on the elevator as:

$$\begin{aligned} \ddot{R}_1 &= \ddot{R}_{CM,x} - \alpha \ddot{R}_{CM,z} + \rho_3 \ddot{\alpha} + \rho_1 [\omega(2\dot{\alpha} - \omega) - \dot{\alpha}^2] \\ \ddot{R}_3 &= \alpha \ddot{R}_{CM,x} + \ddot{R}_{CM,z} - \rho_1 \ddot{\alpha} + \rho_3 [\omega(2\dot{\alpha} - \omega) - \dot{\alpha}^2] \end{aligned} \quad (9)$$

where  $\ddot{R}_{CM,x}$  and  $\ddot{R}_{CM,z}$  are the acceleration components at the elevator's centre of mass along the flight direction (x) and the local vertical (z), respectively. For an

ORIGINAL PAGE IS  
OF POOR QUALITY

unperturbed system aligned along the local vertical,  $\dot{R}_{CM,x} = 0$  and  $\dot{R}_{CM,z}$  coincides with the gravity-gradient acceleration.

Let us assume that the system is stationary and that only the pitch angle  $\alpha$  is oscillating with an amplitude of  $0.57^\circ$  ( $10^{-2}$  rad) at its natural frequency  $\sqrt{b}/2\pi$ . If the test point is located on the yaw axis 2 m from the elevator's centre of mass, from Equations (9) the maximum acceleration components are about  $3.6 \times 10^{-4}$  g along axis-1, and  $3.8 \times 10^{-4}$  g along axis-3. The former is primarily related to the tangential acceleration  $\rho_3 \ddot{\alpha}$ , and the latter to the gravity gradient. Moreover, Equations (9) provide other useful information about the acceleration. Specifically, while the gravity gradient and tangential terms have a natural frequency of  $\sqrt{b}/2\pi$ , the centrifugal term (within square brackets) has two harmonic components at  $\sqrt{b}/2\pi$  (i.e.  $2\omega\dot{\alpha}$ -term) and at  $\sqrt{b}/\pi$  (i.e.  $\dot{\alpha}^2$ -term), respectively. It should also be noted that, for small angles, the gravity-gradient term oscillates at the frequency  $\sqrt{b}/2\pi$  along axis-1 and is constant along axis-3.

The numerical model presented in this paper has proved to be a valuable tool for analysis of the attitude dynamics of a space elevator. The overall system dynamics agree with the results of Reference 1, where a model without the elevator's rotational motion is used.

This paper has shown that the acceleration onboard the elevator is affected by its rotational motion. The rotation-related dynamic noise grows as the distance between the microgravity experiment and the elevator's centre of mass increases. For the particular elevator geometry and inertia adopted in this paper, the two harmonic components of the acceleration have frequencies of  $6.7 \times 10^{-2}$  Hz and  $1.4 \times 10^{-1}$  Hz, which are low enough to affect some microgravity processes.

However, a simulation run with equilibrium initial conditions and environmental perturbations demonstrated that the amplitude of the attitude motion (and hence the related acceleration) is negligible. Consequently, the effect of the attitude dynamics on the acceleration levels is significant only during transient phases.

Further analysis is required with regard to: (i) damping and control of the elevator's attitude motion; (ii) coupling between the elevator's attitude and the tether's vibrations; and, to a lesser extent, (iii) effects of additional disturbances, such as aerodynamic torques, which may be significant for an asymmetric elevator's geometry.

This paper has been supported in the United States by NASA/MSFC Contract NAS8-36606, with J. Harrison and C. Rupp as Programme Directors, and in Italy by Italian Space Agency (ASI) and Ministry for Education (MPI) contracts.

M. Cosmo's support had been provided by Academia Nazionale dei Lincei, Rome, Italy, via the 'Giuseppe Colombo' Fellowship.

## 6. Conclusions

## Acknowledgements

1. Lorenzini E C, Cosmo M, Vetrella S & Moccia A 1988, Dynamics and Control of the Tether Elevator/Crawler System, *AIAA J. of Guidance, Control and Dynamics*, Vol. 12, No. 3, pp. 404-411.
2. Kalaghan P M et al. 1978, Study of the Dynamics of a Tether Satellite System (SKYHOOK), Smith. Inst. Astroph. Obs., Cambridge, USA (prepared for NASA), 138 pp.
3. Vetrella S & Moccia A 1985, Influenza della posizione e dell'assetto del Tethered Satellite System nell'osservazione stereoscopica dallo spazio, Atti VIII Congr. Naz. AIDAA, pp. 789-803.
4. King R L 1978, A Computer Version of the US Standard Atmosphere, NASA CR-150778.
5. Wertz J R (Ed.) 1980, Spacecraft Attitude Determination and Control, D. Reidel Publ. Co., Dordrecht, Holland.

## References

6. Gear C W 1971, Numerical Initial Value Problems in Ordinary Differential Equations, Prentice-Hall, Englewood Cliffs, New Jersey.
7. Cosmo M, Lorenzini E C, Vetrella S & Moccia A 1988, Transient Dynamics of the Tether Elevator/Crawler System, Proc. AIAA/AAS Astrodynamics Conf., Minneapolis, CP8811, pp. 480-489.
8. Vetrella S & Moccia A 1984, Factors Affecting Push-Broom Performance in Future Space Platforms, Proc. Int. Astronautical Fed. XXXV Congr., Lausanne, IAF-84-116, 7 pp.
9. Lemke L G, Powell J D & He X 1987, Attitude Control of a Tethered Spacecraft, *J. Astronaut. Sci.*, Vol. 35, pp. 41-55.

Manuscript received 10 October 1989

#### 4.0 TETHERED SPACE CENTRIFUGE

Tethers with a length of a few kilometer could be used to build a space centrifuge with a very large diameter and a very small rotational rate. Rotational rates higher than 6 rpm produce canal sickness in humans while "apparent" gravity level smaller than 0.3 g are undesirable because they impair motion. The two values above imply a centrifuge with a diameter of at least 16 m. Moreover, if an optimal environment is desired for human habitation, the centrifuge should rotate at a rate smaller than 2 rpm and provide a gravity level of 1 g. These values require a centrifuge with a diameter of at least 420 m. A 1-km tether, connecting two space vehicles and spinning about an axis perpendicular to the tether could be an ideal space centrifuge with an optimum environment (the so called optimum comfort zone) for human habitation.

A tethered centrifuge is proposed for a demonstration flight in LEO in the following paper. A 1-km tether connects a Delta second stage and a General Electric reentry capsule to provide a 1-g gravity level at the capsule with a rotation rate of about 1 rpm.

The paper addresses the issues of: desirable gravity environments for human habitability; quality of the acceleration levels on board the capsule during steady rotation; spinning and despinning of the centrifuge; and stability of the tether oscillations during the steady rotation phase.

See also Quarterly Report No. 16 of this contract for more details.



# Dynamics and Stability of a Tethered Centrifuge in Low Earth Orbit

B. M. Quadrelli<sup>1</sup> and E. C. Lorenzini<sup>2</sup>

## Abstract

The three dimensional attitude dynamics of a spaceborne tethered centrifuge for artificial gravity experiments in low Earth orbit is analyzed using two different methods. First, the tethered centrifuge is modelled as a dumbbell with a straight viscoelastic tether, point tip-masses, and sophisticated environmental models such as non-spherical gravity, thermal perturbations, and a dynamic atmospheric model. The motion of the centrifuge during spin-up, de-spin, and steady-rotation is then simulated. Second, a continuum model of the tether is developed for analyzing the stability of lateral tether oscillations. Results indicate that the maximum fluctuation about the 1-g radial acceleration level is less than  $10^{-3}$  g; the time required for spin-up and de-spin is less than one orbit; and lateral oscillations are stable for any practical values of the system parameters.

## I. Introduction

The planned Space Station and Manned Mission to Mars will require astronauts to endure long periods under weightless conditions detrimental to human physiology. Recent achievements in human endurance to zero gravity notwithstanding, an artificial gravity environment may be far preferable for long missions.

The motivation behind this paper is to prove that a tethered centrifuge is capable of providing the desired level of artificial gravity at low rotational speeds. The advantages of a long tethered centrifuge with respect to a much shorter rotating spacecraft are optimum artificial gravity environment; reduced side Coriolis accelerations, which are unpleasant for human habitability; and simplicity in reconfiguring the centrifuge by reeling the tether in and out. In summary, a tether centrifuge can provide any desired value of fractional-g or a 1-g level by rotating at a much lower rate than a conventional centrifuge.

<sup>1</sup>Visiting Scientist, Radio and Geoastronomy Division, Harvard-Smithsonian Center for Astrophysics, Cambridge, MA 02138.

<sup>2</sup>Staff Scientist, Radio and Geoastronomy Division, Harvard-Smithsonian Center for Astrophysics, Cambridge, MA 02138.

The tethered centrifuge analyzed in this paper is not intended for human habitation, but for carrying out experiments on relatively small samples at various artificial gravity levels in low Earth orbit (LEO), with an emphasis on the 1-g level. The system considered is formed by a 200-kg General Electric (GE) reentry capsule at one end and a Delta II second stage, with an empty mass of 872 kg, at the other end. (See Fig. 1.) The tether length is 1 km as proposed by the Advanced Project Office of the Marshall Space Flight Center [1, 2].

The feasibility of a tethered centrifuge in space has been demonstrated in [1] and [2]. The dynamics during spin-up and de-spin of a tethered centrifuge have been analyzed in [3] for a tether length of 1 km and heavy end masses. In [3], however, the effects of the environment upon the artificial gravity levels were not analyzed.

The three dimensional attitude dynamics of a tethered centrifuge in LEO is investigated in this paper using two different dynamics models.

First, the tethered centrifuge is modelled as a dumbbell system with a straight viscoelastic tether, point tip-masses, and sophisticated environmental models such as non-spherical gravity, thermal perturbations, and a dynamic atmospheric model. These environmental models are currently used for other dynamics studies of tethered systems [4]. Particular attention is given to the acceleration fluctuations on board the capsule at the tether tip during spin-up, de-spin, and steady-rotation phases.

Second, a continuum model of the tether is developed for analyzing the stability of lateral oscillations during the steady-rotation phase as a function of the system parameters. This model has also been used for computing the system's natural frequencies, both analytically and numerically.

## II. Lumped-Mass Model

### *Equations of Motion*

The motion of the system is described with respect to a local vertical local horizontal (LV-LH) orbiting reference frame  $xyz$ , which rotates with orbital mean motion  $\Omega$  and geocentric radius  $R_0$ . The origin of this frame coincides with the initial position of the center of mass of the system and the coordinate axes are  $z$  along the local vertical,  $x$  toward the flight direction, and  $y$  in the out-of-plane

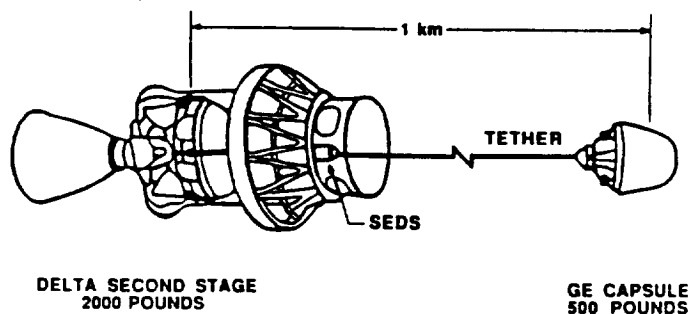


FIG. 1. Artificial Gravity Experiment Configuration.



direction (Fig. 2). The geocentric inertial reference frame  $X_I Y_I Z_I$ , also depicted in Fig. 2, is as follows:  $X_I$  points toward the vernal equinox,  $Z_I$  toward the North Pole, and  $Y_I$  completes the right-handed reference frame.

The system is modelled with  $N$  point masses  $m_i$ , connected by massless springs and viscous dash-pots.  $\rho_i$  is the radius vector of mass  $m_i$  with respect to the orbital reference frame and  $\mathbf{f}_g, \mathbf{f}_d, \mathbf{f}_u$  are the gravitational, drag, and tensional forces on each mass per unit mass. The equation of motion of the generic  $i$ th mass is as follows [4]:

$$\ddot{\rho}_i + \ddot{\mathbf{R}}_o + 2\boldsymbol{\Omega} \times \dot{\rho}_i + \boldsymbol{\Omega} \times (\boldsymbol{\Omega} \times \rho_i) = \mathbf{f}_g + \mathbf{f}_d + \mathbf{f}_u, \quad (1)$$

Substitution of  $\rho_i = x_i \mathbf{i} + y_i \mathbf{j} + z_i \mathbf{k}$  into equations (1) yields:

$$\ddot{x}_i - 2\Omega \dot{z}_i - \Omega^2 x_i = f_{gix} + f_{dix} + f_{uix}$$

$$\ddot{y}_i = f_{giy} + f_{diy} + f_{uiy}$$

$$\ddot{z}_i + 2\Omega \dot{x}_i - \Omega^2 (z_i - R_o) = f_{giz} + f_{diz} + f_{uiz}. \quad (2)$$

If  $\ell = \ell(\cos \varphi \sin \theta \mathbf{i} + \sin \varphi \mathbf{j} + \cos \varphi \cos \theta \mathbf{k})$  is the vector from  $m_1$  to  $m_N$  (Fig. 2), then

$$\begin{aligned} \theta &= \tan^{-1} \left[ \frac{x_1 - x_N}{z_1 - z_N} \right] \\ \varphi &= \sin^{-1} \left[ \frac{y_1 - y_N}{\ell} \right] \end{aligned} \quad (3)$$

are the in-plane and the out-of-plane angles with respect to LV.

Following the assumptions of [5], the kevlar tether is assumed to be perfectly elastic without any bending stiffness. Since, as shown later on, the spring-mass

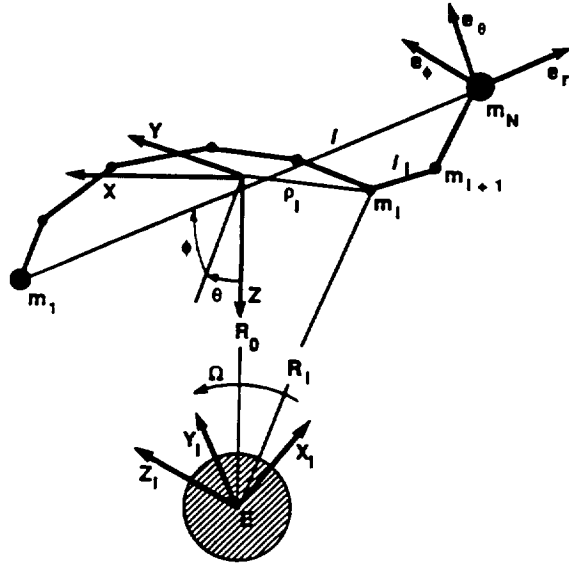


FIG. 2. Schematic of Tethered Centrifuge and Reference Frames.

frequency is too low for the material damping to be effective, a longitudinal damper is added at one of the tether attachment points. From [5] a damper effective in damping the spring-mass mode of the system is tuned to the frequency of that mode and has a damping ratio  $\xi = 0.9$ . Consequently, the damper stiffness  $k_d$  is equal to the tether stiffness per unit length  $k = EA/\ell_o$  where  $EA$  is the tether axial stiffness. Neglecting the tether mass, the damper's damping coefficient is  $b = \xi\sqrt{kM_{eq}}$ , where  $M_{eq} = (m_1 \times m_N)/(m_1 + m_N)$  is the equivalent mass.

The geometry of the tether with the longitudinal damper is depicted in Fig. 3, where  $\ell = \ell_o + \ell_d + \ell_i + \ell_{th}$ , and

$$\ell_{th} = \ell_o \alpha \eta, \quad \text{thermal stretch;} \quad (4)$$

$$\ell_i = \ell_d = T/k, \quad \text{elastic and damper stretches.} \quad (5)$$

Here  $\ell_o$  is the tether natural length,  $\alpha$  is the tether thermal expansion coefficient,  $T$  the average tether tension, and  $\eta$  the tether temperature.

In order to account for the motion of the damper, assumed massless, the following equation,

$$k_{ei} = k_d \ell_d + b \dot{\ell}_d, \quad (6)$$

is added to equations (2). Furthermore, the components of the tensional forces per unit mass in equations (2) are given by:

$$f_{x,i} = (T_{x,i} - T_{x,i-1})/m_i; \quad (7.1)$$

$$T_{x,i} = T_i(x_{i+1} - x_i)/\ell_i; \quad (7.2)$$

$$T_i = \frac{EA}{\ell_o} \ell_{i,i}; \quad (7.3)$$

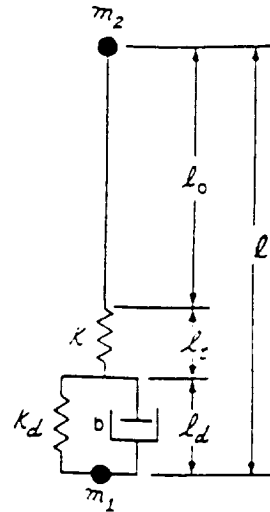


FIG. 3. Schematic of Tether and Damping Element.

where  $\ell_{i,1}$  and  $T_i$  are the elastic stretch and the tension of the  $i$ th tether segment. Similar expressions for  $f_{iy,1}$  and for  $f_{iz,1}$  are obtained by replacing  $x_i$  with  $y_i$  and  $z_i$ , respectively, in equations (7).

### Environmental Models

The system is acted upon by atmospheric, gravitational, and thermal perturbations. An exhaustive description of accurate environmental models normally used for simulating the dynamics of tethered systems is given in [6].

The gravity model adopted for this study has the  $J_0$  and  $J_2$  zonal components of the field. The latter term produces a secular effect on the osculating elements of the orbit, such as mean anomaly, argument of perigee, and right ascension of the ascending node. The  $J_2$ -term also produces a small libration of a long tethered system such as the one under consideration. The gravity acceleration on the  $i$ th mass is given by [7]:

$$\mathbf{f}_{g,i} = [Q] \{-\text{grad}(U_i'^2 + U_i'^0)\}^T \quad (8)$$

where  $[Q]$  is the transformation matrix between the geocentric inertial frame and the orbiting reference frame, and  $U_i'^2, U_i'^0$  are the potential energy components of the Earth's gravity field associated with the  $J_2$  and  $J_0$  terms. Specifically,

$$\begin{aligned} U_i'^0 &= -\frac{\mu}{R_i}; \\ U_i'^2 &= \frac{\mu}{R_i} \left( \frac{R_\oplus}{R_i} \right)^2 \frac{J_2}{2} (3 \sin^2 \lambda_i - 1); \end{aligned} \quad (9)$$

where  $\mu$  and  $R_\oplus$  are the gravitational constant and the equatorial radius of the Earth,  $\lambda_i$  the geocentric latitude, and  $R_i$  the geocentric radius vector of the  $i$ th mass.

With regards to the thermal model, it is assumed that the tether receives thermal energy directly from the Sun, from the Earth's albedo, and from the Earth's infrared radiation. Cooling is provided by emitted radiation only. Furthermore, the reflectance of the Earth is taken to be isotropic and diffuse, and the spectral distribution of the reflected radiation is considered equivalent to the spectral distribution of the incident radiation. Aerodynamic heating is neglected. The tether equilibrium temperature is computed by equating the net thermal flux to the time derivative of the tether thermal energy. The thermal balance equation is taken from [4] and it is not shown here for the sake of brevity.

The atmospheric density model is an analytical function of the exospheric temperature and the local altitude [8], which fits Jacchia's 1977 model. The agreement with Jacchia's 1977 model for the same exospheric temperature is within  $\pm 10\%$ . This atmospheric model takes into account dynamical thermospheric corrections, such as the diurnal variation (function of solar activity) and minor fluctuations like the seasonal-latitudinal variations of the density above 150 km. The atmospheric density profile covers altitudes from the ground up to 1000 km.

The deceleration of the  $i$ th-lump due to the atmospheric drag is

$$\mathbf{f}_{d,i} = -\frac{1}{2} C_d A_i \gamma_i v_i \mathbf{v}_i, \quad (10)$$

where  $A_i$  is the frontal area of  $i$ th mass;  $C_d$  is the drag coefficient ( $=2.2$ );  $\gamma_i$  is the atmospheric density at height  $h_i$ ; and  $\mathbf{v}_i$  is the wind velocity vector.

It is assumed that the atmosphere rotates rigidly with the Earth. Equations (7), (8), and (10) are then substituted into equations (2).

### III. Apparent Accelerations

For a system on a circular, unperturbed orbit of radius  $R_o$  and orbital rate  $\Omega$ , calling  $\mathbf{e}_r$  (radial),  $\mathbf{e}_\theta$  (lateral),  $\mathbf{e}_\varphi$  (tangential) the unit vectors of a body reference frame (tether frame) rigidly attached to the tether, the inertial radius of the GE capsule is

$$\mathbf{R} = [R_o \cos \theta \cos \varphi + \rho] \mathbf{e}_r - [R_o \sin \theta] \mathbf{e}_\theta - [R_o \cos \theta \sin \varphi] \mathbf{e}_\varphi,$$

where  $\rho$  is the radius vector of the capsule (the subscript  $i = 1$  has been dropped in the equation above). The acceleration on board the capsule is

$$\begin{aligned} \ddot{\mathbf{R}} = & \ddot{\mathbf{R}}_o + [\ddot{\rho} - (\Omega + \dot{\theta})^2 \rho \cos^2 \varphi - \rho \dot{\varphi}^2] \mathbf{e}_r \\ & + [(\ddot{\theta} \rho + 2\dot{\rho} \Omega + 2\dot{\rho} \dot{\theta}) \cos \varphi - 2\rho \dot{\varphi}(\dot{\theta} + \Omega) \sin \varphi] \mathbf{e}_\theta \\ & + [\rho(\Omega + \dot{\theta})^2 \sin \varphi \cos \varphi + \rho \ddot{\varphi} + 2\dot{\rho} \dot{\varphi}] \mathbf{e}_\varphi. \end{aligned} \quad (11)$$

Neglecting the drag deceleration, the apparent acceleration  $\bar{\mathbf{a}}$  at the capsule is as follows:

$$\bar{\mathbf{a}} = \mathbf{f}_g - \ddot{\mathbf{R}}. \quad (12)$$

Assuming a spherical gravity field, the gravity acceleration is

$$\mathbf{f}_g = \mathbf{f}_o - \left[ \frac{\partial U'^o}{\partial \rho} \mathbf{e}_r + \frac{1}{\rho \cos \varphi} \frac{\partial U'^o}{\partial \theta} \mathbf{e}_\theta + \frac{1}{\rho} \frac{\partial U'^o}{\partial \varphi} \mathbf{e}_\varphi \right], \quad (13)$$

where  $\mathbf{f}_o$  is the gravity acceleration at  $R_o$ .

Consequently, the radial, lateral, and tangential acceleration components are as follows:

$$\bar{a}_r = -\ddot{\rho} + \rho \dot{\varphi}^2 + (\Omega + \dot{\theta})^2 \rho \cos^2 \varphi - \Omega^2 \rho + 3\Omega^2 \rho \cos^2 \theta \cos^2 \varphi \quad (14.1)$$

$$\begin{aligned} \bar{a}_\theta = & -\ddot{\theta} \rho \cos \varphi - 2\rho(\dot{\theta} + \Omega) \dot{\varphi} \cos \varphi + 2\rho \dot{\varphi}(\dot{\theta} + \Omega) \sin \varphi \\ & - 3\Omega^2 \rho \cos \varphi \sin \theta \cos \theta \end{aligned} \quad (14.2)$$

$$\bar{a}_\varphi = -\rho \ddot{\varphi} - 2\dot{\rho} \dot{\varphi} - \rho(\dot{\theta} + \Omega)^2 \sin \varphi \cos \varphi - 3\Omega^2 \rho \cos^2 \theta \sin \varphi \cos \varphi. \quad (14.3)$$

An accurate estimate of the average steady-spin velocity which provides a 1-g acceleration at the capsule is easily obtained from equation (14.1) after noting that  $\dot{\rho} = \ddot{\rho} = 0$  because for a steady-rotation rate much greater than  $\Omega$  the fluctuation of the tether stretch, owing to the gravity gradient, is negligible with respect to the centrifugal component of the stretch. Moreover, for a centrifuge

with the spin plane initially parallel to the orbital plane and neglecting second order effects due to the  $J_2$ -term,  $\varphi = \dot{\varphi} = 0$ , and equation (14.1) yields

$$\bar{a}_r = \rho(\dot{\theta} + \Omega)^2 - \rho\Omega^2 + 3\Omega^2\rho \cos^2\theta. \quad (15)$$

During the steady-spin phase, the largest contribution to the acceleration is provided by the first term, namely the centrifugal component, while the contribution of the gravitational gradient is negligible. The average inertial spin velocity for a 1-g radial acceleration at the GE capsule of a 1-km long centrifuge is 1.05 rpm. The average tether tension is 1960 N.

#### IV. Simplified Analysis of the Motion of Fast Spinning Systems

The well known linearized equations of motion for a dumbbell system of tether length  $\ell$  are:

$$\begin{aligned} \ddot{\theta} + \frac{2\dot{\ell}}{\ell}(\dot{\theta} + \Omega) - 2\dot{\varphi}(\dot{\theta} + \Omega) \tan \varphi + 3\Omega^2 \sin \theta \cos \theta &= Q_\theta, \\ \ddot{\varphi} + \frac{2\dot{\ell}}{\ell}\dot{\varphi} + \sin \varphi \cos \varphi [(\dot{\theta} + \Omega)^2 + 3\Omega^2 \cos^2 \theta] &= Q_\varphi, \end{aligned} \quad (16)$$

with the assumptions of massless tether, point tip-masses, and circular orbit.  $Q_\theta$  and  $Q_\varphi$  are the in-plane and out-of-plane generalized torque, respectively.

For a constant tether stretch and  $\omega_{IN} \gg \Omega$ , where  $\omega_{IN} = \omega + \Omega$  is the inertial average spin rate and  $\omega$  is the average value of  $\dot{\theta}$ , and for small out-of-plane angles, equations (16) yield:

$$\ddot{\theta} + 3\Omega^2 \sin \theta \cos \theta = Q_\theta, \quad (17.1)$$

$$\ddot{\varphi} + \omega_{IN}^2 \varphi = Q_\varphi. \quad (17.2)$$

Equation (17.2) shows that the out-of-plane motion for spin velocities much greater than the orbital rate has a resonant angular frequency equal to  $\omega_{IN}$ .

#### V. Control Laws for Spin-Up and De-Spin Maneuvers

The space centrifuge is spun up and down by using two thrusters on the tip-masses with equal thrust levels, firing perpendicularly to the spin axis. At the start of the spin-up maneuver, the centrifuge is assumed to be fully deployed and aligned with the local vertical.

The control laws are derived for a system spinning in free-space. They are later implemented into the numerical model described in Section II for simulating the response under more general conditions.

The thrust force  $F$ , during spin-up, is commanded according to a proportional-derivative law as follows:

$$F = -\frac{k_1}{\ell}(\theta - \omega_{ss}t) - \frac{k_2}{\ell}\dot{\theta}, \quad (18)$$

where  $\omega_{ss}$  is the steady-spin velocity.

For any value of  $k_1$  and of the damping ratio  $\xi$  (which is assumed equal to 0.9),  $k_2 = 2\xi\sqrt{M_{eq}}\sqrt{k_1}\ell$  [9]. In order to reach the steady-rotation in about

2000 seconds (one third of the orbital period) with a maximum thrust of about 20 N,  $k_1 = 1670$  Nm/rad and  $k_2 = 9.457 \times 10^5$  Nms/rad.

The control law for the de-spin maneuver is

$$F = -\frac{k_1}{\ell} \theta - \frac{k_2}{\ell} \dot{\theta}. \quad (19)$$

The thrust  $F$  has its maximum value at the initial time because the value of the angular velocity  $\dot{\theta}$  is different from zero.

The total propellant consumption  $G$  is obtained by integrating the total instantaneous thrust  $F$  over the maneuver duration  $\Delta t$  as follows:

$$G = \frac{\int_0^{\Delta t} |F| dt}{I_{sp} g}, \quad (20)$$

where  $I_{sp}$  is the specific impulse. A strategy for reducing the total propellant consumption during the spin-up phase is suggested in [3]: the tether is deployed beyond its final length, the centrifuge spun up to the steady-state value of the angular momentum, and the tether is then reeled in to its final length. Since the total impulse varies inversely with the tether length, the strategy of [3] reduces the propellant consumption with respect to a spin-up maneuver at constant tether length. The conventional technique, however, is followed in this paper because the proposed centrifuge makes use of the Small Expendable-Tether Deployment System (SEDS) [10] for deploying the tether to its final length but the SEDS deployer can not retrieve the tether once it is deployed.

## VI. Motion Of The Tether Treated As A Continuum

### *Equations of Motion*

Restricting the motion of the tether to the orbital plane, the equation of motion for the in-plane transverse vibration of an element of tether of mass  $dm$  at a distance  $R$  from the center of the Earth is (Fig. 4):

$$\ddot{\mathbf{R}} dm = \mathbf{F}_t + \mathbf{F}_g, \quad (21)$$

where  $\mathbf{F}_t$  is the tensional force,  $\mathbf{F}_g$  the gravitational force, and other external perturbation forces have been neglected. Moreover, since the system is stiffened by the centrifugal force, the tether deflections are small.

The tether is assumed to be a uniform string of constant length  $\ell$ , with no bending stiffness, clamped at its ends to the point masses  $m_1$  and  $m_2$ . These geometric boundary conditions imply that  $m_1$  and  $m_2$  always lie on the  $x$  axis of the tether reference frame.

The analysis is also restricted to the steady-rotation phase. The material damping is neglected since it is reasonable to assume that the damping has a significant influence only when transverse deflections are large. The radius vector to the generic tether element is

$$\mathbf{R} = (x - R_o \cos \theta) \mathbf{i} + (y + R_o \sin \theta) \mathbf{j}, \quad (22)$$

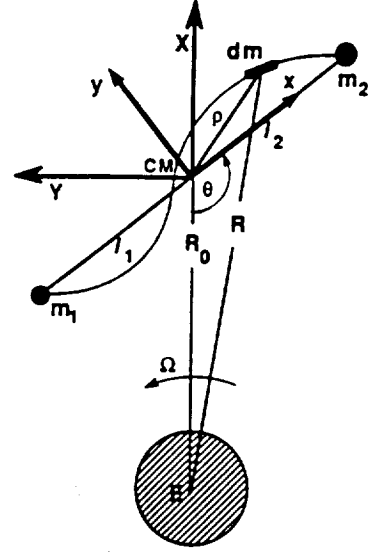


FIG. 4. Reference Frame for the Continuous Model.

and the acceleration

$$\begin{aligned} \ddot{\mathbf{R}} = & [\ddot{x} - \ddot{\theta}y - 2(\dot{\theta} + \Omega)y - x(\dot{\theta} + \Omega)^2 + R_o\Omega^2 \cos \theta]\mathbf{i} \\ & + [\ddot{y} + \ddot{\theta}x + 2(\dot{\theta} + \Omega)\dot{x} - y(\dot{\theta} + \Omega)^2 - R_o\Omega^2 \sin \theta]\mathbf{j}. \end{aligned} \quad (23)$$

Since  $\mathbf{F}_g = -\mu(\mathbf{R}/|\mathbf{R}|^3) dm$ , using a binomial expansion and neglecting second order terms,

$$\begin{aligned} \mathbf{F}_g = & -\Omega^2 dm \{ [x(1 - 3 \cos^2 \theta) + 3y \sin \theta \cos \theta - R_o \cos \theta]\mathbf{i} \\ & + [y(1 - 3 \sin^2 \theta) + 3x \sin \theta \cos \theta + R_o \sin \theta]\mathbf{j} \}. \end{aligned} \quad (24)$$

The tensional force  $\mathbf{F}_t$  is given by [11]:

$$\mathbf{F}_t = \left[ \left( \frac{\partial T}{\partial x} \right) \mathbf{i} + \left( T \frac{\partial^2 y}{\partial x^2} + \frac{\partial T}{\partial x} \frac{\partial y}{\partial x} \right) \mathbf{j} \right] dx. \quad (25)$$

Defining  $\sigma = dm/dx$  as the mass per unit length of the tether, the equations of motion are

$$\ddot{x} - x(\dot{\theta}^2 + 2\dot{\theta}\Omega + 3\Omega^2 \cos^2 \theta) - y \left( \ddot{\theta} - \frac{3}{2}\Omega^2 \sin 2\theta \right) - 2\dot{y}(\dot{\theta} + \Omega) = \frac{1}{\sigma} \frac{\partial T}{\partial x} \quad (26.1)$$

$$\begin{aligned} \ddot{y} - y(\dot{\theta}^2 + 2\dot{\theta}\Omega + 3\Omega^2 \sin^2 \theta) + x \left( \ddot{\theta} + \frac{3}{2}\Omega^2 \sin 2\theta \right) + 2\dot{x}(\dot{\theta} + \Omega) = \\ \frac{1}{\sigma} \left[ T \frac{\partial^2 y}{\partial x^2} + \frac{\partial T}{\partial x} \frac{\partial y}{\partial x} \right]. \end{aligned} \quad (26.2)$$

The assumption of small transverse deflections makes the analysis tractable, as the tension becomes a function of the variable  $x$  only and the Coriolis term

$[-2\dot{y}(\dot{\theta} + \Omega)]$  is negligible. Defining  $s = x + \ell_1$ , where  $\ell_1$  is the distance between the system's center of mass and one of the two tip-masses, the tension along the tether is as follows:

$$T(s) = \sigma(\dot{\theta}^2 + 2\dot{\theta}\Omega + 3\Omega^2 \cos^2\theta) \left[ \frac{(\ell^2 - s^2)}{2} + \frac{M_{eq}\ell}{\sigma} \right]. \quad (27)$$

Substituting equation (27) into equation (26.1), assuming that the system is following its rigid body oscillation forced by the gravity gradient (i.e.  $\ddot{\theta} + (3/2)\Omega^2 \sin 2\theta = 0$ ) and defining the variable  $z = s/\ell$  and the parameter  $A = 1 + 2M_{eq}/\sigma\ell$ , equations (26) yield:

$$\ddot{y} = \frac{1}{2} (\dot{\theta}^2 + 2\dot{\theta}\Omega + 3\Omega^2 \cos^2\theta) \left[ (A - z^2) \frac{\partial^2 y}{\partial z^2} - 2z \frac{\partial y}{\partial z} \right] + (\dot{\theta}^2 + 2\dot{\theta}\Omega + 3\Omega^2 \sin^2\theta)y, \quad (28)$$

with the boundary conditions  $y(0) = y(1) = 0$ .

#### Stability Analysis

Separating the variables in equation (28), after substitution of

$$y(z, t) = \sum_{n=1}^{\infty} F_n(t) G_n(z), \quad (29)$$

equation (28) yields:

$$\ddot{F}_n + [(B_n^2 - 1)(\dot{\theta}^2 + 2\dot{\theta}\Omega) + 3\Omega^2 \cos^2\theta(B_n^2 + 1) - 3\Omega^2]F_n = 0, \quad (30.1)$$

and

$$(A - z^2) \frac{d^2 G_n}{dz^2} - 2z \frac{dG_n}{dz} + 2B_n^2 G_n = 0, \quad (30.2)$$

with  $G(0) = G(1) = 0$ , and  $B_n$  the natural frequency of the  $n$ th mode.

By replacing  $\dot{\theta}$  with its average value  $\omega$  and defining  $\tau = \omega t$ , equation (30.1) simplifies as follows:

$$\ddot{F}_n + [\delta + 2\epsilon \cos(2\tau)]F_n = 0. \quad (31)$$

Equation (31) is Mathieu equation with the parameters given by:

$$\delta = \frac{(B_n^2 - 1)}{\omega^2} \left[ \omega^2 + 2\omega\Omega + \frac{3}{2}\Omega^2 \right] \\ \epsilon = \frac{3}{4} \frac{\Omega^2}{\omega^2} (B_n^2 + 1). \quad (32)$$

Eliminating  $\omega$ , equations (32) yield:

$$\delta = (B_n^2 - 1) + 2 \frac{(B_n^2 - 1)}{(B_n^2 + 1)} \epsilon + \frac{1}{[3(B_n^2 + 1)]^{1/2}} \epsilon^{1/2}. \quad (33)$$



The superposition of this curve onto the Strutt's diagram [12] enables the computation of the boundary values of the parameters  $\delta$  and  $\epsilon$  for stable oscillations. Notice that the shape of this curve depends on the value of the  $n$ th eigenfrequency  $B_n$ , and it is therefore necessary to solve the spatial problem first.

Under the simplifying assumption that the tension is constant along the tether and equal to its average value over one spin period, the time dependent equation of motion yields:

$$\ddot{F}_n + [B_n^2 - \dot{\theta}^2 - 2\dot{\theta}\Omega - 3\Omega^2 \sin^2\theta]F_n = 0, \quad (34.1)$$

and the spatial equation

$$\frac{d^2 G_n}{dz^2} + \frac{\sigma \ell^2}{T} B_n^2 G_n = 0. \quad (34.2)$$

Equation (34.2) represents the motion of a string under constant tension with natural frequencies

$$B_n = \frac{n\pi}{\ell} \sqrt{\frac{T}{\sigma}}. \quad (35)$$

This enables the following formulation of Mathieu equation:

$$\ddot{F}_n + [\delta_1 + 2\epsilon_1 \cos(2\tau)]F_n = 0, \quad (36)$$

with the new parameters

$$\begin{aligned} \delta_1 &= \frac{T}{\sigma \ell^2} \frac{n^2 \pi^2}{\omega^2} - \frac{\Omega^2}{2\omega^2} - 1 \\ \epsilon_1 &= \frac{3}{4} \frac{\Omega^2}{\omega^2}. \end{aligned} \quad (37)$$

The oscillation is unstable for small values of  $\epsilon$  if  $\delta = m^2/4$  where  $m$  is an integer.

For a 1-km-long centrifuge with 1-g artificial acceleration at the capsule  $\omega = 95\Omega$ ,  $\delta_1 = 483.1n^2 - 1$ , and  $\epsilon_1 = 8.31 \times 10^{-5}$ .

From equation (33) a general expression for spinning tethered systems can be derived. Substituting the expression of  $B_n$ , equation (33) yields:

$$\delta_1 = \frac{(r^2 \omega^4 \pi^4 - 1) + 2(r\omega^2 \pi^2 - 1)\epsilon_1 + [3(r\omega^2 \pi^2 + 1)]^{1/2} \epsilon_1^{1/2}}{3(r\omega^2 \pi^2 + 1)}, \quad (38)$$

where  $r = M_{eq}/\sigma \ell$  is the equivalent mass to the tether mass ratio.

Figure 5 shows  $\delta_1$  from equation (38) for small values of  $\epsilon_1$ ,  $n = 1$  (first mode of lateral vibration), and three different values of  $\omega$ . For any practical values of the system parameters and a tether length of 1 km, the lateral tether oscillations are well within the stability boundaries. The faster the system spins and the lighter the tether with respect to the end masses, the more stable the oscillations are. These results are confirmed in [11] and [14].



numerical routine, of a 1-km-long system modelled with 10 lumps. Also in Table 1 are the values of the natural frequencies for a fixed-ends continuous string with constant tension and for an evenly spaced lumpy string with equal lumps and fixed ends, which are given by [15]:

$$\begin{aligned} f_n(\text{longitudinal}) &= \frac{1}{\pi} \sqrt{\frac{EA}{m\bar{\ell}}} \sin\left[\frac{n\pi}{2(N+1)}\right] \\ f_n(\text{transverse}) &= \frac{1}{\pi} \sqrt{\frac{T}{m\bar{\ell}}} \sin\left[\frac{n\pi}{2(N+1)}\right]. \end{aligned} \quad (39)$$

In equations (39),  $n$  is the mode number,  $N$  the number of tether lumps,  $m$  the mass of the lump, and  $\bar{\ell}$  the distance between two successive lumps. Since according to [14], a 4 lumped-mass system provides the lowest natural frequencies with an accuracy of 4% with respect to the continuous model, the 10-lump model adopted for the centrifuge is more than adequate for computing the low order natural frequencies.

## VII. Numerical Results

Numerical results are based on the parameters shown in Table 2. The dynamics simulations have been carried out by using a standard variable step, fourth order Runge-Kutta routine for integrating equations (2). The system is modelled with two lumps only (i.e. the tip-masses) connected by a viscoelastic tether. Because of the high tether tension and the relatively stiff tether, the simulation is very CPU intensive, even with 2 lumps. The addition of more lumps along the tether makes the CPU time prohibitively high and, to a certain extent, unnecessary because thanks to the high tension the tether shape is very close to a straight line.

### *Steady-Rotation Phase*

The centrifuge has its spin axis initially perpendicular to the orbital plane and spins freely, with an initial inertial spin velocity of 1.05 rpm that provides a 1-g gravity level at the GE capsule. The components of the apparent acceleration on board the GE capsule are shown in Figs. 6(a-c). The tangential component is along the tangential velocity, the radial component is along the straight tether, and the lateral component is perpendicular to the spin plane. The lateral and tangential components of the acceleration are negligible. The radial component shows fluctuations smaller than 0.8 mg about the desired value of 1 g. The low- and high-frequency fluctuations are related to tether temperature variations,  $J_2$  effects, and gravity gradient. Because of the low spin rate, an object on board the capsule moving at 3 fps (i.e. the speed of a walking person) in a direction perpendicular to the spin axis is subjected to a side Coriolis acceleration of only 0.02 g.

The centrifugal gradient is  $10^{-3}$  g/m at the steady-rotation rate of 1.05 rpm, which is smaller than the maximum value of the optimal rotational velocity of 2 rpm [16]. As shown in Fig. 7, the tethered centrifuge is long enough to provide a dynamic environment well within the "optimum human comfort zone." The optimum comfort zone is the region of gravity level versus rotational speed that

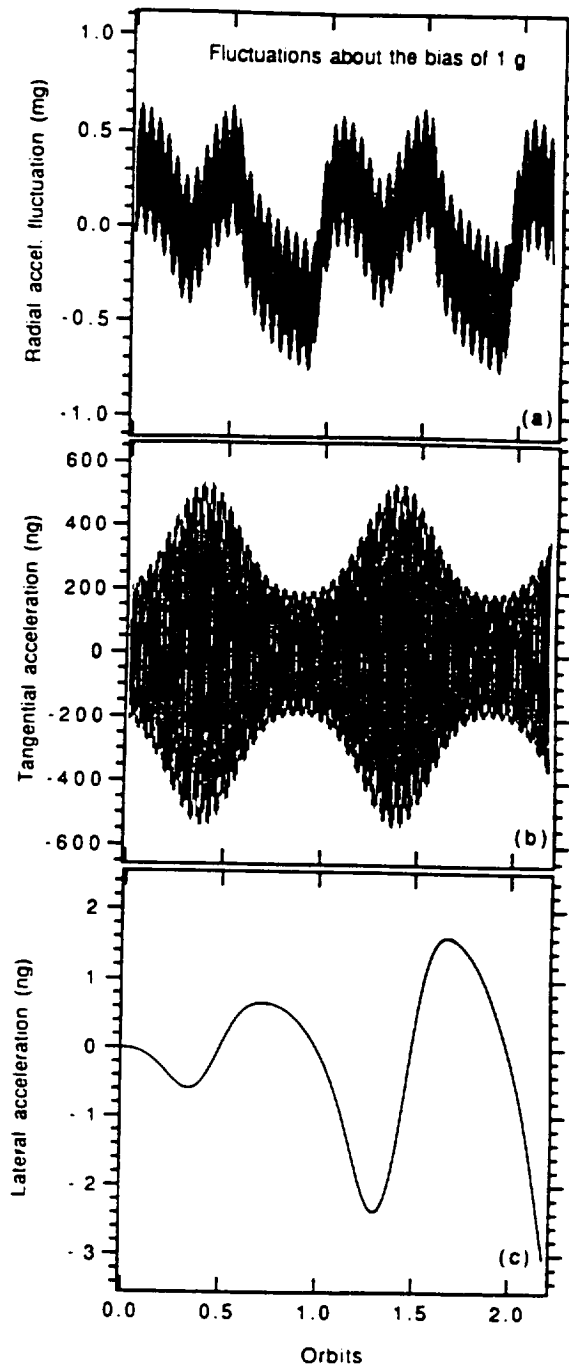
TABLE 2. Orbital and Design Parameters of the Tethered Centrifuge

Orbital Parameters	
Altitude	350 km
Inclination	28.5 deg
Reference Exospheric Temperature	900 °K
Initial Eccentricity	0
Sun Position	Summer Solstice
Design Parameters	
Tether Length	1 km
Tether Diameter	1.7 mm
Tether Thermal Expansion Coefficient	$-2.5 \times 10^{-6} \text{ } ^\circ\text{K}^{-1}$
Kevlar Yield Strength	2500 MPa
Tether Linear Density	3.47 kg/km
Capsule Mass ( $m_1$ )	203.7 kg
Delta II Stage Mass ( $m_2$ )	872.7 kg
Inertial Spin Velocity for 1-g Acceleration at Capsule	1.05 rpm
Longitudinal Wave Speed	3689 m/s
Transverse Wave Speed (Tension = 1960 N)	752 m/s
Tether Axial Stiffness (EA)	47311 N

ground-based tests have demonstrated to be best suited for human physiology [16]. Rotational velocities above 6 rpm produce canal sickness, while gravity levels below 0.3 g impair mobility. Centrifuges with a radius smaller than 8 m are unable to provide an environment suitable for human habitation.

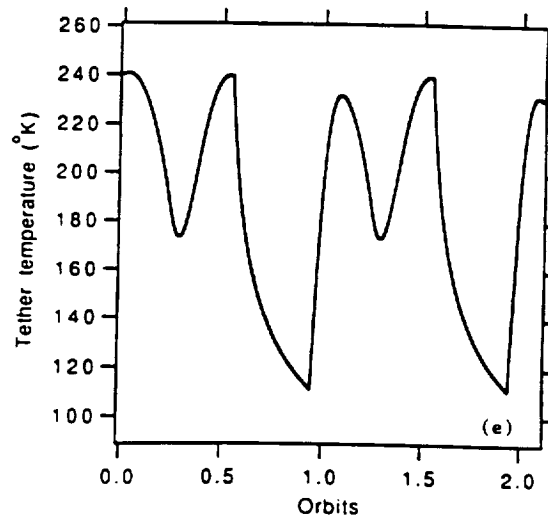
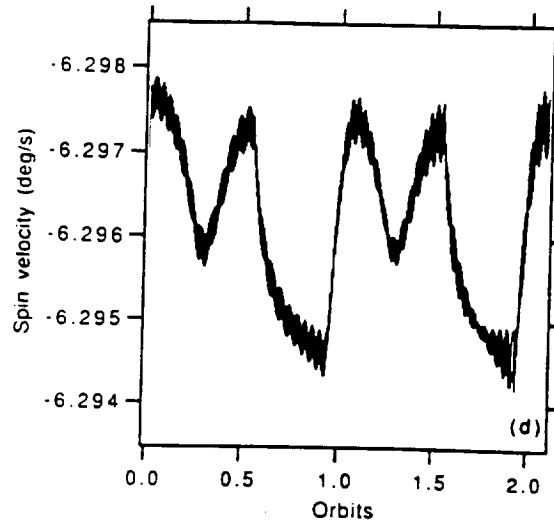
Figure 6(d) depicts the inertial spin velocity. The average spin velocity relative to the rotating frame of  $\theta = 95\Omega$  is very far from the value  $\theta = 1.87\Omega$  at which the out-of-plane motion becomes unstable [17]. The low-frequency variation of the spin rate  $\theta$  is related to the thermal stretch of the tether. The effect of the terminator's crossings at  $t = 3000$  sec and  $t = 5200$  sec is readily seen in Fig. 6(a). A decrease in tether temperature [Fig. 6(e)] produces an increase in tether length and a small decrease in rotational speed. Conversely, a temperature increase produces a small increase of rotational speed.

An interesting result of the centrifuge with its spin axis initially perpendicular to the orbital plane is as follows: the relative angular momentum vector  $\mathbf{H}$  (i.e. about the centrifuge's CM) precesses in inertial space. The  $J_2$  gravity torque, which affects both the orbital and the relative angular momenta, is responsible



FIGS. 6(a)-(f). Dynamic Response during the Steady-Spin Phase of a Centrifuge with the Spin Axis initially Perpendicular to the Orbital Plane.

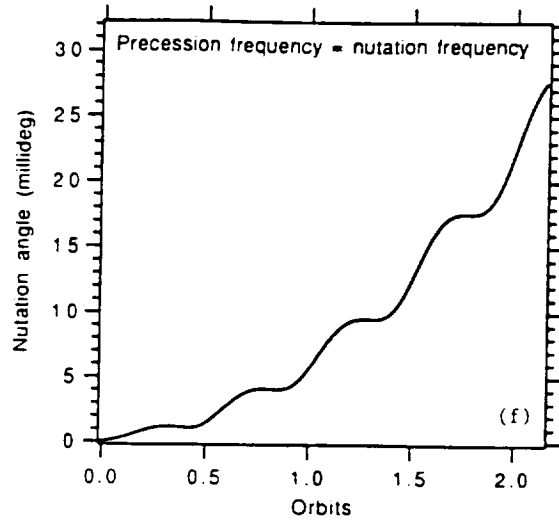
for this phenomenon. As a result, the nutation angle of  $\mathbf{H}$  with respect to its initial orientation increases slowly during the simulation time span as shown in Fig. 6(f). This slow drift of about 5 millideg per orbit is responsible for the slow



FIGS. 6(a)-(f). Cont.

increase of the lateral acceleration component shown in Fig. 6(c). The acceleration level, however, is negligible even after a large number of orbits. A simulation of 20 orbits has shown a linear increase of the lateral acceleration up to a level of 30 nanog after 20 orbits.

Conversely, for a centrifuge with the spin axis initially aligned with the orbital velocity vector, the vector  $\mathbf{H}$  precesses but the maximum amplitude of the nutation angle does not increase with time as shown in Fig. 8(a). Consequently, the amplitude of the lateral acceleration component, shown in Fig. 8(d), is constant. Its magnitude, however, is bigger (but still negligible) than in the previous case



FIGS. 6(a)-(f). Cont.

[compare to Fig. 6(c)] because the lateral acceleration is periodically affected by air drag when the spin axis is initially aligned with the flight direction. Every quarter of an orbit the centrifuge orientation changes from edge-on to head-on with respect to the ram direction. The nonsymmetric behavior of the lateral acceleration is related to the diurnal bulge of the atmosphere whereby the air

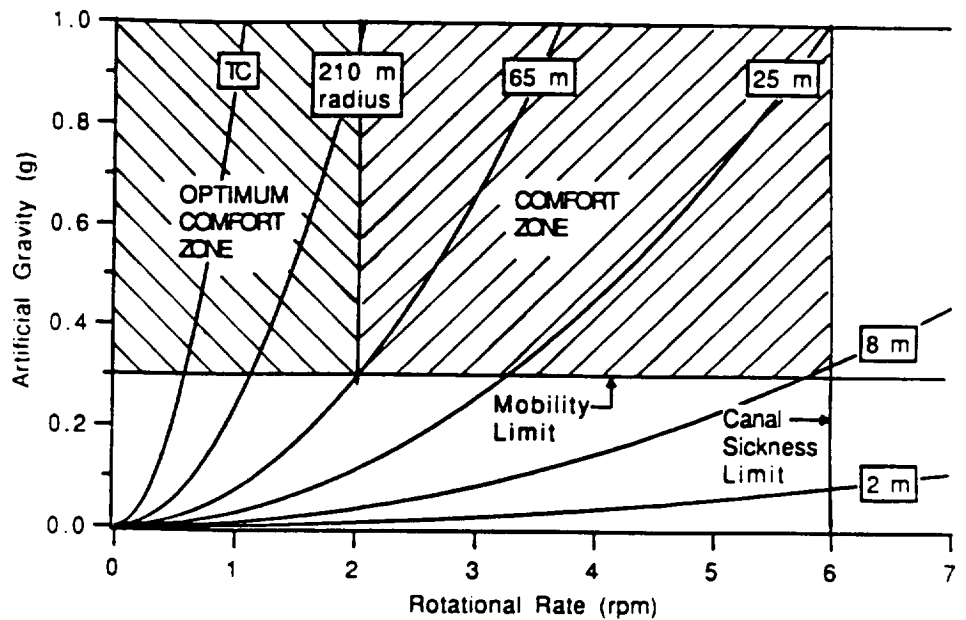
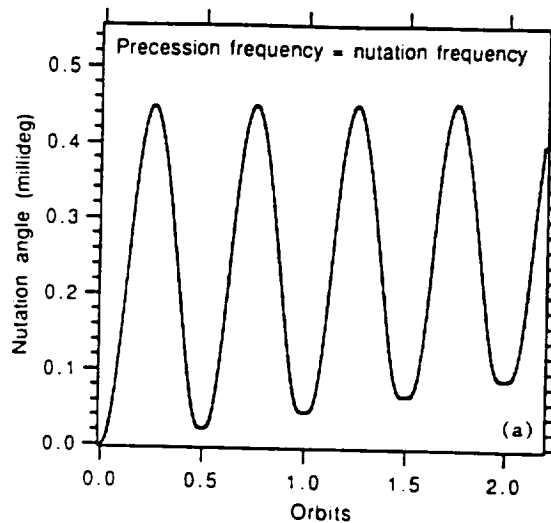


FIG. 7. Artificial Gravity Envelope (Adapted from Ref. [16]). "TC" is the Curve for a 1-km-long Tethered Centrifuge.



FIGS. 8(a)-(d). Dynamic Response during the Steady-Spin Phase of a Centrifuge with Spin Axis initially Aligned with the Orbital Velocity Vector.

density is greater on the sunny side of the orbit. The other components of the acceleration shown in Figs. 8(b) and 8(c), are similar to the previous case. Specifically, the fluctuations of the radial component about the 1-g level are smaller than 0.8 millig.

The analytical treatment of this precession phenomenon is quite complex and beyond the scope of this paper.

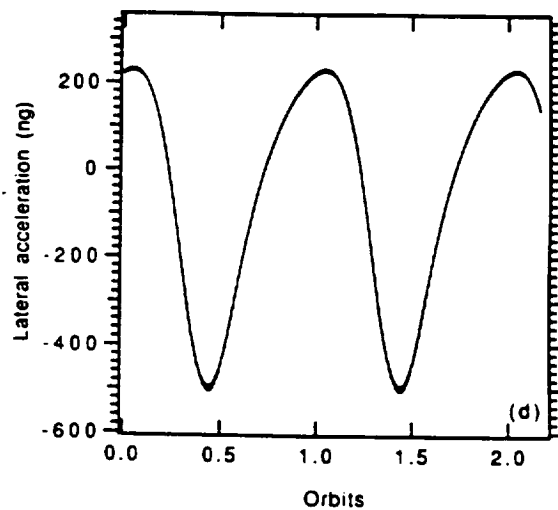
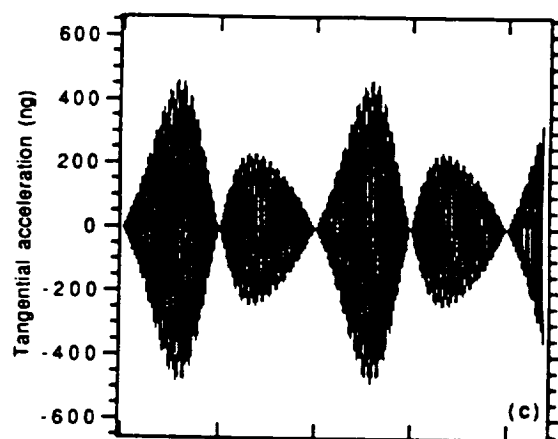
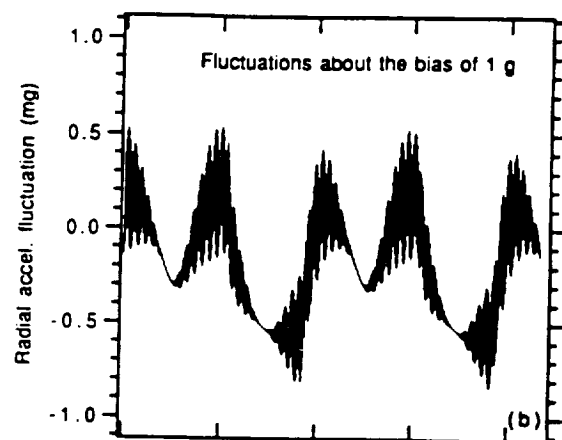
#### *Spin-Up Phase*

The steady-rotation condition is reached in 2000 s as shown in Fig. 9(a). The first rotation takes almost 150 seconds to complete. In the same period of time the instantaneous thrust, shown in Fig. 9(b), grows from zero to 21.5 N. The total propellant consumption is 70 kg for a cold gas system with a specific impulse of 55 s, but only 13 kg if a bipropellant hydrazine propulsion is adopted. Figure 9(c) shows that a 1-g level of radial apparent acceleration is readily attained by the centrifuge.

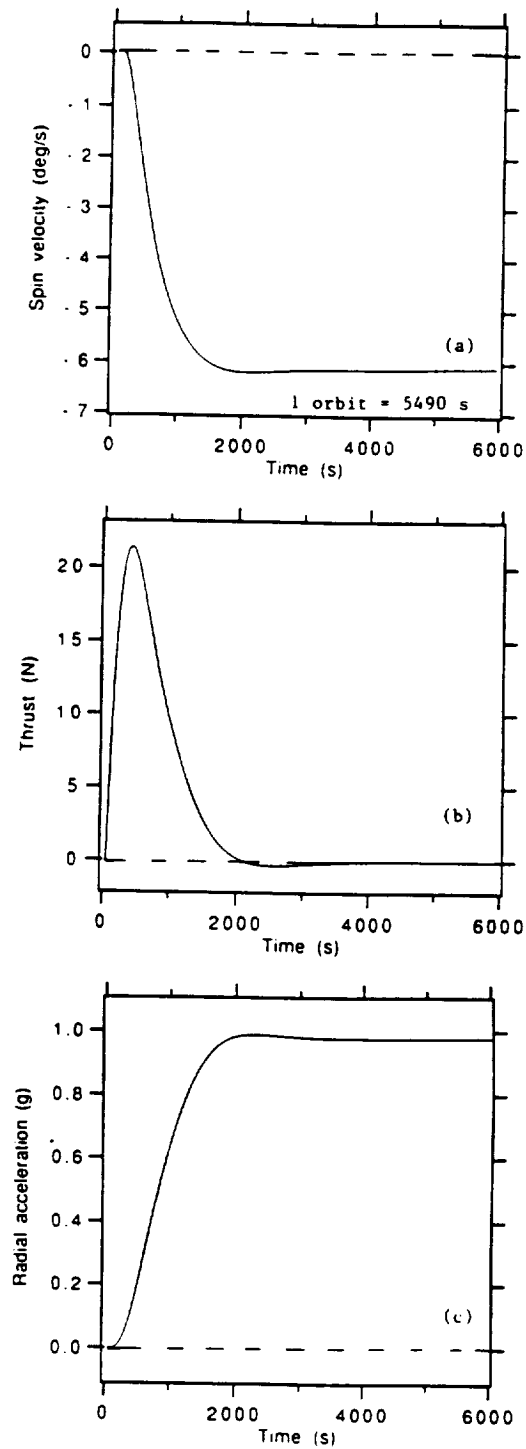
#### *De-Spin Phase*

The system takes 2000 s to reach the quiescent condition [Fig. 10(a)]. The thrusters have no control over the out-of-plane motion, as shown in Fig. 10(b). The thrust level was limited to 40 N, as shown in Fig. 10(c), in this simulation. Once the maneuver is over, the out-of-plane motion changes from a rotation with a spin period of 57.74 s to a libration forced by the  $J_2$ -term with an orbital period of 5492 s. The tension in the tether changes from 1960 N (due almost entirely to the centrifugal force) to 0.13 N due to the gravity gradient. Figure 10(d) shows the radial apparent acceleration, which goes to zero following the variation of tether tension. Since the control law for de-spin is different from the

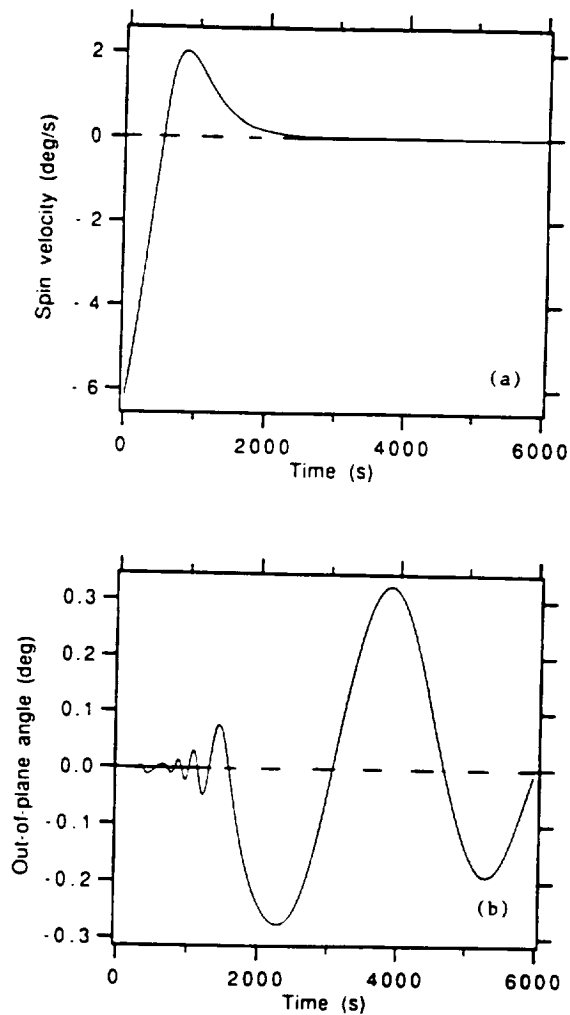




FIGS. 8(a)-(d). Cont.



**FIGS. 9(a)-(c).** Dynamic Response during the Spin-Up Phase of a Centrifuge with the Spin Axis initially Perpendicular to the Orbital Plane.

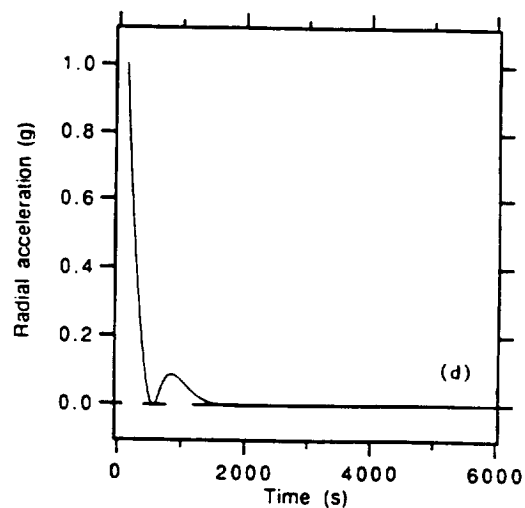
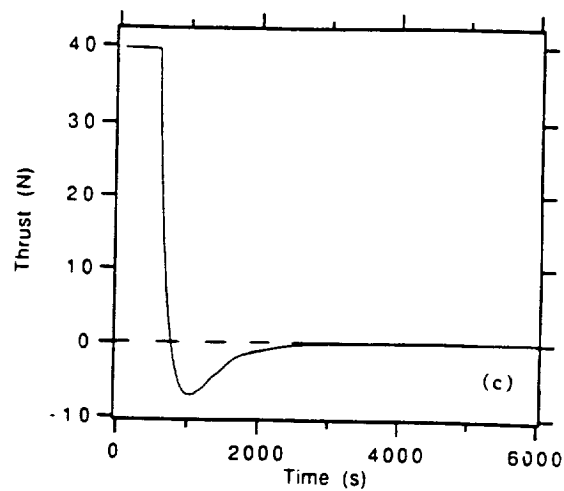


FIGS. 10(a)-(d). Dynamic Response during the De-Spin Phase of a Centrifuge with the Spin Axis initially Perpendicular to the Orbital Plane.

spin-up control law, the propellant consumption is now equal to 110 kg for a cold gas system but only 20 kg for a bipropellant hydrazine propulsion system.

### VIII. Conclusions

The major conclusions on the dynamics and stability of the 1-km space centrifuge are as follows: (1) the analysis of the tether two-dimensional transverse vibrations shows that these oscillations are stable for any practical values of the system parameters; (2) the dynamic environment provided by the tethered centrifuge is in the optimum comfort zone for humans subjected to artificial gravity conditions and the acceleration fluctuations about the 1-g level are smaller than 0.8 mg; (3) because of the  $J_2$  component of the gravity field, the relative angular



FIGS. 10(a)-(d). Cont.

momentum vector precesses and drifts very slowly for a centrifuge with the spin axis initially perpendicular to the orbital plane, conversely the angular momentum precesses without drifting for a centrifuge with the spin axis initially parallel to the orbital plane; and (4) by adopting a proportional-derivative control law for the thrusters, it is possible to spin-up and de-spin the centrifuge in less than one orbit with a moderate propellant consumption.

#### Acknowledgment

This paper has been supported in the United States by NASA/MSFC Contract NAS8-36606 with Charles Rupp and James Harrison as program directors. Marco B. Quadrelli's

support has been provided by Accademia Nazionale dei Lincei, Rome, Italy, with the *Giuseppe Colombo Fellowship*. The authors would also like to thank Prof. Arun Misra for his useful advice.

## References

- [1] RUPP, C., LEMKE, L., and PENZO, P. "An Artificial Gravity Demonstration Experiment," *Tethers in Space Toward Flight*, AIAA, Washington, D.C., 1989, pp. 316-322.
- [2] SCHULTZ, D., RUPP, C., HAJOS, G. A., and BUTLER, J. M. "A Manned Mars Artificial Gravity Vehicle," *Space Tethers for Science in the Space Station Era*, Società Italiana di Fisica, Vol. 14, Bologna, Italy, 1987, pp. 320-355.
- [3] GLAESE, J. R. "The Dynamics of Tethers in Artificial Gravity Applications," *Space Tethers for Science in the Space Station Era*, Società Italiana di Fisica, Vol. 14, Bologna, Italy, 1987, pp. 388-393.
- [4] LORENZINI, E. C., COSMO, M., VETRELLA, S., and MOCCIA, A. "Dynamics and Control of the Tether Elevator/Crawler System," *Journal of Guidance, Control, and Dynamics*, Vol. 12, No. 3, May-June, 1989, pp. 401-411.
- [5] COSMO, M., LORENZINI, E. C., VETRELLA, S., and MOCCIA, A. "Transient Dynamics of the Tether Elevator/Crawler System," Paper No. AIAA-88-4280-CP, AIAA/AAS Astrodynamics Conference, Minneapolis, Minnesota, August 15-17, 1988.
- [6] MISRA, A. K., and MODI, V. J. "A Survey on the Dynamics and Control of Tethered Satellite Systems," *Tethers in Space*, Advances in Astronautical Sciences, Vol. 62, AAS, 1987, pp. 667-719.
- [7] LORENZINI, E. C. "Analytical Investigation of the Dynamics of Tethered Constellations in Earth Orbit (Phase II)," *Smithsonian Astrophysical Observatory Quarterly Report* No. 6, October 1986.
- [8] ROBERTS, C. E. "An Analytical Model for Upper Atmosphere Densities Based Upon Jacchia's 1970 Models," *Celestial Mechanics*, Vol. 4, 1971, pp. 368-377.
- [9] WERTZ, J. R. (Ed.) "Spacecraft Attitude Determination and Control," D. Reidel Publishing Company, 1978, pp. 588-594.
- [10] HARRISON, J. K., RUPP, C. C., CARROLL, J. A., ALEXANDER, C. M., and PULLIAM, E. R. "Small Expendable-Tether Deployer System (SEDS) Development Status," *Tethers in Space Toward Flight*, AIAA, Washington, D.C., 1989, pp. 19-26.
- [11] TARGOFF, W. P. "On the Lateral Vibration of Rotating Orbiting Cables," Paper No. 66-98, AIAA 3rd Aerospace Sciences Meeting, New York, New York, January 24-26, 1966.
- [12] MEIROVITCH, L. *Methods of Analytical Dynamics*, McGraw-Hill, 1970, p. 286.
- [13] CUNNINGHAM, W. J. *Nonlinear Analysis*, McGraw Hill Book Company, 1958, p. 271.
- [14] CRIST, S. A. "Motion and Stability of a Spinning Cable-Connected System in Orbit," NASA Report 67-7, Grant NGR-23-005-131, June 1967.
- [15] MAIN, G. I. "Vibrations and Waves in Physics," Cambridge University Press, 1978, pp. 218-220.
- [16] GILRUTH, R. R. "Manned Space Station-Gateway to Our Future in Space," *Manned Laboratories in Space*, S. F. Singer (editor), D. Reidel Publishing Company, 1968, pp. 1-10.
- [17] THOMPSON, W. S., and GIERMAN, S. "A Preliminary Study of the Dynamical Stability of a Spinning Tether," *Space Tethers for Science in the Space Station Era*, Società Italiana di Fisica, Vol. 14, Bologna, Italy, 1987, pp. 413-415.



## 5.0 TWO-DIMENSIONAL STRUCTURES WITH TETHERS

While the gravity gradient provides positive tension along the vertical direction of Earth-pointing long tethers in space, stabilizing forces in the horizontal direction can be produced by either differential air drag or electrodynamic forces. An alternative to the Earth oriented large structures is a centrifugally stabilized circular structure made of long tethers which form the perimeter of the circle and the spokes. In either case, the final goal is the stabilization of two-dimensional large structures in LEO which make use of long tethers as structural elements.

The work carried out during this contract was the continuation of the investigation conducted under contract NAS8-35497 from NASA/MSFC in which issues of stability of two-dimensional tethered structures had been investigated. The results of that research are best summarized in the following reference: E.C. Lorenzini, "Novel-Connected Two-Dimensional Structures for Low Earth Orbits," *The Journal of the Astronautical Sciences*, Vol. 36, No. 4, pp. 389-405, 1988.

Under the present contract, the research on two-dimensional structures focused on the development of planar phased arrays with extremely high gains.

The following paper focuses on the design and system requirements for spaceborne phased-array antennas for high power transmission of electromagnetic waves in the ULF ( $< 3$  Hz) and VLF (3-30 kHz) frequency bands. The structures proposed in this paper are not only Earth-oriented and stabilized by electrodynamic forces but also centrifugally-stabilized with a spin axis perpendicular to the orbital plane.





# AIAA '89

**AIAA 89-0676**

**One-Dimensional Tethers and Two-Dimensional  
Tethered Structures as Spaceborne Antennas  
for Radio Communications in the Bands  
ULF-to-VLF**

M. Grossi and E. Lorenzini, Smithsonian  
Institution for Astrophysics, Cambridge, MA

**27th Aerospace Sciences Meeting**

January 9-12, 1989/Reno, Nevada

# ONE-DIMENSIONAL TETHERS AND TWO-DIMENSIONALS TETHERED STRUCTURES AS SPACEBORNE ANTENNAS FOR RADIO COMMUNICATIONS IN THE BANDS ULF-TO-VLF

Mario D. Grossi\* and Enrico C. Lorenzini\*  
Smithsonian Institution Astrophysical Observatory  
Cambridge, Massachusetts 02138 USA

## Abstract

A possible application of long conducting tethers in Earth orbit and of spaceborne, two-dimensional tethered structures is to radio communications in a frequency band that extends upwards from about one Hertz to several tens kilohertz. One-dimensional electrodynamic tethers of the self-powered, drag-compensated variety have the potential to function as effective transmitting antennas at the lower end of this band (ULF frequencies), while two-dimensional tethered structures could make it possible to mechanize large-size VLF phased arrays of electric or magnetic dipoles with a gain in excess of 30 dB. Substantial R&D activity is still necessary (involving Shuttle-borne, satellite-borne and rocket-borne experiments) to prove the feasibility of these concepts and to provide experimental data, lacking at this time, on which to base the engineering design of these orbiting systems.

### 1. Single-dimensional tethers

A self-powered, drag-compensated, vertical electrodynamic tether, functioning as a "phantom loop" magnetic-dipole antenna (Grossi, 1987) with a moment in excess of  $10^{10}$  A.m<sup>2</sup> and with a mass smaller than 10 tons could transmit at ULF ( $\sim 1$  Hz) call-up messages and low-data-rate communications to receiving terminals deeply submerged in sea water. The technology of spaceborne tethers, inclusive of the plasma contactors necessary to bridge the tether's terminations to the ionosphere is well on hand at this time and will be experimentally verified in the early '90s. Some of the basic system parameters are given in Table I.

Should the technology of room-temperature superconductivity advance to the point that we could make practical use of it in spaceborne systems, there would be a significant mass reduction. A tether system could be configured with the design parameters given in Table II.

A first experiment on the electromagnetic radiative properties of a vertical electrodynamic tether will be carried out on the occasion of the TSS-1 flight, scheduled for early 1991. A ULF communications system of practical significance, based on the results of this experiment, could be operational a few years later, possibly by 1995.

### 2. Two-dimensional Tethered Structures

Even more impressive are the possibilities offered by two-dimensional tethered structures, that could function as spaceborne reticles made of kevlar wires, capable

\*Also Consulting Scientist, Raytheon Company,  
Portsmouth, Rhode Island 02871  
Associate Fellow Member AIAA

• ORBITAL HEIGHT	500 to 1000 Km
• ORBITAL INCLINATION	<60°
• TETHER LENGTH	25 km
• TETHER CURRENT	10 A
• AVERAGE PRIMARY POWER GENERATED BY TETHER	21.87 KWATT
• TETHER OHMIC RESISTANCE	53 OHM (A WIRE OF ALUMINUM AND KEVLAR THREADS)
• OHMIC LOSSES IN TETHER	53 Kwatt
• PLASMA CONTACTOR RESISTANCE	30 OHM (FOR TWO)
• IONOSPHERIC CIRCUIT RESISTANCE	2 OHM
• TETHER MASS	3 TONS
• CARRIER FREQUENCY	1 Hz
• MODULATION	DPSK
• RECEIVER BANDWIDTH	0.1 Hz
• EXTERNAL SOURCE FOR SYSTEM LOSSES COMPENSATION (15 Kwatt)	2 SOLAR PANELS, EACH WITH $a = 8m$ $b = 6.5m$ (WITH 225 kg BATTERIES IN PARALLEL)
• TOTAL MASS OF ORBITING SYSTEM	6 TONS

Table I. Spaceborne ULF Transmitter Using an Electrodynamic Tether Made of Non-Superconducting Aluminum Wires

• ORBITAL HEIGHT	500 to 1000 Km
• ORBITAL INCLINATION	<60°
• TETHER LENGTH	25 km
• TETHER CURRENT	10 A
• AVERAGE PRIMARY POWER GENERATED BY TETHER	21.87 KWATT
• TETHER OHMIC RESISTANCE	0 OHM (MATERIAL THAT IS SUPERCONDUCTING AT ROOM TEMPERATURE)
• OHMIC LOSSES IN TETHER	0 Kwatt
• PLASMA CONTACTOR RESISTANCE	30 OHM (FOR TWO)
• IONOSPHERIC CIRCUIT RESISTANCE	2 OHM
• TETHER MASS (WITH THERMAL SLEEVE)	2 TONS
• CARRIER FREQUENCY	1 Hz
• MODULATION	DPSK
• RECEIVER BANDWIDTH	0.1 Hz
• EXTERNAL SOURCE FOR SYSTEM LOSSES COMPENSATION (4.4 Kwatt)	2 SOLAR PANELS, EACH WITH $a = 8m$ $b = 3m$ (WITH 64 kg BATTERIES IN PARALLEL)
• TOTAL MASS OF ORBITING SYSTEM	6 TONS

Table II. Spaceborne ULF Transmitter Using an Electrodynamic Tether Made of Room-Temperature Superconducting Material

of supporting an array of dipoles of unprecedented radiation intensity and gain. These large-size structures (circles, ellipses, rectangles, squares, triangles, etc.) can be magnetically stiffened in a plane perpendicular to the geomagnetic field (Lorenzini, 1984) or centrifugally stiffened. Figures 1, 2 and 3 provide examples of stiffening by electrodynamic forces, while in Figure 4, a centrifugally-stiffened configuration is depicted. The large-size,

magnetically-stiffened rectangular array of Figure 5, with dimensions 50 km  $\times$  150 km, containing 1000 loops (elementary magnetic dipoles) could provide in the ELF band (at about 75 Hz) a magnetic moment of  $10^{11}$  A $\cdot$ m<sup>2</sup>, with a total mass smaller than 50 tons.

The VLF band, that extends from 3 KHz to 30 KHz, is where the advantages of tethered structures as electromagnetic radiators in Earth orbit are most striking. At 9 KHz, the 30 km diameter, circular array of Figure 4, rotating at 2.75 rph in a 750 km circular orbit, coplanar with the orbit, could provide a  $2^\circ \times 2^\circ$  beamwidth and radiate into the ionosphere a power level of almost one Megawatt.

This beam, directed downward along the vertical, and kept in that orientation by circular rotation of the phase distribution among the array elements (while the array rotates in its orbital motion) could use hundreds of loops, as indicated in Table III.

FREQUENCY	DIAMETER OF WHEEL	NUMBER OF ELEMENTARY LOOPS
9 KHZ	30 KM	720/360/180 LOOPS, DIA = 200 M EACH
14 KHZ	20 KM	720/360/180 LOOPS, DIA = 152 M EACH
20 KHZ	14 KM	720/360/180 LOOPS, DIA = 136 M EACH

Table III. Array Size (Geometry and Number of Loops) at Three Frequencies  $2^\circ \times 2^\circ$  Beam

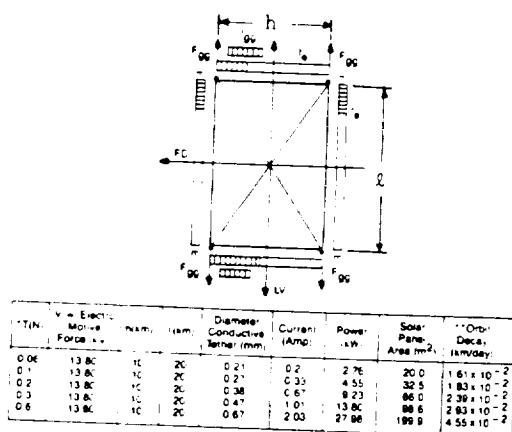


Figure 1. Example of rectangular structure stabilized by electrodynamic forces (tethers are all in aluminum and have the same diameter).

The physical and electromagnetic properties of each loop are illustrated in Table IV. The directivity and the gain that are achievable with the  $2^\circ \times 2^\circ$  array that we have discussed thus far are illustrated in Table V. Such an array would make it possible to achieve a Signal-to-Noise ratio of 0 dB (threshold) in 1 Hz bandwidth, at a distance of 5,000 km from the ionospheric "exit point" in the worst conditions of propagation and noise level, as encountered in Summer daytime. This result is of substantial significance in strategic communications.

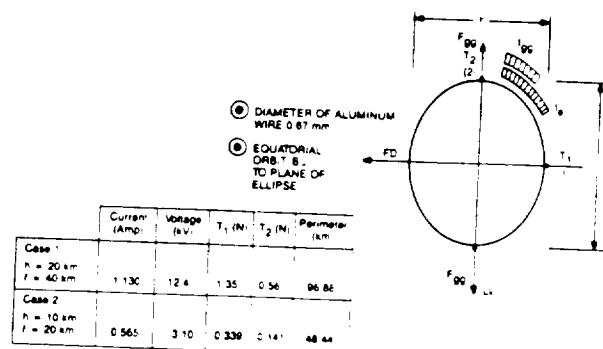


Figure 2. Example of pseudo-elliptical loop also electrodynamically stabilized.

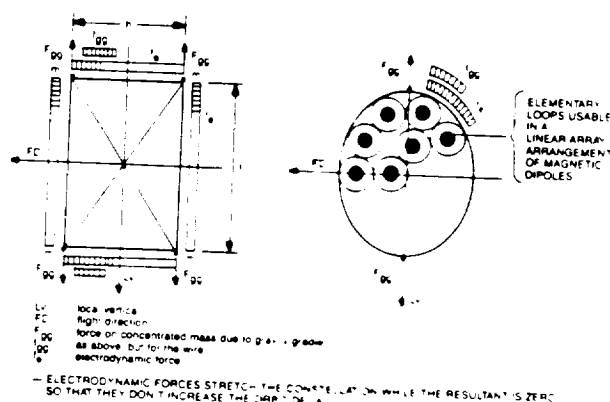


Figure 3. Two-dimensional tethered structure where shape stability is again provided by electrodynamic forces.

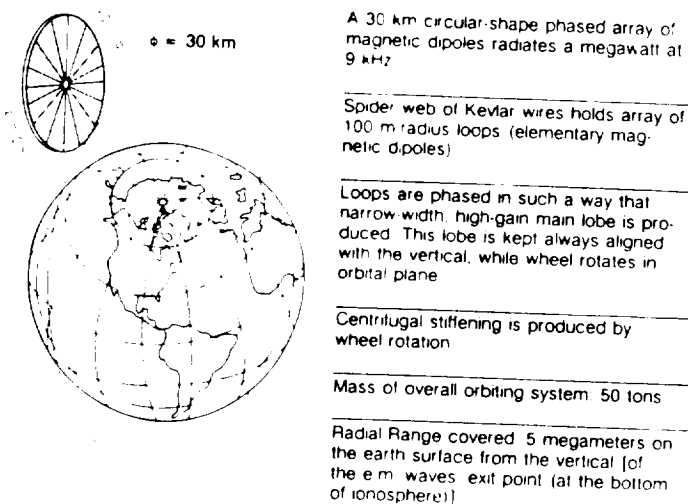
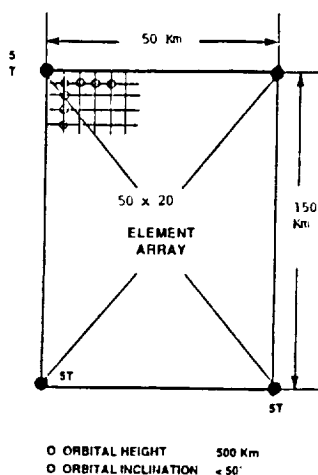


Figure 4. Spaceborne VLF transmitter and antenna for communications at 9 KHz.

The 30-km array (a flat ring with OD (outer diameter) = 30 km and ID (inner diameter) = 10 km) could be mechanized with 18 radial spokes and 10 loops/spoke, the total mass being about 100 tons. When



- REQUIRED TOTAL MAGNETIC MOMENT  $10^{11}$  A.M<sup>2</sup>
- MAGNETIC MOMENT OF EACH ELEMENTARY LOOP (LOOP DIAMETER,  $\phi = 320$  M, LOOP AREA =  $8 \cdot 10^4$  M<sup>2</sup>, CURRENT 12.5 A)  $10^6$  A.M<sup>2</sup>
- NUMBER OF LOOPS IN ARRAY (50x20)  $10^3$
- ACHIEVABLE DIRECTIVITY  $10^2$
- TOTAL ACHIEVABLE MAGNETIC MOMENT ( $10^6 \cdot 10^3 \cdot 10^2$ )  $10^{11}$  A.M<sup>2</sup> (AS REQUIRED)
- POWER FED TO EACH ELEMENTARY LOOP (ALL POWER IS RADIATED) 120 WATT
- TOTAL POWER FED TO ARRAY (ALL POWER IS RADIATED) 120 KWATT
- MASS OF EACH LOOP (DIAMETER 3 MM) 10 Kg
- TOTAL MASS OF  $10^3$  LOOPS 30 TONS
- TOTAL MASS OF ELECTRONICS (10 kg/LOOP) 10 TONS
- MASS OF 4 CORNER PLATFORMS (EACH 2 TONS) 8 TONS
- MASS OF MAGNETICALLY STIFFENED SUPPORT FRAME (100 A STIFFENING CURRENT CABLE MADE OF SUPERCONDUCTING MATERIAL) 15 TONS
- MASS OF SUPPORT RETICLE (MADE OF 40 HORIZONTAL TETHERS AND 20 VERTICAL TETHERS, ALL IN KEVLAR) 3 TONS
- GRAND TOTAL MASS OF ORBITING SYSTEM 66 TONS

Figure 5. Spaceborne ELF transmitter and antenna for communications at 75 Hz.

working at 20 KHz, the array diameter could be limited to 15 km OD and 5 km ID, with the same number of spokes and of loops/spoke as before. In this case the mass could be kept limited to 50 tons.

By assuming to generate the primary power with a few, say three, power plants (such as SP-300 fission reactors), we have to account for distribution losses of the DC power to the single radiators, each one equipped with its VLF transmitter. The power losses in the distribution system are indicated in Table VI. It can be seen that, for each of the four cases that we have considered, these losses are affordable.

Concerning deployment, it is not an easy task to erect in orbit a large-size, two-dimensional structure. However, schemes that are feasible and practical can be worked out, requiring minimal EVA activity or no EVA activity at all.

### 3. Conclusions and Recommendations

There are still several technical issues that need serious study. To name just a few: (a) investigation of possible non-linear effects in the ionosphere, due to the unusually high level of radiated power; (b) establishing a rigorous theory of beam-forming in a magnetoionic medium; (c) perform, in preliminary experiments with rockets and satellites, the space-to-ground channel characterization of the propagation paths, inclusive of determination of Doppler spread and multipath spread, in order to establish the ultimate communication capabilities of these paths.

Finally, the single issue of the uppermost importance, that will decide about the fate of spaceborne tethered structures as radiators of e.m. waves, and make them acceptable to the communications community, if satisfactory technical solutions are found, is cost. Simplicity, low mass, easy deployability are the criteria that system designers must keep prominently under consideration.

FREQUENCY	ELEMENTARY LOOP DIAMETER	WIRE DIAMETER	OHMIC RESISTANCE	MASS
9 kHz	200 m	9.12 mm	0.26 $\Omega$	111 Kg LOOP
14	152	6.137	0.26	87.06
20	136	7.52	0.25	40.24

- NOTES
- 1 WIRE MADE OF ALUMINUM
  - 2 HEIGHT OF ARRAY 750 Km
  - 3 RADIATION RESISTANCE OF EACH LOOP 0.5  $\Omega$  IN ALL CASES
  - 4 INDEX OF REFRACTION 15 AT 9 kHz  
12 AT 14 kHz  
10 AT 20 kHz

Table IV. Properties of Each Elementary Loop

■ Directivity, D  $D = \frac{4\pi R^2}{\Omega_s} = \frac{41,253}{2^\circ \times 2^\circ} = 10,313$   
 $\therefore D \approx 40$  dB

■ Gain, G  $G = kD$ , where k is radiator efficiency  
 $k = \frac{R_{rad}}{R_{rad} + R_{ohmic}} = \frac{0.511}{0.511 + 0.25\Omega} \approx 0.686$   
 $\therefore G \approx 0.686 \times 10,313 = 6,875.33$   
 $G \approx 38.37$  dB

Table V.  $2^\circ \times 2^\circ$  Array's Directivity and Gain

		LOSSES IN FEED LINES ALONG RADIAL SPOKES ONLY	TOTAL LOSSES IN DISTRIBUTION SYSTEM
FIRST CASE	20 KHz Array of 720 loops, 15 km wheel 72 spokes; 10 loops/spoke; spoke length 5 km; feedline resistance ~ 3 ohm; feed voltage 1.2 KV; spoke current 10 A; 24 spokes for each SP-300 generator; 12.5 KW distributed by each spoke; 1.054 KW to each loop	21 KW	27 KW
SECOND CASE	20 KHz Array of 180 loops, 15 km wheel 18 spokes; 10 loops/spoke; spoke length 5 km; feedline resistance ~ 3 ohm; feed voltage 1.2 KV; spoke current 42 A; 6 spokes for each SP-300 generator; 50 KW distributed by each spoke; 5 KW to each loop	91 KW	117 KW
THIRD CASE	9 KHz Array of 720 loops, 30 km wheel 72 spokes; 10 loops/spoke, spoke length 10 km; feedline resistance ~ 2 ohm; feed voltage 1.2 KV; spoke current 10 A; 24 spokes for each SP-300 generator; 12.5 KW distributed by each spoke; 1.054 KW to each loop	15 KW	19 KW
FOURTH CASE	9 KHz Array of 180 loops, 30 km wheel 18 spokes; 10 loops/spoke; spoke length 10 km; feedline resistance ~ 2 ohm; feed voltage 1.2 KV; spoke current 42 A; 6 spokes for each SP-300 generator; 50 KW distributed by each spoke; 5 KW to each loop	63 KW	81 KW

Table VI  
Examples of Computation of Power Loss in Distribution System

#### 4. Bibliographic References

1. Grossi, M.D., 1987, "System Application Study, Section 3 of Final Report Contract NAG8-551, System Engineering Study of Electrodynamic Tether as a Spaceborne Generator and Radiator of E.M. Waves in the ULF/ELF Frequency Band," SAO Report, February.
2. Lorenzini, E.C., 1984, "Analytical Investigation of the Dynamics of Tethered Constellation in Earth Orbit," Final Report Contract NAS8-35497, SAO Report, December.
3. Lorenzini, E.C., 1988, "Novel Tether-Connected Two-Dimensional Structures for Low Earth Orbits," The Journal of Astronautical Sciences, Oct-Dec (in print).



## 6.0 TETHERED HIGH-GAIN ANTENNAS

Conductive Earth oriented tethers can function as high directivity transmitting and/or receiving antennas. The proposed transmitting antennas are traveling wave antennas, i.e., the antennas are non-resonant, terminated by the characteristic impedance.

The three following papers treat the transmitting and receiving antennas as follows:

The first is a white paper which proposes a 4-km vertical, downward tether to transmit e.m. waves in the ULF ( $< 3$  Hz) band and alternatively in the VLF (3-30 kHz) band. The current in the antenna is 12 A for the ULF transmission at 0.25 Hz and 5 A for the VLF transmission at 9 kHz. A second, upward tether is also proposed for transforming orbital energy into electrical energy in order to recharge the batteries for a few times before the orbit decays. Signal-to-noise ratios on the ground are estimated at +6.5 dB and +22.5 dB respectively.

The second paper addresses the propagation of ELF (30-300 Hz) and VLF (3-30 kHz) waves in the ionosphere with particular emphasis on the latter type of waves also called the whistlers. The far field radiation pattern is computed and conditions at the crossing of the E-layer of the ionosphere are evaluated.

The third paper proposes a set of two vertically oriented, traveling-wave antennas orbiting on the same orbit but separated by a distance to provide a high-directivity, narrowly-focused radiation pattern. The two antennas, orbiting at an altitude of 10,000 km are proposed as receiving antennas for radioastronomy in the frequency band 1-30 MHz.





**WHITE PAPER**

**SEDS/Delta-II Electrodynamic Tether Experiment on the Generation and  
Radiation of Electromagnetic Waves from ULF to VLF**

by

Mario D. Grossi, Enrico C. Lorenzini and Mario L. Cosmo

June 1991

Smithsonian Institution  
Astrophysical Observatory  
Cambridge, Massachusetts 02138

<p>The Smithsonian Astrophysical Observatory is a member of the Harvard-Smithsonian Center for Astrophysics</p>
---

## **Table of Contents**

<b>Abstract.....</b>	<b>1</b>
<b>Introduction.....</b>	<b>2</b>
<b>Technical Discussion .....</b>	<b>6</b>
<b>General .....</b>	<b>6</b>
<b>Description of the Proposed Payload .....</b>	<b>6</b>
<b>Orbital Flight Parameters.....</b>	<b>10</b>
<b>Ground-Based Data Collection.....</b>	<b>10</b>
<b>Further Implications of Proposed Experiment.....</b>	<b>14</b>
<b>Brief Outline of the Proposed Program.....</b>	<b>14</b>
<b>References .....</b>	<b>15</b>

## Abstract

An electrodynamic experiment on the generation and radiation of e.m. waves from ULF to VLF frequencies (the specific band of interest extends from about 0.25 Hz to about 30 kHz) can be conducted by taking advantage of one of the future Delta II flights. The proposed payload has a mass of  $\approx 794$  lb, well within the weight margin of 950 lb available for secondary payloads on a Delta II/GPS flight. The payload consists of two SEDS-type deployers, each one to deploy a 4-km-long dielectric-coated copper wire with an overall diameter of 1 mm. The 2x4-km conducting wires are equipped with plasma contactors, Silver-Zinc batteries, modulator, transmitter, DC/AC-AC/DC static converter, programmer/sequencer, etc.

In the ULF mode of operation (carrier frequency of the order of one hertz) the self-powered antenna can draw from the ionosphere a current of 12 A *dc*, under the drive of a maximum electromotive force of 2.1 kV provided by the  $\mathbf{V} \times \mathbf{B} \cdot \mathbf{l}$  mechanism, where  $\mathbf{V}$  is the orbital velocity,  $\mathbf{B}$  the intensity of the Earth magnetic field, and  $\mathbf{l}$  is the antenna's length. At the lower end of the frequency band, the unidirectional current will be modulated by means of a controlled solid-state switch and pulse shaper, from a frequency of 0.25 Hz up to a few Hertz. Existing ground-based receiving stations (e.g. those established by the Smithsonian Astrophysical Observatory and the University of Genova, Italy for the TSS-1 program), as well as existing Magnetic Observatories, will provide a world wide network of receiving terminals to collect and record the signals on the ground.

Based on a phantom-loop radiation model, a signal-to-noise ratio (SNR) of +6.5 dB in  $10^{-2}$  Hz bandwidth is expected at the Earth surface, along the ground track of the orbiting system, for frequencies in the ULF band. This is 27.5 dB better than the SNR of -21 dB that the phantom loop model predicts, under a comparable set of circumstances, for the TSS-1 electromagnetic emissions.

In the ELF mode (30 Hz–60 Hz in our case) and in the VLF mode (3 kHz – 30 kHz) one of the two 4-km tethers is used to generate DC electric power for supplementing the on-board batteries and the other is used as a travelling wave antenna. SNR ratios of +20 to +30 dB are expected on the Earth surface in the VLF band, in a 1 Hz bandwidth.

Optionally, experiments could also be carried out on the potential use of the spaceborne travelling wave antenna as a receiving antenna for scientific uses such as ionospheric physics and low frequency (LF) radioastronomy.

## Introduction

The spaceborne tether concept was first proposed (Grossi, 1973) as a long-wire orbiting antenna usable at frequencies as low as a fraction of 1 Hz. In the area of magnetospheric physics, the usefulness of the tether was identified to reside in the generation of artificial micropulsations of the PC-1 class, and of neighboring classes, thus providing a useful tool to understand several puzzling aspects of this natural phenomenon. In the area of technological applications, the tether was proposed as a generator and radiator of electromagnetic waves in the ULF band (unofficially defined as the band of frequencies  $f < 30$  Hz), in the low-ELF band (the ELF band is officially defined  $30 \text{ Hz} \leq f \leq 300 \text{ Hz}$ ), and in the VLF band (officially defined  $3 \text{ kHz} \leq f \leq 30 \text{ kHz}$ ).

All these bands are of interest to strategic communications. At hertz and subhertz frequencies, the tether could operate as an orbiting terminal capable of transmitting "call-up" bell-ringing signals to deeply submerged receivers. At low-ELF frequencies, namely near the upper end of the allowable band of tether emissions that extends from *dc* to about 60 Hz (Barnett and Olbert, 1986), the tether could operate as an orbiting facility for the transmission of actual information-carrying messages, thus complementing existing ground-based ELF transmitters. At VLF we expect good efficiency in operating the tether as a travelling-wave radiator in the band 3 kHz-to-30 kHz, thus complementing the airborne TACAMO.

The proposed SEDS/Delta-II experiment is expected to provide conclusive evidence about the feasibility of using an electrodynamic tether as a generator/radiator of e.m. waves at frequencies from a fraction of 1 Hz up to 30 kHz. The phantom loop model (Grossi, 1987), that is valid and reasonably accurate at hertz and subhertz frequencies, is indicative of system performance as illustrated in Table I-A.

We have also included provisions in the payload design to perform transmission experiments in the low-ELF band and in the VLF band, by operating the 4-km antenna as a travelling wave radiator. Table I-B provides a first-cut performance appraisal at VLF. We could also add (optionally) e.m. wave receivers that could perform a scientifically valuable detection of naturally occurring ionospheric e.m. waves, especially interesting, should the orbit of SEDS/Delta II include polar regions. In principle, the Delta II satellite could orbit over these regions. Auroral e.m. wave emissions and aurora currents travelling downwards along the lines of force of the geomagnetic field would become detectable because the vertical long-wire antenna would be roughly tangent to these lines.

By applying under comparable circumstances, within the frequency range for which it is valid, the phantom loop model to the TSS-1 mission (20 km length, 0.2 A tether current, and 4 kV e.m.f.), the signal-to-noise ratio (SNR) at the Earth surface is estimated at -21 dB, hence 27.5 dB worse than the SNR expected for the SEDS/Delta-II tether. This is due to the fact that (because of very low tether current) the magnetic moment of the TSS-1 phantom loop is a factor of 24 smaller than the moment, shown in Table I, of the SEDS/Delta-II electrodynamic tether (SNR = +6.5 dB in this case).

**Table I-A. SEDS/Delta-II Electrodynamic Tether Specifications  
for ULF Radiation Experiments**

Tether Length	2x4 km
Electromotive Force	2.1 kVlt
Tether Diameter	1 mm
Tether Ohmic Resistance	2x88 ohm
Tether Current	12 A
Current Switching Frequency	0.25 Hz
Area of the Phantom Loop	$2.88 \times 10^9 \text{ m}^2$
Magnetic Moment of Phantom Loop	$3.46 \times 10^{10} \text{ A m}^2$
Signal Intensity at the Earth Surface, Along Track	+ 36.5 dB wrt $1 \mu\text{V/m}$
Noise Density at 0.25 Hz	+ 50 dB wrt $1 \mu\text{V/mHz}^{-1/2}$
Noise in $10^{-2}$ Hz Bandwidth	+ 30 dB wrt $1 \mu\text{V/m}$
Signal-to-Noise Ratio in $10^{-2}$ Hz Bandwidth	+ 6.5 dB

**Table I-B. SEDS/Delta II Electrodynamic Tether Specifications  
for VLF Radiation Experiments  
(one 4-km tether for DC power generation;  
one 4-km tether for e.m. wave radiation)**

**DC Electric Power Generation**

Tether Length	4 km
Tether Orbital Height	400 km
Electromotive Force (emf)	1.05 kV
Wire Diameter	1 mm (or 1.7 mm)
Tether Ohmic Resistance	88 ohm (or 28 ohm)
Tether Current	6 A (or 20 A)
Gross Primary Power Generated	6.3 kW (or 21 kW)
Primary Power Delivered to Payload	3 kW (or 10 kW)

**Travelling Wave Antenna at VLF**

**1st case – at 9 kHz**

Tether Length	4 km
Wavelength in Ionosphere, $\lambda_{iono}$	3.33 km
Antenna Length in Wavelengths	1.2 $\lambda_{iono}$
Radiation Resistance	130 ohm
Overall Resistance	418 ohm
Antenna Current	4.89 A
Intensity of Electric Field on the Earth Surface (in antenna main lobe, 10° away from vertical)	$\approx 150 \mu\text{v/m}$
Signal-to-Noise Ratio (in 1 Hz bandwidth)	+ 22.5 dB
Required Primary Power	10 kW
Duty Cycle	30% (or 100%)

**2nd case – at 30 kHz**

Required Primary Power	10 kW
Tether Length	4 km
Wavelength in Ionosphere, $\lambda_{iono}$	1 km
Antenna Length in Wavelengths	4 $\lambda_{iono}$
Radiation Resistance	210 ohm
Overall Resistance	500 ohm
Antenna Current	4.47 A
Intensity of Electric Field on the Earth Surface (in antenna main lobe, 10° away from vertical)	$\approx 450 \mu\text{v/m}$
Signal-to-Noise Ratio (in 1 Hz bandwidth)	+ 32 dB

## **Technical Discussion**

### **General**

There are several factors that make it advisable to perform experiments on electrodynamic tethers by taking advantage of the availability of SEDS (Carroll 1987; Harrison et al., 1989) and of the Delta-II flight opportunities (Garvey and Marin, 1989). The most important factor is the long delay that, for various causes, the TSS-1 mission has experienced and is still experiencing. Should we wait for the outcome of the planned sequence of TSS flights to ascertain the feasibility of a tether as generator/radiator of e.m. waves at ULF, low-ELF and VLF frequencies, we would not have the needed answers on hands before the end of the '90s. The situation would be indeed quite discouraging, should not be for the fact that there is a SEDS system, and there are flight opportunities provided by the Delta-II launch vehicle.

This White Paper advocates that an experiment to prove the feasibility of the electrodynamic tether as a generator/radiator from ULF to VLF frequencies be included in the SEDS/Delta-II demonstration program. During the preparation of this document, we have performed a first-cut engineering definition of the required payload for demonstrating its suitability to carry out the required measurements while remaining within the mass, size, and cost constraints typical of a SEDS/Delta-II flight mission.

### **Description of the Proposed Payload**

The simplified block diagram of Figure 1 shows the principal elements of the proposed payload. They are:

- (1) 2 Teflon-coated, conducting tethers, 4 km long, with 2 SEDS deployers; the electrical resistance of each 4-km tether is 88 ohm for the first mission (or in alternative, 28 ohm);



- (2) 3 plasma contactors, complete with power supply and auxiliary units, each rated at 20 A, capable of providing a low-resistance bridge between each end of the tether and the ionosphere, and between the platform and the ionosphere;
- (3) 1 solid state switch operated by a control unit; switching rate from 0.25 Hz to 2.5 Hz; inclusive of a pulse shaper;
- (4) 1 switch control unit;
- (5) 1 programmer/sequencer;
- (6) 1 shunt resistance, 504 ohm, 2 kilowatt;
- (7) Additional Silver-Zinc batteries on the Delta II second stage;
- (8) DC/AC static inverter (high voltage input);
- (9) AC/DC converters (low voltage input);
- (10) E.M. wave receivers, low-ELF band and VLF band, using the conducting tether as a travelling wave receiving antenna (optional items).

Figure 2 shows a possible location for the proposed payload on board the Delta-II. The required space is a fraction of the available toroidal volume (with mean radius 33", width 16" and height 20") all around the guidance section of the Delta-II. The SEDS deployer is accommodated in the shaded area of Fig. 2.

In the ULF mode of operation, the self-powered antenna can draw from the ionosphere a current of 12 A *dc*, under the drive of a maximum electromotive force of 2.1 kV provided by the  $\mathbf{V} \times \mathbf{B} \cdot \mathbf{l}$  mechanism, where  $\mathbf{V}$  is the orbital velocity,  $\mathbf{B}$  the intensity of the Earth magnetic field, and  $\mathbf{l}$  is the antenna's length. At ULF, the current will be modulated by means of a controlled solid-state switch, equipped with a pulse shaper, from a frequency of 0.25 Hz up to approximately 2.5 Hz.

Existing ground-based receiving stations (e.g. those established by the Smithsonian Astrophysical Observatory and by the University of Genova, Italy, for the TSS-1 program), as well as existing Magnetic Observatories, will provide a world-wide network of receiving terminals for collecting and recording the signals generated by the spaceborne system.

Based on a phantom-loop radiation model, a signal-to-noise ratio of + 6.5 dB in  $10^{-2}$  Hz bandwidth is expected at the Earth surface, along the ground track of the orbiting system, for ULF frequencies.

In the VLF mode, one of the two 4-km tethers is used to generate DC electric power and the other tether is used as a travelling wave transmitting antenna, in the frequency band 3 kHz – 30 kHz.

This requires that the high-voltage emf due to the tether (1.05 kilovolt DC) be inverted by a static inverter into a low-voltage AC, that becomes easy to transform into the wanted values (by simple transformers) and converted ultimately into the DC voltages required by the various power supplies. The tether DC electric power generator will supplement the batteries, will trickle-charge them and stay connected with them, in feeding the on-board loads. We have worked out two cases for the DC generator:

(a) a 88 ohm tether, capable of feeding the payload with a 30% duty cycle.

(b) a 28 ohm tether, capable of feeding 100% of the time the same payload.

According to the SEDS deployer's manufacturer (Tether Applications, Inc.) a 4-km  $\times$  1-mm diameter tether with a resistance of 88 ohm can be accommodated into the deployer canister without any substantial modification to the hardware.

This tether will be used for the first mission. For future missions the tether resistance could be reduced to 28 ohm by using a 1.7 mm-diameter Copper wire. In this case the primary power generated by the upper tether would be 21 kW, 10 kW of which are delivered to the load (batteries or VLF

transmitter) with a 100% duty cycle. In this latter case, the SEDS deployer must be enlarged.

In the ELF mode, we will have again one tether functioning as a DC power generator and the other one as a travelling wave antenna. Because the 4 km antenna is now electrically short (for instance at 60 Hz, the wavelength in the ionosphere is 50 km by night and 5 km by day, so that even during the night, the antenna length is  $< 1 \lambda$ ), we would expect a much poorer performance at ELF than at VLF. However, it costs very little to add the ELF band to the VLF system.

An interesting possibility is to use the conducting tether as a long-wire receiving antenna. Should the SEDS/Delta II be launched in a polar, or quasi-polar orbit, the tether would become nearly tangent to the lines of force of the geomagnetic field in that portion of the orbit that overflies the polar regions. Auroral emissions of e.m. waves and aurora currents (the latter being nearly parallel to the conducting wire), could become detectable. To perform an experiment on the feasibility of these measurements, and, more in general, to observe with the tether field-aligned electrodynamic phenomena, we need to add to the SEDS/Delta II payload, receivers to cover the following frequency bands: ULF ( $< 30$  Hz), ELF (30 Hz to 300 Hz), VF (300 Hz to 3 kHz), VLF (3 kHz to 30 kHz), LF (30 kHz to 300 kHz), MF (300 kHz to 3 MHz) and HF (3 MHz to 30 MHz). We expect that a grand total of three receivers will be able to cover the seven frequency bands above. Off-the-shelf units exist, with performance specifications close to what we need, so that no major developmental work is required. As far as size, mass and primary power is concerned, we expect that each one of the three receiver units will have dimensions 3" x 2" x 10", 1 kg mass, and 2 watts primary power requirement.

The total mass of the payload is 360 kg ( $\approx 794$  lb). This includes the tether masses, three plasma contactors inclusive of their power supplies and auxiliary units, 3 receivers, two Marman clamps, and two additional 250 Ah Silver-Zinc batteries on the Delta II which enable a mission duration of 4 days. Two of the three plasma contactors are installed on the end masses of the SEDS tether. One is attached to the platform itself. The

primary power requirement for the payload at ULF is 28 volt *dc*, 5.3 ampere, 146 watt and 10 kW at VLF. Use will be made of the Delta-II telemetry channels available to payloads. This use, however, will be very limited because the scientific data from our experiment are collected and recorded by ULF/ELF/VLF receiving stations on the Earth surface, and not onboard the platform.

### **Orbital Flight Parameters**

The parameters for the orbital flight of the proposed electrodynamic tether experiment could be similar to the parameters of the first SEDS/Delta-II flight (DeLoach et al., 1990), presently scheduled for December 1992, for the measurement of the dynamic properties of the SEDS tether.

We estimate that by adding 260 lb of Silver-Zinc batteries (this figure is already included in the total mass of 790 lb) to the Delta's second stage the mission can last as long as 4 days. The orbital decay will be approximately 2.5 km/orbit during electrodynamic operations.

A nominal inclination of 37° and an orbital altitude greater than 400 km with a circular or a low eccentricity orbit are acceptable. The prior knowledge of the orbital parameters is a particularly important factor in this case because we must establish the precise location of the receiving sites on the Earth surface as a function of the orbital parameters. We must make sure that the orbiting system flies as close as possible over each receiving site. In later flights, we could relax this specification and explore signal detectability at substantial distances from the ground track. For the first electrodynamic mission, however, the receiving stations should be strictly located along the ground track.

### **Ground-Based Data Collection**

Several instrumented sites at various locations on the Earth surface will be used for data collection and recording, equipped with the same instrumentation that has been developed for the TSS-1 electrodynamic mission. The existing instrumentation is mobile and can be relocated at

sites that are on the ground track of the proposed SEDS/Delta-II mission. This instrumentation consists of the following equipment:

(a) Receiving/recording system developed for TSS-1 by Rice University under a subcontract from Smithsonian Astrophysical Observatory. This instrumentation, complete with data recorders, uses the following sensors:

- One set of 3-axis magnetic field sensor BF-4 (a coil magnetometer) for the band 0.3 Hz to 500 Hz;
- Two sets of 3-axis magnetic field sensor BF-6 (also a coil magnetometer) for the band 100 Hz to 100 kHz.

(b) Receiving/recording system developed for TSS-1 by University of Genova, Italy, using sensors that were loaned to University of Genova by US Navy, NUSC, New London, CT (NUSC sensors are encapsulated in Bentos glass spheres suitable for underwater deployment). The sensors are:

- Two sets of 3-axis induction coil magnetometer for the band 0.01 Hz to 100 Hz (Gritzke and Johnson, 1982);
- One set of Varian, optically pumped, cesium vapour magnetometer.

Another magnetometer will be probably added to the sensors that the University of Genova borrowed from the US Navy: a SQUID, multi-axis system that the University of Genova plans to procure in time for the TSS-1 flight.

Given the planned orbital parameters, the schedule of data collection at each of the ground-based sites can be easily formulated with all necessary time accuracy. The number of channels that will be recorded at each site are a function of the number of sensors and of the number of axial components for each sensor. In addition, a channel will be devoted to station's identification and time information consisting of Epoch and of 1-second time marks. Pertinent telemetry data from SEDS/Delta-II will be collected, processed, and formatted by the on-board computer (Rupp, 1988).

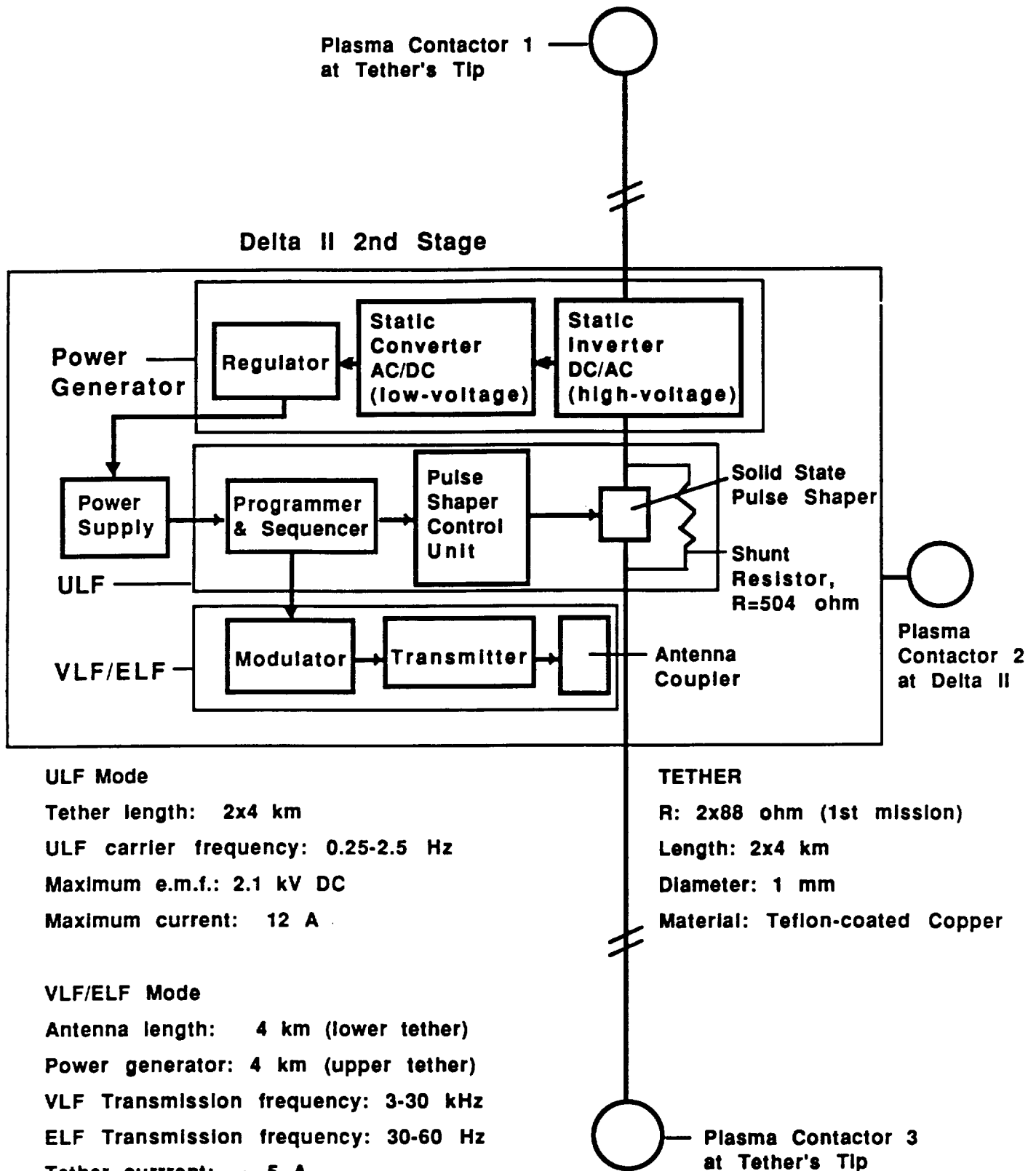


**Figure 1. Simplified Block Diagram of the Proposed Payload**

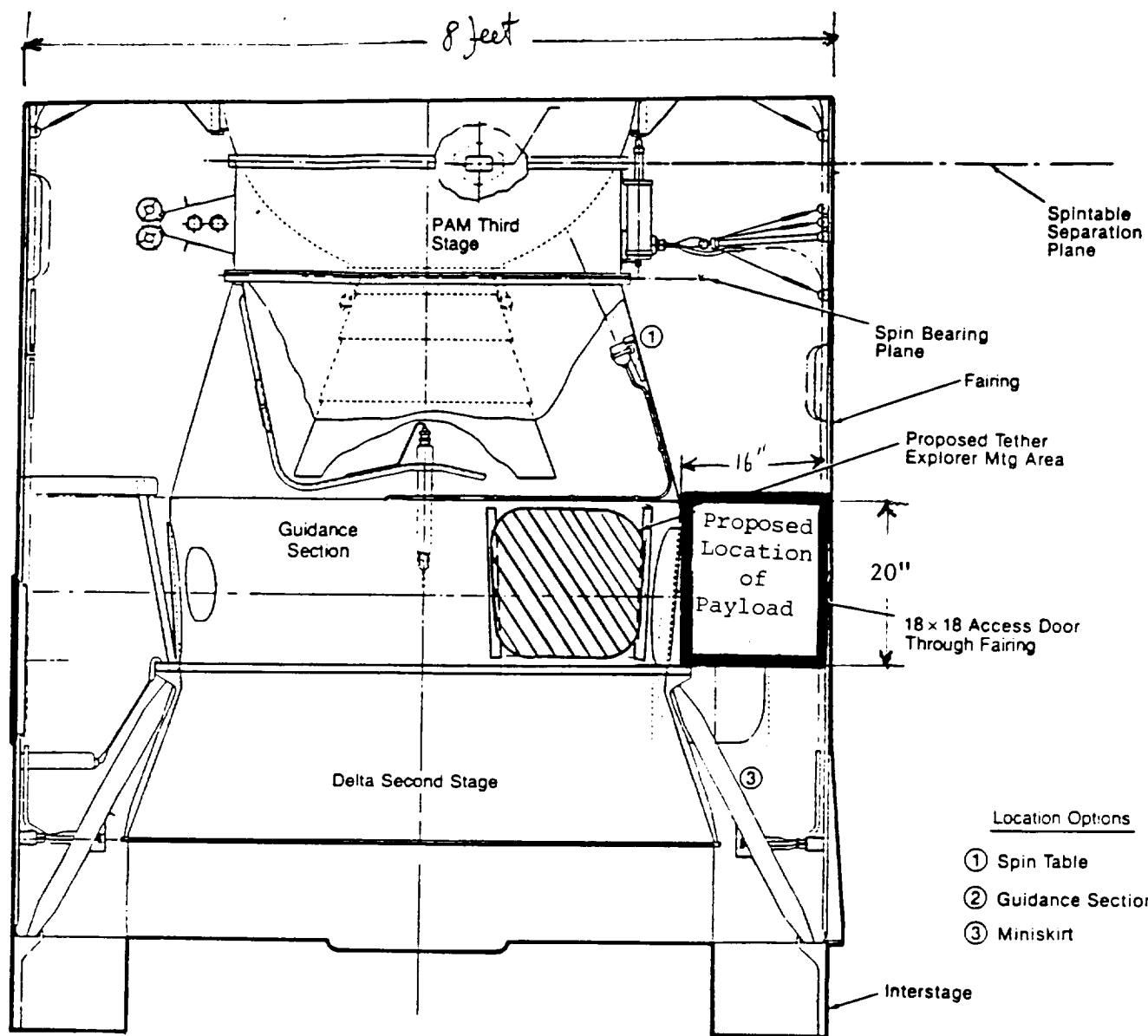


**Figure 2. Proposed Location of the Payload**

Data will then be transmitted to the ground-based telemetry station(s), assigned to the flight, via the Second Stage telemetry link.

### **Further Implications of Proposed Experiment**

The electrodynamic drag associated with DC power generation and with e. m. wave generation and radiation at ULF with a 50% duty cycle produces an orbital decay estimated at 2.5 km per orbit. This orbital decay, while tolerable for the proposed experiment, could not be acceptable for an operational system. The orbital decay, however, can be eliminated completely by removing the DC power generation mode and by eliminating the unidirectionality of tether current (unidirectionality is now present when the tether operates in the ULF mode; it is also necessarily present when generating DC electric power).

We expect the tether to be trackable from the ground (Garvey and Marin, 1989) and its dynamic behavior will, therefore, provide data for model validation.

### **Brief Outline of the Proposed Program**

A program of 2.5 year is presently envisaged for the development, manufacturing, testing, and integration of the flight hardware. The Principal Investigator will be Dr. Mario D. Grossi, SAO, Radio & Geoastronomy Division. Co-Investigators in the program will be Dr. Enrico C. Lorenzini and Dr. Mario L. Cosmo, both from SAO.

The program consists of: (1) an instrumentation hardware development effort to be performed by SAO's Central Engineering Department; and (2) an analytical effort. Specifically, the hardware development effort will include fabrication, integration, and testing. The analytical effort will include: (a) a tether dynamics analysis to verify that a current  $\leq 20\text{A}$  flowing in a single 4 km SEDS tether, or a current of 12 A flowing in the 2x4 km tether does not produce unacceptable dynamic instabilities; (b) an analysis of tether-induced e.m. wave emissions and orbit-to-ground e.m. wave propagation for a more reliable estimate of the signal-to-noise ratio, at



the Earth surface, in the frequency band 0.25 Hz to 60 Hz (ULF/Low ELF) and in the frequency band from 3 kHz to 30 kHz (VLF) (this includes the study of the conducting tether as a travelling wave antenna at ELF and VLF); (c) a system analysis in support of the hardware development; (d) a post-flight data processing and analysis.

Piggy-back accommodations are expected to be provided to the proposed payload on board a USAF (GPS) Delta-II launch (the 950 lb mass available to secondary payloads is well above the mass requirement of the proposed payload) or on any other commercial launch of the Delta II with sufficient mass margin for secondary payloads.

### References

Barnett, A., and S. Olbert, 1986, *Radiation of Plasma Waves by a Conducting Body Moving through a Magnetized Plasma*, JGR, Vol. 19, N.A9, pp. 10117-10135, September 1.

Carroll, J.A., 1987, *The Small Expendable Deployment System (SEDS)*, Space Tethers for Science in the Space Station Era, Conference Proceedings, Vol. 14, Venice, Italy, October 4-8.

DeLoach, R., et al., 1990, *End-Mass Instrumentation for the First SEDS/Delta-II Mission*, 28th Aerospace Sciences Meeting, AIAA-90-0537, Reno, Nevada, January 8-11.

Garvey, J.M. and D.R. Marin, 1989, *Delta-II Secondary Payload Opportunities for Tether Demonstration Experiments*, Tether in Space-Toward Flight, AIAA, San Francisco, CA, May 17-19.

Gritzke A.R. and R.H. Johnson II, 1982, *Ocean Floor Geomagnetic Data Collection System*, Naval Postgraduate School, Monterey, CA, December.

Grossi, M.D., 1973, *A ULF Dipole Antenna on a Spaceborne Platform of the PPEPL Class*, Letter Report to NASA/MSFC, Contract NAS8-28303, May 11.

Grossi, M.D., 1987, *System Application Study*, Section 3 of Final Report on NASA Grant NAG8-551, pp. 59-113, SAO, Cambridge, MA, February.

Grossi, M.D., 1991, *Investigation of the E.M. Properties of a Spaceborne Electrodynamic Tether as a Travelling Wave Antenna*, SAO Proposal (in preparation) to NASA-OSSA, in response to NRA-91-OSSA-11 of 4/12/91, to be submitted on 7/12/91.

Harrison, J.K. et al., 1989, *Small Expendable-Tether Deployer System (SEDS)-Development Status*, Tether in Space-Toward Flight, AIAA, San Francisco, CA, May 17-19.

Rupp, C.A., 1988, *SEDS Computer System*, NASA-MSFC Technical Document, Huntsville, Alabama, November.

---

# AGARD

ADVISORY GROUP FOR AEROSPACE RESEARCH & DEVELOPMENT

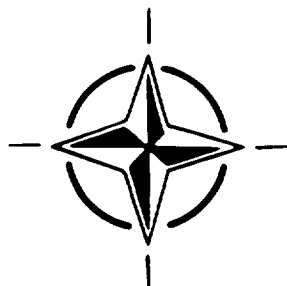
7 RUE ANCELLE 92200 NEUILLY SUR SEINE FRANCE

---

**Paper Reprinted from  
AGARD Conference Proceedings 529**

## **ELF/VLF/LF Radio Propagation and Systems Aspects**

(La Propagation des Ondes Radio ELF/VLF/LF  
et les Aspects Systèmes)



**NORTH ATLANTIC TREATY ORGANIZATION**

---

**PRECEDING PAGE BLANK NOT FILMED**

# ORBITING TRANSMITTER AND ANTENNA FOR SPACEBORNE COMMUNICATIONS AT ELF/VLF TO SUBMERGED SUBMARINES

by

P.R. Bannister  
US Navy-NUWC, New London, CT 06320

J.K. Harrison, C.C. Rupp  
NASA-MSFC, Huntsville, AL 35812

R.W.P. King  
Harvard University, Gordon McKay Laboratory  
Cambridge, MA 02138

M.L. Cosmo, and E.C. Lorenzini  
Harvard-Smithsonian CFA, Cambridge, MA 02138

C.J. Dyer, M.D. Grossi  
Raytheon Co., Submarine Signal Division  
Portsmouth, RI 02871-1087

## Abstract

An orbital emplacement for the transmitter and the antenna of a communications link at ELF (30 to 300 Hz) and VLF (3 kHz to 30 kHz) to submerged submarines, has been considered since the very inception of the space age. Only recently, however, space technology has reached sufficient maturity, for system designers to undertake serious studies of this link configuration.

The optimistic outlook stems from recent space technology developments, such as the design and construction by NASA of long orbiting tethers, and the testing, onboard Shuttle Orbiter ATLANTIS, scheduled for Summer 1992, of the first spaceborne 20 km metal wire. This is known as the Tethered Satellite System #1 (TSS-1, in short), a space mission that might be possibly followed by other flights, with tether lengths that could reach 100 km.

Once deployed at a height of, say, 300 km, from a Shuttle Orbiter, or from another suitable platform, a long, thin tether aligns itself along the local vertical by virtue of the gradient of the Earth gravity field. If made of metal, the tether can function as a VED (Vertical Electric Dipole) transmitting antenna at ELF and VLF.

## 1. INTRODUCTION TO SPACEBORNE TETHERS: AN EMERGING TECHNOLOGY FOR USE IN RADIOPHYSICS AND RADIOENGINEERING

Sometime in Summer 1992, a new structural element will make its appearance onboard the Shuttle Orbiter: a tether consisting of a very long, thin filament attached, at one end, to the Shuttle, and holding "by the leash," at the other end, a satellite. Hence the name "Tethered Satellite System," in short TSS, that has been given to this joint initiative by NASA and ASI (Italian Space Agency).

The Summer 1992 tether, a flexible thread with a diameter of a few millimeters, will have a length of 20 km. However, in later missions, tethers of 100 km length and even longer are a distinct possibility.

The tether aligns itself with the local vertical and stays so aligned, by virtue of the vertical gradient of the Earth gravity field. The tether's orientation, both for upward and downward deployment from the Shuttle, deviates only slightly from the local vertical, and its angular movements about that vertical resemble the angular movements of a pendulum attached to the Shuttle. While the Shuttle Orbiter moves in its orbital flight around the Earth, the tether stays roughly aligned with the center of the Earth.

In a few years, once that such basic operations as deployment and retrieval are thoroughly understood, the tether will find wide-spread use as a flexible structural element (capable of responding to traction) in large space structures of one, two, or three dimensions. This use is similar, in several respects, to the function of ropes in suspended bridges.

While two-dimensional and three-dimensional tethered structures belong to the long-term future, the attention of flexible-spacecraft designers will concentrate, in the short term, on the one-dimensional case. A single vertical tether, notwithstanding its simplicity, is capable of performing a variety of functions, among which, if the tether is made of metal, are the following:

(a) operating as a transmitting antenna (either resonant, or non-resonant, such as a travelling-wave radiator), for the effective radiation of electromagnetic waves. This specific use is the object of this paper. Tethers can be made of such a length that they radiate effectively e.m. waves at frequencies as low as ELF and VLF;

(b) operating as a receiving antenna, again either resonant or non-resonant;

(c) performing as a self-powered antenna, for radiation of e.m. waves at ULF (frequencies of 1 Hz or lower);

(d) generating DC electric energy, at the expenses of the platform's orbital energy. The electromotive force is  $\mathbf{v} \times \mathbf{B} \cdot \mathbf{\ell}$ , where  $\mathbf{v}$  is the orbital velocity (about 7.7 km/sec for a height of 380 km),  $\mathbf{B}$  is the Earth magnetic field (about  $0.3 \cdot 10^{-4}$  Weber/m<sup>2</sup>), and  $\mathbf{\ell}$  is the length of the tether (20 km). The circuit closure is provided by the magneto-ionic plasma of the Earth ionosphere, while the contact between each end of the tether and the ionosphere is provided by a "plasma bridge" also known as a "plasma contactor."

As already told, NASA and ASI will launch in orbit, in Summer 1992 the TSS-1 mission, that uses a 20 km-long metal wire. This mission will verify, first of all, such dynamical issues as the feasibility of safe deployment and retrieval. In addition, it will perform experiments on the electrodynamic and electromagnetic mechanisms (c) and (d) above.

## 2. RADIATION OF E.M. WAVES FROM A TETHER IN THE IONOSPHERE TO THE SURFACE OF THE EARTH, AT ELF AND VLF FREQUENCIES.

### 2.1 Introductory Remarks

The possibility of transmitting electromagnetic waves from a Shuttle Orbiter to the surface of the earth is discussed in a paper by Grossi et al. (1991). The antenna generating the electromagnetic field consists of a vertical wire (the tether) which is driven with the Shuttle as ground. In this Section 2, the electromagnetic aspects of the problem are examined with available knowledge as the basis. Because the existing theory of the properties of the ionosphere and of antennas moving in it are approximate and complicated, quantitative results can be obtained only in terms of a relatively simple model.

### 2.2 The Model

The specific problem to be investigated is the electromagnetic field on the surface of the earth generated by currents in a vertical antenna moving in the F-layer of the ionosphere at a height of 400 km. The length of the antenna is 4 km. It is driven at its upper end by a generator voltage  $V_0$  against the space shuttle as a ground. A schematic diagram is in Fig. 2-1.

The ionosphere is assumed to extend from a height of 150 km to infinity as a homogeneous medium. It is given a sharp boundary with air as a simplification of the gradual layered boundary between 100 and 200 km. With the shuttle orbiting the earth along a great circle over the poles, the earth's magnetic field  $B_0 \sim 0.5 \times 10^{-4}$  Tesla is roughly parallel to the vertical antenna over the poles and perpendicular to it over the equator.

### 2.3 The Properties Of The Ionosphere

The ionosphere is a plasma consisting of electrons, protons, and neutral particles. In the F-layer, the electron and ion densities,  $\eta_e$  and  $\eta_i$ , have the following values:

$$\text{Daytime: } \eta_e = \eta_i = 1.4 \times 10^{12} \text{ per } m^3, \quad (1a)$$

$$\text{Nighttime: } \eta_e = \eta_i = 4 \times 10^{11} \text{ per } m^3. \quad (1b)$$

The electric charges are

$$q_e = -e = -1.6 \times 10^{-19} \text{ Coulombs} \quad (2a)$$

$$q_i = -q_e = 1.6 \times 10^{-19} \text{ Coulombs} \quad (2b) \\ (\text{for protons})$$

The masses are

$$m_e = 9.1 \times 10^{-31} \text{ kg}, \quad (3a)$$

$$m_i = 1836.3 \times 19 m_e = \\ 3.17 \times 10^{-26} \text{ kg} \quad (3b)$$

The reason for including the factor 19 in (3b) is that the lower ionosphere consists of a mixture of ions including  $N^+$ ,  $N_2^+$ ,  $O_2^+$ , with a mean mass of 19 amu.

The plasma frequencies of the electrons and ions for daytime are

$$\omega_{pe}^2 = \frac{\eta_e e^2}{\epsilon_0 m_e} = 44.55 \times 10^{14}, \quad \omega_{pe} = 6.67 \times 10^7, \quad (4a)$$

$$\omega_{pi}^2 = \frac{\eta_i e^2}{\epsilon_0 m_i} = 1.2779 \times 10^{11}, \quad \omega_{pi} = 3.575 \times 10^5 \quad (4b)$$

With

$$B_0 = 0.5 \times 10^{-4} \text{ Tesla}, \quad (5)$$

the gyrofrequencies are

$$\omega_{ge} = \frac{eB_0}{m_e} = 8.8 \times 10^6, \quad (6a)$$

$$\omega_{gi} = \frac{eB_0}{m_i} = 2.53 \times 10^2 \quad (6b)$$

The effective collision frequencies—representing the sum of the electron-ion and electron-neutral collisions—are

$$\text{Daytime: } \nu \sim 10^3; \quad \text{Nighttime: } \nu \sim 4 \times 10^2 \quad (7)$$

## 2.4 Plasma Waves In The Ionosphere

The ionosphere is a complicated medium for the propagation of waves generated by oscillating currents at an angular frequency  $\omega$  in an antenna. The frequencies of interest for the tether experiment are in the following ranges:

$$\text{VLF: } 3 \text{ kHz} \leq f \leq 30 \text{ kHz} \quad \text{or}$$

$$1.88 \times 10^4 \leq \omega \leq 1.88 \times 10^5, \quad (8a)$$

$$\text{ELF: } 30 \leq f \leq 300 \text{ Hz} \quad \text{or} \quad 188.5 \leq \omega \leq 1885 \quad (8b)$$

The specific frequencies to be investigated are

$$f = 9 \text{ kHz and } 30 \text{ kHz}; \quad f = 40 \text{ Hz.} \quad (9)$$

Three types of waves are examined as follows.

### a) Electromagnetic Waves.

The condition for propagating waves of this type is

$$\omega \gg \omega_{pi} = 2.53 \times 10^2 \quad (10)$$

This is satisfied by the entire VLF range (8a), but not by the entire ELF range (8b). For frequencies that satisfy (10), the plasma behaves like a homogeneous medium with the relative effective permittivity and conductivity given by

$$\epsilon_{er} = 1 - \frac{\omega_p^2}{\omega^2 + \nu^2}; \quad \sigma_e = \frac{\nu \epsilon_0 \omega_p^2}{\omega^2 + \nu^2}, \quad (11)$$

when the steady magnetic field  $B_0$  is parallel to the electric field. These are modified when  $B_0$  is in the direction of propagation, as shown in King and Harrison (1969) (Section 2.12). With (11), the wave number is

$$k_i = k_0 \left( \epsilon_{er} + \frac{i\sigma_e}{\omega \epsilon_0} \right)^{1/2} = k_0 \left( 1 - \frac{\omega_p^2}{\omega^2 + \nu^2} \right)^{1/2} (1 + ip)^{1/2} \quad (12)$$

where  $k_0 = \omega/c$ ,

$$p = \frac{\sigma_e}{\omega \epsilon_0 \epsilon_{er}} = \frac{\nu \omega_p^2}{\omega(\omega^2 + \nu^2 - \omega_p^2)} \quad (13)$$

and

$$(1 + ip)^{1/2} = f(p) + ig(p). \quad (14)$$

The quantities  $f(p)$  and  $g(p)$  are tabulated over a wide range in King and Prasad (1986).

When

$$\epsilon_{er} > 0 \quad \text{or} \quad \omega^2 + \nu^2 > \omega_p^2 \quad (15)$$

the wave number becomes

$$k_i = \beta_i + i\alpha_i; \quad \beta_i = k_0 \left( 1 - \frac{\omega_p^2}{\omega^2 + \nu^2} \right)^{1/2} f(p), \quad (16)$$

$$\alpha_i = k_0 \left( 1 - \frac{\omega_p^2}{\omega^2 + \nu^2} \right)^{1/2} g(p) < \beta_i, \quad (17)$$

so that propagation with low attenuation in the form

$$e^{ik_i r} = e^{-\alpha_i r} e^{i\beta_i r} \quad (18)$$

is possible. Alternatively, when

$$\epsilon_{er} < 0 \quad \text{or} \quad \omega^2 + \nu^2 < \omega_p^2, \quad (19)$$

$$k_i = \beta_i + i\alpha_i; \quad \beta_i = k_0 \left( \frac{\omega_p^2}{\omega^2 + \nu^2} - 1 \right)^{1/2} g(|p|) \quad (20)$$

$$\alpha_i = k_0 \left( \frac{\omega_p^2}{\omega^2 + \nu^2} - 1 \right)^{1/2} f(|p|) > \beta_i, \quad (21)$$

so that the high exponential attenuation makes propagation impossible.

With  $\omega_p^2 = 44.55 \times 10^{14}$  and  $\omega^2 + \nu^2 = (1.88 \times 10^4 \text{ to } 1.88 \times 10^5)^2 + 10^6 = 3.53 \times 10^8 \text{ to } 3.53 \times 10^{10}$  for the VLF range,  $\alpha_i > \beta_i$  and no propagation is possible. When the steady magnetic field  $B_0$  is not parallel to the electric field, propagation is likewise generally not possible except in the Whistler mode considered in the next section.

### b) The Whistler Mode

The existence of the steady earth's magnetic field  $B_0$  makes propagation in other modes possible. Because the analytical formulation is extremely complicated, it is necessary to introduce the simplifying approximation of neglecting the losses due to collisions and treating the so-called cold plasma. This has been shown to be a good approximation of hot plasmas in its general description of the wave propagation.

A special range of propagation occurs when the parabolic branch of the dispersion curve is applicable. This is shown by Denisse and Delcroix (1963, page 95). The condition underlying propagation in this mode is

$$\omega < \omega_{pe} = 8.88 \times 10^6 \quad (22)$$

This follows from Fig. 8.7 in Denisse and Delcroix (1963). This is satisfied by the entire VLF range (8a).

The wave number  $k_i$  given by Denisse and Delcroix (1963, p. 98) with  $\omega_{gi}^2 \ll \omega_{pe}^2$  is

$$k_i = \frac{k_0 \omega_{pe}}{(\omega \omega_{ge})^{1/2}} = 2.37 \times 10^4 k_0 \omega^{-1/2} =$$

$$0.749 \times 10^{-4} \omega^{1/2} \quad (23)$$

For the two frequencies  $\omega = 5.65 \times 10^4$  and  $\omega = 1.88 \times 10^5$ , this gives

$$\frac{k_i}{k_0} = \frac{\lambda_0}{\lambda_i} = \begin{cases} 100 & \text{for } f = 9 \text{ kHz} \\ 54.6 & \text{for } f = 30 \text{ kHz} \end{cases} \quad (24)$$

Specifically with

$$k_0 = \begin{cases} 1.88 \times 10^{-4} \text{ m}^{-1} \\ 6.27 \times 10^{-4} \text{ m}^{-1} \end{cases} \text{ or } \lambda_0 = \begin{cases} 33.4 \text{ km} \\ 10 \text{ km} \end{cases} \quad (25)$$

$$k_i = \begin{cases} 1.88 \times 10^{-2} \text{ m}^{-1} \\ 3.42 \times 10^{-2} \text{ m}^{-1} \end{cases} \text{ or } \lambda_i = \begin{cases} 334 \text{ m} \\ 184 \text{ m} \end{cases} \quad (26)$$

The effective permittivities are

$$\epsilon_{ir} = \frac{k_i^2}{k_0^2} = \begin{cases} 10^4 \\ 2975 \end{cases} \quad (27)$$

The antenna (tether) length is  $h = 4 \text{ km}$ , so that

$$\frac{h}{\lambda_i} = \begin{cases} 12 & \text{for } f = 9 \text{ kHz} \\ 21.7 & \text{for } f = 30 \text{ kHz} \end{cases} \quad (28)$$

### c) Alfvén Waves

The ELF range (8b) does not satisfy the conditions for propagation with the Whistler mode. However, it does satisfy the conditions for propagation with Alfvén waves. This condition is

$$\omega \ll \omega_{pi} = 2.53 \times 10^2 \quad (29)$$

For Alfvén waves, the phase velocity is the so-called Alfvén velocity given by

$$a = \frac{c\omega_{pi}}{\omega_{pi}} = 7.077 \times 10^{-4} c = 2.115 \times$$

$$10^5 \text{ m/sec} = 211.5 \text{ km/sec} \quad (30)$$

When  $a/c \ll 1$ , as in (30), the wave number is well approximated by

$$k_a = \beta_a + i\alpha_a \sim \frac{\omega}{a} + i \frac{\omega^2 c^2 \epsilon_0}{2\sigma_0 a^3}; \quad \sigma_0 = \frac{m_e \nu}{\eta_e e^2} \quad (31)$$

For the frequency  $f = 40 \text{ Hz}$  or  $\omega = 251.3$   $\alpha_a$  is entirely negligible so that

$$k_a \sim \beta_a = \frac{\omega}{a} = 1.189 \times 10^{-3} \text{ m}^{-1}; \quad \alpha_a \sim 0. \quad (32)$$

and

$$\lambda_a = \frac{2\pi}{k_a} = 5.288 \text{ km} \quad (33)$$

The antenna length  $h = 4 \text{ km}$  corresponds to

$$\frac{h}{\lambda_a} = 0.76 \quad (34)$$

## 2.5 The Air-Ionosphere Boundary

The electromagnetic field in the ionosphere generated by the current in the antenna travels outward with amplitudes at sufficient distances determined by the far-field pattern. The field incident on the ionosphere-air boundary is locally approximately a plane wave which is reflected and refracted according to Snell's law. Since the Whistler-mode field is incident from the ionosphere (Region i, wave number  $k_i$ ) on the air (Region 0, wave number  $k_0$ ) with  $k_i/k_0 = 100$  when  $f = 9 \text{ kHz}$ , it experiences total internal reflection when  $\Theta > \Theta_{cr}$ , where the critical angle is

$$\Theta_{cr} = \sin^{-1} \frac{k_0}{k_i} = \sin^{-1} (0.01) =$$

$$0.01 \text{ radian} = 0.57^\circ \quad (35)$$

This means that the only field that is transmitted into the air arrives at the boundary within a small cone with angle  $\Theta = 0.57^\circ$ . This suffers reflection and refraction at the boundary. At normal incidence,  $\Theta = 0$ , the reflection and transmission coefficients for the electric field are

$$f_r = -\frac{k_i - k_0}{k_i + k_0} = -\frac{99}{101} = -0.980;$$

$$f_t = \frac{2k_0}{k_i + k_0} = \frac{2}{101} = 0.0198 \quad (36)$$

Thus, there is only a small circular window from the ionosphere into the air. It is directly below the antenna and, at the distance 250 km from the antenna to the boundary, it has the radius 2.5 km. Even in this window, the field incident from the ionosphere is largely reflected back upward with the reflection coefficient  $-0.98$ . The transmission coefficient is 0.0198 for propagation into the air.

In order to transmit a field through the window into the air and down to the earth, the field pattern of the antenna must have a significant amplitude within  $0.57^\circ$  of the perpendicular.

## 2.6 The Antenna

The properties of antennas in magnetoplasmas are very complicated. Analyses have been carried out by Seshadri (1965), (1968) and Bhat (1973) with the steady magnetic field parallel to the antenna and by Wunsch (1967) with the magnetic field perpendicular to the antenna. A detailed study of these investigations and application of their results to the present problem are beyond the scope of this preliminary study. For present purposes, the antenna will be treated as immersed in an infinite homogenous medium with the wave number  $k_i$  characteristic of the Whistler mode for the VLF rate (8a)

and  $k_a$  for the Alfvén mode for the ELF range (8b).

There are two possibilities for the antenna with the length  $h = 4$  km and the radius  $a = 1$  mm. These are: (a) The antenna is coated with a layer of dielectric with the radius  $b \sim 2$  mm. If the dielectric is teflon,  $\epsilon_{dr} = 2.1$ . (b) The antenna is bare (or the insulation is so thin that  $b/a \sim 1$ ). The properties of the antenna are very different in these two cases.

#### a) The Insulated Antenna

A conductor with radius  $a$  and a dielectric coating with radius  $b$ , relative permittivity  $\epsilon_{dr}$ , and wave number  $k_d = k_0 \sqrt{\epsilon_{dr}}$  embedded in an infinite homogeneous ionosphere with the wave number  $k_i$  such that  $|k_i|^2 \gg k_d^2$ , has the properties of a transmission line. The wave number is

$$k_L = k_d \left\{ 1 + \frac{1}{\ln(b/a)} \left[ i \left( \frac{2\pi r_0}{\omega \mu_0} + \frac{\pi}{2} \right) + \ln \frac{2}{|k_i b|} - 0.327 \right] \right\}^{1/2} \quad (37)$$

The characteristic impedance is

$$Z_c = \frac{\omega \mu_0 k_L}{2\pi k_d^2} \ln \frac{b}{a} \quad (38)$$

In these formulas,  $r_0$  is the resistance per unit length of the wire. For the Whistler mode at  $f = 9$  kHz, it follows that

$$k_0 = 1.88 \times 10^{-4} \text{ m}^{-1}, \quad k_d = 2.72 \times 10^{-4} \text{ m}^{-1}, \quad (39)$$

$$k_i = 1.88 \times 10^{-2} \text{ m}^{-1}$$

With radius  $a = 1$  mm,  $r_0 = 2.2 \times 10^{-4} \Omega/\text{m}$  so that  $2\pi r_0/\omega \mu_0 = 0.0195 \Omega/\text{m}$ . This is negligible compared with  $\pi/2$ , which contributes the radiation resistance per unit length. With  $b = 2$  mm,

$$k_L = \beta_L + i\alpha_L = (1.1 + i0.001) \times 10^{-3} \text{ m}^{-1} \quad (40)$$

so that

$$\beta_L = 1.1 \times 10^{-3} \text{ m}^{-1}, \quad \lambda_L = 5.7 \times 10^3 \text{ m} = 5.7 \text{ km}, \quad (41)$$

$$Z_c = 116.4 \Omega \quad (42)$$

For a tether length of  $h = 4$  km,

$$h/\lambda_L = 0.70 \quad (43)$$

The electrical length is sufficiently short so that, regardless of whether the antenna is terminated in its characteristic impedance so that a travelling wave of current is maintained or it is simply driven as a monopole against the space shuttle, the principal lobe of the field pattern is in the equatorial plane  $\Theta = \pi/2$  and no

significant field is maintained in the downward direction near  $\Theta = 0$ . The insulated antenna is ideally suited for a horizontal orientation of the antenna and is essentially useless for the vertical orientation.

#### b) The Bare Antenna

At  $f = 9$  kHz for the Whistler mode, the bare wire of length  $h = 4$  km  $= 12 \lambda_i$  is electrically very long. If it is terminated to produce a travelling wave of current approximately given by  $I_z = I_0 e^{ik_i z}$ , the electric field at large distances from the antenna is

$$E_\theta^r = -\frac{i\omega\mu_0}{4\pi} \frac{e^{ik_i r}}{r} \int_0^h I_z(z') e^{-ik_i z' \cos \Theta} \sin \Theta dz' \quad (44)$$

with

$$I_z(z) = I_z(0) e^{ik_i z}, \quad I_z(0) = -\frac{i2\pi V_0}{\zeta_i \Psi} \quad (45)$$

where

$$\Psi \sim 2 \ln \frac{2h}{a} \quad (46)$$

Since  $\omega\mu_0/k_i \zeta_i = 1$ , the result is

$$E_\theta^r = \frac{V_0}{\Psi} \frac{e^{ik_i r}}{r} f(\Theta) \quad (47)$$

$$|f(\Theta)| = \frac{\sin \Theta}{1 - \cos \Theta} \sin \left[ \frac{1}{2} k_i h (1 - \cos \Theta) \right] \quad (48)$$

The far-field pattern given by  $|f(\Theta)|$  is shown graphically in a polar plot in Fig. 2-2. It is seen that the principal lobe is downward-directed and rotationally symmetric with maximum at  $\Theta_m = 14^\circ.2$ . The field at  $\Theta = 0^\circ$  is, of course, zero. There are eleven minor maxima between the principal one and  $\Theta = \pi/2$ .

The field that enters the air from the ionosphere according to the field pattern in Fig. 2.2 is extremely small since the angle of incidence on the ionosphere-air boundary must be almost vertically down, specifically within  $0.57^\circ$  of the vertical. The magnitude of the field at  $\Theta = 0.01$  rad  $= 0.57^\circ$  is  $f(\Theta) = 0.38$ , whereas it is  $f_m(\Theta) = 7.34$  at the maximum.

In order to direct the maximum of the field pattern vertically down continuously, the antenna must be tilted  $14^\circ.2$  from the vertical and then made to rotate so that its lower end describes a circle. Since the tether normally oscillates through an angle near  $14^\circ.2$ , it is only necessary to impart a small transverse push to have it trace the edge of a cone. The rate of circulation is irrelevant so long as the tether continuously maintains an angle of  $14^\circ.2$  with the vertical.

If the maximum of the field pattern in Fig. 2-2 is directed down, the full field intensity with  $|f(\Theta)| = 7.34$  is directed onto the circular window on the ionosphere-air boundary so that even with the small transmission



coefficient, the effective value of  $|f(\Theta)|$  in the air is  $|f(\Theta)| = 0.15$ . (one orbit).

With  $h/a = 4 \times 10^3 / 10^{-3} = 4 \times 10^6$ ,

$$\Psi = 2 \ln(2h/a) = 31.8, \quad (49)$$

and  $r = 400$  km,

$$|E_\theta^r| = \frac{V_0}{\Psi} \frac{1}{r} \times 0.15 = \frac{V_0}{31.8} \frac{1}{4 \times 10^5} \times 0.15 = V_0 \times 1.18 \times 10^{-8} \quad (50)$$

For an applied driving voltage to the antenna of  $V_0 \sim 1$  kV, the field incident on the surface of the earth is

$$|E_\theta^r| \sim 1.18 \times 10^{-5} \text{ V/m} \quad (51)$$

This is easily measurable. The current at the driving point of the antenna is obtained from (45). It is

$$|I_z(0)| = \frac{2\pi \times 10^3}{12\pi \times 31.8} = 5.2 \text{ Amp} \quad (52)$$

Note that  $\zeta_i = \zeta_0/\epsilon_{ir}^{1/2} = 120\pi/10 = 12\pi$ .

## 2.7 Conclusion

There are several possible modes for the transmission of electromagnetic waves through the ionosphere to the earth surface. The Whistler mode appears to be the most promising for the VLF band when the source is a vertical travelling-wave monopole erected on the lower side of the space shuttle. In order to maintain a continuously significant field on the surface of the earth or sea, it is necessary that the antenna be displaced from the vertical by an angle of  $14^\circ.2$  for  $f = 9$  kHz and rotated so that it traces the surface of a cone.

## 3. SMALL EXPENDABLE-TETHER DEPLOYMENT SYSTEM (SEDS-1)

### 3.1 General Description

The Small Expendable-Tether Deployer System (SEDS-1) is being built by NASA as a low-budget secondary payload for a March 1993 flight on a U.S. Air Force Delta II/GPS mission. SEDS will deploy a 23 kg endmass (or payload) at the end of a 20 km long tether. The experiment purpose is to test and demonstrate the feasibility of the design concept and to verify the computer models that have been built to predict tether dynamic behavior during this type of low tension deployment. The key features of SEDS are its simplicity, low tension deployment with minimum braking, non-retrievability of the tether (the tether is cut after it is fully deployed), and low cost. The 20-km deployment, which is initiated by spring ejection of the endmass at an initial speed of 1.5 meters per second, last about 90 minutes

### 3.2 Design Concept

SEDS consists of four parts: 1) the deployer (tether wound on a core, canister cover and base plate); 2) the brake/cutter assembly; 3) the electronics box; and 4) the endmass (or payload). A view of SEDS is shown in Figure 3.1. The tether unwinds – about 46500 turns – from the outside periphery of a stationary core – there is no rotating reel. After unwinding the tether travels through a small opening in the top of the canister, to a friction brake, a tensiometer, then to the tether cutter, and finally attaches to the payload. The entire system weighs approximately 39 kg most of which is the 23 kg endmass.

The brake cutter assembly contains a running-line tensiometer, stepper motor for turning the brake, the friction brake shaft and gearing, and tether cutter. The friction brake slows the deployment speed by wrapping several turns of the tether around a small shaft when approximately 19-km or 41026 turns of tether have been deployed. The tether is made from a polyethylene synthetic fiber called SPECTRA-1000. The 0.75 mm diameter is much larger than necessary for strength on this first flight but this size gives significant micrometeoroid protection (about a 0.1 percent risk for one orbit).

The endmass (or payload) weighs 23 kg and has an overall size of  $20 \times 33 \times 41$  cm. It contains a three-axis accelerometer, tensiometer, magnetometer, its own power, computer, telemetry system and supporting electronics. Two antennas are mounted on the sides for data transmission directly to the tracking stations during the experiment. The endmass and tether are cut, at the Delta II end, after deployment and burn-up on reentry into the atmosphere.

### 3.3 Electronics System

The SEDS electronics data and control system will record, store, and continuously downlink data over the Delta II S-band telemetry channel. It counts the turns as the tether unwinds from the spool, logs the time for each turn, serves as an event timer, responds to sequencer commands from the Delta II second stage, controls the stepper-motor/brake system, and activates the pyrotechnic charge for the tether cutter. Data stored, besides the turncounts, are tether tension, temperature, and supply voltage. The storage capacity is 160 kilobytes (approximately 115 kilobytes are required) and the downlink capacity ranges from 1 kilobit per second to 64 kilobits per second (requirement is 4.8 kilobits per second). The entire memory can be dumped in six minutes. The system weighs about 3 kg and has an overall size of  $8 \times 13 \times 29$  cm. A block diagram is shown in Figure 3.2.

### 3.4 Mission

The tether deployment begins 3780 seconds after Delta II lift-off at the apogee of a  $204 \times 704$  km orbit. Full deployment of the 20 km tether is reached 5100 seconds later. After full deployment, the tether swings for ten minutes through an angle of approximately 50 degrees toward the local vertical. The tether is cut during the swing when it is near the local vertical position and over the Pacific Ocean at about 150 degrees east longitude. This occurs at 5800 seconds (slightly more than one orbit) after deployment begins. The reentry takes one-third of an orbit so the tether and payload should reenter over the Pacific Ocean near 100 degrees west longitude or just off the coast of Mexico. Table 3.I shows the Delta II/SEDS-1 sequence of events. Figure 3.3 gives the SEDS-1 ground track.

### 3.5 Tether Dynamics Calculations

A major goal of the first SEDS flight is to validate the extensive amount of computer modelling that has been done during the last several years to predict the dynamic behavior of a tether in space. The results of some recent calculations done by Control Dynamics are shown in Figure 3.3 for a 20 km deployment starting at the apogee of a  $204 \times 704$  km orbit and lasting for 5800 seconds (1.6 hours or a little more than one SEDS orbit). Full deployment is reached at 5100 seconds followed by a 50 degree swing to the vertical that is completed at 5800 seconds when the tether is cut. During most of the deployment period the tether position is forward of vertical at an angle of about 50 degrees.

The tether length, deployment speed, and tension are shown in Figure 3.4. Deployment begins with spring ejection of the endmass at a speed of about 1.5 m/s. Tension forces initially are 0.03 to 0.04 n (3 to 4 g) with a slight increase beginning around 2700 seconds reaching a value of 3.0 n at full deployment (5100 seconds) and a maximum value of 4 n just before the tether is cut at 5800 seconds.

### 3.6 Measurements

The key measurements are the turns of the tether versus time as the tether unwinds. This is sensed optically and stored in the electronics system memory. The command times for operating the stepper-motor brake and the cutter are based on this measurement. Also, tether length and payout speed are determined from the turns data.

The time duration of each turn will be compared with similar laboratory test data to evaluate the accuracy of ground test results in predicting flight performance. A reasonably close comparison is important to succeed at developing future tether applications.

Other data collected will be temperature, tension (just before the final exit guide), and supply voltage. Radar data will be collected on the ground giving the Delta II and payload position.

## 4. FEASIBILITY EXPERIMENT

### 4.1 Science And Technology Objectives

There are several issues of feasibility concerning SEDS tethers that must be verified experimentally, before these tethers can be used as antennas in communication systems of practical relevance. First of all, we must verify that the dynamics of tether deployment and station-keeping is well understood, and fully controllable. NASA-MSFC has scheduled several flights of SEDS systems, as piggy-back payloads on board the Air Force Delta-II rocket, to test tether dynamics. There will be a SEDS-1 flight in March 1993, a SEDS-2 flight in March 1994, and a SEDSAT mission in July 1994 (this mission is under study but has not yet been approved). There will also be an electrodynamic mission called PMG in June 1993.

Once that the dynamics is well understood, we should start experimenting with the radiophysics and the radioengineering issues that are fundamental to the use of SEDS tethers as antennas, in communication links from orbit to Earth surface.

The most relevant of the scientific investigations to be carried out are the following:

- (a) guidance of the e.m. waves radiated by the tether, along the lines of force of the Earth geomagnetic field, in the whistler regime, at VLF frequencies;
- (b) Alfvén wave guidance, also along the geomagnetic lines of force, at ELF frequencies, below the ion cyclotron frequency;
- (c) investigation of non-linear effects in the ionosphere, due to the high level of radiated power. This involves determining the threshold of occurrence of non-linear effects, and establishing the analytical dependence of these effects upon the level of radiated power;
- (d) determination of the angular aperture of the cone of capture of e.m. waves by the lines of force of the Earth magnetic field;
- (e) determination of the transmission and of the reflection coefficients at the boundary between the bottom of the ionosphere and the top of the atmosphere, as a function of the angle of incidence (from above) of the e.m. waves radiated by the SEDS tether, when they reach this boundary in their descent toward the Earth surface;
- (f) determination of the spatial extent of the illuminated area on the Earth surface. This is essential information, in order to establish the minimum number of satellites that are required to cover at all times a large

portion of the Earth surface (such as 60%, 80% or 100%).

The investigations listed above have an intrinsic scientific value within the realm of radiophysics. In addition, they represent essential steps that must be undertaken toward the goal of determining the feasibility of using SEDS tethers as antennas in space-to-ground communication links.

## 4.2 Application Goals

Because the ultimate use of the ELF/VLF propagation paths from orbit to Earth surface is in communications, we must characterize these paths as communication channels. The knowledge available on the applicable path properties is extremely limited, so that we must start from the fundamentals, and measure on the occasion of a first experiment, the following parameters:

(1) the response of the path to a "delta function" in the time domain. This will provide the measurement of the group delay, and of the time spread, inclusive of multipath spread;

(2) the response of the path to a "delta function" in the frequency domain. This will provide the measurement on the frequency spread, inclusive of Doppler shift and spread;

(3) the measurement of the path losses and of the noise;

(4) the measurement of the spatial and temporal variability of the channel properties;

(5) the distortion that affects specific communication waveforms, that are transmitted through the channel.

Once that the parameters above have been measured, it will be possible for communicators to select a waveform and to design a link that makes the best use of the available paths.

## 5. A SEDS/DELTA-II PAYLOAD FOR A FIRST FEASIBILITY EXPERIMENT

### 5.1 General

There are several factors that make it advisable to perform experiments on electrodynamic tethers by taking advantage of the availability of SEDS (Carroll 1987; Harrison et al., 1989) and of the Delta-II flight opportunities (Garvey and Marin, 1989). The most important factor is the low cost and the high frequency of flights of SEDS/Delta-II. In this paper we illustrate an experiment for inclusion in the SEDS/Delta-II demonstration program. The payload should be limited to radiation of e.m. waves in the VLF band (experimenting with ELF waves, a more difficult undertaking, should be considered for later times). The tether could be 4 km long, and

should radiate a frequency of  $\sim 9$  kHz. A second tether, also 4 km long, could be used to generate DC electric power, with the objective of recharging the payload's batteries.

### 5.2 Description Of The Payload

The simplified block diagram of Figure 5-1 shows the principal elements of the proposed payload. They are:

- (1) 2 conducting tethers, each 4 km long, each with its deployer; the electrical resistance of each 4-km tether is 88 ohm for the first mission (later-on, it could be lowered to 28 ohm); one tether teflon coated and one tether bare.
- (2) 3 plasma contactors, complete with power supply and auxiliary units, each rated at 20 A, capable of providing a low-resistance bridge between each end of the tether and the ionosphere, and between the platform and the ionosphere;
- (3) one solid-state VLF transmitter to feed one of the two tethers as a travelling-wave (TW) antenna at  $\sim 9$  kHz. To function as a TW radiator, the antenna requires the termination of the free end of the tether with a resistor equal to its equivalent-line characteristic impedance. Thus, the plasma contactor makes the "ground connection" to the ionospheric plasma;
- (4) additional silver-zinc batteries on the Delta-II second stage;
- (5) DC/AC static inverter (high voltage input);
- (6) AC/DC converters (low voltage input).

Figure 5-2 shows a possible location for the payload on board the Delta-II. The required space is a fraction of the available toroidal volume (with mean radius 33", width 16" and height 20") all around the guidance section of the Delta-II. The SEDS deployer is accommodated in the shaded area of Figure 2.

As a DC electric power generator, the tether can draw from the ionosphere a current of 12 A DC, under the drive of a maximum electromotive force of 2.1 kV provided by the  $V \times B \cdot \ell$  mechanism, where  $V$  is the orbital velocity,  $B$  the intensity of the Earth magnetic field, and  $\ell$  is the tether's length.

As already indicated, while one of the two 4-km tethers is used to generate DC electric power, the other tether is used as a travelling wave transmitting antenna, at the frequency of 9 kHz.

This requires that the high-voltage emf due to the tether (1.05 kilovolt DC) be inverted by a static inverter into a low-voltage AC, that becomes easy to transform into the wanted values and converted ultimately into the

DC voltages required by the various power supplies. The tether DC electric power generator will supplement the batteries, will trickle charge them and stay connected with them, while feeding the on-board loads. We have worked out two cases for the DC generator:

(a) a 88 ohm tether, capable of feeding the payload with a 30% duty cycle.

(b) a 28 ohm tether, capable of feeding 100% of the time the same payload.

According to the SEDS deployer's manufacturer (Tether Applications, Inc.) a 4-km x 1-mm diameter tether with a resistance of 88 ohm can be accommodated into the deployer canister without any substantial modification to the hardware.

This tether will be used for the first mission. For future missions the tether resistance could be reduced to 28 ohm by using a 1.7 mm-diameter Copper wire. In this case the primary power generated by the upper tether would be 21 kW, 10 kW of which are delivered to the load (batteries or VLF transmitter) with a 100% duty cycle. In this latter case, the SEDS deployer must be enlarged.

The total mass of the payload is 360 kg (~ 794 lb). This includes the tether masses, three plasma contactors inclusive of their power supplies and auxiliary units, two Marman clamps, and two additional 250 Ah Silver-Zinc batteries on the Delta II which enable a mission duration of 4 days. Two of the three plasma contactors are installed on the end masses of the SEDS tether. One is attached to the platform itself. The primary power requirement for the payload is 28 volt DC, 10 kW at VLF. Use will be made of the Delta-II telemetry channels available to payloads. This use, however, will be very limited because the scientific data from our experiment are collected and recorded by the receiving stations on the Earth surface, and not onboard the platform.

The receiving terminals that were used during the flight of TSS-1 could be moved to new sites that are suitable for the SEDS-1 mission of March 1993.

### 5.3 Orbital Flight Parameters

The parameters for the orbital flight of the proposed electrodynamic/electromagnetic tether experiment could be taken to be similar to the parameters of the first SEDS/Delta-II flight (DeLoach et al., 1990), presently scheduled for March 1993, devoted to the measurement of the dynamic properties of the SEDS tether.

We estimate that by adding 260 lb of Silver-Zinc batteries (this figure is already included in the total mass of 790 lb) to the Delta's second stage, the mission can last as long as 4 days. The orbital decay will be approximately 2.5 km/orbit during electrodynamic operations.

A nominal inclination of 37° and an orbital altitude greater than 400 km with a circular or a low eccentricity orbit are acceptable. The prior knowledge of the orbital parameters is a particularly important factor in our case because we must establish the location of the receiving sites on the Earth surface as a function of the orbital parameters. We must make sure that the orbiting system flies as close as possible over each receiving site. In later flights, we could relax this specification and explore signal detectability at substantial distances from the ground track. For the first electrodynamic/electromagnetic mission, however, the receiving stations should be strictly located along the ground track.

### 5.4 Ground-Based Data Collection

Several instrumented sites at various locations on the Earth surface will be used for data collection and recording, equipped with the same instrumentation that has been developed for the TSS-1 electrodynamic mission. The existing instrumentation is mobile and can be relocated at sites that are on the ground track of the proposed SEDS/Delta-II mission. This instrumentation consists of the following equipment:

- (a) Receiving/recording system developed for TSS-1 by Rice University under a subcontract from Smithsonian Astrophysical Observatory. This instrumentation, complete with data recorders, uses the following sensors:
  - One set of 3-axis magnetic field sensor BF-4 (a coil magnetometer) for the band 0.3 Hz to 500 Hz;
  - Two sets of 3-axis magnetic field sensor BF-6 (also a coil magnetometer) for the band 100 Hz to 100 kHz.
- (b) Receiving/recording system developed for TSS-1 by University of Genova, Italy, using sensors that were loaned to University of Genova by US Navy, NUWC, New London, CT (NUWC sensors are encapsulated in Bontos glass spheres suitable for underwater deployment). The sensors are:
  - Two sets of 3-axis induction coil magnetometer for the band 0.01 Hz to 100 Hz (Gritzke and Johnson, 1982);
  - One set of Varian, optically pumped, cesium vapour magnetometer.

Another magnetometer has been added to the sensors that the University of Genova has borrowed from the US Navy: a SQUID, multi-axis system that was procured for the TSS-1 flight.

Given the planned orbital parameters, the schedule of data collection at each of the ground-based sites can be easily formulated with all necessary time accuracy. The number of channels that will be recorded at each site are

a function of the number of sensors and of the number of axial components for each sensor. In addition, a channel will be devoted to station's identification and time information consisting of Epoch and of 1-second time marks. Pertinent telemetry data from SEDS/Delta-II will be collected, processed, and formatted by the on-board computer (Rupp, 1988). These data will then be transmitted to the ground-based telemetry stations assigned to the flight, via the Second Stage telemetry link.

#### 6. OPERATIONAL USES OF THE ORBITING TERMINAL FOR TACTICAL AND STRATEGIC COMMUNICATIONS TO SUBMERGED SUBMARINES

The orbital emplacement of the transmitting terminal brings with it the potentiality of covering, worldwide, all ocean areas, inclusive of the polar caps, should the orbit have a high-inclination. The waiting time, however, to have available the satellite, for any given location (should a single satellite be in orbit, with its transmitting terminal), would be too long. A constellation of several satellites would make it possible to cover, at any one time, a large portion of the Earth surface.

Figure 6.1 shows that less than ten satellites might be sufficient. A lot depends on the extent of the radius of the illuminated area, that is a quantity not reliably known from theory, and for which the final word will come from an experiment, such as the one illustrated in Section 5. Figure 6.1 shows that, assuming this radius to be somewhere between 3,500 km and 5,000 km, the required number of satellites would range between five and ten, to assure 80% coverage of the Earth surface.

With the constellation in place, assuming that transmissions take place at VLF, the system could be used to transmit EAM (Emergency Action Messages) to submerged submarines. The strategic communications link thus provided, would be a complement to "TACAMO," and would be characterized by a greatly enhanced geographical coverage. Should the ELF capability, then, be added to the satellite, the link would substantially augment the capabilities of the ground-based ELF facilities presently in use by US Navy.

With the present decrease in emphasis in strategic communications, due to the deep changes that have recently occurred in the world's geopolitical situation, tactical uses of the spaceborne transmitting terminal discussed in this paper, may be of greater interest. This system could be used by a Battle Group (Carrier, Destroyers, Submarines, etc.), deployed in remote ocean waters, to enable communications from a surface ship to a deeply submerged vessel.

#### 7. CONCLUSIONS AND RECOMMENDATIONS

Since the early days of radio, long, thin-wire antennas have been a fundamental presence in transmission facilities at LF, VLF and lower frequencies. The orbiting tethers represent the latest addition to this family of long line radiators. It seems natural to perceive the spaceborne tethers as potentially useful to fulfill communications requirements that are world-wide in character, such as the strategic and tactical communications requirements of US Navy.

These authors hold the view that, notwithstanding the lack of pressing motivations to add, at this time, new operational systems to the communications arsenal, R&D activity on this and similar advanced subjects, should be vigorously pursued.

Especially in cases such as ours, in which a fully probative experiment on an entirely novel technological development can be performed at low cost, it is advisable to proceed with it, learn to the fullest what the new technology's capabilities are, and identify unrecognized potentials, possibly leading to even broader and unforeseen applications for this technology.

#### 8. REFERENCES

- Alford, A., 1936, A Discussion of Methods Employed in Calculations of E.M. Fields of Radiating Conductors, *Electrical Communications*, Vol. 16, pp. 70-88, July.
- Barnett, A., and S. Olbert, 1986, Radiation of Plasma Waves by a Conducting Body Moving Through a Magnetized Plasma, *JGR*, Vol. 19, N.A9, pp. 10117-10135, September 1.
- Bhat, B., *Radio Science*, 8(5), 483 (1973).
- Carroll, J.A., 1987, The Small Expendable Deployment System (SEDS), Space Tethers for Science in the Space Station Era, Conference Proceedings, Vol. 14, Venice, Italy, October 4-8.
- DeLoach, R., et al., 1990, End-Mass Instrumentation for the First SEDS/Delta-II Mission, 28th Aerospace Sciences Meeting, AIAA-90-0537, Reno, Nevada, January 8-11.
- Denisse, J.F. and J.L. Delcroix, *Plasma Waves*, Interscience Publishers, New York, 1963.
- Determan, W.R., 1988, SNAP-DYN: Concepts for Multi-kilowatt Space Power Applications, Proceedings 1988 IECEC Conference, Denver, Colorado, July 31-August 5, Volume 3, pp. 203-211.
- Duff, B.M., 1964, "The Resistively-Loaded V-Antenna," NSG-579, Science Report No. 3, Harvard University.
- Garvey, J.M. and D.R. Marin, 1989, Delta-II Secondary

Payload Opportunities for Tether Demonstration Experiments, Tether in Space-Toward Flight, AIAA, San Francisco, CA, May 17-19.

Gritzke, A.R. and R.H. Johnson II, 1982, Ocean Floor Geomagnetic Data Collection System, Naval Postgraduate School, Monterey, CA, December.

Grossi, M.D., 1973, A ULF Dipole Antenna on a Spaceborne Platform of the PPEPL Class, Letter Report to NASA/MSFC, Contract NAS8-28303, May 11.

Grossi, M.D., 1987, System Application Study, Section 3 of Final Report on NASA Grant NAG8-551, pp. 59-113, SAO, Cambridge, MA, February.

Grossi, M.D., 1987, Tether History and Historiography, Second International Conference on Tethers in Space, Venice, Italy, October 4-8.

Grossi, M.D., 1989, A New Class of Large-Size, Spaceborne Antennas Based on Tether Technology, NSF Workshop, PIERS, Boston, MA, 27 July.

Grossi, M.D., 1991, Investigation of the E.M. Properties of a Spaceborne Electrodynamic Tether as a Travelling Wave Antenna, SAO Proposal P2485 to NASA-OSSA, July.

Grossi, M.D., E.C. Lorenzini and M.L. Cosmo, 1991, SEDS/Delta-II Electrodynamic Tether Experiments on the Generation and Radiation of Electromagnetic Waves from ULF to VLF, SAO "White Paper," Rev. No. 3, June.

Harrison, J.K. et al., 1989, Small Expendable-Tether Deployer System (SEDS)- Development Status, Tether in Space-Toward Flight, AIAA, San Francisco, CA, May 17-19.

Iizuka, K., 1967, The Travelling-Wave V-Antenna and Related Antennas, IEEE Trans. AP, AP-15, No. 2, pp. 236-243, March.

Kelly, F.J. et al., 1976, Waveguide-Mode Power Budget for an ELF/VLF Transmitting Satellite, NRL Report 8032, September 17.

King, R.W.P. and C.W. Harrison, Jr., Antennas and Waves, MIT Press, Cambridge, MA, 1969.

King, R.W.P. and S. Prasad, Fundamental Electromagnetic Theory and Applications, Prentice-Hall, New York, 1986.

Myers, C.W., D.J. Kretzchmar, and M.D. Grossi, 1986, Spaceborne E.M. Wave Generation/Radiation Facility for the High-Power Illumination at ULF/ELF of Underwater Targets, DARPA/SPC, Arlington, VA, November 19.

Rupp, C.C., 1988, SEDS Computer System, NASA-MSFC Technical Document, Huntsville, Alabama, November.

Seshadri, S.R., Proc. of the IEE (London), 112(10), 1856 (1965).

Seshadri, S.R., J. Appl. Phys., 39(5), 2407 (1968).

Thompson, G.C., 1988, Design of an ELF/VLF Satellite for Under the Ice Submarine Communications, MS Thesis, Naval Postgraduate School, Monterey, California, September.

Wunsch, A.D., Can. Jour. Phys., 45, 1675 (1967).

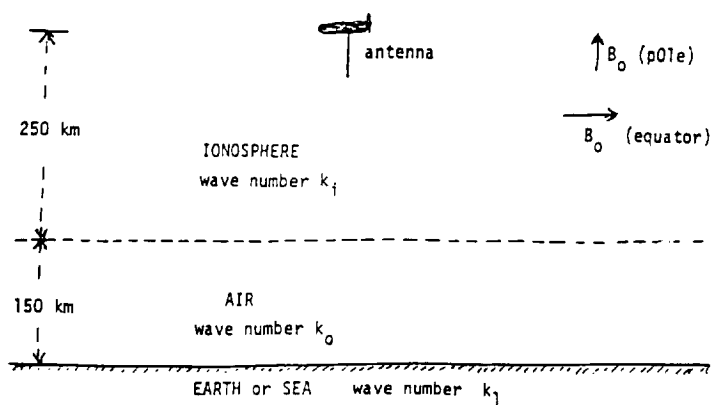


Figure 2-1 Schematic diagram of the Shuttle with a vertical tether antenna in the ionosphere over the Earth

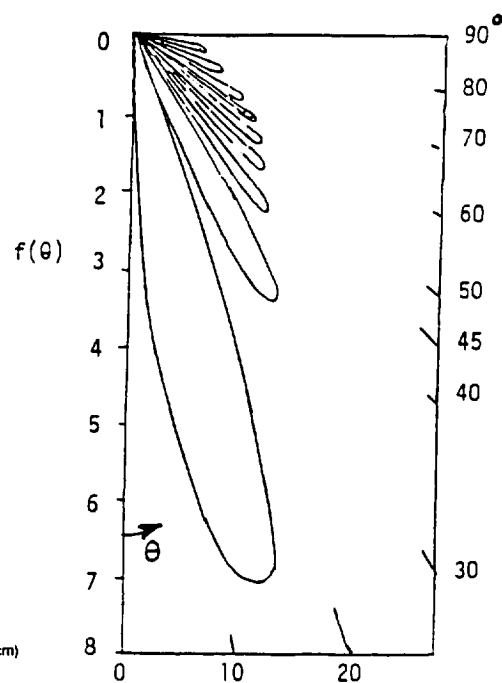


Figure 2-2 Far field of a Travelling-wave antenna in the ionosphere, using the whistler mode

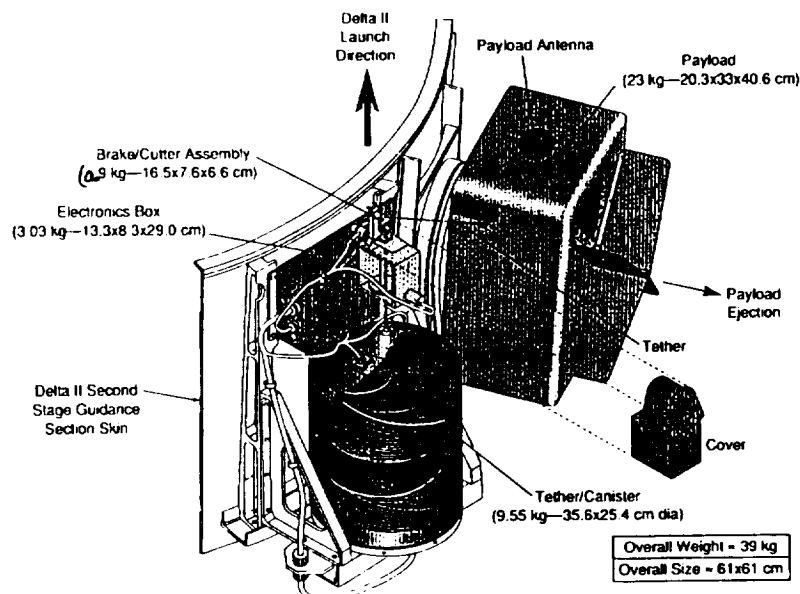


Figure 3-1 SEDS on Delta-II

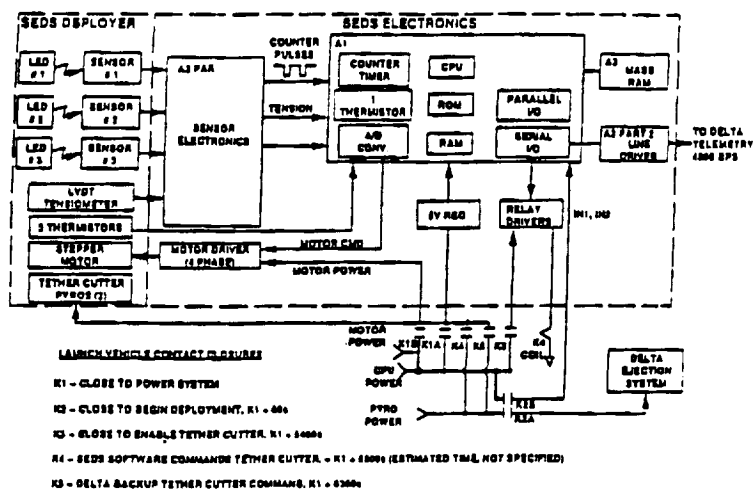


Figure 3-2 SEDS-1 Data System Block Diagram

Event	Delta II Time (sec)	SEDS-1 Time (sec)
Delta II Lift-off	0	
Stage II-III Separation	1262.8	
SEDS Power On	3720.0	0
Guam AOS	3729.4	
Deploy SEDS Endmass	3780.0	60
Begin Roll Maneuver to Tether Deploy Attitude	3785.0	
End Roll Maneuver to Tether Deploy attitude	3795.0	
Maintain Deploy Attitude	3830.0	
Guam LOS	4544.3	
Brake Initiation	8400.0	4680
Deployment Ends - Swing Begins	8570.0	4850
Guam AOS	9717.6	
SEDS Initiated Tether Cut Command	9949.0	6229
Delta Initiated Tether Cut Command (Back-Up)	10,080.0	6360
Guam LOS	10,475.4	
Hawaii AOS	10,777.3	

TABLE 3-1 Delta II/SEDS-1  
Sequence of Events

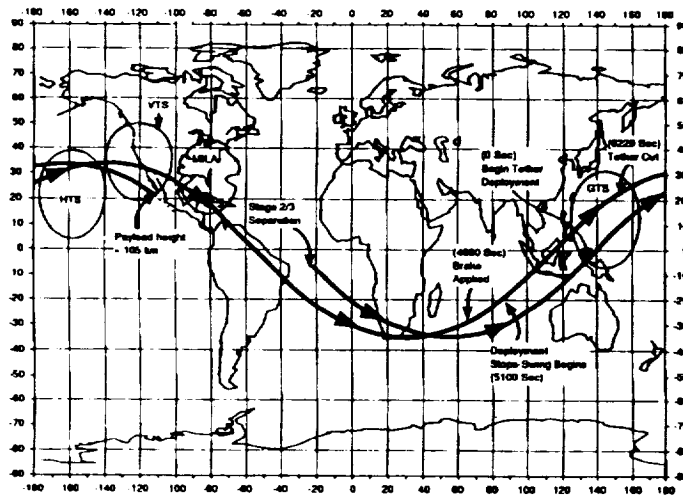


Figure 3-3 SEDS Ground Track

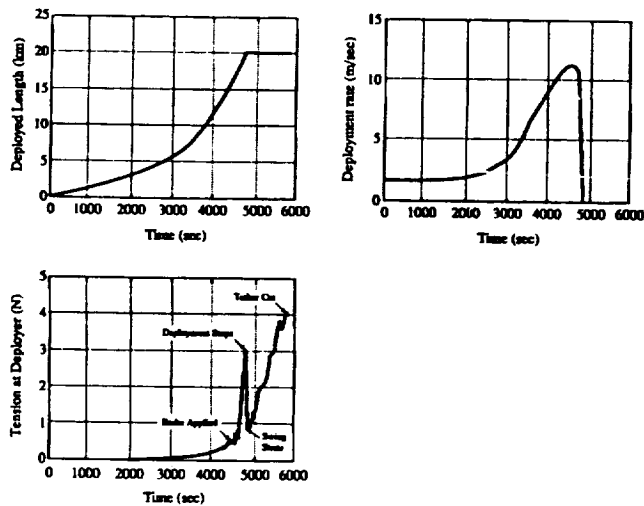


Figure 3-4 SEDS-1 Nominal Deployment  
Case



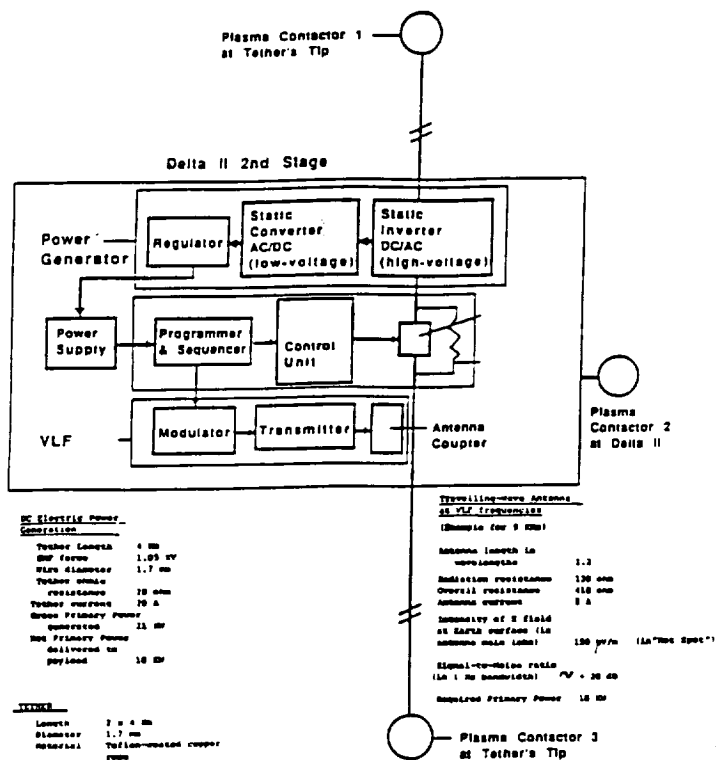


Figure 5-1  
Simplified Block Diagram of the payload

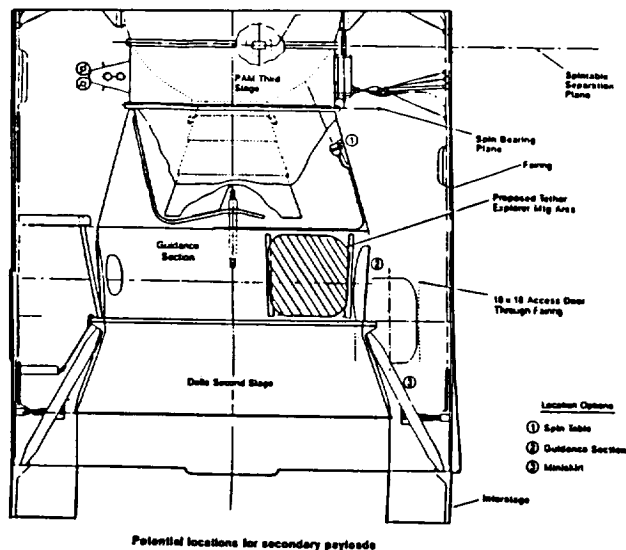


Figure 5-2  
SEDS Accommodation on Delta-II Second Stage

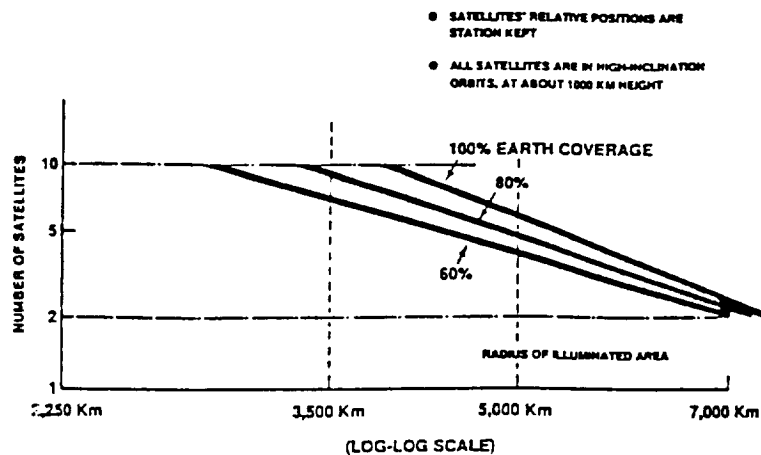


Figure 6-1  
Number of satellites required to cover the Earth surface



Center for Astrophysics  
Preprint Series No. 3470

**A TETHER ARRAY FOR SPACEBORNE LOW-FREQUENCY RADIO ASTRONOMY**

M.L. Cosmo, E.C. Lorenzini, and M.D. Grossi  
Harvard-Smithsonian Center for Astrophysics

## A TETHER ARRAY FOR SPACEBORNE LOW-FREQUENCY RADIO ASTRONOMY

M.L. Cosmo, E.C. Lorenzini, M.D. Grossi

Harvard-Smithsonian Center for Astrophysics, Cambridge, Mass. 02138, U.S.A.

### ABSTRACT

This paper describes a spaceborne array of two long "Travelling Wave" antennas each tethered to a spacecraft. The system orbits the Earth above the ionosphere with an angular separation, thus forming a "V". Gravity gradient forces keep the long tethers taut and aligned along the vertical. The *Small Expendable Deployer System* can be used to deploy and control the tethers. Such an array is proposed for radioastronomical observations in the 1-30 MHz frequency range. The tether V-shaped antenna provides a higher directivity and gain as compared to regular long dipoles, yielding valuable data on the low frequency spectrum characteristics of extragalactic sources, pulsars, supernova remnants and interstellar medium.

### INTRODUCTION

Ground-based radio astronomy in the 1-30 MHz range is difficult if not impossible due to the ionospheric refraction. In the 60's NASA developed and launched the Radio Astronomy Explorers (RAE-1 and RAE-2) to perform such observations from space. Unfortunately, not all the scientific objectives were met due to problems in deploying the long antennas, the Earth radio noise at low frequencies, etc.. Nevertheless some data were of importance and RAE paved the way to future mission in spaceborne radio astronomy.

Tether technology could be the key to these future missions and the Small Expendable Deployer System (SEDS) /1/ offers a simple and inexpensive way to deploy long tethers in space. In the following, an array of two long tethers to be used as Travelling Wave (TW) antennas will be presented.

Long tethers are very stable by aligning themselves along the local vertical while the spacecraft orbits the Earth. The basic advantage in using a TW antenna over a long-wire multiwavelength electric dipole is that the former is non-resonant. TW antennas have high directivity and the frequency band can be made very broad, extending from a fraction of one Hertz up to the upper limit (30 MHz) of the HF band. Another consequence is that the TW antenna is characterized by higher directivity and gain than the resonant dipole. However, the TW antenna, like a resonant dipole is still characterized by a radiation pattern that has a null in the direction of the axis. In most applications this is not a desirable feature. By arranging the antennas in arrays it is possible to produce a pattern with the wanted characteristics. The simplest of all possible array configurations is the "V antenna," consisting of a pair of TW antennas originating from the same point, and angularly separated /2/,/3/. The V antenna's pattern has a maximum along the bisector of the separation angle. This simple array, often in a double-V configuration, has found extensive use in the communications practice on the Earth surface, especially in short-wave communications (frequency range 3 MHz to 30 MHz).

High resolution observations in the 1-30 MHz frequency range could address some important scientific issues such as /4/:

- Study of the properties of radio sources at low frequencies

- Study of physical processes in astrophysical plasmas
- Study of interstellar gas and its distribution
- Study of low energy cosmic rays
- Study of pulsars with flux densities increasing at low frequency
- Study of "old" electrons for fossil remnants of galaxies

## THE TRAVELLING WAVE ANTENNA

A long metal wire in Earth orbit aligned along the local vertical /5/, can naturally function as a long, thin-wire antenna for transmission and reception of electromagnetic waves. An antenna that is well suited to long spaceborne tethers is the "Travelling Wave" (TW) antenna. A TW antenna requires grounding at both ends and must be terminated with a resistance equal to the characteristic impedance of the equivalent transmission line. Such a termination prevents a standing wave (with sinusoidal distribution of maxima and minima) to establish itself along the antenna wire. The standing wave is due to the superimposition of a wave propagating along the wire in one direction, and of a reflected wave moving along the wire in the opposite direction. If the antenna is properly terminated, there is no reflected wave, hence a standing wave is absent.

In space the TW antenna can be grounded by connecting each end to an open-ended  $\frac{1}{4}$  lambda straight wire (a  $\frac{1}{4}$  lambda "stub"). The stub is equivalent to a section of transmission line that is an open-circuit at its free end, and that appears as a short circuit at the point where the stub is attached to the TW antenna, hence the "grounding." The antenna current, if there are no losses in the wire, is constant along the wire.

Ronald W.P. King, Harvard University, has suggested an interesting alternative /6/: the wire of the TW antenna can be made of resistive material, and the current that flows in the wire can be made of an exponentially decreasing intensity. Should this intensity be made equal to zero at the end of the TW antenna, there is no need any longer of any grounding at that end, because no current would flow to the ground (grounding at the other end of the tether is still required). One of the merits of King's suggestion is that the elimination of the  $\frac{1}{4}$  lambda stub (that is a resonant element) keeps fully broadbanded the TW antenna. An example of pattern in free-space conditions is shown in figure 1. The tether is assumed to be 5 km long and the antenna frequency is 1 Mhz. Figure 1 shows that a TW antenna in free space conditions has a null along the axis of the wire. Its main lobe is "cave" and the cross section of the lobe is an annulus, at variance with the circular cross section that normally characterizes the lobe of a high-directivity antenna. This undesirable feature can be corrected by using in orbit several TW antennas, and by combining their outputs. A two-element array, the "V-antenna", produces by coherent summation, a beam with the main lobe that is filled rather than cave. The angle  $\beta$  of the maximum radiation measured from the axis of the wire is a function of the ratio  $l/\lambda$ , where  $l$  is the tether length and  $\lambda$  the wavelength (see Table 1). The maximum gain is achieved when the angular separation  $\alpha$  between the two arms of the V antenna is equal to  $2\beta$  as shown in figure 2. The pattern is referred to a V-antenna with arms 5 km long and with an angular separation  $\alpha$  equal to  $24.6^\circ$ .

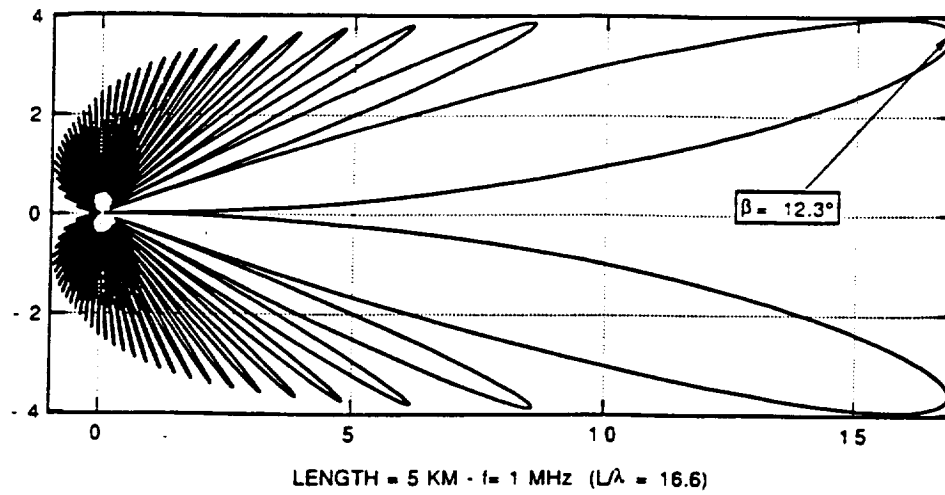


Fig. 1. Radiation pattern of a single Travelling Wave Antenna 5 km long at 1 MHz ( $L/\lambda = 16.6$ )

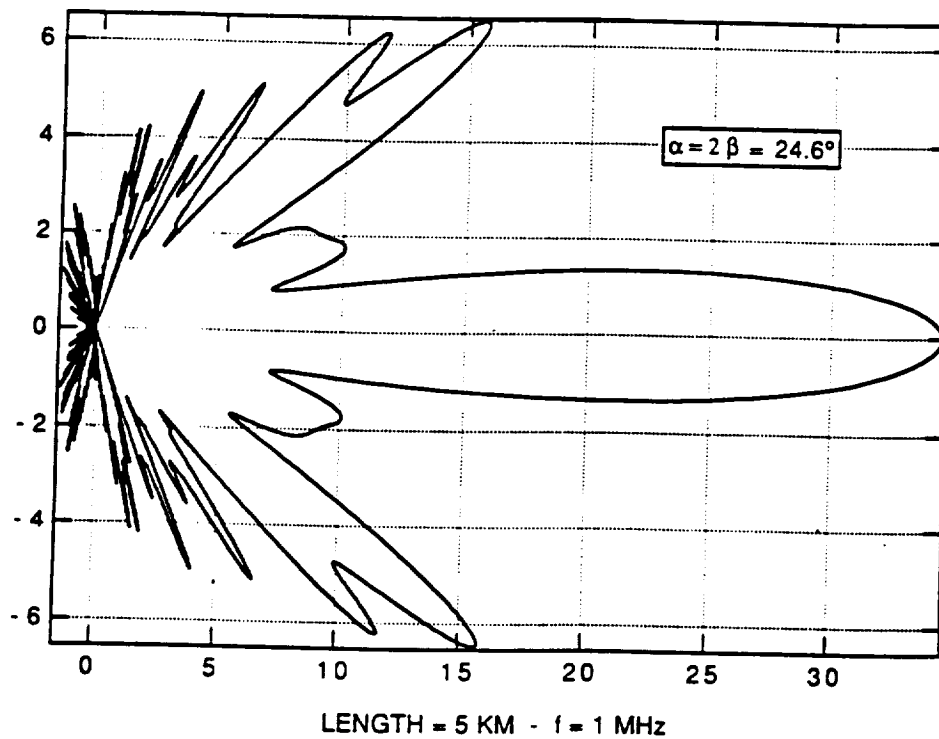


Fig. 2. Radiation pattern (E-plane) of a V-Travelling Wave Antenna with arms 5 Km long and an angular separation of  $24.6^\circ$  at 1 MHz

**Table 1.** Angle  $\beta$  of Maximum Radiation as a Function of  $l/\lambda$  for two frequencies for a Travelling Wave Antenna

TETHER LENGTH (Km)	$l/\lambda$ [1 MHz]	$\beta$ ( $^\circ$ )	$l/\lambda$ [30 MHz]	$\beta$ ( $^\circ$ )
5	16.67	12.3	500	2.25
10	33.33	8.66	1000	1.65
20	66.67	6.06	2000	1.06
50	166.67	3.86	5000	0.7

### THE SMALL EXPENDABLE DEPLOYER SYSTEM

The Small Expendable Deployer System (SEDS) was developed by the Energy Science Laboratories, and at the present by Tether Applications, under the sponsorship of NASA/Marshall Space Flight Center. SEDS does not retrieve the payload and consequently it has a very simple design. The first SEDS flight is scheduled in March 1993. An instrumented box will be deployed with a 20 km long tether from the second stage of a Delta II /1/.

SEDS consists of a canister where the tether is spooled, a brake system, a turn counter, a tensiometer and a computer. With reference to figure 3, the tether goes through the exit guide of the canister, passes through the brake, the tensiometer and a guillotine and then to the end-mass. In the first flight the brake will be activated by the stepper motor at about 19 km bringing the payload to a smooth stop. When the payload reaches the vertical the tether is severed and reenters into the atmosphere. SEDS mass characteristics are given in table 2.

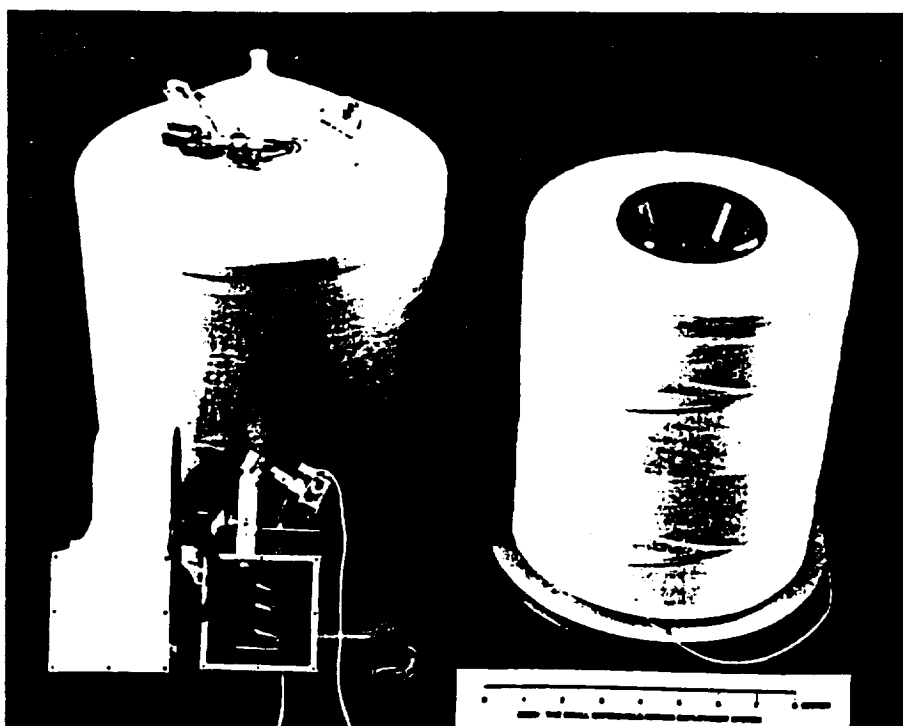


**Fig. 3.** SEDS Hardware

Table 2. SEDS mass and size (first mission)

	Mass(kg)	Size (cm)
Deployer canister	3	25 X 33
Tether (Spectra)	7	20 km X 0.75mm
Brake/Cutter	1	8 X 8 X 20
Electronics	2	8 X 13 X 25
End-mass	25	20 X 30 X 40
Brackets/Clamps	4	
Total	42	

### SYSTEM DESCRIPTION

The system consists of two spacecraft . Since the pattern is function of the ratio  $l/\lambda$ , the tether length and the angular separation between the two spacecraft must be chosen in such a way as to keep the antenna system capable of providing the wanted directivity in the frequency band of interest. In our preliminary study, the orbital height of the system is 10,000 Km, the 50-km long tethers are made of Spectra with an aluminum or copper core and are 50 km long. The two spacecraft are separated by a geocentric angle of  $2^\circ$ . The patterns of the V-antenna are shown in figure 4, 5, and 6 for 3, 15 and 25 MHz, respectively. The antenna characteristics are given in table 3.

Table 3. V-Antenna characteristics

$f$ (MHz)	$l/\lambda$	HPBW ( $^\circ$ )
3	500	6
10	1667	0.7
25	4167	0.5

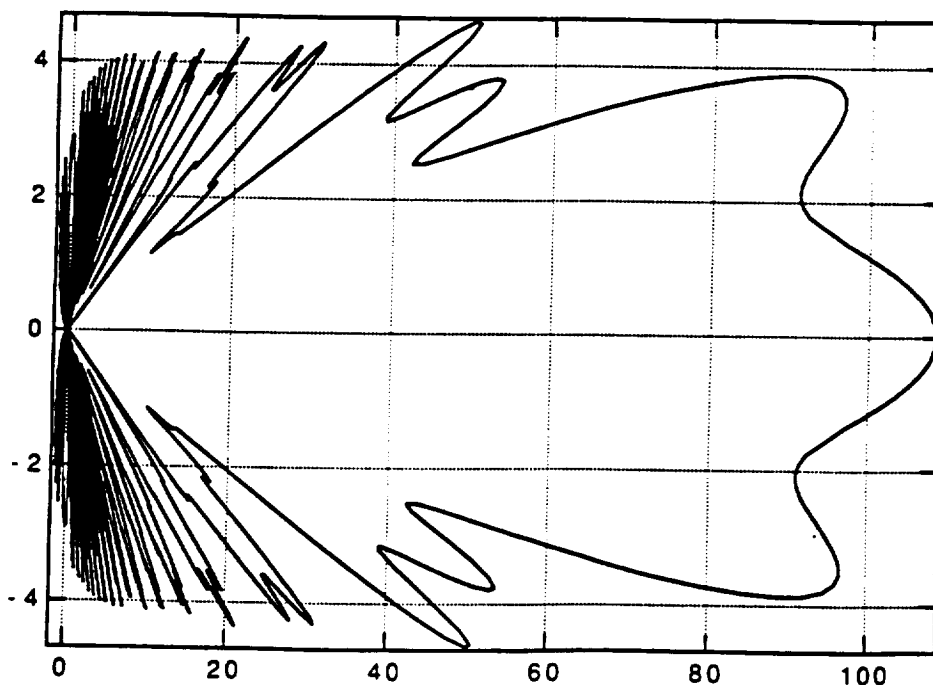


Fig. 4. Radiation pattern (E-plane) of a V-Travelling Wave Antenna with arms 50 Km long and an angular separation of  $2^\circ$  at 3 MHz



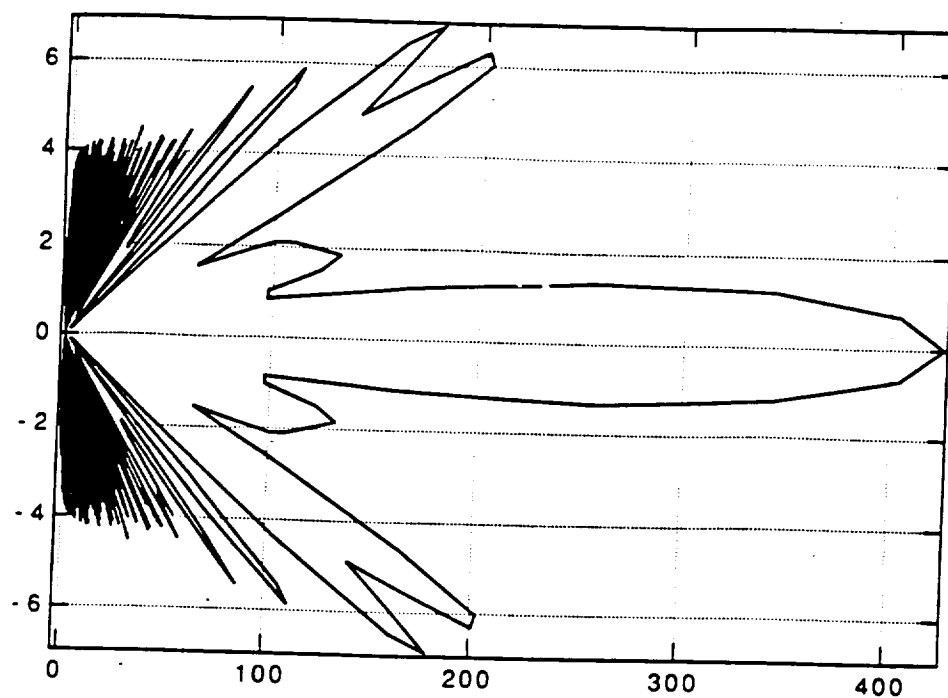


Fig. 5. Radiation pattern (E-plane) of a V-Travelling Wave Antenna with arms 50 Km long and an angular separation of  $2^\circ$  at 10 MHz

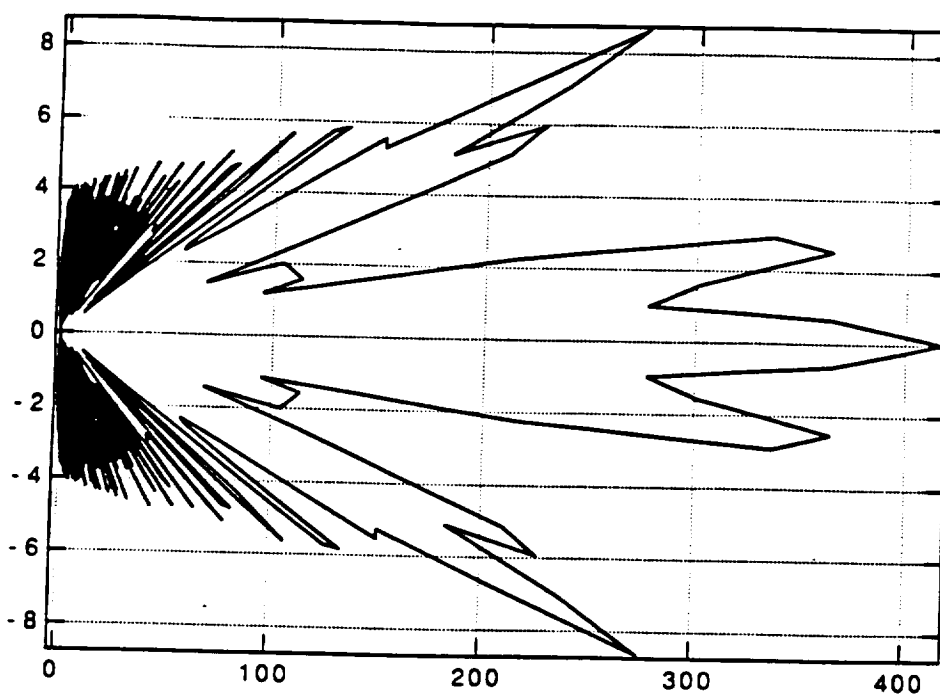


Fig. 6. Radiation pattern (E-plane) of a V-Travelling Wave Antenna with arms 50 Km long and an angular separation of  $2^\circ$  at 25 MHz

The two antennas orbit along coplanar orbits and are separated, ideally, by a constant geocentric angle  $\Delta\theta$ . The angular separation must be maintained within 10% in order to avoid degradation of the resultant radiation pattern (i.e. the combination of the two antennas' patterns). Alternatively, a differential attitude motion between the two antennas greater than 10% of the separation angle will produce a degradation of the resultant radiation pattern.

At an altitude of 10,000 km above the Earth's surface, the aerodynamic drag is negligible. The major perturbations to the relative position of the antennas, and hence to the relative angular separation, are from differential forces due to: Sun's and Moon's gravity; Earth's  $J_2$  gravity component; solar pressure.

Likewise, the major disturbances to the relative attitude of the antennas are from differential torques due to: Earth's  $J_2$  and solar pressure.

#### - Earth's $J_2$ Differential Effects -

##### Differential Forces

The differential force acting on the antennas separated by a geocentric angle  $\Delta\theta$  is obtained from the  $J_2$  perturbing potential. The radial (R), in-flight ( $\theta$ ), and lateral (L) components of the differential force are

$$\begin{aligned}\delta f_R &= \frac{3}{2} A \sin^2 i \sin(2\theta) \Delta\theta \\ \delta f_\theta &= -A \sin^2 i \cos(2\theta) \Delta\theta \\ \delta f_L &= -\frac{1}{2} A \sin(2i) \cos\theta \Delta\theta\end{aligned}\tag{1}$$

where  $A = 3\mu_E J_2 R_E^2 / r^4$ ,  $i$  is the orbital inclination,  $\mu_E$  and  $R_E$  the gravitational constant and the equatorial radius of the Earth, and  $\theta$  the argument of longitude of the antenna closer to the equator.

The differential precession of the two antennas is then as follows:

$$\frac{d\Omega}{dt} = \frac{\delta f_L \sin\theta}{V \sin i} \Delta\theta\tag{2}$$

which leads to:

$$\frac{d\Omega}{d\theta} = \frac{A}{2r\omega_0^2} \sin(2\theta) \cos i \Delta\theta\tag{3}$$

The integral of eqn (3) is null over any number of half orbits implying that no secular effect is produced by this differential force component. The integral of eqn (3) reaches a maximum value over a quarter of an orbit. The maximum error of the separation angle is, therefore, as follows:

$$\epsilon = \left( \frac{d\Omega}{\Delta\theta} \right)_{\pi/2} = \frac{3}{2} J_2 (R_E/r)^2 \cos i\tag{4}$$

At an altitude of 10,000 km, the maximum angular error is 0.002%.

##### Differential Torques

From eqn (1.1), the  $J_2$  torque with respect to the center of mass of a dumbbell antenna (the tether mass has been neglected) is

$$T_{J_2} = 6J_2 \omega_0^2 \left( \frac{R_E}{r_{cm}} \right)^2 l^2 m_R \sin^2 i \sin(2\theta) \quad (5)$$

where  $r_{cm}$  is the geocentric distance of the antenna's center of mass (cm),  $l$  the antenna's length, and  $m_R = m_1 \cdot m_2 / m_{tot}$  the reduced mass of the two tip-masses of the antenna  $m_1$  and  $m_2$ .

The maximum differential attitude occurs when the antennas are on opposite sides of the equator, i.e.  $\theta = n\pi/2$  with  $n$  an integer. Then the differential torque is

$$\delta T_{J_2} = 6J_2 \omega_0^2 \left( \frac{R_E}{r_{cm}} \right)^2 l^2 m_R \sin^2 i \Delta\theta \quad (6)$$

After equating eqn (6) to the gravity gradient restoring torque for small attitude angles  $\beta$ ,

$$T_{GG} = 3m_R \omega_0^2 l^2 \beta \quad (7)$$

the relative maximum attitude error is

$$\epsilon = 2J_2 \left( \frac{R_E}{r_{cm}} \right)^2 \sin^2 i \quad (8)$$

At an altitude of 10,000 km, the maximum attitude errors for polar orbits are 0.03%.

- Third-body Differential Effects -

The third-body perturbation force, obtained from the third-body effective potential, is as follows:

$$\vec{f} = \frac{\mu_{III}}{r_{III}^2} \left( 3 \frac{\vec{r}_{III} \cdot \vec{r}}{r_{III}^2} \hat{r}_{III} - \frac{\vec{r}}{r_{III}} \right) \quad (9)$$

where the subscript III is referred to either the Sun or the Moon,  $\vec{r}_{III}$  and  $\vec{r}$  are the vector radii from the Earth to the third body and to the antennas respectively, and  $\hat{r}_{III}$  is the unit vector.

The components of the differential force on the two antennas are obtained by transforming eqn (5) to the orbiting reference frame  $R\theta L$ , taking the partial derivative with respect to  $\theta$ , and assuming that the third body has zero declination. Hence

$$\begin{aligned} \delta f_R &= -3 \frac{\mu_{III}}{r_{III}^2} \frac{r}{r_{III}} [\sin(2\alpha) \cos(2\theta) + \sin(2\theta) \cos(2\alpha)] \Delta\theta \\ \delta f_\theta &= -3 \frac{\mu_{III}}{r_{III}^2} \frac{r}{r_{III}} \cos i [\sin(2\alpha) \sin(2\theta) - \cos(2\alpha) \cos(2\theta)] \Delta\theta \\ \delta f_L &= -3 \frac{\mu_{III}}{r_{III}^2} \frac{r}{r_{III}} \sin i [\sin(2\alpha) \sin(2\theta) - \cos(2\alpha) \cos(2\theta)] \Delta\theta \end{aligned} \quad (10)$$

where  $\alpha$  is the right ascension of the third body.

Eqn (2), then, yields the differential precession between the two antennas. Here again there is no secular effect and the maximum angular error occurs over one quarter of an orbit as follows:

$$\epsilon = \left( \frac{d\Omega}{d\theta} \right)_{\pi/2} = \left( \frac{\omega_{III}}{\omega_0} \right)^2 [2 \sin(2\alpha) + \cos(2\alpha)] \quad (11)$$

where  $\omega_{III}^2 = \mu_{III}/r_{III}^3$  and  $\omega_0$  is the orbital rate of the antennas.

The maximum angular error occurs for a third-body right ascension of 40 deg and 140 deg. The errors are 0.0003% due to the Moon and 0.0001% due to the Sun for an orbital altitude of 10,000 km.

## - Solar Pressure Differential Effects -

### Torques

At high altitudes the solar pressure torque may be relatively significant with respect to other external torques. For the travelling wave antenna, the tether and the solar panels provide independent torque components as indicated in the following formula that gives the attitude misalignment with respect to the local vertical

$$\delta\theta = \frac{M_F}{3\omega_0^2} [ASP K_{SP}/(l m_1) + r K_T \sin\gamma/m_D] \quad (12)$$

where  $M_F$  is the solar momentum flux equal to  $4.4 \times 10^{-6} \text{ N/m}^2$ ,  $ASP$  the area of the solar panels perpendicular to solar rays,  $r$  and  $l$  the radius and length of the tether,  $\gamma$  the solar view angle of the tether,  $K_{SP}$  and  $K_T$  the reflectances of the solar panels and the tether respectively, and  $m_D = m_1 \cdot m_2 / (m_2 - m_1)$ . If  $m_2 < m_1$  the tether torque contribution (second term in square brackets) has a sign opposite to the solar panels contribution. The two contributions depend upon system geometry, values of  $K_{SP}$  and  $K_T$ , and power requirement. It is possible, however, to have a zero total torque with realistic and appropriate values of the system parameters.

In a more general situation, an upper bound of the solar radiation torque can be obtained by neglecting the tether contribution and by assuming typical values of system parameters as follows: 1 kW of power delivered by the solar panel with an efficiency of 10%,  $\gamma = 90^\circ$ ,  $K_{SP} = 1.5$ ,  $r = 1 \text{ mm}$ ,  $l = 10 \text{ km}$ . At an altitude of 10,000 km, the attitude misalignment is  $\delta\theta = 0.002^\circ$ . A relative attitude error equal to this misalignment value can be reached across the terminator with one antenna in the light and the other in the shade.

### CONCLUSIONS

The possibility of performing high resolution observations from orbit of radioastronomical sources in the band 1-30 MHz, can be greatly enhanced by the advent of spaceborne tethers.

There is now a substantial larger flexibility in configuring a radioastronomical observatory in Earth orbit, where tethers can be used as structural elements to provide support to a large array of dipoles. The requirement of simplicity will be, however, the prevailing criterion, and we would expect that, in the conceivable future, the dual-platform V-antenna discussed in this paper will be considered for implementation

### REFERENCES

1. E.C. Lorenzini and J.A. Carroll, In-Orbit Experimentation with the Small Expendable-Tether Deployment System, *ESA Journal*, Vol. 15, 27-33 (1991)
2. B.M. Duff, The Resistively-Loaded V-Antenna, NSG-579, Sci. Report 3, Harvard University, Cambridge, Mass., U.S.A. (October 1964)
3. K. Iizuka, The Traveling-Wave V-Antenna and related Antennas, *IEEE Transactions on Antennas and Propagation*, Vol. AP-15, No.2, 236-243 (1967)

4. N.E. Kassim and K.W. Weiler (Eds.), Low Frequency Astrophysics from Space, 562, Springer-Verlag, 1990
5. Colombo, G., E.M. Gaposhkin, M.D. Grossi, and G.C. Weiffenbach, Shuttle-borne Skyhook: A New Tool for Low-Orbital Altitude Research, Reports in Geoastronomy 1, Smithsonian Astrophysical Observatory, Cambridge, Mass., U.S.A. (1974)
6. R.W.P. King, private communication (1991)



## **7.0 PROPAGATION OF ELF WAVES INTO THE IONOSPHERE**

The research conducted on this topic focused on the development of a method for the numerical calculation of the electromagnetic wave field on the Earth's surface associated with the operation of an electrodynamic tethered satellite system of constant or slowly varying current orbiting in the ionosphere. One of the experiment of the TSS-1 mission calls for the detection on the Earth's surface of the electromagnetic waves emitted from TSS. The development of this numerical model is therefore instrumental for evaluating the strength of the signal on the ground.

The following paper summarizes the results of the investigation mentioned above.

See also Quarterly Reports No. 18, No. 19, and No. 20 of this contract for more details.





Robert D. Estes  
Harvard-Smithsonian Center for Astrophysics  
Cambridge, MA 02138

### Abstract

This paper outlines a method for numerical calculation of the electromagnetic wave field on the Earth's surface associated with the operation of an electrodynamic tethered satellite system of constant or slowly varying current high in the ionosphere. The model used allows for arbitrary angles between the geomagnetic field lines and the horizontal plane and for vertical variations in plasma density, ion species, and ion-neutral collision frequency. The shear Alfvén wave-packet generated by an electrodynamic tether in an infinite, uniform magnetoplasma is taken as the incident wave. The functional forms of the Fourier components of the incident and reflected shear Alfvén waves and the upwardly decreasing evanescent compressional Alfvén solution are known in the upper ionosphere. The form of the solution in the atmospheric cavity is easily obtained. This knowledge enables us, in principle, to obtain the wave field at the ionospheric boundary and, hence, on the Earth's surface by numerical integration. Preliminary conclusions based on general principles are that the ionospheric waves do not propagate into the atmosphere and that the image of the Alfvén "wings" from a steady-current tether should be greatly broadened on the Earth's surface and will probably be too weak to detect, even for high current values.

### Introduction

The problem of electromagnetic wave generation by an electrodynamic tethered satellite system is important both for the ordinary operation of such systems and for their possible application as orbiting transmitters. The tether's ionospheric "circuit closure" problem is closely linked with the propagation of charge-carrying electromagnetic wave packets away from the tethered system.

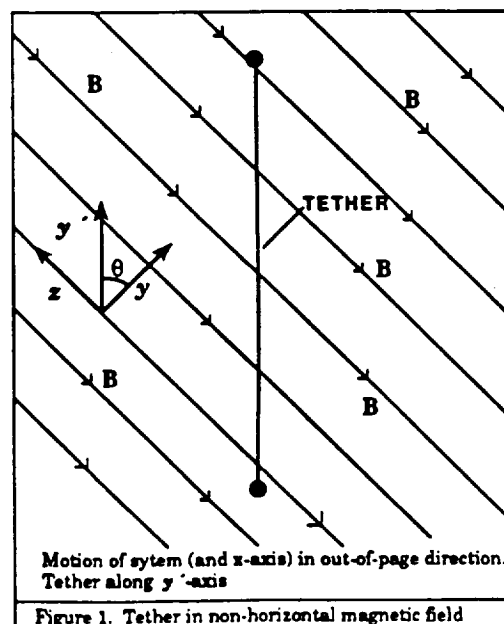
Previous analyses of the waves generated by large conductors moving through a magnetoplasma<sup>1-6</sup> (in our case a tethered system moving through the ionosphere) have considered the

conductor to be immersed in an infinite plasma medium. When the boundary with the atmosphere is far enough away, this serves as a useful approximation for calculating the ionospheric waves and estimating their contribution to the tethered system's electrical impedance; but it tells us nothing about the electromagnetic signal we should expect to be associated with the tethered system in the atmosphere or on the Earth's surface.

Heretofore there has not been a systematic treatment of the wave reflections and other effects of nonuniformities in the plasma medium. The inclusion of ion-neutral collisions introduces the possibility of coupling to the fast magnetosonic (compressional Alfvén) wave modes. The work reported here represents a step towards a solution to the problem that takes into account the effects of boundaries and of vertical variations in plasma density, collision frequencies, and ion species.

### Generalization of Previous Results

As a first step, we generalize our previous results on steady-current tethers to the case where the geomagnetic field makes an arbitrary angle with the horizontal plane, in which the tethered system moves (See Figure 1).



This paper is declared a work of the U.S. Government and is not subject to copyright protection in the United States.

This would approximately correspond to a system at its maximum excursion in latitude for a non-equatorial orbit. Having previously demonstrated the equivalence of an orbiting "ribbon" current distribution and the idealized dumbbell tether current distribution used in the earlier analysis<sup>6</sup>, we can conveniently define the tether current distribution as

$$j = \frac{\hat{y}I}{L_x} \left[ H\left(x' - \frac{L_x}{2}\right) - H\left(x' + \frac{L_x}{2}\right) \right] \cdot \left[ H\left(y' - \frac{L}{2}\right) - H\left(y' + \frac{L}{2}\right) \right] \quad (1)$$

where  $x' = x - v_x t$  and  $\hat{y}'$  lies along the vertical with  $y'=0$  at the middle of the tether. The  $y$ -axis, which is orthogonal to  $B$  (the  $z$  axis) is also indicated in Figure 1.  $H(x)$  is the Heaviside function defined by

$$\begin{aligned} H(x) &= 1, x \geq 0 \\ H(x) &= 0, x < 0 \end{aligned} \quad (2)$$

and  $I$ ,  $L$ , and  $L_x$  are the tether current, tether length, and system dimension in the line-of-flight direction, respectively.

We now need  $k \cdot j_k$ , where  $j_k$  is the Fourier transform of the tether current density. This is most conveniently calculated in the  $(x, y', z')$  co-ordinate system, where

$$k \cdot j_k = k_{y'} j_{k,y'} \quad (3)$$

It is easy to obtain

$$j_{k,y'} = \frac{2I}{\pi} \delta(\omega - k_x v_x) \frac{\sin\left(\frac{k_x L_x}{2}\right)}{k_x L_x} \frac{\sin\left(\frac{k_{y'} L}{2}\right)}{k_{y'}} \quad (4)$$

The Fourier transform of the plasma current along the field lines is

$$J_z = \frac{ic^2}{4\pi\omega} k_x k \cdot E, \quad (5)$$

and

$$k \cdot E = \frac{4\pi\omega}{c^2} \frac{k \cdot j}{\left(k_x^2 - \epsilon_1 \left(\frac{\omega}{c}\right)^2\right)} \quad (6)$$

where  $\epsilon_1$  is the diagonal component of the cold plasma dielectric tensor perpendicular to the magnetic field<sup>6</sup> and Gaussian units are used. The only difference from the horizontal magnetic field case is in the argument of the second sin factor in (4).

When the inverse Fourier integrals of (5) are carried out, the result is once again field-line sheet currents at the ends of the system; only the charge-exchange regions at the ends of the system are now located at  $y = \pm \frac{L}{2} \cos \theta$ . The top and bottom wings are connected by the condition of current continuity but otherwise they appear to be independent phenomena generated by the disturbances at their respective ends of the system. Except for the shift in lines of discontinuity in  $J_z$  to coincide with those traced by the charge exchange terminals, the Alfvén wing solutions are the same as before.

#### Electrodynamic Tether in a Bounded, Non-Uniform Ionosphere: Basic Physics

The first significant new feature we introduce to the problem is the presence of boundaries: the one between the ionosphere and the atmosphere and the one between the atmosphere and the Earth. For simplicity, we begin our analysis with the atmospheric cavity considered as a vacuum and the Earth as a perfect conductor. For electromagnetic problems the first approximation is reasonable, and the second approximation greatly simplifies the boundary value problem at the Earth. If the ocean surface is considered, it is justifiable as a first approximation since its main consequence is a small horizontal electric field component at the surface.

We make the assumption that the tethered system is sufficiently far from the atmospheric boundary (or any steep gradients in plasma parameters) that we need not be concerned with the boundaries' effects on the system. That is, we assume that the infinite-medium solution previously obtained is a reasonable approximation to the "incident" wave-packet generated by the system operating in the bounded ionosphere. For now we assume a tethered system high in the ionosphere above a flat Earth. We first re-

strict ourselves to the steady-state operation of such a system. We allow only vertical variations in ionospheric quantities.

The complexity of our problem, even in the simplified form stated above, requires a numerical analysis. There are, however, a number of observations that can be made based on the fundamental physics of the system under consideration. Our approach follows the general outlines of the analyses of ionospheric waves made by P. Greifinger<sup>7</sup>, C. and P. Greifinger<sup>8</sup>, and Rudenko, et al.<sup>9</sup>. The particularities of our moving source require some modifications to the analysis from the outset, however.

### Horizontal Plane-Wave Components

In order to utilize the formalism of the above-mentioned authors, we seek an incident wave solution written in terms of plane waves in the horizontal plane. The amplitudes of these wave components depends on the vertical coordinate,  $y'$  in our notation. A number of transformations are required to obtain this form for our incident wave-packet. We must also take into account the relationship that exists between the  $x$ -component of the wave vector and the frequency (as seen in the plasma, i.e. the terrestrial, rest frame) for the steady-state operation of an electrodynamic tethered system: namely, the Döppler relation  $\omega = k_x v_x$ . At this initial stage of our analysis we restrict ourselves to the Alfvén region  $k_x v_x \ll \Omega_a$  ( $\Omega_a$  is the ion cyclotron frequency), which is consistent with our consideration of systems in the upper regions of the ionosphere.

Following the reasoning used to derive expression (4), we obtain the following expressions for the Fourier transformed electric field components

$$E_{x,y} = \frac{8i\omega I}{k_{\perp}^2 c^2} \delta(\omega - k_x v_x) \cdot \left[ \frac{\sin\left(\frac{k_x L_x}{2}\right)}{k_x L_x} \frac{\sin\left(\frac{k'_y L}{2}\right)}{\left(k_x^2 - \epsilon_{\perp}\left(\frac{\omega}{c}\right)^2\right)} k_{x,y} \right] \quad (7)$$

where the  $\perp$  subscript refers to components perpendicular to the magnetic field, which lies along the negative  $z$  direction\*.

\*In all that follows we will use the notation  $k'_y \equiv k_y$ , etc. to represent vector components in the primed system of co-ordinates.

Thus Maxwell's equations give us

$$B_z = -\frac{c}{\omega}(k_x E_y - k_y E_x) = 0 \quad (8)$$

Since  $E_z = 0$  by assumption, Maxwell's equations further yield

$$B_{y,x} = \pm \frac{k_x c}{\omega} E_{x,y} \quad (9)$$

We now carry out the inverse Fourier integration over  $k_x$ . Since we are considering downward moving waves, which correspond to the negative  $z$  direction in our co-ordinate system, we close the contour of integration in the lower half of the complex  $k_x$  plane and pick up the contribution of the pole at

$$k_x = -\frac{\omega}{v_A} \quad (10)$$

Using

$$k_y y + k_z z = k'_y y' + k'_z z' \quad (11)$$

and the transformation of variables

$$\int \int \int d\omega dk_x dk_y = \sin \theta \int \int \int d\omega dk_x dk'_y \quad (12)$$

we obtain

$$E_x = \frac{-2Iv_A \sin \theta}{\pi L_x c^2} \int \int \int d\omega dk_x dk'_y \delta(\omega - k_x v_x) \left\{ \exp(-i[\omega t - k_x x - k'_y y' - k'_z z']) \frac{\sin\left(\frac{k_x L_x}{2}\right)}{k_{\perp}^2} \sin\left(\frac{k'_y L}{2}\right) \right\} \quad (13)$$

$$E_y = \frac{-2Iv_A \sin \theta}{\pi L_x c^2} \int \int \int d\omega dk_x dk'_y \delta(\omega - k_x v_x) \left\{ \exp(-i[\omega t - k_x x - k'_y y' - k'_z z']) \frac{\sin\left(\frac{k_x L_x}{2}\right)}{k_{\perp}^2} \sin\left(\frac{k'_y L}{2}\right) (k'_y \cos \theta - k'_z \sin \theta) \right\} \quad (14)$$

where

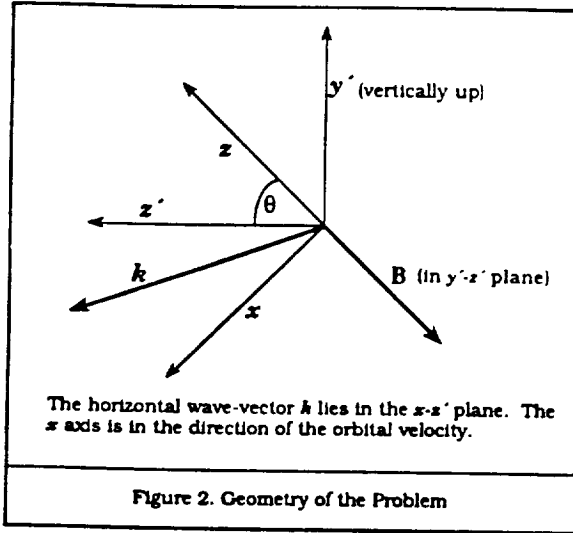
$$k'_y = -\frac{\omega}{v_A \sin \theta} - k'_x \cot \theta \quad (15)$$

and

$$k_\perp^2 = k_x^2 + (k'_y \cos \theta - k'_x \sin \theta)^2 \quad (16)$$

Equations (9) and (10) imply

$$B_{x,y} = \pm \frac{c}{v_A} E_{y,x} \quad (17)$$



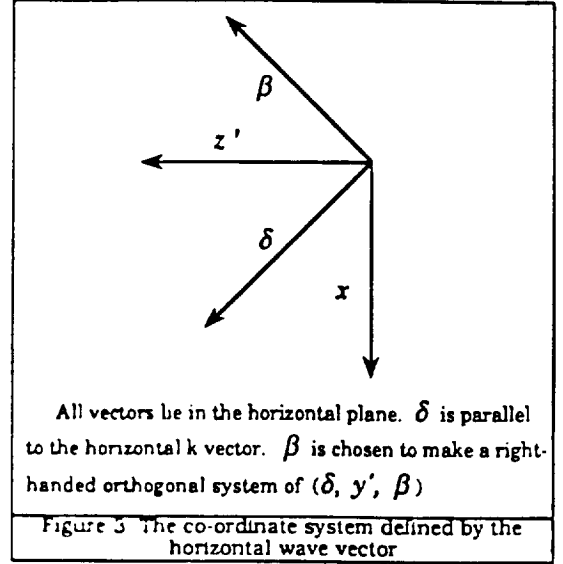
The horizontal components of the field are now at hand. The  $x$ -component is one horizontal component. The other horizontal component of the wave field (the  $z'$ -component) is easily obtained utilizing  $E_z = B_z = 0$ :

$$E'_z = -E_y \sin \theta \quad (18)$$

The corresponding expression holds true for the  $B$  field components.

Following the approach of the references mentioned earlier (particularly Rudenko, *et al.*), we now need to obtain the horizontal wave field components parallel and perpendicular to the

horizontal wave vector. Figures 2 and 3 show the co-ordinates to which we refer.



Note that each horizontal wave vector  $(k_x, k'_x)$  defines a different co-ordinate system  $(\delta, \beta)$ . This implies that the numerical integration must be carried out separately for each  $(k_x, k'_x)$  pair. In all that follows the vector  $k$  with no subscript refers to the horizontal wave vector of magnitude

$$k = \sqrt{k_x^2 + k'^2_x} \quad (19)$$

In the  $(\delta, \beta)$  system the wave electric field components are

$$E_\delta = \frac{\mathbf{E} \cdot \mathbf{k}}{k} \quad (20)$$

$$E_\beta = \hat{y}' \cdot \left( \frac{\mathbf{E} \times \mathbf{k}}{k} \right) \quad (21)$$

The corresponding expressions hold for the components of the  $B$  field.

Having obtained the components of the incident wave packet, we can consider some of the general physical characteristics of the system. Since the only variations in our model are in the vertical direction, the dependence of our incident Alfvén wing wave-packet components on the horizontal co-ordinates is given everywhere by the horizontal plane wave factor. Thus each component of the incident wave-packet arrives at the ionospheric boundary with the same

horizontal wave vector that it had high in the ionosphere. This has important consequences for the solutions in the atmosphere and on the Earth.

### Atmospheric Cavity Solution

The equations for the horizontal electric field components in the atmospheric cavity are

$$\frac{d^2 E_{\delta, \beta}}{dy'^2} + \left( \frac{\omega^2}{c^2} - k^2 \right) E_{\delta, \beta} = 0 \quad (22)$$

where  $k$ , the magnitude of the horizontal wave vector, has the same value as in the ionosphere. Similarly, the frequency is unchanged across the boundary. The identical equations hold for the horizontal magnetic field components.

The incident wave components contain the factor  $\delta(\omega - k_x v_x)$ , a consequence of the steady-state operation that we have assumed up until now. An immediate consequence of this is that the factor  $\left( \frac{\omega^2}{c^2} - k^2 \right)$  in the second term of equations (22) is always negative, since  $|k_x v_x| < |kc|$  always.

This means that the Alfvén wings generated by the steady state operation of an electrodynamic tethered satellite system will not propagate into the atmospheric cavity. That is, there is total reflection at the atmosphere's boundary with the ionosphere. Our solution corresponds to a surface wave at the ionospheric boundary.

Taking into account the perfect conductor boundary condition at the Earth's surface, we obtain the solution in the atmospheric cavity

$$E_{\delta, \beta} = E_{\delta, \beta}(y'_b) \frac{\sinh(p(y' - (y'_b - H)))}{\sinh(pH)} \quad (23)$$

$$B_{\beta} = \frac{i\omega}{pc} E_{\delta}(y'_b) \frac{\cosh(p(y' - (y'_b - H)))}{\sinh(pH)} \quad (24)$$

$$B_{\delta} = -\frac{ipc}{\omega} E_{\beta}(y'_b) \frac{\cosh(p(y' - (y'_b - H)))}{\sinh(pH)} \quad (25)$$

where

$$p = \sqrt{k^2 - \frac{\omega^2}{c^2}} \quad (26)$$

and  $y'_b$  and  $H$  are the values of  $y'$  at the ionospheric boundary and the distance of this boundary from the Earth's surface, respectively.

Equations (24)-(25) show that the ratio of the magnetic field on the Earth's surface to that at the ionospheric boundary is

$$\frac{B_{\delta, \beta}(y'_b - H)}{B_{\delta, \beta}(y'_b)} = (\cosh(pH))^{-1} \quad (27)$$

The height of the ionosphere may be taken to be around 100 km. The consequence of equations (23)-(26) is that the image of the Alfvén wings on the Earth's surface will be much wider than the wings are in the ionosphere, since only the wave-packet components with horizontal wavelengths of hundreds of kilometers will escape severe attenuation. Since such long wavelength components make up only a small fraction of the wavepacket for a reasonably sized tethered system and since the noise level is much higher for the lower regions of the ULF band, we tentatively conclude that the magnetic field image of the Alfvén wings on the Earth's surface will probably be too weak to detect in the case of a steady-current tether, even one with a high current.

Hughes and Southwood<sup>10</sup> reached similar conclusions about the "shielding" of ionospheric disturbances with short horizontal wavelengths. These authors emphasized the role of Hall currents in the lower part of the ionosphere in reducing the  $B_{\beta}$  component of the ionospheric waves; but it is obvious from the analysis that the result is a general consequence of Maxwell's equations that would hold for different models of the ionospheric conductivity

### The Ionospheric Wave-Guide

So far we have not discussed the possible effects of vertical variations in plasma density and ionic composition. Since the Alfvén speed depends directly on these quantities, their variation changes the effective dielectric constant of the plasma. This has consequences for the waves that can propagate in the ionosphere. The dispersion relation for the anisotropic Alfvén wave is approximately

$$\omega = k_x v_A \quad (28)$$

The dispersion relation for the fast magnetosonic (isotropic Alfvén) wave is

$$\omega^2 = k_{\perp}^2 v_A^2 \quad (29)$$

where  $k_{\perp}$  is the total wave vector, including horizontal and vertical components. For a given horizontal wave-vector, frequency, and Alfvén speed combination it may be impossible to find a real vertical wave vector component that satisfies the dispersion relation (29).

In this case the fast magnetosonic mode is evanescent. This is the case for the steady-current electrodynamic tether, which excites waves satisfying (28), but by virtue of the  $\omega = k_z v_z$  condition cannot satisfy (29) for any real vertical wave vector component. The fast magnetosonic mode has thus been discarded in our calculations of the Alfvén wings.

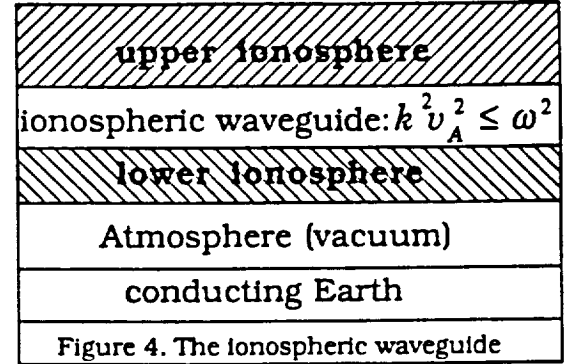
We have seen that for a given horizontal  $k$  vector and frequency  $\omega$ , the isotropic wave will propagate or not depending on the Alfvén speed. The Alfvén speed has a minimum value in the F-region of the ionosphere, so an isotropic wave can be confined to the region around this minimum—the ionospheric wave guide. Figure 4, illustrates the ionospheric wave-guide. The Greifinger and Rudenko references<sup>7-8</sup> discuss the ionospheric wave-guide and note the occurrence of wave-guide resonances. Rudenko, et al.<sup>9</sup> make the point that an Alfvén wave, incident from high in the ionosphere, couples to the fast magnetosonic wave within the ionospheric wave-guide region for the particular frequency and wave-vector combination.

The ionospheric wave-guide traps electromagnetic energy in a horizontal layer of the ionosphere. Stimulating resonances of the ionospheric wave-guide with an electrodynamic tether would seem to be a possible way of overcoming the difficulties in obtaining a measurable signal on the Earth's surface.

It is easy to see that no steady-current electrodynamic tethered system can achieve this in the Earth's ionosphere, however. Since an orbiting steady-current tether cannot stimulate propagating fast magnetosonic waves even in the region of minimum Alfvén speed, it is impossible for Alfvén waves generated by a steady-current tether anywhere in the ionosphere to excite propagating fast magnetosonic waves. There is no ionospheric wave-guide for steady-current tethers.

The next phase of our research into the problem of tether-generated electromagnetic

waves will focus on the ionospheric wave-guide and its possible excitation by electrodynamic tethered satellite systems with time-varying currents. In the next section we map out the method we plan to use in our numerical investigation of this question.



#### Numerical Integration of the Wave Equations

Our method applies to systems that directly excite only shear Alfvén waves. We would expect the method to have its greatest utility in the case of slowly-varying tether currents with frequency components such that coupling to ionospheric wave-guide modes occurs.

It should be noted that we are talking only about variations in the tether current sufficiently slow that the tether current distribution can still be considered as independent of the vertical coordinate along the tether's length. The tether is not functioning as an antenna in the normal sense of the word in this case; it is still a source of varying current to the ionospheric transmission line, a concept that we have emphasized in our previous analysis.

#### Slowly Varying Current

We assume a tether current distribution that is just expression (1) multiplied by  $\cos(\omega_0 t)$ , where  $\omega_0$  is the oscillation frequency of the tether current. Let us suppose that the tethered system is equipped with a suitable power supply to enable it to reverse the current. Any time variation can be broken into its Fourier components, so the choice is not restrictive, except that we are explicitly excluding spatial variations in the tether current along its length, which implicitly limits the range of frequencies we can consider.

Expressions (13) and (14), which define the incident wave packet, are modified only by the replacement of the delta function  $\delta(\omega - k_z v_z)$  by

$$\frac{(\delta(\omega + \omega_0 - k_x v_x) + \delta(\omega - \omega_0 - k_x v_x))}{2} \quad (30)$$

### The Ionospheric Model and Equations

Having derived the incident Alfvén wave-packet in the desired form, we now turn our attention to the numerical methods we propose to use for solving the problem. We are following the method outlined in Rudenko, et al.<sup>9</sup> However, our notation differs in some respects from that used in the Rudenko reference. In addition there are a few serious typographical errors in that paper. For these reasons, we will outline the method here.

Maxwell's equations for the horizontal wave field components in the ionosphere can be written in the following compact way :

$$-i \frac{dF}{dy'} = GF \quad (31)$$

where we define  $F$  as the four-component vector

$$F = (E_\delta, E_\beta, H_\delta, H_\beta) \quad (32)$$

with the third and fourth components given by

$$H_\delta = -\left(\frac{v_0 \bar{\omega}}{c}\right) B_\beta \quad (33)$$

$$H_\beta = \left(\frac{v_0 \bar{\omega}}{c}\right) B_\delta \quad (34)$$

For our numerical work we use dimensionless quantities. The dimensionless frequency is defined by

$$\bar{\omega} = \frac{\omega \lambda}{v_0} \quad (35)$$

where  $\lambda$  is a scaling length and  $v_0$  is the Alfvén speed in the region in which the wave-packets originate. The variable  $y'$  is just the vertical spatial co-ordinate in units of  $\lambda$ .

The 2x2 submatrices

$$g_3 = \begin{pmatrix} \frac{\bar{\omega}^2}{\bar{v}^2} \mu_1 \left( \frac{\bar{k}^2 - \bar{k}_x^2 \cos^2 \theta}{\bar{k}^2 \sin^2 \theta} \right) & \frac{\bar{\omega}^2}{\bar{v}^2} \left( \frac{\mu_1 \bar{k}_x \bar{k}_x \cot^2 \theta}{\bar{k}^2} - \frac{\mu_2}{\sin \theta} \right) \\ \frac{\bar{\omega}^2}{\bar{v}^2} \left( \frac{\mu_1 \bar{k}_x \bar{k}_x \cot^2 \theta}{\bar{k}^2} + \frac{\mu_2}{\sin \theta} \right) & \frac{\bar{\omega}^2}{\bar{v}^2} \mu_1 \left( \frac{\bar{k}^2 - \bar{k}_x^2 \cos^2 \theta}{\bar{k}^2 \sin^2 \theta} \right) - \bar{k}^2 \end{pmatrix} \quad (36)$$

$$g_1 = \begin{pmatrix} -\bar{k}_x \cot \theta & -\bar{k}_x \cot \theta \\ 0 & 0 \end{pmatrix} \quad (37)$$

$$g_2 = \begin{pmatrix} 1 & 0 \\ 0 & 1 \end{pmatrix} \quad (38)$$

$$g_4 = \begin{pmatrix} -\bar{k}_x \cot \theta & 0 \\ -\bar{k}_x \cot \theta & 0 \end{pmatrix} \quad (39)$$

define the the 4x4 matrix

$$G = \begin{pmatrix} g_1 & g_2 \\ g_3 & g_4 \end{pmatrix} \quad (40)$$

In the expressions above,  $\bar{k}_x$  and  $\bar{k}_z$  refer to the dimensionless horizontal wave-vector components defined by the scaling factor  $\lambda$ . The normalized Alfvén speed  $\bar{v}$  is defined by  $\frac{v_A}{v_0}$ .

The quantities

$$\mu_1 = \frac{\left(1 + i \frac{v_i}{\omega}\right)}{\left(1 + \left[\frac{(v_i - i\omega)}{\Omega_{ci}}\right]^2\right)} \quad (41)$$

and

$$\mu_2 = i \left( \frac{\omega}{\Omega_{ci}} \right) \left[ 1 + i \frac{v_i}{\omega} \right] \mu_1 \quad (42)$$

along with the Alfvén speed, express the dielectric properties of the ionospheric medium. Here  $v_i$  and  $\Omega_{ci}$  are the ion-neutral collision frequency and the ion cyclotron frequency, respectively. The Alfvén speed,  $v_i$ , and  $\Omega_{ci}$  all vary with altitude in our model.

For the frequency range and horizontal wave-vectors to which we are limiting our analysis, there are four well-defined independent solutions to equation (31) in the upper ionosphere: two shear Alfvén solutions, corresponding to positive and negative vertical wave-vector components, and two isotropic Alfvén solutions, one that grows exponentially with increasing  $y'$  and another that falls off exponentially with  $y'$ .

The shear Alfvén solution with negative vertical wave-vector component corresponds to the incident wave, whose components we have calculated. The upward traveling shear Alfvén solution then corresponds to a reflected wave. Of the two isotropic solutions, only the upwardly decreasing one makes physical sense. It corresponds to leakage of the ducted fast magnetosonic wave from the ionospheric wave-guide. Thus we are left with three physically meaningful solutions to equation (31) at "infinity" (the location of our tethered system, high in the ionosphere).

While we know the amplitude of the incident wave-packet solution at infinity, the amplitudes of the other two solutions are unknown. It turns out that knowledge of the functional form of these solutions at infinity, combined with the boundary conditions at the ionosphere/atmosphere interface and the functional form of the solutions in the atmospheric cavity, determines the solution at the ionospheric boundary and, hence, on the Earth's surface.

#### The Admittance Matrices

Let us now sketch the means by which this can be accomplished. First we introduce the admittance matrices, which are variations of those defined by Budden<sup>11</sup>. We define the admittance matrix  $A^{(i,j)}(\bar{\omega}, \bar{k}, \bar{y}')$  as the  $2 \times 2$  matrix that satisfies the equation

$$\begin{pmatrix} \alpha F_3^i + \beta F_3^j \\ \alpha F_4^i + \beta F_4^j \end{pmatrix} = A^{(i,j)}(\bar{\omega}, \bar{k}, \bar{y}') \begin{pmatrix} \alpha F_1^i + \beta F_1^j \\ \alpha F_2^i + \beta F_2^j \end{pmatrix} \quad (43)$$

where  $F^i$  and  $F^j$  are two solutions of (31) and  $\alpha$  and  $\beta$  are two arbitrary complex constants. The admittance matrix transforms a linear combination of the electric field components of the two independent solutions into the same linear combination of the corresponding magnetic field components, as defined by equations (32)-(34).

It is straightforward to obtain from (31) and (43) the following differential equation for an admittance matrix  $A$  defined as in (43):

$$-i \frac{dA}{dy'} = -AA - Ag_1 + g_4A + g_3, \quad (44)$$

where the  $g_i$  are the matrices defined in (36)-(39).

The admittance matrices contain the ratios of electromagnetic field components rather than their absolute values. This has an important advantage for numerical integrations down through the ionosphere, since it avoids the problem of numerical swamping brought on by the exponential growth of an initially small mix of the downward growing solution.

Since we know the functional form of the solutions at infinity, we can construct the admittance matrices at infinity in the following way:

$$A^{(i,j)}(\omega, k) = \begin{pmatrix} X_3^i & X_3^j \\ X_4^i & X_4^j \end{pmatrix} \begin{pmatrix} X_1^i & X_1^j \\ X_2^i & X_2^j \end{pmatrix}^{-1} \quad (45)$$

where the  $X^i$  are the known functional forms of the  $F^i$  solutions at infinity. These can then be taken as the initial values for numerical integration down to the boundary with the atmosphere.

$A^b$ , the boundary matrix at the atmosphere/ionosphere boundary is defined by

$$\begin{pmatrix} F_3(\bar{y}'_b) \\ F_4(\bar{y}'_b) \end{pmatrix} = A^b \begin{pmatrix} F_1(\bar{y}'_b) \\ F_2(\bar{y}'_b) \end{pmatrix} \quad (46)$$

where the  $F$  corresponds to the total solution at the boundary, including the contributions from the reflected and ducted waves, as well as the incident wave.

For the case of a perfectly conducting Earth this corresponds to

$$A^b = i\lambda \coth(pH) \begin{pmatrix} \left(\frac{\omega^2}{c^2 p}\right) & 0 \\ 0 & -p \end{pmatrix} \quad (47)$$

#### The Solution at the Ionospheric Boundary and on the Earth's Surface

The solution at the boundary may be written as

$$F(\bar{y}'_b) = B_1 F^1(\bar{y}'_b) + B_2 F^2(\bar{y}'_b) + B_3 F^3(\bar{y}'_b) \quad (48)$$



where  $F^1$  and  $F^2$  denote the reflected and incident shear Alfvén solutions, respectively, and  $F^3$  denotes the ducted wave solution, with the  $B_i$  complex constants. The coefficient  $B_2$  is known from the incident shear Alfvén solution at infinity.

An obvious consequence of the definition of the admittance matrices (43) is that

$$(A^{(i,j)}(\bar{\omega}, \bar{k}, \bar{y}') - A^{(k,j)}(\bar{\omega}, \bar{k}, \bar{y}')) \begin{pmatrix} F_1^j \\ F_2^j \end{pmatrix} = 0 \quad (49)$$

for  $i \neq k$ .

We can utilize expressions (43), (46), (48), and (49) to obtain the following equation, which is true on the boundary between the ionosphere and the atmosphere:

$$(A^b(\bar{\omega}, \bar{k}) - A^{(1,3)}(\bar{\omega}, \bar{k}, \bar{y}_b')) \begin{pmatrix} F_1 \\ F_2 \end{pmatrix} = \quad (50)$$

$$(A^{(2,3)}(\bar{\omega}, \bar{k}, \bar{y}_b') - A^{(1,3)}(\bar{\omega}, \bar{k}, \bar{y}_b')) B_2 \begin{pmatrix} F_1^{(2)} \\ F_2^{(2)} \end{pmatrix}$$

This expression, which relates the electric field components of the total solution (48) on the boundary to the electric field components of the incident wave solution on the boundary by means of the admittance and boundary matrices, is the basis for our numerical method. We invert the matrix  $(A^b(\bar{\omega}, \bar{k}) - A^{(1,3)}(\bar{\omega}, \bar{k}, \bar{y}_b'))$  on the left hand side of (50) to obtain the electric field components on the boundary. Then the boundary matrix  $A^b$  yields the magnetic field components on the boundary. The atmospheric cavity solution (24)-(25) yields the magnetic field on the Earth's surface and anywhere in the atmosphere. The required admittance matrices and the incident wave solution on the boundary are to be obtained by means of numerical integration of the equations (44) and (31).

All of the analysis outlined in the preceding paragraphs must be carried out for each horizontal wave vector component. The complete solution on the Earth's surface is obtained by summing over all these solutions to obtain the inverse Fourier transform. We have begun software development to carry out the program of numerical analysis.

## Acknowledgments

I have benefited from numerous discussions with Mario Grossi on the subject of tethers in the ionosphere. This work has been supported by NASA (NAG8-638 and NAS8-36606).

## References

1. Drell, S.D., H.M. Foley, and M.A. Ruderman, Drag and propulsion of large satellites in the ionosphere: An Alfvén engine in space, *J. Geophys. Res.*, 70, 3131, 1965
2. Belcastro, V., P. Veltri, and M. Dobrowolny, Radiation from long conducting tethers moving in the near earth environment, *Nuovo Cimento*, C, 5, 537, 1982
3. Rasmussen, C.E., P.M. Banks, and K.J. Harker, The excitation of plasma waves by a current source moving in a magnetized plasma: The MHD approximation, *J. Geophys. Res.*, 90, 505, 1985
4. Dobrowolny, M. and P. Veltri, MHD power radiated by a large conductor in motion through a magnetoplasma, *Nuovo Cimento Soc. Ital. Fis. C*, 9, 27, 1986
5. Barnett, A. and S. Olbert, Radiation of plasma waves by a conductive body moving through a magnetized plasma, *J. Geophys. Res.*, 91, 10, 117, 1986
6. Estes, R.D., Alfvén waves from an electrodynamic tethered satellite system *J. Geophys. Res.*, 93, 945, 1988
7. Greifinger, P., Micropulsations from a finite source, *J. Geophys. Res.*, 77, 2392, 1972
8. Greifinger, C. and P. Greifinger, Wave guide propagation of micropulsations out of the plane of the geomagnetic meridian, *J. Geophys. Res.*, 78, 4611, 1973
9. Rudenko, G.V., S.M. Churilov, and I.G. Shukhman, Excitation of the ionospheric waveguide by a localized packet of Alfvén waves, *Planet. Space Sci.*, 33, 1103, 1985
10. Hughes, W.J. and D.J. Southwood, The Screening of Micropulsation Signals by the Atmosphere and Ionosphere, *J. Geophys. Res.*, 81, 3234, 1978
11. Budden, K.G., The propagation of radio waves: The theory of radio waves of low power in the ionosphere and magnetosphere, Cambridge Univ. Press, 1985



## 8.0 REENTRY OF TETHERED CAPSULES


A vertical or alternatively a swinging tether can provide the initial  $\Delta V$  to force the reentry of a capsule attached at the tip of a downward tether. Once the tether is cut, the capsule can reenter with the long tether attached to it. Upon entering the dense atmosphere, the tether drags the capsule by decelerating the reentry at high altitudes and, consequently, strongly reducing the maximum temperature experienced by the capsule. For this effect to be fully exploited, the tether must be made of heat-resistant materials such as graphite, silicon carbide, boron carbide or similar.

The small satellite of SEDS-I reentered with the tether attached to it and its tensiometer (load cells to be more precise) clearly shows the beginning of an exponentially increasing deceleration provided by the tether before the telemetry link was lost. In the case of SEDS-I, the tether was Spectra-1000 with a very low melting temperature of 140 °C. Consequently, the tether burnt at an altitude somewhat lower than 105 km, i.e., without slowing down the satellite during the most critical phase of reentry.

Conversely, a heat-resistant tether could reduce the maximum temperature of the capsule during reentry from 2700 K to less than 500 K. The maximum temperature of the tether would be about 1000 K which is well below the melting temperatures of the candidate materials mentioned above (e.g., several materials suitable for tethers have a maximum operating temperature well above 1000 K).

A paper is included herewith which highlights the numerical results obtained for the reentry of a tethered capsule. Moreover, the reentry of SEDS-I is also simulated in order to estimate the altitude at which the tether and the satellite burn in the upper atmosphere. Maximum temperatures and reentry trajectories are then computed for the three following cases: (1) a heat resistant tether attached to the reentry capsule; (2) a low-melting-point tether (i.e., SEDS-I); and (3) a reentry capsule without tether.

See also Quarterly Reports No. 25 and No. 26 of this contract for more details.







**IAF-92-0822**

**A HYPERSONIC PARACHUTE FOR LOW-TEMPERATURE REENTRY**

**M. Krischke<sup>1</sup>, E. Lorenzini<sup>2</sup> and D. Sabath<sup>3</sup>**

**<sup>1</sup>Kayser-Threde GmbH, München, Germany**

**<sup>2</sup>Harvard-Smithsonian Center For Astrophysics, Cambridge, USA**

**<sup>3</sup>Technische Universität München, Germany**

**43rd CONGRESS OF THE  
INTERNATIONAL ASTRONAUTICAL FEDERATION**

**August 28-September 5, 1992/Washington, DC**

# A HYPERSONIC PARACHUTE FOR LOW-TEMPERATURE REENTRY

M. Krischke<sup>1</sup>, E. Lorenzini<sup>2</sup> and D. Sabath<sup>3</sup>

<sup>1</sup> Kayser-Threde GmbH München, Germany

<sup>2</sup> Harvard-Smithsonian Center For Astrophysics, USA

<sup>3</sup> Technische Universität München, Germany

## Abstract

Atmospheric reentry, even when initiated from a circular low Earth orbit, requires heavy heat shields, ablative materials or radiative dissipation techniques.

Semianalytical and numerical simulations of the atmospheric reentry from low Earth orbits of a capsule with a 20-km, attached, heat resistant tether have shown that the thermal input flux on the capsule is reduced by more than one order of magnitude with respect to a comparable reentry without tether.

Long tethers have low ballistic coefficients and a large surface for heat dissipation. Moreover, a long tether is stabilized by gravity gradient and consequently tends to maintain a high angle of attack with respect to the wind velocity. The exposed surface of a 20-km-long 1-mm diameter tether is 20 m<sup>2</sup>, which is much larger than the cross section of a reentry capsule. The resulting strong drag decelerates the capsule during reentry like a conceivable hypersonic parachute would do.

This paper describes the methods and results of the simulation of the SEDS endmass reentry with different tethers.

## Introduction

Most of the fundamental work concerning atmospheric reentry was done in the sixties. Facing projects such as the Space Station, S nger, and Hermes the research activities in aerothermodynamics and the interest in atmospheric reentry missions have been growing over the last years. In several countries new reentry capsules are under development, e.g. the American Westar capsule and the German Express and Mirka capsules.

During atmospheric reentry a part of the vehicles total energy is dissipated and transferred to the surrounding medium by two heat transfer mechanisms, convection and radia-

tion. Typical values for the heat load on a reentering capsule are between 1.3 MW/m<sup>2</sup> and 4 MW/m<sup>2</sup>. These heat loads require a special protection which consists in general of a heavy ablative heatshield and thermal insulation.

The reentry of a spacecraft is usually initiated by firing a retrorocket, which decelerates the vehicle down to reentry velocity. Tethers have long been proposed as a means to provide the necessary  $\Delta V$  for reentry. They have the advantage of not polluting the orbit and transferring the angular momentum from the lower to the upper spacevehicle. During our research on the atmospheric reentry of tethered spacecraft and our simulation of the reentry of the SEDS (Small Expendable Tether Deployer) endmass a new surprising application of tethers has been found. A heat resistant tether which is attached to the reentering body works like a hypersonic parachute. This hypersonic parachute slows down the vehicle already in very high altitudes and thus lowers the heat loads during the reentry in the denser atmosphere.

## SEDS

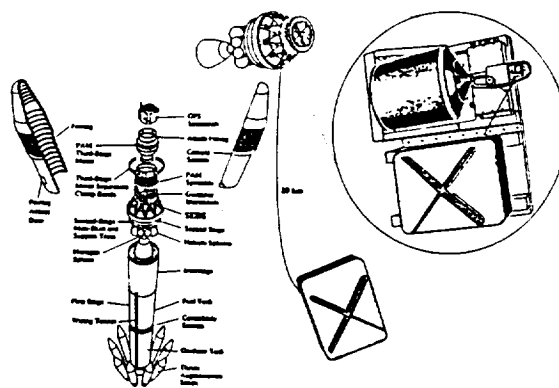


Fig. 1: The Small Expendable Tether Deployer (2)

The need for inorbit experimentation and demonstration of tether technology before flying major missions led to the development of an inexpensive tethered space system for carrying out precursor flights, the Small Expendable-Tether

carrying out precursor flights, the Small Expendable-Tether Deployment System (SEDS <sup>(1)</sup>). Unlike TSS1, SEDS does not retrieve the payload attached to the end of a 20km-long thin tether. By avoiding the complex control system necessary for retrieval, the design of the deployer is drastically simplified. SEDS flies as a secondary payload on a Delta II rocket. The Hardware of the SEDS project is already built, tested, and ready for the flight, which is scheduled for 1993.

The SEDS System consists of the tether deployer with the tether and an instrumented endmass. The endmass, which is connected to the deployer by the tether, is ejected by a spring-loaded marman clamp. After a period of 1.5 h the deployment of the 20 km-long tether is completed and the tether is cut at the deployer end. This operation puts the endmass and the tether on a reentry ellipse. During the reentry the tether and the endmass are supposed to burn up in the upper atmosphere.

In our research we consider also the use of a reentry capsule and a heat resistant tether in the SEDS configuration.

## Modelling

For the simulation of the reentry of a tethered spacecraft two different models have been used. The first model was developed within the Harvard Smithsonian Center for Astrophysics <sup>(3)</sup> for the simulation of orbital tether dynamics. The original computer code which is called Master20 has been modified to simulate reentry.

The tether dynamics are simulated in three dimensions by modelling the tether with 7 point masses connected by massless springs and viscous dashpots. The endmass is represented by an additional pointmass.

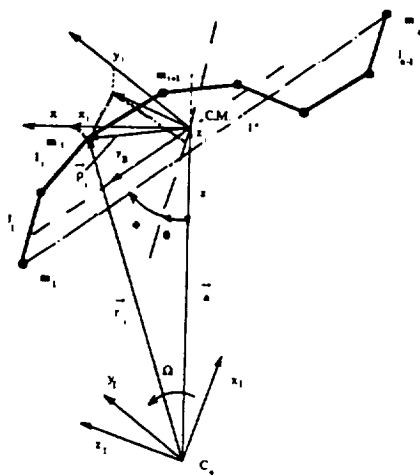


Fig. 3: Kinematics of the lumped masses model

The aerodynamic forces are computed on the basis of a rotating US Standard Atmosphere 1976 <sup>(4)</sup>. The gravitational model is a J0+J2 model. Lifting effects on the tether are not

considered. In addition the tensional forces are provided by the visco-elastic tether segments that connect two adjacent lumps. The aerothermodynamic heating is computed by using the formulas for heat transfer analysis by Lees <sup>(5)</sup>.

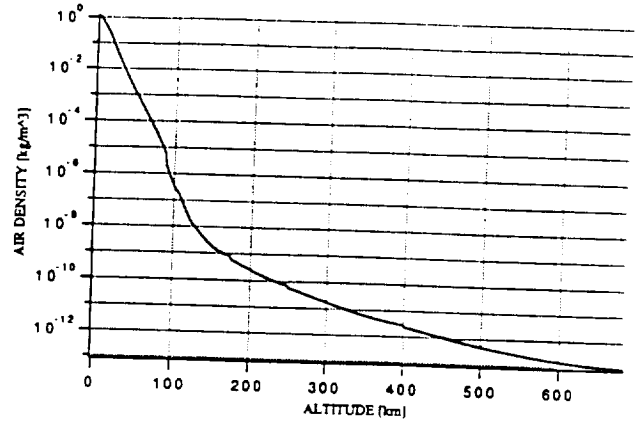


Fig. 3: The density profile of the lumped masses model

In addition to the model described above a much simpler model was developed to prove the plausability of the numerical simulation with the Master20 software code. The tether is assumed to be rigid and straight with a constant angle of attack. The endmass is modelled by an attached point mass.

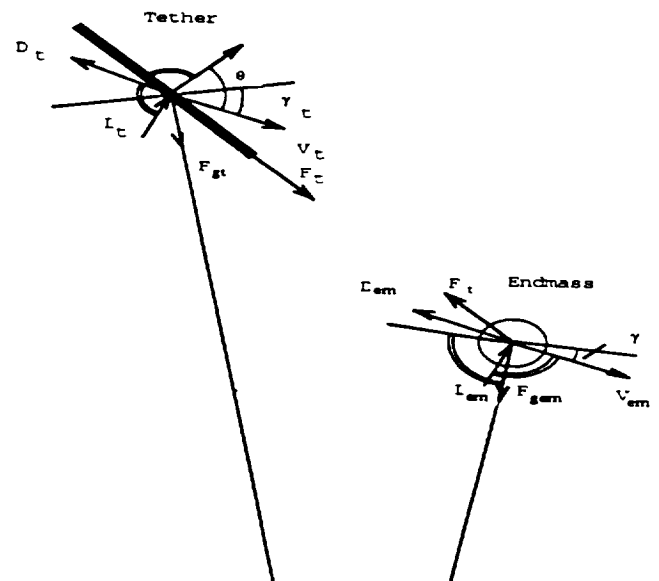


Fig. 4: Kinematics of the simple model

The aerodynamic forces are computed with a simple exponential density profile.

## Simulations

The differential equations of both models are numerically integrated by using a 4th order Runge-Kutta Integrator. In addition to these numerical solutions a semianalytical solu-

tion similar to the 'second order solution of entry dynamics' by W.H.T. Loh <sup>(6)</sup>, of the simple model could be found.

The comparison of the different solutions showed a very good agreement. In this paper only the results of the simulation of the lumped masses model are discussed.

The simulations start at the time of the tether cut at an altitude of 700 km. The orbital velocity of the endmass is 7276 m/s.

## Solutions of the lumped masses model

We have simulated different reentry cases. One with a heat resistant tether which is connected to the endmass during the whole reentry, one with the tether disconnected all the time or in other words endmass without tether, and one with a melting tether (>420 K) which is the case in the first SEDS mission.

The simulations show (see Fig. 5) that the shape of the tether is very stable up to the region where the endmass enters the atmosphere. Fig.5 represents a series of snapshots of the reentry of the tether and the endmass. The snapshots are taken every 100 s. The distances are with respect to the Delta's second stage which rotates around the Earth on the elliptical orbit. For a better understanding, the altitudes at the beginning and at the end of the snapshots are shown. In the figure.

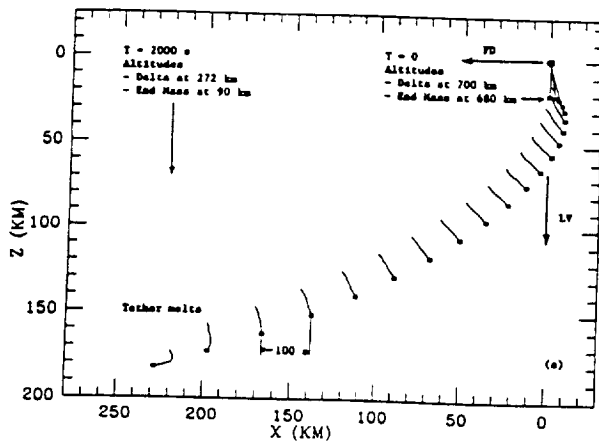


Fig. 5: Snapshots of a part of the reentry of the endmass and the tether

In Fig. 6 the separation of the endmass and the tether when the tether reaches the melting temperature of 420 K for spectra is very clear. The system is entering the dense atmosphere after about 1850 sec from release.

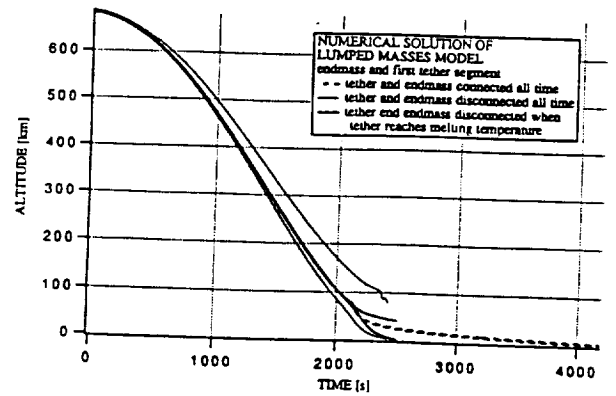


Fig. 6: Altitude of first tethersegment and endmass for three different cases

The velocity profiles of the endmass and the first tethersegment (Fig. 7) are very interesting. It shows that the tether decelerates the endmass in a higher altitude which means that the system enters the denser atmosphere with a much lower velocity. Since the melting temperature of the material of the SEDS tether is very low (420 K), the velocity profile of the case whereby the tether and the endmass are disconnected when the tether starts to melt is very similar to the case whereby the tether and the endmass are disconnected all the time.

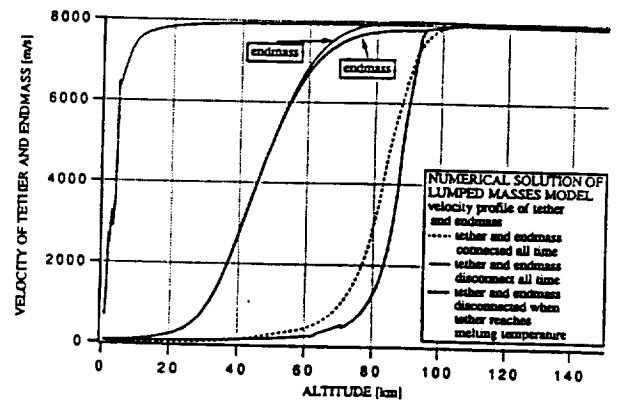


Fig. 7: Velocity profile of endmass and first tethersegment over the altitude

The plot of the tether tension (Fig. 8) shows that the vibrations following the cut of the tether are damped out after a while and the tension swings smoothly around the value of the gravity gradient. When the system enters the atmosphere tension rapidly grows up to a maximum of more than 2000 N.



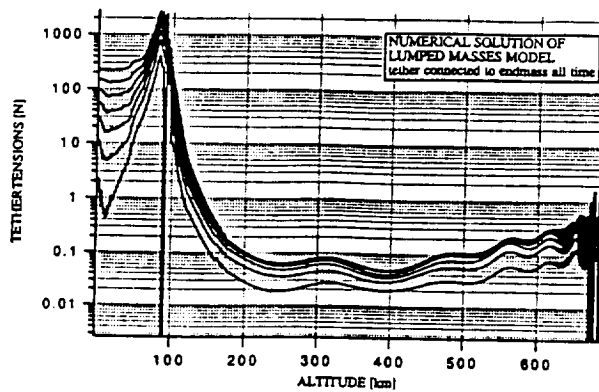


Fig. 8: Tension of tethersegments over the altitude

The heat fluxes on the endmass which are shown in Fig. 9 demonstrate the dramatic change for a reentry with a heat resistant tether compared to the case without tether or with a melting tether. The maximum heat flux is diminished by about one order of magnitude.

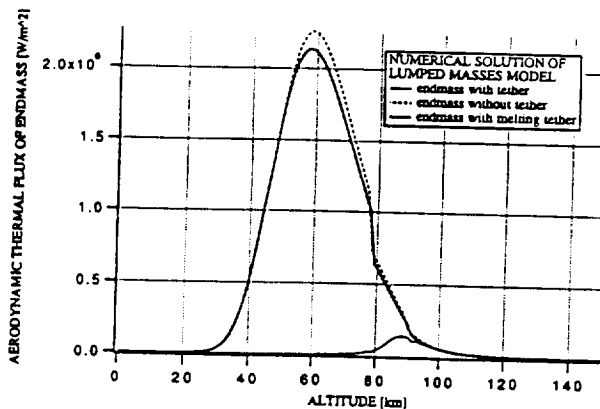


Fig. 9: Aerodynamic thermal flux of endmass

With the computed heat flux on the endmass we made a simple calculation of the temperature of the endmass. By using only the mass of the aluminium box (7kg) for the heat capacity of the endmass (total mass of 23kg) in the thermal equations we assume that the heat transfer between the outer aluminium shell and the inner instrumentation is very low. We consider only the incoming aerothermodynamic heat flux and the outgoing radiation heat flux. The temperature of the endmass for the three cases, as shown in Fig. 10, demonstrates also very well the influence of the tether. Whereas for the connected tether and endmass the temperature stays far below the melting temperature, the disconnected endmass evaporates in the atmosphere.

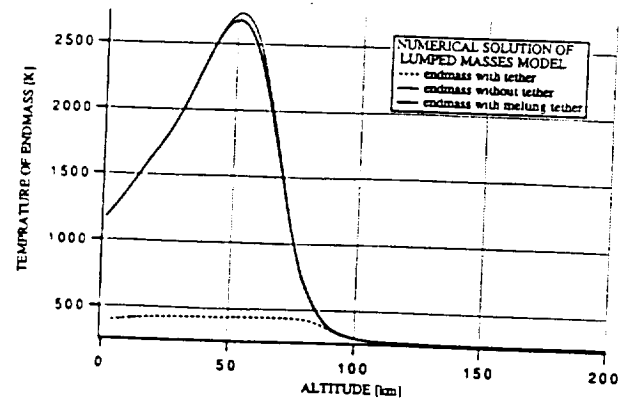


Fig. 10: Temperature of endmass

As we can see in the snapshot display (Fig. 5) the orientation of the tether is almost constant with respect to the windvelocity as long as the tether is out of the dense atmosphere. Fig. 11 shows the same effect. Once the tether enters the atmosphere it tends to align itself with the wind-velocity vector.

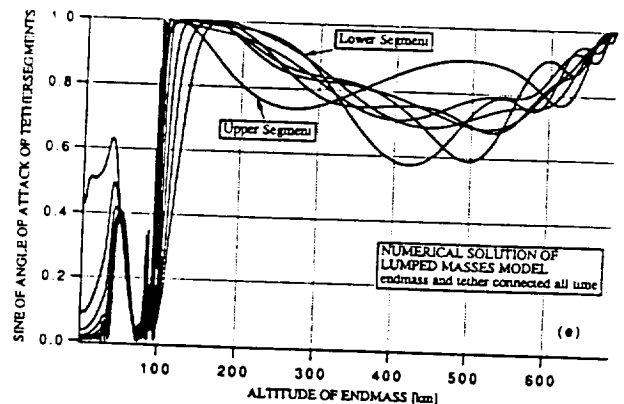


Fig. 11: Orientation of the tethersegments

The tethersegments reach different maximum temperatures and fluxes. The aerodynamics fluxes of the tethersegments depend strongly on the angle of attack of the segments. The computation of the tether temperatures (Fig. 12) shows that the tether does not reach temperatures higher than 1000K. For modern materials such as quartz or graphite this temperature is not too high.

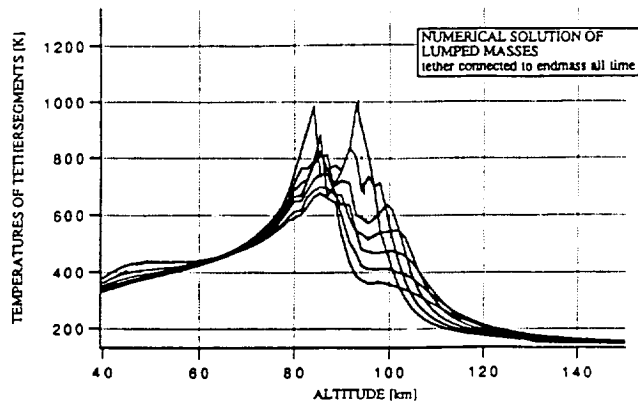


Fig. 12: Temperatures of the tethersegments

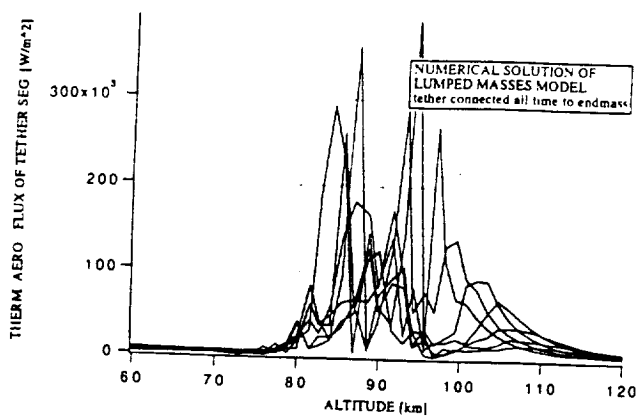


Fig. 13: Thermal aerodynamical fluxes of the tethersegments

## Conclusions

The simulations of the reentry of the SEDS endmass shows a new and very promising application of tethers. A heat resistant tether attached to a reentry body acts as a hypersonic parachute and reduces the heat loads of reentry body of about one order of magnitude. The tether which already replaces the retrorocket for the initiation of the reentry also simplifies the necessary heat protection of the reentry capsule. A heat resistant tether would be very advantageous for sample returns from the Space station. A tether does not produce pollution like a retrorocket and can drastically reduce the mass required for the heatshield of the reentry spacecraft. The same considerations apply for unmanned Mars missions, whereby a heat resistant tether could not only be used for aeroassisted breaking <sup>(7)</sup> and for a low altitude tethered Mars probe <sup>(8)</sup> but also for a low temperature reentry

on the Martian surface. Many other applications could be conceived in the future.

Even with current technology and materials a first test mission seems to be feasible. Testing this attractive alternative could readily be carried out in connection with the American SEDS, the German-Russian RAPUNZEL project or using one of the frequent piggy back opportunities of different launchers.

A suitable capsule could be the German MIRKA capsule which is under development at JENA OPTRONIC in Jena and at KAYSER-THREDE GmbH in Munich or a small Russian capsule which will be developed by the SAMARA AVIATION INSTITUT, Russia in Cooperation with the TECHNICAL UNIVERSITY OF MUNICH and KAYSER-THREDE GmbH.

## References

1. E. C. Lorenzini, J. A. Carroll, "In orbit Experimentation with the Small Expendable Tether Deployment System", ESA Journal, Vol.15, 1991
2. K. Grumbly and J. Harrison, "SEDS Project Status Review", NASA Hdqs/LaRC/MSFC/GSFC, July 1991
3. E.C. Lorenzini et al. Quarterly Reports NASA contract NAS8-36606, Smithsonian Institution Astrophysical Observatory, Cambridge, MA, USA
4. US Standard Atmosphere 1976 Washington, DC, 1976
5. Lester Lees, Frederick W Hartwig, and Clarence B. Cohen, "Use of Aerodynamic Lift During Entry into the Earth's Atmosphere", ARS Journal, September 1959
6. W.H.T. Loh, "Dynamics and Thermodynamics of Planetary Entry", Prentice-Hall, Inc., Englewood Cliffs, N.J. 1963
7. James M. Longuski, Jordi Puig-Suari, "Hyperbolic Aerocapture and Elliptic Orbit Transfer With Tethers", 42nd Congress of the IAF, Montreal, Canada, 1991
8. E. C. Lorenzini, M. D. Grossi, M. Cosmo, "Low Altitude Tethered Mars Probe", Acta Astronautica, Vol.21, No.1, p 1-12, 1990
9. Manfred Krischke, "Atmospheric Reentry of Tethered Spacecraft", Diploma thesis, Lehrstuhl für Raumfahrttechnik, Technische Universität München, Dez.91

## 9.0 DEPLOYMENT DYNAMICS OF SEDS-I

### Figure Captions

- Figs. 9.1(a-i) Dynamics during deployment of SEDS-1. Initial conditions and orbital characteristics as follows: 198x723 km elliptical orbit; ejection velocity = 1.64 m/s; ejection angle = -4.7 deg (backwards); orbital anomaly at satellite ejection = 170 deg (i.e., 10 deg before apogee). The minimum tension in these simulation runs varies from 10 mN to 40 mN.
- Figs. 9.2(a-d) Simulation runs of SEDS-1 for relatively high values of the minimum tension, i.e., from 50 mN to 70 mN. The system and orbital characteristics are as in Figs. 9.1.

~~PRECEDING~~ PAGE BLANK NOT FILMED

## 9.1 SEDS-I deployer

The SEDS deployer is a passive (i.e., without any retrieval capability) system designed and built by Tether Applications Inc. of San Diego, California.

The deployer is a large, stationary spool of tether which deploys along the axial direction, from the outer perimeter of the spool. Upon exiting the deployer canister, the tether, as it unwinds, cuts through two light beams which shine on two photodetectors thereby counting the numbers of deployed tether turns. Subsequently, the tether goes through a brake, a tensiometer, and a tether cutter. The brake is a barber pole that, when engaged, forces the tether to spiral around the pole, hence producing a friction force that varies exponentially with the number of brake turns.

The SEDS deployer can handle satellites with a mass of up to 30,000 kg for short tethers of 4 km and a mass of 90 kg for the longest tether of 80 km. In its present configuration the small satellite at the tether tip is only 23 kg and the tether is 20 km long made of a carbon fiber called Spectra-1000. The satellite, in the current configuration (i.e., SEDS-I and SEDS-II) is ejected by a spring device (Marmam clamp) which provides an ejection velocity of 1.64 m/s.

The potential application of the SEDS deployer are many, especially in the fields of atmospheric science, reentry of spacecraft, and injection of spacecraft to different orbits without the use of thrusters.

The first paper included at the end of this section gives a concise description of the SEDS deployer, the small satellite utilized for SEDS-I and SEDS-II, the characteristic of the tether and the potential applications of the system.

The second paper included at the end of this section describes the complex attitude dynamics of SEDS-I end-mass and a passive device to reduce the attitude oscillations.

## 9.2 Simulation of SEDS-1 Deployment Dynamics

The deployment dynamics of SEDS-1 was analyzed for the initial conditions and orbital parameters expected for the first mission. They are as follows: 198x723 km elliptical orbit; ejection velocity = 1.64 m/s; ejection angle = -4.7 deg (backwards); orbital anomaly at satellite ejection = 170 deg (i.e., 10 deg before apogee).

The frictional tension model adopted in the following simulations is the model developed by J. Carroll and documented by J. Glaese in Ref. [1]. The friction is modeled as the sum of two terms: a static term (the minimum tension) and a dynamic term proportional to the velocity squared. The brake amplifies the two terms above by increasing them exponentially with the wrap angle of the tether around the brake-post time the friction coefficient.

An additional friction multiplier is provided by the exit angle between the tether and the exit guide of the deployer. This effect is also modeled with an exponential function with the exit angle time the friction coefficient as the exponent. In formulas:

$$T = (T_0 + I\rho V^2 A_{rel} e^E) e^{B f n \text{Abs}(\theta - \theta_0)} \quad (9.1)$$

where:

- $A_{rel}$  =  $1 - A_{sol}XL/L_{full}$
- $L$  = tether deployed length,
- $L_{full}$  = fully-deployed tether length,
- $A_{sol}$  = tether annulus solidity,
- $B$  = brake parameter =  $2\pi f n$ ,
- $f$  = friction coefficient = 0.18
- $n$  = number of tether turns around the brake post,
- $T_0$  = minimum tension,
- $\rho$  = linear density of the tether =  $3.3 \times 10^{-4}$  kg/m,
- $\theta$  = in plane libration angle,
- $\theta_0$  = null exit angle = 65 deg,
- $I$  = inertia multiplier,
- $E$  = area exponent.

The minimum tension is determined by the frictional force in the absence of any braking action. This tension component is, in first approximation, velocity independent

and consequently we will call it the static component of the tension. The other component of the tension is a dynamic component which depends upon the velocity squared. The first exponential term in eqn (9.1) models the effect of the braking action whereby the brake parameter B is proportional to the number of brake turns. The second exponential function models the effect of the friction due to the exit angle of the tether with respect to the deployer exit guide.

The static component of the tension dominates the deployment dynamics in the early part of deployment. The static term also affects the duration of the deployment whereby at a higher tension corresponds a faster deployment and vice versa for a lower static tension. The dynamic tension affects the deployment profile at comparatively high velocities, i.e., for the latter part of deployment.

Figures 9.1(a)-9.1(i) show the deployment dynamics for different values of the minimum tension. A higher minimum tension implies a deployment which is slower than nominal before 7 km of deployed tether length (cross over point) and higher than nominal after the cross over point (see Fig. 9.1(a)). The net effect is a faster deployment for higher values of the minimum tension. The maximum tether speed is also higher for higher minimum tether tension (see Fig. 9.1(b)).

In the above simulations, the brake is activated at a tether length of 18.94 km (i.e., 95% of the fully deployed tether length). The final tether speed is about 7 m/s. For a brake-post rotational speed of 0.0145 turn/s and a minimum tension ranging from 10 mN to 40 mN, the number of brake turns before reaching the tether end ranges between 1.4 and 1.8 (see Fig. 9.1(e)) where the lower number of turns corresponds to the higher value of the minimum tension. The tether tension vs time for various values of the minimum tension are shown in Figs. 9.1(f)-9.1(i).

The following tension model parameters were considered nominal before the flight of SEDS-I [2]:

Minimum tension	= 20 mN,
Inertia multiplier	= 3,
Annulus solidity	= 0.96,
Area exponent	= -0.8.

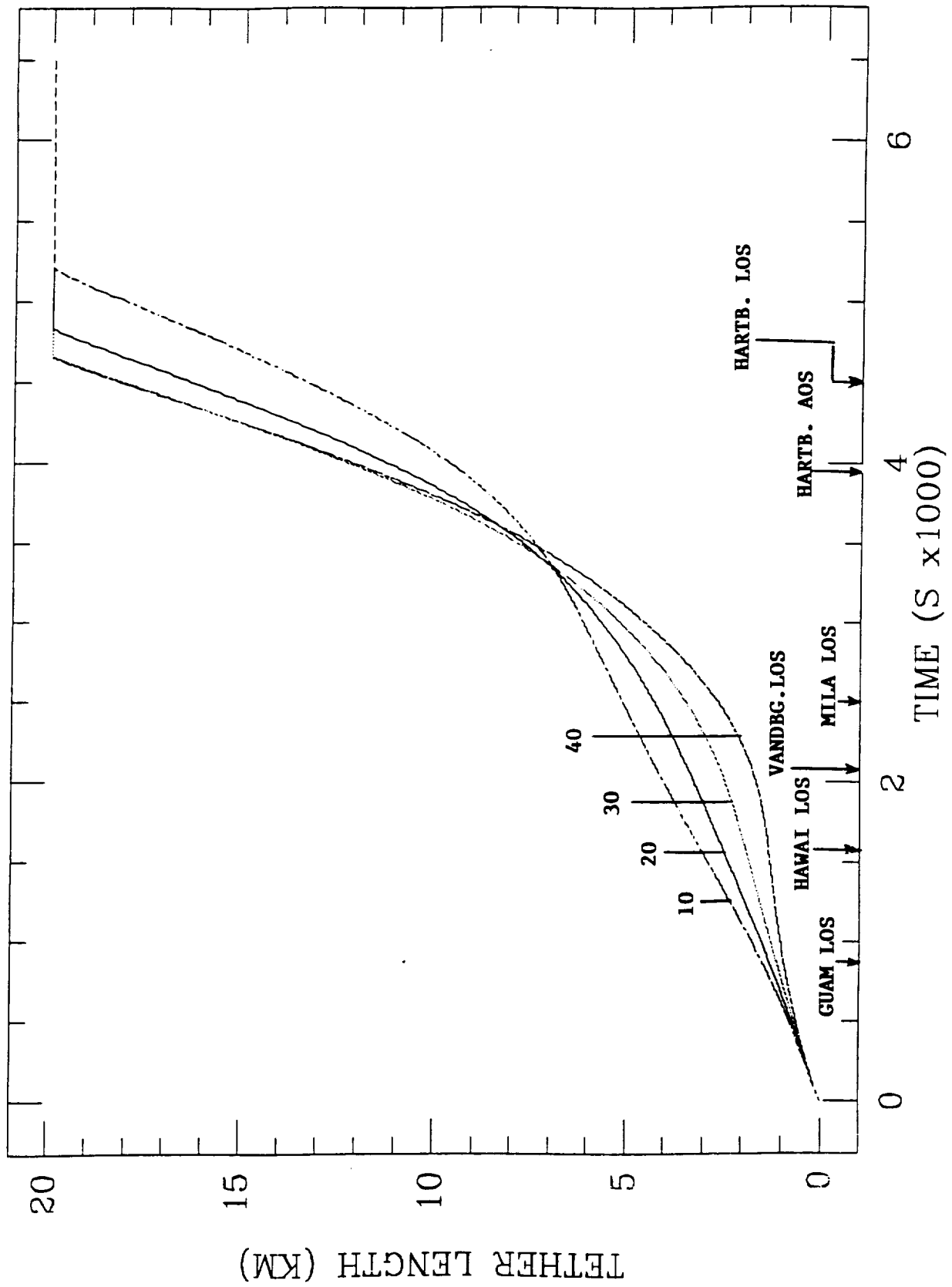


Figure 9.1(a)

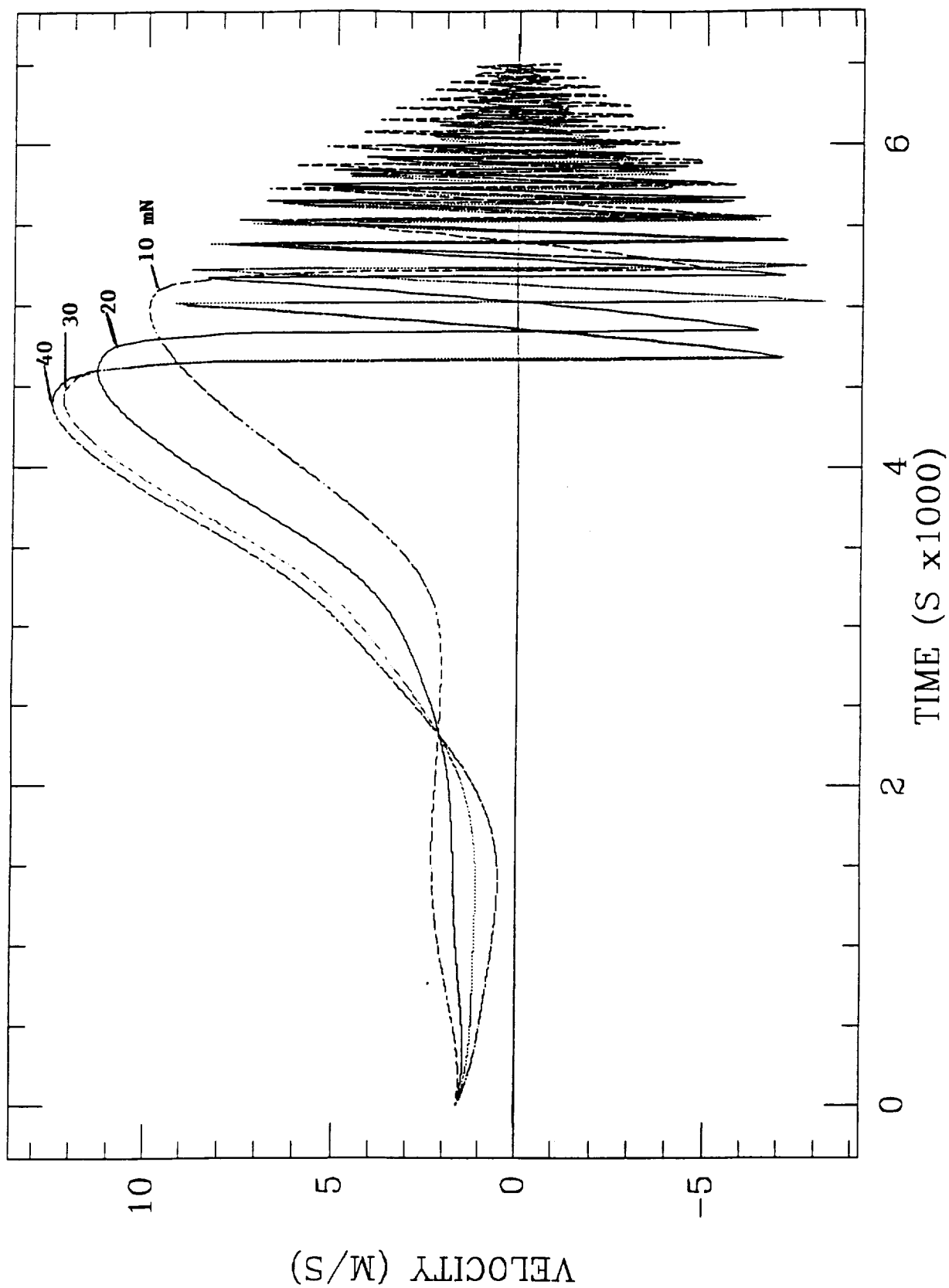


Figure 9.1(b)



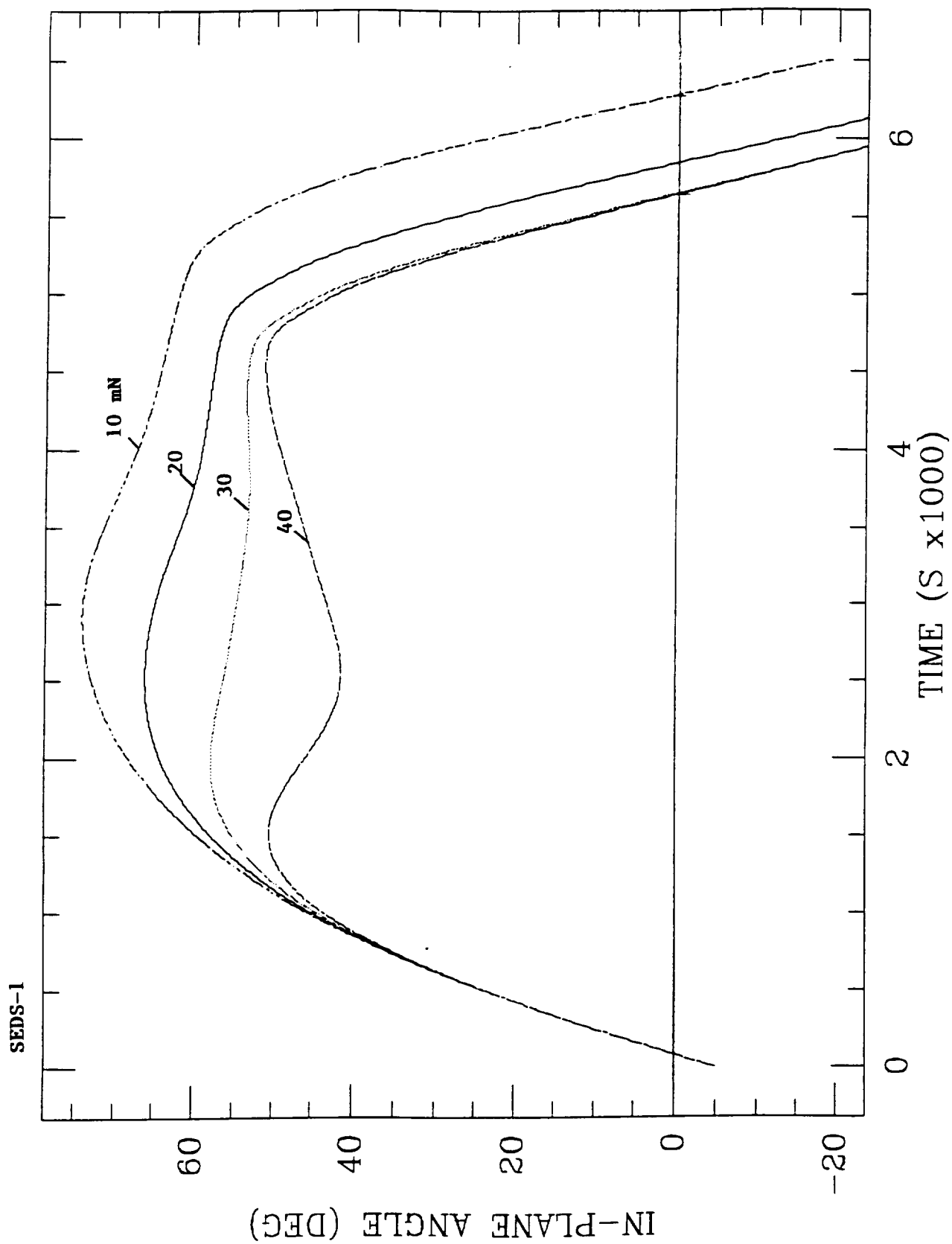


Figure 9.1(c)

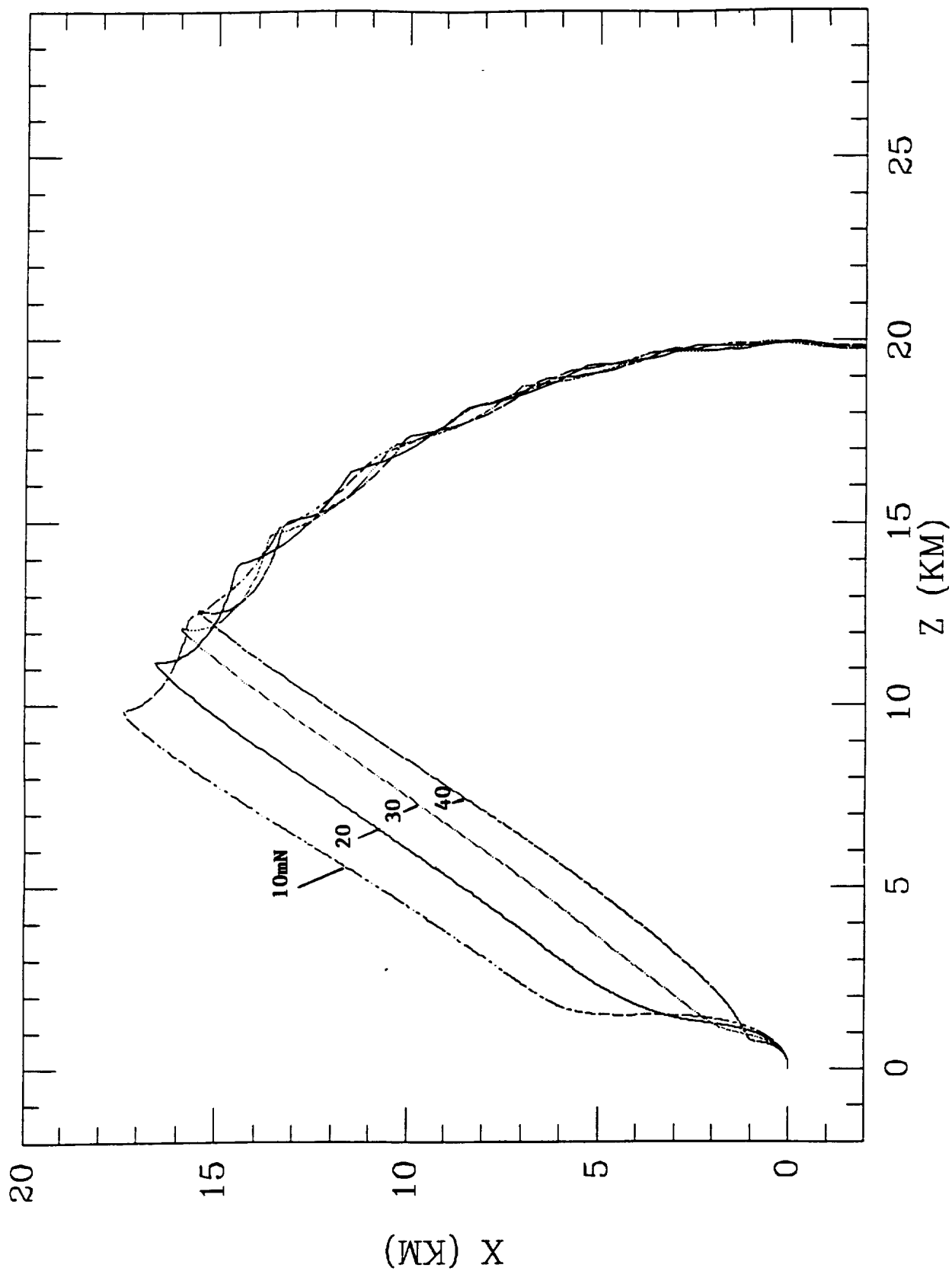


Figure 9.1(d)

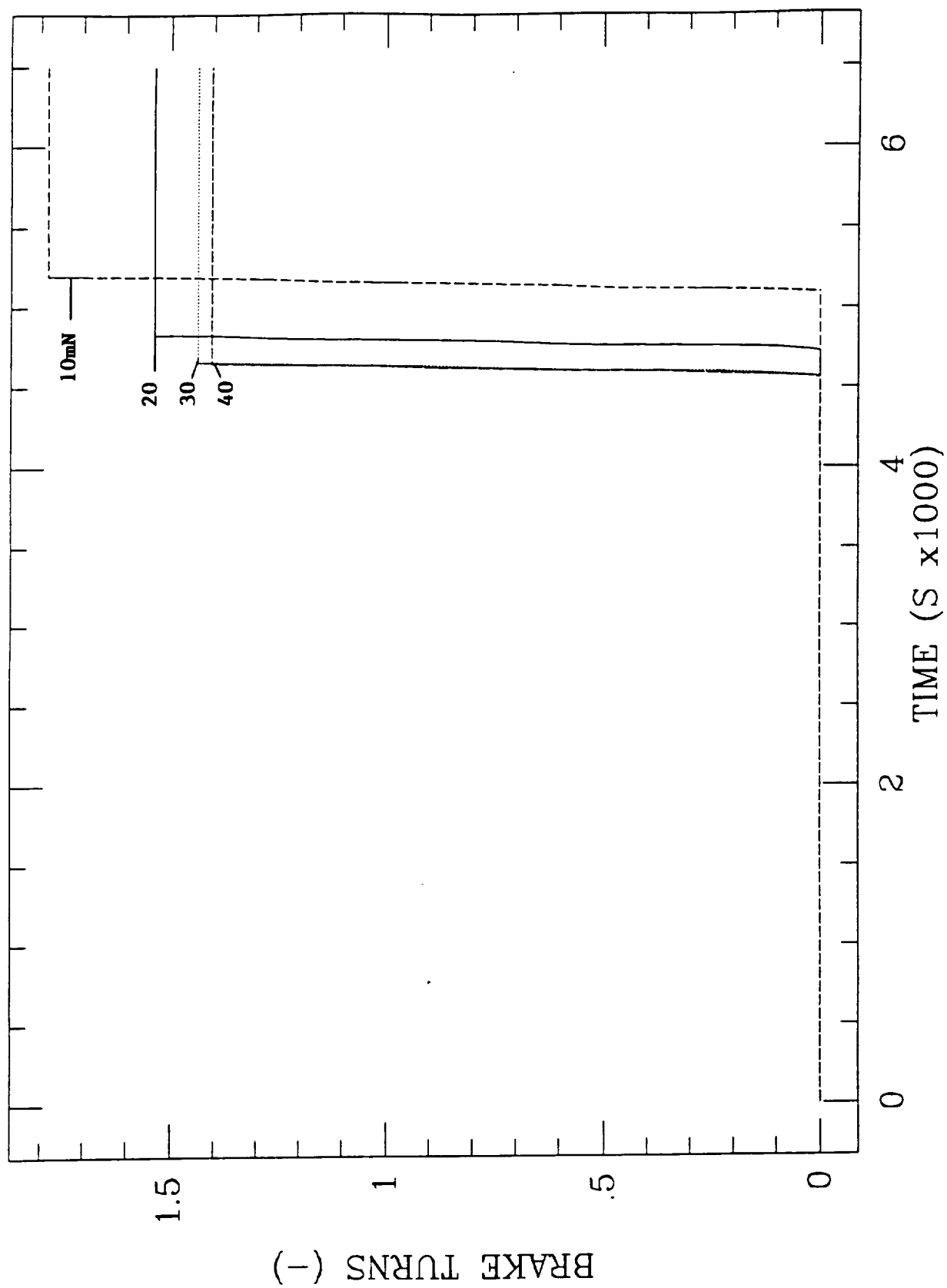


Figure 9.1(e)

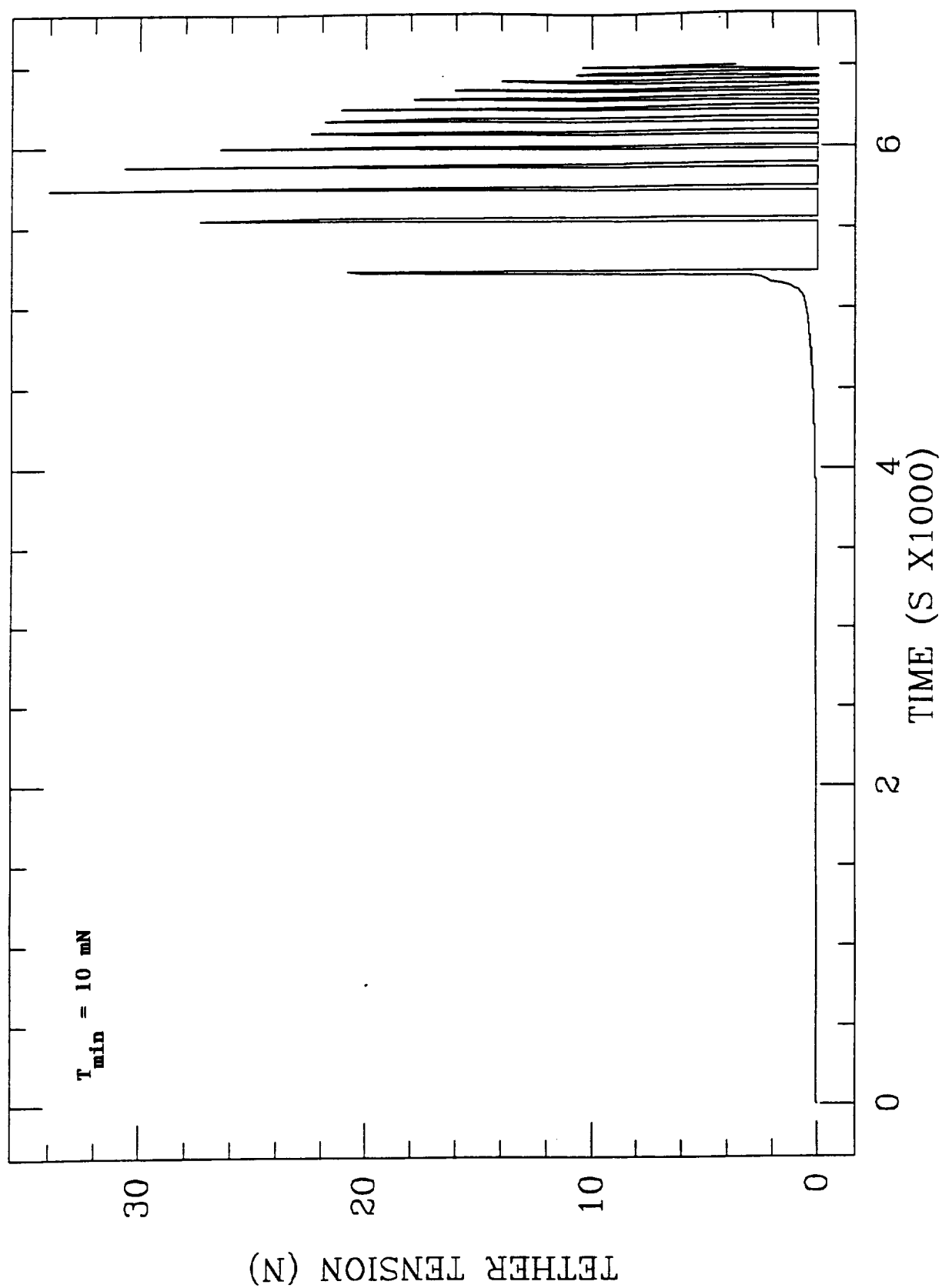


Figure 9.1(f)

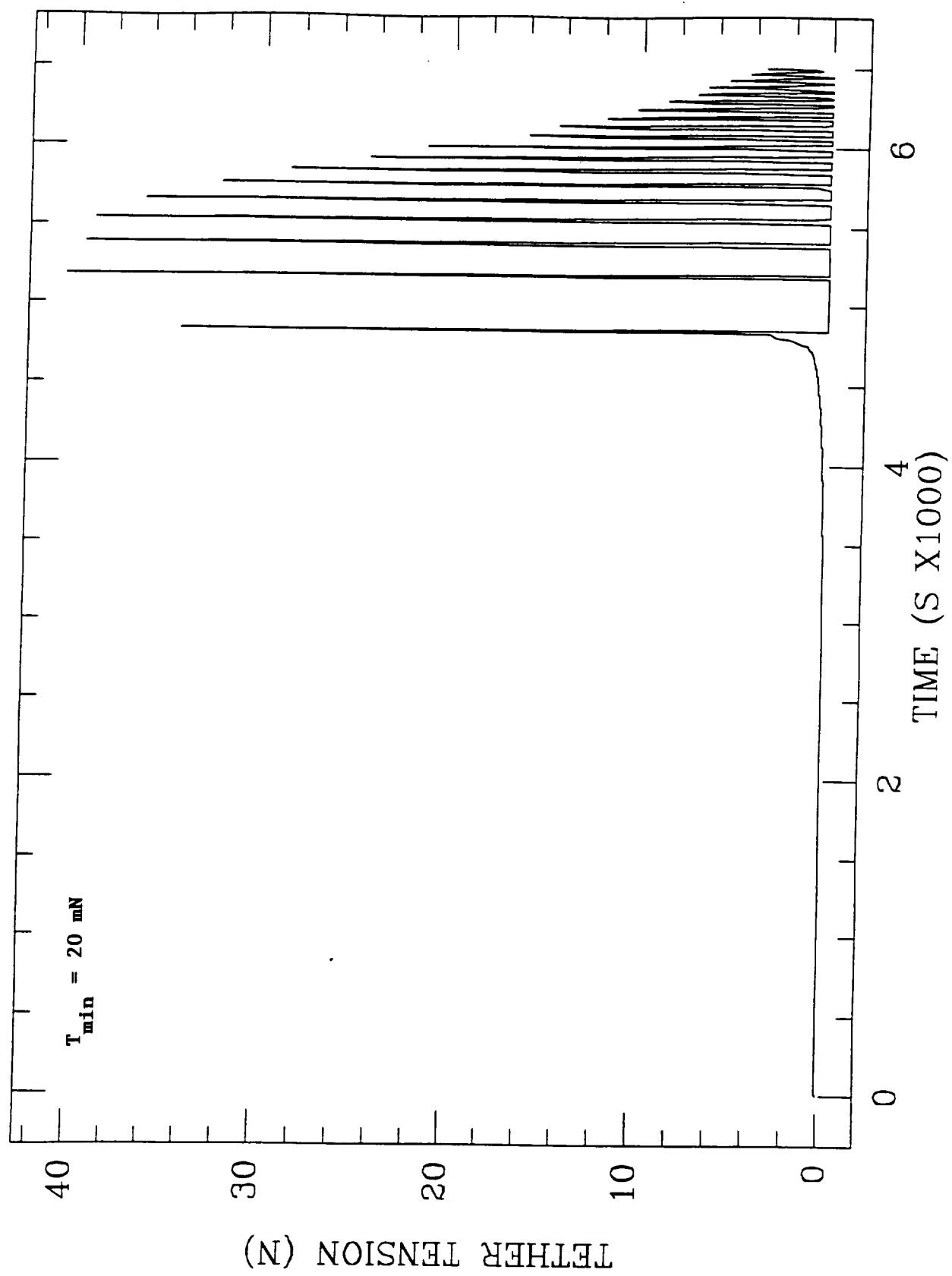


Figure 9.1(g)

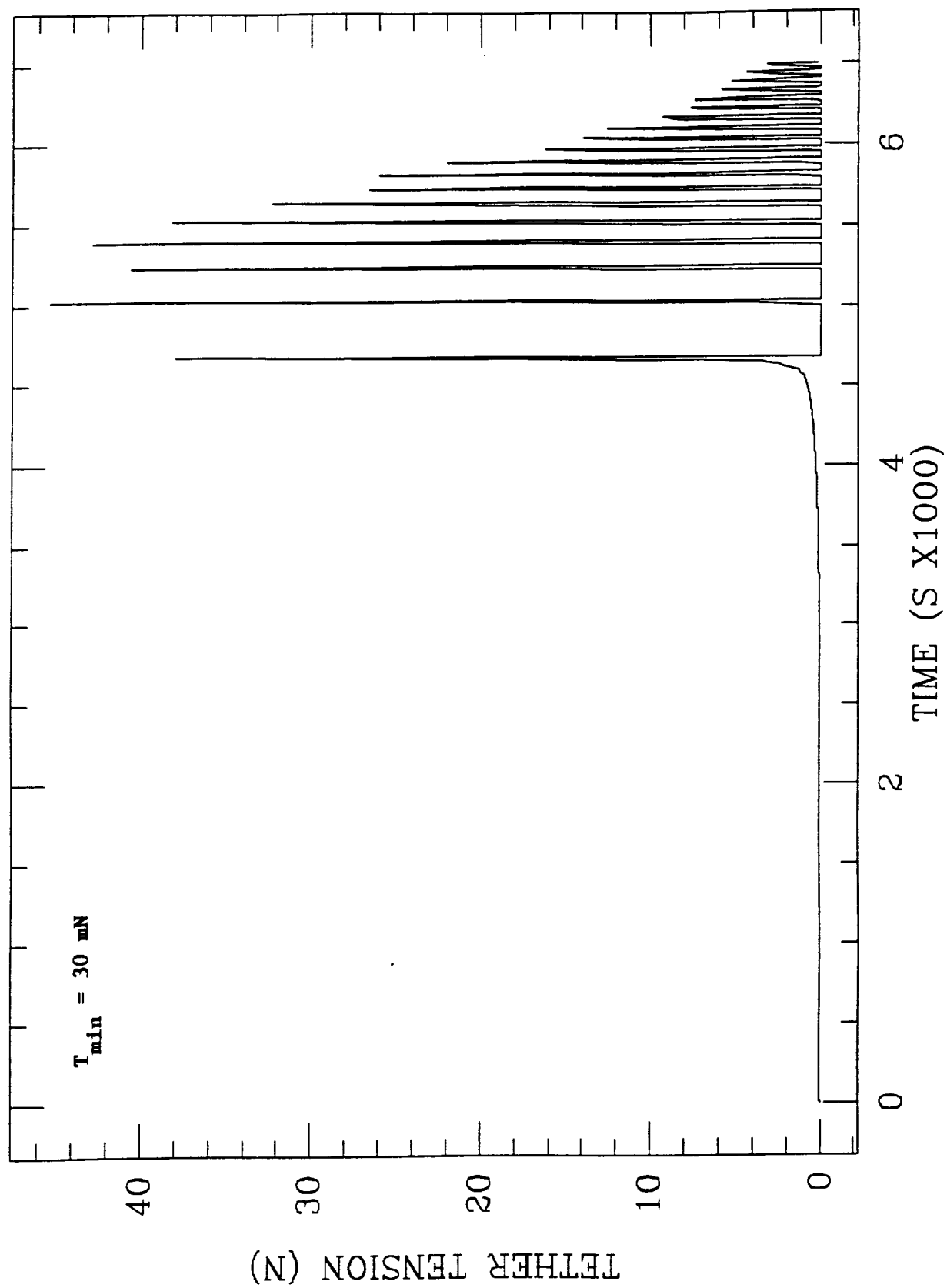


Figure 9.1(h)

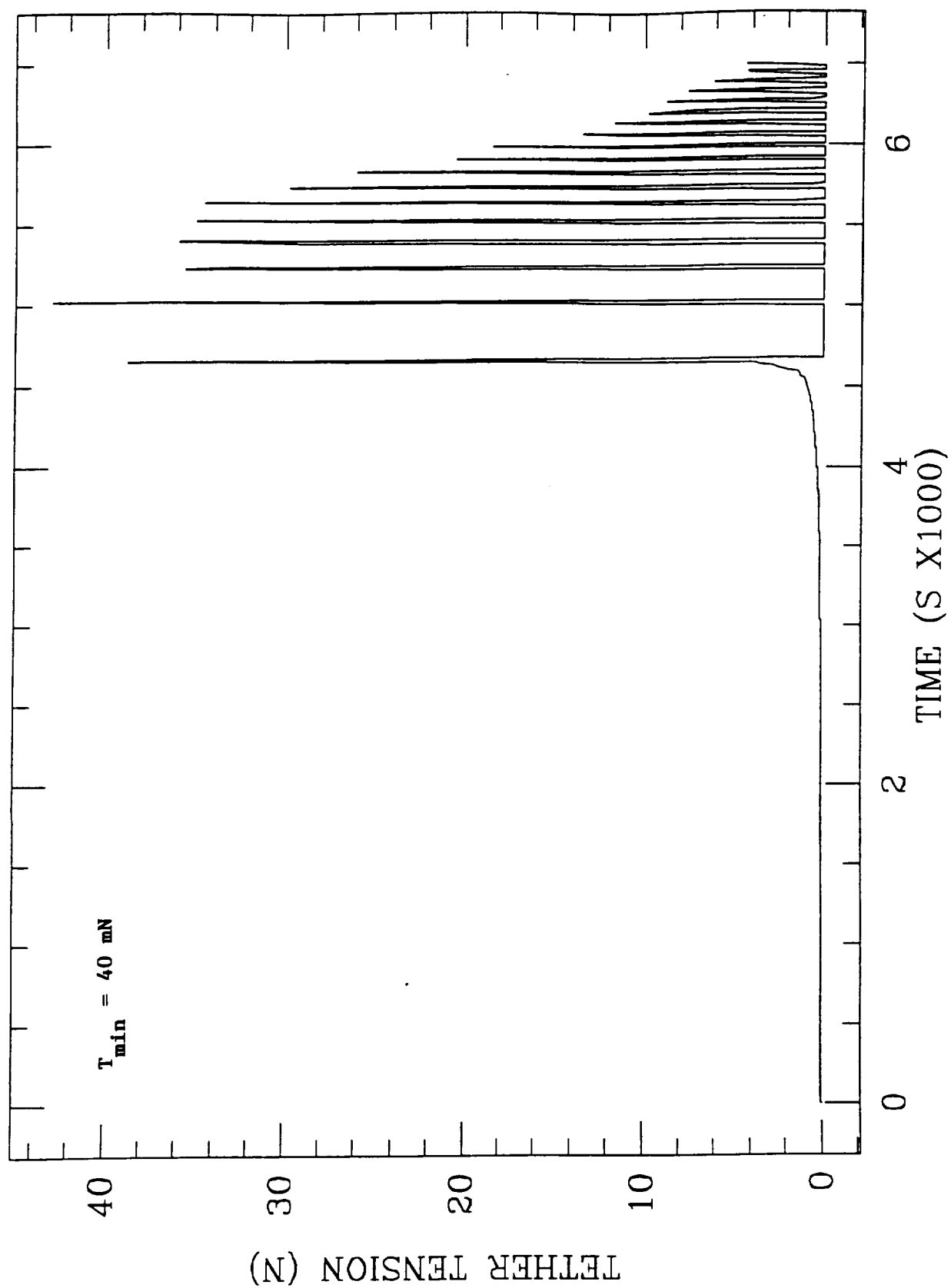


Figure 9.1(i)

## 9.2 Off-Nominal Deployment Cases

If the minimum tether tension is high, the momentum imparted to the end-mass at ejection can be entirely dissipated by the frictional forces. In the following simulation runs, shown in Figs. 9.2(a)-9.2(d), the minimum tension is increased up to values as high as 70 mN.

Full deployment is attained for values of minimum tension lower than 65 mN. Moreover, the deployment stops temporarily for values of minimum tension between 50 mN and 65 mN. The deployment stops temporarily at a tether length that ranges between 0.55 km and 0.85 km where the shorter length corresponds to the higher minimum tension. The pull of the gravity gradient against the frictional forces is responsible for resuming the deployment in those cases whereby the minimum tension is less than 65 mN.

For a minimum tension of 70 mN, the deployment stops at a tether length of 0.5 km. Since the gravity gradient is too weak at that tether length and the friction is too high, the deployment does not resume.



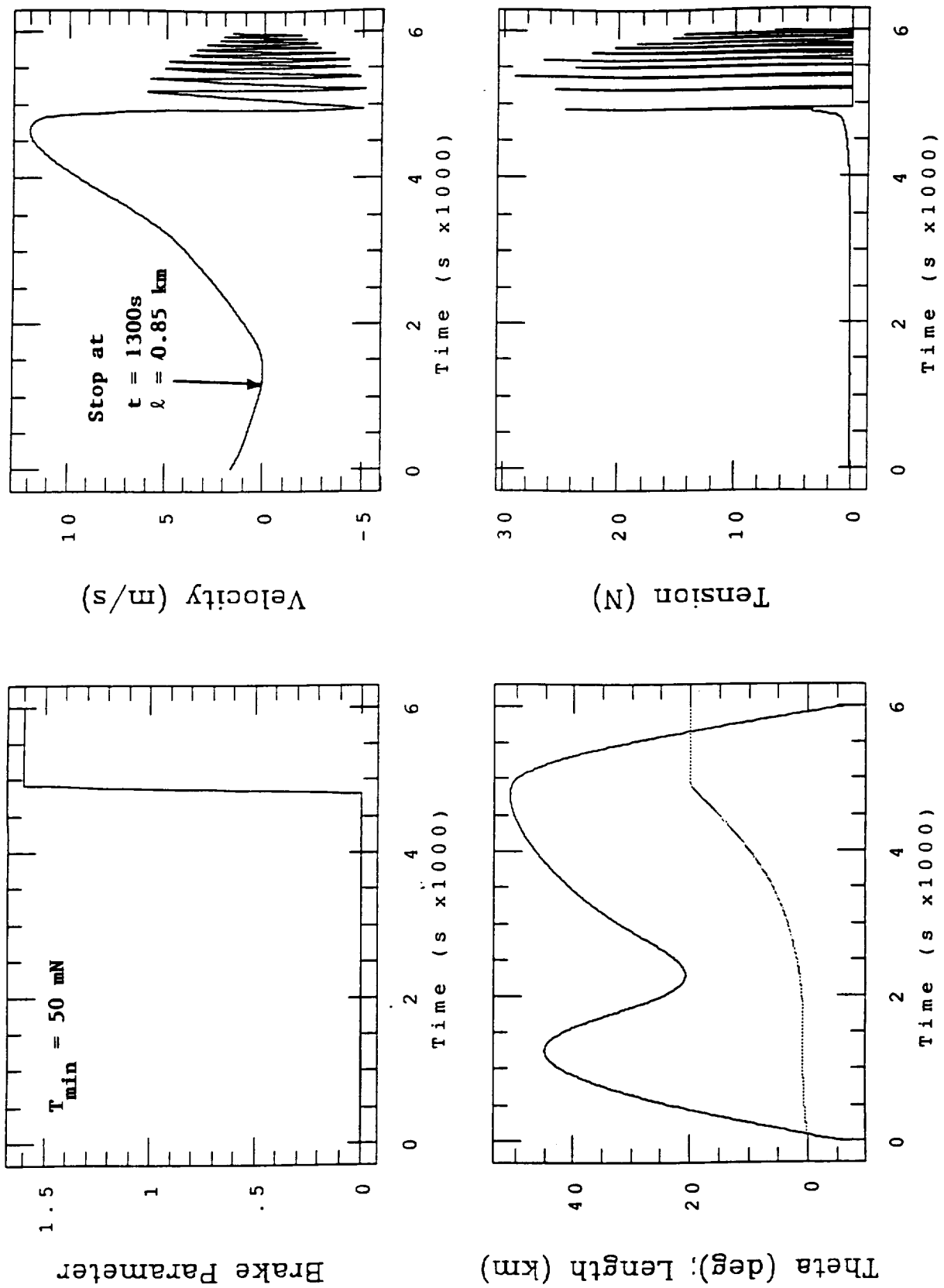


Figure 9.2(a)

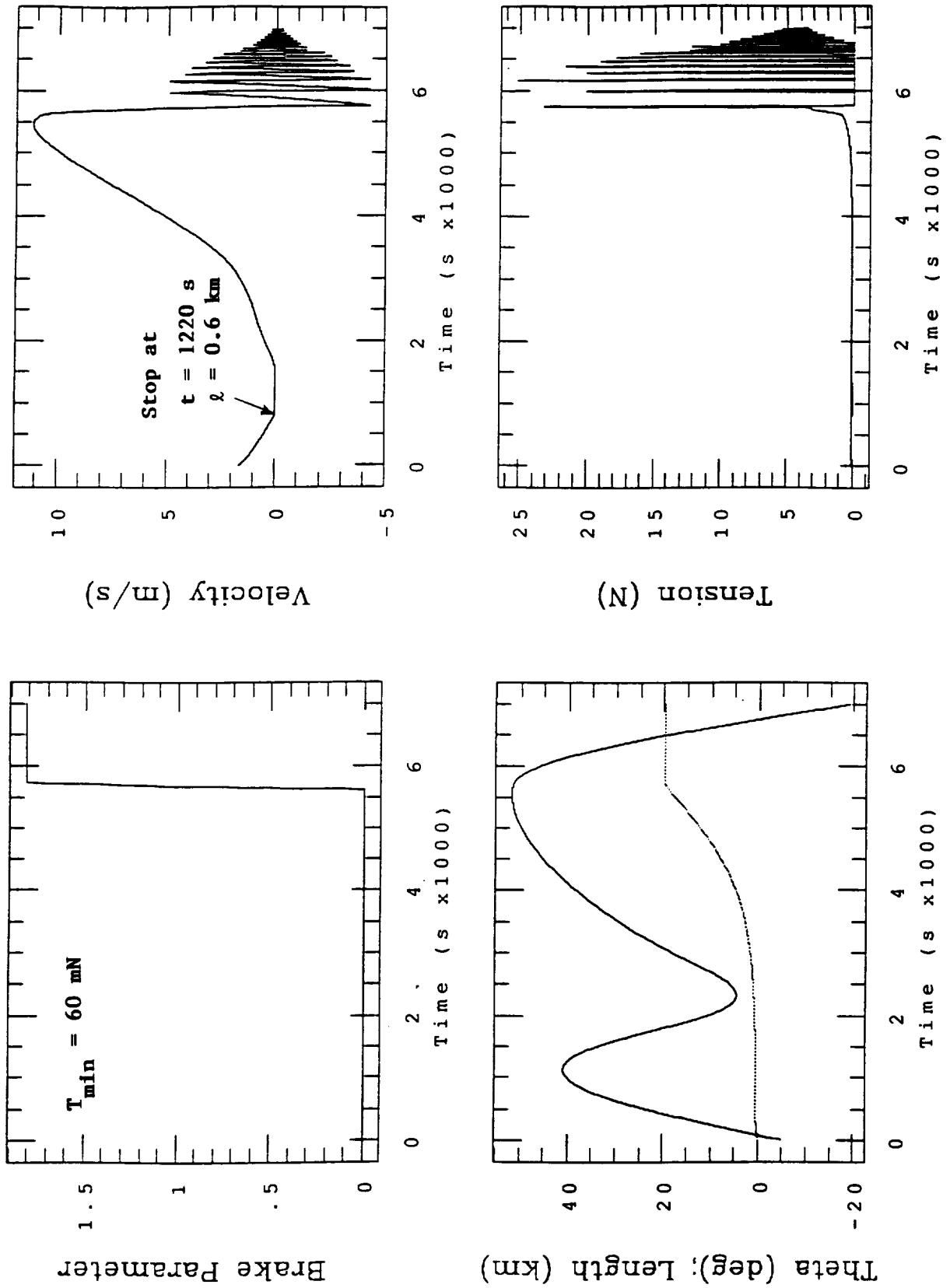


Figure 9.2(b)

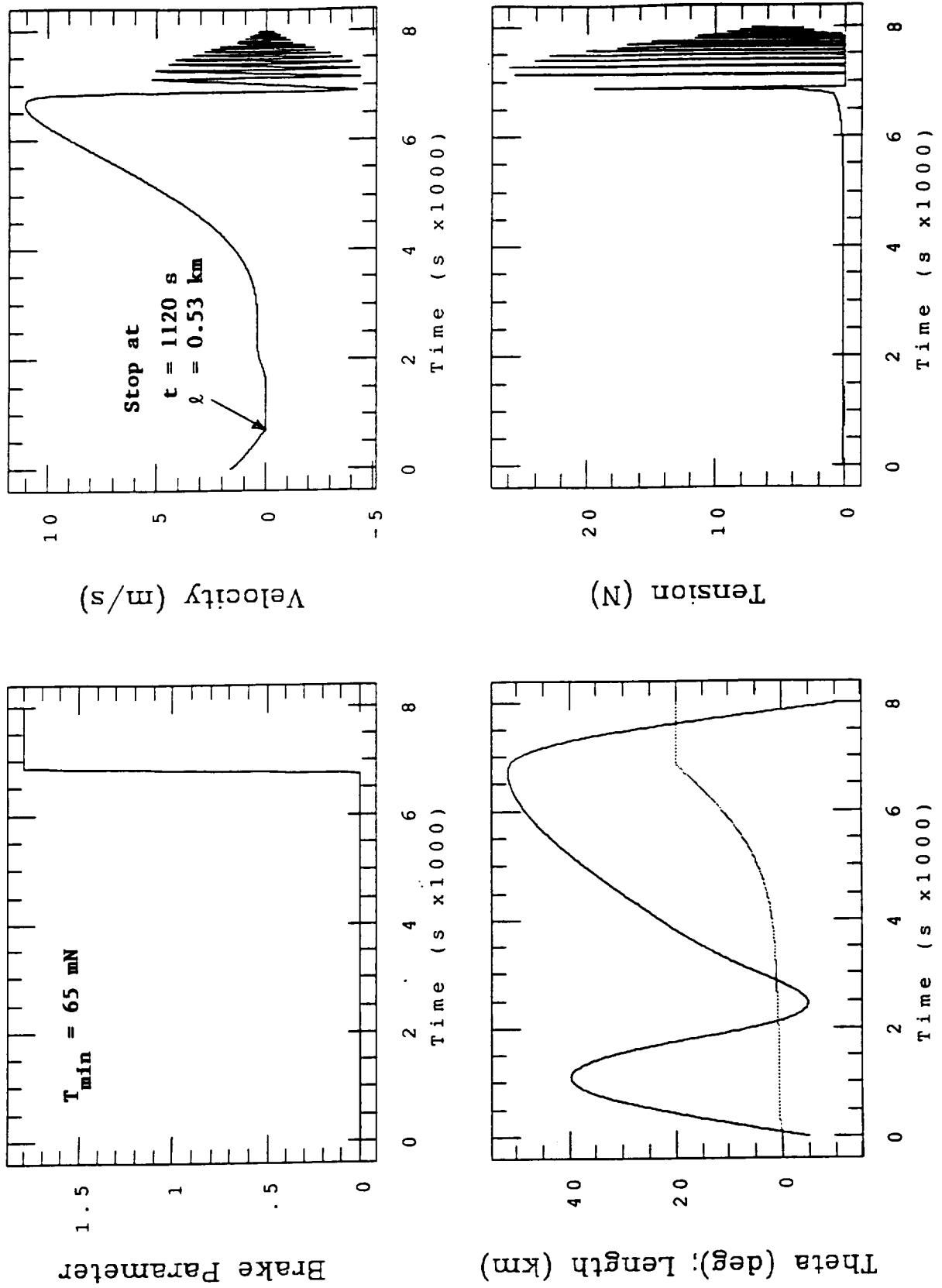


Figure 9.2(c)

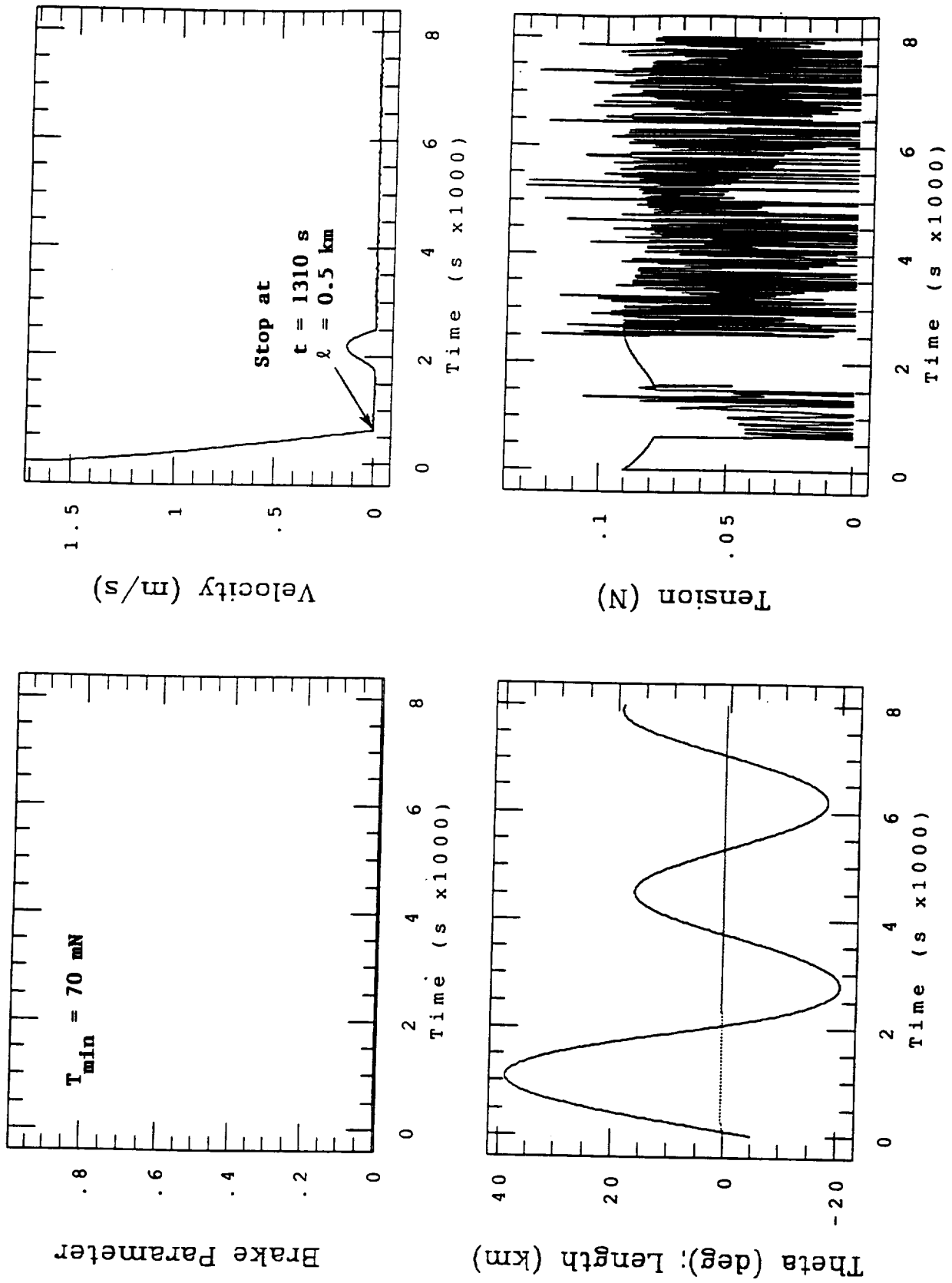


Figure 9.2(d)

### 9.3 Conclusions on the simulation of SEDS-1 deployment

The results of the pre-flight deployment simulations, indicate that SEDS-I can reach the fully deployed length of 20 km if the minimum tension is below 65 mN.

For a minimum tension between 50 mN and 65 mN, the deployment stops temporarily at a tether length ranging from 0.85 km for the lower tension to 0.55 km for the higher tension. The deployment subsequently resumes thanks to the gravity gradient.

For a minimum tension of 70 mN, the deployment stops at a tether length of 0.5 km and never resumes.

For values of the minimum tension between 10 mN and 40 mN, the deployment never stops. The deployment profile is qualitatively the same for all these cases. The maximum in-plane angle ranges from 52 deg to 75 deg. The time to reach the final tether length ranges from 4,650 s to 5,200 s. The time from ejection to the tether swinging across the local vertical ranges from 5,610 s to 6,250 s. The shorter times correspond to high minimum tensions.

From the SEDS-1 flight data, it can be inferred that the value of the minimum tension was about 35 mN, the maximum angle of libration 57 deg, the maximum length of tether of 19.94 km was reached after 4602 s from ejection, the end of the tether was reached with a velocity of about 7 m/s. The brake was ramped up at constant speed at about 19 km of deployed tether length. The brake post had turned 1.5 turn before the end of deployment. This was not sufficient to bring the tether velocity to zero before the end of deployment, demonstrating the need for a close-loop control for improving the brake performance. The tether was cut at  $t = 5611$  s when the tether was close to the local vertical. The satellite with the tether attached reentered and burnt in the upper atmosphere 1/3 of an orbit after release. Visual observations from the ground showed the last pieces of burning fragments at 48 km of altitude. From the last-transmitted telemetry data, the tether was still attached to the satellite at an altitude of 107 km.

### 9.4 References

- [1] J. Glaese and R. Issa, "SEDS DRM Preliminary Presentation". Control Dynamics Company, Huntsville, AL, June 1992.
- [2] J. Carroll, *Input file to BEADSIM*, Tether Application Inc., January 1993.



E. C. Lorenzini

*Harvard-Smithsonian Center for Astrophysics, Cambridge, Massachusetts, USA*

J. A. Carroll

*Tether Applications, San Diego, California, USA*

## **In-Orbit Experimentation with the Small Expendable-Tether Deployment System\***

### **Abstract**

The Small Expendable-Tether Deployment System (SEDS) is a lightweight deployer capable of deploying instrumented packages and other tethered payloads, with a mass limit of 1 metric ton, to a distance of up to 20 km. Since the payloads are not retrieved, the system is simple and inexpensive. On its first flight, presently scheduled for 1992, the deployer will be attached to the second stage of a Delta-II rocket, which will provide the stabilised platform for the deployment of the tethered payload.

SEDS is particularly suitable for complementing the Tethered Satellite missions by providing a flexible system for experimenting with the tether-in-space technology. SEDS can also provide a convenient means of testing instruments and/or procedures that require the use of long tethers.

---

\* Based on a paper presented at the 41st IAF Congress, Dresden, Germany, 6-12 October 1990.

## 1. Introduction

The need for in-orbit experimentation and demonstration before flying major missions that involve innovative technology is stimulating the development of inexpensive space systems for carrying out precursor flights. The Small Expendable-Tethered Deployment System (SEDS) falls into this category, having been developed by Energy Science Laboratories (ESL)\*, with NASA/Marshall Space Flight Center sponsorship to provide capabilities complementary to the Tethered-Satellite System (TSS).

Unlike TSS, SEDS does not retrieve the payload attached to the end of a 20 km-long thin tether<sup>1</sup>. By avoiding the complex control system necessary for retrieval, the design of the deployer is drastically simplified. Moreover, since SEDS flies as a secondary payload, it can take advantage of the frequent Delta flights<sup>2</sup>. This makes a SEDS launch possible every few months, starting with the first mission presently scheduled for 1992.

## 2. Hardware description

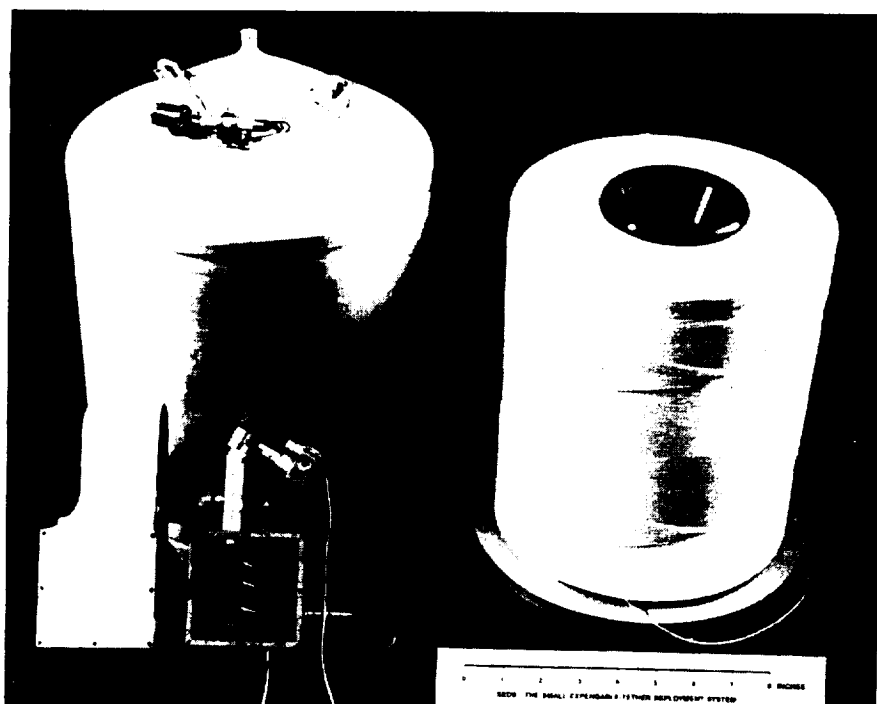
SEDS consists of a tether spool housed in a 33 cm × 25 cm (diameter) cylindrical canister. The tether unwinds from the end of a stationary reel (Fig. 1). While unwinding from the spool, the tether crosses two light beams, generating an electrical pulse every half a turn. There are no moving parts within the canister other than the tether itself. The tether tension at the exit is solely due to tether inertia, stiffness and friction. After passing through the canister's exit guide, the tether goes through a brake, a tensiometer, and a guillotine<sup>3</sup>.

The tensiometer is a spring-loaded device which measures the lateral pull produced by the tension, since the tether is at an angle to the measuring device. The brake is a 'barber's pole' activated by a stepper motor (Fig. 1). When the gear rotates, the tether is forced to spiral around the brake axle thereby producing a controllable frictional force. This 'adjustable-path' braking method provides a tension that varies exponentially with the number of turns wrapped around the brake axle up to the breaking strength of the tether. The guillotine is a pyro-activated cutting device for disposing of the tether and the payload at the end of the mission.

SEDS' deployer has an overall mass of 13 kg, including a 7 kg, 20 km-long tether. This tether is capable of handling payloads weighing up to 1 metric ton. The first payload, however, will have a mass of only 23 kg. A summary of the masses and dimensions of the SEDS components<sup>4</sup> is given in Table 1.

The tether has a diameter of 0.75 mm and a linear density of 0.33 kg/km. The tether material is Spectra-1000, a high-strength polyethylene synthetic fibre, which yields a

Figure 1. Tether spool, brake and cutter of the SEDS deployer



\* ESL personnel who developed SEDS have recently split off to form Tether Applications.



**Table 1. SEDS mass and size data**

Item	Mass (kg)	Size (cm)
Deployer Canister	3	25 × 33
Tether	7	20 km × 0.75 mm
Brake/Cutter	1	8 × 8 × 20
Electronics	2	8 × 13 × 25
End Mass	23	20 × 30 × 40
Brackets/Clamps	4	n/a
Total	40	

**Table 2. Characteristics of tether materials**

	Density (g/cm <sup>3</sup> )	Tensile Strength (GN/m <sup>2</sup> )	Specific Strength (m × 10 <sup>5</sup> )	Tensile Modulus (GN/m <sup>2</sup> )
Spectra-1000	0.97	2.99	3.1	172
Kevlar-29	1.44	2.76	1.9	131
Steel	7.85	1.45	0.2	207
Aluminium	2.64	0.31	0.1	69

breaking strength of 850 N for the SEDS tether. The characteristics of Spectra-1000 are compared with those of Kevlar-29, steel and aluminium in Table 2. It has the highest tensile-strength/weight ratio (i.e. specific strength) of the four materials.

Since Spectra has a melting point of only 147°C and rapidly loses its strength above 80°C, this material is suitable for high-altitude missions like SEDS and TSS1, but not for low-altitude atmospheric missions. The estimated tether temperature for SEDS during deployment varies from 20°C to about -110°C. The minimum temperature is reached during eclipses and the maximum occurs before tether deployment. These temperatures are well within the Spectra operating limits of +66°C and -267°C.

The canister will be attached to a Delta second stage above the 'Miniskirt' in the Guidance Section<sup>2</sup> (Fig. 2). An end mass, connected to the tether tip, is mounted side-by-side with the deployer before deployment (Fig. 3). This end mass is ejected by a spring-loaded Marman clamp (Fig. 4) and deployed to a distance of 20 km in 1.5 h period<sup>3</sup>. At the end of the mission, the tether will be cut at the deployer end.

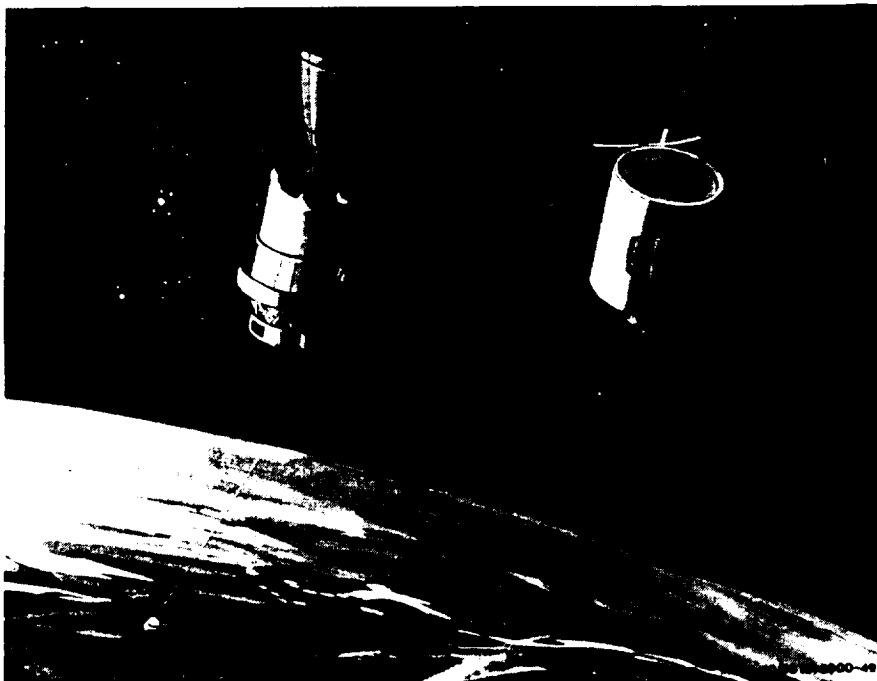
**Figure 2. SEDS' location on the Delta-II second stage**



Figure 3. Flight assembly of SEDS' deployer and end mass

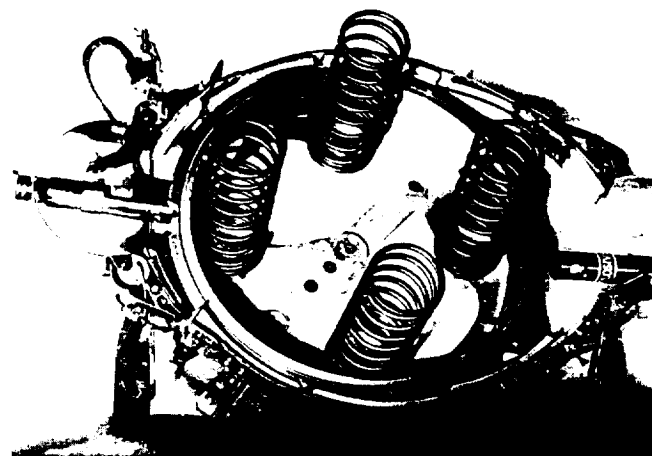


Figure 4. End-mass ejection mechanism (Marman clamp)

This operation deorbits the payload and the tether, which then burn up in the upper atmosphere one-third of an orbit after being cut loose.

The end mass, which is a rectangular box of Aluminium-6061 with a radar corner reflector, is instrumented with a three-axis gyro package, a three-axis tensiometer mounted at the tether attachment point, a three-axis magnetometer, and temperature sensors<sup>4</sup>. The characteristics of these instruments are given in Table 3. The accelerometers and the three-axis tensiometer have three channels each with three different measurement ranges. In this way, a high relative accuracy is provided over a large dynamic range.

Data from the instruments on the end mass are collected at a rate of either 1 Hz or 10 Hz by the onboard computer and stored in the 0.5 Mbyte RAM memory<sup>5</sup>. Data are continually transmitted by means of an S-band transmitter and recorded whenever SEDS is in sight of a ground station. The transmission rate for the payload data is 1.25 kbit/s. The deployer data are transmitted on a different channel through the Delta's telemetry link at a rate of 4.8 kbit/s. The modulation scheme is IRIG-compatible and the data are time-tagged in order to correlate events on the end mass and on the deployer.

Table 3. End-mass instrument characteristics

	Range	Resolution	
Three-Axis Magnetometer	$\pm 600$ mG	4.7 mG	
Three-Axis Accelerometer	$\pm 1$ mg	8.3 $\mu$ g	low range
	$\pm 5$ mg	42 $\mu$ g	medium range
	$\pm 50$ mg	0.42 mg	high range
Three-Axis Tensiometer	$\pm 100$ mN	0.83 mN	low range
	$\pm 1$ N	8.3 mN	medium range
	$\pm 10$ N	83 mN	high range

### 3. Orbital dynamics

On the first mission, the Delta second stage is expected to follow a  $100 \times 400$  nautical mile orbit (not yet finalised). The deployment of the tethered payload starts at apogee by triggering the pyros of the Marman clamp, thereby ejecting the end mass with 1.6 m/s initial velocity. The end mass pulls the tether out of the canister while following a trajectory dictated by the initial  $\Delta V$  and the tether tension produced by frictional forces<sup>6</sup>. When the gravity gradient overtakes the other forces at about 1–2 km distance from the Delta, the deployment rate increases. At a distance of

19 km, the brake is activated, the speed of the end mass is smoothly reduced to zero and the system librates toward the local vertical (*LV*). As the end mass approaches *LV*, about 1020 s after braking begins, the tether is cut loose. The end mass and the tether follow a reentry trajectory and burn up in the upper atmosphere one-third of an orbit later.

The duration of the first mission is limited by the energy provided by the launcher's silver-zinc batteries. Mission duration can be increased, at a price, on future flights by adding an extra battery to the Delta.

Figure 5a shows the trajectory of the end mass and the tether (side view) from  $t=0$  to  $t=5600$  s with snapshots taken every 200 s. Figure 5b shows the tether tension, speed and length as a function of time. Figure 5c shows snapshots (side view) every 10 s for the last 700 s of the deployment. Some features of the transverse waves along the tether are visible in this figure.

SEDS' tether dynamics is simulated by modelling the tether with seven point masses connected by massless springs and viscous dashpots. The Delta-II second stage and the end mass are modelled with two additional point masses. In the computer simulation used to derive the above results, the environmental models are as follows: aerodynamic forces are based on a Jacchia 1977 density model, while the gravity forces are computed by means of a  $J_0+J_2$  gravity model. In addition, the tensional forces are provided by the visco-elastic tether segments connecting two adjacent lumps<sup>7</sup>.

SEDS' first mission is designed to explore the dynamics of a long tethered system, and to analyse specifically: the motion of the end-mass during deployment; the tether motion; the wave propagation along the tether; and the material damping characteristics.

To assist the investigation of tether dynamics, a set of radar dipoles has been embedded into the tether at its mid-point. These dipoles will be tracked, together with the Delta-II stage and the end mass, by radars on the ground, in order to provide an absolute reference frame for studying the motion of the system. The radar dipoles will also make the first lateral harmonic of the tether motion detectable.

In addition, three 3 m-long lead wires have been embedded into the tether at the 17.9, 18.3, and 18.7 km points. Each will produce a tensional pulse, close to the end of the tether's deployment, lasting 0.3 s and with an amplitude 2.5 times higher than the tension's unperturbed value. These tensional pulses will excite waves along the tether, which will be detected by the tensiometer and/or accelerometers. Consequently, it will be possible to analyse wave propagation, tether-material damping, and elasticity characteristics.

## 4. First mission profile

Several future missions are being planned which go beyond the investigation of tether dynamics. These are precursor flights for<sup>5</sup>:

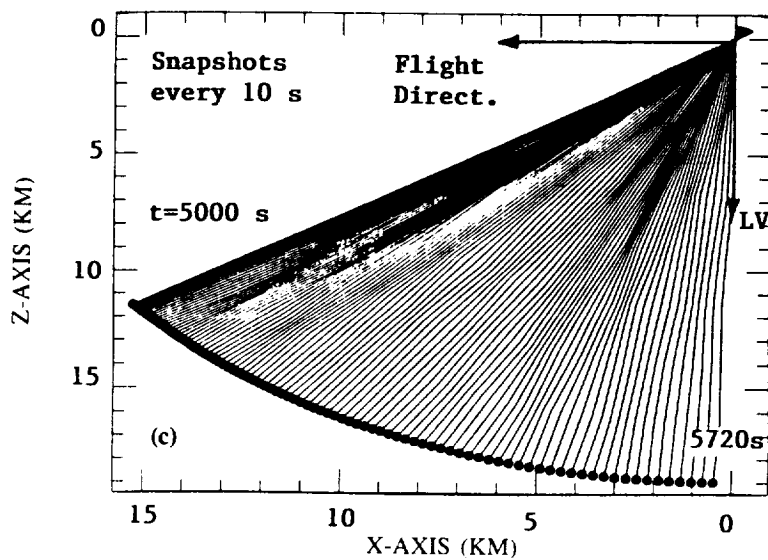
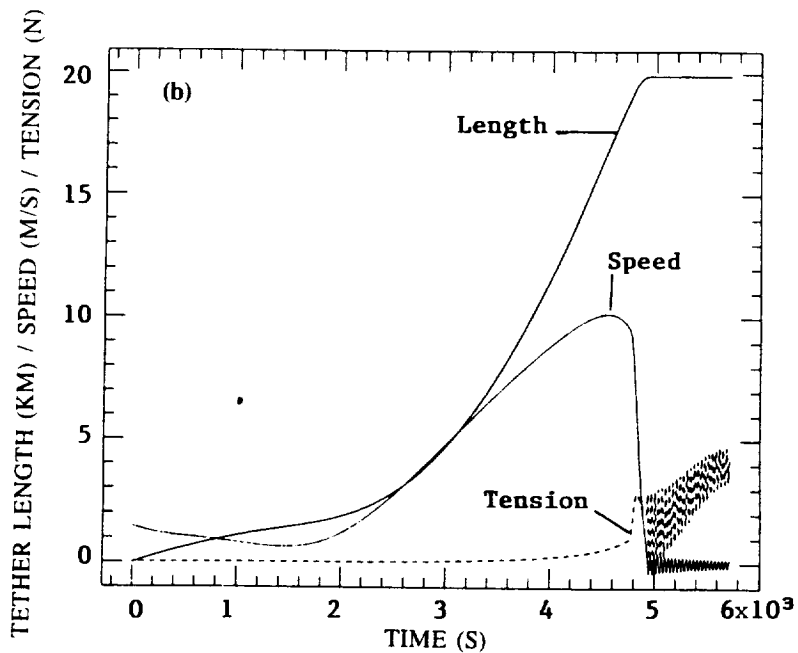
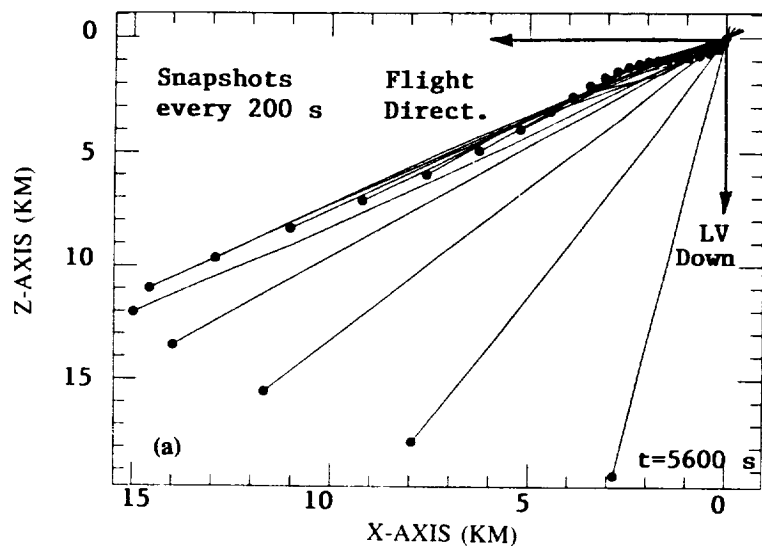
- (i) electrodynamic experiments with short, highly conductive tethers;
- (ii) payload orbit circularisation;
- (iii) reentry-capsule deorbit;
- (iv) data collection by means of atmospheric probes (either while tethered or after release);
- (v) precision attitude control of the end-mass using tether-induced control torques;
- (vi) low-altitude spaceborne gravity gradiometry or other remote-sensing activities.

## 5. Future flights

Since tether retrieval is inherently unstable, large tether oscillations excited during station-keeping are very difficult to damp out during retrieval. Consequently, the excitation of large tether oscillations must be limited in a tethered system that needs to retrieve the end mass. Since SEDS does not retrieve the tethered payload, the system can be used to conduct experiments that involve large dynamic disturbances.

For example, SEDS is ideal for carrying out electrodynamic experiments with high

Figures 5a-c. Results of simulation of SEDS orbital dynamics



currents and consequently large electrodynamic drag. For similar reasons, SEDS is best suited for aerothermodynamic research at very low altitudes. The strong atmospheric drag at low altitudes or the strong electrodynamic drag at high tether currents excites large tether oscillations, which makes the retrieval of the payload very difficult if not impossible.

The expendability of the hardware calls for a focus on low-cost payloads (an exception is the use of SEDS to de-orbit a reusable re-entry capsule or probe). The fact that the host vehicle is unmanned should speed up the development and flight of innovative experiments by eliminating potential delays associated with human safety issues. Consequently, SEDS is suitable for carrying out early precursor flights for demonstrating the validity of tether technology in space and evaluating the performance of prototype scientific instrumentation which is being developed for future flights on more ambitious systems.

The Small Expendable-Tether Deployment System (SEDS) provides a low-cost facility for conducting experiments that require the use of long tethers. Such experiments range from precursor flights for investigating the dynamics of tethered systems, to electrodynamic and aerothermodynamic flight experiments. Specifically, the first mission (TDE-I) is a dynamic-explorer mission for providing data complementary to the Tethered Satellite flight data.

Because of SEDS' low cost, and because of the frequent flight opportunities, scientists will be able to obtain a quick turnaround of their experimental results. In some instances, SEDS lends itself to more adventurous and innovative experiments, where the low cost of a flight will make the taking of risks more acceptable than on a Shuttle-based mission.

Support for this research was provided by NASA/Marshall Space Flight Center (NASA/MSFC) with Mr C. Rupp and Mr J. Harrison as technical monitors. SEDS was developed under SBIR contracts and follow-on funding from NASA/MSFC between 1983 and 1989, with the same technical monitors. We would also like to thank Dr. M. Cosmo of the Smithsonian Astrophysical Observatory for providing part of the dynamic-simulation results.

## 6. Conclusions

## 7. Acknowledgements

## References

1. Rupp C C 1988, Early Tether Dynamic Flight Experiments, in *Space Tethers for Science in the Space Station Era* (Eds. L Guerriero & I Bekey), Società Italiana di Fisica Conf. Proc. Vol. 14, Bologna, Italy.
2. Garvey J M & Marin D R 1989, Delta II Secondary Payload Opportunities for Tether Demonstration Experiments, in *Tethers in Space — Toward Flight*, AIAA, Washington, DC.
3. Harrison K J, Rupp C C, Carroll J A, Alexander C M & Pulliam E R 1989, Small Expendable-Tether Deployment System (SEDS) Development Status, in *Tethers in Space — Toward Flight*, AIAA, Washington, DC.
4. DeLoach R, Diamond J, Finley T & Rhew R 1990, End-Mass Instrumentation for the First SEDS/Delta-II Mission, Proc. AIAA 28th Aerospace Sciences Meeting, 8–11 January 1990, Reno, Nevada (Paper AIAA-90-0537).
5. Carroll J A 1990, Users Guide to SEDS, The Small Expendable-Tether Deployment System, Tether Applications, La Jolla, Calif., April 1990.
6. Carroll A J 1988, The Small Expendable Deployment System (SEDS), in *Space Tethers for Science in the Space Station Era* (Eds. L Guerriero & I Bekey), Società Italiana di Fisica Conf. Proc. Vol. 14, Bologna, Italy.
7. Lorenzini E C, Cosmo M, Vetrella S & Moccia A 1989, Dynamics and Control of the Tether Elevator/Crawler System, *ESA Journal*, Vol. 14, No. 3, pp. 303–312.



**STUDY OF THE ATTITUDE DYNAMICS  
OF THE  
SMALL EXPENDABLE-TETHER DEPLOYMENT SYSTEM**

**Michele Grassi**

**Institute of Gasdynamics, University of Naples "Federico II",**

**P.le Tecchio 80, 80125 Naples, Italy**

**Tel:+39-81-7682158 Fax:+39-81-7682160**

**and**

**Mario L. Cosmo**

**Smithsonian Astrophysical Observatory,**

**60 Garden Street, Cambridge(MA), U.S.A.**

**Tel:001-617-495-7412 Fax:001-617-496-7670**

**Abstract**

The Small Expendable-Tether Deployment System (SEDS) provides a low-cost facility for deploying tethered payloads in space. Among various objectives, SEDS' first flight, scheduled in March '93, will assess the capability of tethered platforms to carry out measurements in the upper atmosphere. The performance of onboard instruments is seriously affected by the payload's attitude dynamics. In this paper, SEDS' attitude dynamics and stability are analitically and numerically analysed for the nominal mission. It is shown that although a passive damper can be used to reduce the amplitudes of the attitude angles, appropriate control techniques are required for scientific instrumented platforms.

## 1. Introduction

The first mission of the Small Expendable-Tether Deployment System (SEDS), scheduled for flight in March 1993, will be a precursor flight for investigating the dynamics of long tethers in space. A 25 kg payload will be deployed with 20 km-long tether from the second stage of a Delta II. At the end of the deployment when the end-mass swings toward the local vertical the tether is cut and payload and tether re-enter the atmosphere[1-3].

The instrumentation on board the payload[4] is mainly intended to collect data on the dynamics of spaceborne tethers and the orientation of the end-mass. These data, however, provide also the opportunity to assess the performance of tethered payloads as scientific platforms for in-situ measurements of the Earth's upper atmosphere and ionosphere[5]. To this end payload attitude stability and control are necessary to maximize the mission's scientific return[6].

Since in a tethered system the largest external torque is provided by the tether tension, the attitude dynamics of tethered payloads has unique features with respect to classical satellite configurations[7-10].

SEDS adopts a low-tension strategy at the beginning of the deployment to minimize the momentum exchange between deployer and payload during major part of the deployment. Therefore attitude perturbations from other sources and/or initial conditions could be significant.

This paper deals with the end-mass attitude dynamics and stability. To this end a simplified analytical model of the payload attitude is developed under the assumption of small angles. Then the satellite attitude model is implemented in the numerical code that simulates SEDS' deployment, to analyze the dynamics of the end-mass during the nominal mission. The results show that the initial phase of deployment is characterized by tumbling of the end-mass. A passive damping device is proposed to limit the



amplitudes of the attitude angles and a numerical simulation is run to assess its effectiveness.

## 2. Small attitude oscillations and stability

Fig.1 shows a schematic representation of the payload when (a) it is attached to the Delta Second Stage and (b) during the deployment. The payload is assumed to be a rigid body. The moments of inertia ( $I_1, I_2, I_3$ ), the products ( $I_{12}, I_{13}, I_{23}$ ), and the body coordinates of the tether attachment point ( $x_1, x_2, x_3$ ) of SEDS-1 payload are listed in Table 1. In the following, in order to simplify the analysis the body frame (1-2-3) is assumed to coincide with the payload's principal axes.

The attitude dynamics is described considering the yaw ( $\gamma$ ), pitch ( $\beta$ ) and roll ( $\alpha$ ) angles as the Euler's angles of the body axes (1-2-3) with respect to a right-handed reference frame, whose origin is at the payload's center of mass, the z-axis coincides with the position vector and it is directed toward the Earth, the y-axis is perpendicular to the orbital plane and the x-axis is directed along the flight direction, (Fig.1). Due to the location of the tether attachment point, the pitch angle has a non-zero mean value  $\beta_0$ .

### 2.1. Equations of motion

The equations of motion have been derived under the following assumptions[11]:

- the payload's center of mass is in Keplerian circular orbit;
- the tether is assumed to be straight and unelastic;
- the gravitational potential is linearized;
- small attitude angles.

Moreover, since the tether tension slightly changes during the first part of the deployment[1], it will be considered constant ( $3 \cdot 10^{-2}$  N).

$$\ddot{\alpha} + \Omega^2 k_1 (1 + 3 \cos^2 \beta_0) \alpha - (\sin \beta_0) \ddot{\gamma} - [\Omega(1 - k_1) \cos \beta_0] \dot{\gamma} - (\Omega^2 k_1 \sin \beta_0) \gamma = \left( \frac{T x_2 \sin \beta_0}{I_1} \right) \beta - \frac{T x_2 \cos \beta_0}{I_1} + \left( \frac{T x_3 \cos \beta_0}{I_1} \right) \alpha \quad (1a)$$

$$\ddot{\beta} + (3\Omega^2 k_2 \cos \beta_0) \beta = T \frac{x_1 \cos \beta_0 + x_3 \sin \beta_0}{I_2} + T \frac{x_3 \cos \beta_0 - x_1 \sin \beta_0}{I_2} \beta + -3\Omega^2 k_2 \sin \beta_0 \cos \beta_0 + (3\Omega^2 k_2 \sin^2 \beta_0) \beta \quad (1b)$$

$$\ddot{\gamma} - [\Omega(1 - k_3) \tan \beta_0] \dot{\gamma} + (\Omega^2 k_3) \gamma + \frac{\Omega(1 - k_3)}{\cos \beta_0} \dot{\alpha} + (3\Omega^2 k_3 \sin \beta_0 \cos \beta_0) \alpha = -T \frac{x_2}{I_3} \tan \beta_0 - T \frac{x_2}{I_3} \beta - T \frac{x_1}{I_3} \alpha \quad (1c)$$

where  $k_1$ ,  $k_2$  and  $k_3$  are the inertia ratios

$$\begin{aligned} k_1 &= \frac{I_2 - I_3}{I_1} = .648 \\ k_2 &= \frac{I_1 - I_3}{I_2} = .406 \\ k_3 &= \frac{I_2 - I_1}{I_3} = .328 \end{aligned} \quad (2)$$

$\Omega$  the orbital angular velocity,  $T$  the tether tension, and  $\beta_0$  is given by the solution of the following equation:

$$T \frac{x_1 \cos \beta_0}{I_2} + T \frac{x_3 \sin \beta_0}{I_2} - 3\Omega^2 k_2 \sin \beta_0 \cos \beta_0 = 0 \quad (3)$$

which is the equilibrium between the tension and gravity gradient torques around the pitch axis.

Note that the pitch equation is decoupled from the roll and yaw equations.

## 2.2. Stability Analysis

If we neglect the roll-yaw coupling due to the tether, after Laplace transforming eqns. (1a) and (1c) for null initial conditions, we obtain the characteristic equation:

$$s^4 + \left[ (3k_1 \cos^2 \beta_0 + 3k_3 \sin^2 \beta_0 \cos \beta_0 + 1 + k_1 k_3) \Omega^2 - T \frac{x_3 \cos \beta_0}{I_1} + T \frac{x_1 \sin \beta_0}{I_3} \right] s^2 + \Omega^2 \left[ \Omega^2 k_1 k_3 (1 + 3 \cos^2 \beta_0) + 6 \Omega^2 k_1 k_3 \sin^2 \beta_0 \cos \beta_0 - k_3 T \frac{x_3 \cos \beta_0}{I_1} + k_1 T x_1 \left( \frac{1}{I_1} + \frac{\Omega^2}{I_3} \right) \sin \beta_0 \right] = 0 \quad (4)$$

Since  $\frac{\Omega^2}{I_3} \ll \frac{1}{I_1}$  in the previous equation, by applying the Routh-Hurwitz criterion[12] the conditions of yaw-roll stability can be derived:

$$\Omega^2 k_1 k_3 (1 + 3 \cos^2 \beta_0) + 6 \Omega^2 k_1 k_3 \sin^2 \beta_0 \cos \beta_0 - k_3 T \frac{x_3 \cos \beta_0}{I_1} + k_1 T \frac{x_1 \sin \beta_0}{I_3} > 0 \quad (5a)$$

$$\left( 3k_1 \cos^2 \beta_0 + 3k_3 \sin^2 \beta_0 \cos \beta_0 + 1 + k_1 k_3 \right) \Omega^2 - T \frac{x_3 \cos \beta_0}{I_1} + T \frac{x_1 \sin \beta_0}{I_3} > 2 \Omega \sqrt{\Omega^2 k_1 k_3 (1 + 3 \cos^2 \beta_0) + 6 \Omega^2 k_1 k_3 \sin^2 \beta_0 \cos \beta_0 - k_3 T \frac{x_3 \cos \beta_0}{I_1} + k_1 T \frac{x_1 \sin \beta_0}{I_3}} \quad (5b)$$

Eqns. (5) show that the end-mass attitude stability is a function of the inertia ratios, the tether tension torque, and  $\beta_0$ . The roll-yaw stability region in  $k_1 - k_3$  plane is shown in figure 2. The shaded area is the locus of the values of  $k_1$  and  $k_3$  that satisfy the roll-yaw stability condition. The angle  $\delta$  between  $k_1$ -axis and the line delimiting the stability area (Fig. 2) can be expressed as a function of the location of the tether attachment point as:

$$\delta \equiv \text{tg}^{-1} \left[ - \left( \frac{x_1}{x_3} \right)^2 \frac{I_1}{I_3} \right] \quad (6)$$

Notice that as  $x_1$  increases, the stability region moves toward the right half plane as  $\delta$  goes to  $-\frac{\pi}{2}$ .

The Pitch stability condition is:

$$3\Omega^2 k_2 \cos\beta_0 - 3\Omega^2 k_2 \sin^2\beta_0 - T \frac{x_3}{I_2} \cos\beta_0 + T \frac{x_1}{I_2} \sin\beta_0 > 0 \quad (7)$$

Under the assumption of small angles, conditions (5) and (7) are satisfied and the payload attitude dynamics is then stable.

### 3. Numerical Model

The attitude dynamics of SEDS' end mass has been simulated numerically. Both end-platforms and tether are modelled as lumped masses connected by massless spring-dashpots systems[13]. The motion of the system is described with respect to an orbiting reference frame (ORF) that rotates at constant orbital rate  $\Omega_0$  and radius  $R_0$ . The origin of this frame coincides with the initial position of the system center of mass. The  $x_o$ -axis is along ORF velocity vector, the  $z_o$ -axis is along the local vertical toward the Earth, and the  $y_o$ -axis completes the right-handed reference frame[13]. The external perturbations considered in this analysis are the tether tension, the gravitational force, including the second zonal harmonic of the gravity field, and the aerodynamic forces.

The payload attitude dynamics is computed by integrating the Kinematics and Euler equations as follows:

$$\begin{Bmatrix} \dot{\phi} \\ \dot{\theta} \\ \dot{\psi} \end{Bmatrix} = \frac{1}{\sin \theta} \begin{bmatrix} \sin \psi & \cos \psi & 0 \\ \cos \psi \sin \theta & -\sin \psi \sin \theta & 0 \\ -\sin \psi \cos \theta & -\cos \psi \cos \theta & \sin \theta \end{bmatrix} \begin{bmatrix} \omega_1 \\ \omega_2 \\ \omega_3 \end{bmatrix} \quad (8)$$

$$\begin{Bmatrix} \dot{\omega}_1 \\ \dot{\omega}_2 \\ \dot{\omega}_3 \end{Bmatrix} = I^{-1} \begin{Bmatrix} \bar{\delta}_1(\omega_1, \omega_2, \omega_3) \\ \bar{\delta}_2(\omega_1, \omega_2, \omega_3) \\ \bar{\delta}_3(\omega_1, \omega_2, \omega_3) \end{Bmatrix} + I^{-1} \begin{Bmatrix} N_1 \\ N_2 \\ N_3 \end{Bmatrix} \quad (9)$$

where  $I$  is the inertia matrix[12],  $N_i$  the external torques and

$$\begin{Bmatrix} \bar{\delta}_1(\omega_1, \omega_2, \omega_3) \\ \bar{\delta}_2(\omega_1, \omega_2, \omega_3) \\ \bar{\delta}_3(\omega_1, \omega_2, \omega_3) \end{Bmatrix} = \begin{bmatrix} I_2 - I_3 & -I_{12} & I_{13} & -I_{23} & 0 & 0 \\ I_{12} & I_3 - I_1 & -I_{23} & 0 & -I_{13} & 0 \\ -I_{13} & I_{23} & I_1 - I_2 & 0 & 0 & -I_{12} \end{bmatrix} \begin{Bmatrix} \omega_2 \omega_3 \\ \omega_1 \omega_3 \\ \omega_1 \omega_2 \\ \omega_3^2 - \omega_2^2 \\ \omega_1^2 - \omega_3^2 \\ \omega_2^2 - \omega_1^2 \end{Bmatrix} \quad (10)$$

The unknowns in the above equations are the Euler's angles  $(\phi, \theta, \psi)$  of the body axes (1-2-3) with respect to an inertial reference frame (IRF) X,Y,Z and the body-frame components of the inertial angular velocity vector  $(\omega_1, \omega_2, \omega_3)$ .

The Euler's angles are defined as a 3-1-3 rotation sequence of the body frame with respect to IRF, whose origin is located at the Earth's center with the X axis pointed toward the Vernal Equinox, the Z axis pointed toward the North pole and the Y axis completes the right handed reference frame.

The torques are computed taking into account the tether visco-elastic force and the gravity gradient. The payload yaw, pitch and roll angles are then evaluated by using transformation matrices[7].

#### 4. Numerical Results

The simulation starts with the payload deployment from Delta second stage at the apogee (716 km) of an orbit with inclination of 34 deg and perigee of

202 km. At the beginning of the deployment the payload is ejected with an initial velocity of about 1.6 m/s.

The tension at the deployer, the deployed length and the deployment rate are shown in Fig.3.

Payload pitch, roll and yaw angles are shown in Figs. 4-6. Large attitude oscillations start as soon as the payload is ejected. Moreover, tumbling is observable around roll and yaw axes. From our previous analysis we can deduce that this dynamics is mainly caused by the initial phase of the deployment. The low-tension deployment is unable to provide enough restoring torque. Despite the increasing tension payload tumbling around roll and yaw axes is observable throughout the whole deployment.

## 5. Tumbling analysis

In this section we analyze the influence of the initial conditions (see Tab. 2) on the payload tumbling.

With reference to Fig. 7, we limit our analysis to the payload's rotation in the (x-z) plane. Since the variation of the payload's rotational energy must be balanced out by the work done by the external torques, we can write:

$$\int_{t_0}^t (\vec{M} \cdot \vec{\dot{\theta}}) dt = E_{c,t} - E_{c,t_0} \quad (11)$$

where  $\vec{M}$  represents the external torques,  $\vec{\dot{\theta}}$  the angular rate in the (x-z) plane and  $E_{c,t_0}$  and  $E_{c,t}$  the payload rotational energy at  $t_0$  and  $t$ , respectively. In our case eq. (11) becomes:

$$\frac{I_1}{2} (\dot{\theta}^2 - \dot{\theta}_0^2) = Tb [\cos\theta_1 \sin\theta + (1 - \cos\theta) \sin\theta_1] \quad (12)$$

where  $\dot{\theta}_0$  is the initial angular rate, and  $\theta_1$  and  $b$  (Fig. 7) are given by:

$$b = \sqrt{x_2^2 + x_3^2} \quad (13a)$$

$$\theta_1 = \sin^{-1} \left( \frac{|x_2|}{\sqrt{x_2^2 + x_3^2}} \right) = 9.3(\text{deg}) \quad (13b)$$

By substituting eqs. (13) in eq. (12) we obtain:

$$\dot{\theta}^2 = \dot{\theta}_0^2 - 2 \frac{T}{I_1} [ |x_3| \sin \theta + |x_2| (\cos \theta - 1) ] \quad (14)$$

By assuming  $\dot{\theta}_0 = 0$ , the maximum amplitude of the payload rotation can be computed by setting  $\dot{\theta} = 0$ . Then we have:

$$\theta = \pi - 2\theta_1 \quad (15)$$

Therefore, in our case the initial value of  $\bar{\theta}$ , determined by the initial conditions of the deployment and the tether tension, causes large attitude oscillations of the payload. Furthermore, this analysis did not take into account the roll-yaw coupling which also affects the amplitudes of the payload attitude angles.

## 6. Attitude Stabilization

Our analysis shows that some attitude stabilization must be introduced in order to avoid tumbling. Considering the low-tension deployment strategy and the payload design, a displacement of the tether attachment point appears to be the simplest solution to adopt. Since the payload tumbling is limited to the roll and yaw axes (1 and 3 axes, respectively), the tether attachment point can be moved along the 2-axis to provide the required stabilization by increasing the tether restoring torque. With reference to fig.7, by applying the work and energy principle, the following expression of  $x_2$  can be obtained:

$$|x_2| = -\left(\frac{\sin\theta}{(1-\cos\theta)}\right)|x_3| - \frac{I_1}{2T} \frac{(\dot{\theta}^2 - \dot{\theta}_0^2)}{(1-\cos\theta)} \quad (16)$$

Figure 8 shows  $|x_2|$  for different amplitudes of the roll angle given an initial roll rate ( $\dot{\theta}_0=2.7$  deg/s). Considering the physical dimensions of the end mass an appendix can be used to provide the desired displacement of the tether attachment point toward the negative direction of the pitch axis.

The numerical analysis shows that the solution is effective in stabilizing the satellite around both roll and yaw axes.

In the following simulation we have chosen  $|x_2|=11\text{cm}$  which gives a roll amplitude of about 120 deg. Given the actual configuration of the end mass the length of the appendix is 5 cm.

Figures 9 and 10 show the roll and yaw angles of the payload when the appendix is introduced. Due to the increased restoring torque, no more tumbling is observable around roll and yaw axes except at the end of the deployment when the tether goes slack. This can be avoided by controlling the tension in order to bring the payload to a smoother stop.

The displacement of the tether attachment point along the body 2-axis causes the roll angle to oscillate around a large mean value (Fig. 9) which actually limits the length of the appendix. Therefore, although the appendix is effective in avoiding the payload tumbling, it does not satisfy more stringent attitude requirements.

## 7. Conclusions

The attitude dynamics and stability of the payload of the Small Expendable Tether Deployment System have been analytically and numerically studied. The analysis has considered the first nominal mission as reference case.



Our study showed that the end-mass attitude stability is strongly affected by the initial conditions of the deployment: tumbling around roll and yaw axes starts as soon as the payload is ejected from Delta Second Stage.

The introduction of a rigid appendix at the tether attachment point is effective in stabilizing the payload attitude dynamics. Nevertheless, if SEDS is used to deploy platforms with scientific instruments only very long appendices allow more stringent attitude requirements to be satisfied. Therefore, considering that the payload's reduced dimensions cannot accomodate inertia wheels and/or a mobile tether attachment point, different control techniques must be considered; such as:

- rigid appendices and viscous dampers;
- gas jets;
- drag stabilization.

The authors will focus their research on these issues by refining the attitude dynamics model.

## **Acknowledgements**

Mario Cosmo's work has been supported by NASA/MSFC contract NAS8-36606. The authors would like also to thank NASA/LaRC, the Smithsonian Institution, and the Italian Ministry for University and Research for the support provided.

## References

1. E.C. Lorenzini and J.A. Carroll, In-Orbit Experimentation with the Small Expendable-Tether Deployment System. *ESA Journal*, **15**, 27-33 (1991).
2. J.A. Carroll, The Small Expendable Deployment System (SEDS). Conference Proceedings, Space Tethers for Science in the Space Station Era, Venice, Italy, pp.43-50(1987).
3. K.J. Harrison, C.C. Rupp, J.A. Carroll, C.M. Alexander and E.R. Small Expendable-Tether Deployment System (SEDS) Development Status. Conference Proceedings, Tethers in Space-Toward Flight, San Francisco, CA, pp.19-26(1989).
4. R. DeLoach, J. Diamond, T. Finley and R. Rhew, End-Mass Instrumentation for First SEDS/Delta-II Mission. Proceedings of the AIAA 28th Aerospace Sciences Meeting, (Paper AIAA-90-0537), Reno, Nevada (1990).
5. J.A. Carroll, Users Guide to SEDS, The Small Expendable-Tether Deployment System. Tether Application, La Jolla, Calif (1990).
6. W.J. Webster, Engineering Tethered Payloads for Magnetic and Plasma Observations in Low Orbit. *Journal of Spacecrafts and Rockets*, **26**, 80-84(1989)
7. S. Vetrella, A. Moccia, E.C. Lorenzini and M.L. Cosmo, Attitude Dynamics of the Tether Elevator/Crawler System for Microgravity Applications. *ESA Journal*, **14**, 303-312(1990).
8. R. Fan and P.M. Bainum, Dynamics and Control of a Space Platform with a Tethered Subsatellite. *Journal of Guidance, Control and Dynamics*, **4**, 377-381(1988).
9. A. Moccia and S. Vetrella, Dynamics and Control of Two Space Platforms Connected by a Short Tether. Conference Proceedings, Space Tethers for Science in the Space Station Era, Venice, Italy, pp.104-110(1987).

10. F. Venditti, B. Cibario and B. Musetti B, Dynamics Simulation of the TSS actively Controlled Satellite. Conference Proceedings, Space Tethers for Science in the Space Station Era, Venice, Italy, pp.116-129(1987).
11. L.G. Lemke, J.D. Powell and X. He, Attitude Control of Tethered Spacecraft. *J. of the Astronautical Science*, 1, 41-55(1987).
12. L. Meirovitch, *Methods of Analytical Dynamics*, pp. 222-224. McGraw-Hill Publishing Company, New York, U.S.A. (1970).
13. E.C. Lorenzini M.L. Cosmo, S. Vetrella and A. Moccia, Dynamics and Control of the Tether Elevator/Crawler System. *Journal of Guidance, Control and Dynamics*, 3, 404-411(1989).

## **Figure and Table captions**

Fig.1. Schematic representation of SEDS's payload when attached to Delta Second Stage (a) and during deployment (b).

Fig.2. Roll-yaw stability region.

Fig.3. Tether tension, length and length rate during SEDS deployment.

Fig.4. Payload pitch angle versus time.

Fig.5. Payload roll angle versus time.

Fig.6. Payload yaw angle versus time.

Fig.7. Schematic of payload's roll rotation.

Fig.8. Displacement of tether attachment point on pitch axis versus roll angle.

Fig.9. Payload's roll angle versus time with appendix.

Fig.10. Payload's yaw angle versus time with appendix.

Tab.1. Payload inertia characteristics and body coordinates of tether attachment point.

Tab.2. Deployment initial conditions.

Tab.1 Payload inertia characteristics and body coordinates of tether attachment point.

$I_1(\text{kg} - \text{m}^2)$	.372
$I_2(^{\circ})$	.436
$I_3(^{\circ})$	.195
$I_{12}(^{\circ})$	.005
$I_{13}(^{\circ})$	-.011
$I_{23}(^{\circ})$	.022
$x_1(\text{m})$	-.184
$x_2(^{\circ})$	-.027
$x_3(^{\circ})$	-.165

Tab.2 Deployment initial conditions

angular rates(deg/s) :	
$\omega_1$	2.701
$\omega_2$	0.120
$\omega_3$	-3.168
ejection velocity(m/s)	1.6

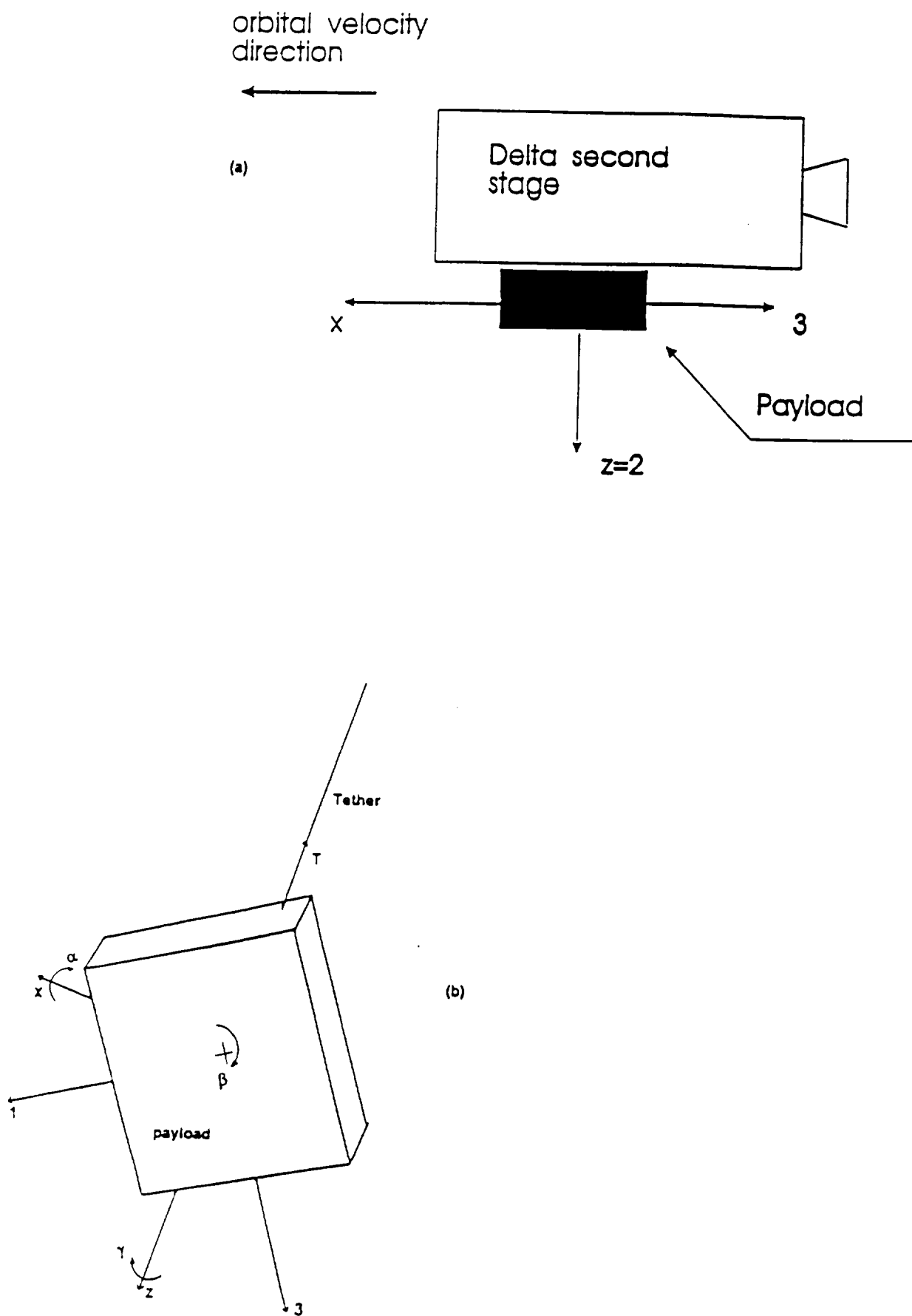


Figure 1

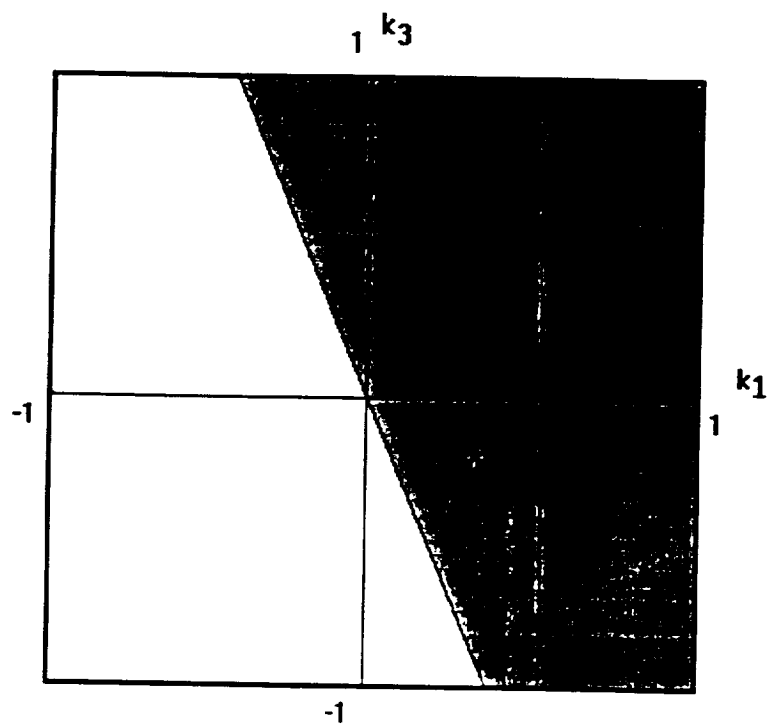


Figure 2



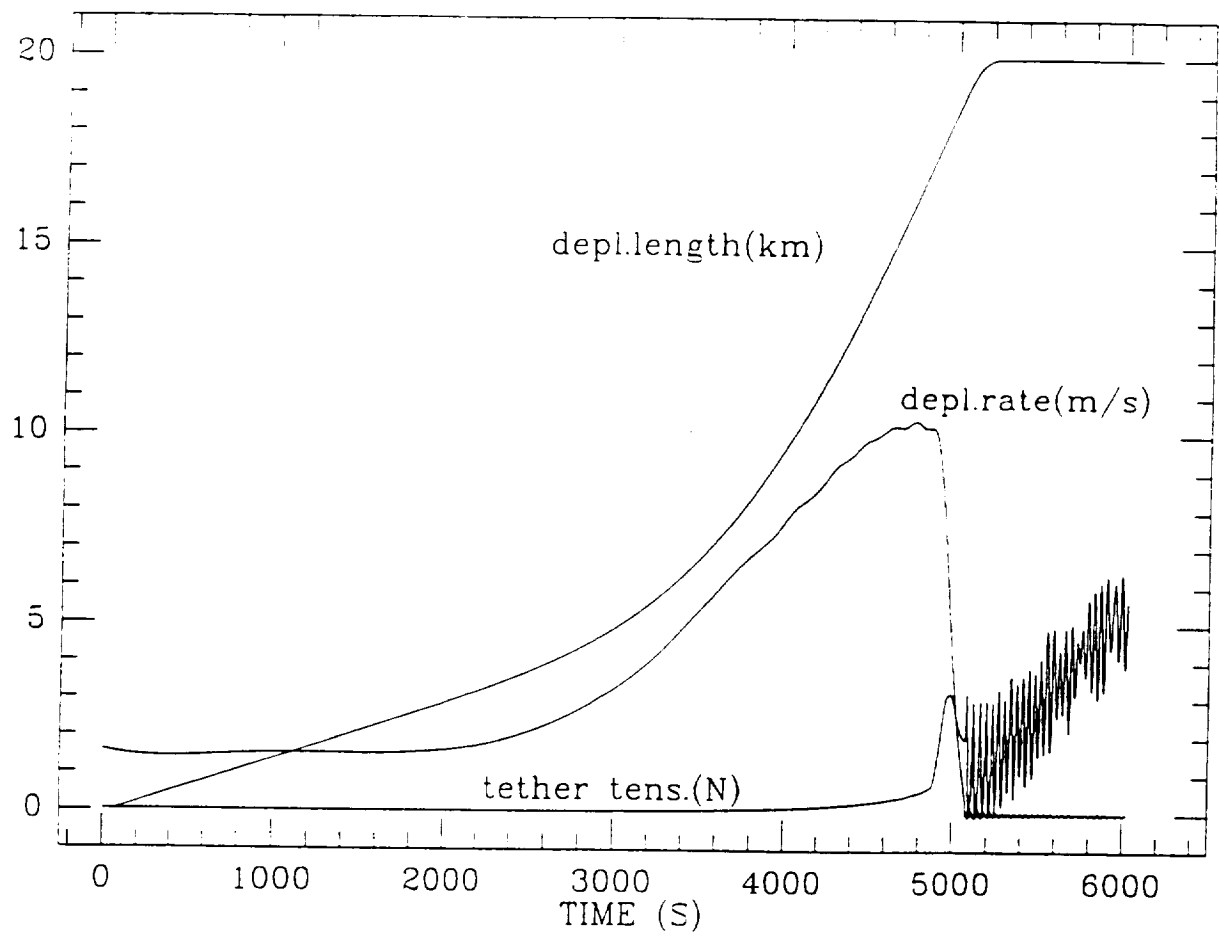


Figure 3

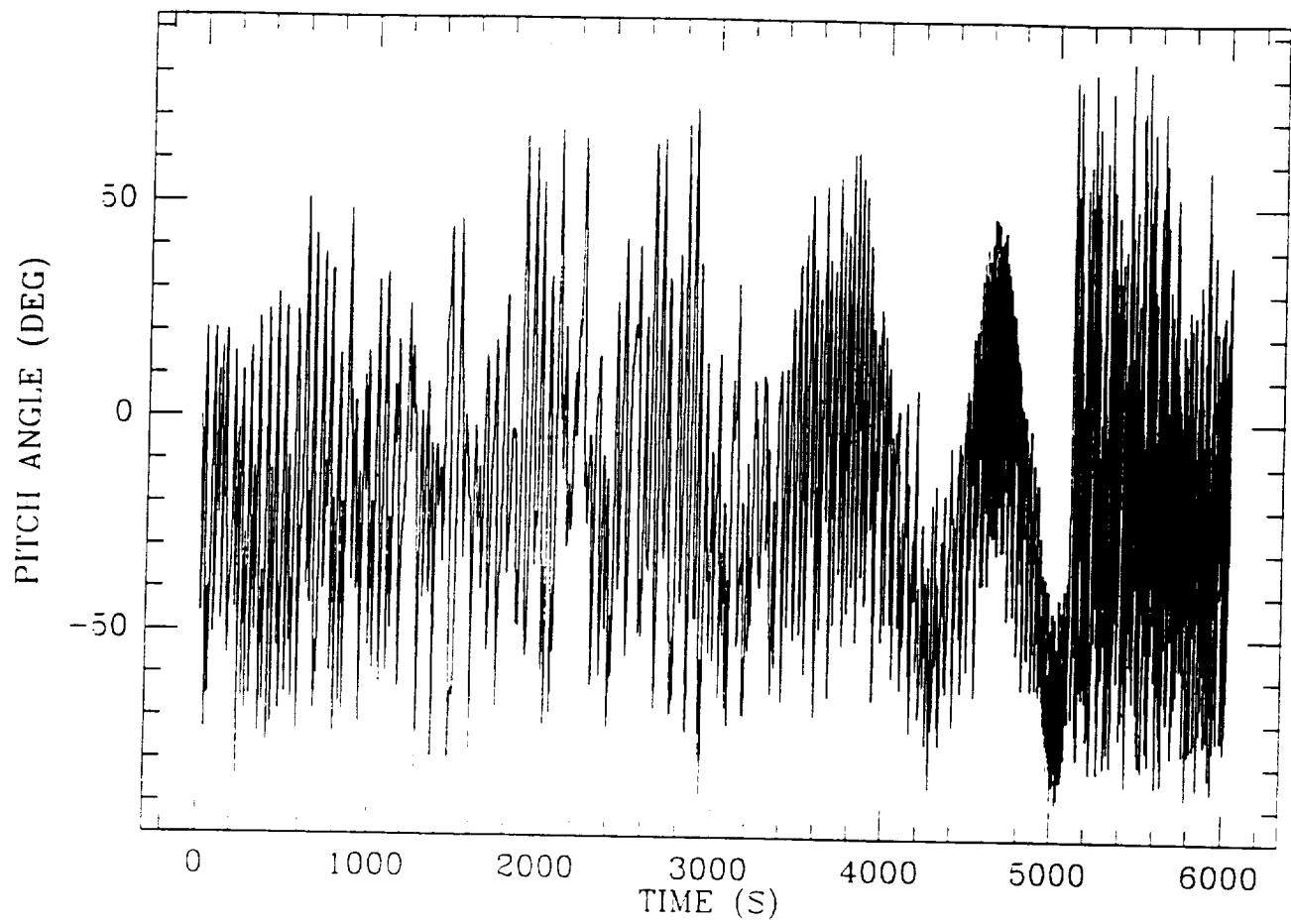


Figure 4

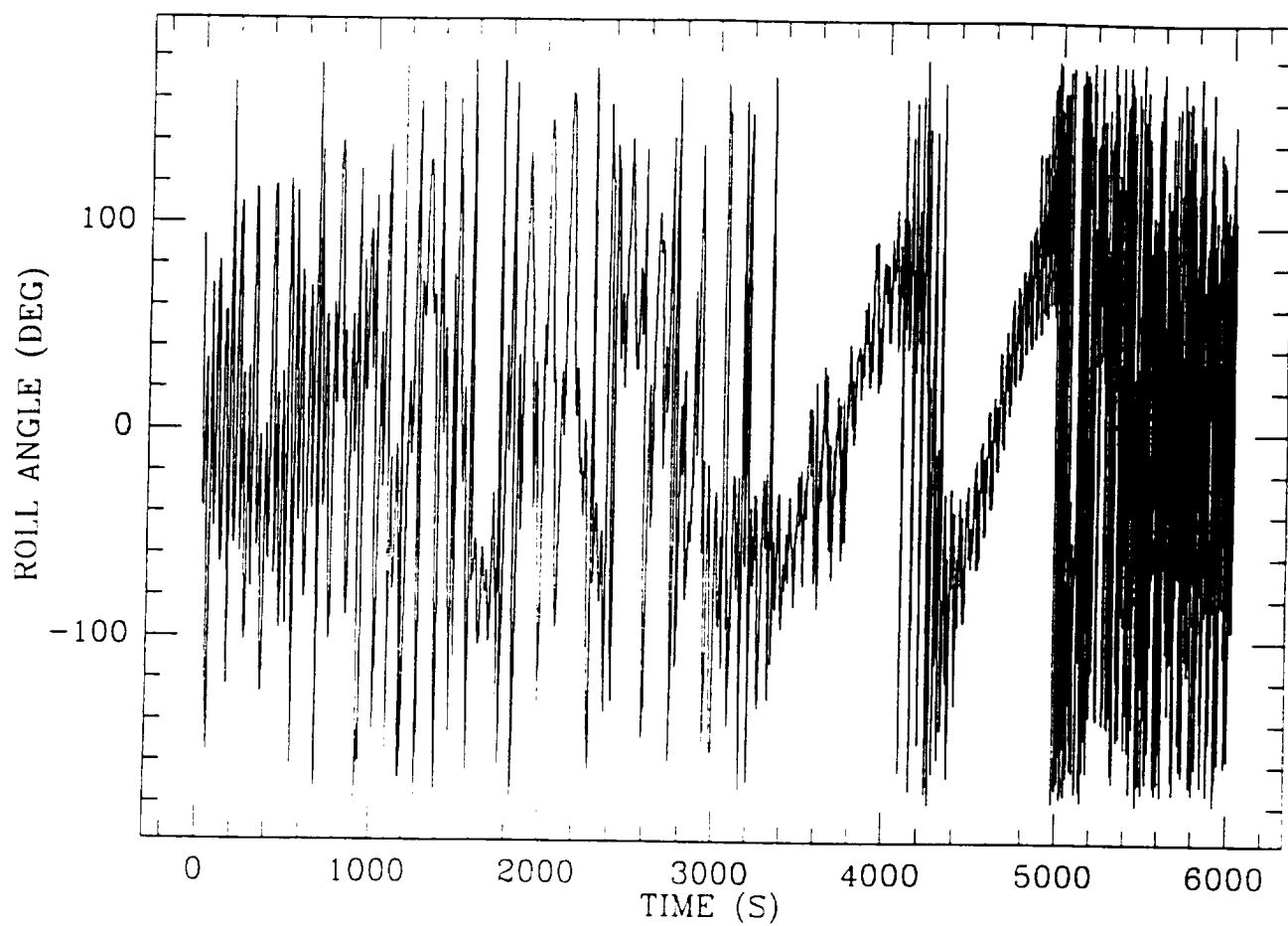


Figure 5

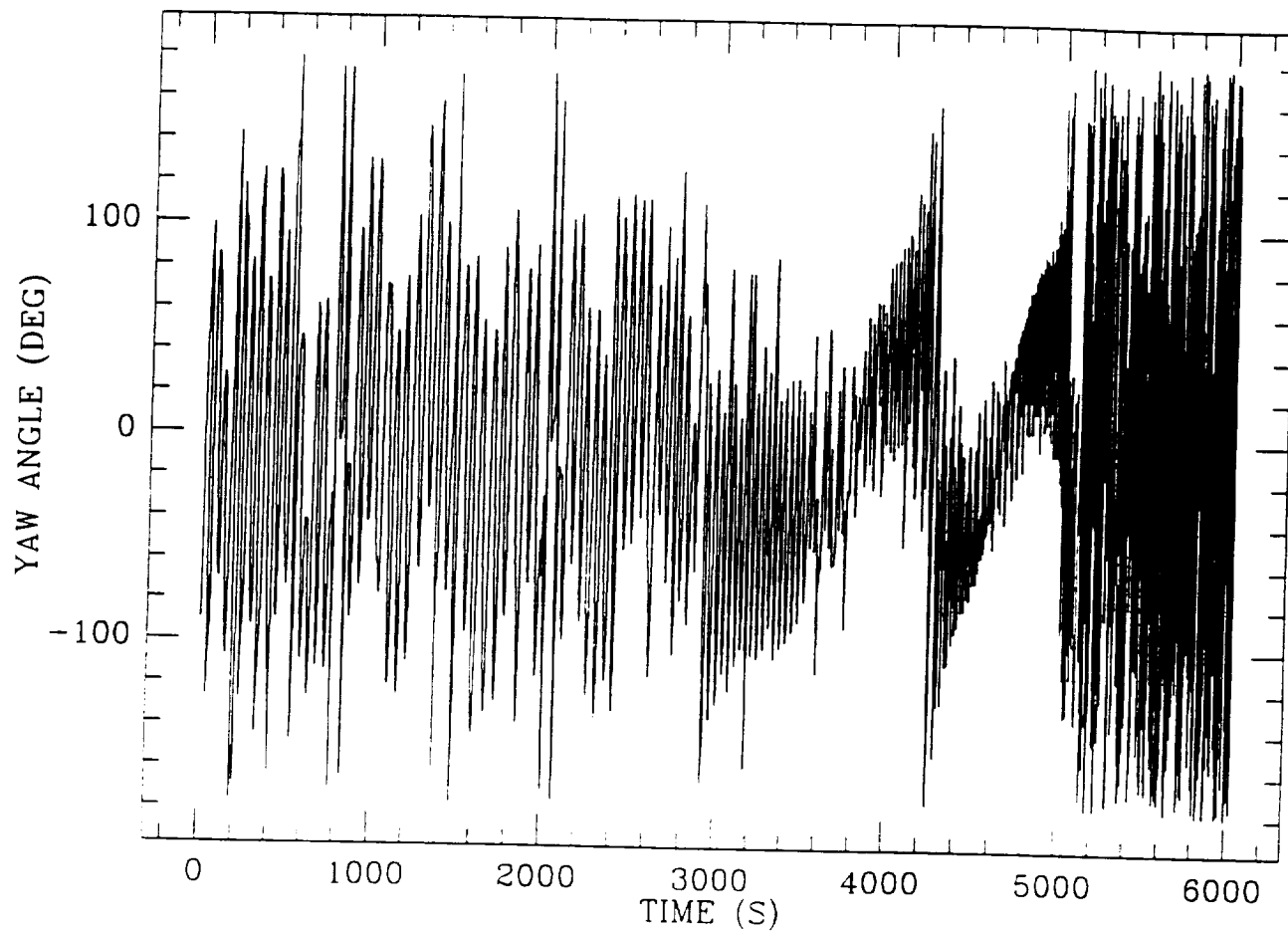


Figure 6

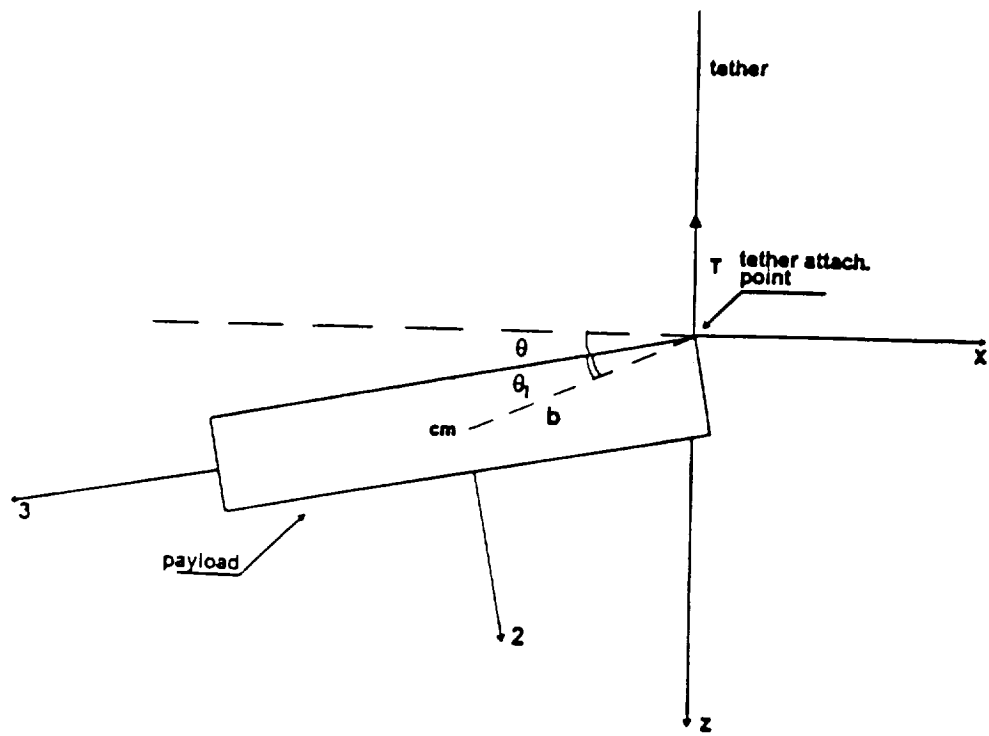


Figure 7

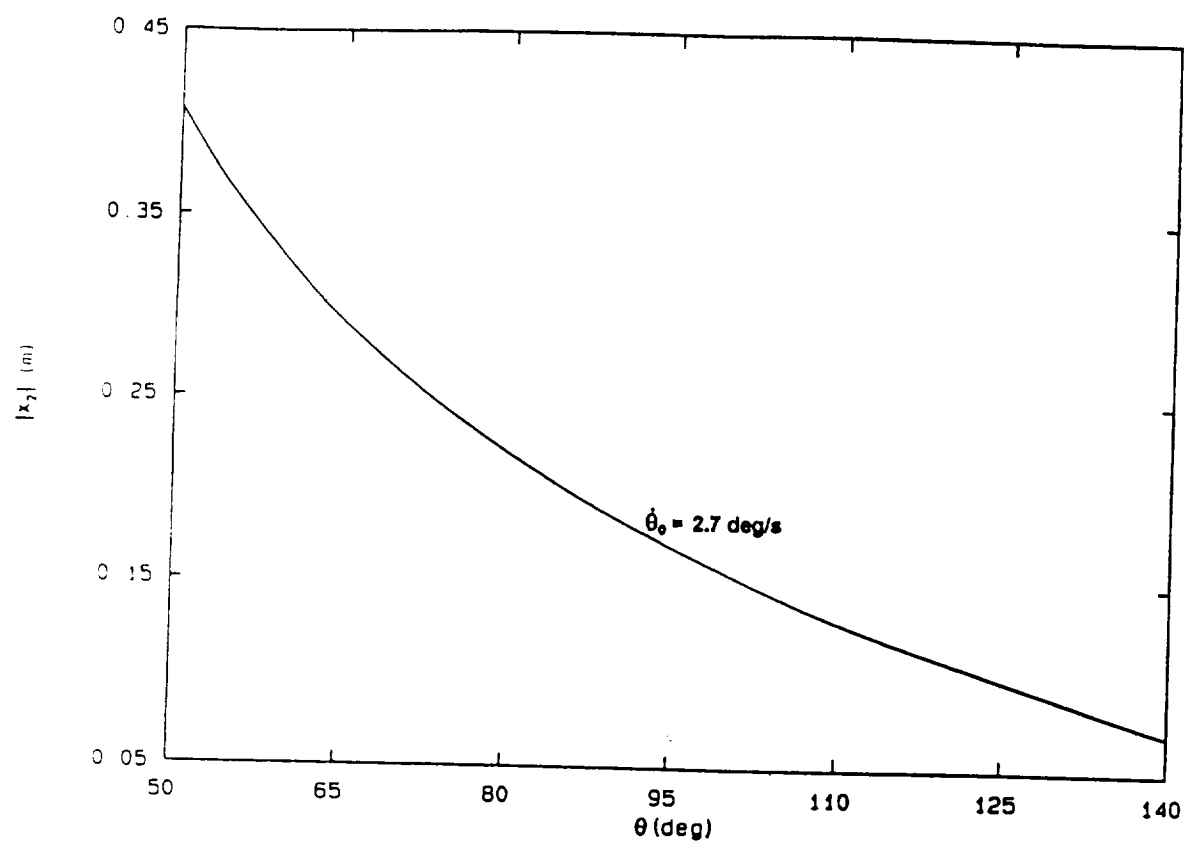


Figure 8

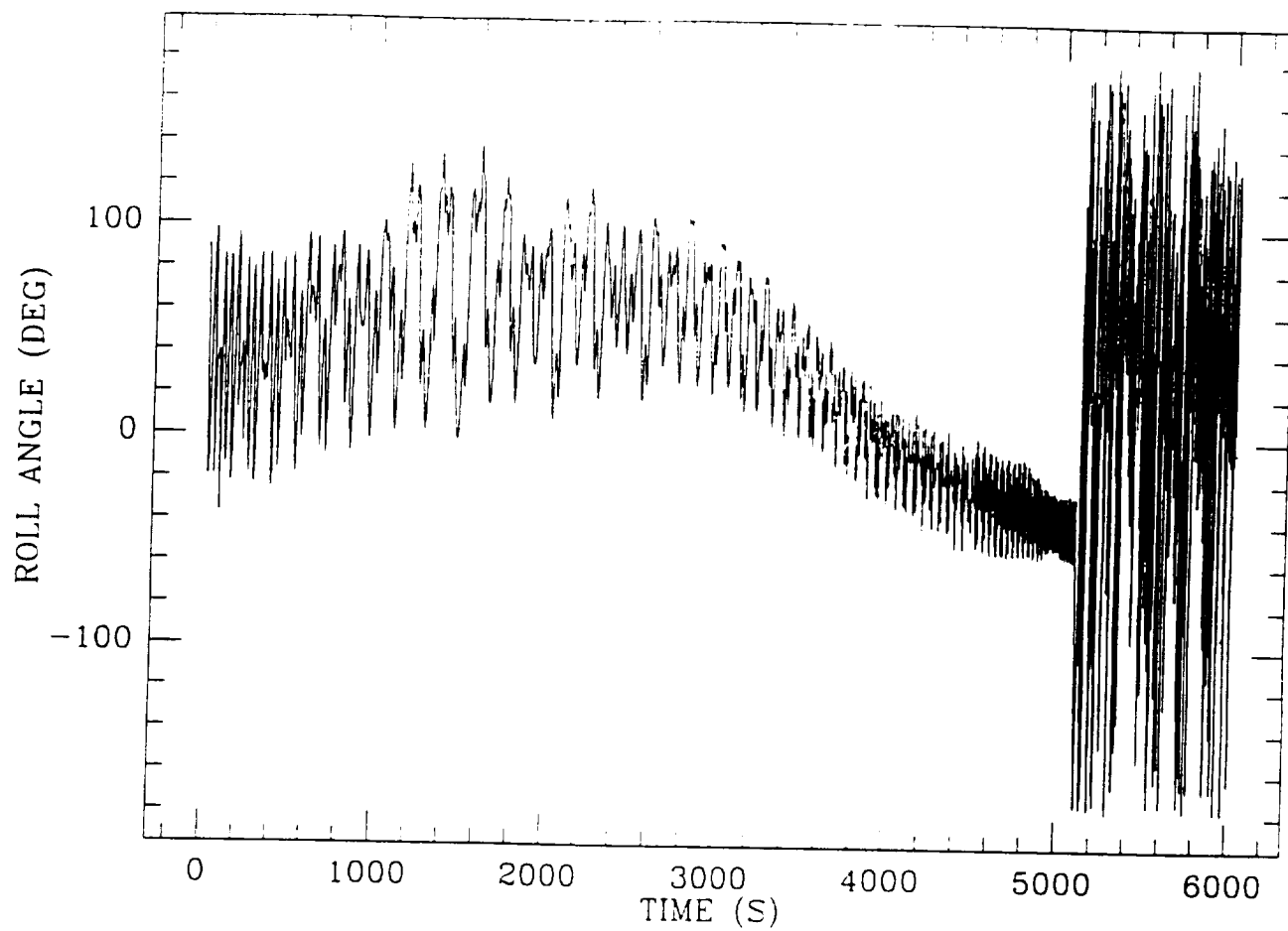


Figure 9

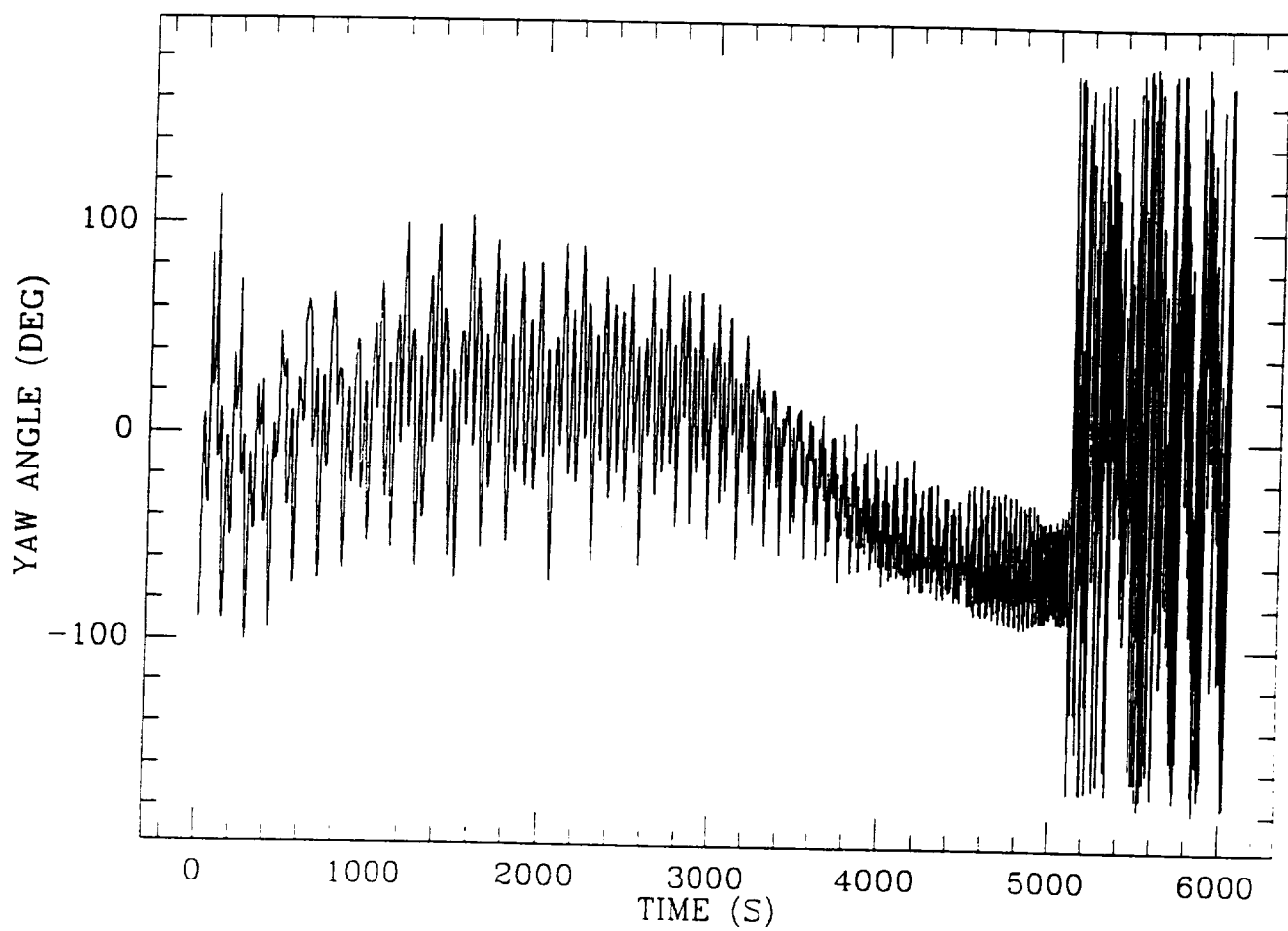


Figure 10



## 10.0 ANALYSIS OF SEDS-I FLIGHT DATA

### Figure Captions

Fig. 10.1	SEDS-1 Magnetic field modulus
Fig. 10.2	Magnetic Field Modulus corrected for bias
Fig. 10.3	Scalar product of reference and measured unit vectors
Fig. 10.4 a-c	End-mass angular rates components
Fig. 10.5 a-c	End-mass angular accelerations components
Fig. 10.6 a-c	Difference between computed and flight angular acceleration components
Fig. 10.7	Load Cells Angular Accuracy
Fig. 10.8	Magnetometer Angular Accuracy
Fig. 10.9	Angular estimation accuracy
Fig. 10.10	Angle between x and y load cells components
Fig. 10.11	x,y and z magnetometer components
Fig. 10.12 a-c	End-mass Euler angles vs. time
Fig. 10.13 a-b	FFT of load cells and accelerometer x and z component
Fig. 10.14 a-b	FFT of load cells and magnetometer x and z component
Fig. 10.15	SEDS-1 theoretical modes frequency vs deployed length.
Fig. 10.16a-b	Comparison of best fit simulation with flight data: length and length rate.

## 10.1 Introduction

The estimation of the SEDS-1 end-mass orientation has been a major undertaking of our investigation. The payload was equipped with a three-axis magnetometer and three-axis tensiometer to measure the orientation with respect to the geomagnetic field and the line connecting the two end-mass, respectively.

As it will be shown in the following, the use of the load cells as attitude sensor and the lack of a third attitude sensor (e.g. horizon sensor, sun sensor, gyro package, etc.) is the limiting factor in getting a complete picture of the whole SEDS-1 mission as well as on the accuracy of estimated results. The lack of redundancy also puts a limit on the observations. Namely, if the tether was slack or the tether line was parallel to the Earth's magnetic field the end-mass orientation could not be computed.

The accuracy of attitude measurements is affected by the following sources of error:

- Error in the orbital state of the payload affecting inertial orientation of the line connecting the two end-masses and to a lesser degree computation of the Earth's magnetic field
- Error due to the natural angular displacement from the line connecting the two end-masses due to the tether bowing. This is particularly true when the tension is low, or the payload goes through phases of slack and taut tether.

Also, the tether curvature is not an observable with the SEDS instrumentation.

The direction of the line connecting the end-masses is strictly dependent on our ability in simulating SEDS-1 deployment and whenever the tether is not slack. Therefore we have limited our analysis to the first 4604 seconds of the mission before the load cells went out of range for the first time. After the brake was applied to the last hundred meters of tether, the end-mass reached an abrupt stop going through phases of bouncing before being cut and reentering into the atmosphere. The accuracy of our simulations could be checked only during the deployment since we have the data of the turn counter to produce length and length rate time profiles.

Another problem that was encountered was that the magnetometer modulus showed a high frequency (1 to 2 minutes) variation around the reference profile (e.g. Earth magnetic field model), as shown in figure 10.1. After several hypotheses SEDS IWG suggested that

this variation could be caused by a dipole moment inside the end-mass even though the cause for the bias is not clear yet. Moreover from preliminary discussions it seems that the same kind of problem has affected SEDS-2 end-mass magnetometer. To the moment of this writing there is no direct evidence of the cause of the bias, however we hope to clarify this issue soon.

Therefore we treated the magnetometer data as affected by a bias and we applied our least-square bias estimator obtaining the following results

$$\text{Bias X} = 31.8 \text{ mGauss} \quad \text{Bias Y} = -34.04 \text{ mGauss} \quad \text{Bias Z} = -43.17 \text{ mGauss}$$

$$\text{Bias Modulus} = 63.5 \text{ mGauss}$$

The modulus of the magnetometer signal corrected in this way is shown in figure 10.2

## 10.2 Data Check and Validation

In this scenario it became clear to us that a series of tests to validate and check the flight data was as important as estimating the attitude itself. One straightforward test was to compare the signal of the load cells to the accelerometers, the major difference being the rotational acceleration terms. We carried out this test by Fourier transforming the load cells and accelerometers data and then comparing the harmonic content. Since, the data were time-varying we divided the time series in short subsets and then applied the FFT routine.

Another test we run consisted in comparing the scalar products of the reference and the measured unit vectors. Within the limitations of our hypotheses on the measurement and modeling errors the angle between the reference fields should be similar to the angle subtended by the measured fields. The result of this test is shown in figure 10.3. The general agreement is quite evident. The oscillations between 1000 and 300 seconds as well as the offset after 4000 seconds are mainly due to the angular displacement between the tangent to the tether and the line connecting the two end-platforms. Moreover we noticed that some high frequency oscillations of the magnetometer original data were not completely removed even after being treated for a bias.

Unfortunately, there was no straightforward test to compare the magnetometer output with. To this end we computed the angular body rates using the load cells and magnetometer data and then computed the angular accelerations. These acceleration can then be compared to the signal of the accelerometers. Details of the algorithms are given in

the Quarterly Report #33/34. We limit ourselves to show the angular rates, the angular accelerations and the residuals  $\delta$  given by:

$$\delta = \underline{A} - \underline{T}/M - \underline{A}_c - \underline{A}_t$$

where  $\underline{A}$ ,  $\underline{T}$ ,  $M$  are the accelerometer signal, the load cells signal and the EMP mass respectively and  $\underline{A}_c$  and  $\underline{A}_t$  are the estimated centrifugal and tangential accelerations.

This test, however, has some limitations, namely:

A) The only external perturbation acting upon the end mass is the tether tension. This is true at the beginning and at the end of the deployment when the end-mass is at apogee.

B) The end-mass rotates around its center of mass. This is true when the tether tension is low.

C) The angular derivatives are computed using the Euler equations assuming that the end-mass axis are principal axes. This limitation, though, can be removed easily in a second order of approximation by introducing the other inertia terms.

The angular rates are shown in figure 10.4(a-c) and the comparison between flight angular accelerations and estimated accelerations are shown in figure 10.5(a-c). The residuals  $\delta$  are shown in figure 10.6(a-c). The agreement between flight and estimated angular acceleration is generally good and, as expected, the match is poor at the beginning after ejection and when the tension ramps up. The rms values of the residuals  $\delta$  for the whole data set are:

$$\delta_x = 0.00017 \text{ m/s}^2 (= 0.0044 \text{ N})$$

$$\delta_y = 0.00029 \text{ m/s}^2 (= 0.0075 \text{ N})$$

$$\delta_z = 0.00025 \text{ m/s}^2 (= 0.0065 \text{ N})$$

The maximum residual values are at the end of the deployment and are of the order of  $0.001 \text{ m/s}^2$ .

This test is also highly sensitive to the load cells data. While processing and calibrating the flight data NASA/LaRC noticed that the load cells were affected by a time varying bias depending on the temperature. As a matter of fact, when we processed the data for the first time we noticed that the residuals followed closely the temperature variation.

Ray Rhew of NASA/LaRC provided us with an improved version of the load cells data and the final results are shown in this report.

### **10.3 Covariance Analysis**

By assuming that the magnetometer data were affected only by a bias, the accuracy of the end-mass orientation was mostly affected by the load cells performance as angular sensor. Figures 10.7 and 10.8 show the angular accuracy of the load cells and magnetometer, respectively. As expected the angular accuracy of the load cells plays a major role during most of the deployment since the tension is low. As soon as the tension increases the accuracy ( $1\sigma$ ) improves. Figure 10.9 shows the accuracy in estimating the Euler angles as given by the covariance analysis.

### **10.4 End-mass Orientation**

The orientation of the end-mass was estimated with the QUEST and TRIAD algorithms. Even though the covariance analysis did not show a good accuracy in the estimation, we still tried through physical reasoning to get the picture of the end-mass attitude dynamics and orientation's time-history.

Figure 10.10 shows the angle between load cells x and y as compared to the angle in the x-y plane of the tether attachment point. As the figure shows the end-mass tends to align itself with the tether line. As the time progresses and the tension increases the amplitudes of the oscillations decrease. The other interesting result is that, by looking at the magnetometer data, the three components show a peak-to-peak oscillation at the same frequency, as shown for a short portion of the deployment in Figure 10.11. From a FFT analysis this frequency is "seen" only by the magnetometer and it is the same frequency that showed up in the original magnetometer modulus. Provided that the magnetometer was only affected by the dipole moment, we can assume that the end-mass was spinning throughout the whole deployment around the tether. Since it was an almost constant spin it did not appear in the accelerometer being the DC value and it did not appear in the load cells signal because it could be not detected. We checked this possibility with John Glaese and after some discussions and numerical simulations we agreed that this scenario was plausible. It was also emphasized that the last part of the tether, the "shrink-wrap" section played a major role in damping out the oscillations perpendicular to the tether line. On the other end, rotations about the tether line cannot be damped since there is no restoring torque and it seems plausible that the end-mass initial energy, picked up during ejection, spilled into that degree of freedom.

Even though it is hard to visualize the orientation of a body, for the sake of completeness we are including the three plots of the Euler angles in figure 10.12(a-c). The Euler representation assumes a 3-1-3 rotation sequence of the body frame with respect to the inertial frame. The end-mass spinning is quite evident. As expected, QUEST and TRIAD produced the same results.

### **10.5 Data Analysis and Validation: An Example**

Physical considerations have helped us in the analysis and validation of SEDS-1 data. In the following we will give an example of the type of analysis we have done during the course of the study.

The data set under consideration spans from 3580 to 4092 seconds. Load cells and accelerometers are averaged at 1 second to compare their signal with the magnetometer.

Figures 10.13(a-b) and 10.14(a-b) show the comparison of the FFT analysis of the X and Z components of the load cells and accelerometer and load cells and magnetometer, respectively. The three FFT are shown in the same scale being divided by their highest peak. The load cell and accelerometer comparison is quite direct since both measure the same dynamics. The agreement is quite evident on both axis. We also computed the theoretical frequencies of the tether system as shown in figure 10.15 versus tether length for the data set under consideration. The flight data show that the lateral frequencies and the pitch frequency are excited and are very close to the theoretical values. We call pitch the motion of a tethered platform around the z-axis ( $\simeq$  out of plane). The z component show two frequencies at about 0.7 and 0.9 Hz that appear also in the rotation rates. These are typical attitude frequencies but their theoretical derivation is not simple since in this case the small angles assumption is not valid. The FFT also show that the load cells worked well as strain sensors.

The comparison between load cells and magnetometer is not as direct as the previous one. Nonetheless both instruments measure the same rates of variation with respect to their respective reference fields. Therefore the frequency content of the signal is what matters not the peak of the harmonic. Both instrument show the same frequencies, the major and only difference being at the spin rate frequency in the magnetometer.

## 10.6 Conclusions

The analysis of SEDS-1 end-mass orientation has given interesting results even though with a low accuracy. The load cells have provided excellent results as strain sensors but their use as angular sensors is not very accurate. Too many assumptions on the orientation of the tether line have degraded the covariance of the estimated angles. The magnetometer, on the other hand, has shown an almost constant frequency suggesting a spin of the end-mass around the tether line. Unfortunately this spin cannot be checked for with other instruments.

We have carried a series of tests and computed the angular rates and the angular accelerations of the end-mass. All the tests agree, within our modeling and instruments' errors.

The final result of the estimation has a physical sense and confirms that, as expected, the attitude dynamics of SEDS-1 is a very complicated process. We hope that SEDS-2 flight data will provide us with some more data to answer some questions still open.

## 10.7 Pulse Propagation Analysis

Tethered systems are subject to disturbances at the end masses and, in exceptional circumstances such as a micrometeorite impact, in the body of the tether itself. Any such disturbance will excite vibratory modes of the system. If the disturbance is relatively brief, it can be profitable to think of it as generating an impulse or pulse propagating along the tether which can impact on the other end mass and be measured by instrumentation there. Both transverse (string like) and axial (column like) waves in the tether have similar formal descriptions, although transverse waves have little damping and travel much slower than axial waves. We concentrate on the transmission of axial disturbances.

Three attachments follow which summarize our work on this topic.

Paper One considers a system with one large end-mass (idealized as a fixed end) at which the perturbation takes place and a smaller end-mass whose response is desired. The tether is a uniform viscoelastic. Both the frequency and impulse response functions are given, the latter in terms of an inverse Laplace transform. An exact solution is given for the zero damping case, and numerical results plotted which include damping.

Paper Two (an appendix from Quarterly Report # 26) discusses a model in which an impulse propagates into a semi-infinite viscoelastic tether with no gravity gradient force and no secondary end mass. Numerical results are presented using a Laplace formalism.

Paper Three presents data from pulses generated as three mass enhancements embedded in the SEDS-1 tether were deployed. The broadening of the pulse is clearly seen, and is probably due to tether damping.

### 10.8 Fit of Simulation to Flight Data

The program MASTERDEP0 was used to perform a number of simulations of the SEDS-1 deployment. Parameters were varied and the end-mass trajectory compared to flight length and length-rate data. The best "fit" was judged visually and is presented here; for more details see Quarterly Report #33/34.

The deployer orbital parameters were provided by McDonnell-Douglas and John Glaese of Control Dynamics and were not varied.

The end-mass properties and initial conditions were also nominal, except that a slight increase in the ejection velocity (from 1.60 to 1.62 m/s, well within the expected range) gave a better fit to the tether velocity in the first part of deployment.

A tension control law provided by Joe Carroll was used:

$$T_{Dep} = [T_{Min} + J \rho A^{-\epsilon} (dl/dt)^2] K_{Br} K_{Ex}$$

$$K_{Br} = \exp(K_1 \tau)$$

$$K_{Ex} = \exp(K_2 \alpha)$$

where:

$T_{Min}$  = Minimum Deploying Tension (constant)

$J$  = Inertia Multiplier (constant, dimensionless)

$A$  = Relative ratio (dimensionless) =  $1 - A_{Sol} (L/L_{max})$

$L$  = Instantaneous length

$L_{max}$  = Maximum length to be deployed = 19940 m

$A_{Sol}$  = constant

$\epsilon$  = Constant

$\rho$  = Linear density

$dl/dt$  = Deployment rate



$\tau$  = Brake turns (a function of deployed length)

$\alpha$  = Angle between tether exit guide and tether

$K_1$  and  $K_2$  = friction coefficients = constants

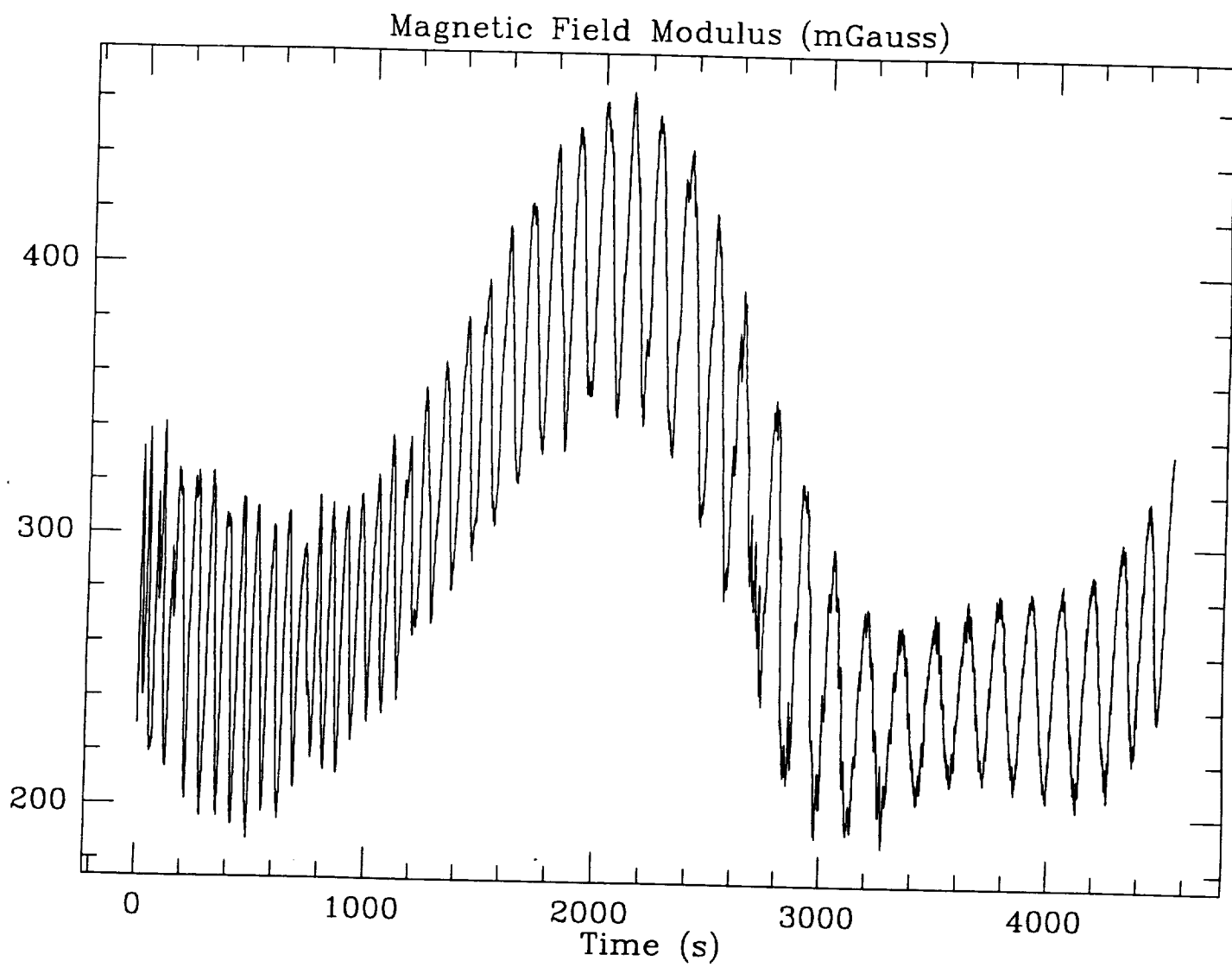
The brake is activated when about 18900 m of tether are deployed. The exit angle term influences the deployment for the first 3675 sec of deployment, then the deployer was aligned with the tether .

Numerous simulations led us to adopt brake parameters somewhat different from the nominal ones in the Design Reference Mission:

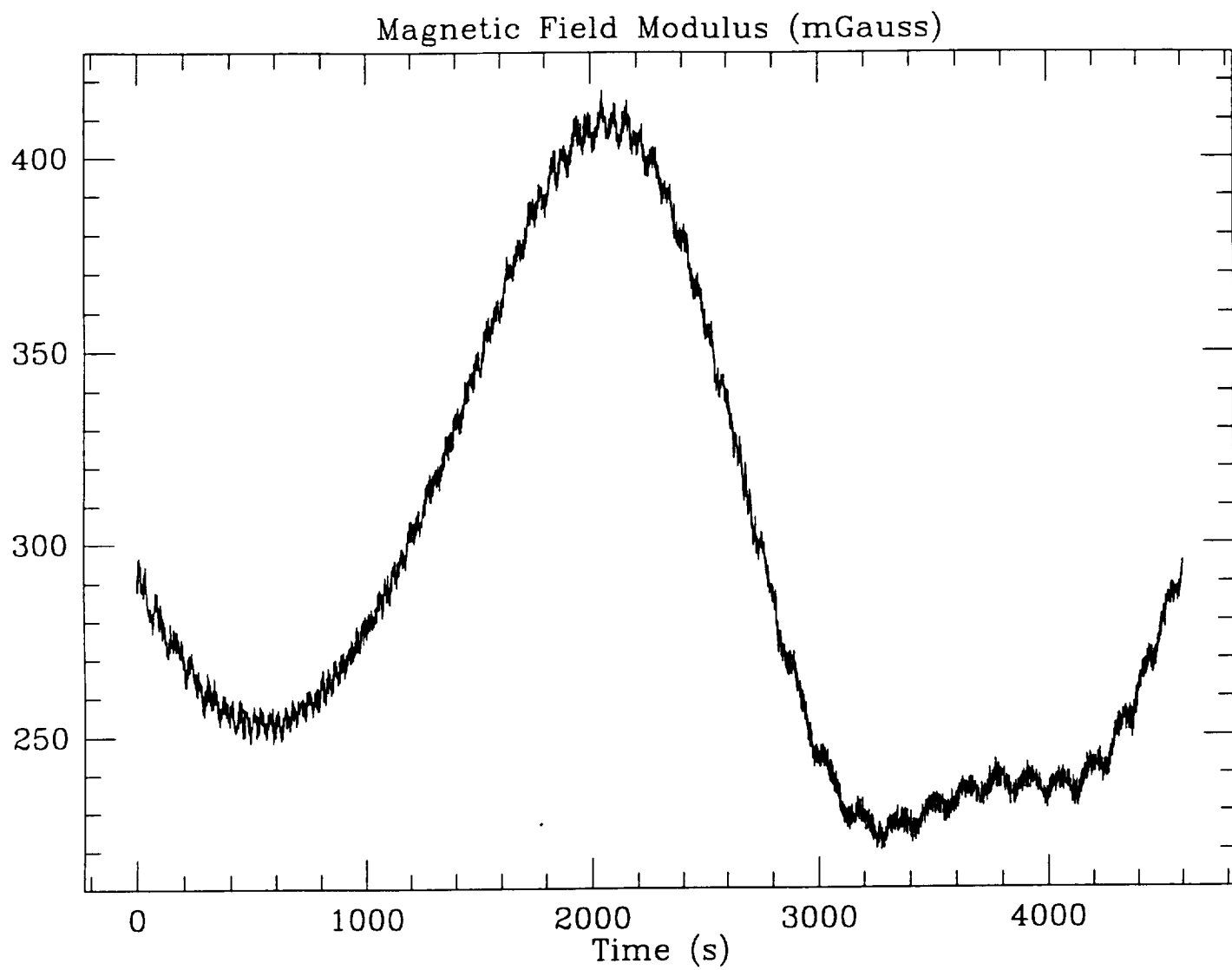
	Nominal	Final Fit
$T_{Min}$	0.028N	0.035N
J	3	5
$A_{sol}$	0.96	0.942
$\epsilon$	0.8	0.61
$K_1, K_2$	0.18	0.18

Figure 10.16a shows the tether deployed length compared to the flight data. The deployment at the beginning is slower. The deployed length is about 200 m shorter than the flight data. From perigee (~2800 s) up to 4000 seconds the fit is very satisfactory. Thereafter the numerical integration goes faster than the data reaching the final length of 19940 m 17 seconds earlier.

Figure 10.16b shows the deployment rate as compared to the flight data. Note that the fit is not very accurate at the beginning of the deployment yielding a maximum difference of 0.2 m/s lower than the data. The flight data show a linear decay of the velocity with respect to time. This also gives an error in the acceleration produced by the tension (see Eqs. 1). After perigee the numerical integration gives a faster deployment velocity (~0.3 m/s). Other measured quantities (magnetometer and load cell data) also show close agreement with the simulation; see Quarterly Report #33/34.



**Figure 10.1**



**Figure 10.2**

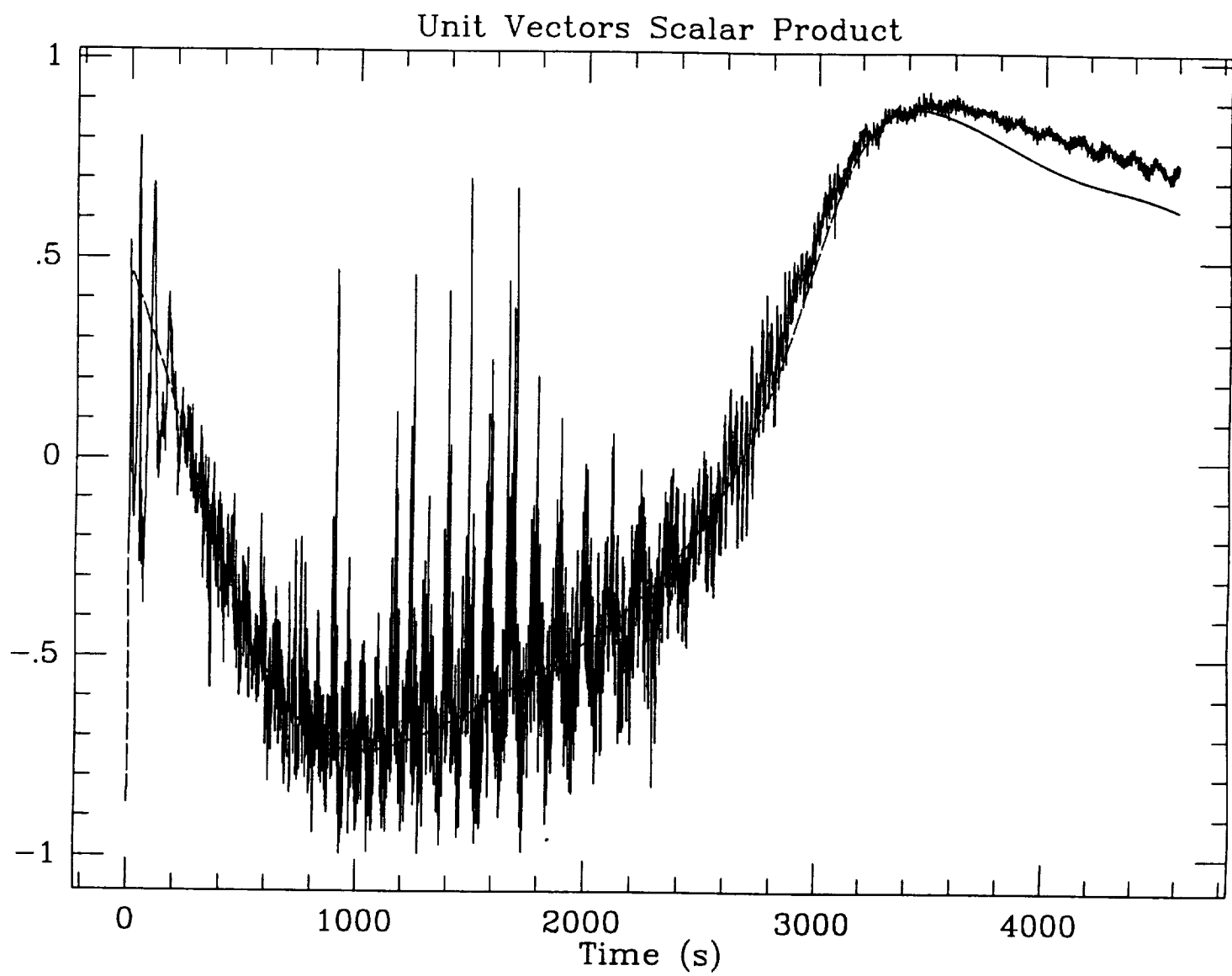
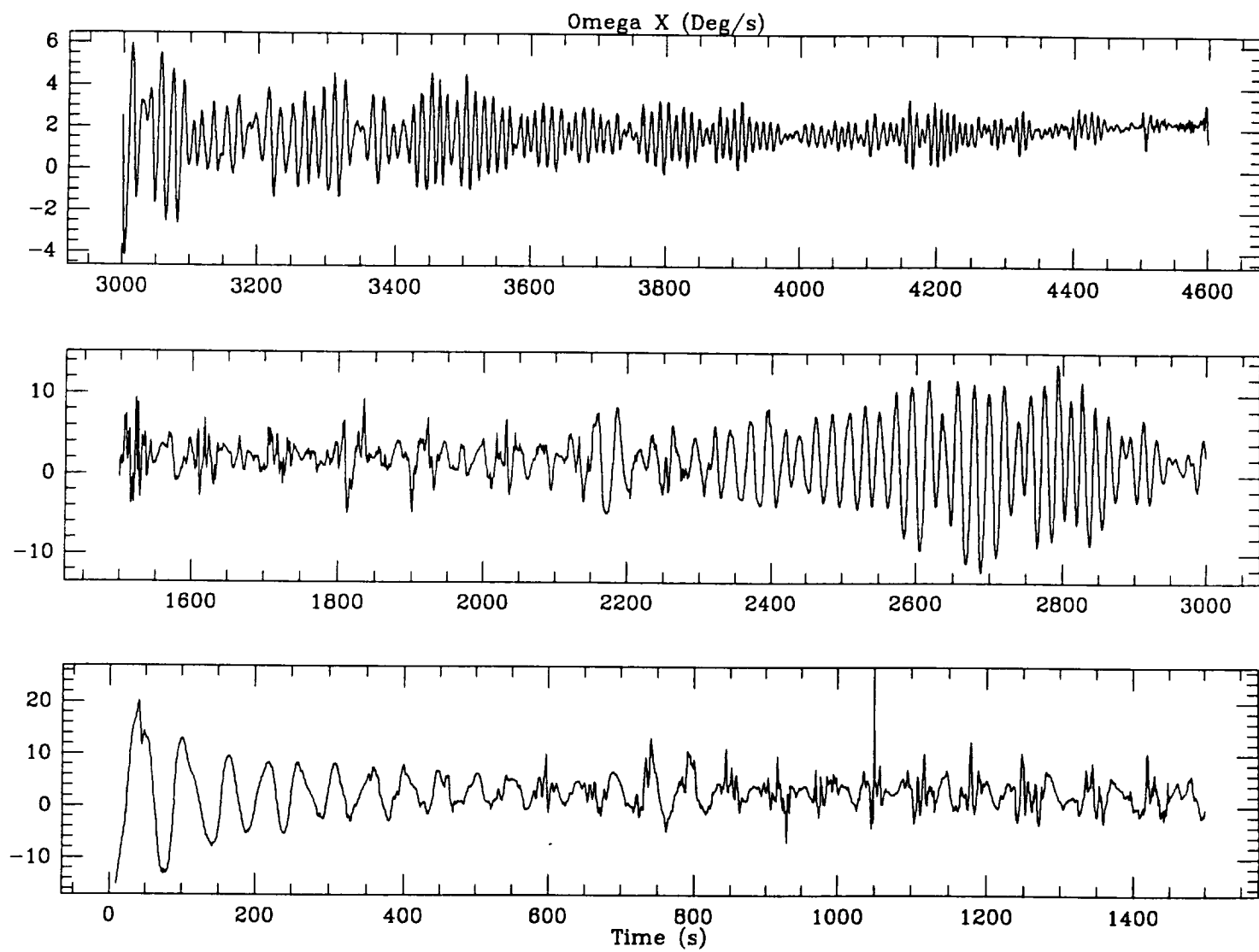
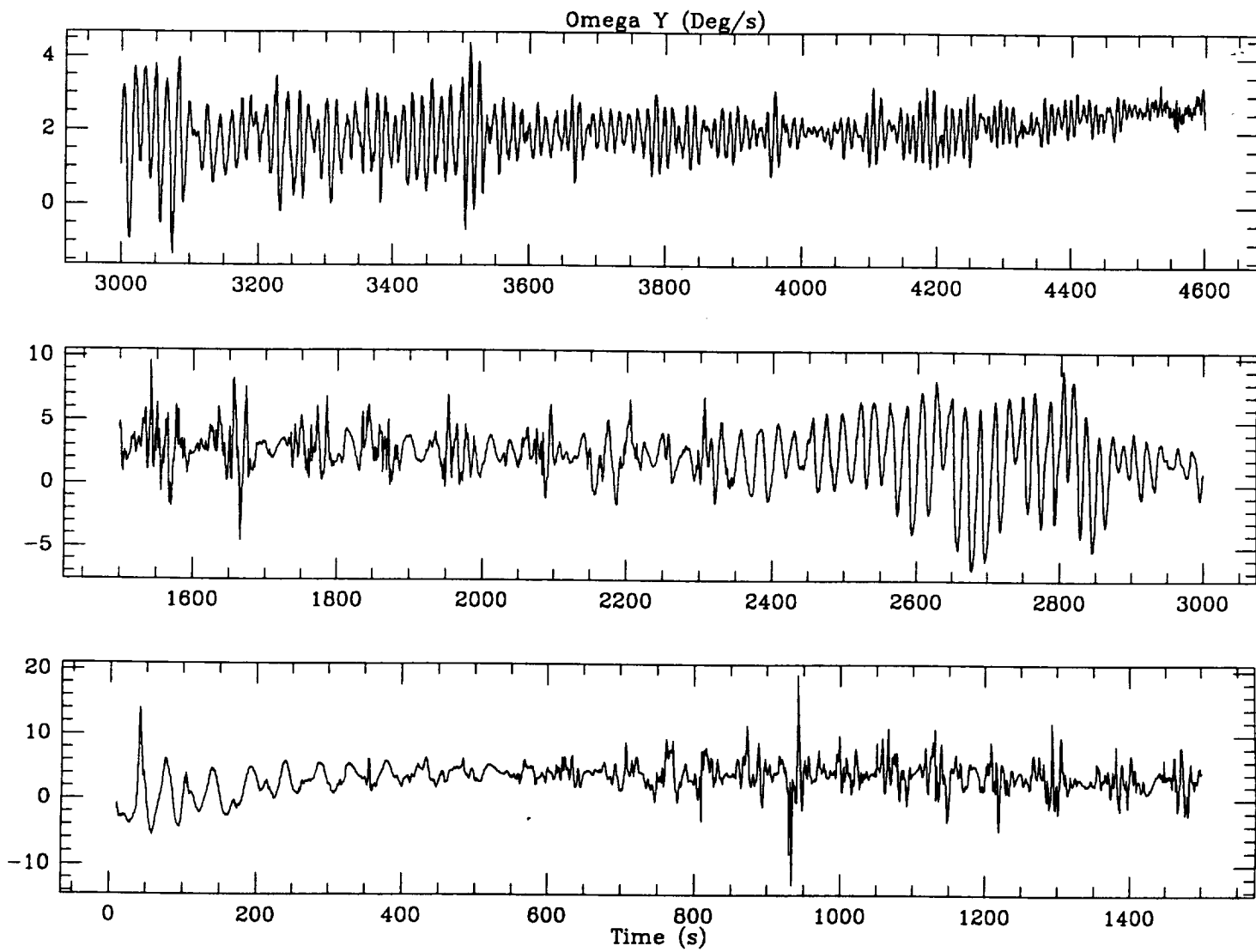


Figure 10.3



**Figure 10.4(a)**



**Figure 10.4(b)**

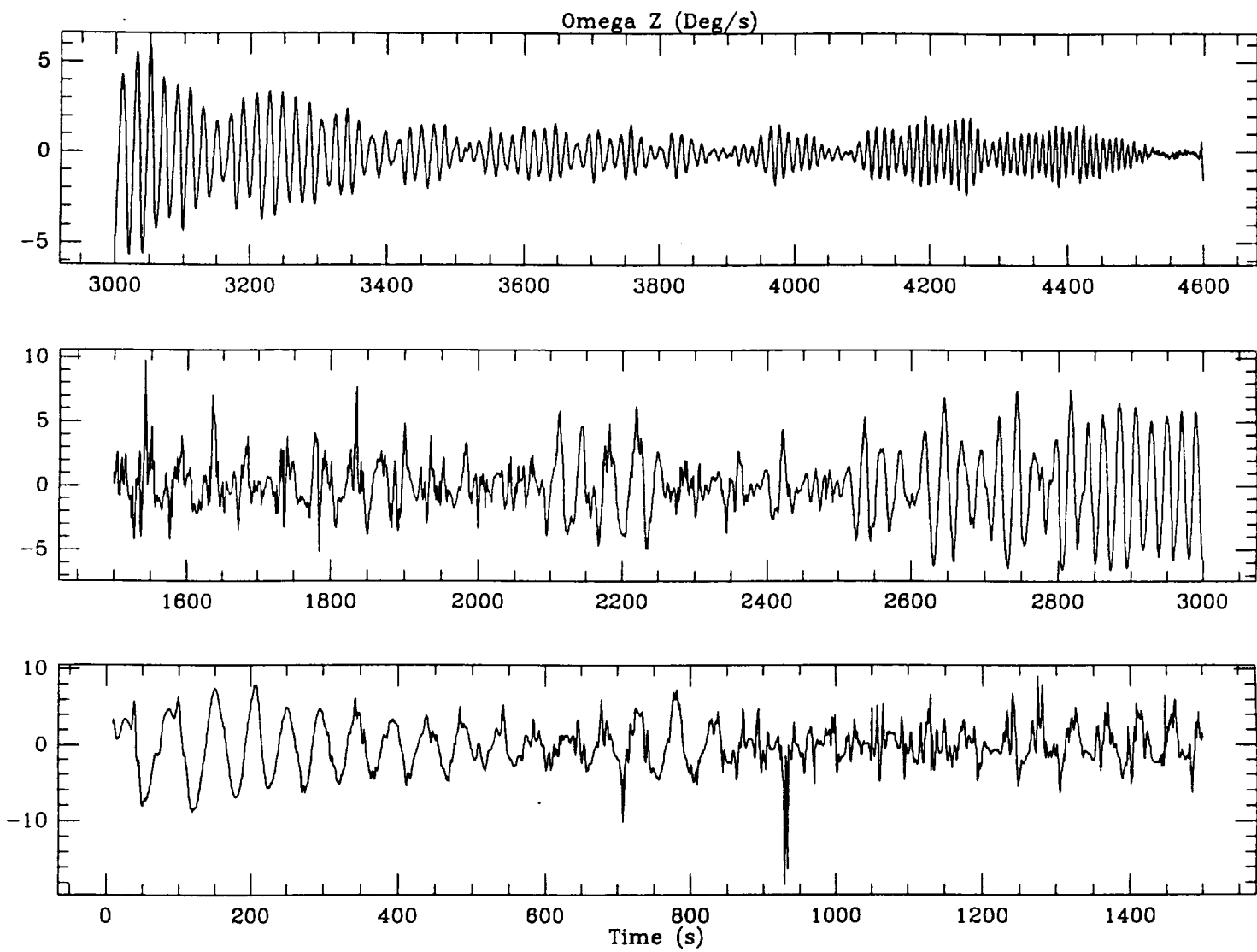


**Figure 10.4(c)**

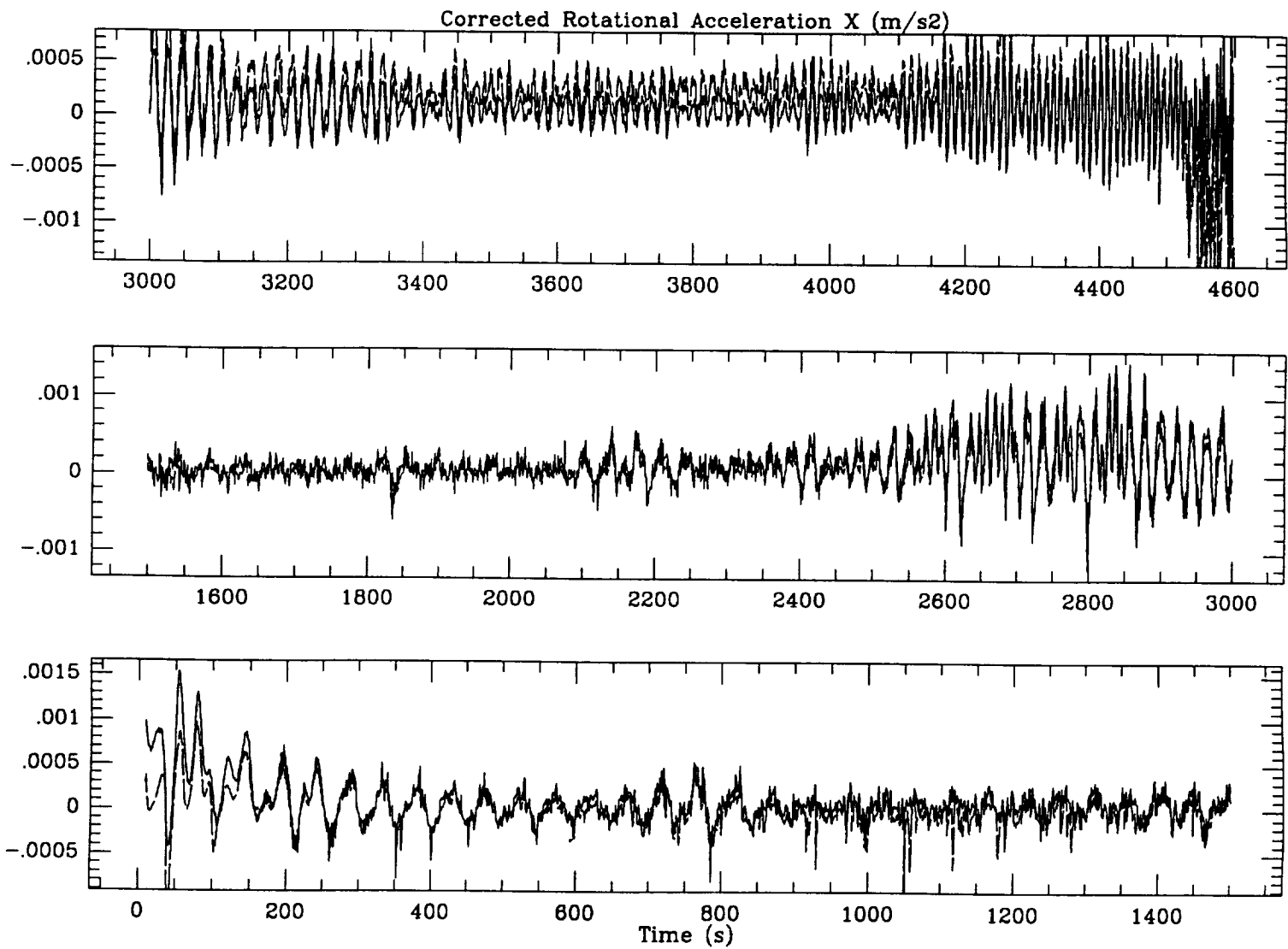


**Figure 10.5(a)**



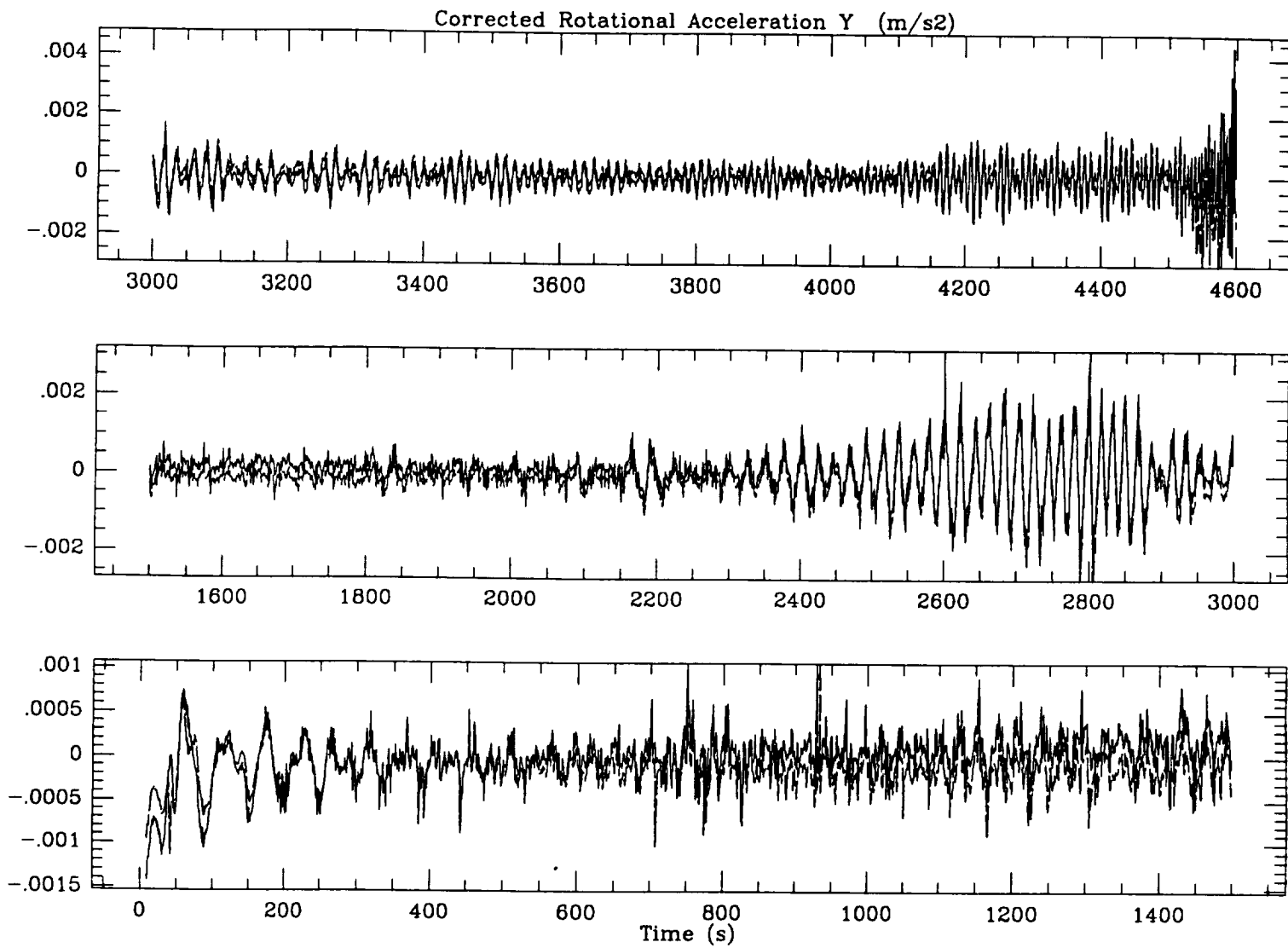


**Figure 10.5(b)**

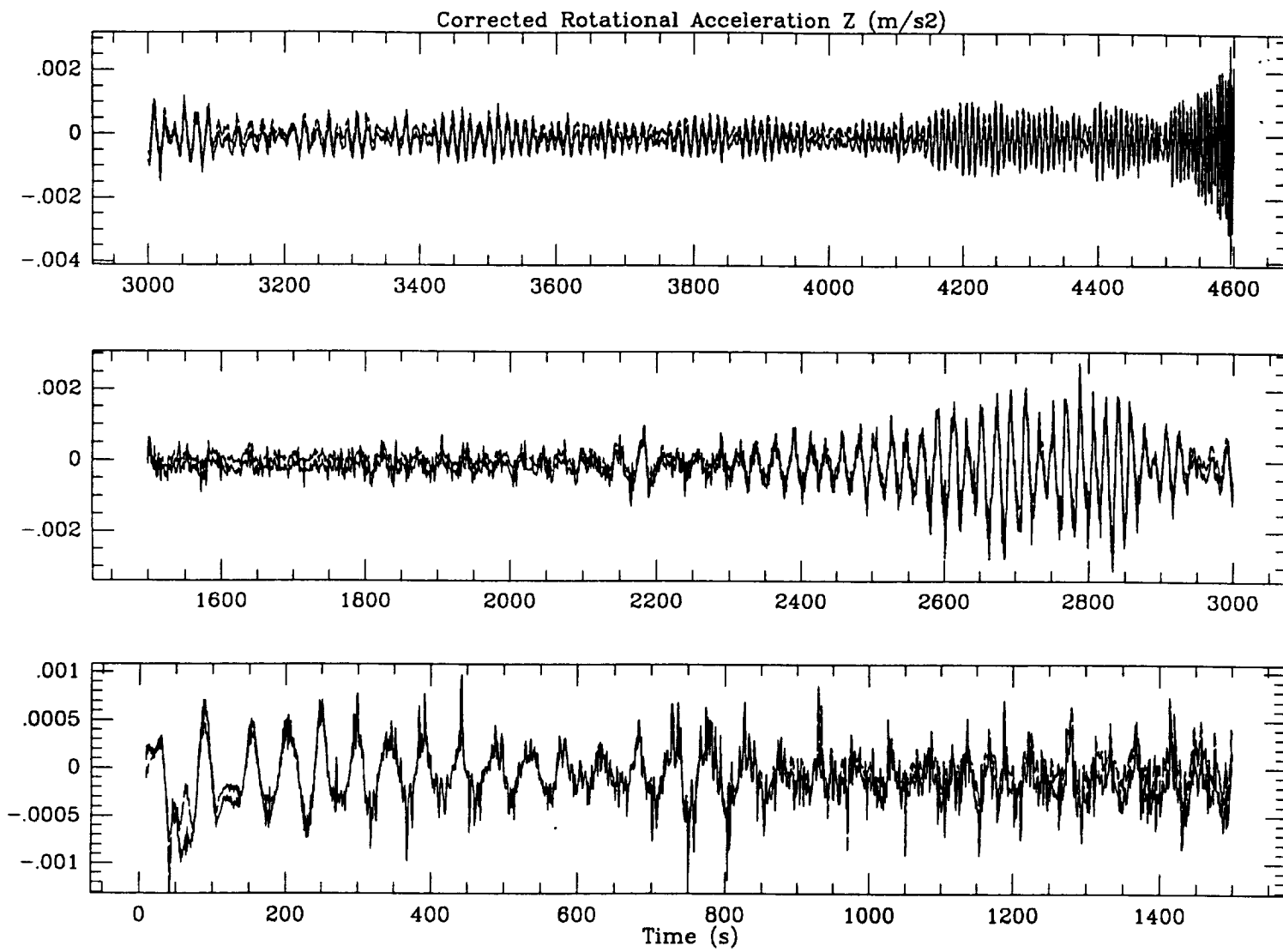
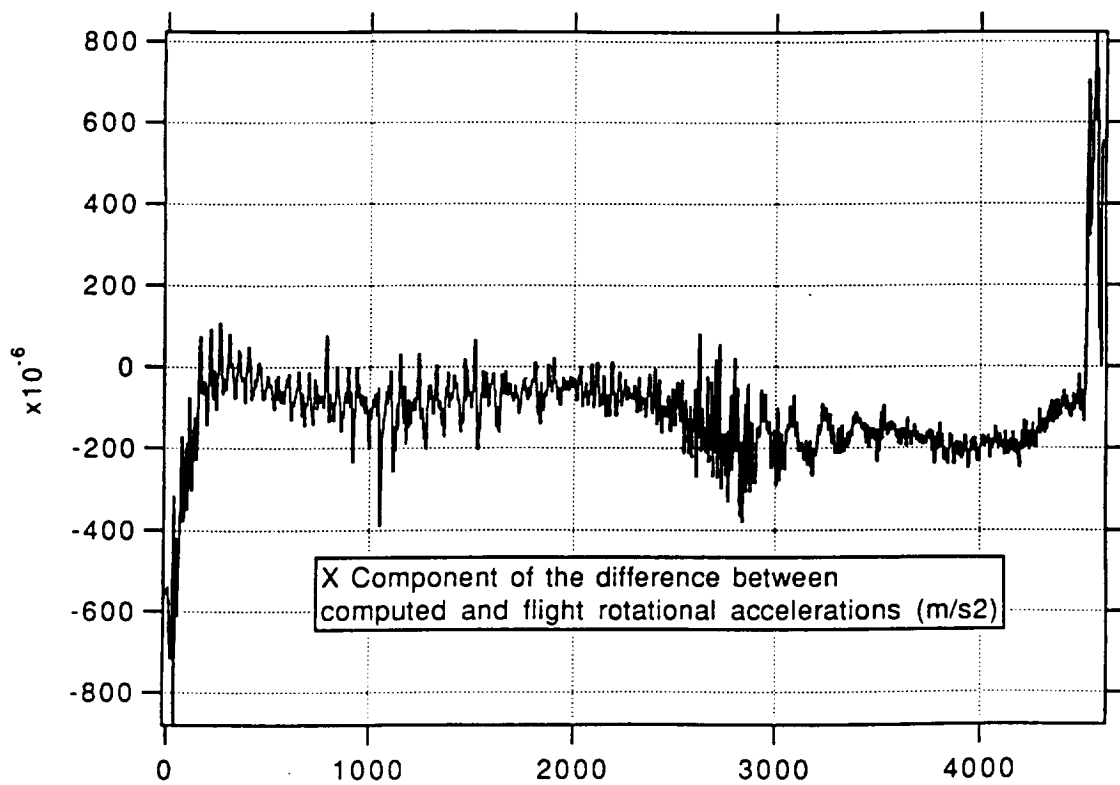
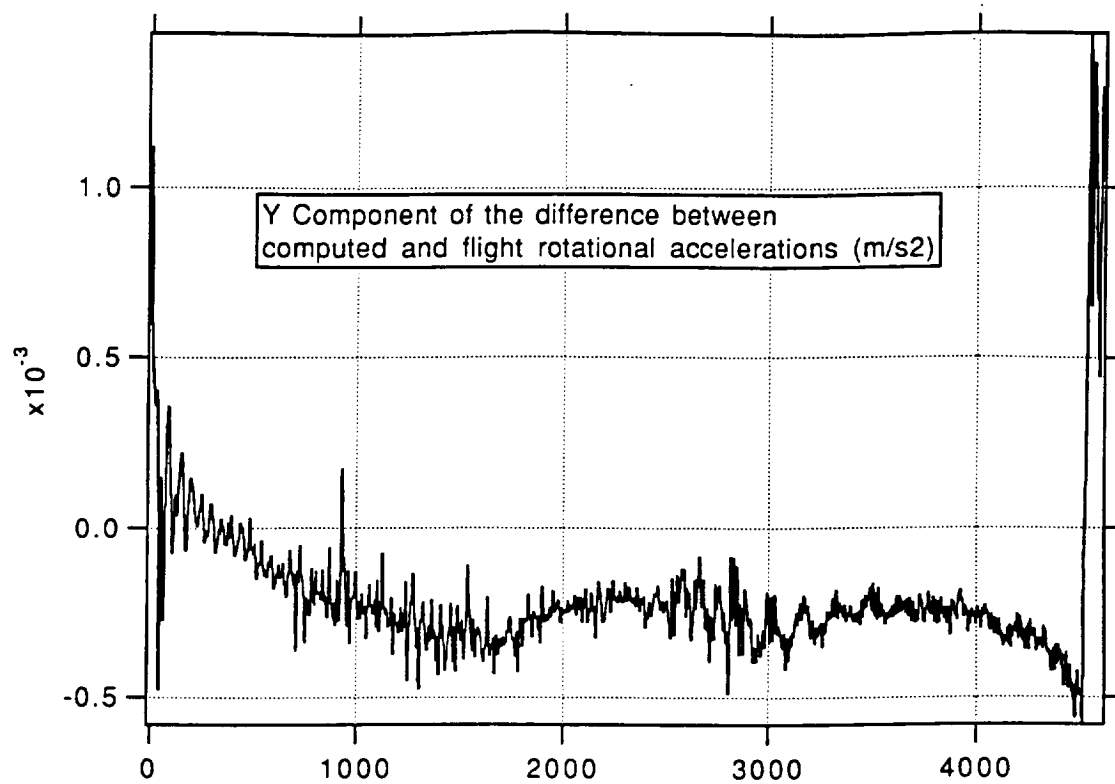
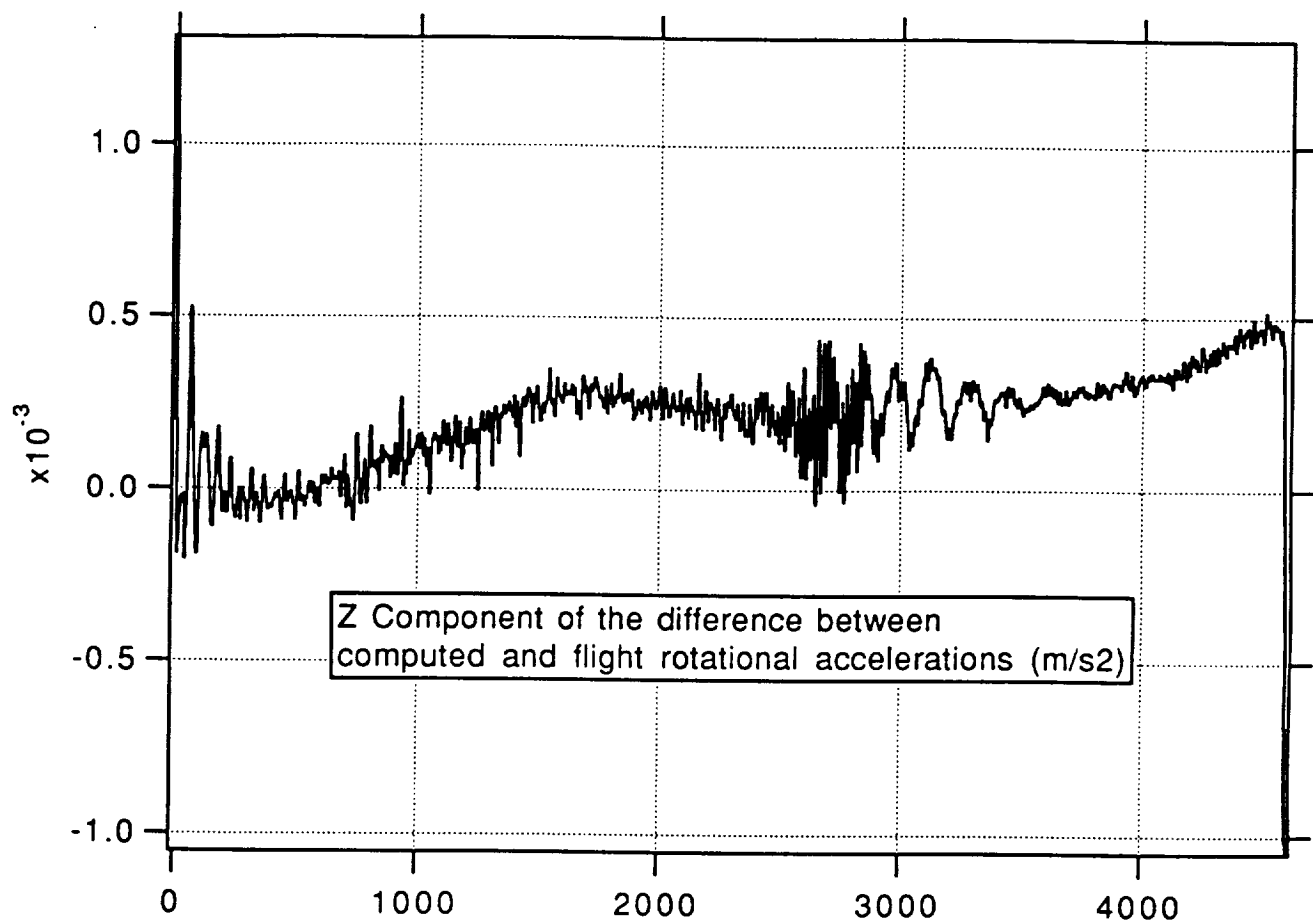


Figure 10.5(c)



**Figures 10.6(a) and 10.6(b)**



**Figure 10.6(c)**

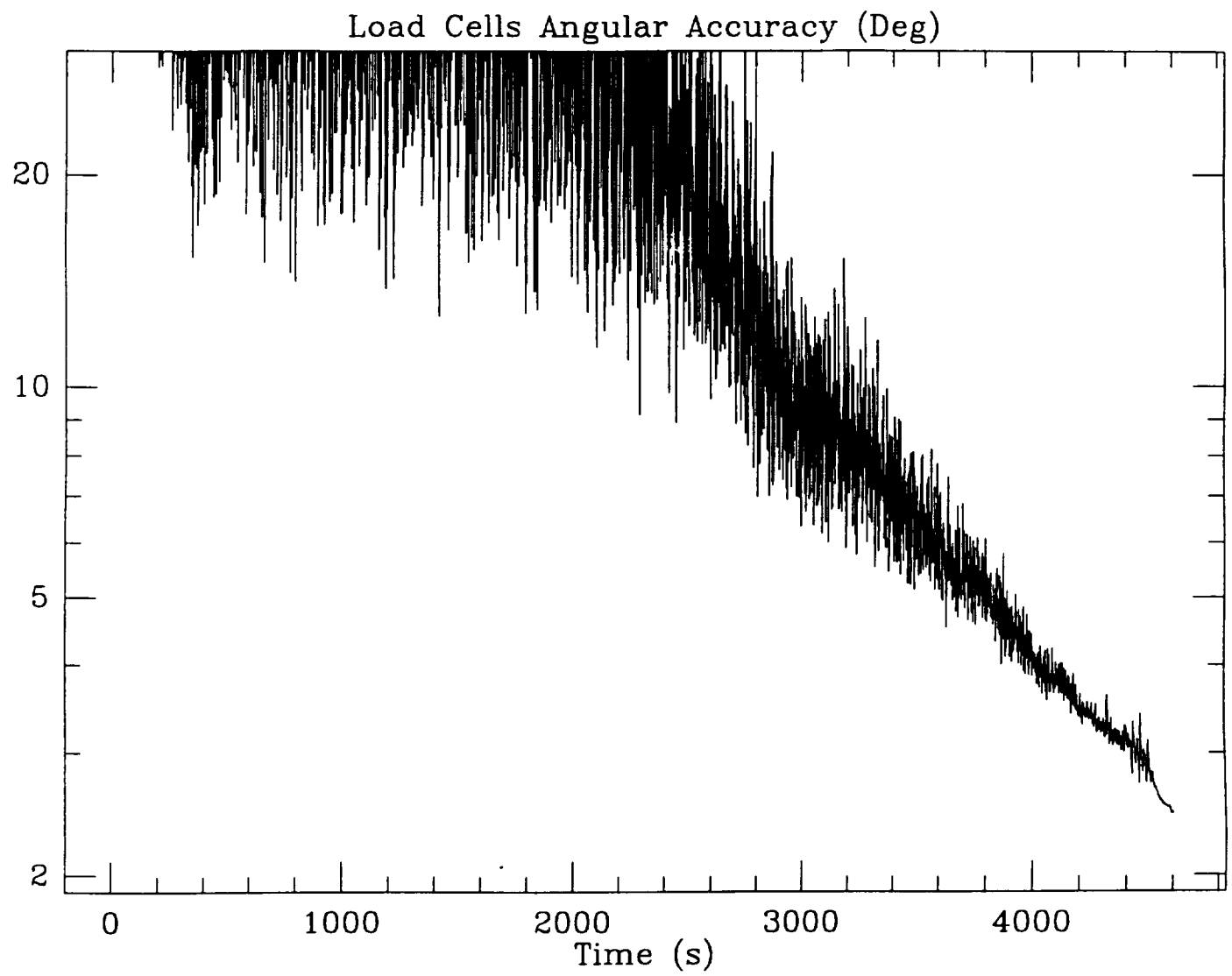


**Figure 10.7**

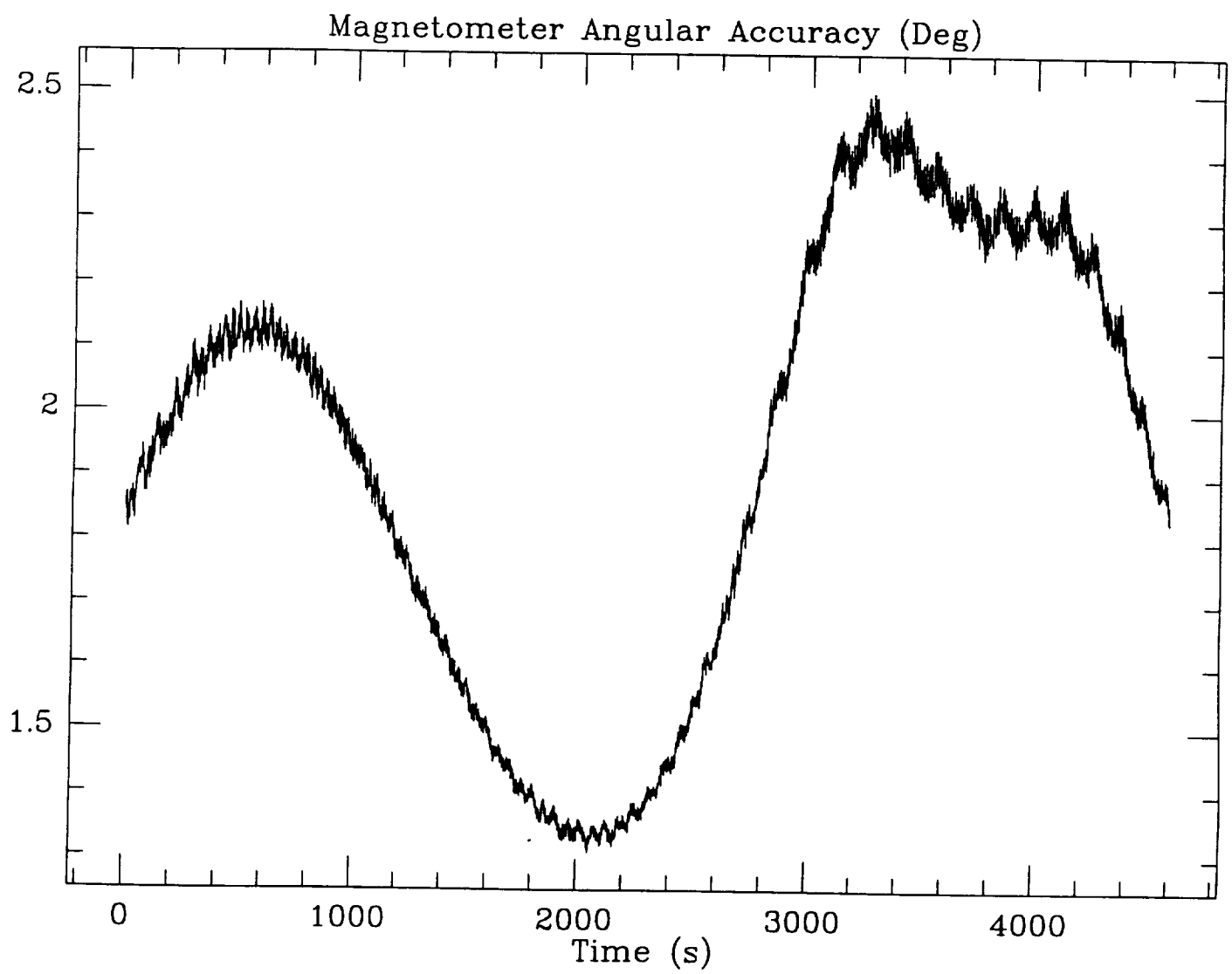


**Figure 10.8**

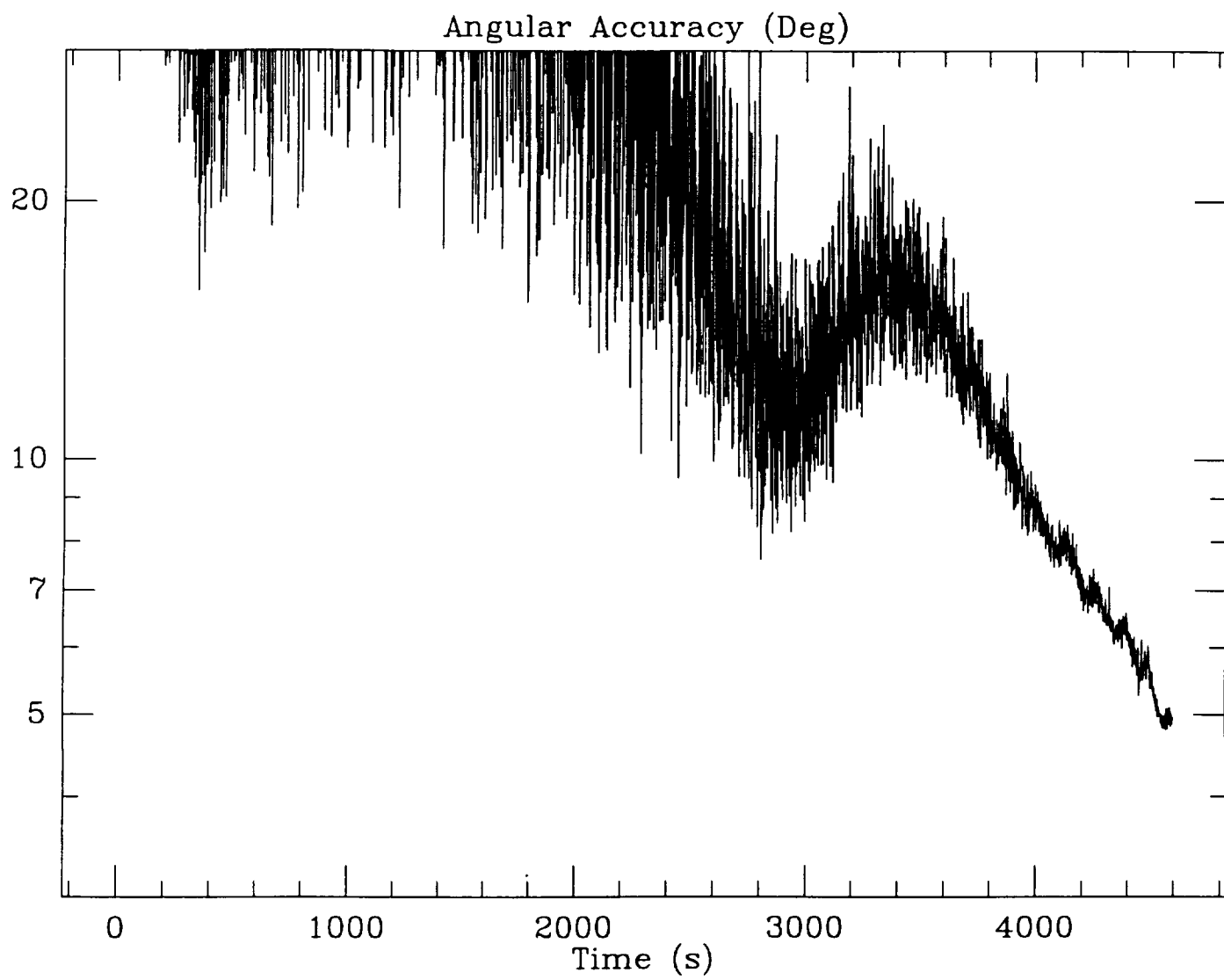


**Figure 10.9**

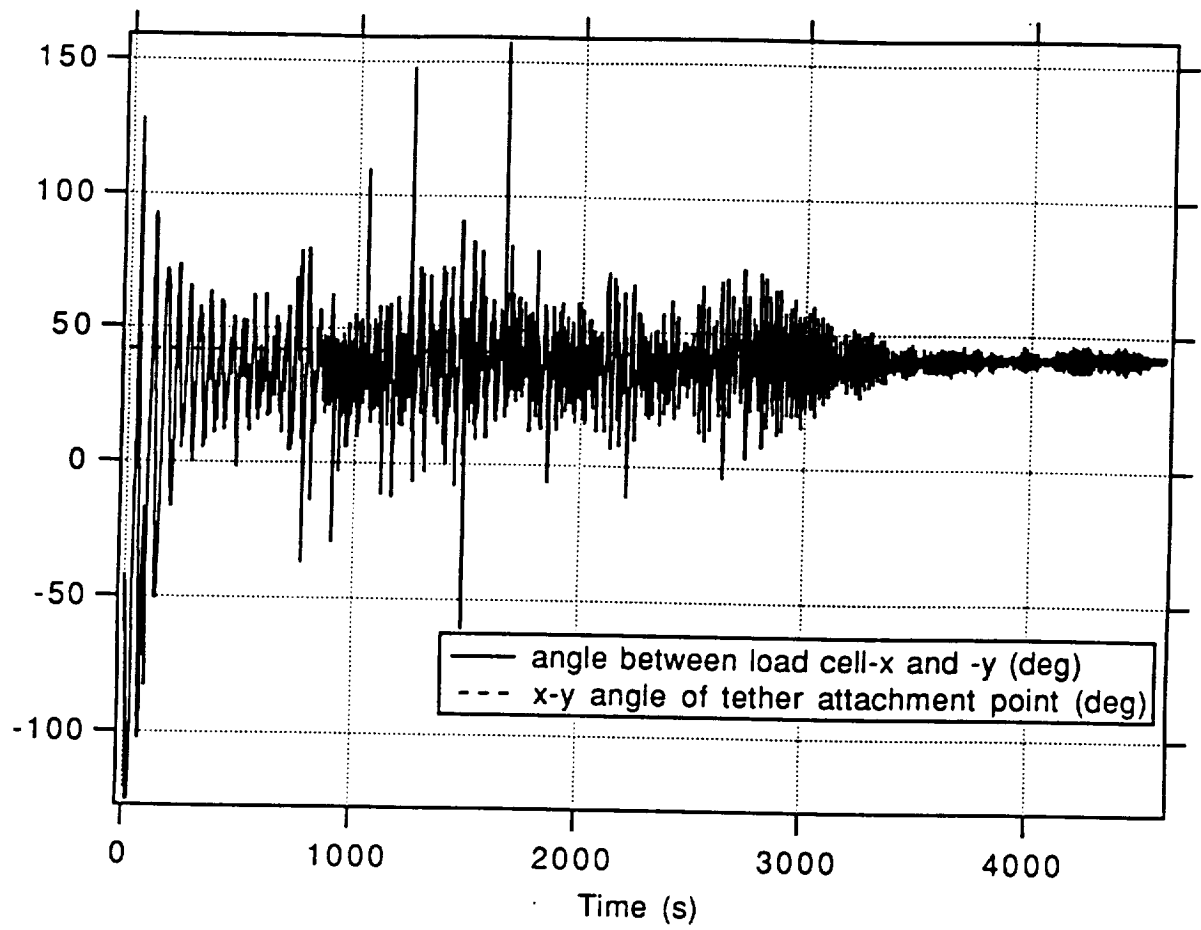


**Figure 10.10**



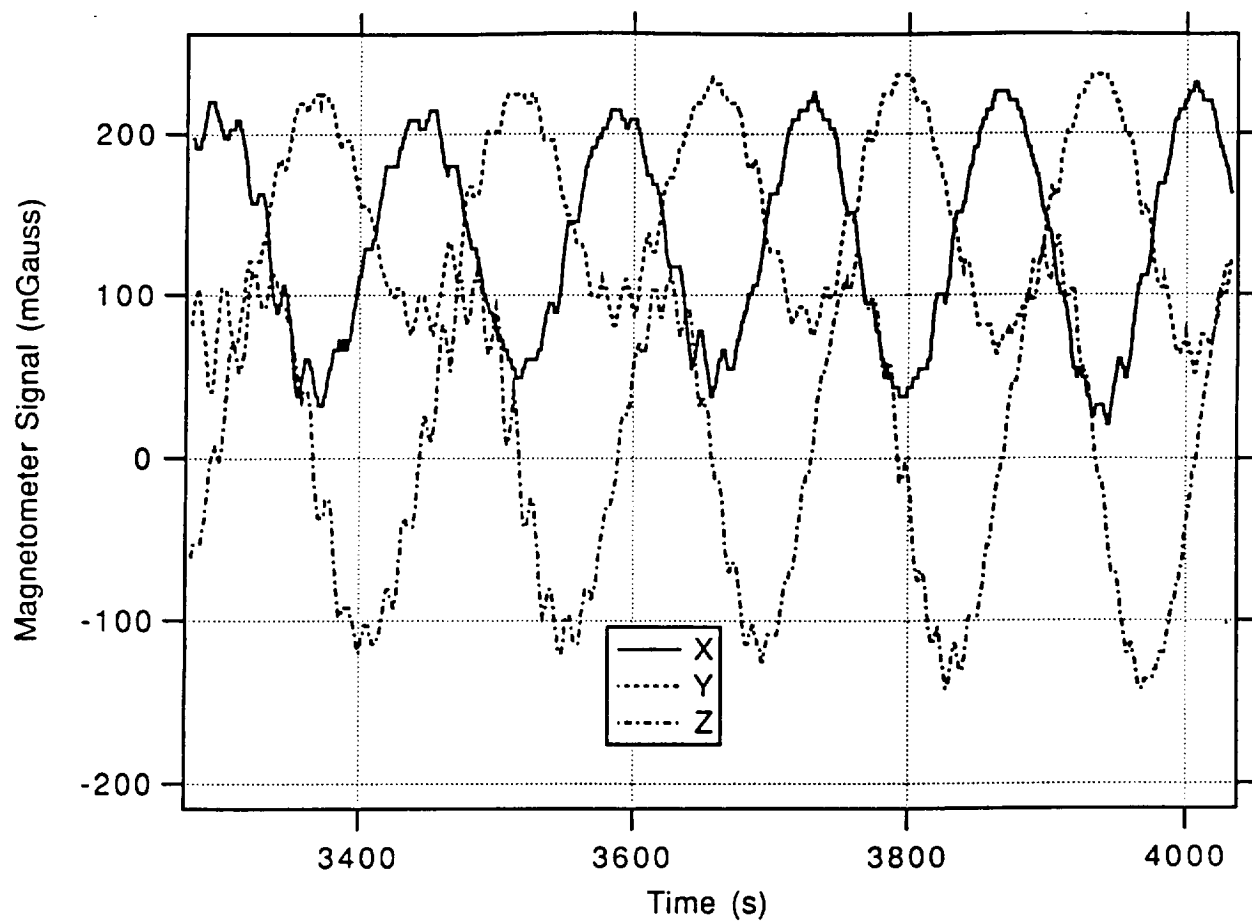
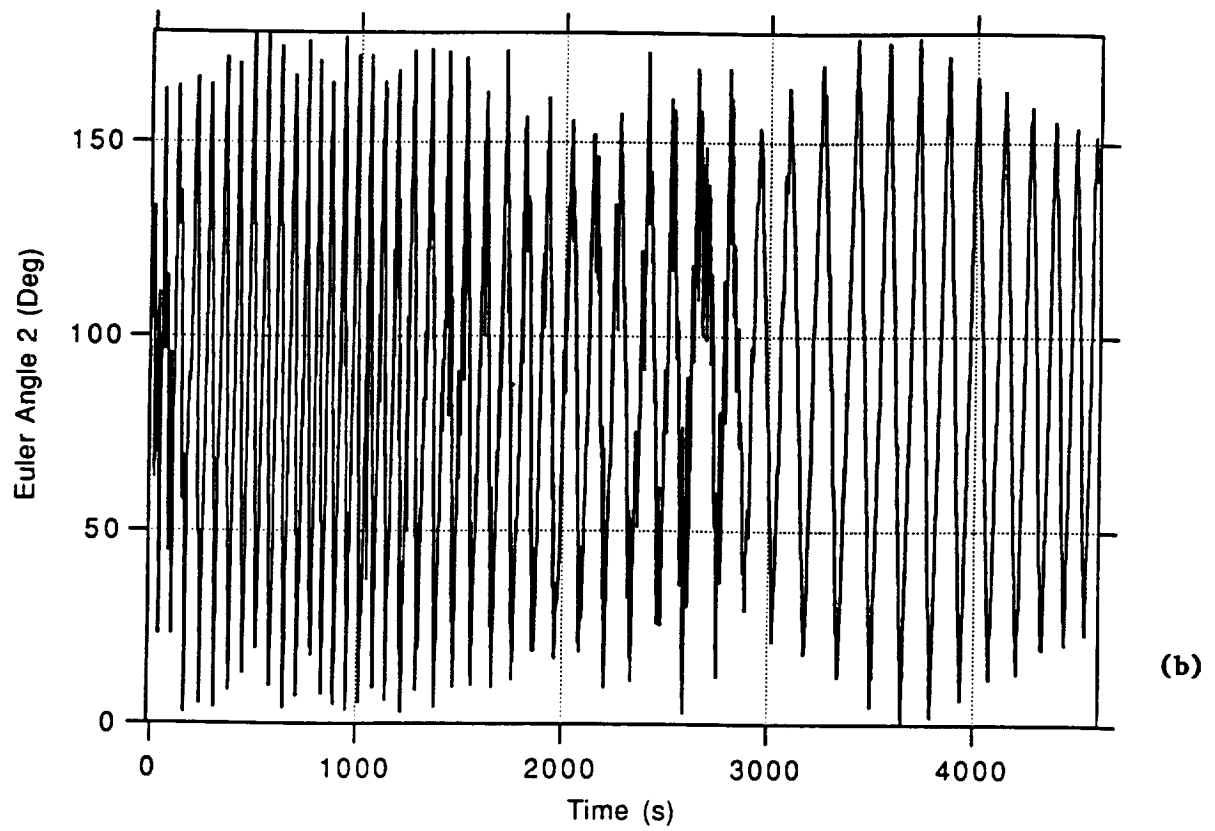
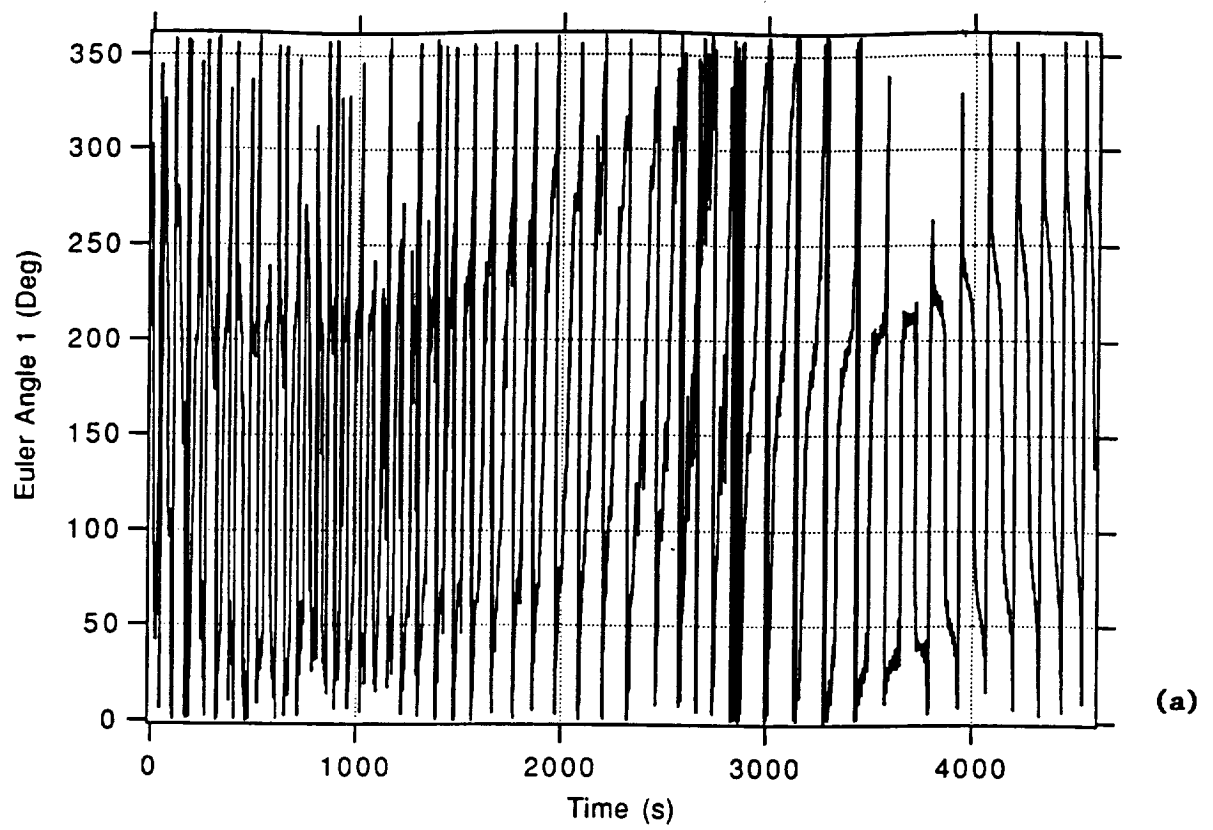


**Figure 10.11**



Figures 10.12(a) and 10.12(b)

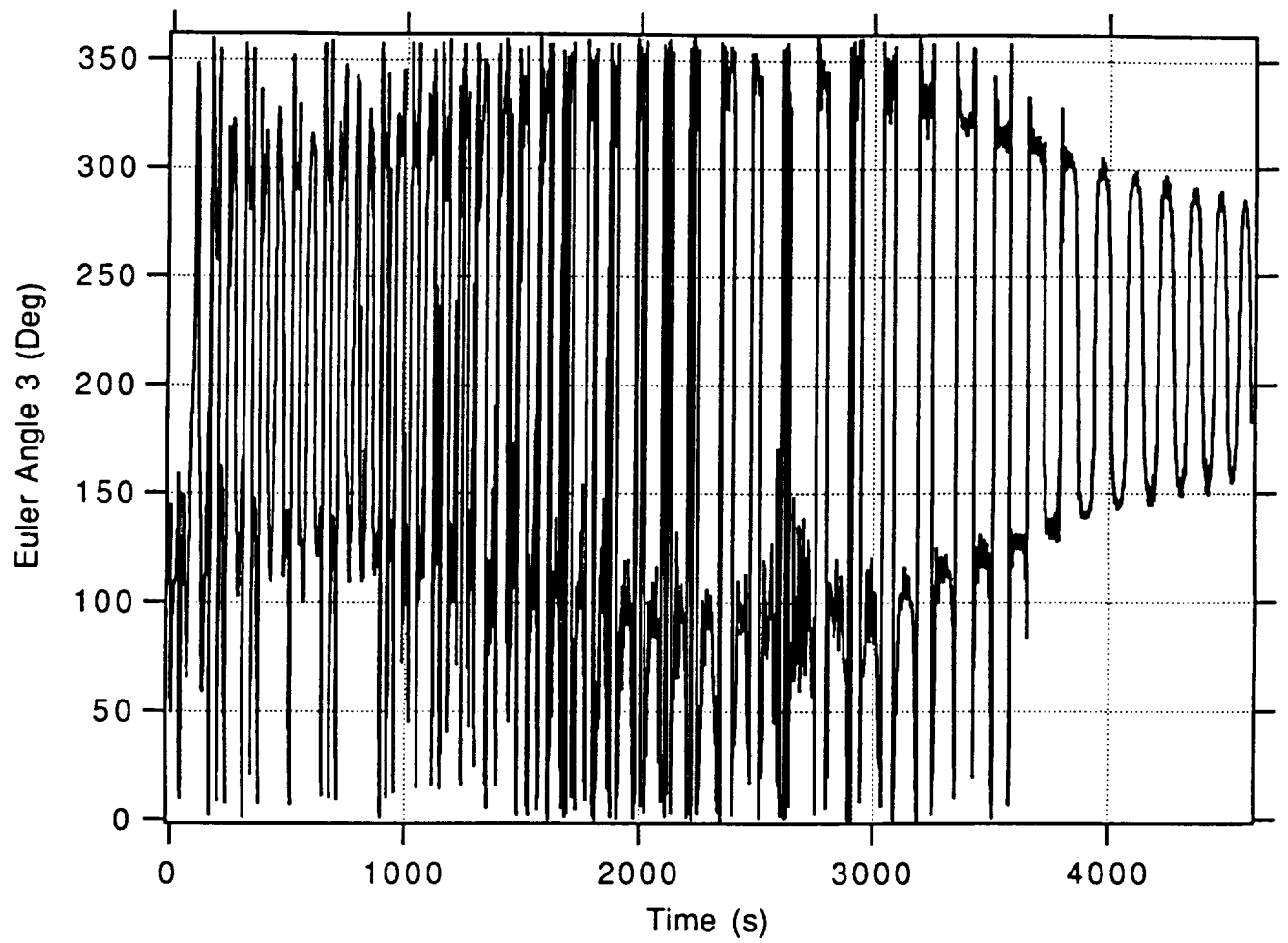
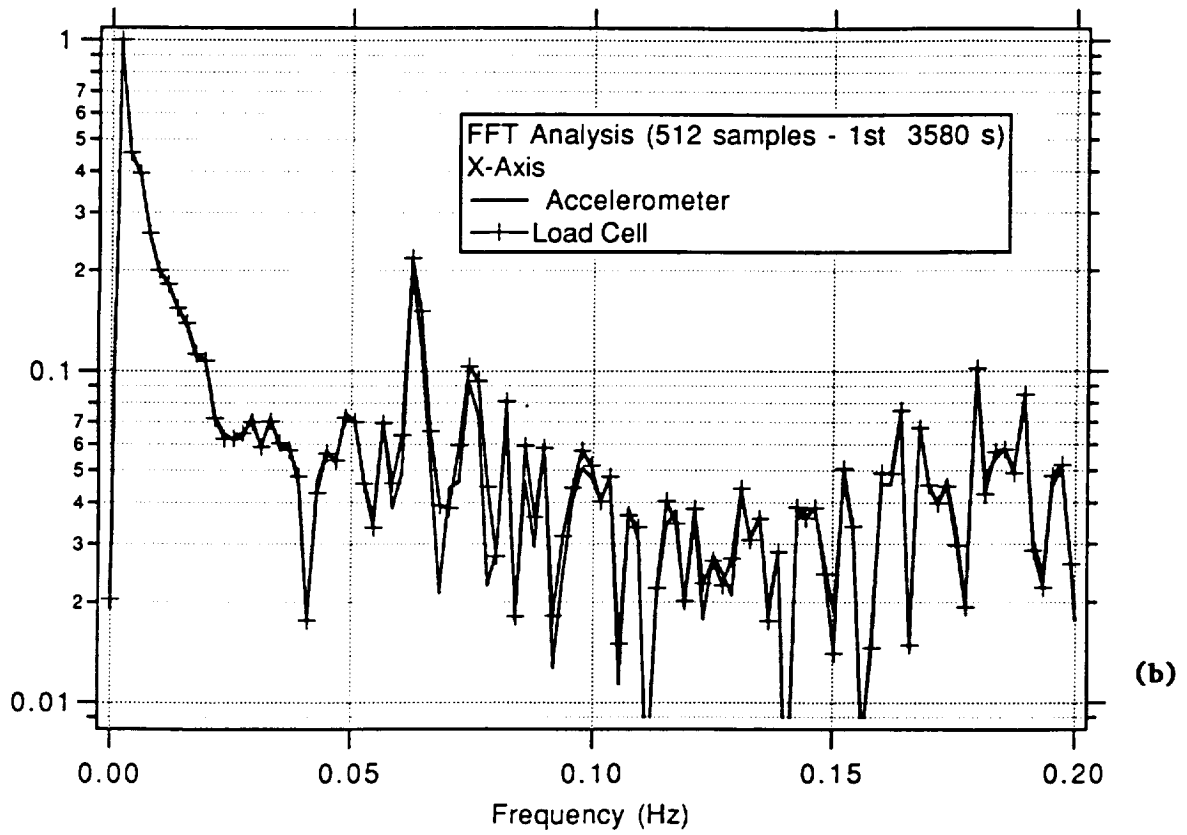
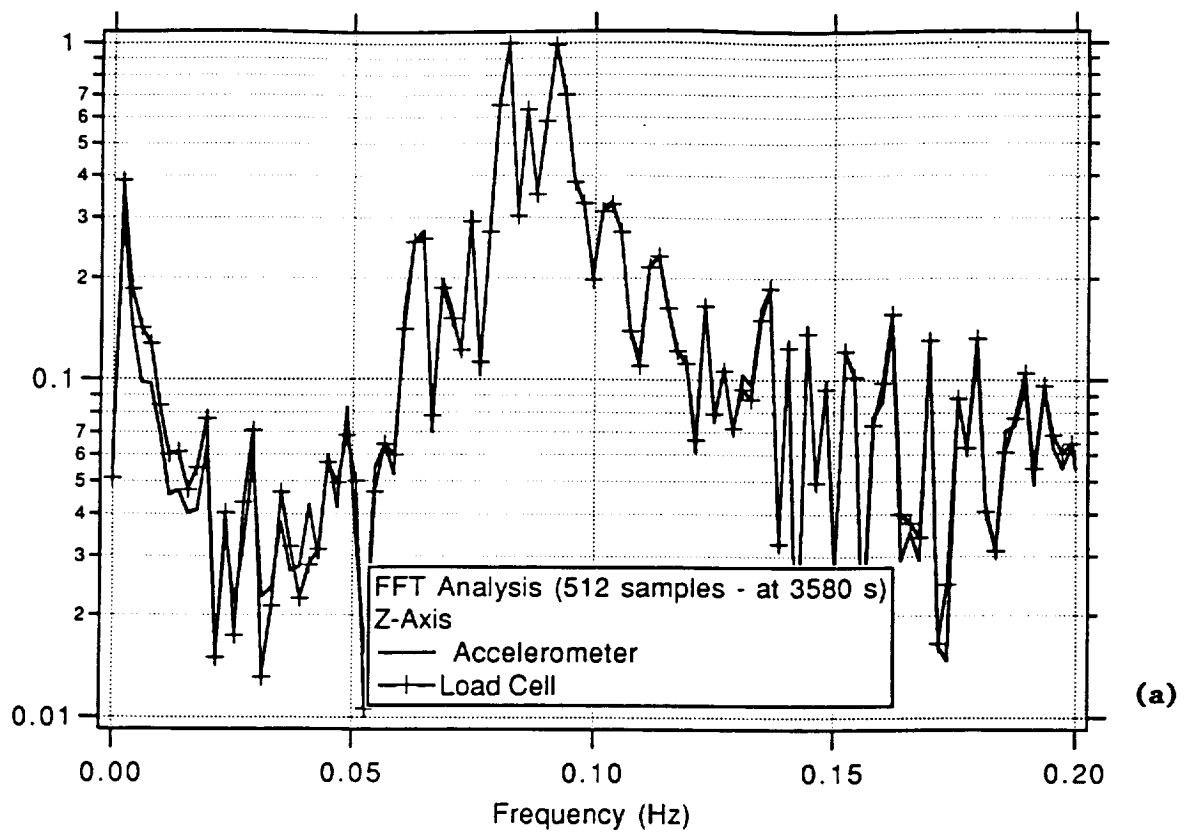
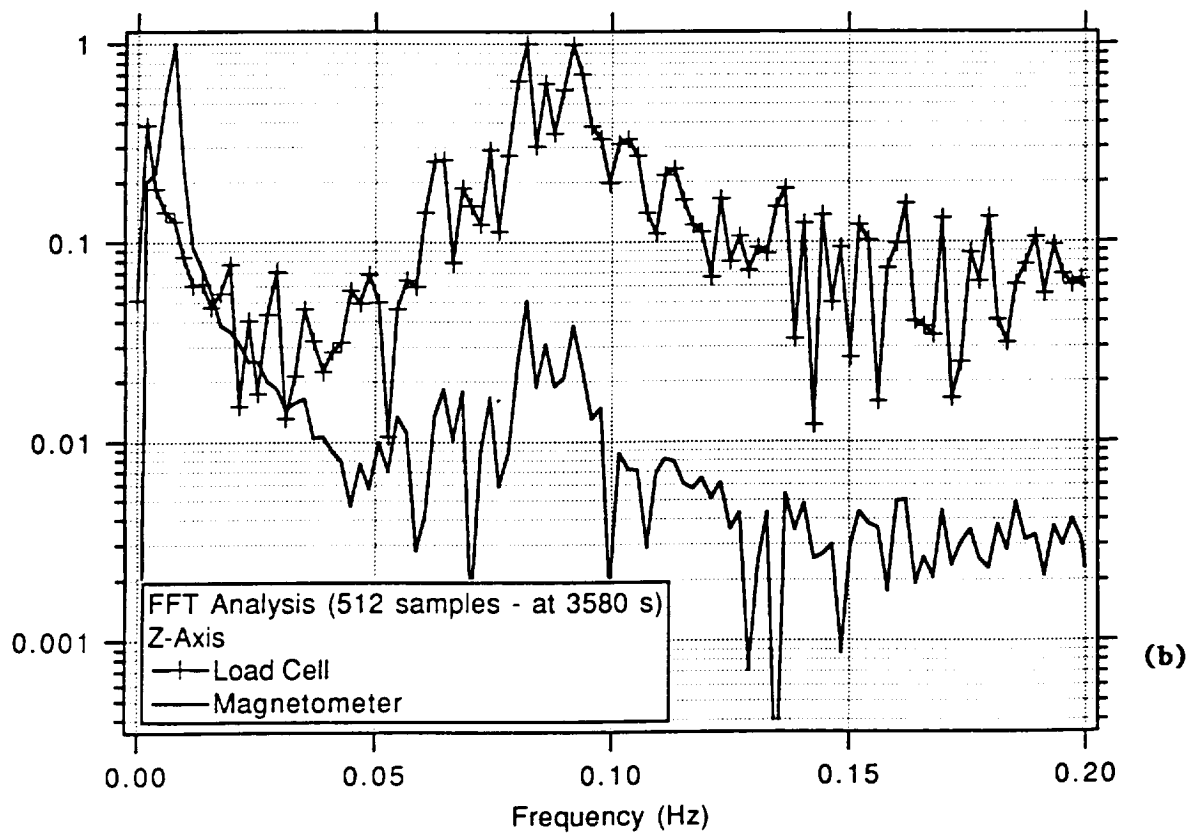
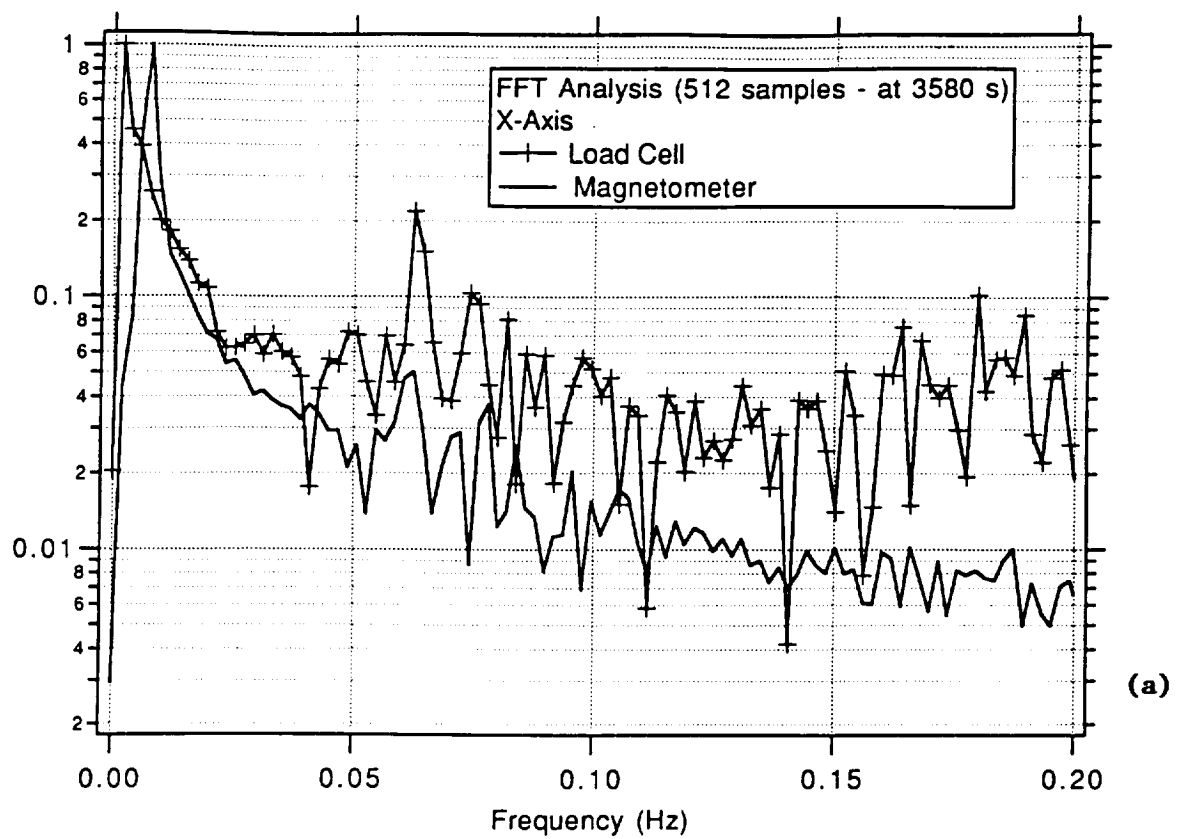


**Figure 10.12(c)**



Figures 10.13(a) and 10.13(b)



Figures 10.14(a) and 10.14(b)

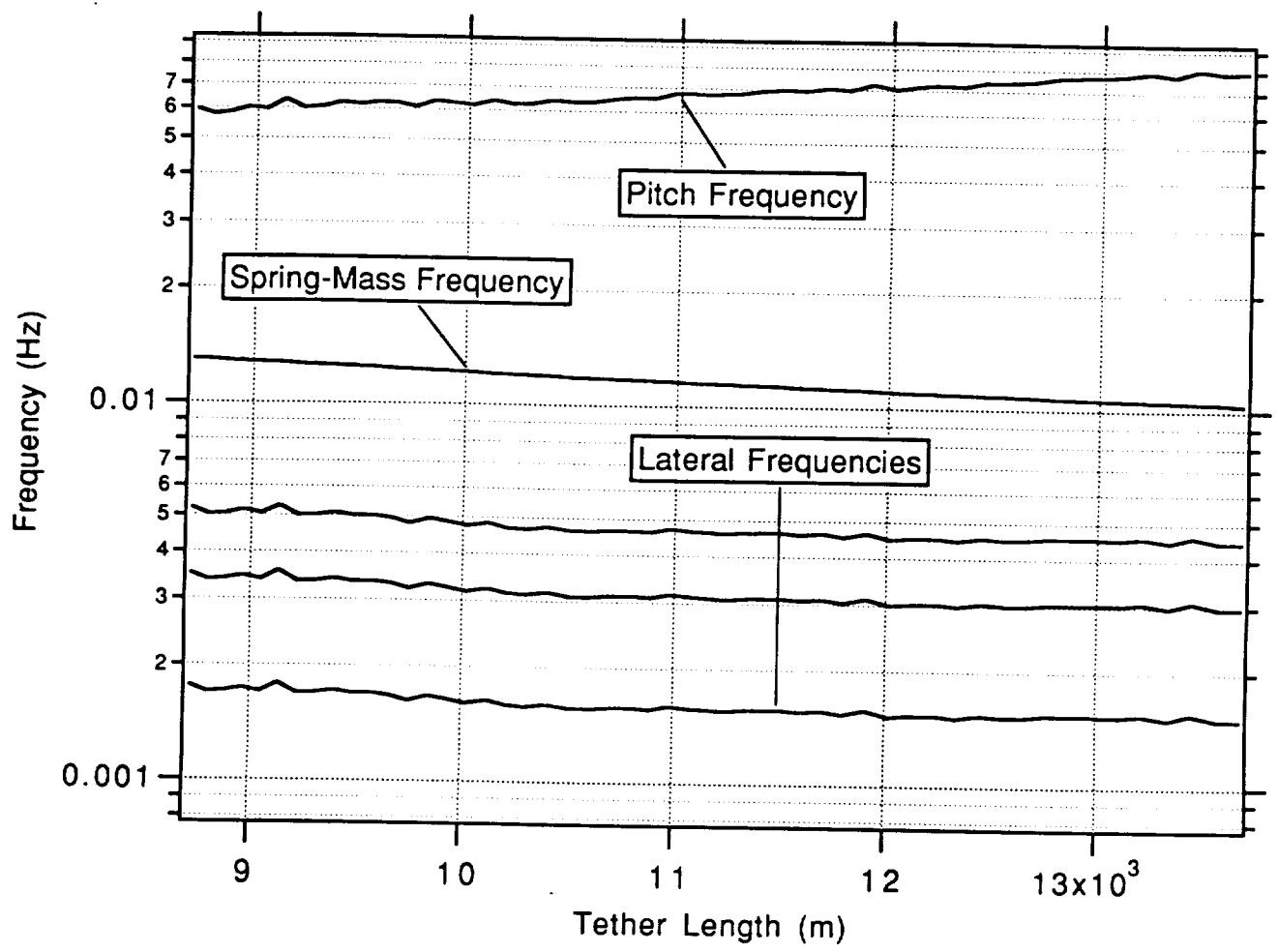
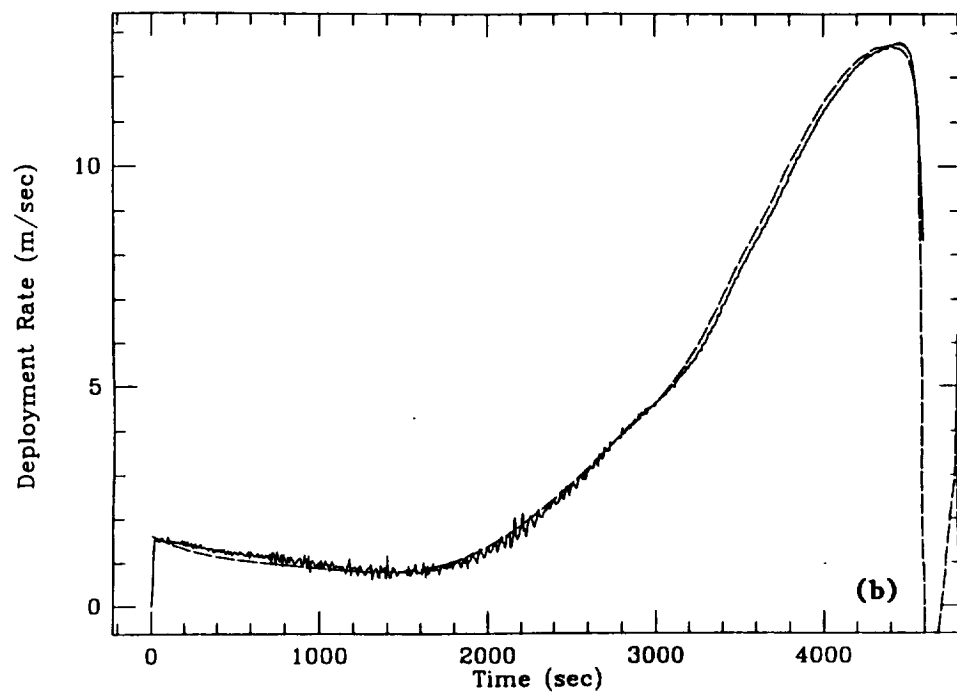
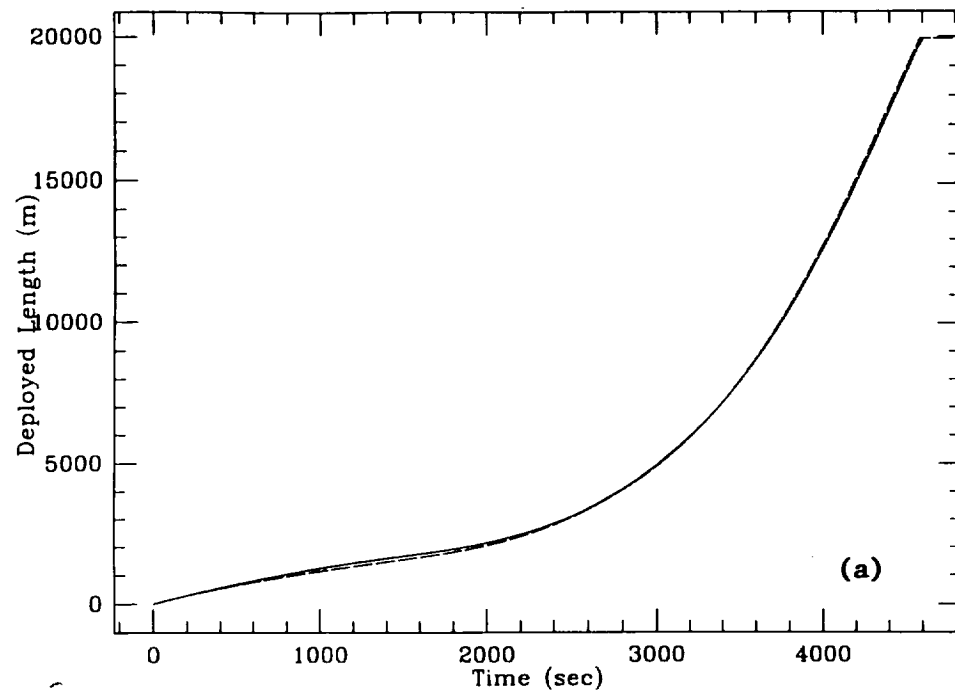


**Figure 10.15**



Figures 10.16(a) and 10.16(b)





# TETHER AS A DYNAMIC TRANSMISSION LINE

Gordon E. Gullahorn\*  
Harvard-Smithsonian Center for Astrophysics  
Cambridge, Massachusetts

Robert G. Hohlfeld†  
Boston University  
Boston, Massachusetts

## ABSTRACT

In a number of possible tether applications, *e.g.* gravity gradiometry and a variable gravity facility, isolation of the instrumented platform from disturbances on the base (Shuttle or Space Station) is critical. The tether is sometimes spoken of as a "low pass filter", implying that only the effects of the overall spring-mass system are significant. However, we have analyzed the effect of longitudinal impulses on the satellite when a continuum tether (subject to viscoelastic damping and gravity gradient force) is included, and find that in typical systems the effects of propagating waves will be substantial. The results are applied to the first two TSS missions and a variable gravity facility.

## I. Introduction

Certain platforms which have been proposed for deployment on gravity gradient stabilized tethers require isolation from dynamical disturbances upon their base (Shuttle or Space Station), which will be subject to a variety of perturbations from human and other activities. Such platforms include gravity gradiometers for determining the Earth's gravity field, platforms with sensitive pointing requirements and variable gravity facilities tethered to the Space Station. On TSS1 we hope to observe the effects of prescribed impulses such as firing of a Shuttle thruster, sudden application of the brakes on the deployer reel, or impact of a crew member on the Shuttle structure.

Apparently based on the idealization of the tether as a massless spring, it is sometimes claimed<sup>1</sup> that the tether acts as a "low pass filter" of dynamic noise. This claim is then used to infer either that there will be no problem with high frequency dynamic interference on the above mentioned dynamic platforms, or that in the case of planned TSS1 experiments, impulsive perturbations will never be observed on the satellite.

\* This work was partially supported by contracts NAS 8-36810 and NAS 8-36606.

† Assistant Professor, Electrical, Computer & Systems Engineering

This is not the whole story. We demonstrate below that, taking the continuum nature of the tether into account, the sharp onset of a forcing impulse at the Shuttle end is perceived on board the satellite. The magnitude of the satellite response is diminished from that of the forcing impulse, and the response exhibits a broadened exponential tailoff; these are due, however, primarily to the coupling between the tether and the satellite and its influence on an impinging impulsive wave, and not on the whole system as in the spring-mass model. The full impulse response function can be quite complex, showing repeated impulses as the tether wave bounces back and forth between the satellite and Shuttle, having a different shape at each impingement on the satellite.

## II. Equations of Motion

The physical system under consideration consists of (a) a uniform, viscoelastic tether of natural length  $L$ , (b) a point mass satellite attached to one end whose response we desire, and (c) an attachment at the other end whose motion we will specify but which is otherwise fixed, *i.e.* which provides a forcing boundary condition. The fixed end is in circular orbit around the Earth, and the system is small enough that the linear approximation to the gravity gradient along the local vertical may be used:

$$F_{gg} = 3GMm \frac{x}{R_{orbit}^3} = g_{gg}xm \quad (1)$$

where  $x$  is the vertical distance from the orbiting reference point ("fixed" attachment),  $m$  is the satellite mass, and  $M$  is the Earth's mass. The coefficient is conveniently computed as  $g_{gg} = 3g/R_{orbit}$ , for a low orbit with  $g \sim 10 \text{ m s}^{-2}$  and  $R_{orbit} \sim 6.5 \times 10^6 \text{ m}$ , we get  $g_{gg} \sim 0.5 \times 10^{-5} \text{ s}^{-2}$ .

We consider only the gravity gradient force (exclude air drag and Coriolis forces), and only longitudinal tether motion and a point mass (excluding transverse "string" motions and satellite attitude variations).

Let  $\tilde{\ell}$  be the natural coordinate along the string, from 0 at the fixed end to  $L$  at the satellite. (We shall soon scale to dimensionless variables, and  $\tilde{\cdot}$  denotes unscaled physical variables.) The system starts in initial hanging equilibrium. Let  $\tilde{u}(\tilde{\ell}, \tilde{t})$  denote displacement from this equilibrium. The

usual method of balancing forces on mass elements and taking limits leads to

$$\begin{cases} \mu \ddot{u}_{\tilde{t}} = \{EA + E'A \frac{\partial}{\partial \tilde{t}}\} \ddot{u}_{\tilde{t}} + g_{gg} \mu \ddot{u}, & 0 < \tilde{t} < L, \\ m \ddot{u}_{\tilde{t}} = -\{EA + E'A \frac{\partial}{\partial \tilde{t}}\} \ddot{u}_{\tilde{t}} + mg_{gg} \ddot{u}, & \tilde{t} = L \end{cases} \quad (2)$$

where  $\mu$  is the tether mass per unit length, and  $EA$  and  $E'A$  are the elastic and damping coefficients. The boundary condition at  $\tilde{t} = 0$  depends on whether we are trying to compute the impulse response function (IRF, time profile of response to a single impulse) or frequency response function (FRF, strength of steady state response to a sinusoidal forcing function, as a function of frequency). The two cases are

$$\begin{cases} \text{IRF: } \ddot{u}(0, \tilde{t}) = \delta(\tilde{t}) \\ \text{FRF: } \ddot{u}(0, \tilde{t}) = e^{i\omega \tilde{t}} \end{cases} \quad (3)$$

Scale these equations by

$$\begin{cases} \ell = \tilde{t}/L \\ t = \tilde{t}/(L/c) \end{cases} \quad (4)$$

where  $c = \sqrt{EA/\mu}$  is the speed of longitudinal waves in the tether. Then with  $u(\ell, t) = \ddot{u}(L\ell, \frac{L}{c}t)$ , we get

$$\begin{cases} u_{tt} = [1 + b \frac{\partial}{\partial t}] u_{\ell\ell} + \gamma u, & 0 < \ell < 1, \\ u_{tt} = -a[1 + b \frac{\partial}{\partial t}] u_{\ell} + \gamma u, & \ell = 1, \\ \text{IRF: } u(0, t) = \frac{1}{L/c} \delta(t) \\ \text{FRF: } u(0, t) = e^{i\omega t} \end{cases} \quad (5)$$

where  $\omega = \tilde{\omega} \frac{L}{c}$ . The dimensionless parameters,  $a$ ,  $b$ , and  $\gamma$  are defined by  $a = EAL/mc^2 = \mu L/m$ , i.e. the ratio of tether mass to satellite mass,  $b = E'c/EL = E'A/\mu Lc = \frac{E'A}{L} \sqrt{\frac{1}{EA\mu}}$ , and  $\gamma = g_{gg} \frac{L^2}{c^2} = g_{gg} \frac{\mu L^2}{EA}$ . In practice, we solve the dimensionless IRF problem for a unit dimensionless impulse and scale the result to the dimensioned response; dimensionless IRF's shown are for unit impulse in (5).

The damping term ( $b \frac{\partial}{\partial t}$ ) in the  $\ell = 1$  boundary condition of (5) is important for some purposes; it is omitted in at least one previous paper<sup>2</sup>. Tests performed without this term show that the overall damping (in the spring-mass mode) is substantially reduced; the effect on the character of the response to individual impulses (e.g. rise times) is less pronounced.

Note that (5) is a linear system. Most practical concerns deal with acceleration and not displacement as such. The derivative is a linear operator; hence, IRF's and FRF's computed for (5) apply equally well if interpreted as the IRF or FRF of acceleration response to an acceleration input.

We consider three systems in this paper: the first and second tethered satellite missions, TSS1 and TSS2; and a variable gravity facility, VG. Typical parameters are shown in Table I, with the VG at 1 km deployment. (Note that the VG is a much more complicated system, with three tethers and four masses; we consider only the Space-Station/tether/facility portion.) Except for TSS1, these values should be taken as quite uncertain; even in TSS1 the damping  $E'A$  is poorly known.

### III. FRF Solution

We solve (5) with the FRF boundary condition by attempting a steady state solution

$$u(\ell, t) = R(\ell) e^{i\omega t}, \quad (6)$$

where complex  $R$  allows for a phase shift along the tether. Substitution produces an ordinary differential equation which is readily solved. The FRF is then just  $R(1)$  and is found to be

$$\text{FRF} = \frac{1}{\cos \beta - \frac{\beta}{a} \sin \beta} \quad (7)$$

where

$$\beta = \omega \sqrt{\frac{1 + \gamma/\omega^2}{1 - i b \omega}}. \quad (8)$$

Note that this is for a displacement forcing function and measured displacement output. In a proposed experiment for TSS1, the deployer reel will oscillate with known displacement amplitude and acceleration response will be measured. The FRF for this system is

$$\text{FRF}_{\text{DA}} = -\omega^2 \text{FRF} \quad (9)$$

Both forms of FRF are shown in Figures 1 and 2 for the TSS1 system with nominal damping. A comparison FRF for the equivalent spring-mass system is shown in each plot (the lower curve with only one peak). Even for the direct FRF there is substantial response in the first few modes, while for the acceleration response these modes strongly dominate the spring-mass mode.

### IV. IRF Solution by Laplace Transform

The derivation will be presented in a further paper<sup>3</sup>, but by taking the Laplace transform of (5) with respect to time, we obtain a soluble set of ordinary differential equations in space with the Laplace domain variable  $s$  as a parameter. The impulse response function is then

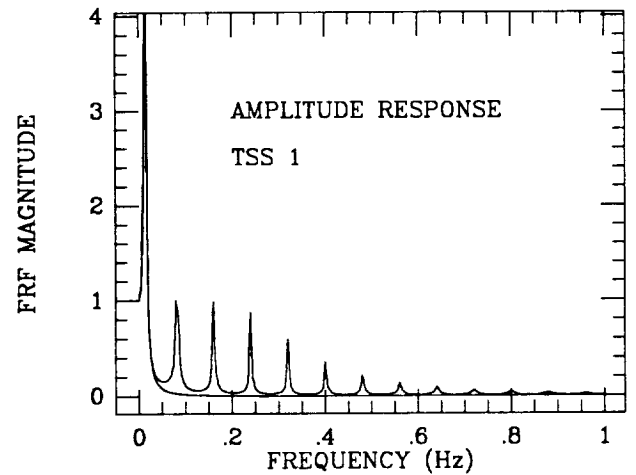


Figure 1 – Amplitude Frequency Response Function, TSS1.

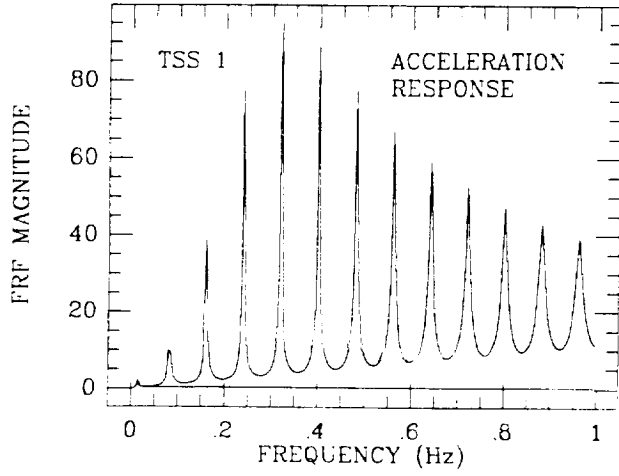


Figure 2 - Frequency Response Function for output acceleration, TSS1.

$$\text{IRF} = \mathcal{L}^{-1} \left\{ \frac{1}{\cosh \nu + \frac{\nu}{a} \sinh \nu} \right\} \quad (10)$$

where

$$\nu = s \sqrt{\frac{1 - \gamma/s^2}{1 + bs}}. \quad (11)$$

In the case  $\gamma = b = 0$  an exact inverse has been found, evaluable with modest effort at any time. Otherwise, it appears that some form of numerical method must be used.

## V. Limit Case, Exact Solution

If there is no damping and no gravity gradient, we expect an initial pulse to propagate distortion free through the tether. By matching ingoing and outgoing waves at the satellite end, the IRF can be found<sup>3</sup>:

$$\text{IRF} = 2e^{-\bar{t}/\tau}/\tau \quad (12)$$

where

$$\tau = \frac{m}{\mu c} \quad (13)$$

is the decay constant after an initial sharp rise to  $2/\tau$  at  $\bar{t} = 0$ , which is taken as the moment the wave reaches the satellite.  $\tau$  is tabulated in Table I. The reflected part of the wave is also computed, its reflection from the Shuttle, and a more complicated response is found on the satellite due to this second, spread out, impulse; this process repeats indefinitely to give<sup>3</sup>, in physical variables,

$$\text{IRF} = \sum_{k=1}^{k_{\max}} u_k(\bar{t}) \quad (14)$$

where

$$k_{\max} = \left[ \frac{1}{2} \left( \bar{t} \frac{L}{c} + 1 \right) \right] \quad (15)$$

$$u_k(\bar{t}) = \frac{2}{\tau} H \left( \bar{t} - \frac{2k-1}{L/c} \right) q_k \left( \left( \bar{t} - \frac{2k-1}{L/c} \right) / \tau \right) e^{-(\bar{t} - \frac{2k-1}{L/c})/\tau} \quad (16)$$

and the polynomials  $q_k$  are defined by recursion

$$q_{k+1}(\xi) = q_k(\xi) - 2 \int_0^\xi q_k(\eta) d\eta \quad (17)$$

with  $q_1(1) = 1$ .  $[\bullet]$  in (15) is the greatest integer function and  $H(\bullet)$  in (16) is the Heavyside function.

TABLE I

	TSS1	TSS2	VG
$\mu$	$0.82 \times 10^{-2} \text{ kg m}^{-1}$	$0.49 \times 10^{-2}$	$0.49 \times 10^{-2}$
$c$	$3.2 \times 10^3 \text{ m s}^{-1}$	$3.2 \times 10^3$	$3.2 \times 10^3$
$EA$	$8.4 \times 10^4 \text{ kg m s}^{-2}$	$5.0 \times 10^4$	$5.0 \times 10^4$
$E'A$	$200 \text{ kg m s}^{-1}$	100	100
$m$	550 kg	550	$5 \times 10^3$
$L$	$2 \times 10^4 \text{ m}$	$10^5$	$10^3$
$g_{gg}$	$0.5 \times 10^{-2} \text{ s}^{-2}$	$0.5 \times 10^{-2}$	$0.5 \times 10^{-2}$
$a$	0.30	0.89	$10^{-3}$
$b$	$0.4 \times 10^{-3}$	$0.6 \times 10^{-4}$	$0.6 \times 10^{-2}$
$\gamma$	$0.2 \times 10^{-3}$	$0.5 \times 10^{-2}$	$0.5 \times 10^{-4}$
$L/c$	6.25 s	31	0.31
$\tau$	21 s	35	320

This form of the solution (14)–(17) can also be derived<sup>3</sup> directly from (10) with  $b = \gamma = 0$ , and numerical evaluations, though difficult, confirm the result also. Thus, in a sense, *this superposition of reflected pulses contains all the physics of the problem.*

If we scale this result as in (4), the decay constant becomes  $1/a$  and the pulses initiate at  $t = 1, 3, 5, \dots$ . Cases with a broad response ( $a = 0.3$ ) and a narrow response ( $a = 3.0$ ) are shown in Figure 3. Figure 4 shows the undamped IRF equivalent to TSS1, along with the equivalent spring-mass IRF. Note the increasing phase lag relative to the spring-mass IRF.

## VI. Numerical Inversions

The rather elegant form of (14)–(17) does not seem to be easily obtained when  $\gamma$  or  $b$  is non-zero. We are reduced to some form of numerical solution.

The approach we have adopted is to use a routine from the IMSL<sup>4</sup> library. A program was prepared which evaluates (10) along with (14) and the equivalent spring-mass IRF. If we are near a sharp rise, as in the cases with zero or small damping, the routine is not robust: numerical overflows, oscillations, and failure due to excessive function evaluations are experienced. One case (Figure 12, below) even appears to have failed without issuing a warning.

Evaluation of (10) by the integral inversion formula via the residue theorem and a Bromwich contour produces an infinite sum of residues at the poles of (10). This has been done in the  $\gamma = b = 0$  case, and the series converges slowly. If  $\gamma$  or  $b$  is non-zero, (11) introduces complications in the function domain and in the choice of appropriate contour; this case has not yet been fully solved.

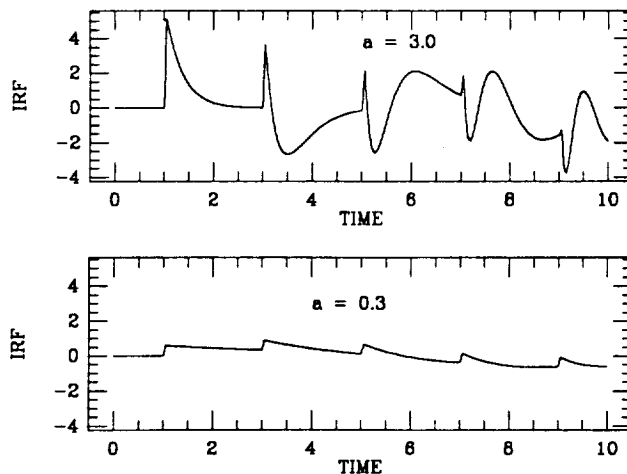


Figure 3 – Effect of parameter  $a$  on the IRF in undamped case,  $\gamma = b = 0$ .

Using the IMSL routine we have performed some studies of the effects of damping and gravity gradient remaining in dimensionless variables ( $a = 0.3$  being used throughout), and have evaluated IRF's for the three systems in Table I.

## Effects of Gravity Gradient

Gravity gradient introduces no energy dissipation, i.e. no damping, and the initial rise is as steep as for  $\gamma = 0$ , to the resolution of the numerical computations (Figure 5). Note the “ringing” in the numerically computed solution,  $\gamma = 0.3$ ; this is an artifact, and occurs if the  $\gamma = 0$  case is treated numerically.

Gravity gradient has a substantial effect on the longer time scale response as shown in Figure 6. (The finite rise times seen are due to the coarse resolution; numerical solution proved difficult near the rises.)

## Effects of Damping

A comparison of damped and undamped solutions for TSS1 is shown in Figure 7. Damping is ten times nominal for clarity; however, there is reason to expect higher damping in the space environment due to increased friction between fibers, and in any case the nominal figure for damping is very uncertain. Note the progressive broadening of the rise profiles in successive pulses.

Figure 8 demonstrates the effect of damping on the rise time of the initial pulse. Note the large effect possible from a small  $b$ .

Figure 9 compares a heavily damped IRF with the spring-mass equivalent. They are very similar, with a slight phase shift.

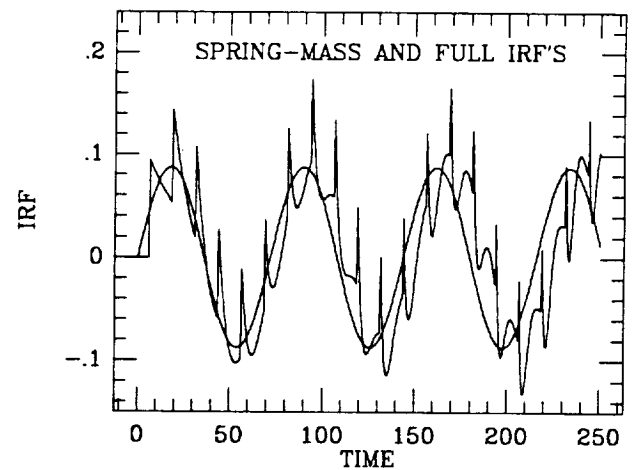


Figure 4 – Undamped and spring-mass IRF's for TSS1.

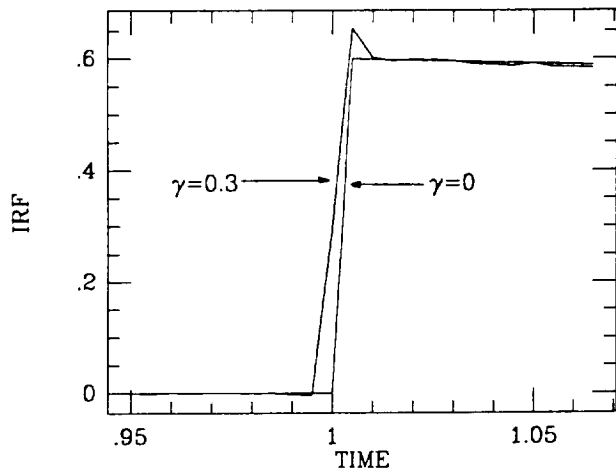


Figure 5 - Effect of gravity gradient on initial IRF rise.

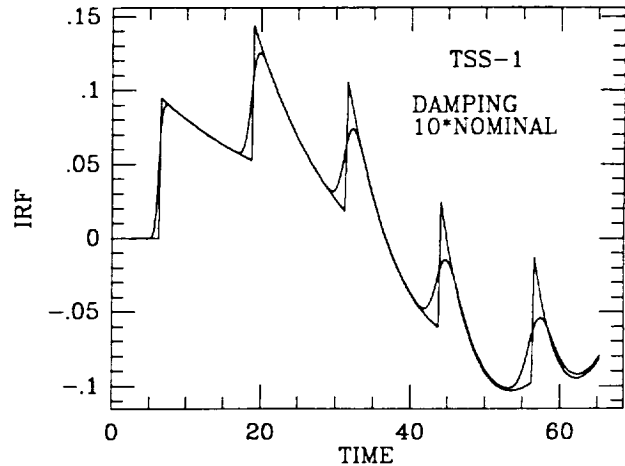


Figure 7 - Effect of damping in TSS1.

### Case Studies

The IRF's for the three cases in Table I are shown in Figures 10, 11, and 12. The cases are TSS1, TSS2, and a variable gravity facility. Higher damping than nominal was used in the first two cases to facilitate numerical solution.

The sharper appearance of TSS2 as compared to TSS1 is due more to the longer interval between pulses (due to longer  $L/c$ ) than to increased sharpness of individual pulses.

The very different appearance of the variable gravity facility case results from the larger satellite mass and the short tether. Almost all the pulse energy is reflected, and the relaxation time for the mass is large. Thus, we see a series of essentially identical pulses which rise only. The linear section above  $t = 4$  is probably a numerical artifact.

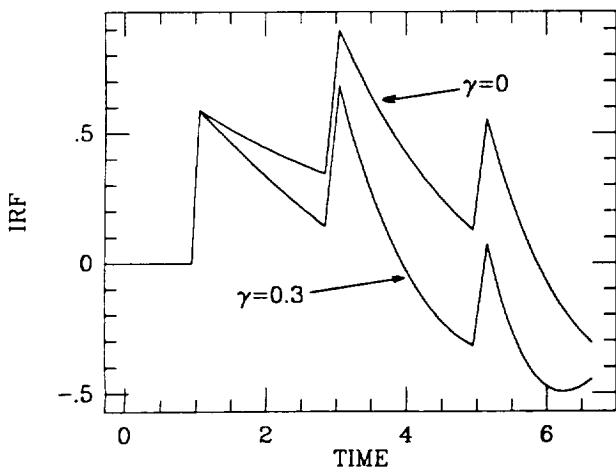


Figure 6 - Long scale influence of gravity gradients.

### VII. Future Investigation

The only immediate prospect for physical verification of these results is on TSS1 and TSS2, which will fly accelerometers on the satellites. Perturbations designed to provide impulses have been requested and a variety of normally occurring operations will also produce such impulses. A ground test of impulse response would also seem quite feasible and worthwhile.

Within the model and methods we have used here, several lines of work are open. The Laplace inversion technique could be made more robust. Approximate results for small  $b$  and  $\gamma$  could be attempted via the Bromwich integral or a method similar to that used to get an exact inverse when  $b = \gamma = 0$ . The integral inversion method needs to be analyzed properly when  $b$  or  $\gamma$  is non-zero. The resulting series of residues may be capable of convergence enhancement.

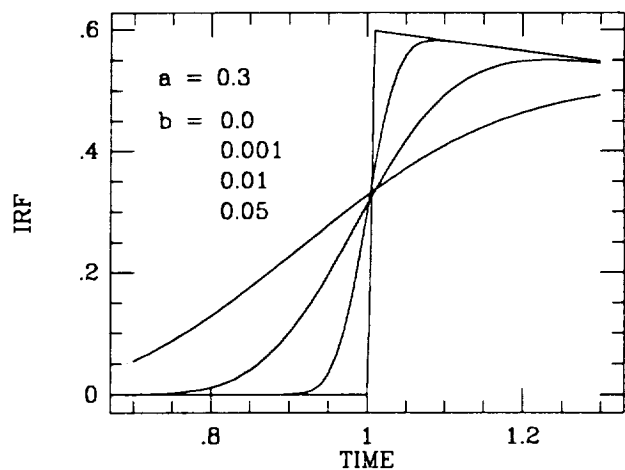


Figure 8 - Effect of damping on initial rise time.

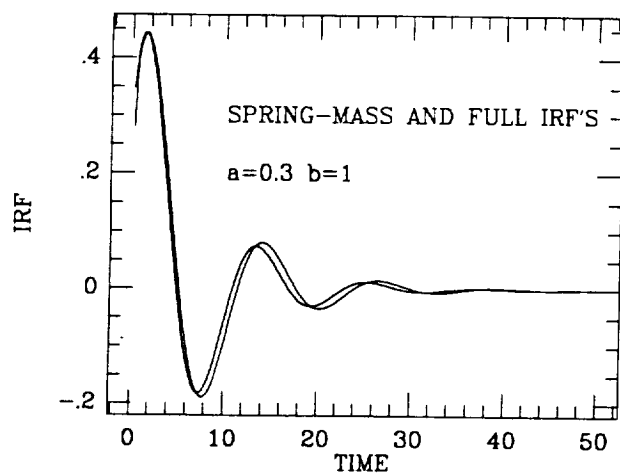


Figure 9 - Comparison of heavily damped IRF with equivalent spring-mass IRF.

The model itself could be extended using essentially the same methods. A finite mass Shuttle could be readily included, as would a flexible deployment boom. Attitude dynamics of the satellite will be more difficult: the resulting equations are non-linear (in the boundary condition) even for small angles. Multi-tether systems could also be solved, providing a more realistic model for the variable gravity facility.

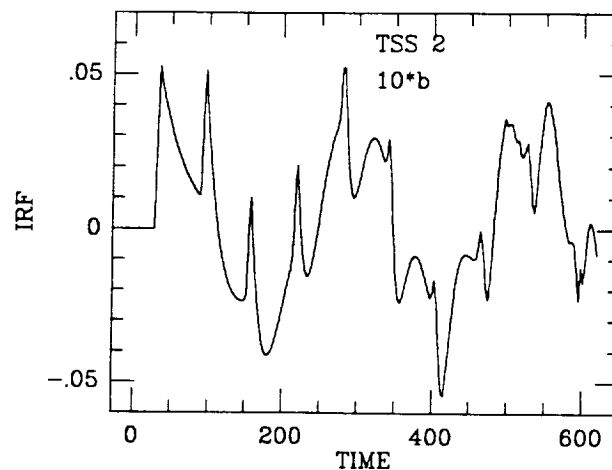


Figure 11 - TSS2 impulse response function

### References

- <sup>1</sup> Various verbal communications
- <sup>2</sup> S. Bergamaschi, W. Lazzarin, and A. Sinopoli, "Dynamical Effects of Tether Structural Damping: A Preliminary Model", in *Tethers in Space*, vol. 62, *Advances in the Astronautical Sciences*, (Bainum, Bekey, Guerriero, Penzo, eds.), 1986
- <sup>3</sup> G. E. Gullahorn and R. G. Hohlfeld, in preparation
- <sup>4</sup> IMSL, "User's Manual, IMSL Library", Routine FLINV, 1984

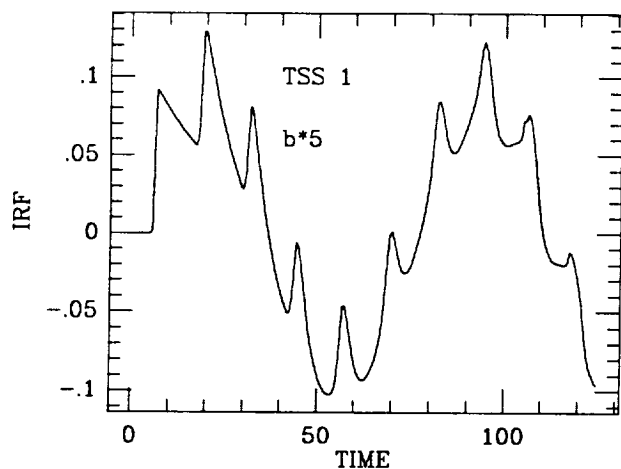


Figure 10 - TSS1 impulse response function.

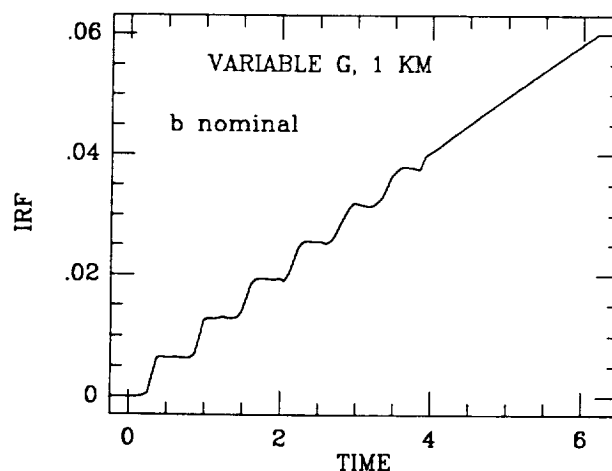


Figure 12 - Variable gravity facility impulse response function. The straight section above  $t = 4$  is probably an artifact.

# VISCOELASTIC DAMPING OF A PULSE IN AN UNTERMINATED TETHER

## DEFINITION OF THE PROBLEM

The mathematical problem describing a tension pulse propagating into a tether terminated with a finite mass is very difficult, even when damping or gravity gradient forces are not considered (Gullahorn and Hohlfeld, 1987 and in preparation, provide a closed form solution). Attempting to solve for the broadening of a pulse due to damping seems formidable when the complication of the terminating mass is included.

The problem becomes more tractable when the terminating mass is removed and the pulse is allowed to propagate into a (semi)infinite tether, with an end condition only at the originating end (assumed to be a relatively large deployer). Ignoring the end mass should still give a good idea of the forces on that mass due to the initial pulse (the reflected pulses, though, may still be important); perhaps in future work, given the solution to the unterminated problem, we may be able to solve the problem with end mass by appropriately reflecting that solution. We also neglect gravity gradient forces; some numerical work with the end mass case seems to indicate that the gravity gradient does not have a smoothing or pulse broadening effect. Also, gravity gradient forces in an infinite tether do not make physical sense: Once a certain length has been exceeded, the force (proportional to tether length) causes the tether to extend indefinitely.

The equations describing tether motion are the same whether the variable being considered is the tension, the position, the acceleration, etc., since these are all related by linear differential operators and the equations are also linear. Because it is the most primitive physical variable, the one typically used to derive the equations, we shall work with the tether position. To be more precise, we imagine the tether fixed at one end so that we may completely control that end's motion, and extending to infinity in a straight line; all tether motion is confined to that line, i.e. is along the axis of the tether, with no lateral or 'string' motion. (In a more complete treatment, this axial or 'column' motion is easily decoupled from the string motion and for small displacements they may be treated independently.) We suppose that the tether is initially at rest in an equilibrium state, in this case simply unstretched, or alternately consider an equivalent reference tether. Divide it into infinitesimal 'elements', each described by its position ' $x$ '

along the reference. We can now disturb the tether, and in the ensuing motion each element will be displaced but still carry with it the 'tag'  $x$ . We describe the motion of element ' $x$ ' at time ' $t$ ' by this displacement from equilibrium,  $u(x,t) =$  (position at time  $t$ ) - (reference position).

The equation describing the tether motion is derived by balancing the acceleration of each tether element with the forces on that element. The model assumed for the tether material determines what these forces are. In general there will be three kinds of force: elastic restoring force; dissipative forces due to energy loss, such as friction; and external (body) forces such as gravity gradient. More complex scenarios might involve changes in tether properties due to, for instance, heating and cooling of the tether. In our work here, we will use as simple a model of tether properties as possible while retaining the features of interest. The results will not be an exact and precise prediction of expected tether response in a specific mission, but are intended as an exemplar against which to compare actual results (to see if any additional physics need be included to explain actual behavior), and as at least an approximate description of reality which can give us information on the relation between damping and pulse velocity, or total energy loss vs. pulse width, etc.

Specifically, we consider two forces on each tether element: A perfect, Hooke's law, elastic restoring force due to the extension of the tether on either side. And an internal, viscous damping force, proportional to the rate of stretch of the tether on either side; this differs from the more commonly considered viscous damping due to friction with a fixed external fluid, which is proportional to the velocity, and something similar might also be due to, say, friction between tether fibers. The arguments of such a derivation are familiar from numerous physics and structural engineering texts and will not be repeated here. The end result is:

$$\mu \cdot \frac{d^2 u}{dt^2} := AE \cdot \frac{d^2 u}{dx^2} + AE' \cdot \frac{d}{dt} \cdot \frac{du}{dx} \quad \square$$

where  $\mu$  is the mass per unit length of the tether,  $AE$  is the tether axial stiffness (elasticity) and  $AE'$  is an equivalent damping constant. To simplify the equations, scale the distance variable by the speed of sound in the undamped tether, ' $c$ ', where



$$c := \sqrt{\frac{AE}{\mu}}$$

and the equation of motion becomes

$$u_{tt} := \left[ 1 + b \cdot \frac{d}{dt} \right] \cdot u_{xx} \quad t > 0, \quad 0 < x < \infty$$

where  $b$  is a dimensionless damping parameter:

$$b := \frac{AE' \cdot \mu}{AE}$$

Here we very cavalierly ignore the details of the scaling and the difference between the original variable  $x$  (in meters or whatever) and the scaled  $x$  (in seconds). From now on,  $x$  refers to the scaled variable. A value of  $x = 2$ , for instance, corresponds to the distance traveled at velocity  $c$  in 2 seconds.

(We could scale both the space and time variables, and totally eliminate parameters in the partial differential equation of motion! However, this scaling does not have a simple interpretation as the above does, and it is complicated enough that it is difficult to see the effect of, say, very small damping. This dimensionless problem might be useful for strictly numerical work where only one problem need be solved by difficult computation and stored, and all problems with arbitrary  $\mu$ ,  $AE$  and  $AE'$  are solved by scaling and lookup.)

To complete the mathematical statement of the problem, we need initial and boundary conditions. For IC, we assume an initial state of rest:

$$\begin{aligned} u(x,0) &:= 0 & 0 < x < \infty \\ \frac{d}{dt} u(x,0) &:= 0 \end{aligned}$$

For boundary conditions, the end at  $x = 0$  is controlled; for our case, we shall assume that the end is held fixed except for very sharp impulse at time  $t = 0$ , idealized as a delta function. At the  $x \rightarrow \infty$  'end', a simple boundedness requirement appears to suffice in the later analysis.

$$u(0,t) := \delta(t)$$

$$u(x,t) \text{ remains bounded as } x \rightarrow \infty$$

## TRANSFORMATION TO LAPLACE DOMAIN

The problem as defined above is a partial differential equation, with both  $x$  and  $t$  derivatives. Such problems are seldom soluble directly. One common way to simplify such a problem is to perform a Laplace transformation in one of the independent variables. The Laplace transform is an integral transform, one of a family of generalized Fourier transforms, which carries one from a domain in which problems are expressed in terms of a given variable, say ' $t$ ', to one in which the variable is typically called ' $s$ '. The Laplace transform of a function  $f(t)$  is called  $F(s)$ , and defined by

$$F(s) := \int_0^{\infty} e^{-s \cdot t} \cdot f(t) dt$$

The advantage of Laplace transformation for differential equations is that it converts derivatives with respect to  $t$  into simple multiplications by  $s$ . We shall not reproduce the details of the transformation of our problem: they are found in numerous applied mathematics books and are routine. We choose to transform the variable  $t$ :  $u(x,t) \rightarrow U(x,s)$ . The result is

$$s^2 \cdot U(x,s) := (1 + b \cdot s) \cdot U_{xx} \quad 0 < x < \infty$$

$$U(0,s) := 1$$

$$U(x,s) \text{ bounded as } x \rightarrow \infty$$

We have effectively decoupled the two independent variables. For the purpose of solving the above, which is now an ordinary differential equation, we can consider  $s$  to be a parameter of the problem. When we have solved the problem for each  $s$  independently, we will then have the complete function  $U(x,s)$ .

For the moment ignoring the dependence on the parameter  $s$ , simply writing  $U(x)$ , and denoting derivatives by  $U'(x)$ , etc., we get a linear boundary value problem:

$$U''(x) - v^2 \cdot U(x) := 0$$

$$U(0) := 1$$

$$U(\infty) \text{ bounded}$$

where

$$v^2 := \frac{s^2}{1 + b \cdot s}$$

Note that  $v$  is constant for the purposes of solving the ODE, and that for real  $v > -1/b$ , the coefficient is negative. The solution is then almost trivial, and again including the dependence on  $s$ , we may write

$$U(x,s) := e^{-v \cdot x}$$

ORIGINAL PAGE IS  
OF POOR QUALITY

or

$$U(x,s) := \exp \left[ -x \cdot s \cdot \sqrt{\frac{1}{1 + b \cdot s}} \right]$$

This is the complete solution expressed in the Laplace domain. Unfortunately it does us little direct good. Physical insight, as well as application to simulation of specific missions, requires again converting from the Laplace domain to the time domain, i.e. taking the inverse Laplace transform.

#### COMPUTING THE INVERSE LAPLACE TRANSFORM

Unfortunately, computing the inverse Laplace transform is not usually as simple as the direct Laplace transform, except for certain classes of functions. Additionally, the function whose inverse transform is sought often exhibits complicated behavior, as for our  $U(x,s)$ . Indeed, it is likely that there often is no closed form inverse for even seemingly simple problems. Approximation techniques can be tricky since the inverse transform is not well behaved.

A direct expression for the inverse transform does exist. However, it requires extending the solution to the entire complex domain. This is not too difficult with our present function, although some care must be taken to stay on the correct branch of

the multiple valued square root function. Then we may write

$$u(x,t) := \frac{1}{2\pi i} \int_{g-i\infty}^{g+i\infty} e^{s \cdot t} \cdot U(x,s) ds$$

Note that here we are integrating along a vertical line in the complex plane. The constant  $g$  is any arbitrary number to the right of all singularities of the function  $U(x,s)$ .

A common way to approach computing this integral is to form a Bromwich contour in the complex plane: consider a limited segment of the vertical line along which the above integral is taken, from  $g-iR$  to  $g+iR$ . Complete a contour by a large circle about the origin intersecting the vertical line at those points (other forms may be used). If there are any branch cuts, distort the contour so as to enclose them with some tolerance  $\epsilon$ . By Cauchy's integral formula the integral around the complete contour may be expressed as a sum of the residues of  $U(s)$  at all the poles within the contour. We let  $R \rightarrow \infty$  (and  $\epsilon \rightarrow 0$ , if applicable), and compute the contributions of the large circle segment and of any contour segments along branch cuts and around their termini, in the limit. Typically, the contribution of the portion going to infinite radius vanishes. Then we may express the solution as the sum of residues minus any branch cut contributions. (This is all standard complex analysis, at least in outline.)

Our example has no poles at all, but does have a branch cut along the negative real axis (this is somewhat arbitrary) terminating at  $-1/b$ . Some progress has been made, at considerable effort, in demonstrating that the outer perimeter does indeed have zero contribution and in evaluating the contribution along the branch cut and around the branch cut point. This work is still preliminary; it is not likely to result in a precise expression, but may be able to provide physical insight (e.g., an approximation for small damping) or convenient numerical methods.

As an interim expedient (partly done to check the derivation to that point) we have decided to evaluate the integral expression for  $u(x,t)$  directly. This evaluation is made relatively simple using the MathCAD software package, a report writing and numerical mathematics tool. The attached reports detail that evaluation, but a brief introduction and some observations are given here.

Three items are attached: First, a report showing how we evaluate the integral expression; we indeed do see the expected broadened pulse at the expected position. But there appears to

be some residual disturbance near the fixed tether end; a second report shows that this is do to numerical problems evaluating the integral at a distance from the actual pulse. Third, we include a consistently displayed set of examples of pulse shapes for a wide range of damping.

Essentially, MathCAD allows us to evaluate the integral expression fairly directly. We simply parameterize a contour segment as a function on a real interval, and integrate the resulting complex function. We set a specific time  $t$  (we always choose  $t = 1$ ) and compute the pulse shape as a function of  $x$ . For each  $x$  value (we typically take 40 to 50) a separate numerical integral must be computed, which can take moderate to substantial computation time. The real and imaginary components of the solution  $u(x,1)$  are plotted; as expected, the real component looks like a damped pulse, and the imaginary component is very small, essentially roundoff.

The integral is performed along a finite segment from  $g - iR$  to  $g + iR$ . This leaves us two parameters  $g$  and  $R$  to choose. The choice can strongly affect the efficiency, or even possibility, of evaluating the integrals. We plot the integrand along the line for a typical  $x$  value; MathCAD's interactive nature allows us to this readily for a variety of parameters  $g$  and  $R$ , and a variety of  $x$ ,  $t$  and  $b$ , for evaluation on the computer screen. In general, the integrand is much more tractable for values of  $x$  on the pulse. Examples of tractable integrands are shown in the first report and in the example pulse shape pages: the integrand may oscillate mildly, or hardly at all, and has an envelope which essentially vanishes within a few oscillations.  $R$  should be chosen to encompass the region of non-negligible integrand.  $g$  affects the integrand itself, and an improper choice can lead to extremely large values or to envelopes which vanish slowly forcing numerical integration over very many oscillations. For points far from the region of the pulse on the  $x$  axis, it seems impossible to find values of  $g$  leading to an easy integration. Such intractable integrands are shown in the second attached report which demonstrates the numerical problems near  $x = 0$ .

Computing a pulse shape can take anywhere from a few minutes to an hour or so, depending on the damping, the range of  $x$  over which the pulse is to be computed, and the parameters  $g$  and  $R$  (on an i386sx machine with coprocessor). Since MathCAD is highly interactive, and since some time must be spent exploring for appropriate  $g$  and  $R$ , these computations are expensive in person time. There is little hope of automating the process within the context of MathCAD, but it is likely that a more prescriptive and less exploratory method may be found to choose  $g$  and  $R$ , and then the pulse computation could be performed by a standard integration routine in Fortran or C.

A set of pulse shapes is displayed at time  $t = 1$  for values of the dimensionless damping  $b = 0.001, 0.01, 0.1$  and  $0.5$ . The lower left plot on each page is the significant one: the top plots show typical integrands, and the lower right is the vanishing imaginary component of the integral. It is seen that even moderate  $b$  values significantly broaden the pulse. Rather than slowing the transmission, damping speeds it on two counts. To first order, the pulse peak travels at the speed of the undamped pulse (indicated by the vertical line at  $x = 1$  on each plot); hence, half of the pulse precedes the peak. Second, for larger damping values, it is seen that even the pulse peak outspeeds the undamped pulse.

# VISCOELASTIC DAMPED TETHER

## DIRECT INVERSE LAPLACE EVALUATION

The Laplace approach to solving the damped pulse problem leads to an inverse Laplace transform, not readily expressed in elementary functions. The inverse may be expressed as an integral along a vertical line in the complex plane. This is typically evaluated by completing the contour (Bromwich contour) and taking advantage of any poles within, as well as branch cuts etc., but let us just try to evaluate it directly for a sample damping and time, to make sure we are on the right track. If we define

$$U(x,s) := \exp \left[ -x \cdot s \cdot \frac{1}{\sqrt{1 + b \cdot s}} \right]$$

where  $b$  is a dimensionless damping parameter,  $x$  is position along the tether (suitably scaled) and  $s$  is the Laplace domain variable. Then the profile at time  $t$  is

$$u(x,t) := \frac{1}{2 \cdot \pi \cdot i} \int_{g - i \cdot \infty}^{g + i \cdot \infty} \exp(s \cdot t) \cdot U(x,s) \, ds$$

where  $g$  is any value such that the cut is to the right of all singularities.

In practice, although we can use complex numbers in the integrand, we must parameterize the contour and then define the contour integral as an integral over a real range (and of course can't actually use an infinite range). E.g.,

$$s(r) := g + i \cdot r \quad \Rightarrow \quad ds = i \cdot dr$$

$$u(x,t) := \frac{1}{2 \cdot \pi} \int_{-R}^R \exp(s(r) \cdot t) \cdot U(x,s(r)) \, dr$$

We are interested in some particular time and damping, say:

$$t \equiv 1 \quad b \equiv .1 \quad (\text{note global definitions})$$

and also a couple of parameters for the integration:

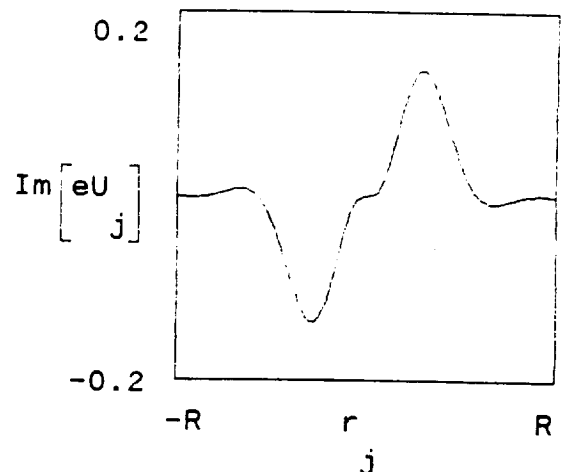
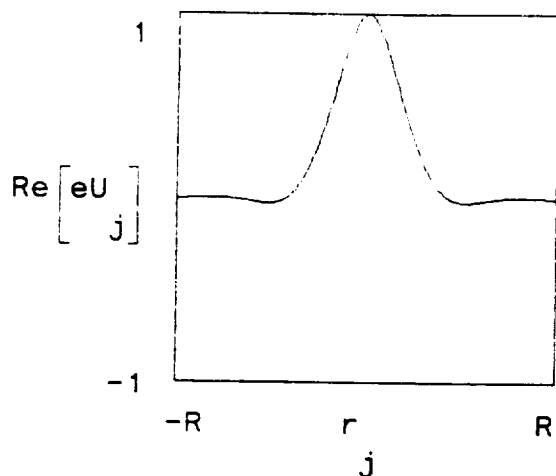
First let's look at the integrand:

```
jmax := 201    j := 0 ..jmax
```

```
dr :=  $\frac{2 \cdot R}{jmax}$     r_j := -R + j \cdot dr
```

calculate a whole vector of functions for a typical x:

```
x := 1
eU := (exp(s(r) \cdot t) \cdot U(x,s(r)))
```



Some lessons from experimenting with the above:

- The real part is symmetric, the imaginary part anti-symmetric, and hence integrating to 0.
- $g=0$  seems like a good choice. For largish positive  $g$ , the real part becomes oscillatory. For  $g$  approaching  $-1/b$ , it becomes closely restricted near 0 but becomes very large (e.g.,  $10^{**8}$ ).
- As  $x$  goes away from  $x=1$  (in the case  $t=1$ , where we expect a pulse near if not at  $x=1$ ) the integrand becomes oscillatory, and the integral hence likely gets smaller.

Let's evaluate  $u(x,t)$  for a few sample values and then do a pulse profile:

```
recall    t = 1    b = 0.1    integration params    R = 20    g = 0
```

```
u(1,t) = 1.247
```

```
u(2,t) = 0.031
```

```
u(.5,t) = 0.201
```

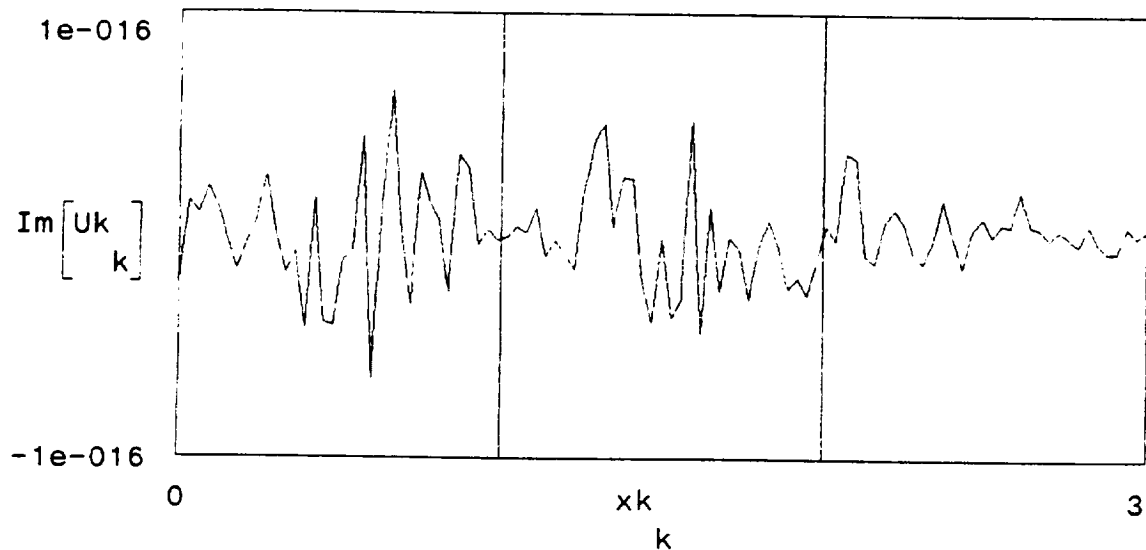
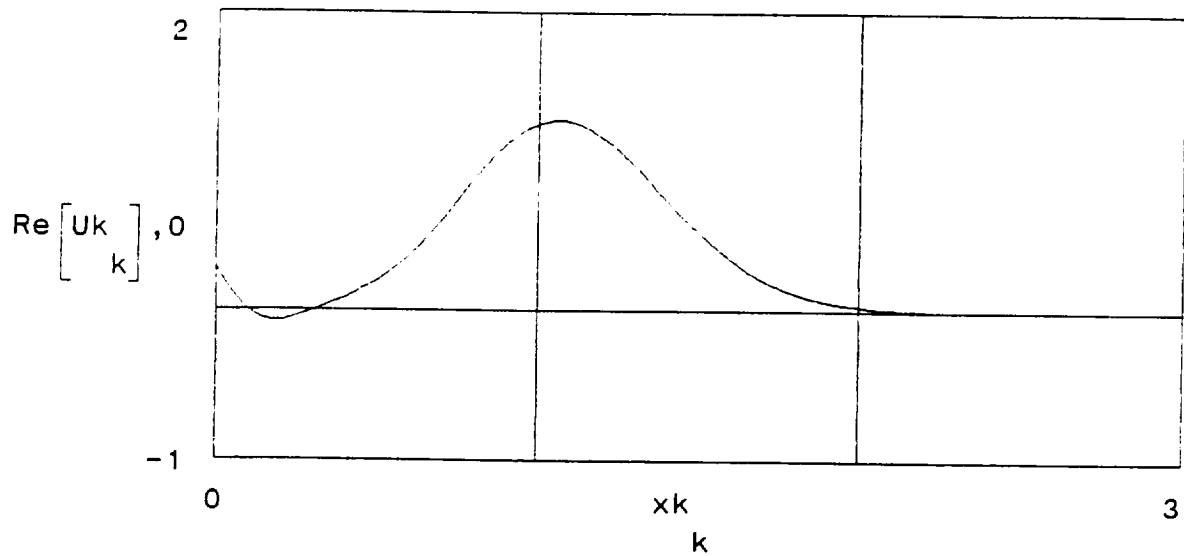
```
u(.1,t) = -0.003
```



```
kmax := 100    k := 0 .. kmax    xmax := 3 · t
```

```
dx :=  $\frac{x_{\max}}{k_{\max}}$     xk := k · dx
```

```
Uk := (u(xk,t))    recall    t = 1    b = 0.1    R = 20    g = 0
```



The little tweak near  $x=0$  appears to be a ubiquitous feature. We will look at it more closely in a separate file.

Note that the real part looks like a pulse at the expected position after one time unit, and the imaginary part is essentially zero (very small roundoff errors keep it from being precisely zero).

# VISCOELASTIC DAMPED TETHER

## DIRECT INVERSE LAPLACE EVALUATION

### BEHAVIOR NEAR $x = 0$

In computing the pulse shape for sample times and damping, we noted a typical behavior near  $x = 0$  that is counter-intuitive: the pulse profile dips below zero for  $x$  around  $1/3$  or so (the major pulse peak is about  $x = 1$ , for  $t = 1$ ) and then increases to some fraction of the peak value as  $x \rightarrow 0$ . Is this real, or an artifact of our limited integration range and limits of Mathcad's integration routine? Here we reproduce the analysis in the previous paper in such a fashion that we can examine the region near  $x = 0$  in greater detail. We eliminate most of the intervening prose and make the integration parameters  $R$  and  $g$  explicit function arguments (rather than global variables) so that a series of plots for varying  $R$  and  $g$  can be presented.

$b := 0.1$       typical, fairly strong damping

$$U(x,s) := \exp \left[ -x \cdot s \cdot \sqrt{\frac{1}{1 + b \cdot s}} \right]$$

$$s(r,g) := g + i \cdot r \Rightarrow ds = i \cdot dr$$

$$u(x,t,g,R) := \frac{1}{2 \cdot \pi} \cdot \int_{-R}^R \exp(s(r,g) \cdot t) \cdot U(x,s(r,g)) \, dr$$

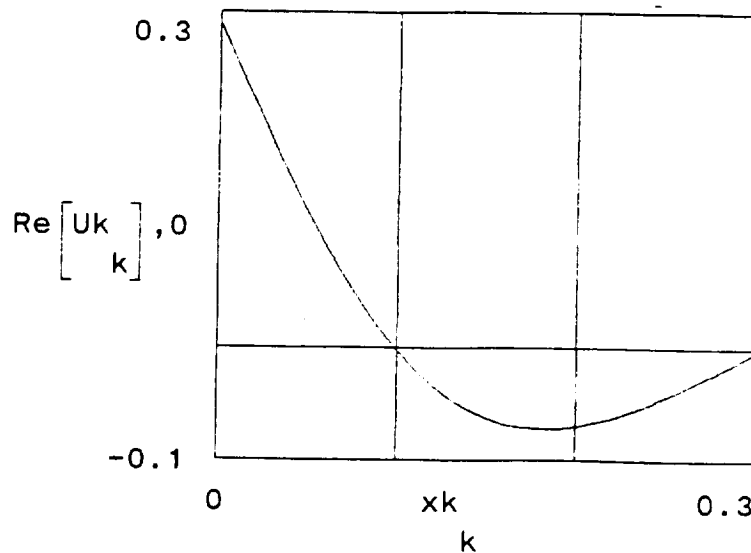
$$k_{\max} := 30 \quad x_{\max} := 0.3$$

$$k := 0 \dots k_{\max} \quad dx := \frac{x_{\max}}{k_{\max}} \quad x_k := k \cdot dx$$

$t := 1 \quad g := 0 \quad R := 20$

---

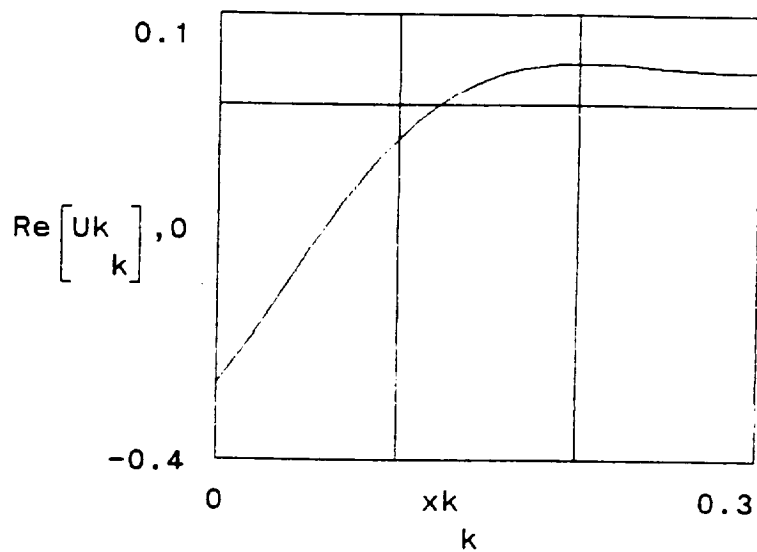
$U_k := (u(x_k, t, g, R))$



$t := 1 \quad g := 0 \quad R := 30$

---

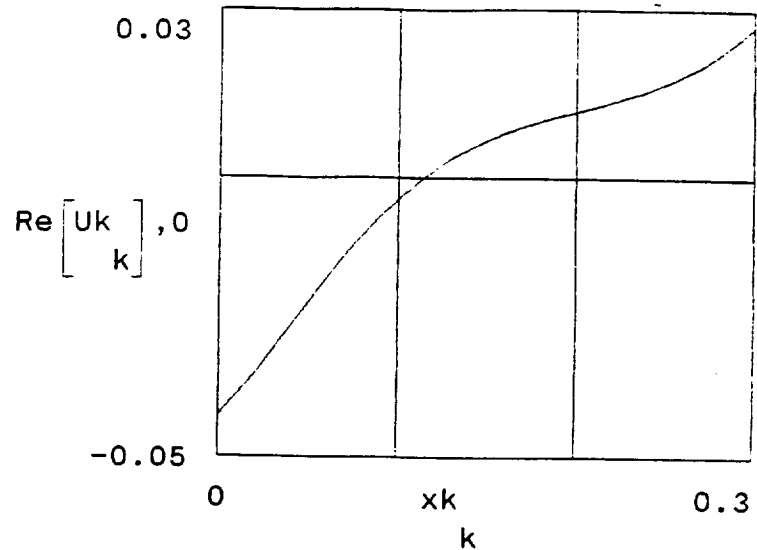
$U_k := (u(x_k, t, g, R))$



$t := 1$     $g := -2$     $R := 30$     $TOL = 1 \cdot 10^{-3}$    (default TOL)

---

$U_k := (u(x_k, t, g, R))$

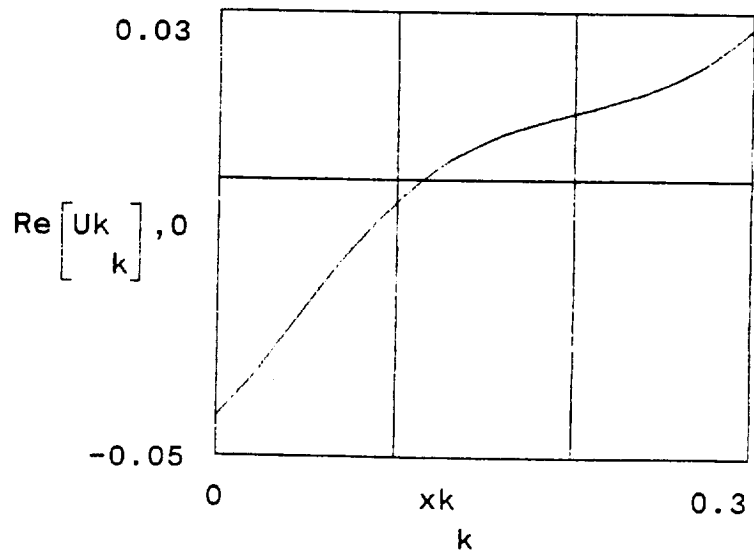


Clearly, from these three examples, the behavior of the profile near  $x = 0$  depends very much on the integration parameters chosen. It is not clear from the above whether the Mathcad integral routine breaks down, or if the inaccuracy is due to the neglected part of the integrand ( $R$  determines what is neglected;  $g$  alters the character of the integrand). We will try two approaches. First, change the default integral convergence TOL. Second, plot the integrand for small  $x$  and varying  $g$  to see what is going on.

$t := 1$     $g := -2$     $R := 30$     $TOL := 1 \cdot 10^{-4}$

---

$U_k := (u(x_k, t, g, R))$



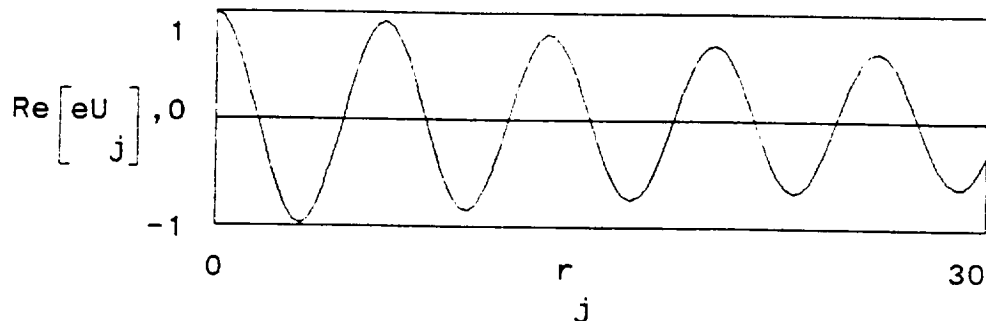
The result looks virtually unchanged. So it does not seem to be numerical error. Now look at integrand.

```
t := 1  R := 30  g := 0  x := 0.05
```

```
-----  
jmax := 100  j := 0 .. jmax
```

```
      R  
dr := ----  
      jmax  
      r  
      j := j · dr
```

```
-----  
eU := (exp(s(r,g)·t)·U(x,s(r,g)))
```

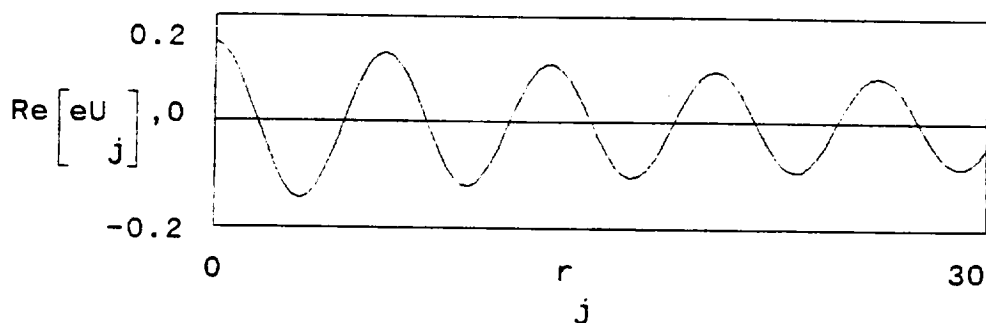


```
t := 1  R := 30  g := -2  x := 0.05
```

```
-----  
jmax := 100  j := 0 .. jmax
```

```
      R  
dr := ----  
      jmax  
      r  
      j := j · dr
```

```
-----  
eU := (exp(s(r,g)·t)·U(x,s(r,g)))
```



The above examples clearly illustrate that the integrand for small  $x$  is highly oscillatory and decreases in amplitude only slowly with increasing variable of integration  $r$ . Thus it would require integrating over very many oscillations to approach a correct answer. In contrast, the behavior of the integrand for values of  $x$  nearer the pulse peak was seen to be much more amenable to accurate integration. Note also that as  $g$  becomes significantly smaller than 0 the integrand decreases substantially.

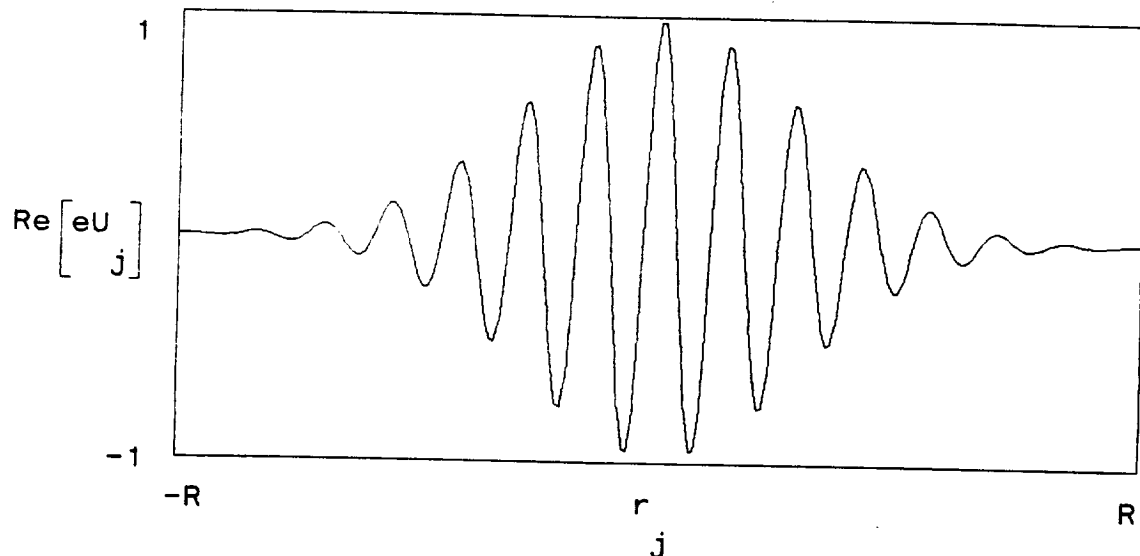
# VISCOELASTIC DAMPED TETHER

## DIRECT INVERSE LAPLACE EVALUATION

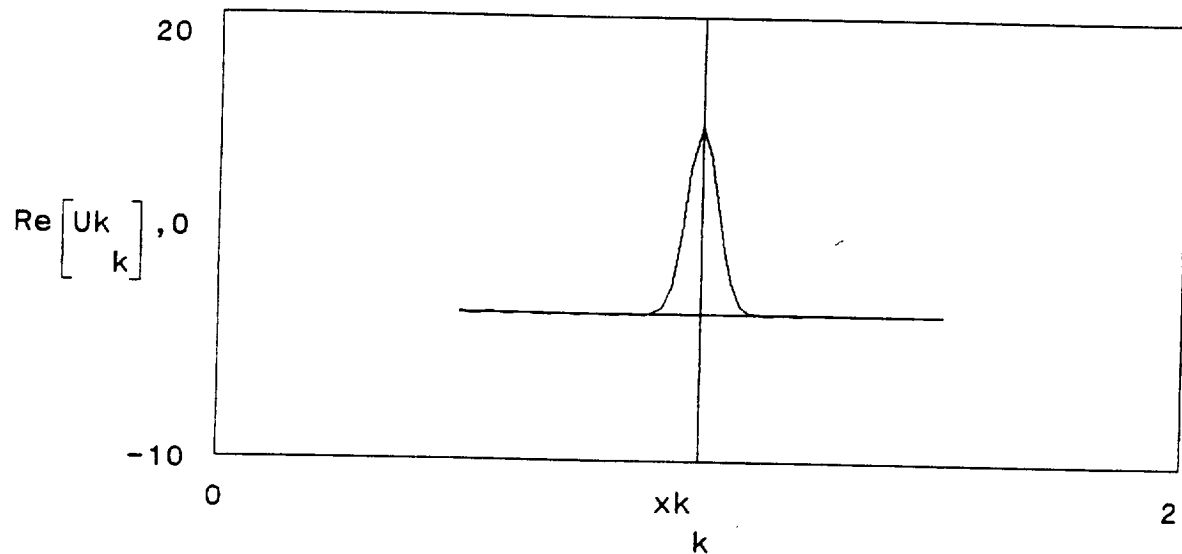
DIMENSIONLESS DAMPING:  $b \equiv 0.001$       TIME:  $t \equiv 1$

INTEGRATION PARAMETERS:  $g \equiv 0$        $R \equiv 90$

INTEGRAND FOR A TYPICAL VALUE OF  $x$ :  $x \equiv 1.5$



INTEGRAL (PULSE SHAPE) on interval:  $x_{\min} \equiv 0.5$        $x_{\max} \equiv 1.5$   
 number of points:  $k_{\max} \equiv 50$



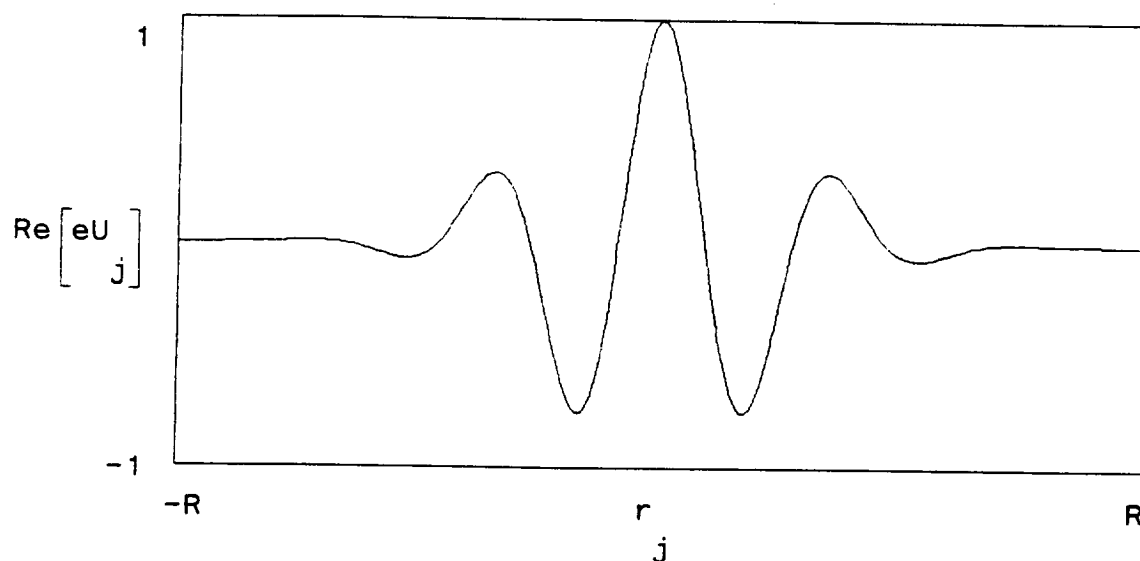
# VISCOELASTIC DAMPED TETHER

## DIRECT INVERSE LAPLACE EVALUATION

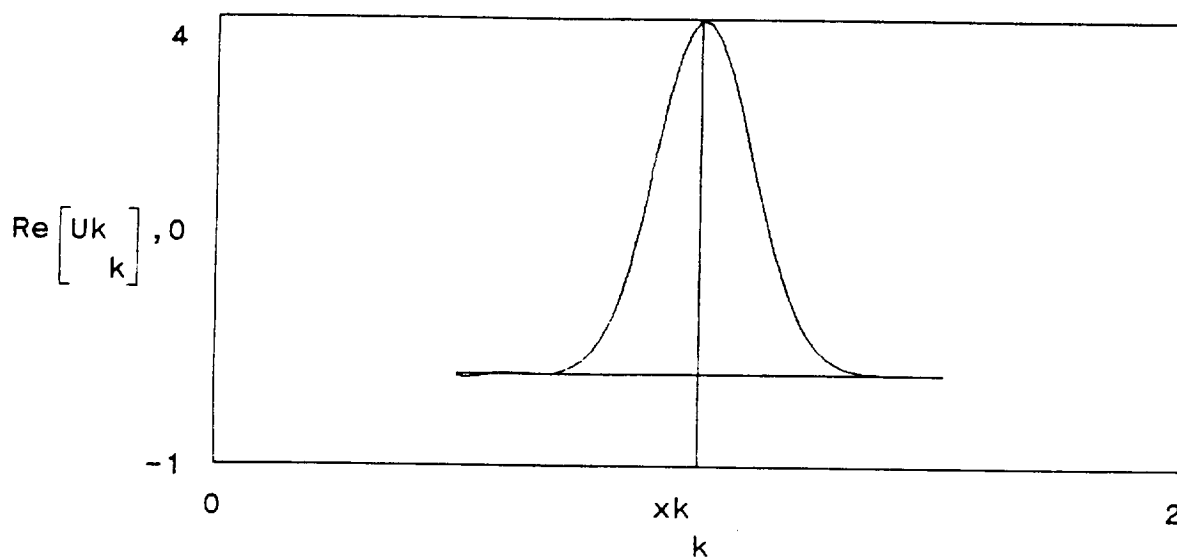
DIMENSIONLESS DAMPING:  $b \equiv 0.01$       TIME:  $t \equiv 1$

INTEGRATION PARAMETERS:  $g \equiv 0$        $R \equiv 35$

INTEGRAND FOR A TYPICAL VALUE OF  $x$ :  $x \equiv 1.5$



INTEGRAL (PULSE SHAPE) on interval:  $x_{\min} \equiv 0.5$        $x_{\max} \equiv 1.5$   
 number of points:  $k_{\max} \equiv 50$



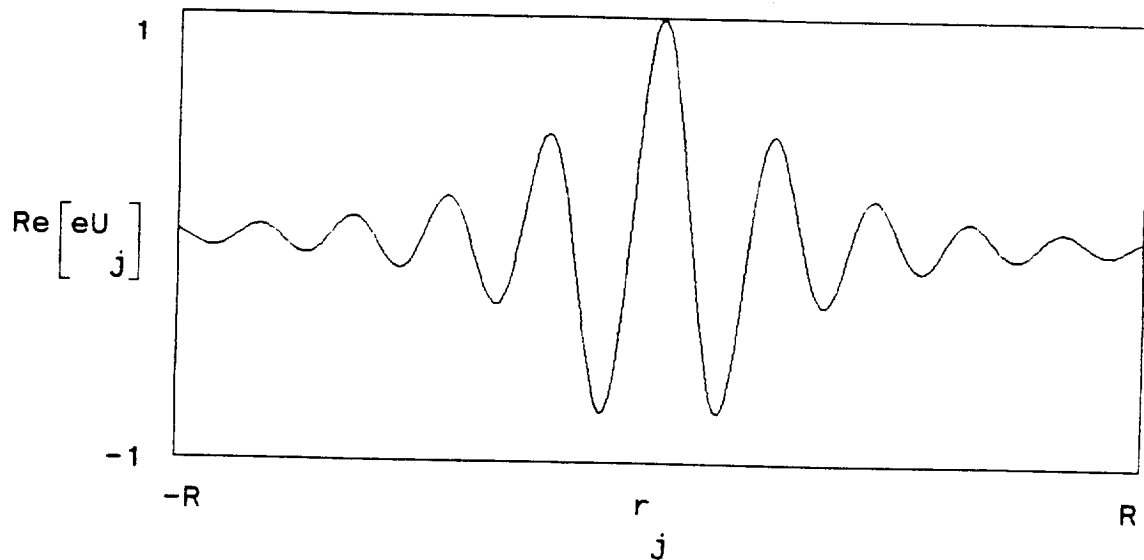
# VISCOELASTIC DAMPED TETHER

## DIRECT INVERSE LAPLACE EVALUATION

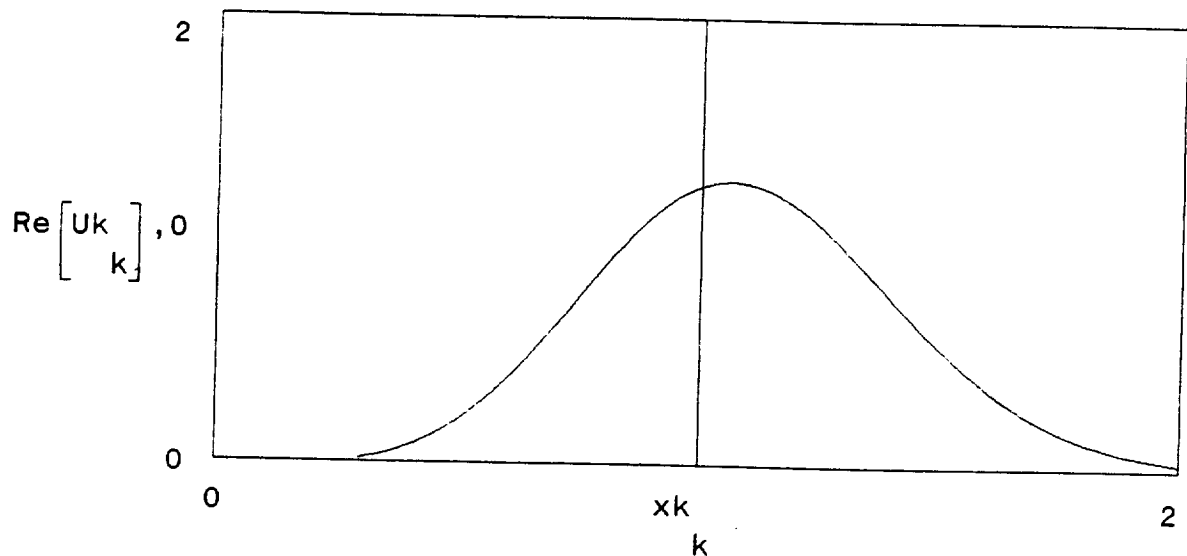
DIMENSIONLESS DAMPING:  $b \equiv 0.1$       TIME:  $t \equiv 1$

INTEGRATION PARAMETERS:  $g \equiv 0$        $R \equiv 35$

INTEGRAND FOR A TYPICAL VALUE OF  $x$ :  $x \equiv 0.3$



INTEGRAL (PULSE SHAPE) on interval:  $x_{\min} \equiv 0.3$        $x_{\max} \equiv 2.0$   
 number of points:  $k_{\max} \equiv 60$





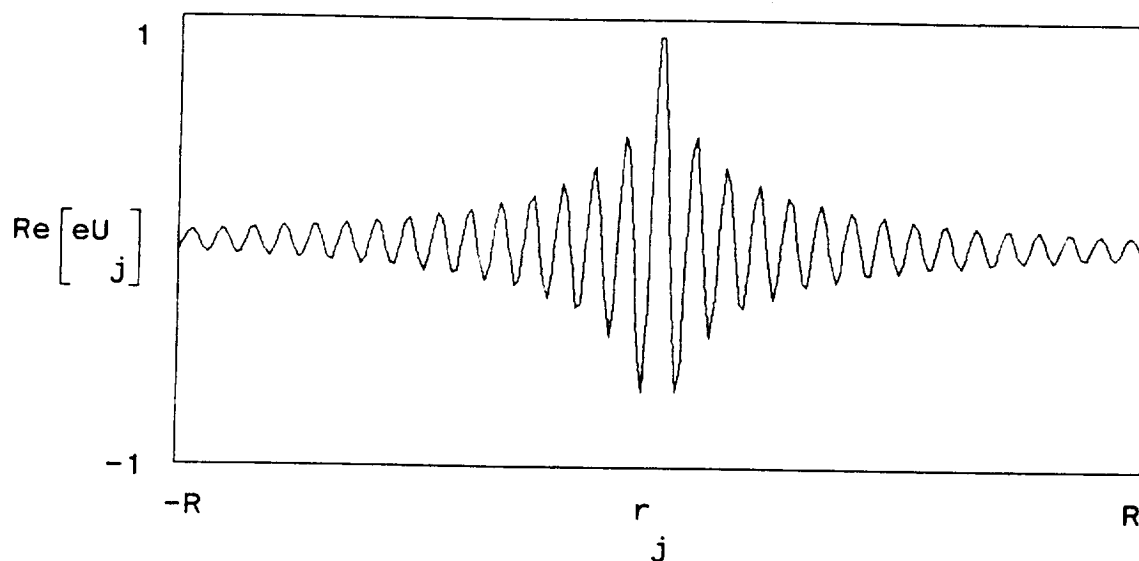
# VISCOELASTIC DAMPED TETHER

## DIRECT INVERSE LAPLACE EVALUATION

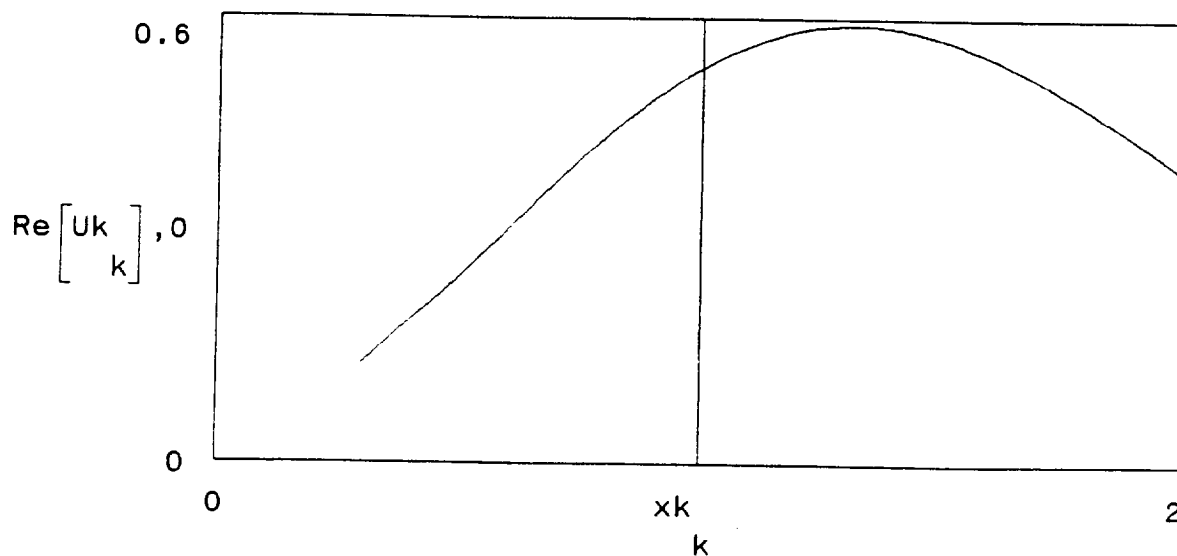
DIMENSIONLESS DAMPING:  $b \equiv 0.5$       TIME:  $t \equiv 1$

INTEGRATION PARAMETERS:  $g \equiv 0$        $R \equiv 100$

INTEGRAND FOR A TYPICAL VALUE OF  $x$ :  $x \equiv 0.3$



INTEGRAL (PULSE SHAPE) on interval:  $x_{\min} \equiv 0.3$        $x_{\max} \equiv 2.0$   
 number of points:  $k_{\max} \equiv 60$



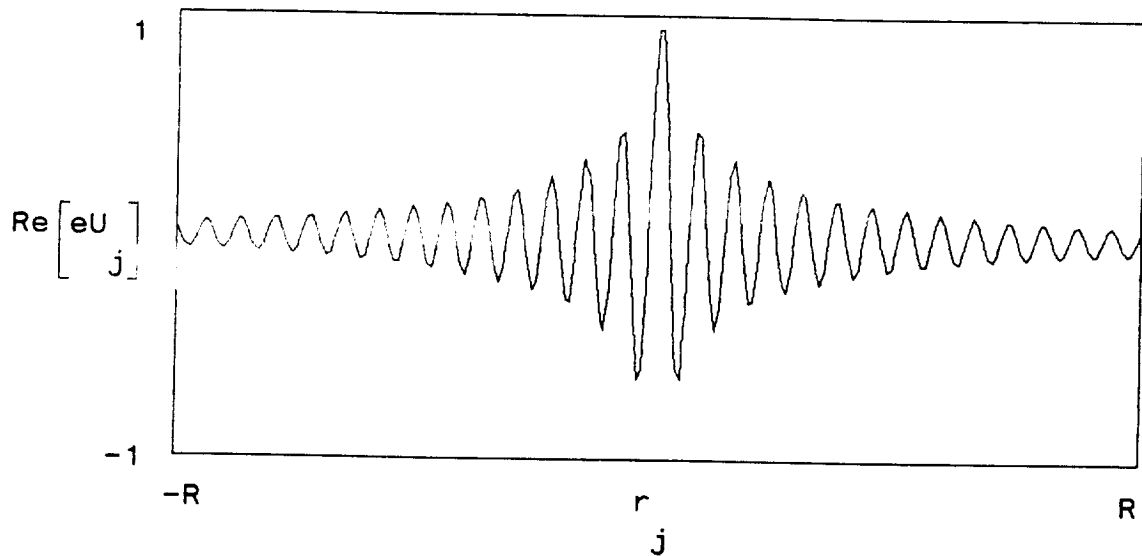
# VISCOELASTIC DAMPED TETHER

## DIRECT INVERSE LAPLACE EVALUATION

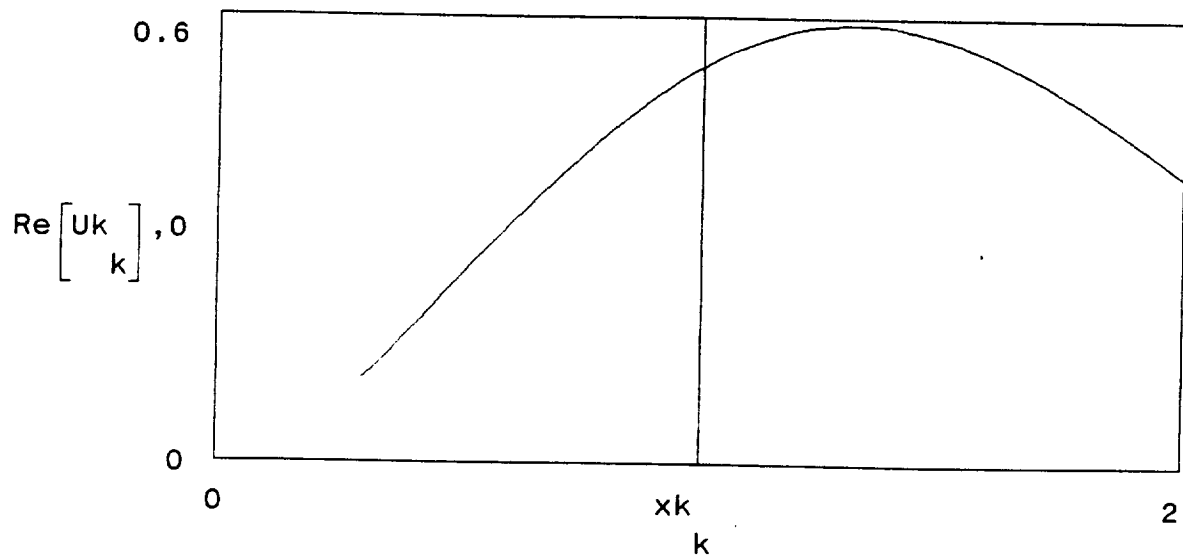
DIMENSIONLESS DAMPING:  $b \equiv 0.5$       TIME:  $t \equiv 1$

INTEGRATION PARAMETERS:  $g \equiv 0$        $R \equiv 90$

INTEGRAND FOR A TYPICAL VALUE OF  $x$ :  $x \equiv 0.3$



INTEGRAL (PULSE SHAPE) on interval:  $x_{\min} \equiv 0.3$      $x_{\max} \equiv 2.0$   
 number of points:  $k_{\max} \equiv 60$





AIAA 93-4765

**ANALYSIS OF SEDS-1 DYNAMICS FROM ON BOARD  
INSTRUMENTATION**

M. L. Cosmo, G.E. Gullahorn, E.C. Lorenzini, M.Grassi  
Smithsonian Astrophysical Observatory  
Cambridge, MA

**AIAA Space Programs  
and Technologies Conference  
and Exhibit**

**September 21-23, 1993 / Huntsville, AL**

# ANALYSIS OF SEDS-1 DYNAMICS FROM ON BOARD INSTRUMENTATION

M. L. Cosmo\* , G.E. Gullahorn, E.C. Lorenzini \*\*, M.Grassi+  
Smithsonian Astrophysical Observatory  
Cambridge, MA 02138

## Abstract

The data of the instruments on board the SEDS-1 end-mass can be used to verify models of the dynamic behavior of long space borne tethers. The purpose of this paper is to estimate the end mass orientation and validate the numerical codes. Our survey is limited to the analysis of only the accelerometer data. Preliminary analysis of some results is presented. A series of three tension pulses generated as density enhancements is the tether deployed are also examined using both satellite and deployer data.

## 1. Introduction

SEDS-1 successful flight has provided the scientific community with valuable data on the dynamic behavior of long space borne tethers. These data can validate theoretical models and check their applicability. Furthermore the elastic properties of long tethers in space can be assessed and compared to the laboratory tests run on the ground.

SEDS-1 data consists of three main sets:

- Deployer Data: number of spool turns, deployment rate and the deploying tension

- Endmass Data: magnetic field, accelerations and tether tension vectors.

- Ground-based Data: radar and optical observations of the deployer, the end-mass and a radar dipole located at the tether midpoint.

The scope of this paper is the study of the dynamics of space borne tethers from the end mass instrumentation data, namely:

- 1) Three-axis magnetometer to measure the orientation of the end-mass with respect to the geomagnetic field
- 2) Three accelerometers to measure non-gravitational accelerations
- 3) Three axis tensiometer to measure the three components of the tether tension and its torque.

The characteristics of the end-mass instruments are listed in Table 1.

In the following, the preliminary results of the analysis of the end-mass instrumentation data will be presented.

Thus far the effort has been concentrated on:

---

\* AIAA Member

\*\*AIAA Senior Member

+AIAA Member. Visiting Scientist also PhD Candidate at University of Naples, Italy.

— "This paper is declared a work of the U.S. Government and is not subject to copyright protection in the United States."

- Estimation of end-mass orientation
- Low-tension deployment
- Tether longitudinal dynamics

## 2. Estimation of End-mass orientation

In order to estimate the orientation of a rigid body in space two reference vectors are needed. In our case only the magnetometer was dedicated to such measurements by using the geomagnetic field as the reference. As second vector we have used the "tether" vector. Specifically, the direction of the line connecting the end-mass to the deployer has been compared to the load cell unit vector.

For both sets of measurements the end-mass orbital parameters are needed in order to compute the inertial components of the line connecting the end mass and the geomagnetic field. In our preliminary analysis the results of our computer program that SEDS-1 deployment have been compared to the delta orbital track and tether length and length rate from the deployer data set. Table 2 shows the orbital elements of the end mas at the moment of the ejection. The results of this fit are shown in figures 1 where the time histories of the end-mass magnetic flux, height above the reference ellipsoid, latitude and longitude are shown, respectively. The agreement with flight data is quite satisfactory. It is also planned to compare these data with the ground based data set and those obtained from other computer simulators and optimal estimators<sup>1,2</sup>.

The two sets of observations can be combined to yield the attitude matrix A and therefore the three euler angles. We use two algorithms

to estimate the end-mass orientation: QUEST (**Q**uaternion **E**stimation) and TRIAD (algebraic method).

The quest algorithm<sup>3</sup> uses a set of n observation at each time to compute the attitude matrix A given a quaternion q that minimizes in the least square sense the so called Wahba's cost function L(A):

$$L(A) = \sum_1^N a_k \left| \underline{w}_k - A \underline{v}_k \right|^2$$

where:

n = number of sets of unit vector observations

$a_k$  = weights =  $1/\sigma_k^2$

$\sigma_k$  = measurement standard deviation

$\underline{w}_k$  = k-th set of unit vector observation in the body reference frame

$\underline{v}_k$  = k-th set of unit vector representation with respect to the reference frame

It can be shown that the solution that minimizes L(A) is also the maximum likelihood estimate of the attitude for the particular choice of weights<sup>4</sup>.

The TRIAD algorithm<sup>3</sup>, also referred as the algebraic method<sup>5</sup>, uses only two reference unit vectors to determine the three Euler angles. Even though this is not an optimal method it can be easily implemented to check QUEST results. It can be shown that when there are only two measurements, as in our case, QUEST and TRIAD are equivalent.

## 2.1. Magnetometer Error Analysis

The magnetometer error  $\sigma_{mag}$  is given by three main contributions: measurement error  $\sigma_{meas}$ , modeling error  $\sigma_{mod}$  and orbital error  $\sigma_{orb}$ .

The error budget of the magnetometer measurement error is as follows:

Linearity = +/- 0.5% FS = +/- 3 mGauss

Noise = +/- 1% FS = +/- 6 mGauss

Ripple Output = 10 mV rms = 2.4 mGauss

Stability = +/- 1% FS = +/- 6 mGauss

The total error  $\sigma_{meas}$  (rms) is 9.31 mGauss.

The strength and orientation of the geomagnetic field is known with high accuracy. In a case like SEDS-1 the modeling problem plays a minor role. Nevertheless an estimate of its contribution can be taken into account as a function of the end-mass height<sup>5</sup>:

$$\sigma_{mod} (mGauss) = \frac{1.43 \times 10^{12}}{(R + h)^3} - 2.7$$

where  $h$  is the height above the ellipsoid expressed in km and  $R$  is the earth equatorial radius.

The knowledge of the end-mass position plays an important role in computing the reference field. An error in estimating the end-mass position results in an error in the reference magnetic field that can be expressed as:

$$\sigma_{orb}^2 = \left( \frac{\partial B}{\partial r} \right)^2 \sigma_r^2 + \left( \frac{\partial B}{\partial \vartheta} \right)^2 \sigma_{\vartheta}^2 + \left( \frac{\partial B}{\partial \phi} \right)^2 \sigma_{\phi}^2$$

where  $B$  is the reference magnetic field and  $r, \vartheta, \phi$  are the end-mass radius, colatitude and longitude, respectively.

The magnetometer attitude error is

$$\sigma_{mag}^2 = \frac{\sigma_{orb}^2 + \sigma_{mod}^2 + \sigma_{meas}^2}{B^2}$$

where  $B^2$  is the modulus of the magnetic field.

## 2.2. Load Cell Error Analysis

According to a NASA/LaRC study<sup>6</sup> that takes into account several sources of error, the measurement error (RMS) of a load cell is  $7\mu V$ . Since the full range corresponds to  $5000 \mu V$  we obtain for each scale of the load cell:

$$\sigma_{low} = 7 \times 10^{-1} / 5000 = 1.4 \times 10^{-4} N$$

$$\sigma_{med} = 7 \times 1 / 5000 = 1.4 \times 10^{-3} N$$

$$\sigma_{high} = 7 \times 10 / 5000 = 1.4 \times 10^{-2} N$$

No data on the instruments biases is available yet, consequently it is not taken into account.

For sake of brevity we do not give here the expressions of the error in measuring the "tether unit vector"  $\sigma_{meas}$  and the error in estimating the orientation of the unit vector connecting the two end-masses in the inertial frame  $\sigma_{orb}$ <sup>7</sup>.

We can then write that the tensiometer attitude error  $\sigma_T$  is:

$$\sigma_T^2 = \sigma_{meas}^2 + \sigma_{orb}^2 + \sigma_{mod}^2$$

where  $\sigma_{\text{mod}}$ , the modeling error, takes into account that the line connecting the two end platforms does not coincide with the direction measured by the tensiometer. In the preliminary stage  $\sigma_{\text{mod}}$  will be kept constant and equal to 2.44 deg<sup>8</sup>.

The accuracies in determining the attitude from the tensiometer and magnetometer data are shown in figure 2 for SEDS-1 deployment. At the moment of this writing no data are available to give a preliminary estimate of the end-mass orientation.

### 3. Early Deployment Tether Dynamics

In order to validate our theoretical models as well as improve our understanding of tether dynamics it is necessary to go through the whole sets of data to find correlations and be able to test some hypotheses. Unfortunately our survey will be limited to the accelerometer data, being the only validated set so far.

The accelerometer data provide the basic information to analyze SEDS-1 dynamics. However, additional information on the end-mass orientation and rotation rates are needed in order to provide the complete model.

The comparison between the moduli of the acceleration measured on board the end-mass and the acceleration computed by the numerical simulation is shown in figure 3. The flight acceleration has been averaged over 60 seconds in order to reduce the periodic rotational terms.

The overall agreement is quite evident even though the fit needs further refinement. It is likely that the assumed tension profile is a principal source of disagreement.

Several interesting features have been observed on small time scales. Figures 4, for example, show the three accelerations at 100 second after ejection.

The arc tangent of the y and x component is plotted in figure 5. We can see that between 150 and 160 seconds the payload aligns itself with the tether (X-Y plane) and oscillates around that value with amplitudes of about 30-40 deg. Moreover the X-Y plane lies in the orbital plane and the out-of-plane component is mostly unaffected oscillating around 0 with amplitudes of about 0.002 m/s<sup>2</sup>. After 180 seconds it looks as the payload is going through phases of tether slackness, or at least very low tension and consequent bouncing. Similar alternating periods of slack and taut behavior were observed on TSS-1<sup>9</sup>. This behavior seems to suggest how the tether was being deployed.

### 4. Tension Pulses

Embedded in the SEDS tether were three linear lumps of flexible metal 3 m long at 400 m intervals. When the tether containing these lumps deployed, the tension increased due to the increased tether density, giving a nominally square wave tension pulse which propagated into the tether. This pulse was detected by both the load cell and the accelerometers on the satellite. As will be seen below, the four relevant measurements (the z acceleration does not show the pulses, being closely orthogonal to the tether direction, and the z tension is not yet available) are very nearly equivalent in form; one example, the x acceleration, is shown in Figure 6 for a period of 100 seconds containing all three pulses. The pulses are clearly

distinct from the background signal.

Visual inspection of Figure 6 seems to show some regularity in the behavior following each pulse. Figure 7 shows the three pulses with both coordinates shifted so that they appear stacked one on top of the other. The structure is not so apparent because of the expanded time scale, but the similarities remain: a sudden decline at about 6 seconds after the peak, lasting for 1 to 2 seconds, followed by a rise until about 15 to 17 seconds after the peak. Whether these regularities are real or simply psychological artifacts will need further analysis.

Figure 8 shows all four measurements for each pulse, for the four seconds surrounding the peak. On this time scale the individual samples (1/8 second) are distinct. The four traces (the top two are tension, the bottom two accelerations) show closely similar structure. Before the first pulse is received at the satellite, note that the two accelerations (and two tensions) are very close, indicating that the satellite is in the 45 degree neutral hang angle. After, the signals diverge, indicating a departure from this attitude, presumable due to the tension pulse. Similar changes in attitude occur across the other two pulses. Since the four measurements are so similar in character, we arbitrarily choose one (the x acceleration) and in Figure 9 superpose the three pulses as in Figure 7, except with a more detailed time scale.

To within the resolution of the sampling, the appearance of the pulses is quite similar: a fairly sharp rise, no more than 3 samples (3/8 s), a peak about 1 to 2 samples wide (1/8 s), and a tail of exponential appearance, with a time constant of about 4 samples

(1/2 s). Before ascribing the measured pulse shape to tether material damping, we should eliminate other possibilities. One such is suggested by Gullahorn and Hohlfeld<sup>10</sup>, who show that even in the absence of damping the finite mass of the satellite will result in an impulse response function (IRF) with a sharp rise and exponential tail. The decay constant is

$$\tau = M/\mu c$$

where M is the satellite mass, c the speed of sound in the tether and  $\mu$  the tether linear density. For nominal SEDS values of  $M = 26$  kg,  $EA = 1.5 \times 10^4$  N,  $\mu = 3.3 \times 10^{-4}$  kg m<sup>-1</sup>, we get  $\tau = 12$  s. Clearly this effect cannot contribute to the structure seen in Figure 7.

Another possibility is that some effect causes the pulse injected at the deployer to be broadened beyond the expected width: the pulses in Figure 7 are 31.1 s apart, corresponding to lump separation of 400 m; so 3 m lumps should give a pulse width of  $(3/400) 31.1 = 0.23$  s. There is a tension measurement at the deployer, but the data is averaged to give a sample rate of 1 s. However, two brief "snapshots" were at a high sampling rate, 0.002 s; one snapshot covered the period when a lump was being deployed, corresponding to the first pulse. The snapshot data has some very short scale, large amplitude, oscillation which makes direct plots of little use (Figure 10a). If we average over 25 samples, the pulse is easily discerned at fairly high resolution, and is seen to be close to a square wave of width 0.2-0.3 (Figure 10b). Now if we average over 62 samples, i.e. over 0.124 s, this gives data at very nearly the sample rate (0.125 s) of the satellite data. These are both plotted in Figure 11, and clearly some of the



apparent structure of the satellite measurements could be due to the sampling; but also clearly, the slightly broadened rise time, and the exponentially decaying tail, are not in the input signal, no matter how sampled. The most likely explanation is that the pulse structure is due to transmission effects in the tether, either nonlinear elasticity or damping.

## 5. Acknowledgments

Support for this research was provided by NASA/Marshall Space Flight Center and NASA Langley Research Center.

## 6. References

1. Glaese, J., SEDS-1 Best Fit Input Data Files for Tether Simulations, Technical Memorandum #10321000-93-2, June 21, 1993.
2. Carrington, C.K., "Kalman Estimation for SEDS Measurements Analysis." NASA/ASEE Summer Faculty Fellowship Program Final Report, NASA/MSFC, August 1989.
3. Shuster, M.D. and S.D. Oh, "Three-Axis Attitude Determination from Vector Observations." Journal of Guidance, Control and Dynamics, Vol. 4, No. 1, January-February 1981, pp.70-77.
4. Shuster, M.D., "Maximum Likelihood Estimation of Spacecraft Attitude." The Journal Of Astronautical Sciences, Vol. 37, No. 1, January-March 1989, pp. 79-88.
5. Wertz, J.R., ed. "Spacecraft Attitude Determination and Control." D. Reidel Publishing Co., Dordrecht, The Netherlands, 1978.
6. R. DeLoach, Private Communication, 1993.
7. E. C. Lorenzini, G.E. Gullahorn, M. L. Cosmo."Analytical Investigation of the Dynamics of Tethered Constellations in Earth Orbit (Phase II)." Contract NAS8-36606, Quarterly Report No.31, July 1993, pp. 22-35.
8. E.C. Lorenzini, G.E. Gullahorn, M. L. Cosmo."Analytical Investigation of the Dynamics of Tethered Constellations in Earth Orbit (Phase II)." Contract NAS8-36606, Quarterly Report No.29, July 1992, pp. 32-91.
9. G.E. Gullahorn, R.G. Hohlfeld and C. Bonifazi. "Observations of Tethered Satellite System (TSS-1) Dynamics," in press, Proceedings of the AAS/AIAA Astrodynamics Conference, August 16-19, Victoria, British Columbia, 1993.
10. G.E. Gullahorn and R.G. Hohlfeld, "Tether as a dynamic transmission line," in Space Tethers for Science in the Space Station Era, ed. L. Guerriero and I. Bekey, 1988, Societa Italiana di Fisica, pp. 163-168.

Table 1. End-mass Instrumentation

	Range	Resolution
Accelerometer		
Low Scale	$\pm 1$ mg	8.3 $\mu$ g
Medium Scale	$\pm 5$ mg	42. $\mu$ g
High Scale	$\pm 50$ mg	0.42 mg
Tensiometer		
Low Scale	$\pm 100$ mN	0.83 mN
Medium Scale	$\pm 1$ N	8.3 mN
High Scale	$\pm 10$ N	83 mN
Magnetometer	$\pm 600$ mGauss	4.7 mGauss

Table 2. End-mass Orbital Elements at ejection

Date	March 30, 1993
Time	4:12:00
Right Ascension (deg)	27.26
Inclination (deg)	33.97
Argument Perigee (deg)	182.64
Semimajor axis (Km)	6832.14
Eccentricity	0.0401
Time since Perigee (sec)	2661.28
Ejection velocity (m/sec)	1.62

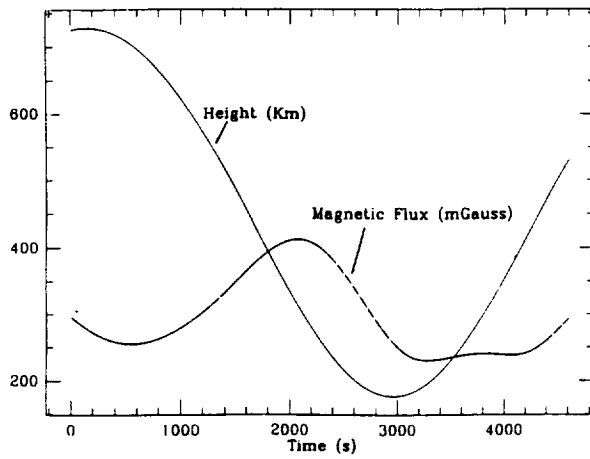


Fig. 1a. End-mass height and magnetic field

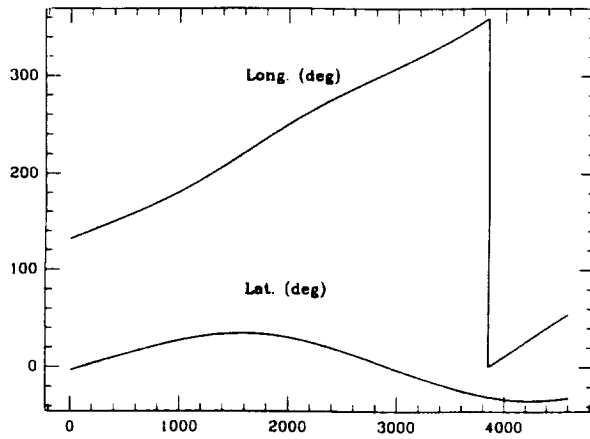


Fig. 1b. End-mass longitude and latitude

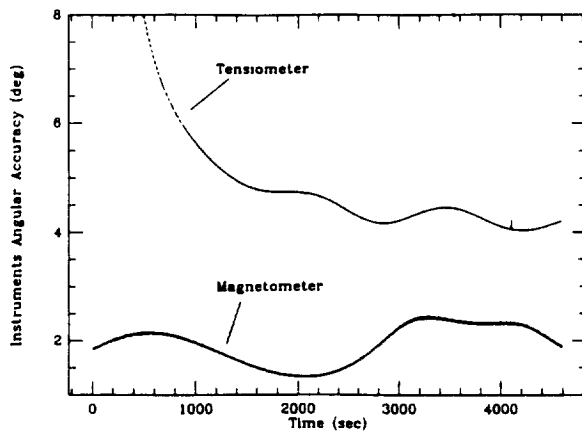


Fig. 2. Angular accuracies of load cells and magnetometer.

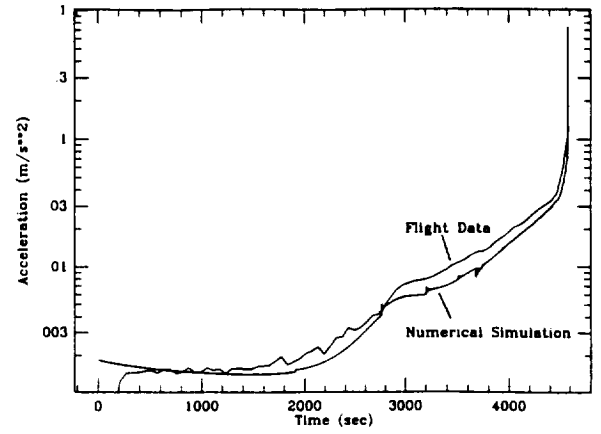


Fig. 3. Time history of flight and numerical acceleration.

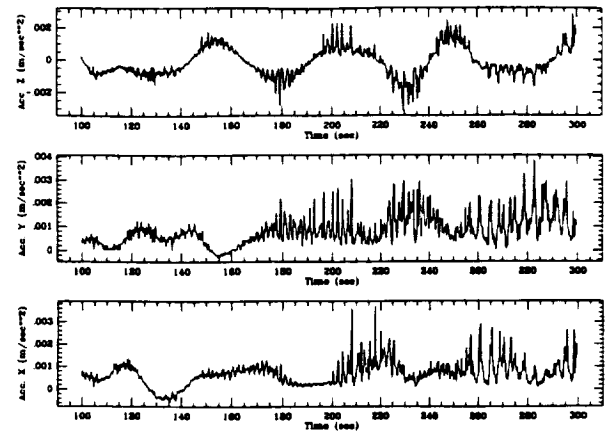


Fig. 4. X, Y, and Z Acceleration components.

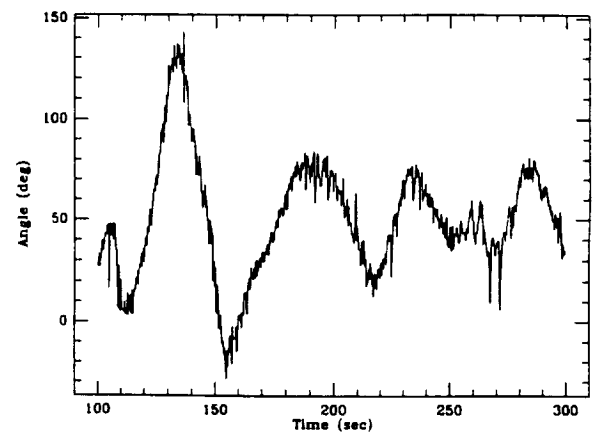


Fig. 5. Angle between X and Y acceleration components.

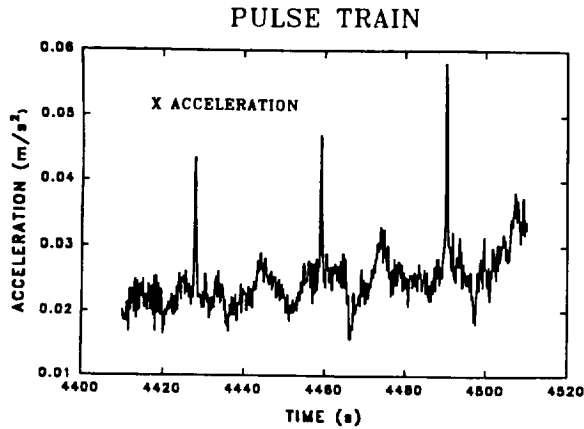


Figure 6. The response on the satellite to three tension pulses produced at the deployer by incorporating regions of enhanced density (metal core) in the tether. One component of acceleration is shown; other relevant measurements are similar.

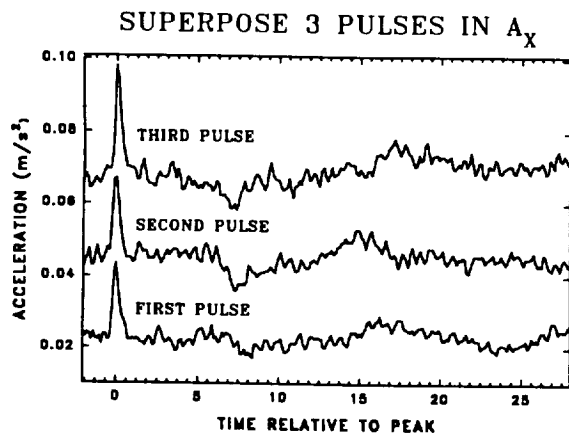


Figure 7. The three pulses of Figure 6, stacked so that similarities in the responses may be discerned. Each pulse is plotted with the time scale shifted to the peak of the pulse, and the second and third pulses are also shifted vertically to avoid interference.

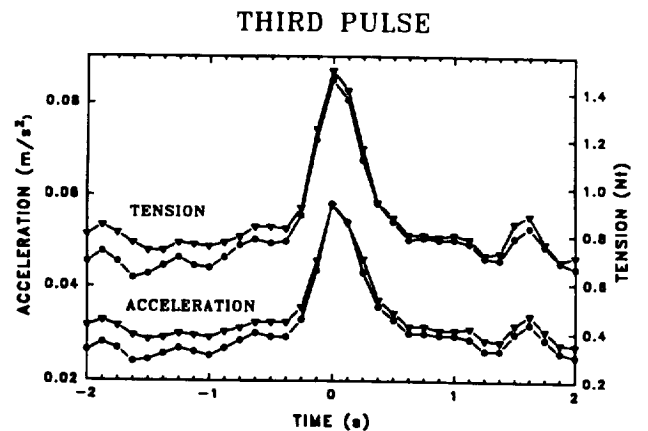
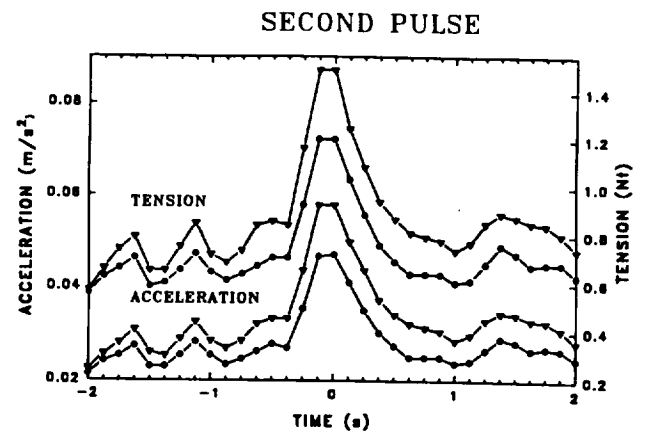
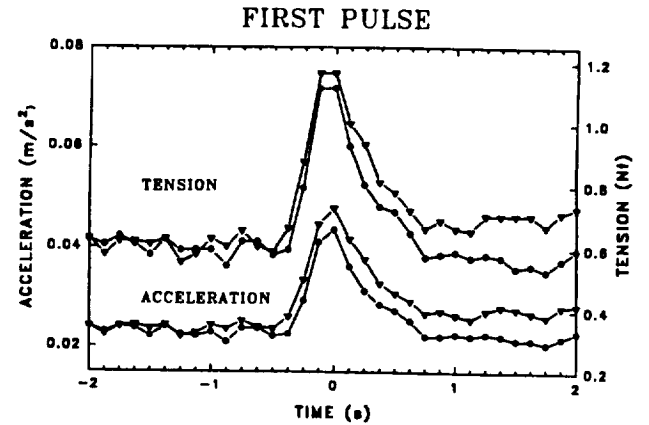


Figure 8. For each pulse the four relevant measurements are plotted. The top two traces are the x and y tension measurements, and the bottom two traces are the x and y accelerations.

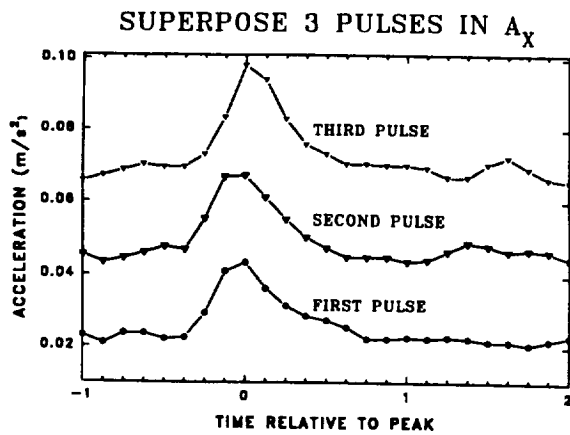


Figure 9. The three pulses are stacked as in Figure 7, except with an expanded time scale to show the pulse structure.

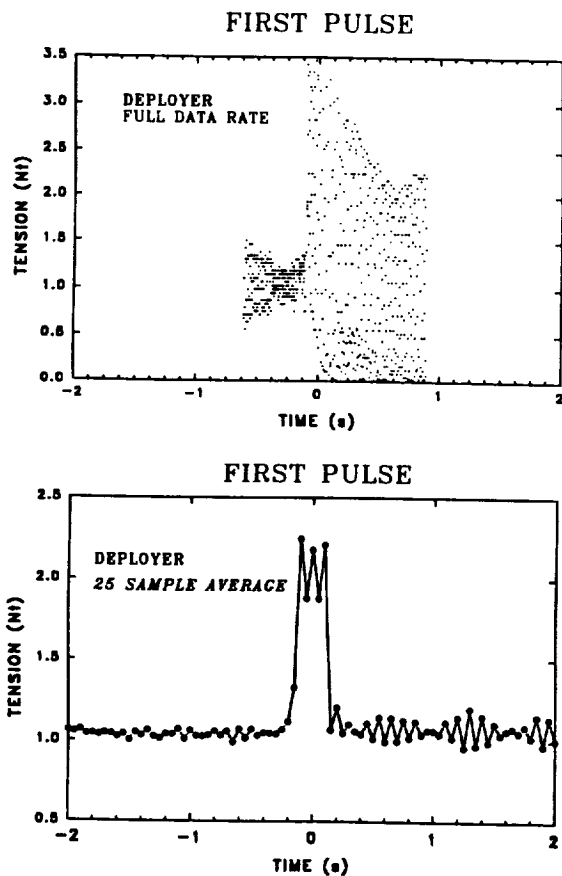


Figure 10. Data from the tensiometer on the deployer about the time of deployment of one of the density enhanced regions producing the tension pulses: (a) at the full data rate of 500 samples per second, there is so much short time scale oscillation that the pulse cannot be discerned; (b) if 25 samples are averaged together to form each plotted point, the square wave nature of the generated pulse is easily seen.

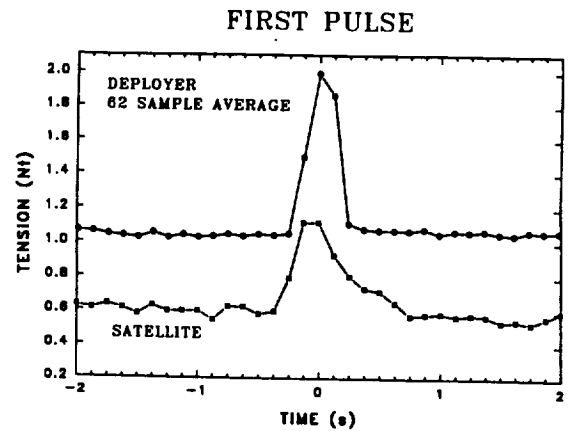


Figure 11. Comparison of the pulse measured aboard the satellite (x component of the tension) with the deployer data averaged to achieve similar "sample" rate. Even though the averaging makes the square wave nature less discernible, the pulse on the satellite is clearly broadened relative to the input (deployer).

## 11.0 DYNAMICS AND CONTROL OF SEDS-II

### Figure Captions

- Fig. 11.1 Deployment trajectories of the satellite with respect to the Delta second stage at various stages during the convergence of the optimization process for finding reference deployment profiles.
- Figs. 11.2(a-c) Reference profiles: (a) length (m), rate (m/s), and brake (turn); (b) spool turn (turn), spool rate (turn/s), and brake (turn); and (c) reference simulation output for perfect reference conditions (i.e., no aerodynamic, massless tether, no sling/scrub transition, no Delta drift): in-plane angle, swing velocity, and tether tension.
- Figs. 11.3(a-b) Deployment dynamics of SEDS-2 with an "additive" (see text) feed-forward/feedback control law for: (a) reference minimum tension  $T_0 = 30$  mN; (b)  $T_0 = 10$  mN; and (c)  $T_0 = 40$  mN.
- Fig. 11.4 Block diagram of SEDS-2 control law.
- Fig. 11.5 Response of low-pass filter for  $a = 1$ , different values of  $c$  and sampling time  $T = 1$  s.
- Fig. 11.6 The filter of SEDS-2 is tested on the flight data of SEDS-1 to smooth out the velocity. The filter parameter are:  $a = 1$ ,  $c = 0.125$ , and  $T = 1$  s.
- Figs. 11.7(a-b) Dynamic response for reference case with "proportional" (see text) control law:  $T_0 = 30$  mN along the whole tether; annulus solidity = 0.96; area exponent = -0.8; and inertia multiplier = 3. Tether is massive, Delta drifts 2000 s after end-mass ejection, aerodynamic drag is present, sling/scrub transition occurs at about  $L \geq 18.8$  km.
- Figs. 11.8(a-e) Sensitivity of system response to uncertainties affecting the tension model. Deployment dynamics for values of the minimum tension ranging from 10 m N to 60 mN.
- Fig. 11.9 Maximum libration amplitude at end of deployment for: (1) an ejection velocity = 1.64 m/s (SEDS-2 springs); (2) an hypothetical ejection velocity = 2.4 m/s (PMG springs); and (3) SEDS-1.

- Figs. 11.10(a-b) Sensitivity to uncertainties affecting the brake response as follows: (a) the friction coefficient is 0.1, i.e. 50% lower than the reference value of 0.18; and (b) the friction coefficient is 0.26, i.e. 50% higher than the reference value.
- Figs. 11.11(a-b) Sensitivity to tension random fluctuations as follows: (1) an additive component that fluctuates  $\pm 2$  mN with respect to the baseline value; and (2) a multiplicative component that fluctuates  $\pm 50\%$  of the baseline value.
- Figs. 11.12(a-b) Sensitivity to saw-tooth noise affecting the tension. Saw-tooth noise for  $L \geq 17$  km, with a fluctuation of  $\pm 0.5$  N and a period of 30 s.
- Fig. 11.13 Maximum libration amplitude at end of deployment for: (1)  $V_0 = 1.64$  m/s,  $\theta_0 = -4.7^\circ$  (nominal conditions); (2)  $V_0 = 1.56$  m/s,  $\theta_0 = -6.7^\circ$ ,  $f = 0.1$ , and  $H_{apo} - H_{per} = 50$  km (conditions of maximum dispersion); and (3) SEDS-1.
- Figs. 11.14(a-e) Comparison simulation between the SAO and NASA/MSFC computer codes for the reference case ( $T_0 = 30$  mN).
- Figs. 11.15 New (January 1994) baseline case with temperature  $\tau = 13^\circ\text{C}$  and the following model parameters:  $T_0 = 12.5$  mN for 19.7-km new and cleaned tether and  $T_0 = 70$  mN for 300-m old tether at the end; annulus solidity = 0.9424; area exponent = -0.6; inertia multiplier = 4.1.
- Figs. 11.16 Same parameters as above except for  $T_0 = 15$  mN for the new tether (cold case with  $\tau = 2^\circ\text{C}$ ).
- Figs. 11.17 Same parameters as above except for  $T_0 = 8$  mN for the new tether (hot case with  $\tau = 35^\circ\text{C}$ ).
- Figs. 11.18(a-b) Effect of heavy tensional noise on the dynamics according to the new (nominal) baseline. The noise structure is as follows: an additive component of  $\pm 10$  mN; a multiplicative component of  $\pm 50\%$ ; and a saw-tooth noise of  $\pm 0.5$  N with a period of 30 s active for  $L \geq 17$  km.

Figs. 11.19(a-b) Flight data of SEDS-2: (a) raw tension from the deployer's tensiometer; and (b) filtered tension after the end of deployment. From the analysis of the filtered tension, the maximum libration amplitude at the end of deployment is 3.2 deg.

Figs. 11.20(a-b) Flight data of SEDS-2: (a) raw tether exit velocity from the turn counter (one turn counter was declared failed at  $t = 2200$  s); and (b) raw tether length.

Figs. 11.21(a-b) (a) 10-s average of tether velocity after having eliminated the spurious velocity values  $> 10$  m/s due to the turn counter's failure; and (b) in-plane angle estimated by feeding the 10-s average of tether velocity to the SEDS-2 deployment simulator. According to this estimate, the maximum libration amplitude at the end of deployment is 4 deg.

Figs. 11.22(a-b) (a) 100-s average of tether velocity after having eliminated the spurious velocity values  $> 10$  m/s due to the turn counter's failure; and (b) in-plane angle estimated by feeding the 100-s average of tether velocity to the SEDS-2 deployment simulator. According to this estimate, the maximum libration amplitude at the end of deployment is 2 deg.

Fig. 11.23 The actual brake turns from the SEDS-2 flight are compared to the reference brake profile.

## 11.1 SEDS-2 Closed-loop Control Law

### 11.1.1 Control Scheme

Difficulties in devising a control law which provides small librations at the end of deployment stem from the stringent hardware limitations of the SEDS system. Namely: a brake with highly non-linear characteristics (i.e., exponential response); a deployer which can not reverse the deployment velocity; a Z-80-based computer with limited computational speed and 28 Kbytes of memory available for the control software; only one sensor with a repeatability adequate for a feedback control loop, i.e. a turn counter which measures the number of tether turns deployed from the spool with an accuracy of one turn.

The goal of the control law is to control a non-linear plant both in terms of dynamics and actuator response in the presence of uncertainties affecting the actuator and the plant. The performance goal is a libration of less than 10 deg at the end of deployment for large (and unpredictable) variations of the tension values. One additional requirement calls for the activation of the brake only after the first kilometer of tether has been deployed because, since the tether tension is too low at short tether lengths, an over braking could stop the deployment at short range.

The strategy followed to derive the control law splits the control problem into two parts: (1) finding the solution of a two point boundary value problem; and (2) developing a local linear feedback controller.

The solution of the boundary value problem, by means of a parametric optimization, provides the reference length  $L_{ref}$  and velocity  $\dot{L}_{ref}$  profiles and an associated reference brake profile  $B_{ref}$  (reference control input) [1,2]. The reference brake profile is the non-linear part of the control law which is fed forward to the actuator. This non linear part enables a linearization of the perturbed response of the system around the non-linear solution. For this reason, this technique of splitting the control law into a feed-forward non-linear component and a linear feedback is sometime called feedback linearization.

The linear feedback control, which is the subject of this report, is a PD controller which forces the system to follow the reference length and velocity profiles by canceling the length and velocity errors with respect to the reference.



### 11.1.2 Implementation of Control Law

#### Tension Model

The tension model for the SEDS deployer was derived empirically from the analysis of deployment tests on the ground, supported by physical considerations. In summary the tension model consists of a static component  $T_0$  (the minimum tension) and a dynamic component, proportional to the square of the deployment velocity. The actuator (brake) is modeled as an exponential function  $e^B$  that multiplies the input tension. A second exponential function models the friction between the tether and the exit guide. See eqn. (9.1) in Section 9.2 for the mathematical expression of the tension model.

#### Reference Profiles

The feed-forward part of the control law is the reference brake profile which enables the system to follow the desired length  $L_{ref}$  and speed  $\dot{L}_{ref}$  profiles under reference conditions and a reference tension model.

The reference profiles are computed with an iterative process aimed at minimizing the value of a cost function at the end of a deployment of desired duration. The optimization process is briefly outlined in the following. The brake profile is expressed in terms of a finite (and small) numbers of parameters, for example by means of a cubic spline with a few fixed points. A cost function is constructed in such a way that its value approaches zero for the desired values of the state vectors at the end of deployment. An optimization routine, suitable for minimizing generic (non-smooth) functions, is adopted to search for the optimal set of parameters of the brake profile. For each trial of brake parameters, the numerical integration of the deployment trajectory enables the computation of the cost function at the end of deployment. The optimization routine selects different sets of brake parameters based on the trend of the cost function from iteration to iteration. Figure 11.1 shows the convergence of the optimization routine by depicting selected deployment trajectories during the iteration process. The minimum tension and the target state vector for this particular optimization run were as follows:  $T_0 = 20$  mN,  $X_{goal} = 0$  m,  $Z_{goal} = 20$  km,  $\dot{X} = 0$  m/s,  $\dot{Z} = 0.8$  m/s where  $X$ ,  $Z$  and  $\dot{X}$ ,  $\dot{Z}$  are the components of the satellite displacement and satellite velocity with respect to an local horizontal-local vertical (LH-LV) reference frame centered at the Delta second stage. For a more detailed description of the optimization process see Ref. [1] and Ref. [2].

The reference profiles  $L_{ref}$ ,  $\dot{L}_{ref}$ , and  $B_{ref}$  are memorized in the on-board computer in a 3x900 array of data (reference table) in fixed point format with a three digit accuracy. The reference table for the flight software of SEDS-II was derived for the numerical values of the system parameters shown here below. These values were based on the flight data of SEDS-I.

*Tension model and system parameters*

$T_0$	= Minimum tension	= 30 mN
$A$	= Tether annulus solidity	= 0.96
$E$	= Area exponent	= -0.8
$I$	= Inertia multiplier	= 3
$m$	= Satellite mass	= 25.9 kg
$t_D$	= Deployment duration	= 6,500 s

*Orbital parameters and initial conditions*

$H$	= Orbital altitude	= 350 km
$\theta_0$	= Ejection angle	= -4.7 deg (backward wrt LV)
$V_0$	= Ejection velocity	= 1.64 m/s

The  $L_{ref}$ ,  $\dot{L}_{ref}$ , and  $B_{ref}$  profiles are shown in Figs. 11.2(a). The flight software reference profiles, which are expressed in terms of spool turns and turn rates, are shown in Fig. 11.2(b). The simulation output, i.e. in-plane libration angle  $\theta$ , swing rate  $\dot{\theta}$  and tether tension, for perfect reference conditions (i.e., no aerodynamic drag, massless tether, no sling/scrub transition, no Delta drift) are shown in Fig 11.2(c). For a tabulation of SEDS-II flight reference table, called Ref1\_14June93, see Ref. [3].

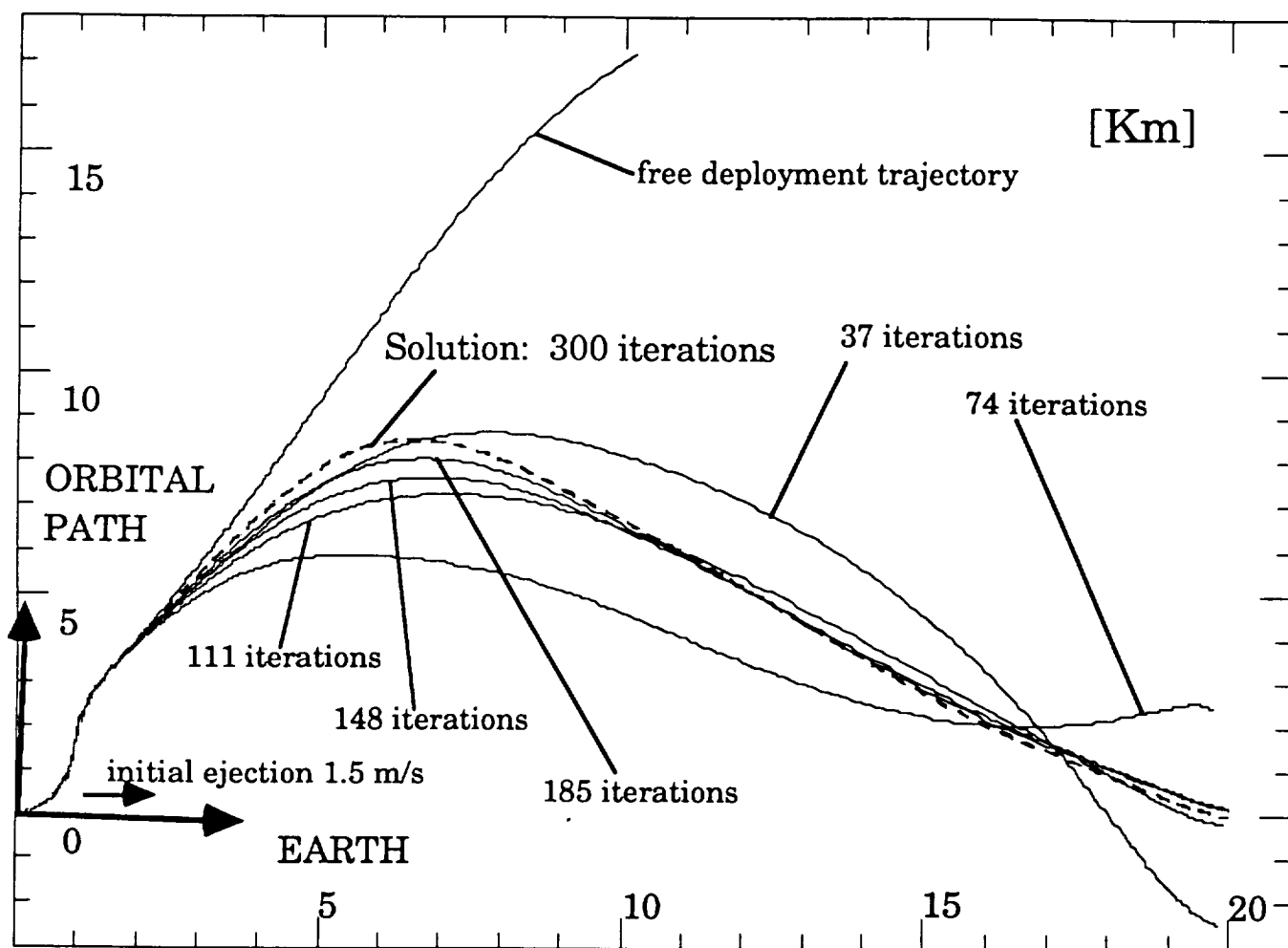


Figure 11.1

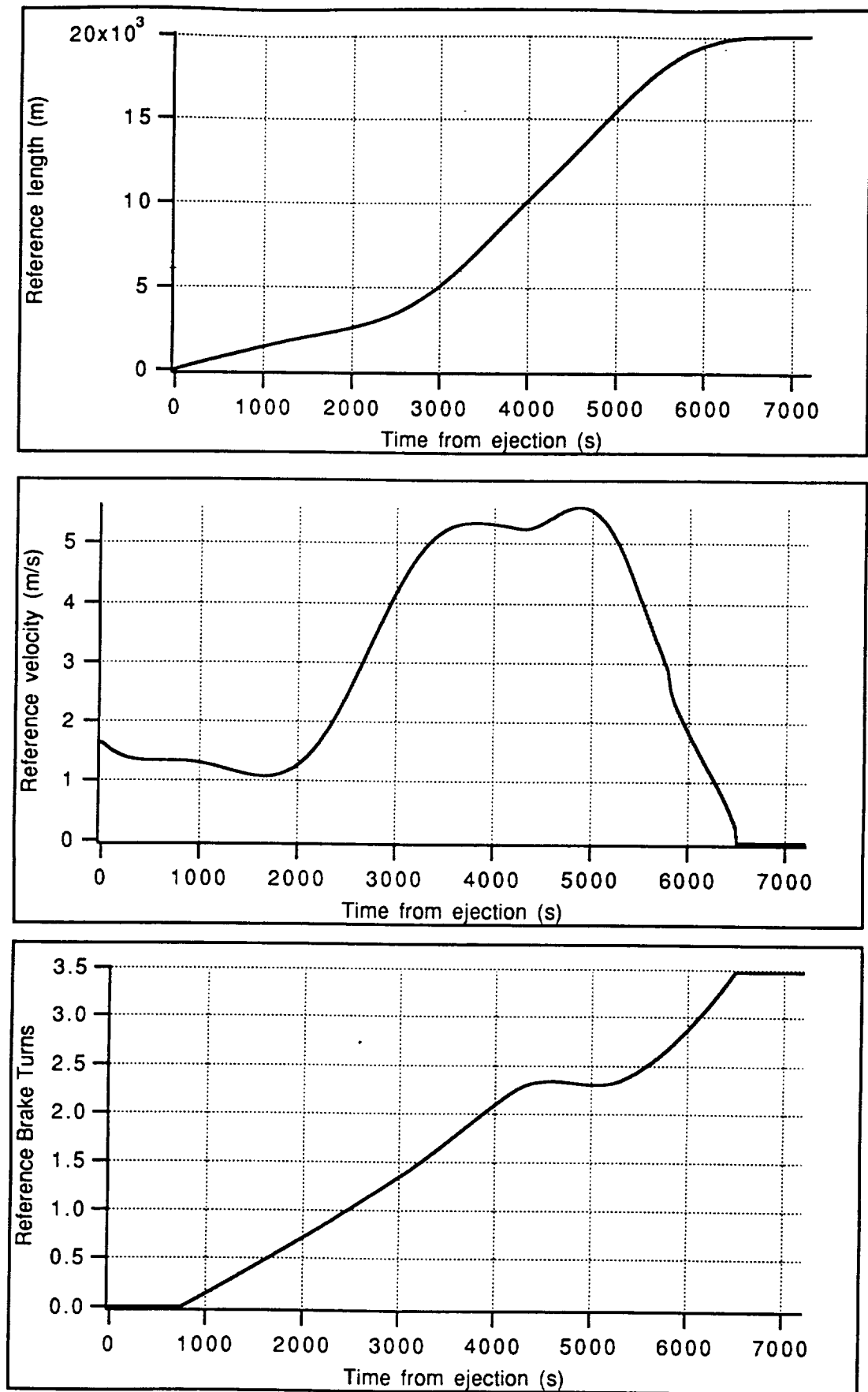


Figure 11.2(a)

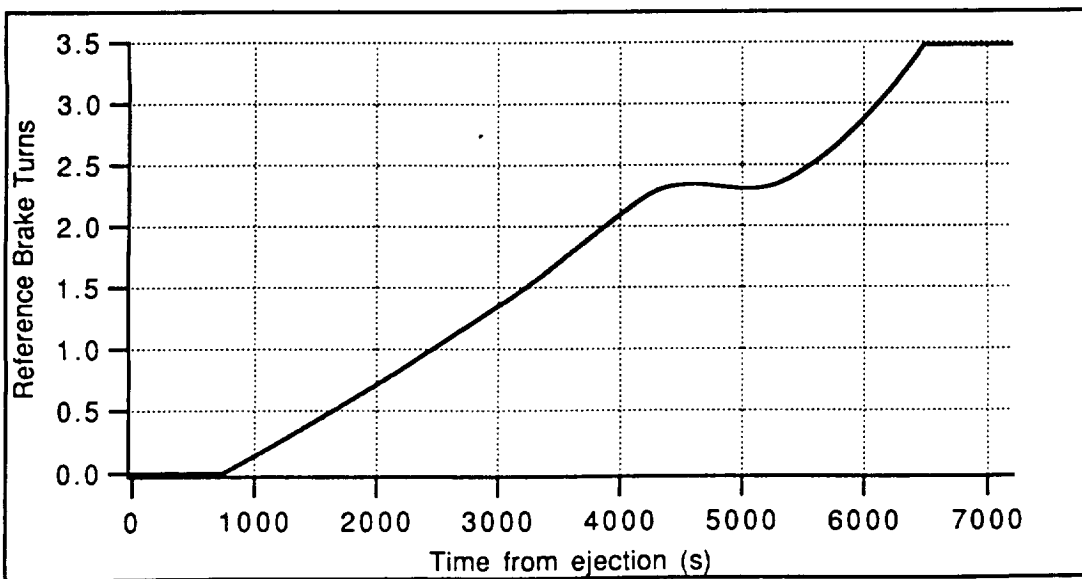
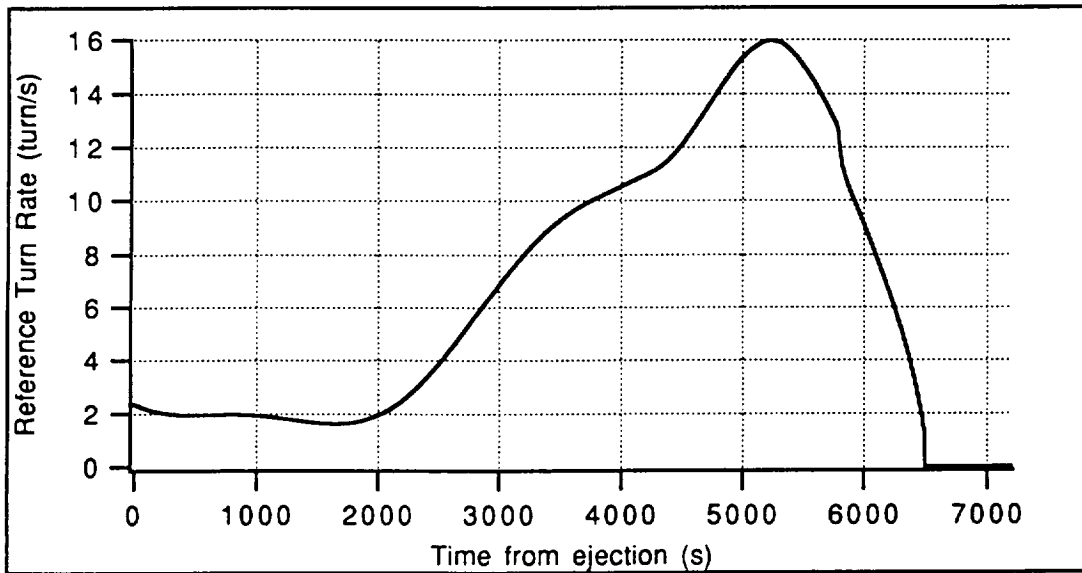
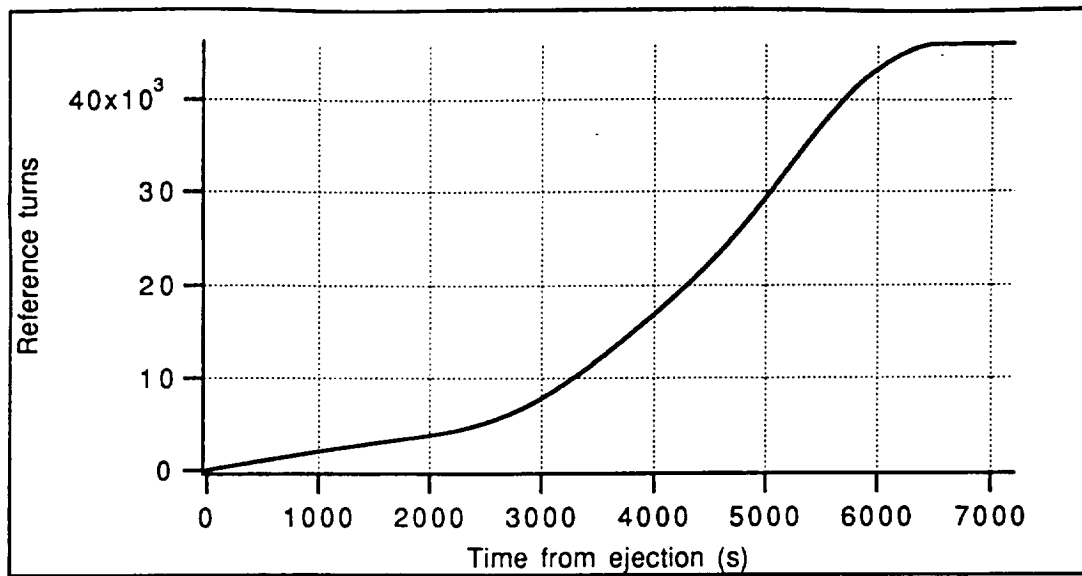


Figure 11.2(b)

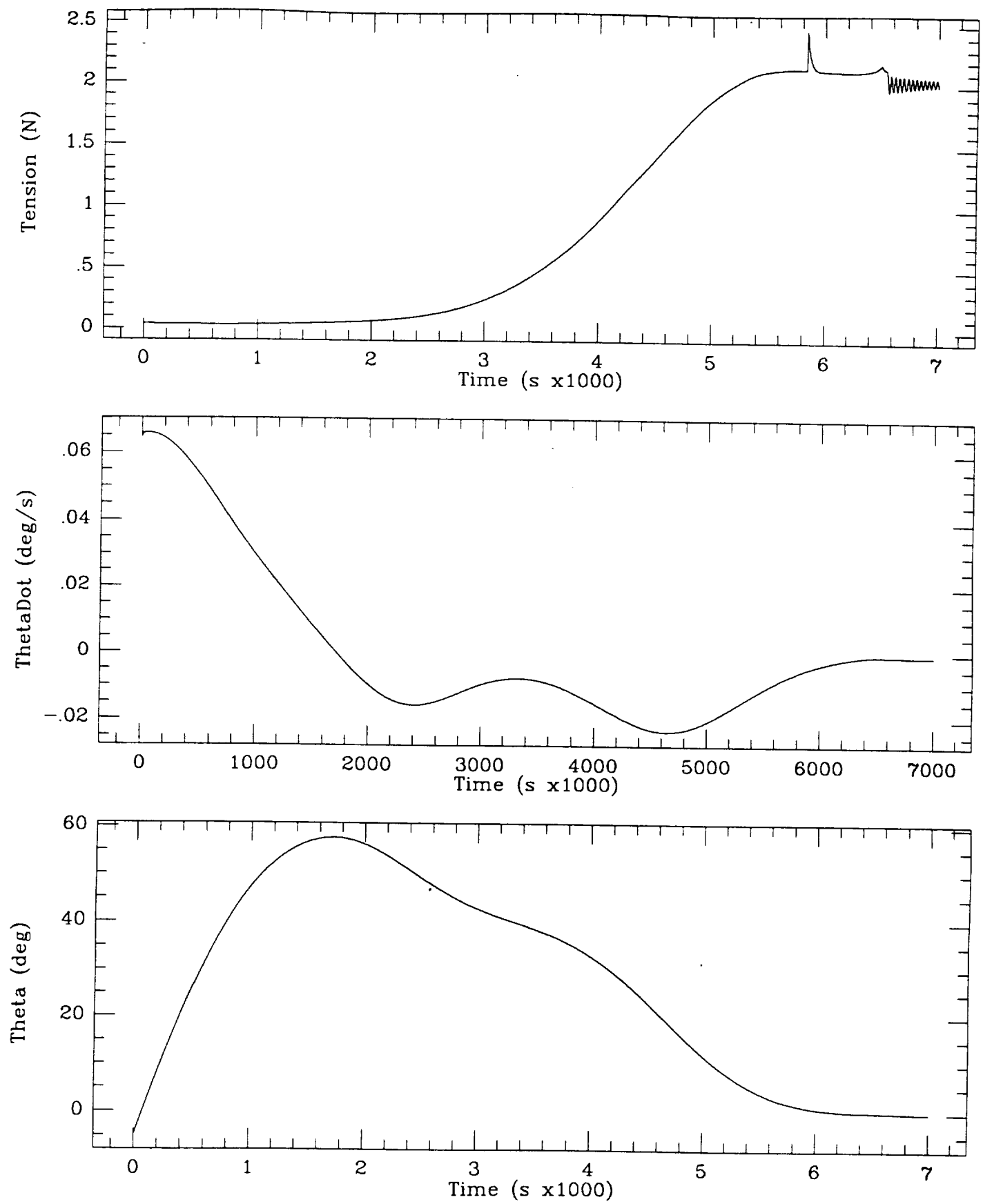


Figure 11.2(c)

The following numerical values have been adopted for nominal orbital and system parameters of the SEDS-2 flight: circular orbit at an altitude of 350 km (orbital rate  $\Omega = 1.144 \times 10^{-3}$  rad/s); orbital inclination = 30 deg; end-mass  $m = 25.9$  kg; tether linear density  $\rho = 0.33$  kg/km; tether diameter = 0.75 mm; tether stiffness  $EA = 15,000$  N; tether axial viscosity  $E'A = 1,000$  N-s; and tether final length  $L_{\text{end}} = 20$  km. The end-mass is ejected with a speed  $V_0 = 1.64$  m/s at an angle  $\theta_0 = -4.7$  deg (backward of the downward local vertical).

### Feedback

By following the reference  $B_{\text{ref}}$  profile, an ideal system without any errors or disturbances and under reference initial and orbital conditions will follow the reference length and length rate profiles and hence reach the end of deployment with a zero libration amplitude in a given time. However, while the ejection conditions are known within a  $\pm 5\%$  error, much larger uncertainties affect the tension model and the brake response. A feedback is needed in the control law to make it more robust by correcting for the effects of the uncertainties in the tension model and actuator response.

The feed-forward part of the control law (without feedback) has the form  $B = B_{\text{ref}}$  where  $B_{\text{ref}}$  is the reference brake profile. If uncertainties and/or errors are present, the system will not follow the length and length-rate profiles and consequently the libration response will be different from the desired response. One way to compensate for the effects of errors and uncertainties is to implement a feedback controller that forces the system to follow the reference length and length-rate profiles under off-reference conditions.

The classic approach, encountered in the literature [4], for implementing the feedback control law is to add the feedback controller to the non-linear component (i.e., to the feed-forward component) of the control law. Consequently, the formulation of the control law would be:

$$B = B_{\text{ref}} + F \quad (11.1.1)$$

$$F = k_1 \delta L + k_2 \delta \dot{L} \quad (11.1.2)$$

$$\delta L = L - L_{\text{ref}} \quad (11.1.3)$$

$$\delta \dot{L} = \dot{L} - \dot{L}_{\text{ref}} \quad (11.1.4)$$

where  $F$  is the feedback and  $\delta L$  and  $\delta \dot{L}$  are the length and length-rate errors with respect to the reference respectively. Because of its mathematical formulation we call this control law "additive". Results from simulations carried out with the additive control law are shown in Figs. 11.3(a-b) for off-reference tension values of 10 mN and 40 mN. When compared to the analogous curves shown in Figs. 11.8 relevant to the control law formulation (explained later on) adopted for SEDS-2, the simulation results clearly show that the additive control law is unable to provide a system response robust enough with respect to variations of the tension model parameters.

Another formulation of the control law was attempted whereby the feedback corrects the reference brake profile proportionally to the instantaneous value of that profile as follows:

$$B = B_{\text{ref}} (1 + F) \quad (11.2)$$

We call this control law "proportional" because the feedback is proportional to the reference brake profile.

### Control Gains

The equations of motion for a dumbbell system with a massless and straight tether are as follows

$$\ddot{\theta} + 2 \frac{\dot{L}}{L} (\dot{\theta} - \Omega) + \frac{3}{2} \Omega^2 \sin(2\theta) = 0 \quad (11.3.1)$$

$$\ddot{L} - L (\dot{\theta} - \Omega)^2 - L \Omega^2 (3\cos^2(\theta) - 1) = - \frac{T_{\text{ref}}}{m} \quad (11.3.2)$$

where the tension  $T_{\text{ref}}$  is given by eqn (9.1) of Section 9.2. Eqns (11.3) can be linearized around the solution provided by the reference profiles to yield:

$$\delta \ddot{\theta} + 2 \frac{\dot{L}_{\text{ref}}}{L_{\text{ref}}} \delta \dot{\theta} + 3 \Omega^2 \cos(2\theta_{\text{ref}}) \delta \theta - 2 \frac{\dot{L}_{\text{ref}}}{L_{\text{ref}}^2} (\dot{\theta}_{\text{ref}} - \Omega) \delta L + \frac{2}{L_{\text{ref}}} (\dot{\theta}_{\text{ref}} - \Omega) \delta \dot{L} = 0 \quad (11.4.1)$$



$$\begin{aligned} \delta \ddot{L} + 2 \frac{a \dot{L}_{\text{ref}}}{m} \delta \dot{L} - [\dot{\theta}_{\text{ref}}^2 - 2 \dot{\theta}_{\text{ref}} \Omega + 3 \Omega^2 \cos^2(\theta_{\text{ref}})] \delta L \\ + 6 L_{\text{ref}} \Omega^2 \cos(\theta_{\text{ref}}) \sin(\theta_{\text{ref}}) \delta \theta - 2 L_{\text{ref}} (\dot{\theta}_{\text{ref}} - \Omega) \delta \dot{\theta} = - \frac{T_{\text{ref}}}{m} \left( \delta B + \frac{\delta T_0}{T_{\text{ref}}} \right) \end{aligned} \quad (11.4.2)$$

where  $\delta T_0$  represent the departure of the minimum tension from its reference value and  $a = I_p (1 - A L/L_{\text{end}})^E$ . In deriving eqns (11.4), the dependence of the tension model of eqn. (9.1) on the variables  $\theta$  and  $L$  was neglected by replacing the relevant terms with their average values. Moreover, since  $\delta B \ll 1$ ,

$$e^B = e^{(B_{\text{ref}} + \delta B)} \approx e^{B_{\text{ref}}} (1 + \delta B)$$

For the additive feedback of eqn. (11.1.1),

$$\delta B = F \quad (11.5.1)$$

and for the proportional feedback of eqn. (3),

$$\delta B = B_{\text{ref}} F \quad (11.5.2)$$

After defining  $\lambda = L/L_{\text{ref}}$  and  $\tau = \delta T_0/T_{\text{ref}}$ , eqn. (11.5.2) can be expressed in a non-dimensional form as follows:

$$\delta \ddot{\lambda} + d_1 \delta \dot{\lambda} + d_2 \delta \lambda + d_3 \delta \theta + d_4 \delta \dot{\theta} = - \frac{1}{m} \frac{T_{\text{ref}}}{L_{\text{ref}}} (\delta B + \delta \tau) \quad (11.6)$$

where 
$$d_1 = 2 \frac{\dot{L}_{\text{ref}}}{L_{\text{ref}}} \frac{I_p}{m} (1 - A L/L_{\text{end}})^E$$

$$d_2 = 2 \dot{\theta}_{\text{ref}} \Omega - 3 \Omega^2 \cos^2(\theta_{\text{ref}}) - \dot{\theta}_{\text{ref}}^2 \quad (11.7)$$

$$d_3 = 6 \Omega^2 \cos(\theta_{\text{ref}}) \sin(\theta_{\text{ref}})$$

$$d_4 = 2(\Omega - \dot{\theta}_{\text{ref}})$$

After numerical evaluation and considering that  $\delta \dot{\theta} \approx \Omega \delta \theta$ , the last two terms on the left hand side of eqn. (11.6) can be neglected with respect to the other terms for the expected ranges of the variables in question. For the reference tension model  $\delta \tau = 0$ , and

after neglecting the terms mentioned above and substituting eqn. (11.5.2), eqn. (11.6) yields

$$\delta\ddot{\lambda} + \left(d_1 + \frac{B_{\text{ref}} T_{\text{ref}}}{m L_{\text{ref}}} \kappa_2\right) \delta\dot{\lambda} + \left(d_2 + \frac{B_{\text{ref}} T_{\text{ref}}}{m L_{\text{ref}}} \kappa_1\right) \delta\lambda = 0 \quad (11.8)$$

In first approximation, this equation can be used to compute the non-dimensional control gains  $\kappa_1 = L_{\text{ref}} k_1$  and  $\kappa_2 = L_{\text{ref}} k_2$  disregarding, for the time being, eqn. (11.4.1). Since eqn. (11.8) has variable coefficients, it must be analyzed at frozen times during deployment in order to estimate the dynamic response analytically.

The mid-deployment time of SEDS-2 is  $t = 3250$  s. At this time, the values of the parameters in the equation are as follows:

$$\begin{aligned} d_1 &= 8 \times 10^{-8} \\ d_2 &= 4 \times 10^{-6} \\ \frac{B_{\text{ref}} T_{\text{ref}}}{m L_{\text{ref}}} &\approx 4 \times 10^{-6} \end{aligned} \quad (11.9)$$

At frozen time, eqn. (11.8) is a canonical second-order equation. Consequently, the rotational frequency, damping ratio, and time constant are respectively

$$\begin{aligned} \omega &= \left(d_2 + \frac{1}{m} \frac{T_{\text{ref}}}{L_{\text{ref}}} \kappa_1\right)^{1/2} \\ \xi &= \frac{1}{2\omega} \left(d_1 + \frac{1}{m} \frac{T_{\text{ref}}}{L_{\text{ref}}} \kappa_2\right) \\ \gamma &= \frac{1}{2\xi\omega} \end{aligned} \quad (11.10)$$

A time constant  $\gamma \approx 100$  s and a damping ratio  $\xi = 0.7$  were selected for the control system, leading to  $\kappa_1 = 12.76$  and  $\kappa_2 = 2500$  or equivalently  $k_1 = 2 \times 10^{-3}$  N/m and  $k_2 = 0.4$  N/ms<sup>-1</sup>.

Extensive simulation runs have indeed verified the validity of the value selected for  $k_1$  while the value of  $k_2$  has been reduced to  $0.2$  N/ms<sup>-1</sup> in order to make the control system less susceptible to the abrupt tension variations at the end of deployment caused by the mechanization of the deployer (i.e. two-way transitions between sling and scrub modes for

low deployment velocity and small diameter of the spool). In summary, the values adopted for the control gains of SEDS-2 are

$$k_1 = 2 \times 10^{-3} \text{ N/m} \quad (\text{position gain}) \quad (11.11.1)$$

$$k_2 = 0.2 \text{ N/ms}^{-1} \quad (\text{velocity gain}) \quad (11.11.2)$$

### Block Diagram

The flight control software is based on an outer loop sampled at every 8 seconds and an inner loop sampled at every 1 second. The output of the turn counter (see Fig. 11.4), sampled at every second, is filtered (see next subchapter) and the turn count rate is computed by taking the numerical derivative of the filtered turn counts over 8-s intervals. This process provides a smooth turn count rate despite the high noise level of the turn count signal. At every 8-s, the smoothed turn count and turn rates are compared to the reference turn count and rate for computing the correction (feedback) to apply to the reference brake  $B_{\text{ref}}$  profile in order to track the reference length and rate profiles.

It is important to stress that the control software is based on number of turn counts and turn count rate as opposed to length and length rate. Because of the spool geometry, the two set of variables are linked by quadratic relationships as follows:

$$L = a_1 T_c^2 + a_2 T_c + a_3 \quad (11.12.1)$$

$$\dot{L} = 2 a_1 T_c + a_2 \quad (11.12.2)$$

where  $T_c$  is the number of turn counts. Consequently, the derivatives of eqn. (11.1.2) with respect to  $\delta L$  and  $\delta \dot{L}$  yield the relationships between the L-based control gains and the turn-based control gains as follows:

$$K_1 = k_1 (a_2 + 2 a_1 T_c) \quad (11.13.3)$$

$$K_2 = k_2 (a_2 + 2 a_1 T_c) \quad (11.13.2)$$

where  $K_1$  and  $K_2$  are the turn-based control gains which appear in the turn-based corrective term (feedback)

$$F = \Delta T_c + \Delta \dot{T}_c \quad (11.14)$$

where  $\Delta T_c = K_1 \delta T_c$  and  $\Delta \dot{T}_c = K_2 \delta \dot{T}_c$ .

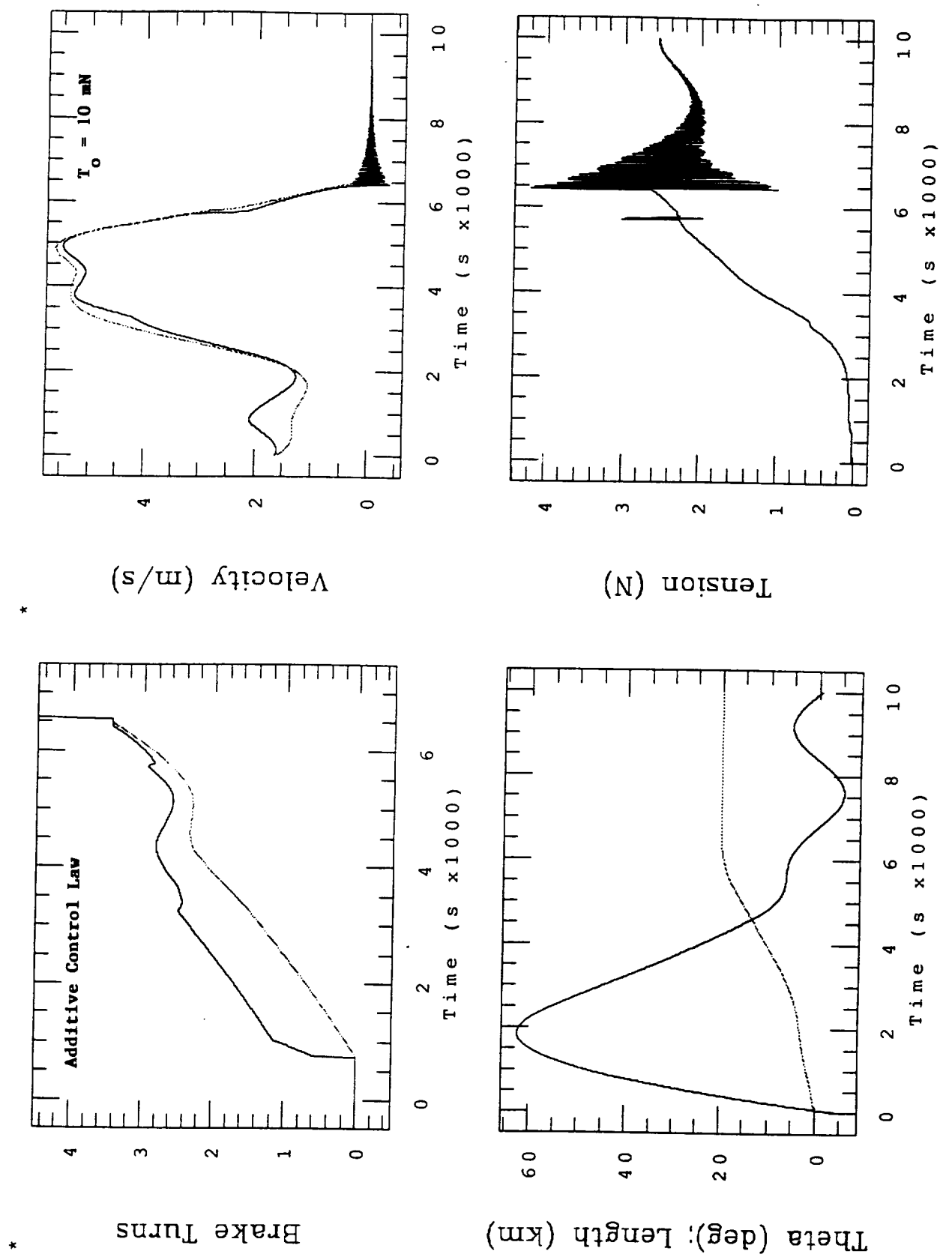
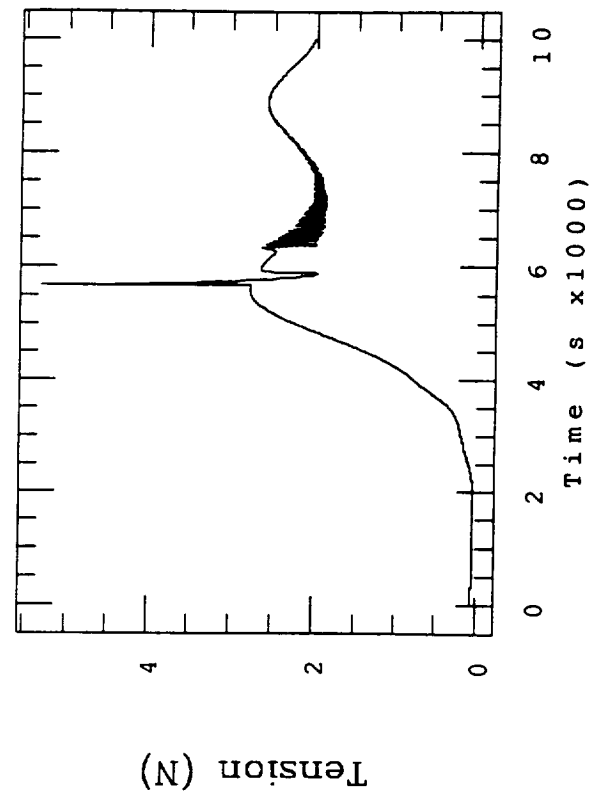
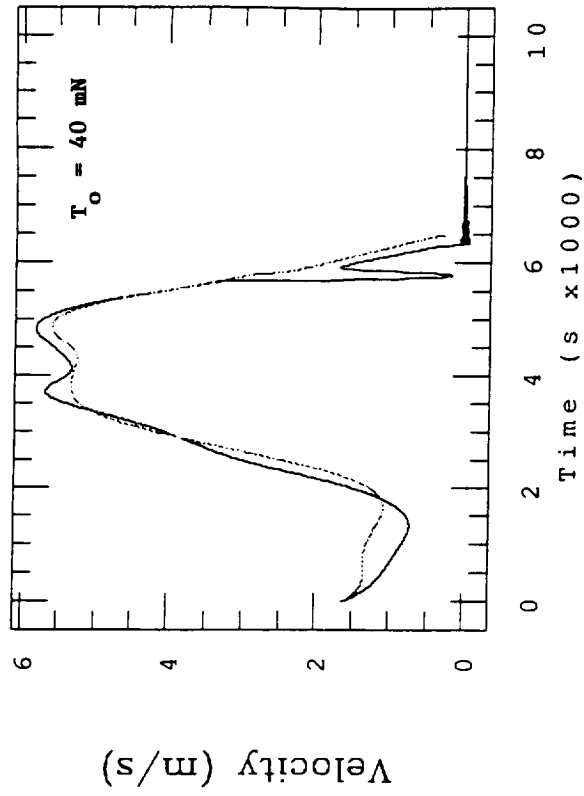


Figure 11.3(a)

\*



\*

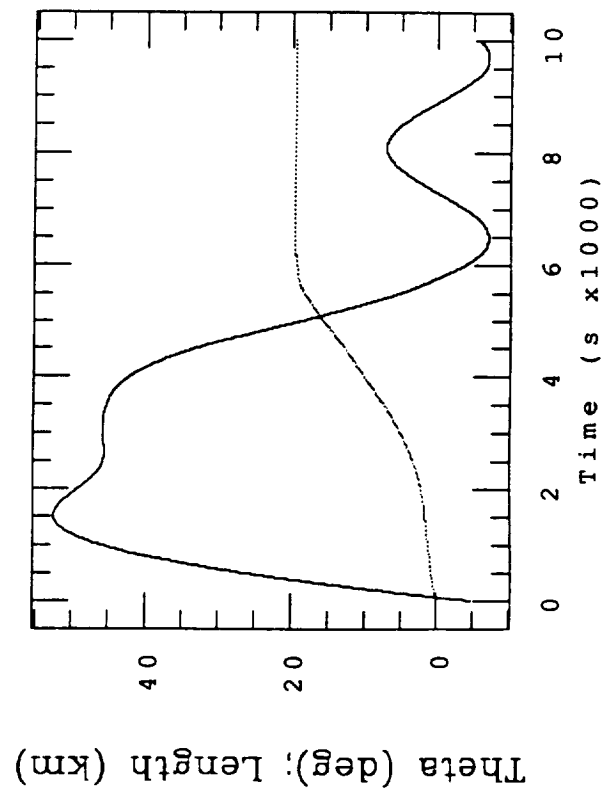
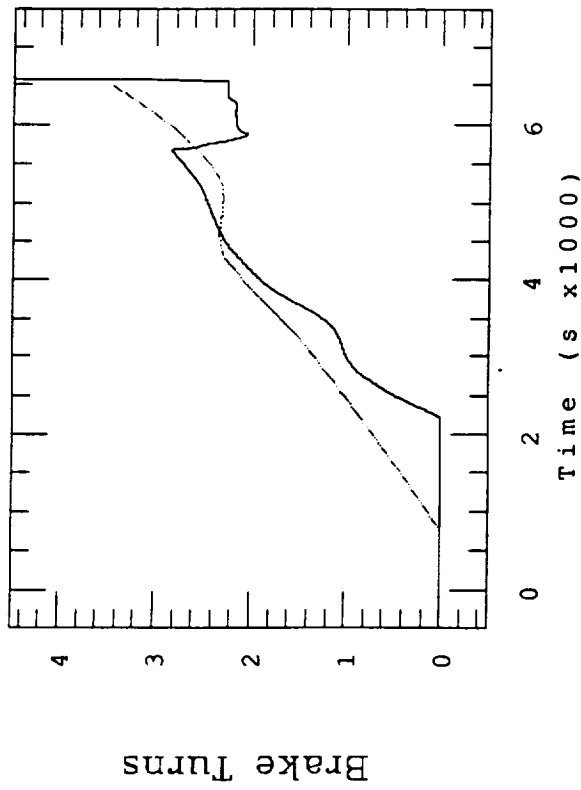


Figure 11.3(b)

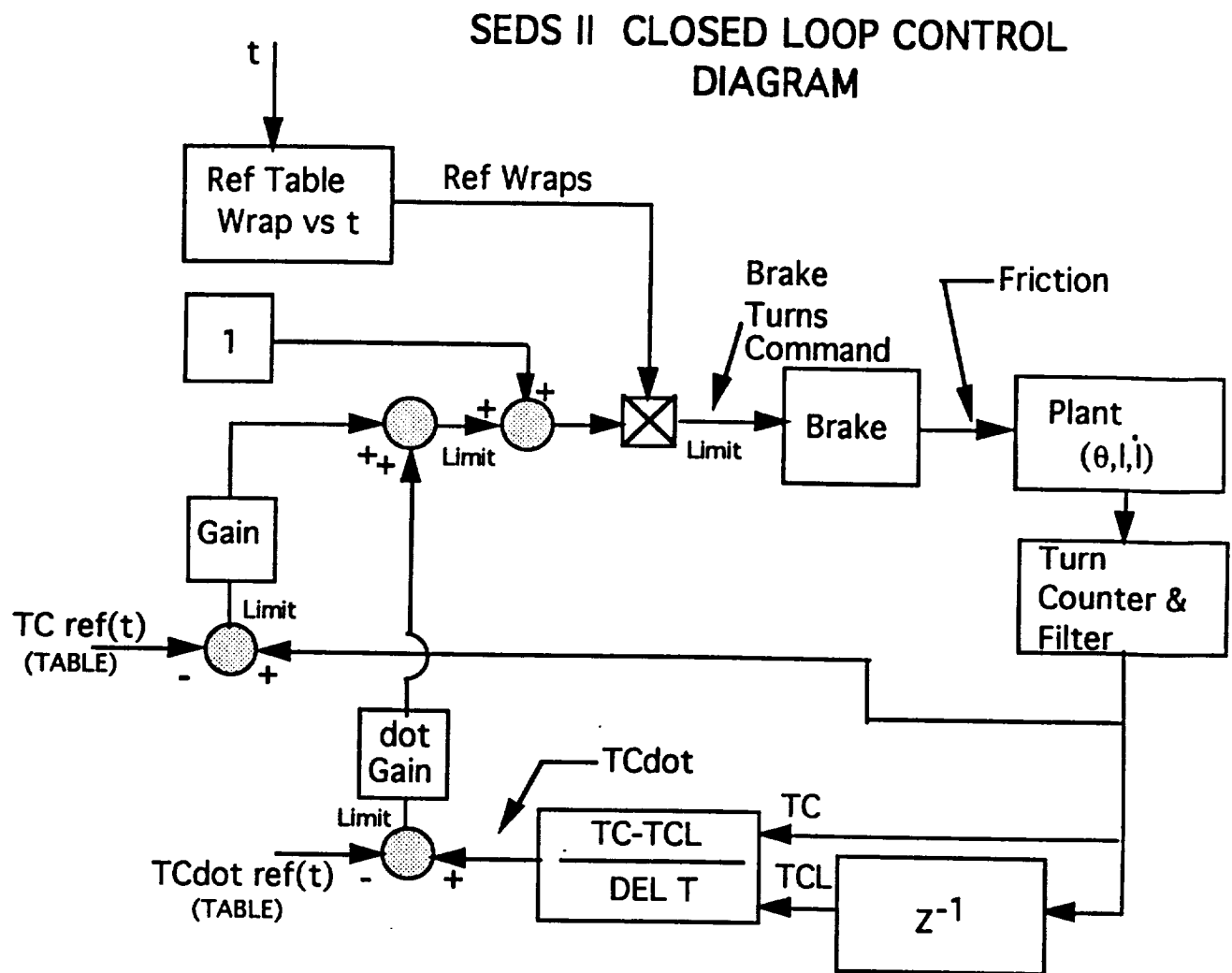


Figure 11.4

Once the individual components of the feedback  $\Delta T_c$  and  $\Delta \dot{T}_c$  are computed, they are checked for saturations and thresholds according to the following logic (similar expressions hold for  $\Delta \dot{T}_c$ ):

```

if:          abs ( $\delta T_c$ )  $\leq$   $\delta T_{irc}$ 

then:          $\Delta T_c = 0$ 

elseif:      abs ( $\delta T_c$ )  $>$   $\delta T_{sat}$ 

then:          $\Delta T_c = K_1 (\delta T_{sat} - \delta T_{irc}) \text{ sign } (\delta T_c)$ 

else:         $\Delta T_c = K_1 (abs (\delta T_c) - \delta T_{irc}) \text{ sign } (\delta T_c)$ 

```

where  $\delta T_{sat}$  and  $\delta T_{irc}$  are the saturation and threshold values respectively.

Once the correction term (eqn. 11.14) is computed, it is also checked for saturations:

```

if:           $F < -1$                 then           $F = -1$ 

if:           $F > F_{sat}$             then           $F = F_{sat}$ 

```

where  $F_{sat}$  (i.e., the upper bound of the feedback) limits the control authority. For SEDS-2,  $F_{sat}$  was equal to unity.

Finally, the brake command is computed according to

$$B = B_{ref} (1 + F) \quad (11.15)$$

The number of allowable brake turns  $B$  is also limited as follows:

```

if:           $B > B_{max}$                 then           $B = B_{max}$ 

```

where for SEDS-2,  $B_{max}$  is equal 6.

### Filtering

Deploying from a passive spool with a tether rubbing on various metal surfaces is dominated by the stick-slip mechanism as it is easily inferred from the data of the SEDS-1 flight. This mechanism gives rise to an output signal from the turn counter with a high

noise level. Effective filtering is, therefore, important in order to eliminate the high frequency components from the turn counter output signal and consequently compute a noise-free turn rate by means of numerical derivation.

The filter adopted in this control scheme is a recursive filter with the following formulation [5]:

$$y(i+1) = a y(i) + c [u(i+1) - a y(i)] \quad (11.16)$$

where  $u(i)$  is the measured value at the  $i$ -th step,  $y(i)$  is the filtered variable at the same step,  $a$  determines the type of filtering and  $c$  the cut-off frequency. In particular, for  $a = -1$ , the filter in eqn. (11.16) is a high-pass filter and for  $a = 1$ , (which is the value we will adopt from now on) it is a low-pass filter.

The amplitude of the filtered variable is given by

$$M = c [a^2 (c - 1)^2 + 2a (c - 1) \cos(\omega T) + 1]^{-1/2} \quad (11.17)$$

where  $T$  is the sampling frequency of the measured variable.

Figure 11.5 depicts the attenuation provided by the filter for  $T = 1$  s,  $a = 1$  (low-pass), and different values of the parameter  $c$ . Specifically, for  $c = 0.1$ , the cut-off frequency (defined as the frequency at -3 dB) is about 0.02 Hz. A cut-off frequency of 0.02 Hz is adequate for SEDS-2 since, from experimental data, the lowest-frequency noise component is at about 0.033 Hz.

Moreover, the performance of the filter and the velocity computation routine (by numerical derivation) was tested on the deployment data of SEDS-1. In Figure 11.6, the deployment velocity, obtained through filtering of the turn count data, is compared to the unfiltered velocity. The filter parameters are those adopted for SEDS-2 as follows:  $a = 1$ ,  $c = 0.125$ ,  $T = 1$  s.



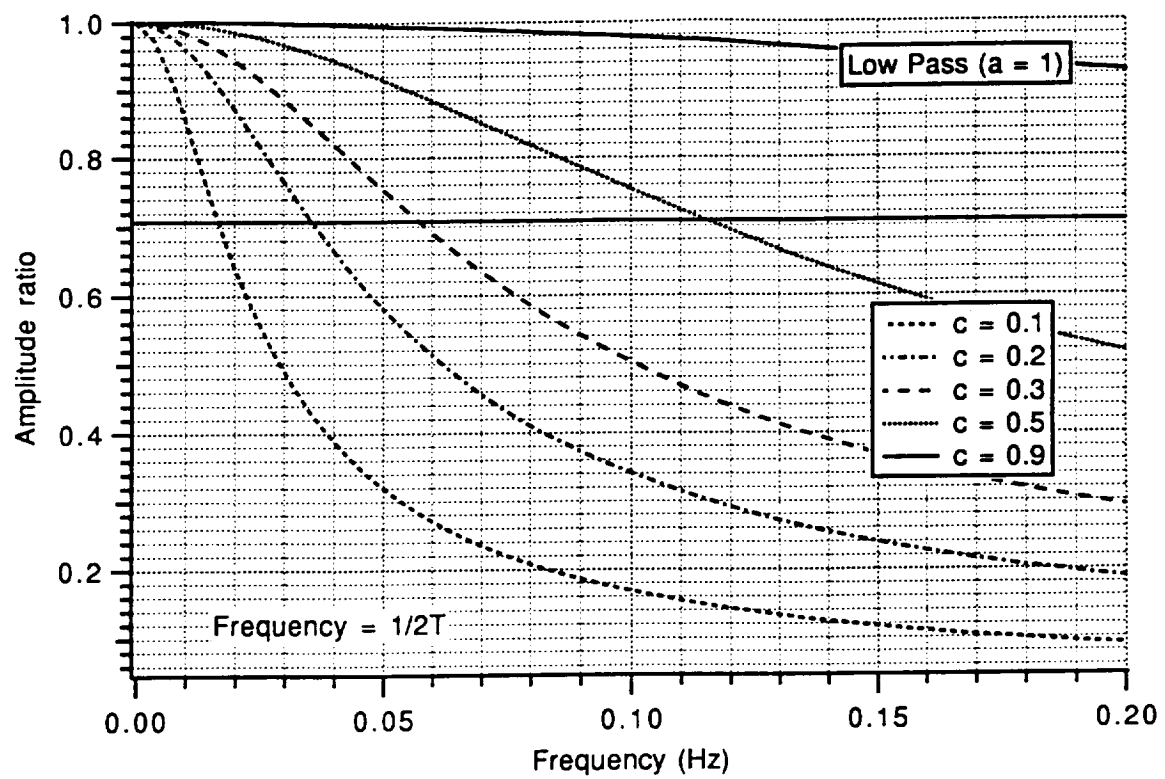


Figure 11.5

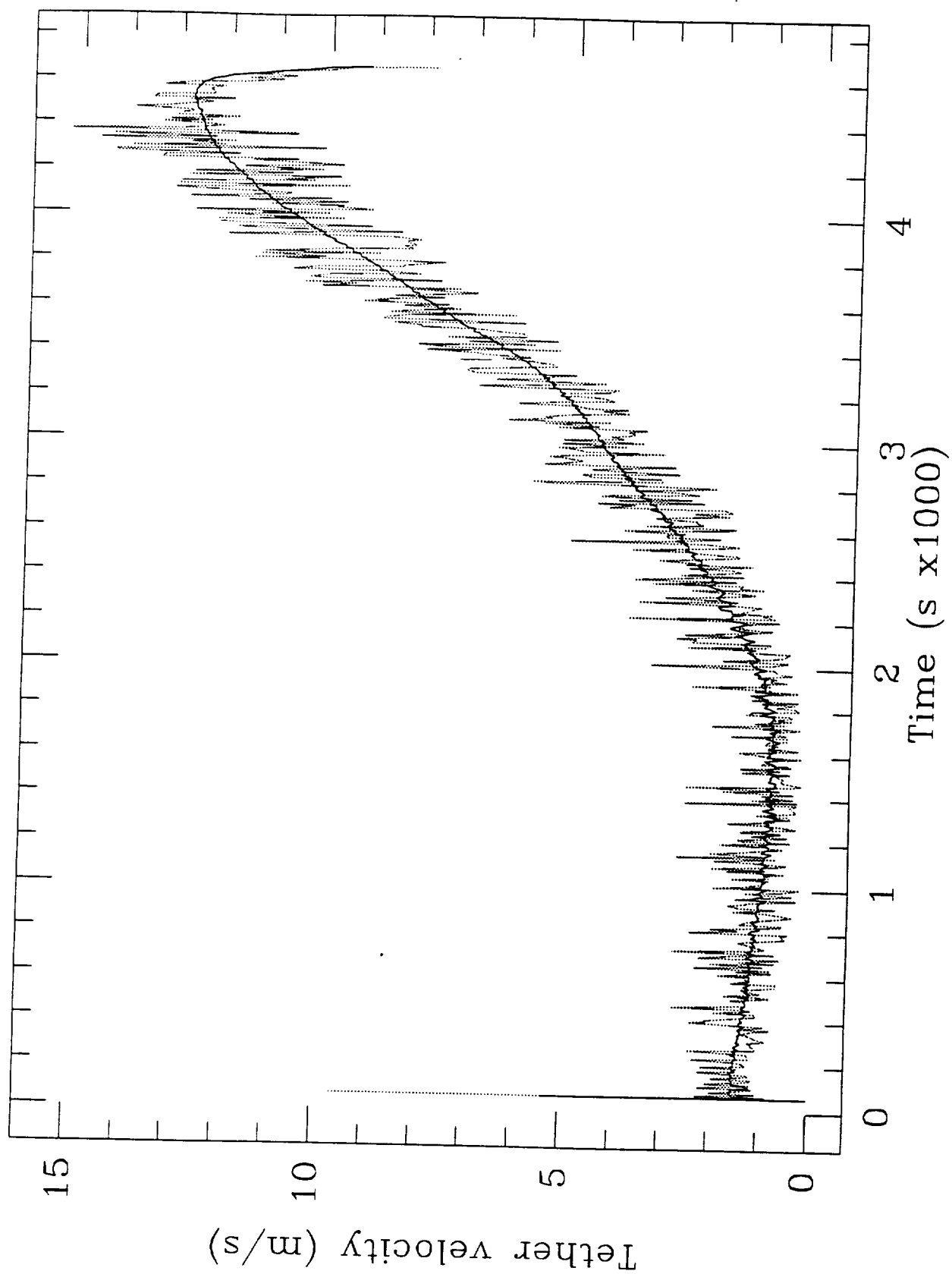


Figure 11.6

### 11.1.3 Robustness of Control Law

#### Reference Case

The simulation runs have been carried out with the DUMBBELL computer code which has the following characteristics: in-plane dynamics, generic orbit, point end-masses, aerodynamic drag, spherical gravity model, straight and visco-elastic tether.

The dynamics for the reference case is shown in Figs. 11.7(a-b). In the reference case, the minimum tension is equal to 30 mN and it is assumed constant along the entire tether length. The following values were adopted for the other parameters of the reference tension model: annulus solidity = 0.96, inertia multiplier = 3, and area exponent = -0.8 [6]. The reference case does not have perfect reference conditions as opposed to what was assumed for the simplified model for the derivation of the reference profiles. The reference case adopts more realistic reference conditions: the tether is massive, the Delta second stage drifts from its flight attitude 2000 s after the end-mass ejection, the aerodynamic drag is present, the sling/scrub transition occurs for a tether turn rate  $< 13$  turn/s at about  $L = 18.8$  km and  $t > 5,700$  s.

The tension model is one of the main source of errors because it is affected by large uncertainties due to the unpredictability of frictional forces in the deployer. Specifically, values of the minimum tension can range, most likely, between 10 mN and 40 mN while the friction coefficient  $f$  can exhibit variation of  $\pm 50\%$  with respect to the most likely value of 0.18. Since the friction coefficient appears in the argument of an exponential function (i.e. the brake multiplier  $e^B$ ), it has a dramatic effect on the tension. For the average number of brake turns of 3, a  $\pm 50\%$  change of the friction coefficient corresponds to a  $\pm 500\%$  variation of the tension. For the maximum number of brake turns of 6, a  $\pm 50\%$  change of the friction coefficient corresponds to a  $\pm 3000\%$  variation of the tension.

For the reason above, it is important to demonstrate the robustness of the control law with regards to large uncertainties in the tension model and the actuator response.

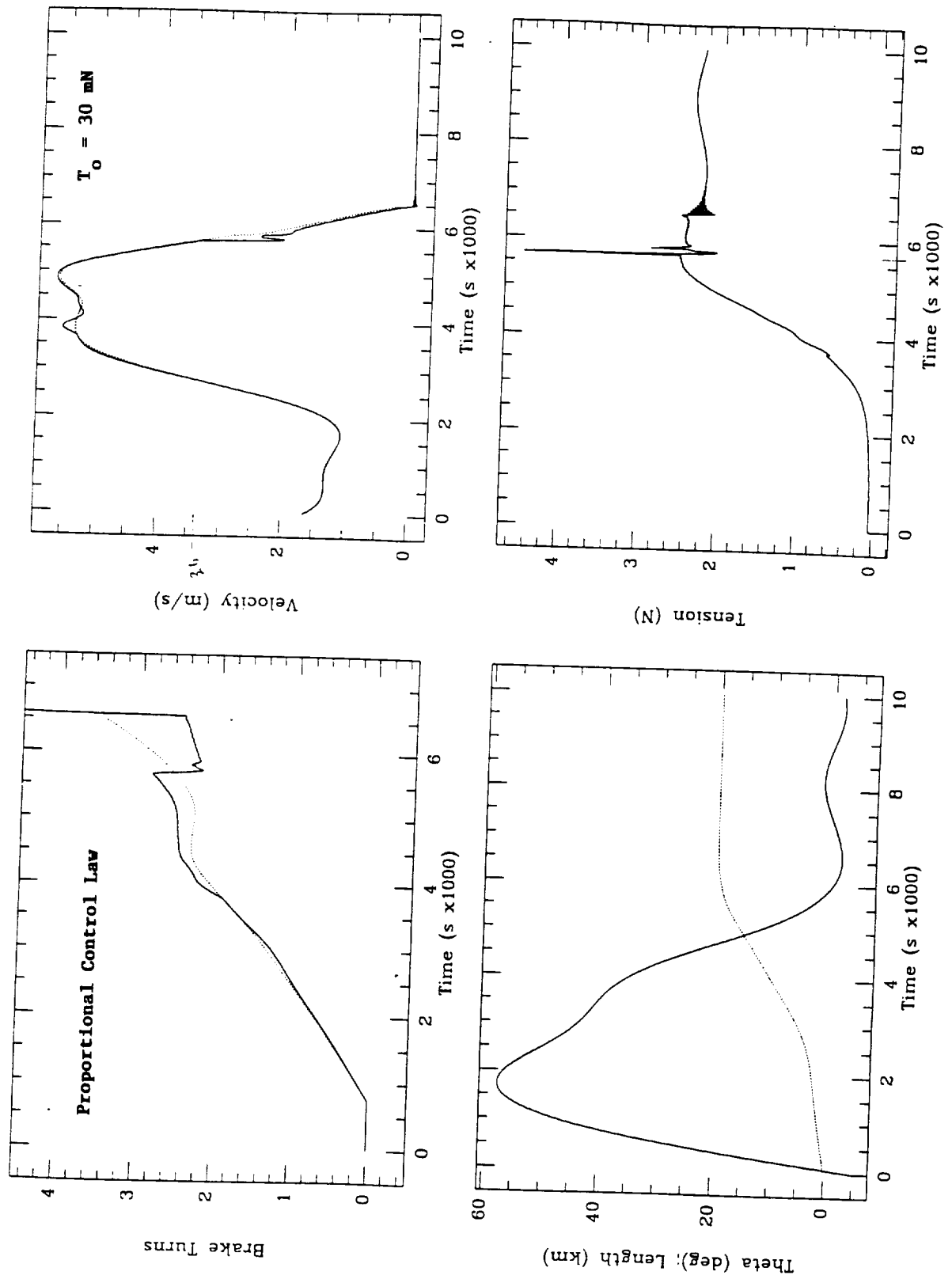


Figure 11.7(a)

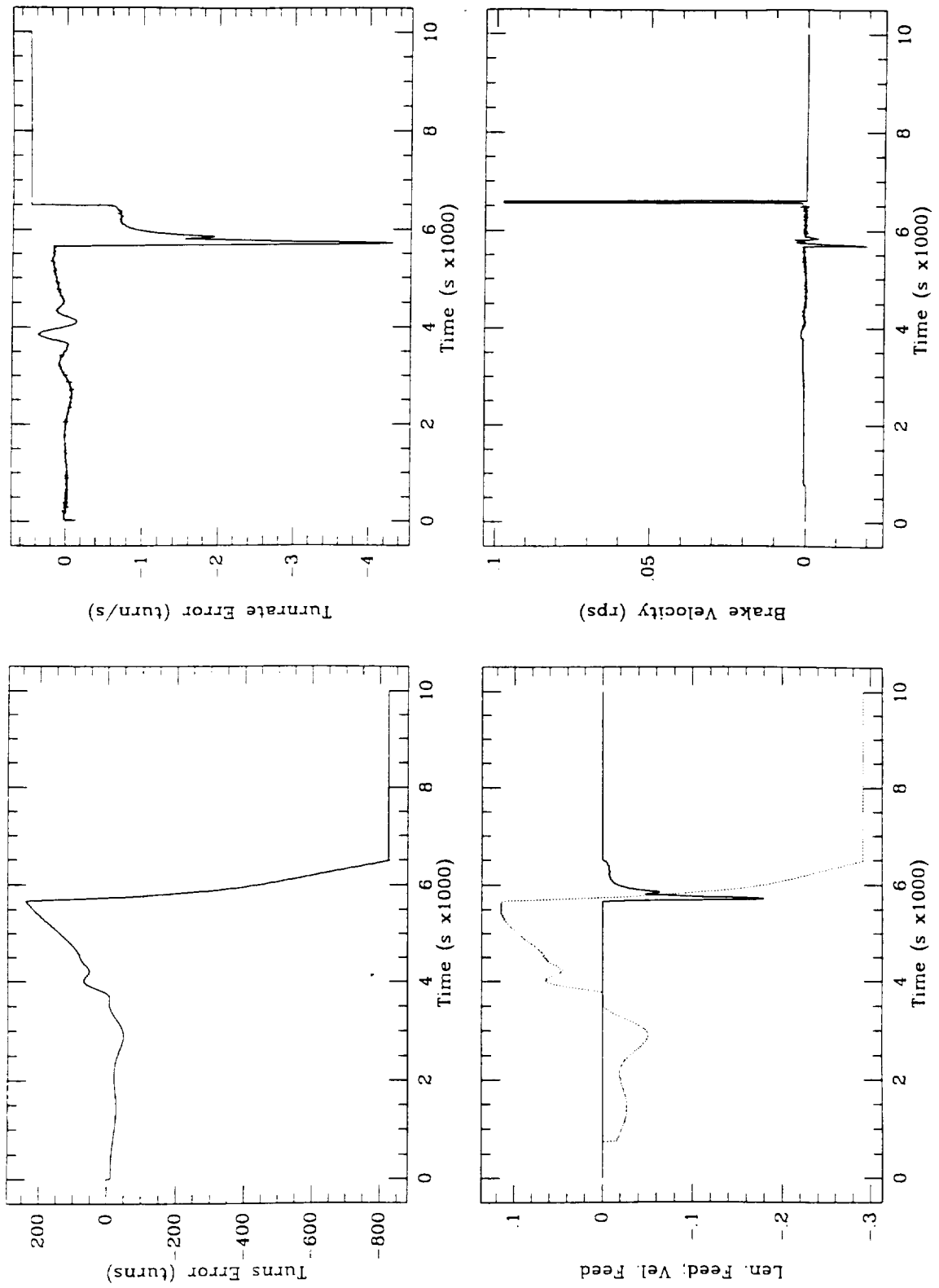


Figure 11.7(b)

### Sensitivity to Uncertainties in the Tension Model

In this subsection we investigate the sensitivity of the SEDS-2 control law to departures of the tether tension from the baseline model.

Specifically, for the values of deployment velocity of SEDS-2 ( $< 6$  m/s), the dominant contribution in the tension model is from the static tension  $T_0$ . Figures 11.8(a-e) show the dynamic responses during deployment for static tensions ranging from 10 mN to 60 mN (excluding the reference tension of 30 mN shown in Figs. 11.7). In Figure 11.9, the maximum libration amplitudes of SEDS-1 and SEDS-2 at the end of deployment are shown vs the static tension  $T_0$ . The control law of SEDS-2 provides a maximum libration amplitude that ranges between 2 deg and 10 deg for  $10 \text{ mN} \leq T_0 \leq 45 \text{ mN}$ . The deployment would stop at short range ( $< 1$  km) without resuming for a static tension  $\geq 65$  mN.

The drop-off of the control law performance for static tension  $> 45$  mN is due to lack of initial momentum (i.e., a low ejection velocity) rather than lack of robustness of the control law. The brake can only slow down the deployment velocity and the gravity gradient is not able to speed it up for high values of the static tension if the initial momentum is insufficient. Consequently, if the ejection velocity is small and the static tension is high the brake can only command the brake not to intervene. The robustness of the control law to variation of the static tension is clearly demonstrated by the curve in Fig. 11.9 relevant to an ejection velocity of 2.4 m/s (PMG-type of ejection mechanism). In this case the drop-off in the performance of the control law is for  $T_0 > 60$  mN while the deployment would stop at short range for  $T_0 > 95$  mN.

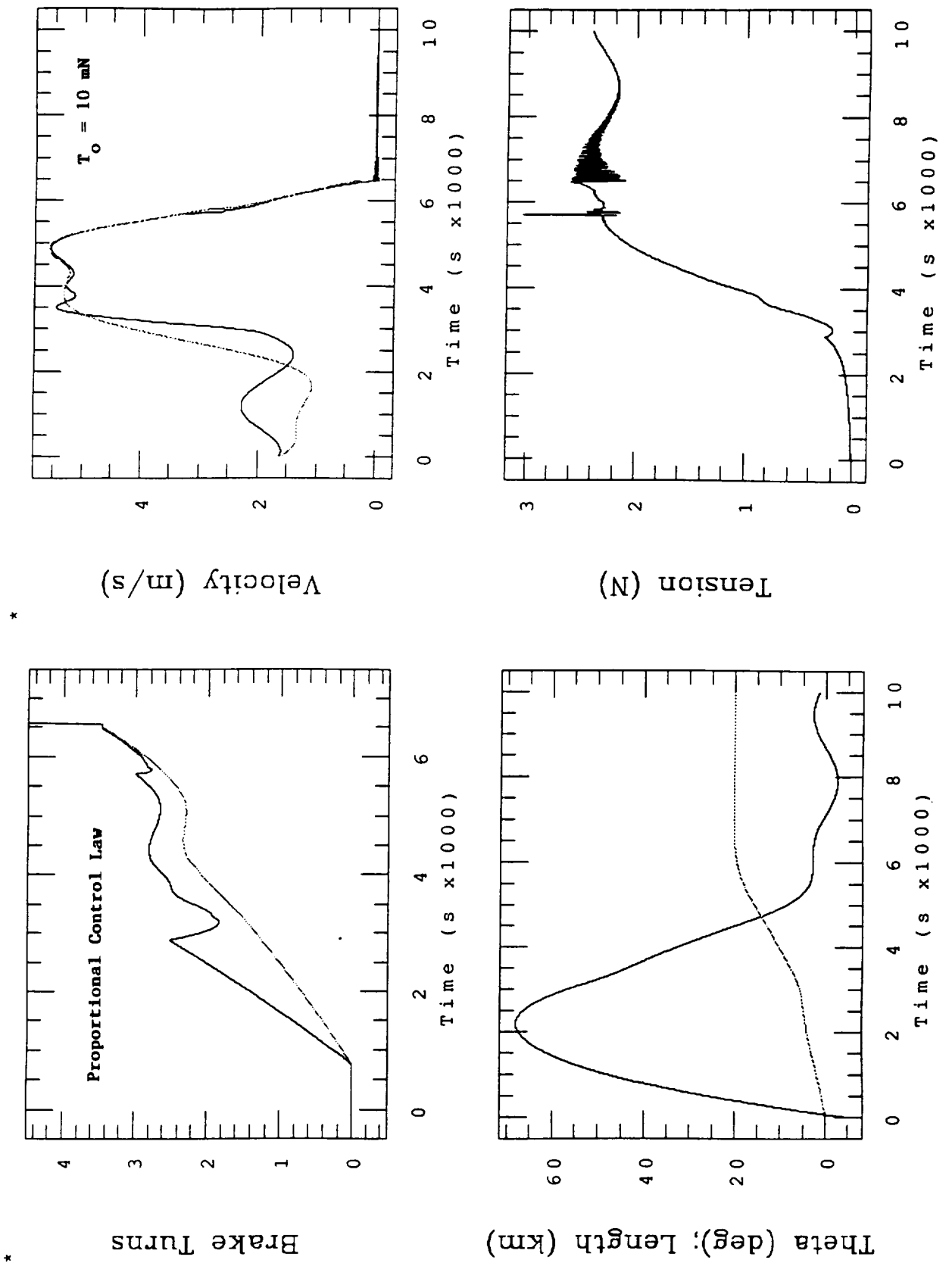


Figure 11.8(a)

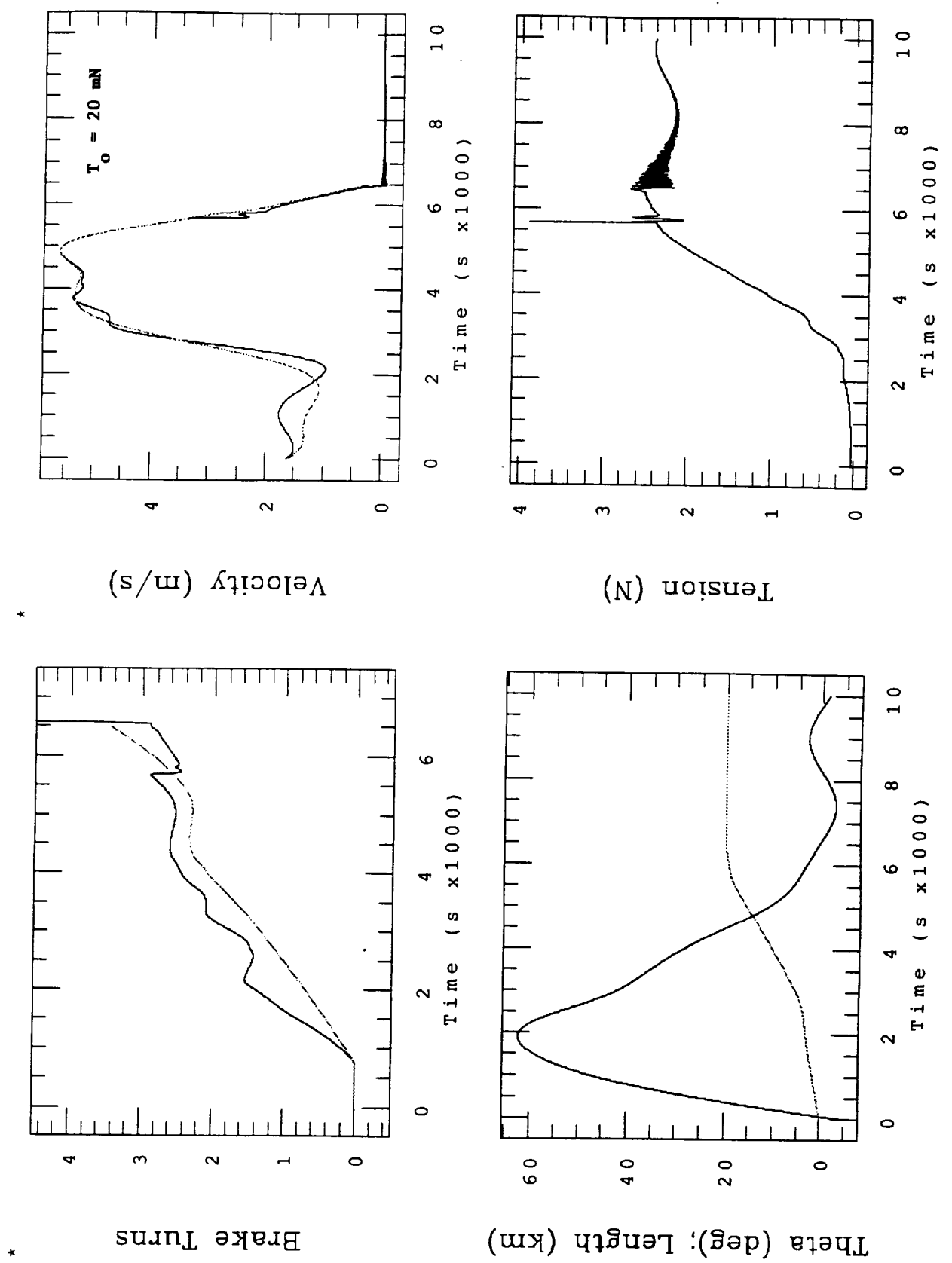
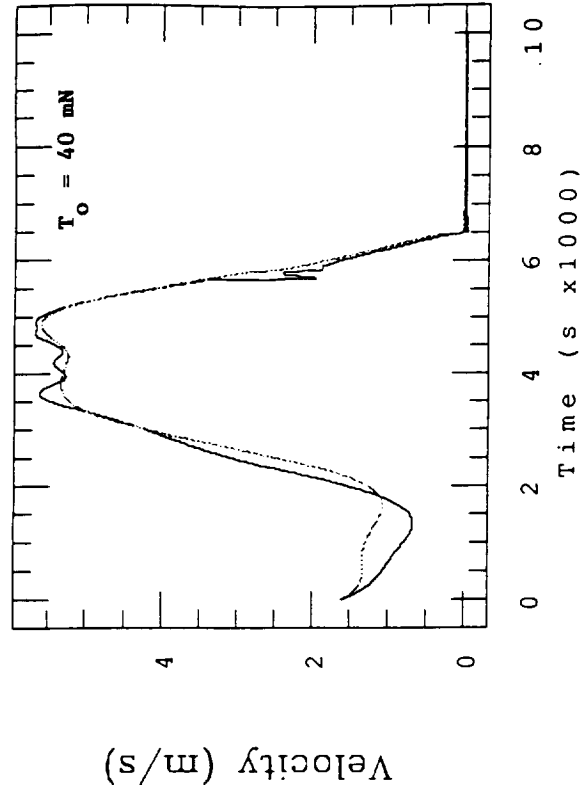


Figure 11.8(b)



\*



\*

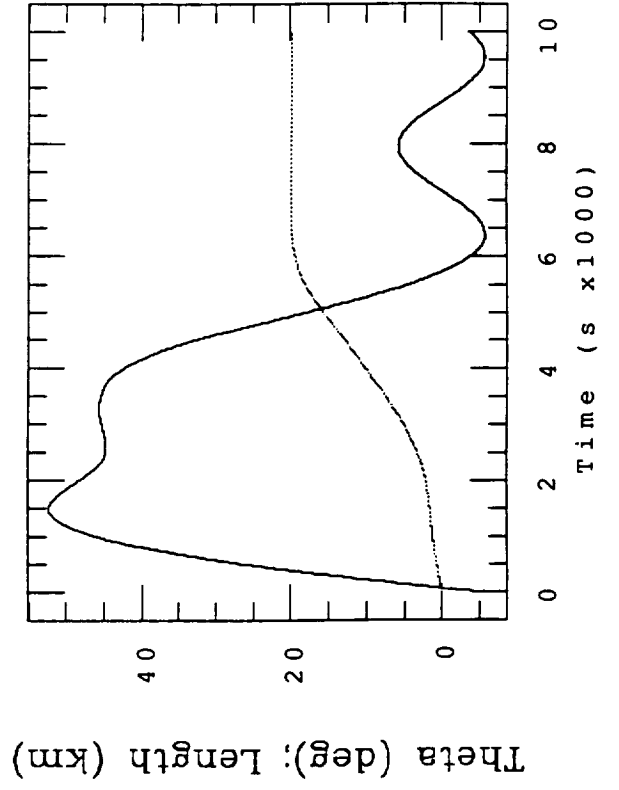
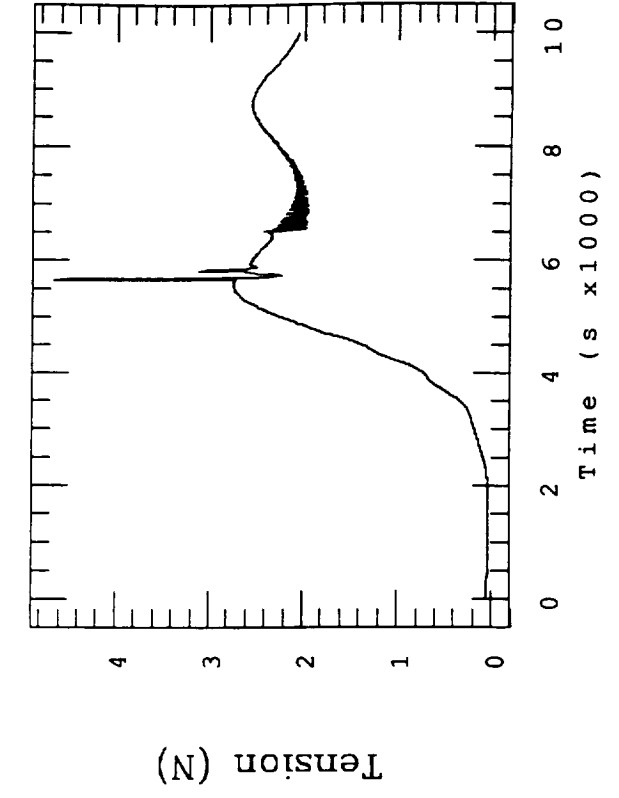
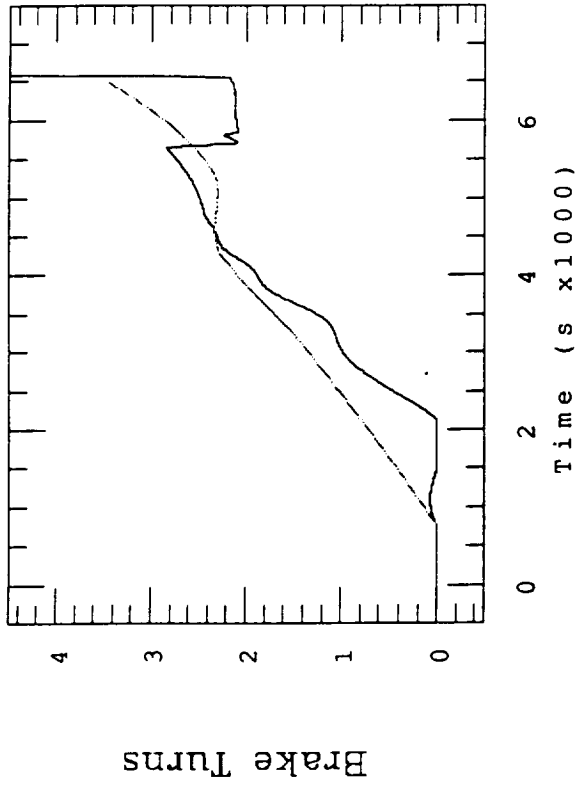
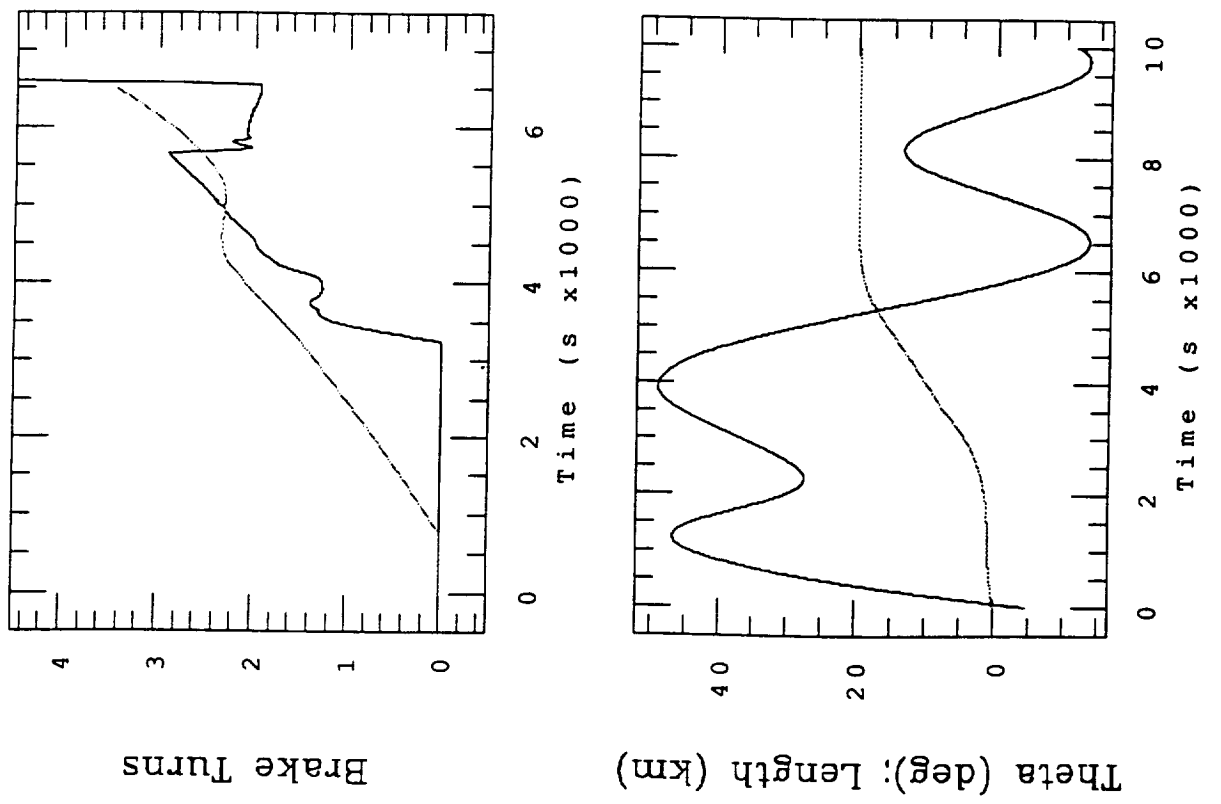


Figure 11.8(c)

\*



\*

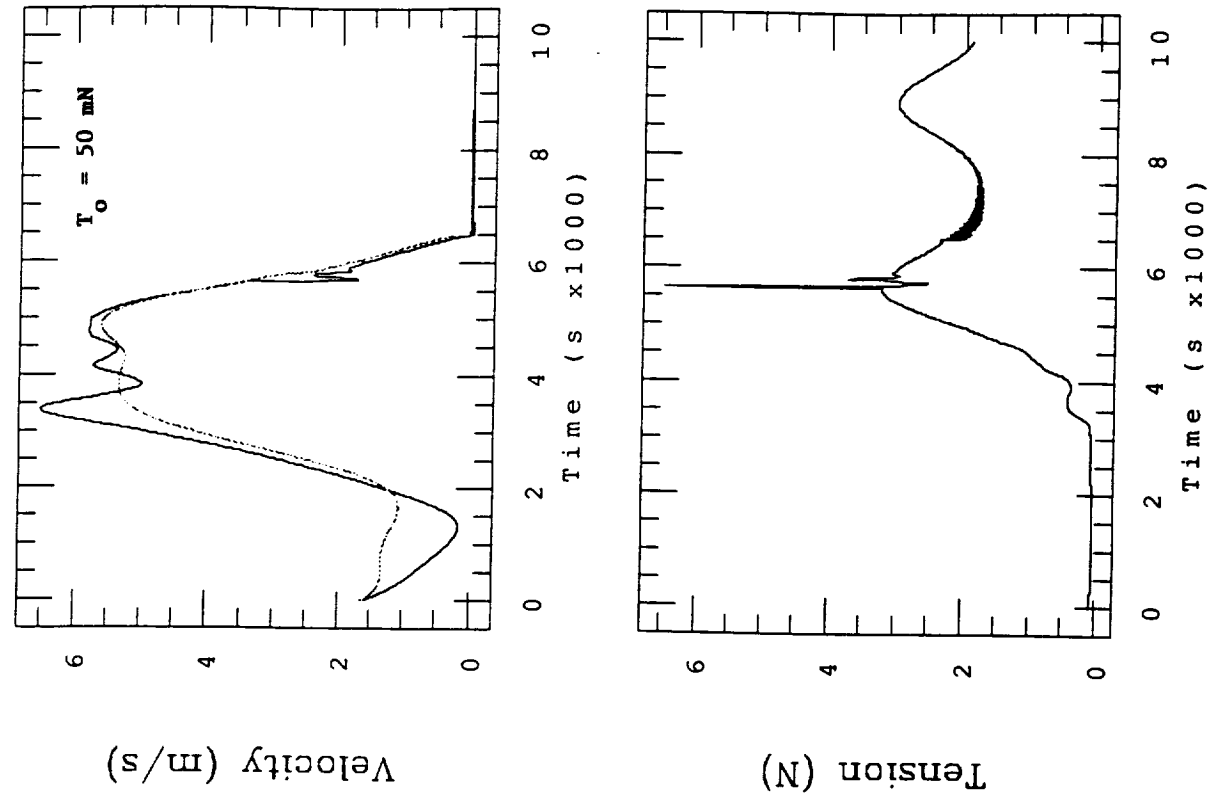
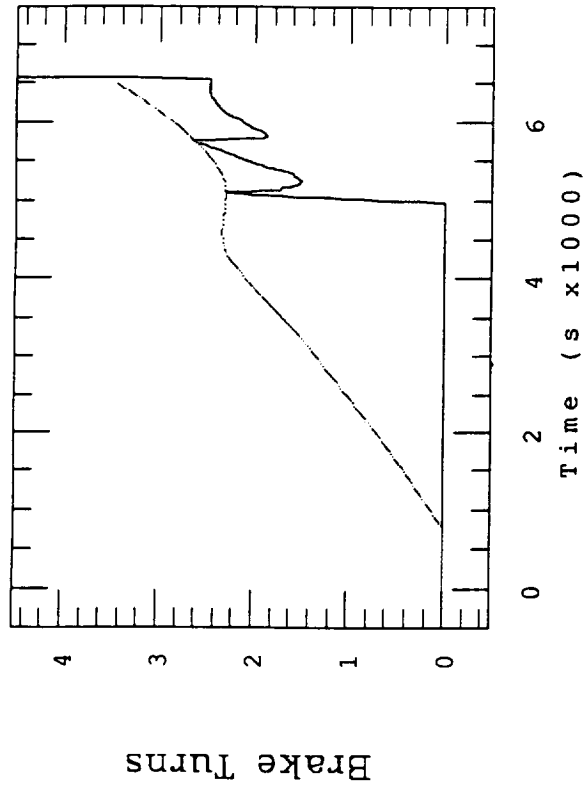


Figure 11.8(d)

\*



\*

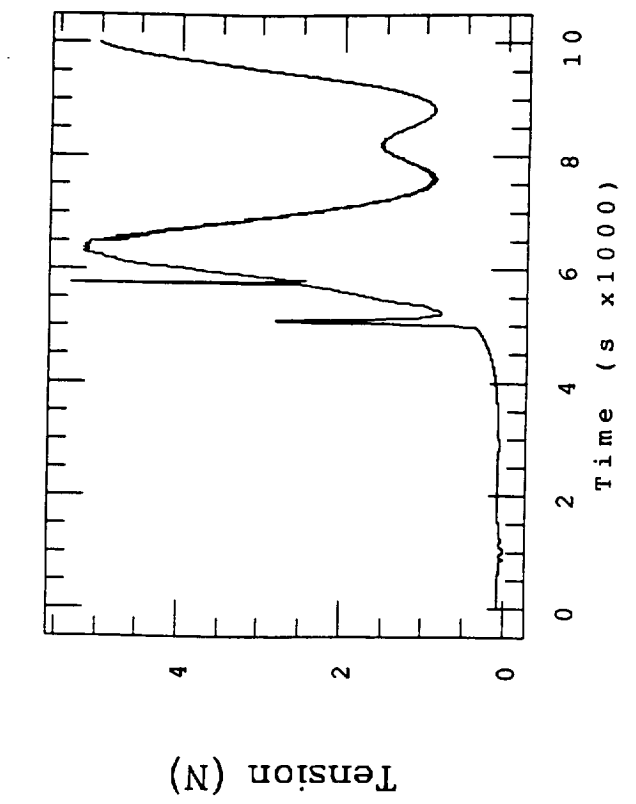
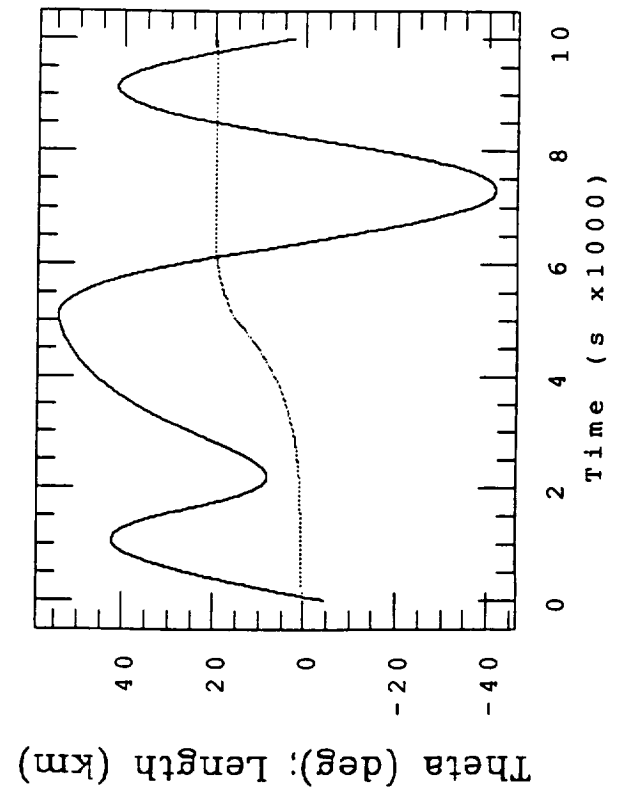
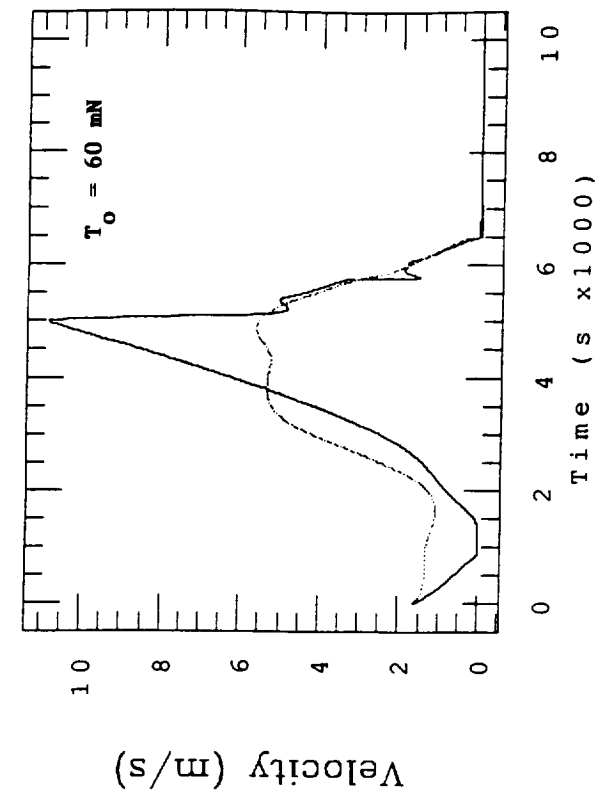


Figure 11.8(e)

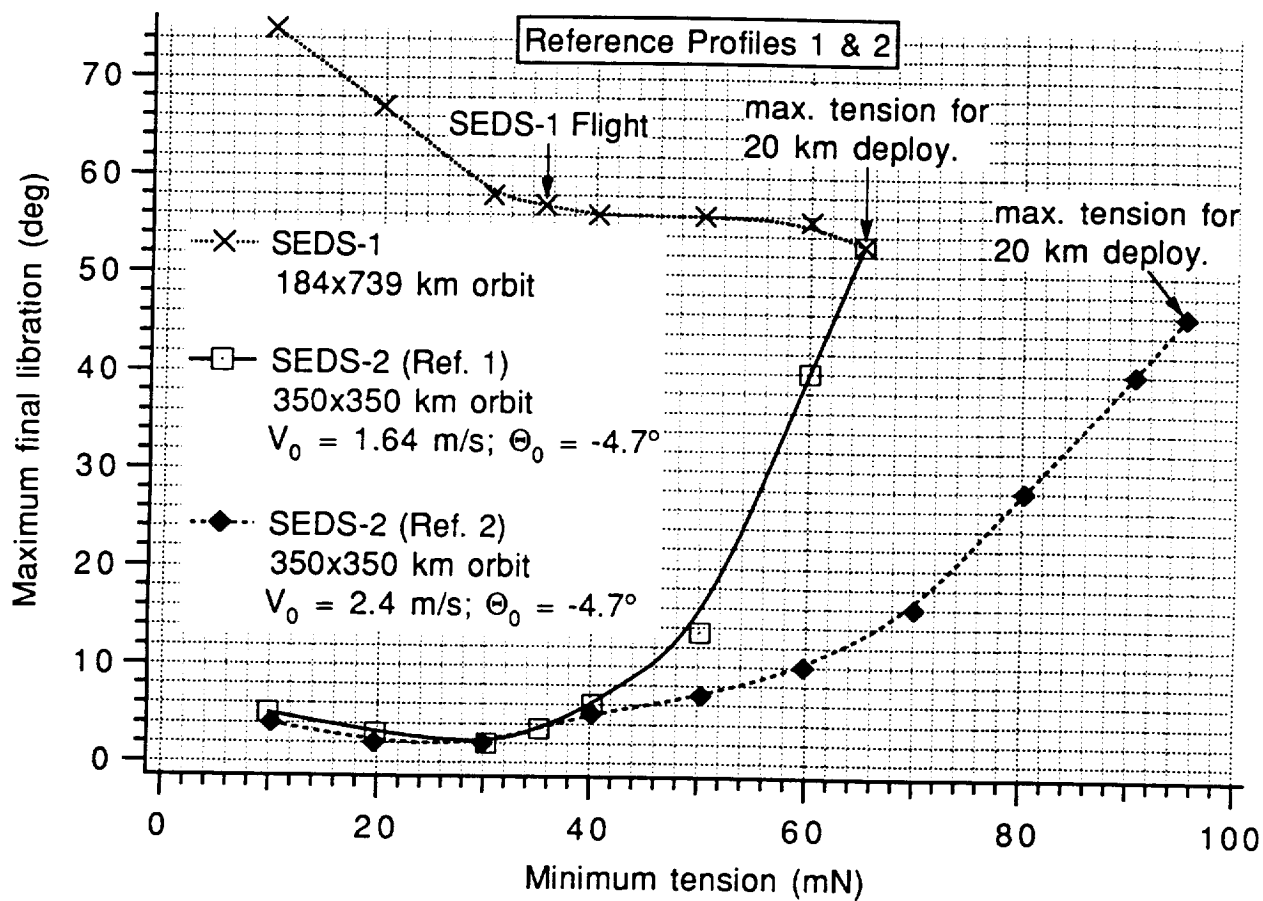


Figure 11.9

### Sensitivity to Uncertainties in the Actuator Response

The response of the brake is also highly uncertain as pointed out before. A change in the brake effectiveness is best modeled as a variation of the friction coefficient. Figures 11.10(a-b) show the dynamic response during deployment for values of the friction coefficient ranging from 0.1 to 0.26. The baseline value of the friction coefficient is 0.18. Independent experimental measurements of the friction coefficient of Spectra-1000 on Aluminum were carried out at the "Staatl Materialprüfamt für Textilstoffe" in Reutlingen, Germany in June 1993. The tests were directed by Dieter Sabath of the Technical University of Munich. The tether was a sample of the flight tether (the new tether before cleaning) and the rubbing material was the actual brake post of the SEDS deployer. The tests were done at two different temperatures  $\tau$  of the tether while the brake post was at the room temperature of 23 °C. Measured values of the friction coefficient  $f$  were as follows:  $f = 0.15$  for  $\tau = 0$  °C and  $f = 0.16$  for  $\tau = 15.5$  °C. A detailed report on the friction tests is in Appendix B of Ref. [3].

The conclusions from the sensitivity to uncertainties affecting the brake response is that variations as high as  $\pm 50\%$  with respect to the baseline value of 0.18 for the friction coefficient still lead to a maximum libration amplitude  $\leq 10$  deg at the end of deployment.

### Sensitivity to Random Noise

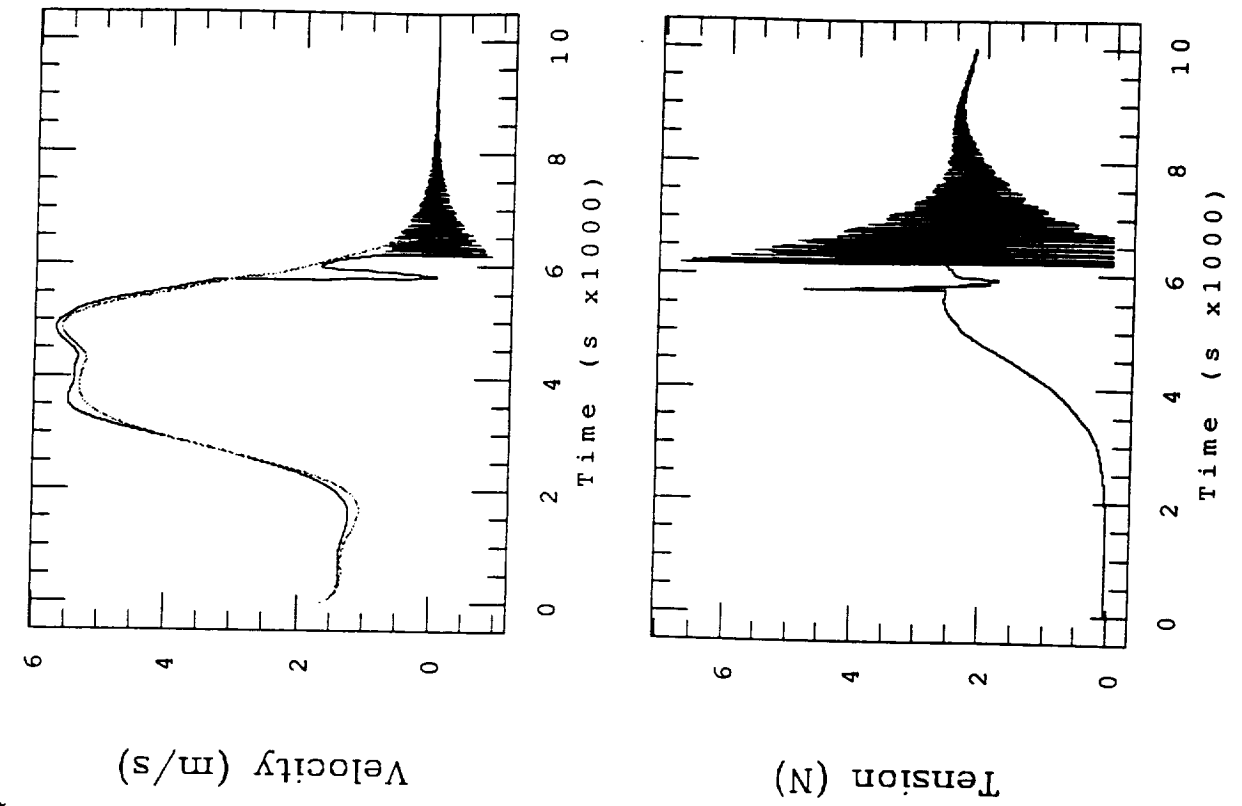
In order to test the effect of broad-band random noise upon the control law, noise is superimposed on the tether tension. Specifically, the structure of the tension affected by noise is as follows:

$$T_N = S_T + N_a + T (1 + N_m) \quad (11.18)$$

where  $T$  is the noise-free tether tension,  $N_a$  and  $N_m$  are broad-band random noise components, and  $S_T$  is a saw-tooth, low-frequency noise component.  $N_a$  and  $N_m$  are generated by zero-bias white noise routines which have been filtered (with a high-pass filter) to eliminate the noise components with a frequency  $< 0.35$  Hz. If this frequency is interpreted as the number of turns per second inside the deployer, 0.35 turn/s corresponds to a tether exit speed of roughly 0.15 m/s which is rarely encountered.

This strategy of filtering the white-band noise was adopted in order not to introduce unrealistic low-frequency noise components. The noise component with the lowest frequency is represented by the function  $S_T$  which models the fluctuations, observed

\*



\*

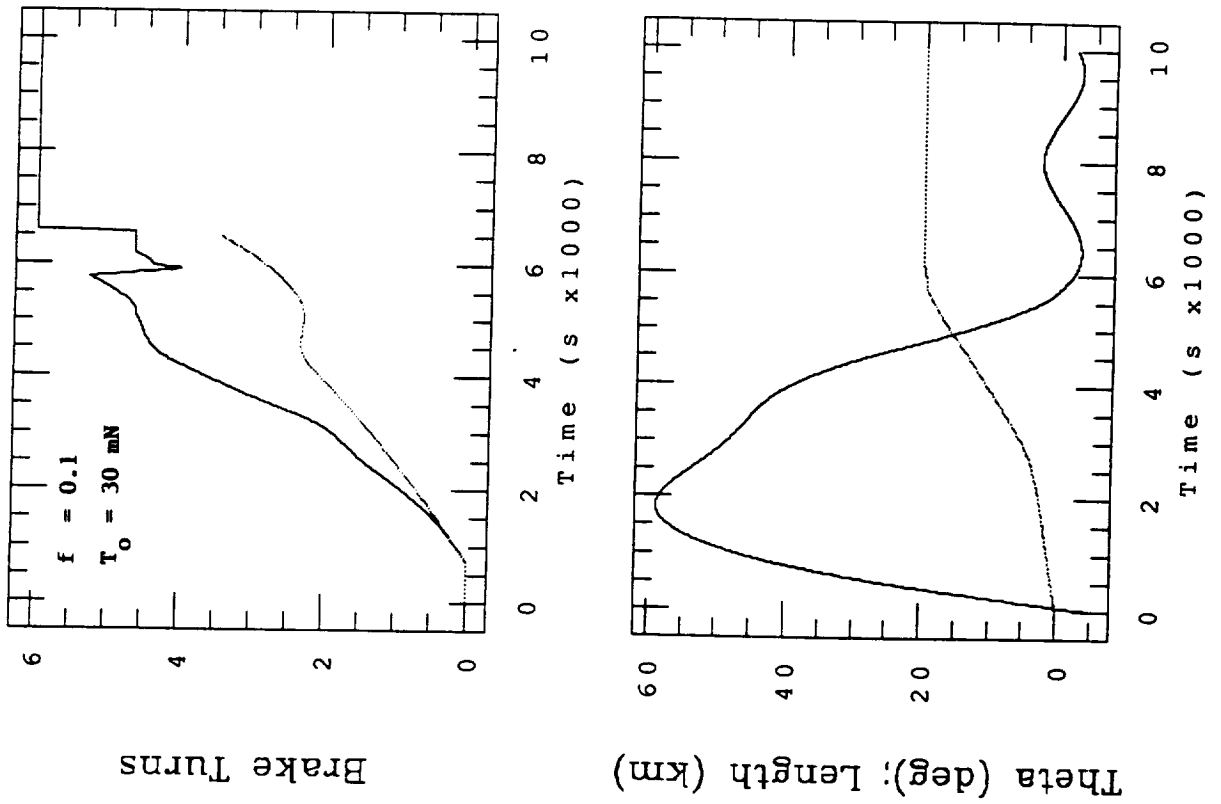
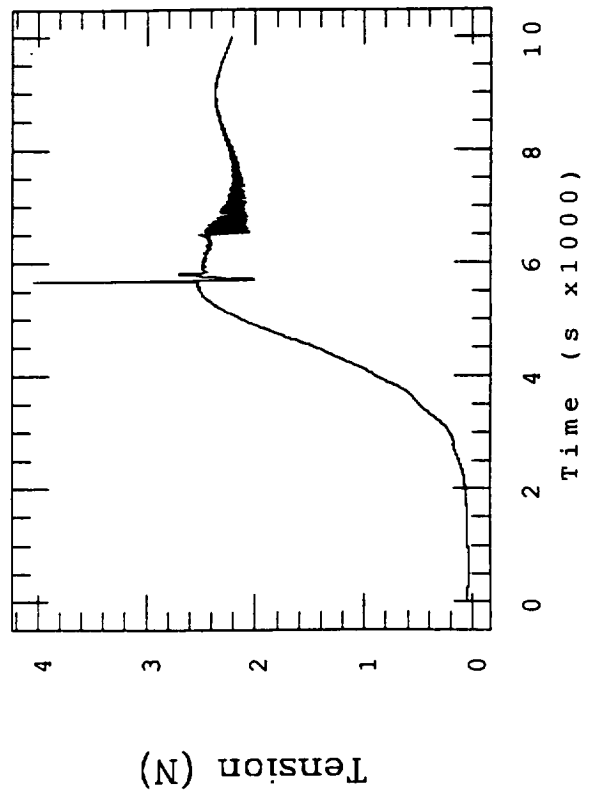
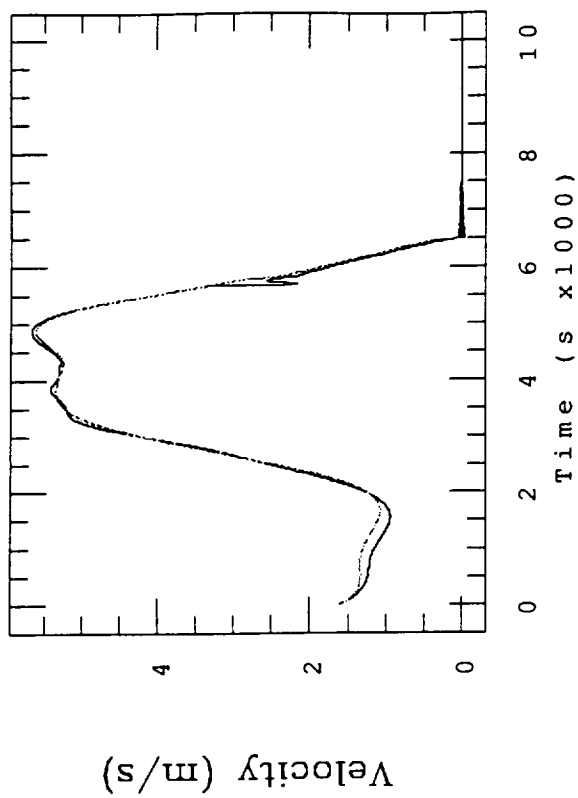


Figure 11.10(a)

\*



\*

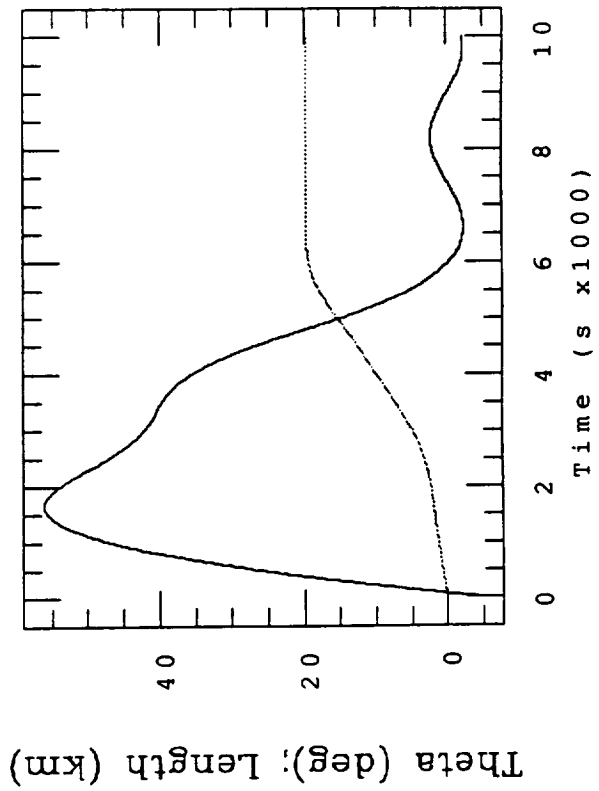
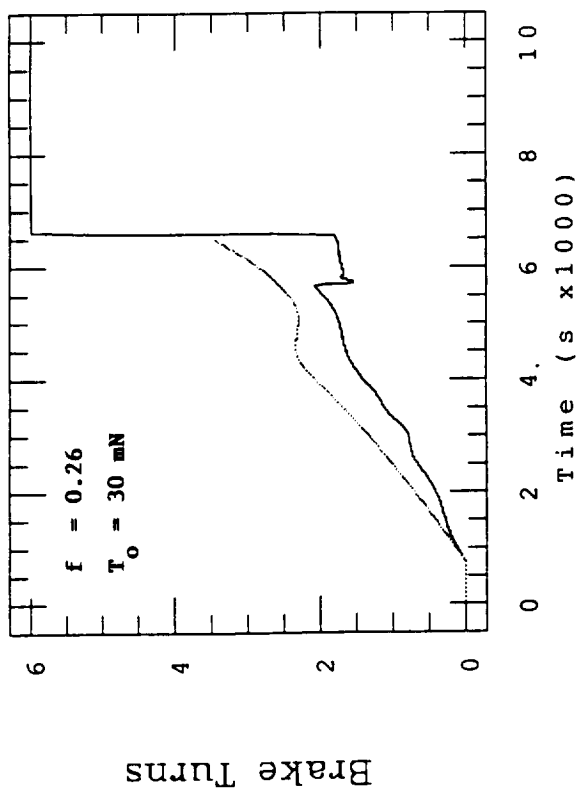


Figure 11.10(b)

during the SEDS-2 deployment tests on the ground and also in the SEDS-1 flight data, produced by the parallel winding of the tether on the spool. For SEDS-2, parallel winding starts at a tether length of about 17 km and the period of the associated noise component is about 30 s.

A tension fluctuation (as modeled in eqn. 11.18) produces a speed and hence a turn count fluctuation. The tension is, therefore, the most effective way of introducing noise into the system dynamics.

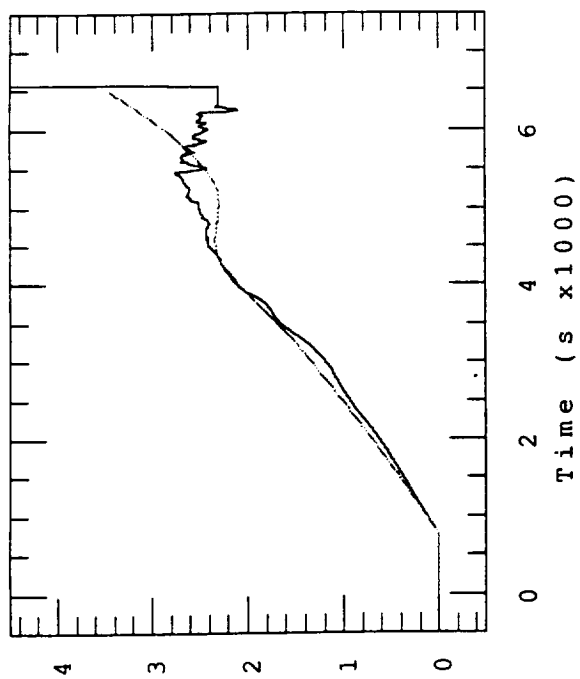
As mentioned before, the tether tension is assumed to be affected by an additive and a multiplicative noise component. Specifically, the additive noise component is important in the early phase of deployment when the tension is low. This component represents the effect of the stick-slip which dominates the low tension deployment up to a tether length of about 2 km. The multiplicative term represents the increase of tension fluctuations proportionally to the instantaneous value of the tension at later stages of deployment.

In the case shown in Fig. 11.11(a-b), the additive noise component is  $\pm 2$  mN and the multiplicative component fluctuates  $\pm 50\%$  with respect to the baseline value. Unbiased noise components were adopted because the effects of biases in the tension model are better represented by a variation of the minimum tension and variation in the brake effectiveness are better represented by variations in the friction coefficient (see relevant subsections of this report). In general, relatively high levels of random noise do not affect appreciably the system performance during deployment.

When the tether winding on the spool switches from universal (criss-cross type) to parallel, the tension fluctuations are dominated by a low frequency noise best described by a saw-tooth function. From deployment tests on the ground of SEDS-2, the amplitude of the tension fluctuation is conservatively less than  $\pm 0.5$  N with a period of roughly 30 s. The parallel winding starts at a tether length of about 17 km.

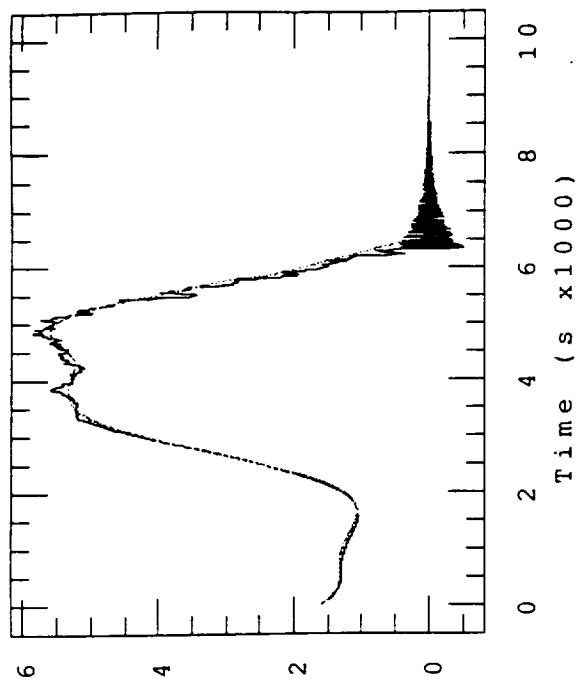


\*

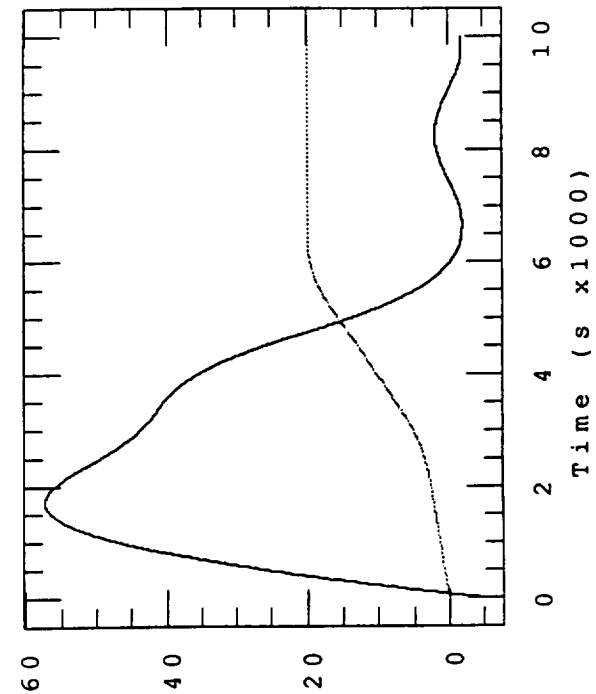


\*

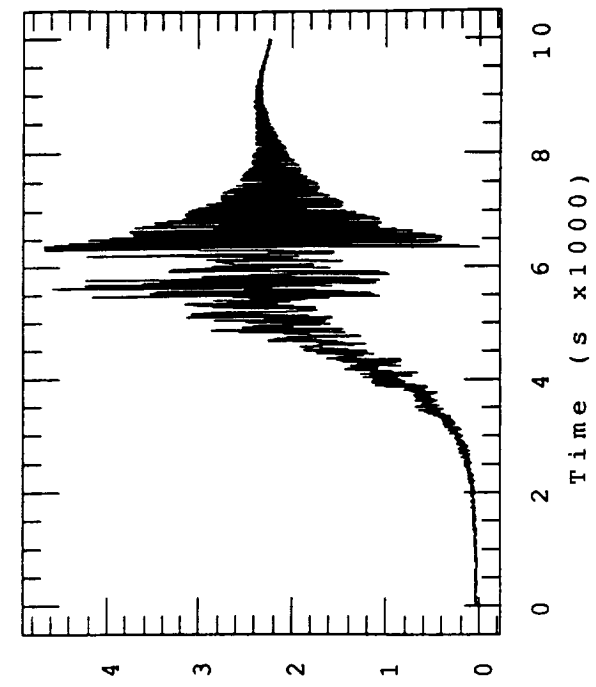
Brake Turns



Velocity (m/s)



Theta (deg); Length (km)



Tension (N)

Figure 11.11(a)

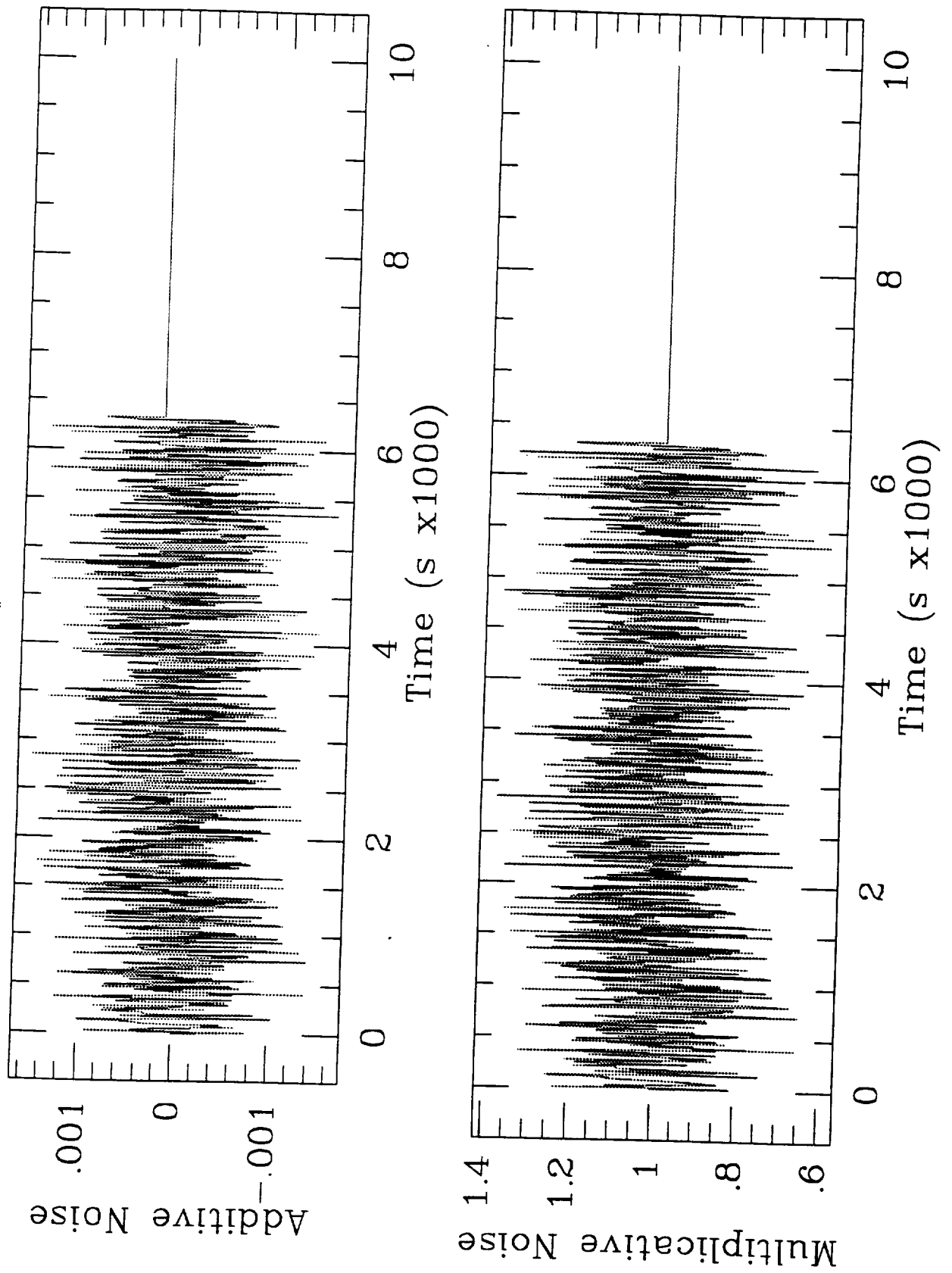


Figure 11.11(b)

The effect of the saw-tooth-shaped noise was simulated separately from the random noises and the results are shown in Figures 11.12(a-b). Since tension fluctuations influence the tether speed, the response to tension fluctuations is a test of the effectiveness of the filter in the control loop. In this particular control system which lacks a speedometer, the performance of the filter is especially important because, since the speed is computed from numerical derivation of the turn count, it is very sensitive to noise that affects the turn count. The most damaging noise components are the low-frequency components such as the saw-tooth noise.

The plots show that the recursive filter is very effective in abating the low-frequency noise and the filtered turn rate exhibits a smooth behavior. In conclusion, the deployment response is not significantly affected by this low-frequency noise component.

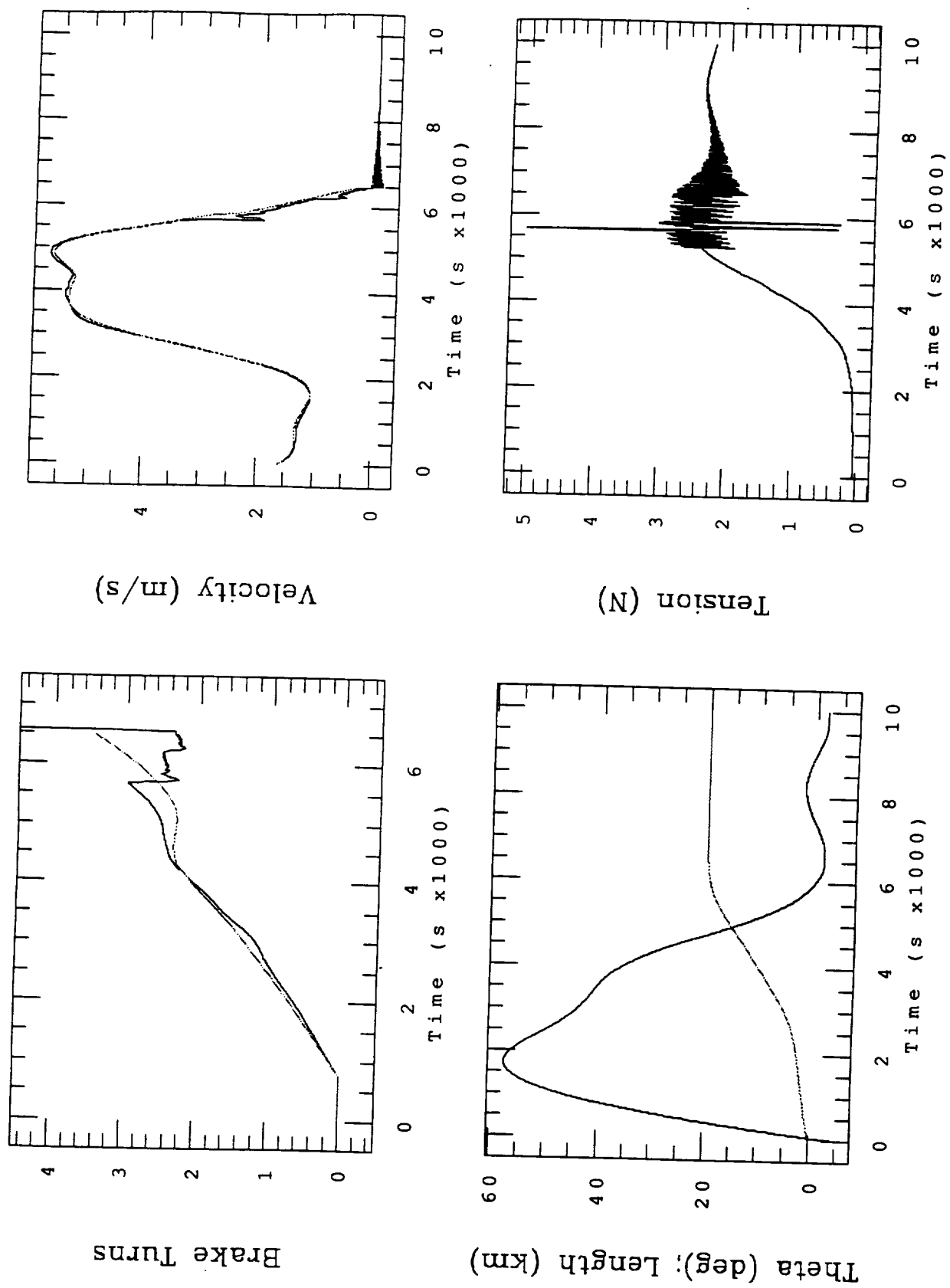


Figure 11.12(a)

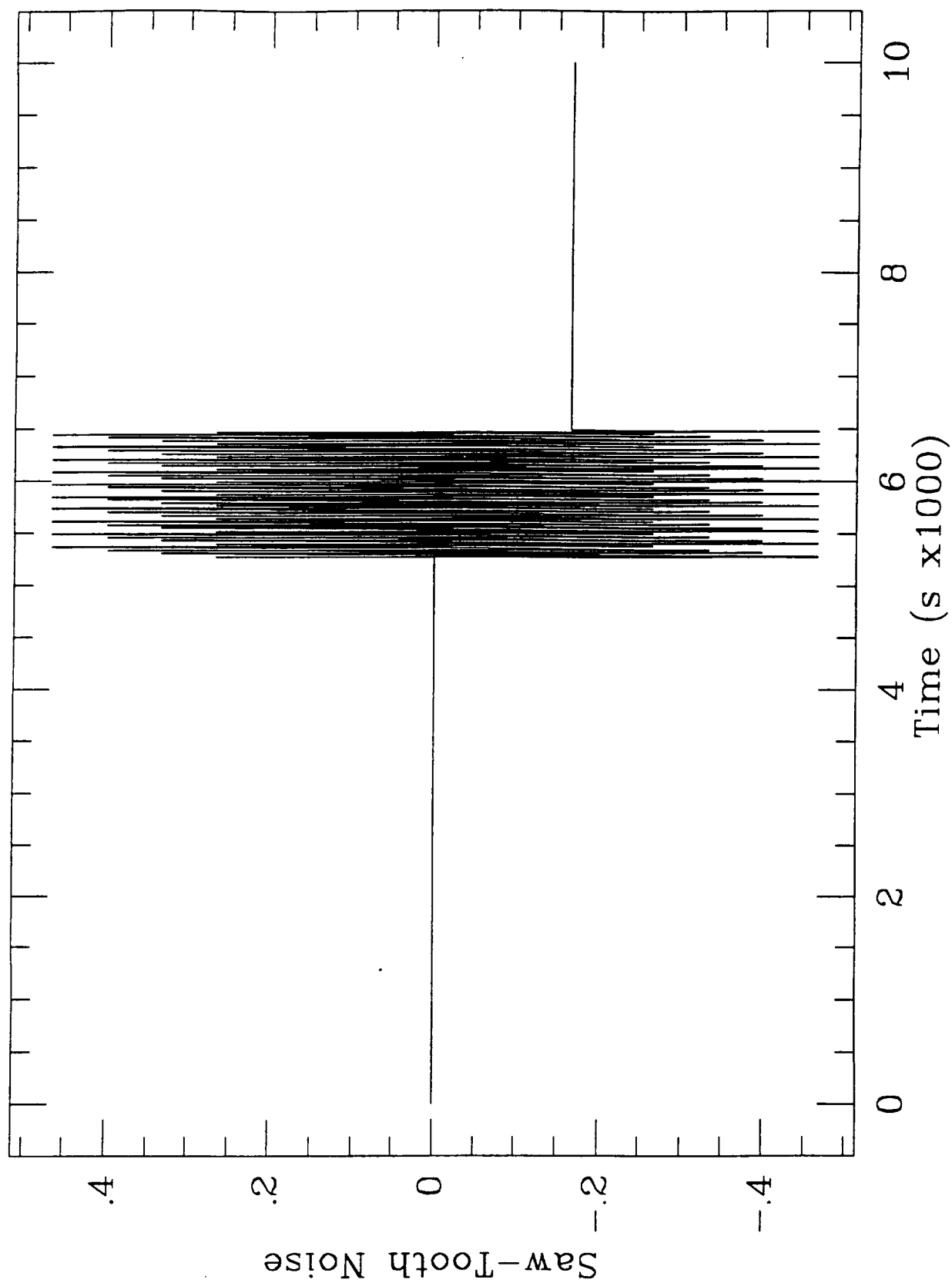


Figure 11.12(b)

### Combined Effect of Noise and Errors

Besides the uncertainties affecting the minimum tension and the brake response (modeled as a variation of the friction coefficient), the ejection velocity and direction also affect the final libration amplitude. The reference profiles are in fact derived for the nominal set of values for the initial conditions and any deviations from those values imply a non-null final libration. An orbital ellipticity also forces a non-null libration amplitude because the eccentricity pumps the libration through variations of the in-plane gravity gradient torque at the orbital frequency. Moderate value of eccentricities, however, have a weak effect on the libration. All these contributions to a non-null final librations are combined in the most destructive way to produce the dispersion plot shown in Figure 11.13 where the final libration amplitude is shown vs the minimum tension for two cases as follows: (1) nominal conditions  $V_0 = 1.64$  m/s,  $\theta_0 = -4.7^\circ$ ,  $f = 0.18$ , 350x350 km orbit; and (2) off-nominal conditions  $V_0 = 1.56$  m/s (5% less than nominal);  $\theta_0 = -6.7^\circ$  ( $-2^\circ$  with respect to nominal),  $f = 0.1$  (50% less than nominal), and an altitude difference between apogee and perigee of 50 km. The boundary values adopted for the dispersion of orbital and other parameters are representative of the system expected performance.

The plot in Fig. 11.13 clearly shows that the worst possible combination of uncertainties and errors can degrade the control law performance by increasing the final libration amplitude by as much as  $5^\circ$  over the expected span of minimum tension values (i.e.,  $10 \text{ mN} \leq T_0 \leq 45 \text{ mN}$ ). However, the worst possible combination of uncertainties is unlikely to occur.

#### **11.1.4 Validation of SEDS-2 Control Law**

A validation of the simulated performance of SEDS-2 control law was carried out by means of test-case simulations run in parallel at SAO and NASA/MSFC [7]. Since the computer codes at SAO and NASA/MSFC are completely independent, this comparison provides a comprehensive test of the control law and the simulation software. In particular, the specific code used to develop the SEDS-2 control law at SAO assumes the tether to be straight while the NASA/MSFC computer code models the bowing of the tether. A successful validation, therefore, acquires the additional meaning that the bowing of the tether and the additional vibrational modes have a negligible effect on the performance of the control law. Another, less important, difference between the two codes

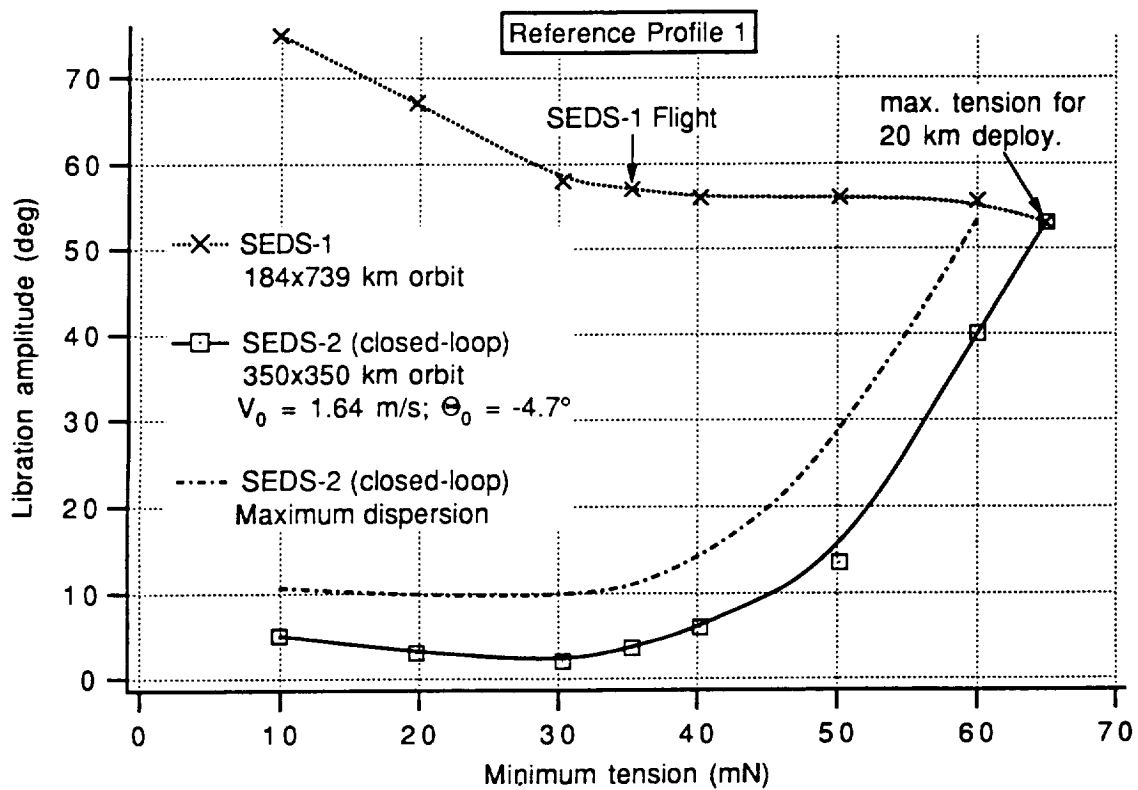


Figure 11.13

involves the gravity model: the SAO code used for SEDS-2 has a spherical gravity model while the NASA/MSFC code has a  $J_0 + J_2$  gravity model. This difference accounts for the small discrepancies in the plot of the tether libration angle.

The simulation results for the most important variables from the two computer codes are shown in Figures 11.14(a-e). This simulations adopt the reference values of the parameters as indicated in Section 11.1.2.

The results from the SAO simulators were also compared to the results obtained by Logicon Control Dynamics which are reported in Ref. [8]. In this case, the comparison was qualitative because it was based on the analysis of plots, rather than files, relative to same simulation cases. Unlike the comparison with the NASA/MSFC code, the comparison covered not only the reference case but also the low-static-tension and the high-static-tension cases. The agreement between the results is impressive with maximum differences between the libration angles from the two codes of less than 1 deg.

#### **11.1.5 Simulation of latest baseline deployments**

The latest configuration of the flight tether consists of 19.7 km of the new (cleaned) tether and 300-m of the old (SEDS-1 type) tether spliced to the new tether at the deployer end. From the deployment tests conducted on the ground and analyzed by NASA/MSFC, the most likely values of the static tension for the new (cleaned) tether are as follows:  $T_0 = 10\text{-}15$  mN for a temperature of 13 °C (55 °F, nominal case);  $T_0 = 10\text{-}15$  mN for a temperature of 2 °C (36 °F, cold case); and  $T_0 = 8\text{-}10$  mN for a temperature of 35 °C (95 °F, hot case). The old tether, instead, exhibits a rather high and uncertain static tension, estimated, at the time of this writing, at 40-100 mN. The tension model parameters have also been slightly modified as follows: annulus solidity = 0.9424; area exponent = -0.6; and inertia multiplier = 4.1.

The new tension model parameters do not affect significantly the control law and the deployment response. The addition of the 300-m old tether segment at the end of the new tether, however, alters the deployment speed profile in the last phase of deployment.

The new parameters are adopted for the new baseline simulations as explained in the following.



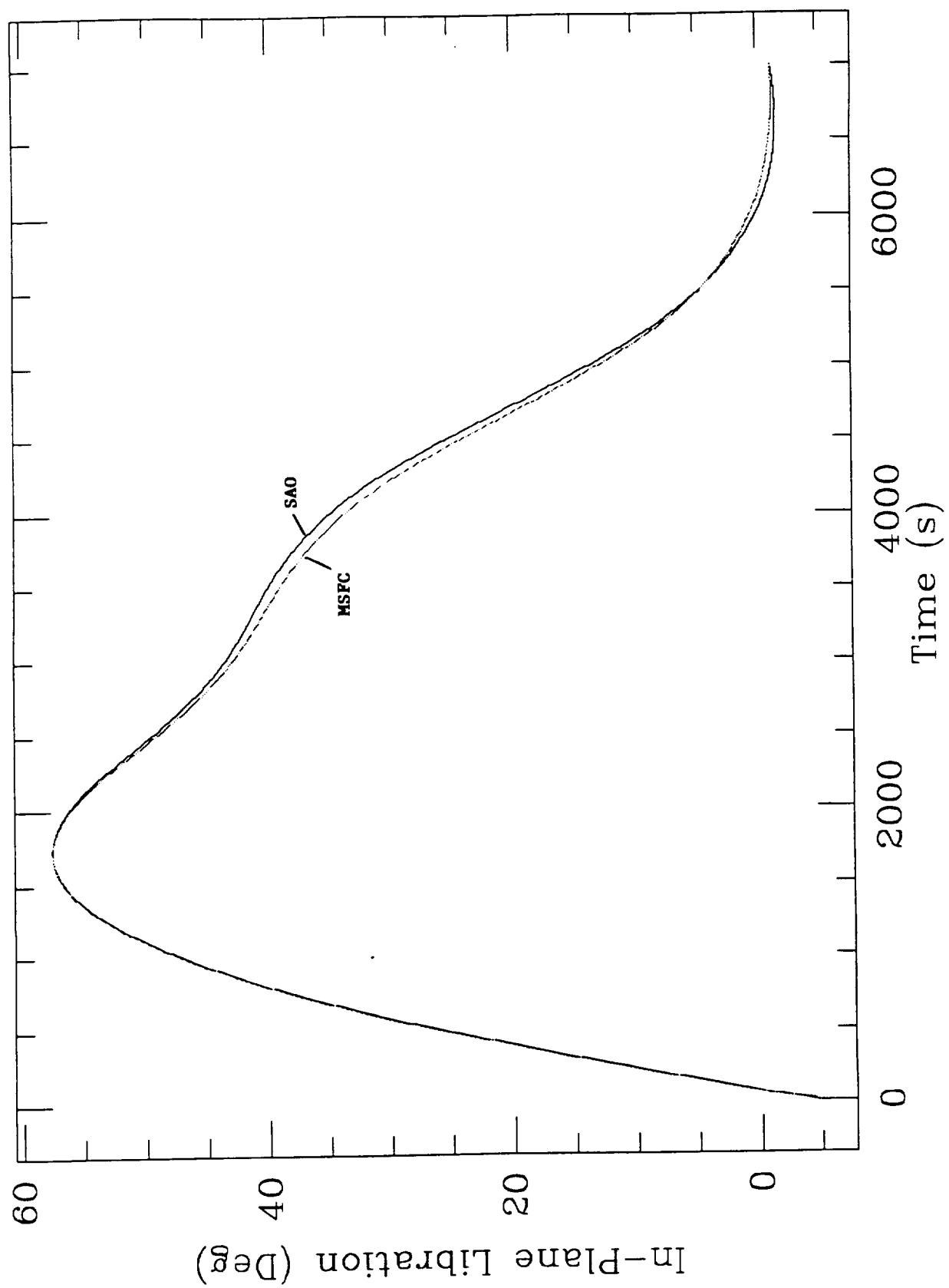


Figure 11.14(a)

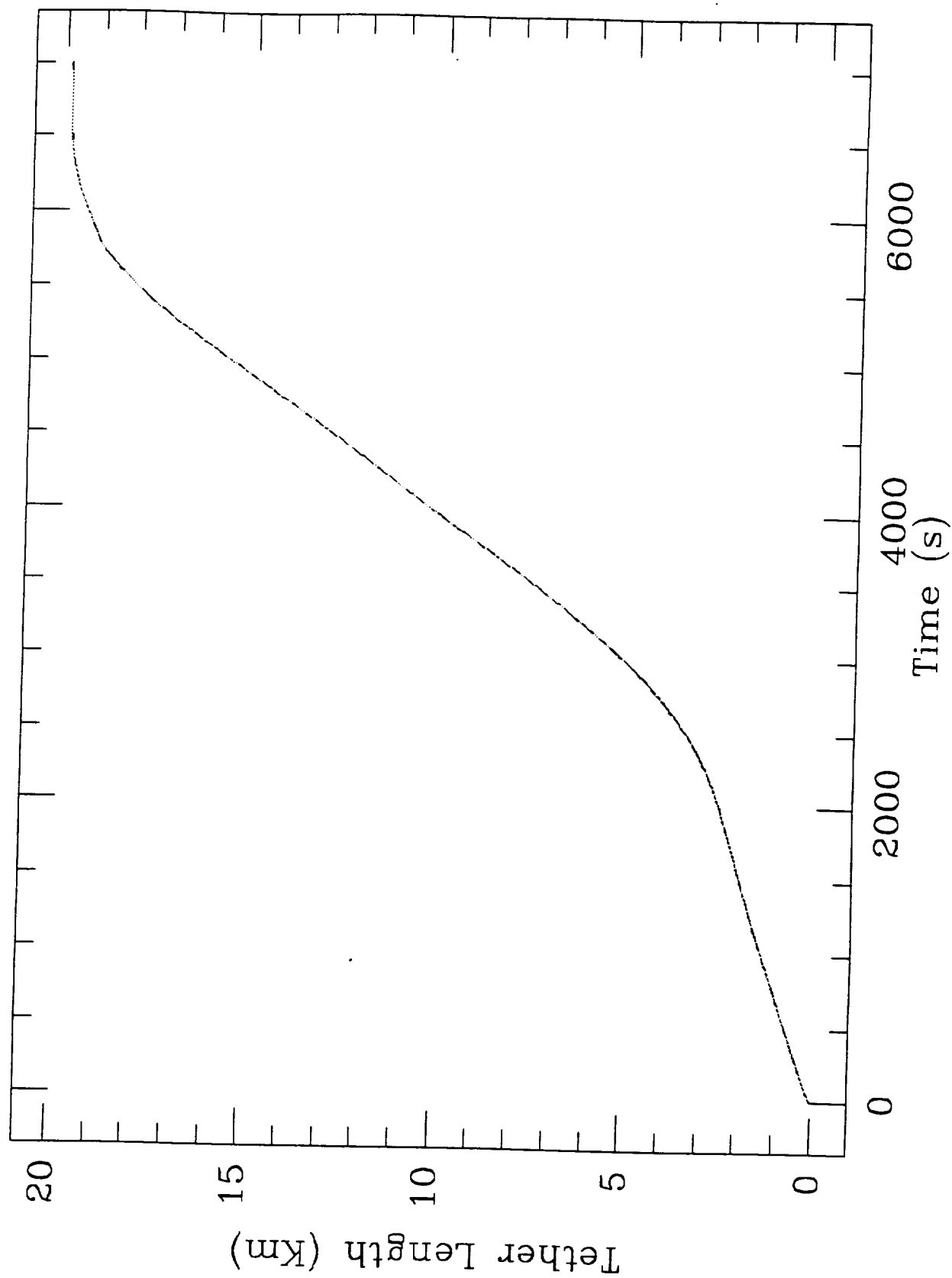


Figure 11.14(b)

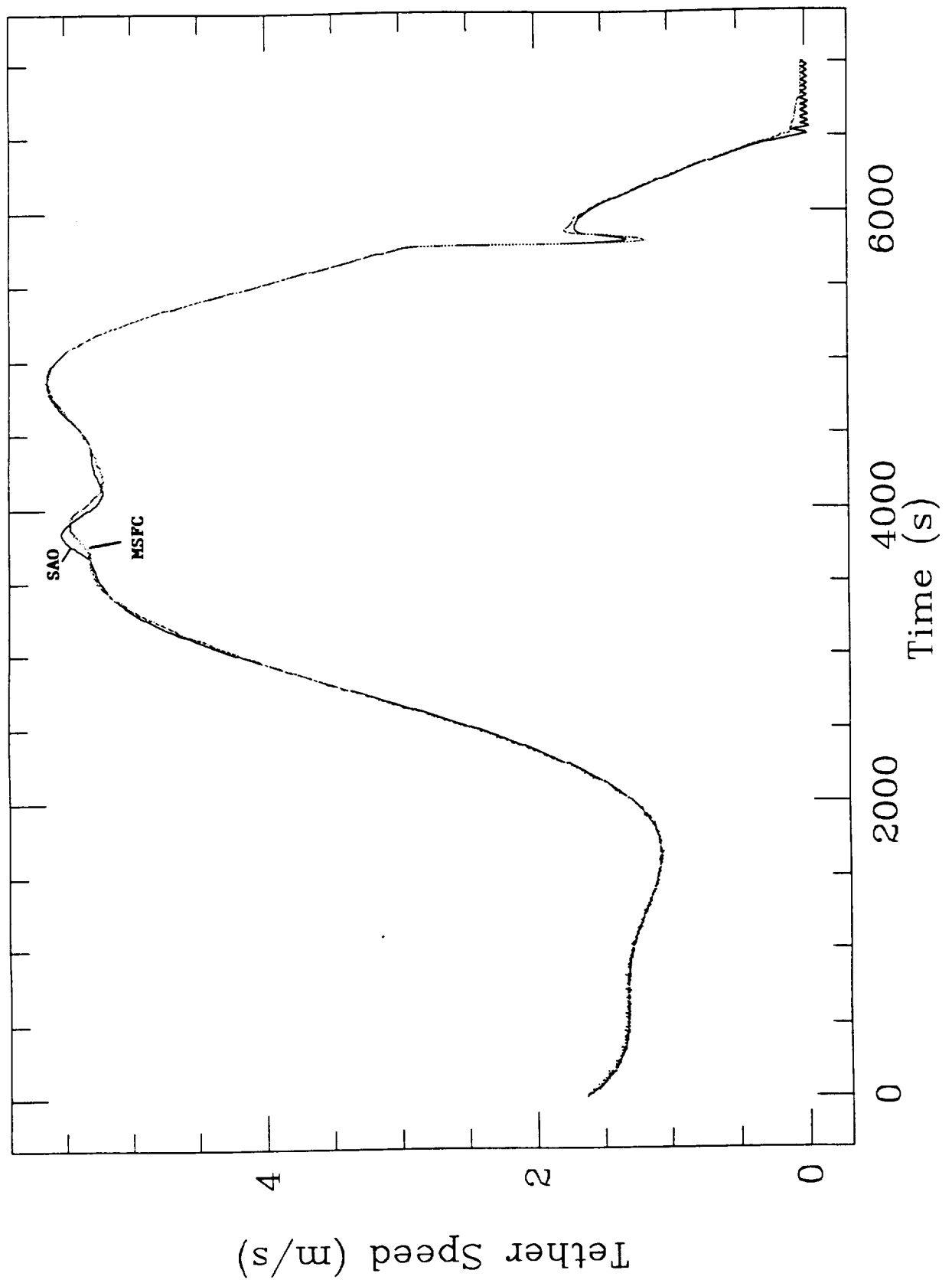


Figure 11.14(c)

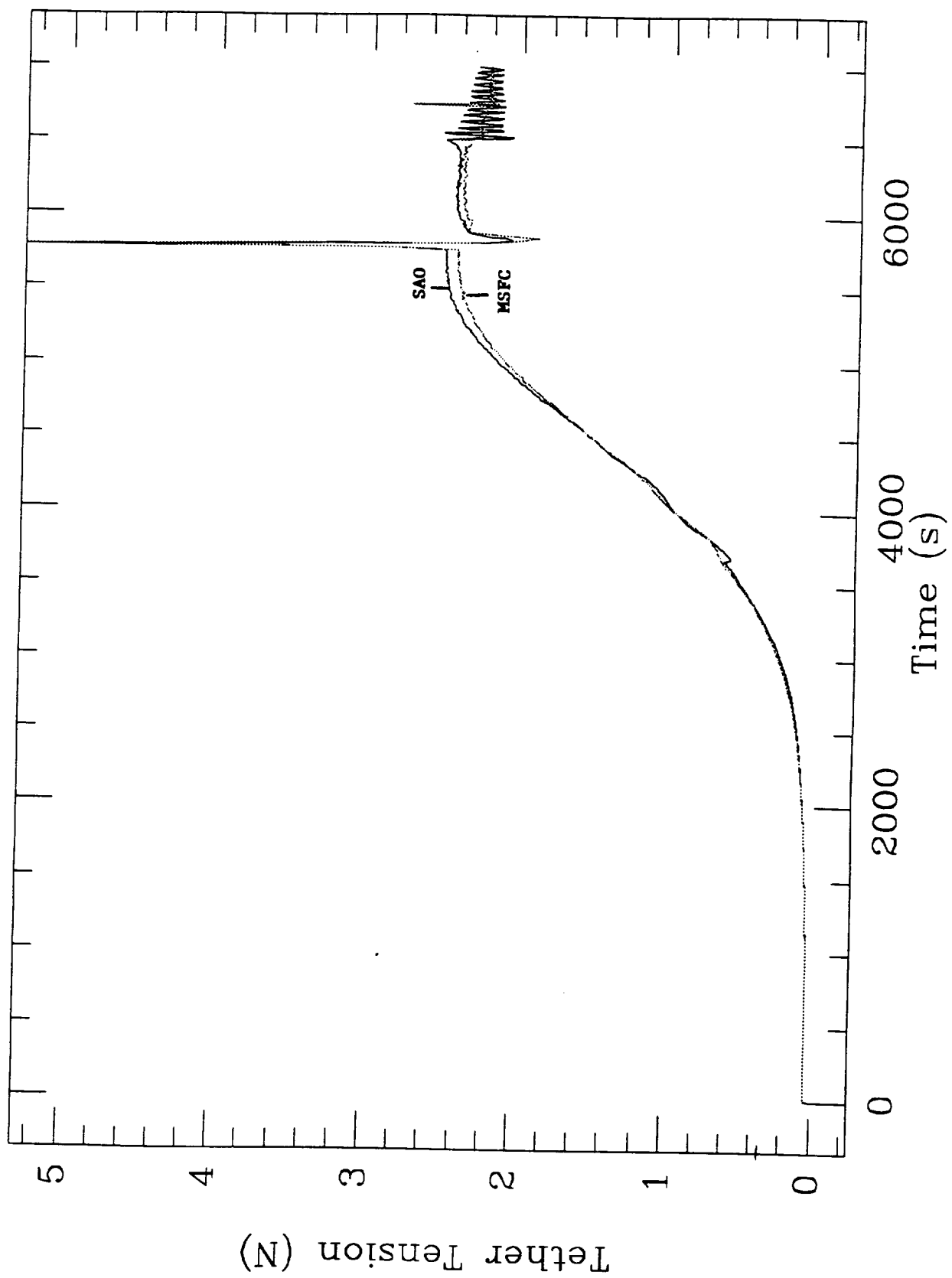


Figure 11.14(d)

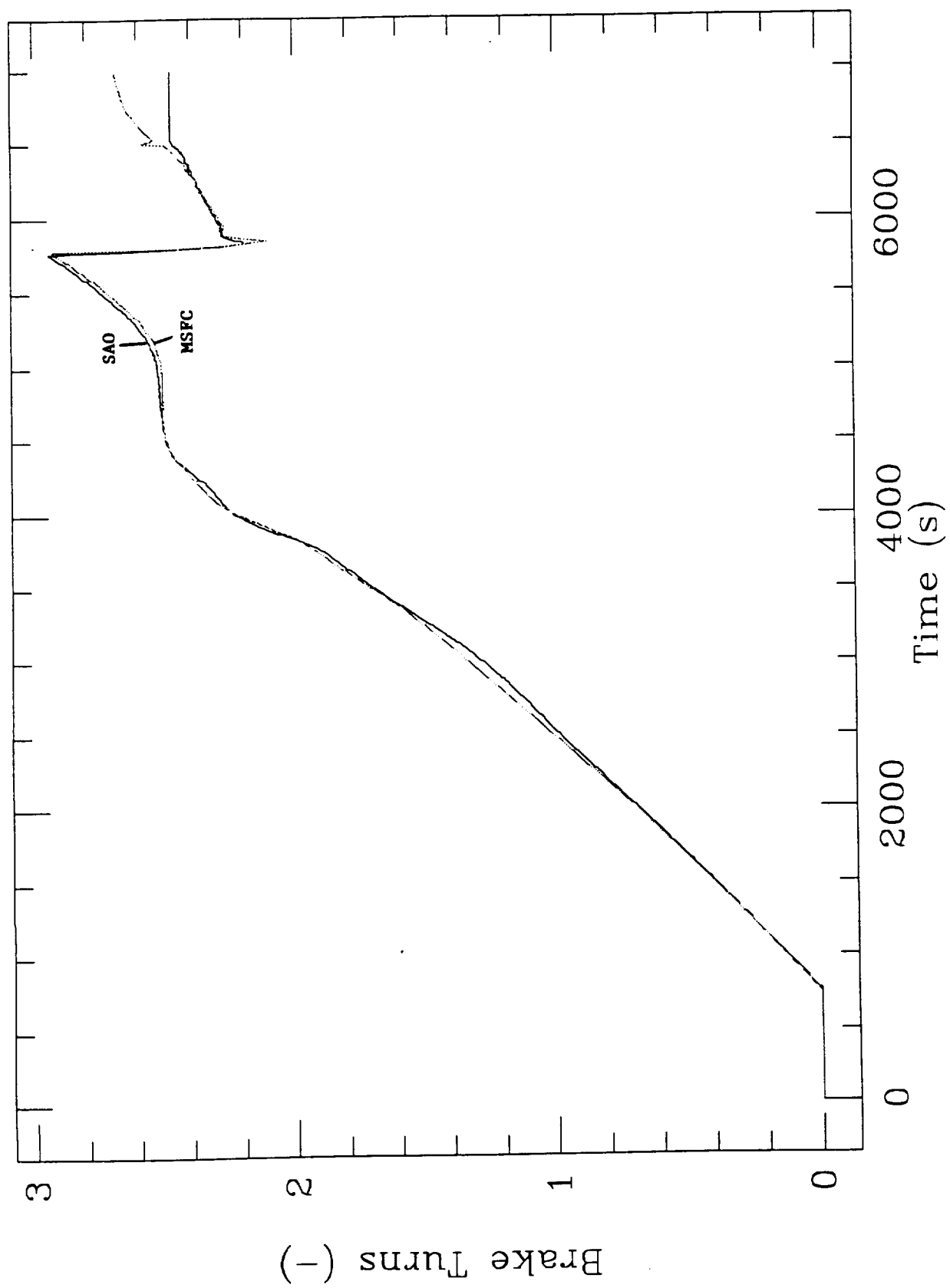


Figure 11.14(e)

Simulation results for the nominal case are depicted in Figures 11.15 in which a static tension of 12.5 mN was adopted for the new tether and 70 mN for the last 300-m old tether.

Results for the cold case, with  $T_0 = 15$  mN for the new tether and 70 mN for the old tether, are shown in Fig. 11.16. Results for the hot case, with  $T_0 = 8$  mN for the new tether and 70 mN for the old tether, are shown in Fig. 11.17.

In conclusion, the addition of the old tether does not affect the libration response of the system during deployment. It does affect significantly the tether speed profile in the last phase of deployment because of the abrupt change of the tether minimum tension (from roughly 10 mN to 70 mN) at a time when a high number of brake turns is applied. The control law compensates by reducing the number of brake turns by 1.5 turns. Deployment comes to a stop at about 19.78 km and  $t = 6,560$  s when the brake is ramped up.

Finally, a simulation was run to show the effect of heavy tensional noise on the new nominal case. The tension is assumed to be affected by noise structured as follows: an additive component of  $\pm 10$  mN, a multiplicative component of  $\pm 50\%$  (the spectra of these two components is cut below a frequency of 0.33 Hz), and a saw-tooth noise of  $\pm 0.5$  N with a period of 30 s active for tether lengths  $\geq 17$  km. Figure 11.18(a-b) show the simulation results. The control law performs rather well in the presence of high noise levels: the final libration amplitude is almost unaffected with respect to the (latest) nominal, the final velocity is similar to nominal (in which the final phase is significantly impacted by the presence of the 300-m old tether segment), and the brake actuation is not excessively jittery.

One important remark, the term "baseline" should not be confused with the term "reference". The non-linear control law adopted for SEDS-2 necessitates reference profiles as explained before. The reference profiles for SEDS-2 were derived according to the values of parameters indicated in Section 11.1.2. The most important of this reference parameter is the value of the static tension. The reference value of the static tension ( $T_0 = 30$  mN) is closer to the baseline value of the cold case than to the baseline value of the hot case. However, thanks to the robustness of the control law, especially with respect to low values of the static tension, the librational response for the cold and hot cases are completely satisfactory.

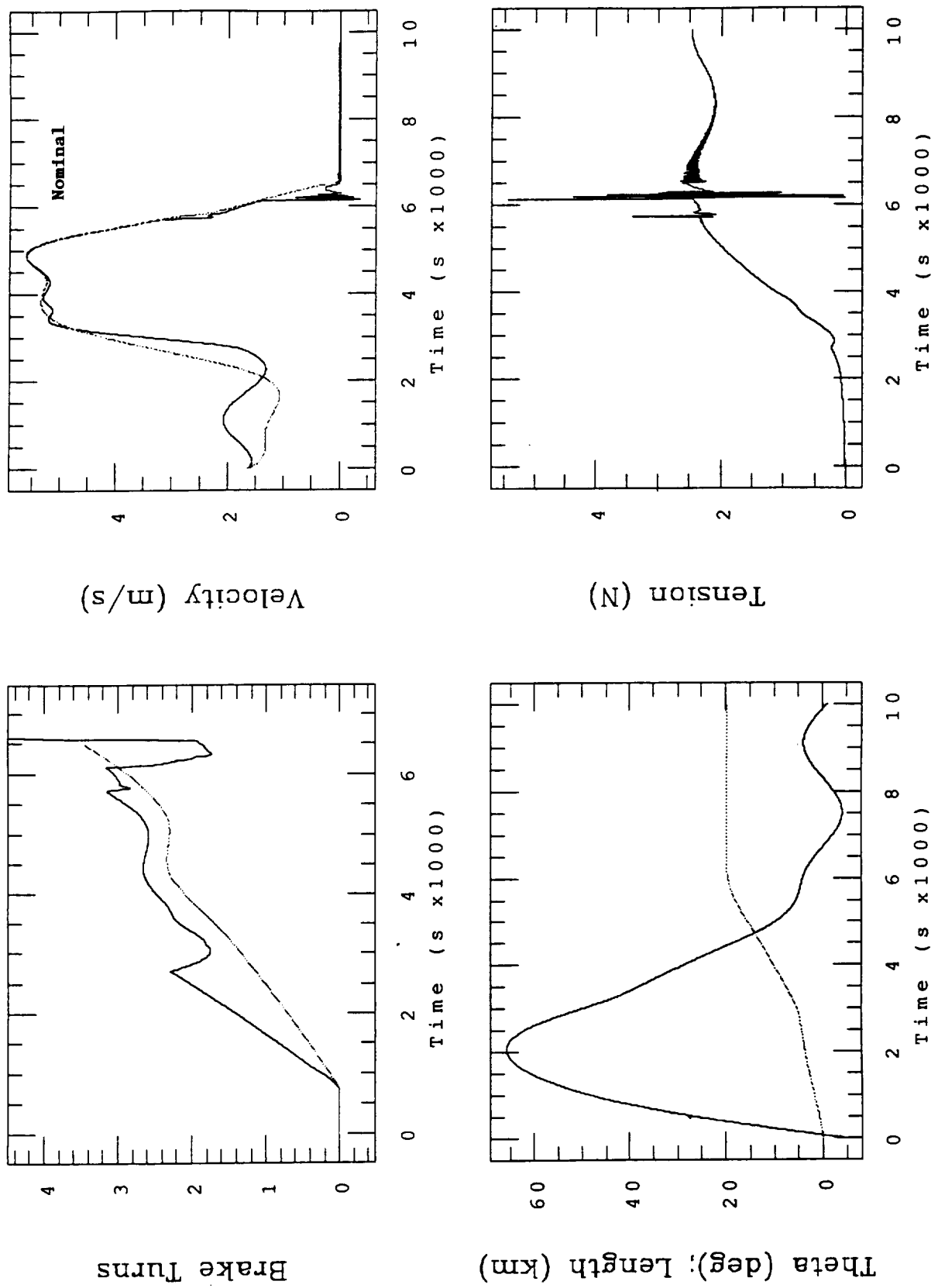


Figure 11.15

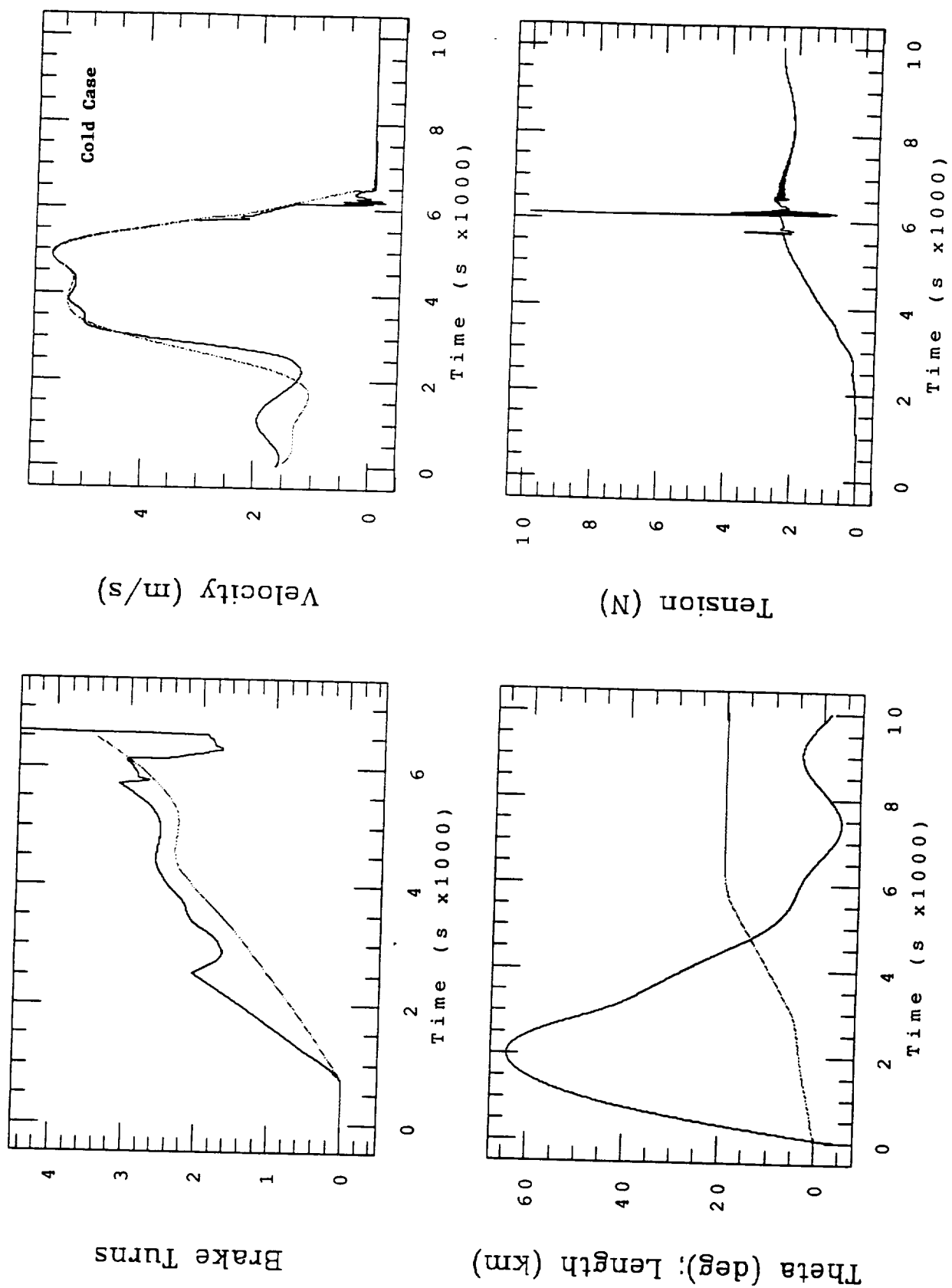


Figure 11.16



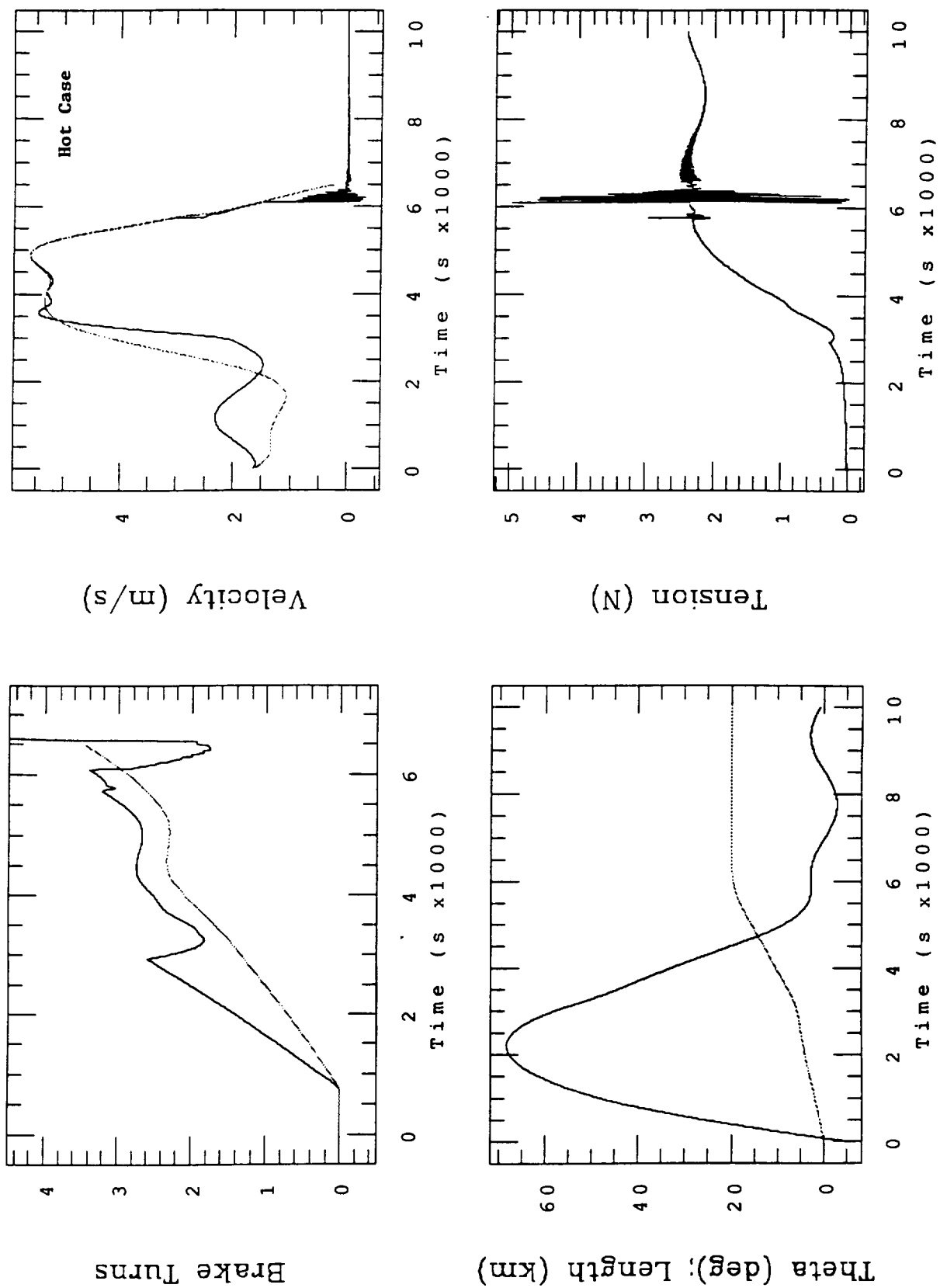


Figure 11.17

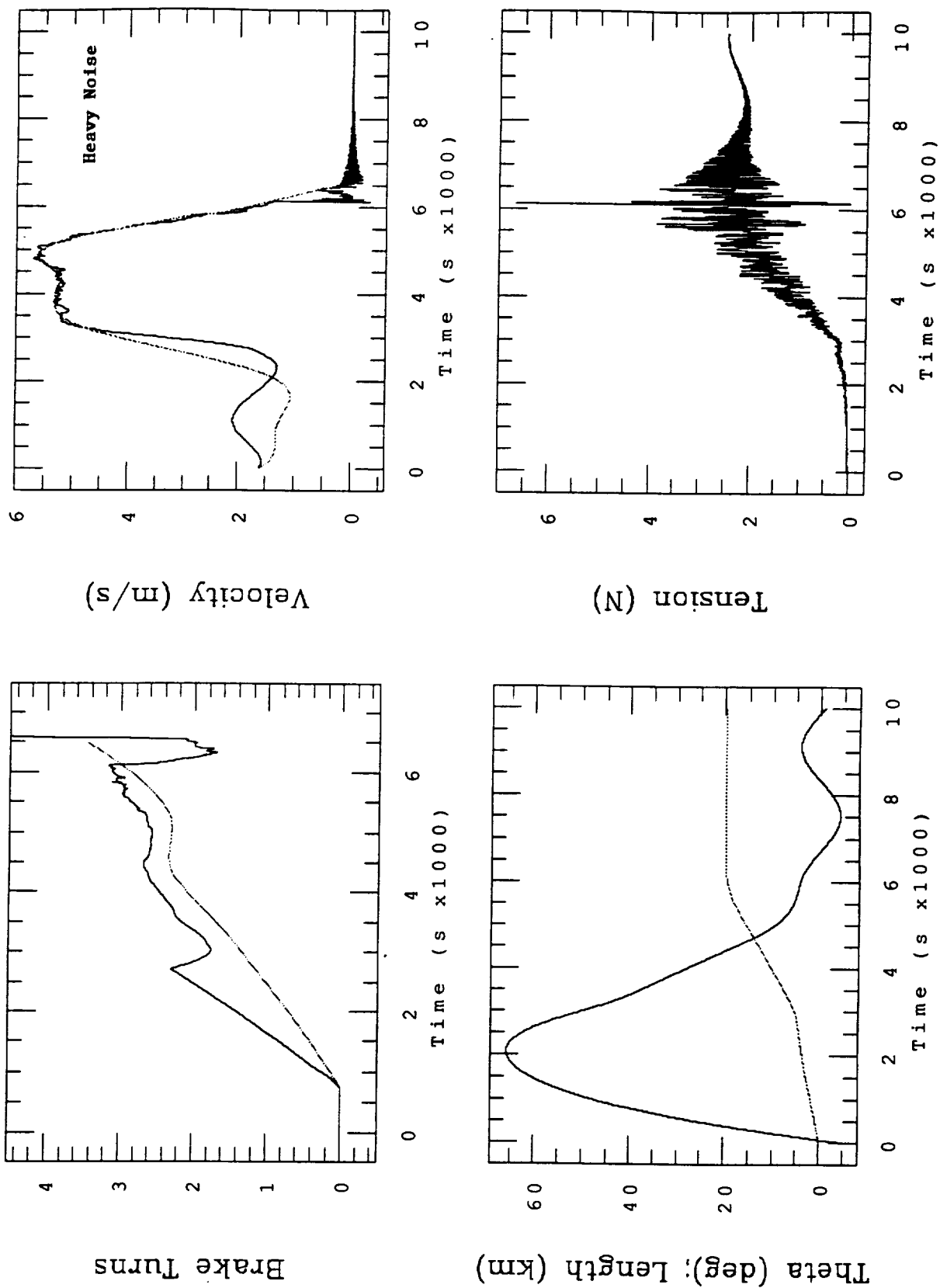


Figure 11.18(a)

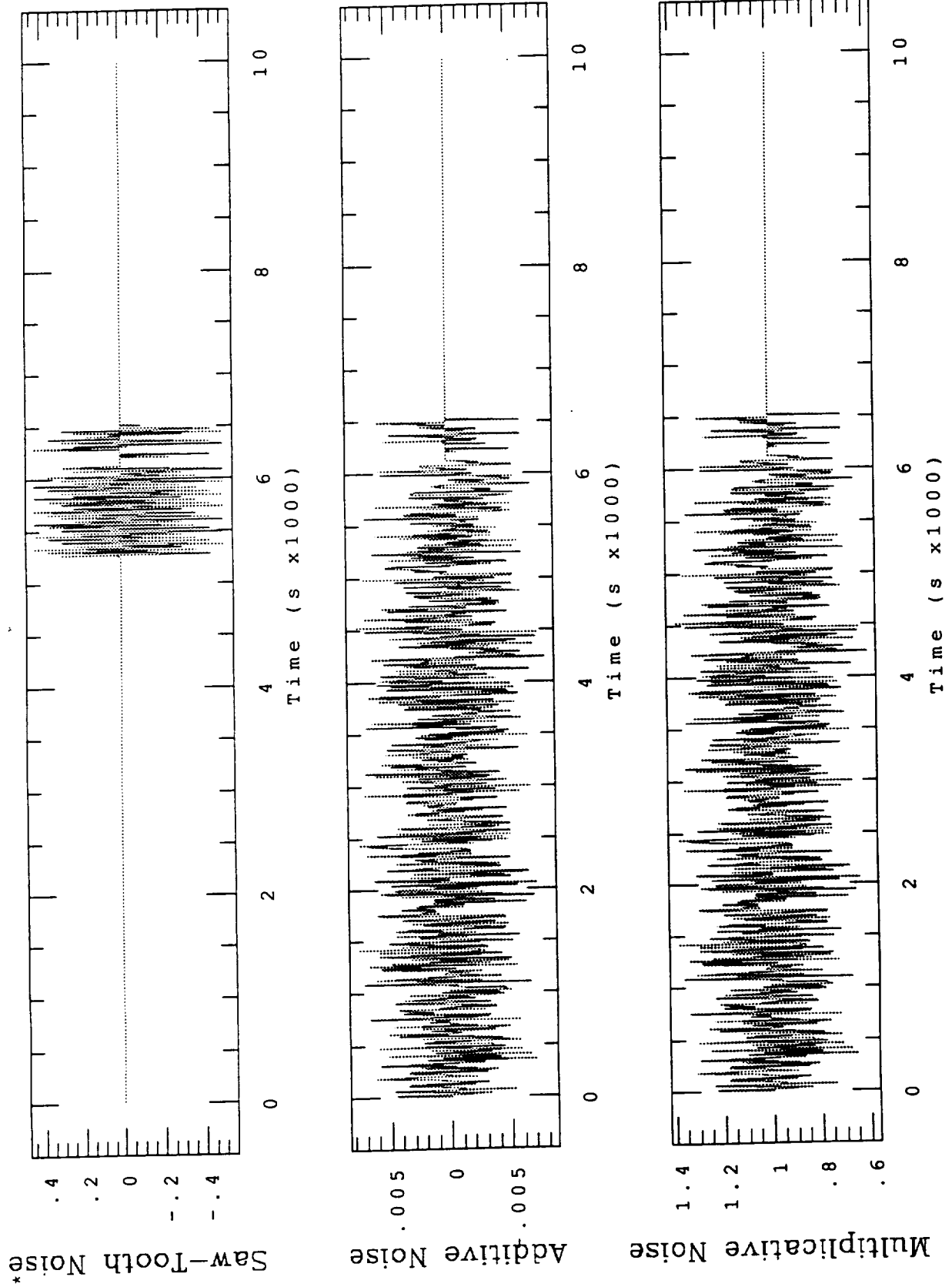


Figure 11.18(b)

## 11.2 Control law performance during the flight

### 11.2.1 Estimate of the maximum libration at the end of deployment

The libration amplitude of SEDS-2 at the end of deployment must be estimated indirectly because there are no on-board sensors to measure that variable directly.

The estimate of the maximum tether libration is, therefore, carried out with the following two methods: (1) by analyzing the tether tension variation for constant tether length (i.e., after deployment); and (2) by simulating the deployment libration dynamics for the tether velocity and length deployment profiles of the actual flight.

#### Tension method

The tether tension contains the information of the tether libration amplitude because the libration modulates the tension at the frequency of the libration. For an inextensible tether and two-dimensional librations in the orbital plane:

$$\frac{T}{m_r} = [(\dot{\theta} + \Omega)^2 + \Omega^2(3\cos^2\theta - 1)] L \approx [(\dot{\theta} + \Omega)^2 + 2\Omega^2] L \quad (11.19)$$

where  $T$  is the tether tension,  $m_r$  the reduced mass,  $\theta$  the libration angle with respect to the local vertical,  $L$  is the deployed tether length, and  $\Omega$  the orbital rate. The approximation in eqn (11.9) is valid for small libration amplitudes. The tension can be further subdivided into a static part owing to the gravity gradient and a dynamic part owing to the libration as follows:

$$T_0 = 3\Omega^2 m_r L \quad (11.20.1)$$

$$\Delta T = (\dot{\theta} + 2\Omega) \dot{\theta} m_r L \quad (11.20.2)$$

where  $\Delta T$  is the amplitude of the tension fluctuation due to libration.

For free in-plane librations whereby  $\dot{\theta} = \sqrt{3}\Omega\theta$ , eqn (11.20.2) leads to the following quadratic equation:

$$\theta_m^2 + \frac{2}{\sqrt{3}} \theta_m - \frac{\Delta T_m}{2\sqrt{3}\Omega^2 m_r L} = 0 \quad (11.21)$$

from which the maximum libration amplitude  $\theta_m$  can be readily obtained.

Presently, the tether tension is available only from the tensiometer at the deployer for a duration of approximately 15,500 s from satellite ejection. The flight tension contains not only the libration-related fluctuations but also tension oscillations due to many other natural oscillations and external perturbations. The libration component, however, has a distinct signature because of its very long period of 3200 s.

The libration component was extracted from the flight tension data through filtering. Figure 11.19(a) shows the flight raw tension while Fig. 11.19(b) shows the filtered tension after deployment. The curves in Fig. 11.19(b) are for: (1) a 100-s running average; (2) a recursive low-pass filter with a cut-off frequency of about  $10^{-3}$  Hz (i.e., a period of 1000 s); and (3) a smoothed version of the recursive filter output in solid line. The peak-to-peak amplitude of the tension component related to libration is about 0.3 N which corresponds to a maximum tension amplitude  $\Delta T_m = 0.15$  N.

After substitution of the numerical value above, eqn (11.21) yields a maximum libration amplitude of 3.2 deg.

The estimate of the libration amplitude with the tension method could be improved in the near future with the release of the load cell and accelerometer data from the satellite. The duration of the satellite data is longer as it covers about 7 orbits and will, therefore, enable an even more accurate estimate of the low-frequency libration-related tension fluctuations.

#### Velocity method

The second method adopted to evaluate the amplitude of libration at the end of deployment is by feeding the tether-dynamics simulator with the length and velocity profiles from the flight data.

The velocity profile, however, is corrupted because of the failure of one turn counter after  $t = 2200$  s as shown in Fig. 11.20(a). The tether length flight profile is shown in Fig. 11.20(b). Furthermore the flight velocity profile exhibits a strong variability at high frequencies which disturbs the simulator. For the reasons above, the velocity profile must be cleaned as much as possible of the spurious values due to the turn counter malfunctions and subsequently filtered to remove the high frequency fluctuations. It is important to note that the high frequency fluctuations have an almost negligible effect on the low frequency librations.

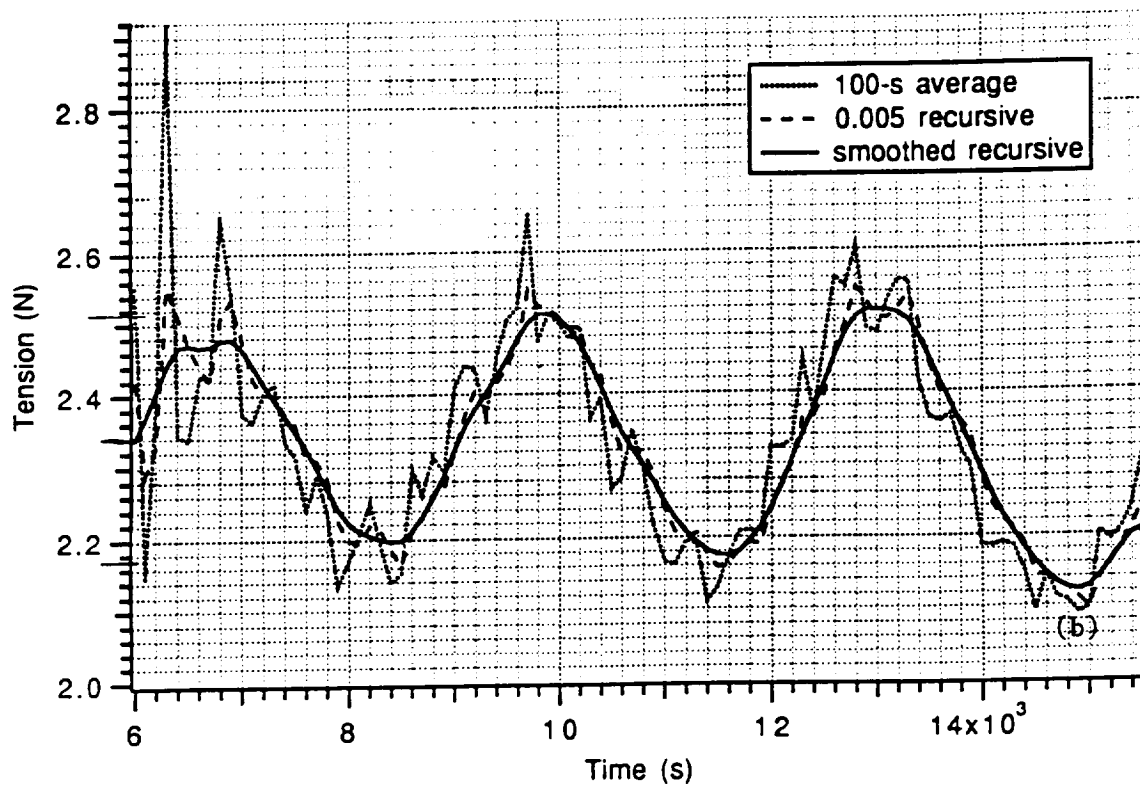
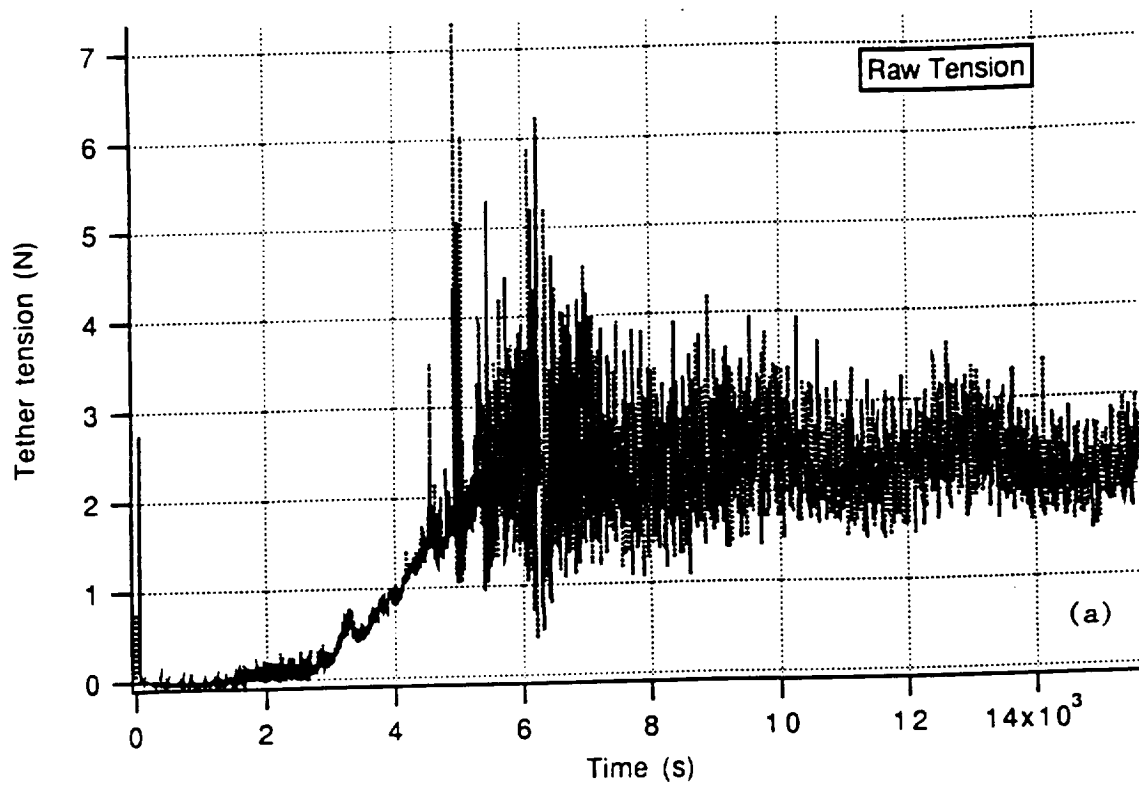
The spurious counts of tether velocity were eliminated by discarding all the velocity values greater than 10 m/s. Subsequently, the velocity profile was filtered with a 10-s and a 100-s moving average filter.

Figure 11.21(a) and 11.21(b) show the the 10-s running average velocity and the associated libration response for the actual orbital parameters of the SEDS-2 mission. The 100-s running average velocity and the associated libration response are shown in Figures 11.22(a) and 11.22(b).

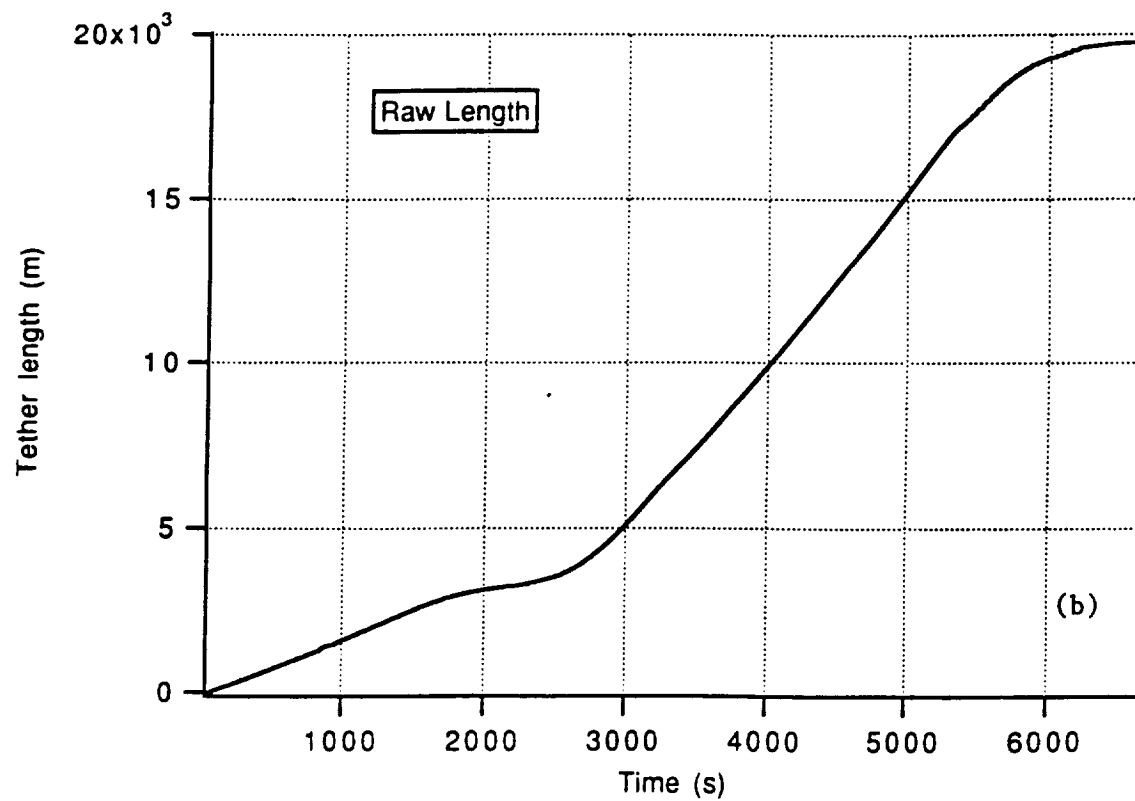
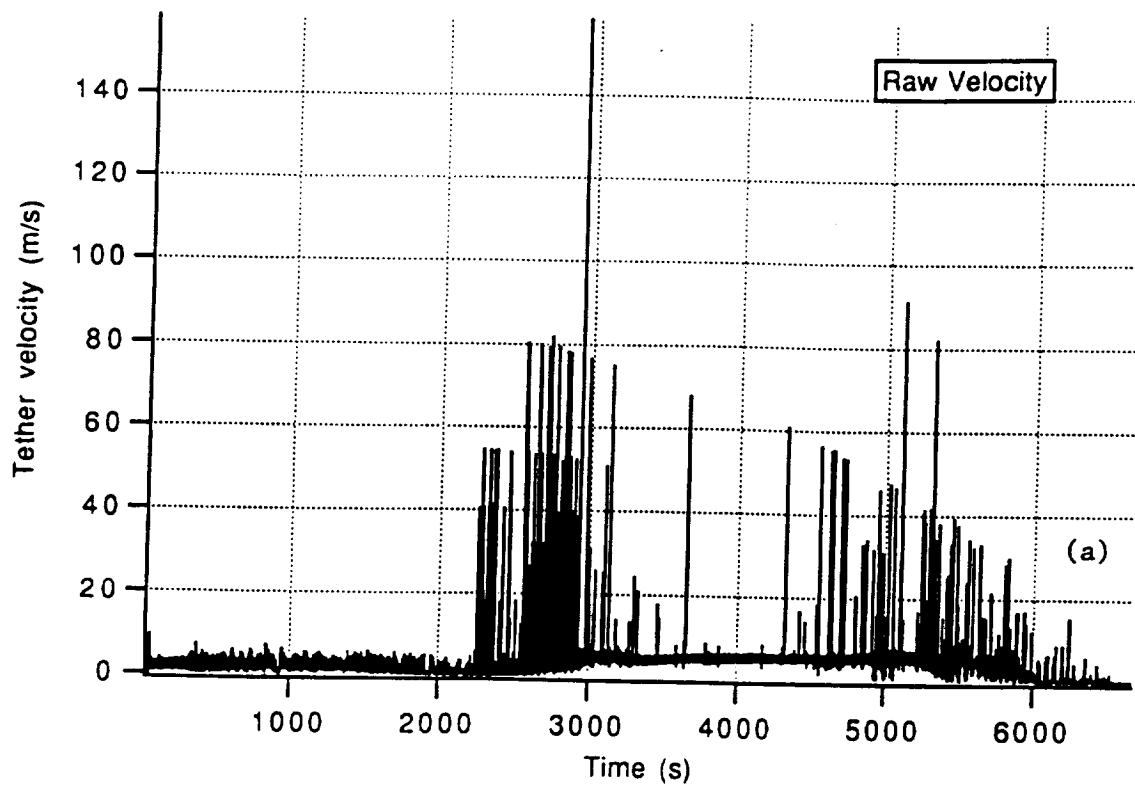
The maximum libration amplitude at the end of deployment for the two case is 4 deg and 2 deg respectively which are in line with the estimate from the tension method.

The tension method, however, is more accurate because it is a more direct measurement of libration. In conclusion, it is reasonable to assume at this point in time that the maximum libration amplitude at the end of deployment was about 3 deg.

This estimate could be validated and maybe refined in the near future when the data from the load cells and the accelerometers on board the satellite become available.

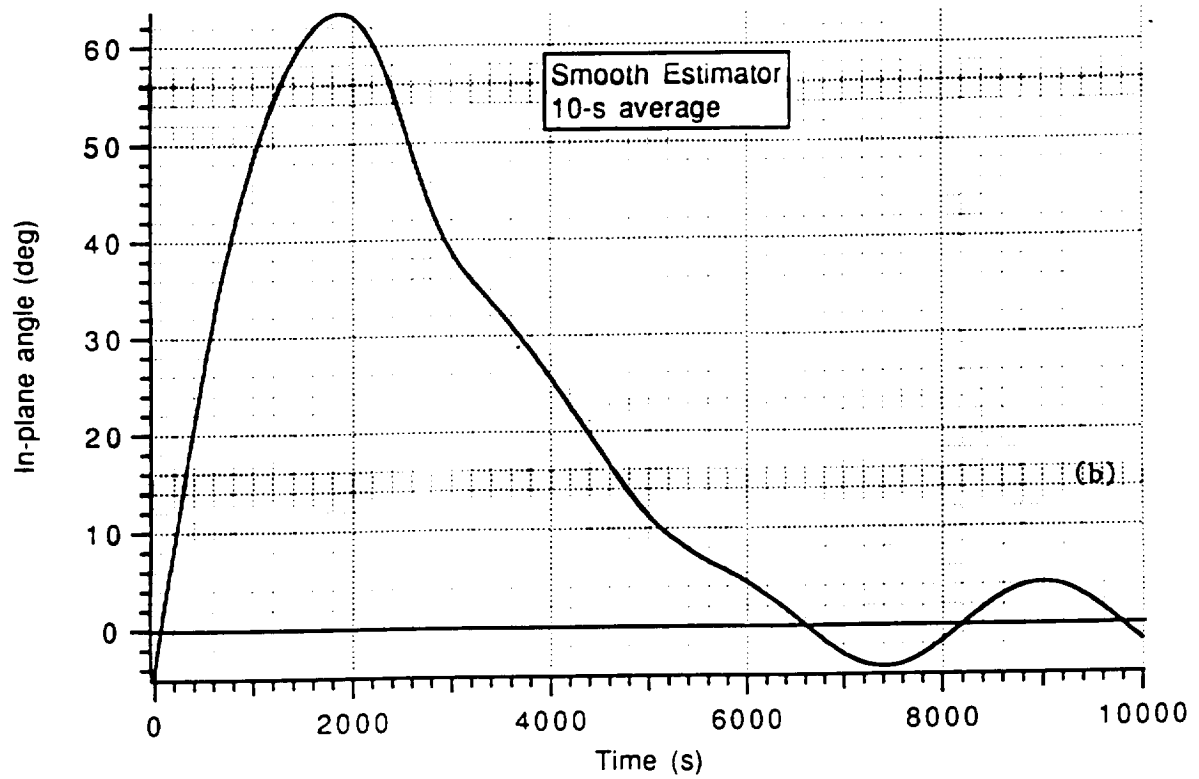
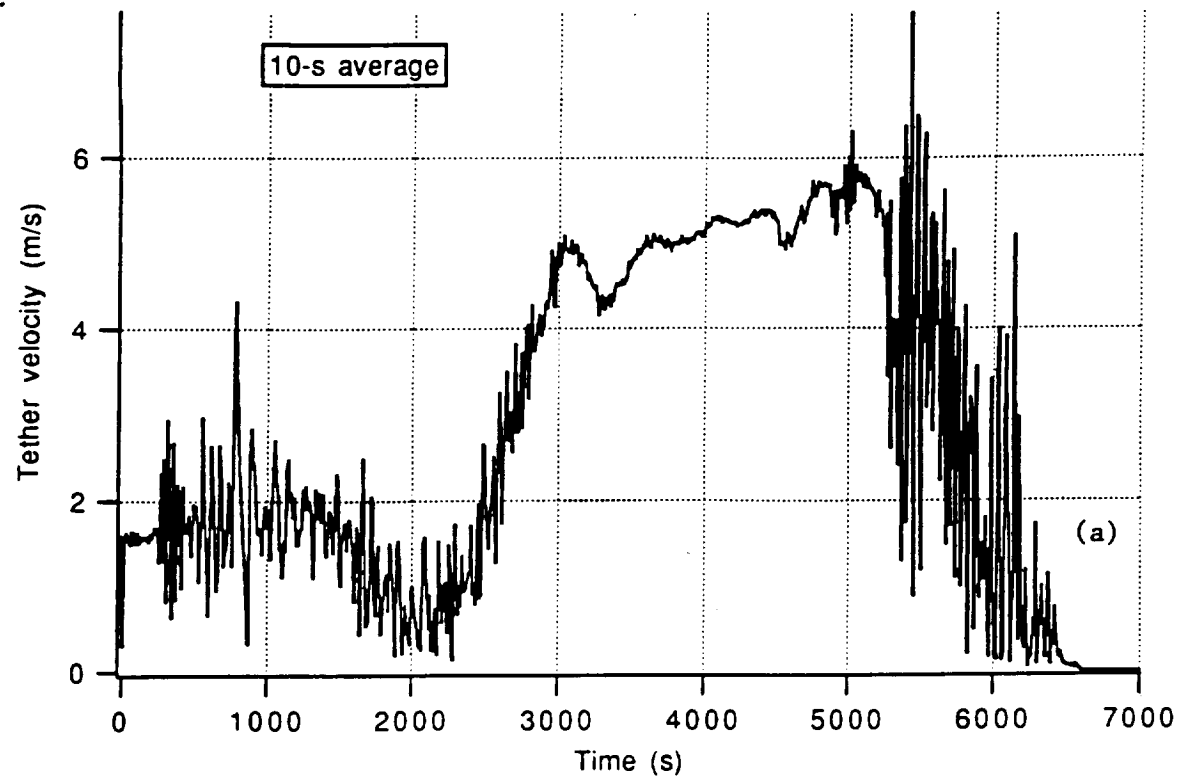


Figures 11.19(a) and 11.19(b)

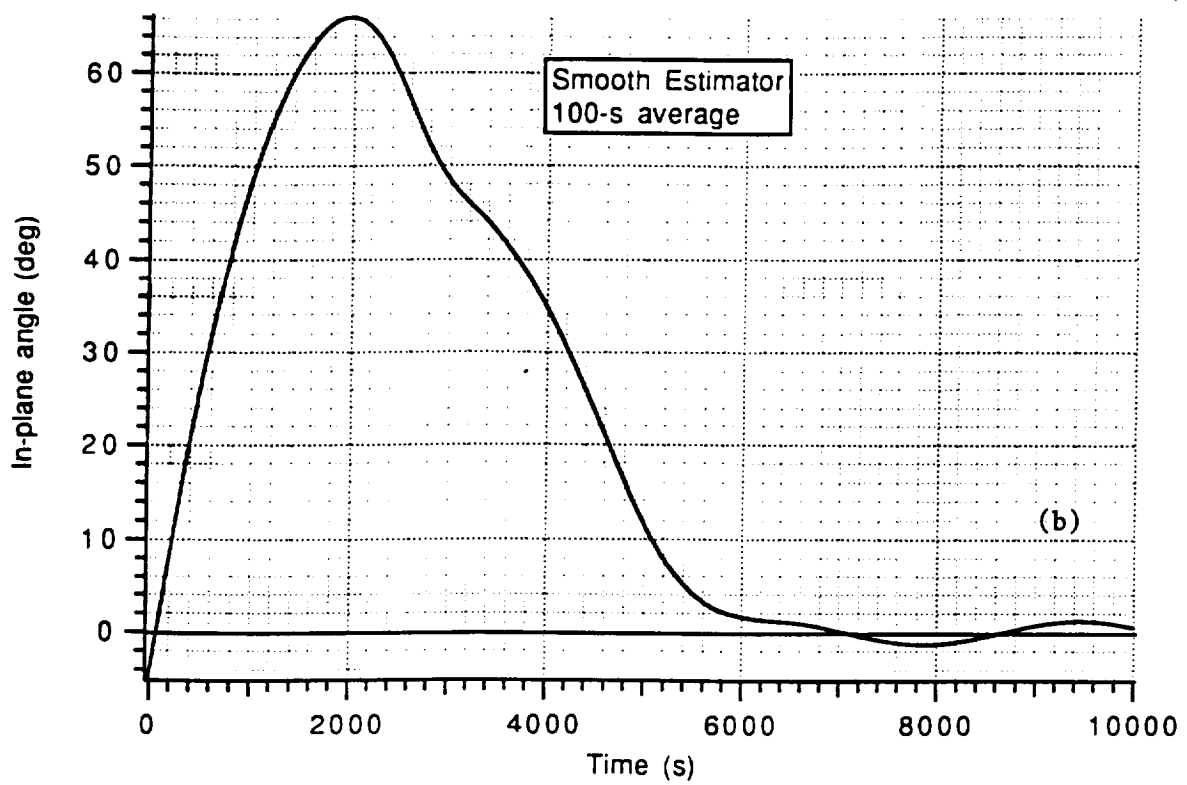
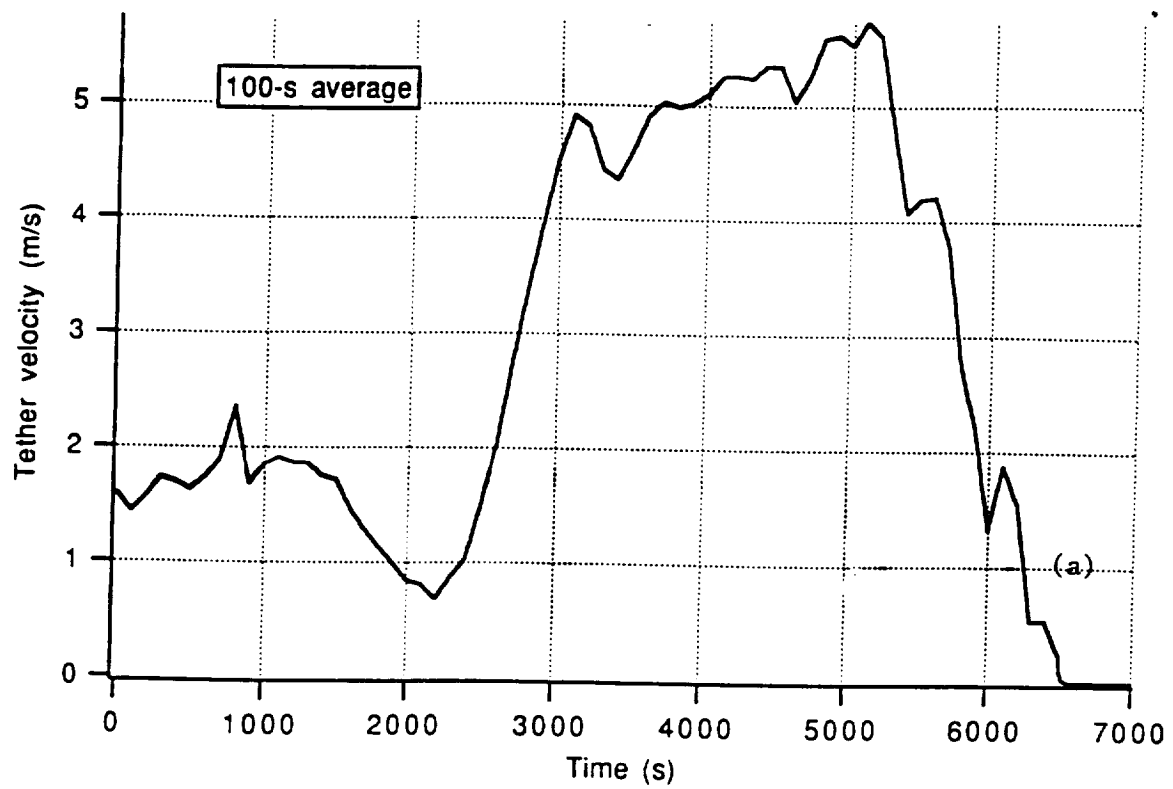


Figures 11.20(a) and 11.20(b)





Figures 11.21(a) and 11.21(b)



Figures 11.22(a) and 11.22(b)

### 11.2.2 More on the performance of the control law

The deployment of SEDS-2 stopped when the brake was ramped up to its maximum number of turns equal to 6. The ramping up started at  $t = 6560$  s from ejection and terminated at  $t = 6590$  s. The ramping up from about 3 turns to 6 turns of the brake post took approximately 30 s due to the brake speed of 0.1 turn/s. At  $t = 6560$  s, the tether longitudinal speed was 0.018 m/s and the (corrected) final length was 19,745 km. Because of the failure of 1 turn counter at  $t = 2200$  s and a tether length of 3.3 km, this final tether length has been adjusted by taking into account the  $\approx 380$  spurious turn counts computed by the remaining turn counter.

It is remarkable to see that the actual final value of the tether length is only 35 m shorter of the 19,780 m estimated before the flight for the nominal deployment (see Section 11.1.5). The deployment stop shortly before reaching 20 km should be attributed to the 300 m segment of old tether that forms the last portion of the tether. This segment of tether has much higher friction than the rest of the tether.

The final portion of the deployment was sufficiently smooth to provide a very gentle ride for the satellite without any loss of tether tension.

We would like to stress the excellent behavior of the control law notwithstanding the strong fluctuations of the velocity as measured by the turn counter(s) which were caused by the detected failure of one turn counter. The filtering and numerical technique for evaluating the velocity adopted in the control law provided a smooth actuation of the brake notwithstanding the high noise levels in the turn counts and turn rate.

The brake actuation, as shown in Fig. 11.23, was not jittery for most of the deployment. The more jagged behavior of the brake for  $t > 5300$  s can be attributed to the multiple sling/scrub transitions that occur for a small diameter of the tether spool (i.e., at the end of deployment and for small velocities the tether starts scrubbing on an aluminum flange with a consequent steep increase of the friction) and to the change in winding pattern of the tether spool.

The estimation of the minimum deployment tension is related to refining of the tension model. The tension model adopted for the pre-flight simulations was adequate but it is not refined enough to provide a high fidelity fit between the flight data and the simulated data. At this point, the minimum tension can be estimated to be in the range 10-20 mN. The nominal value of the minimum tension from the most recent ground tests was in the range

10-15 mN. Consequently, the actual deployment, from the friction standpoint, was close to nominal.

The control law for SEDS-2 was based on predefined reference profiles for length, length rate and brake. It is worth mentioning that nominal deployment does not mean reference deployment. The reference for SEDS-2 was derived for a minimum tension of 30 mN. This choice was based on the data of SEDS-1, which exhibited a higher minimum tension, and on the effort for increasing the robustness of the control law with respect to variations of the minimum tension. The successful performance of SEDS-2 during deployment proved that the control law was indeed robust.

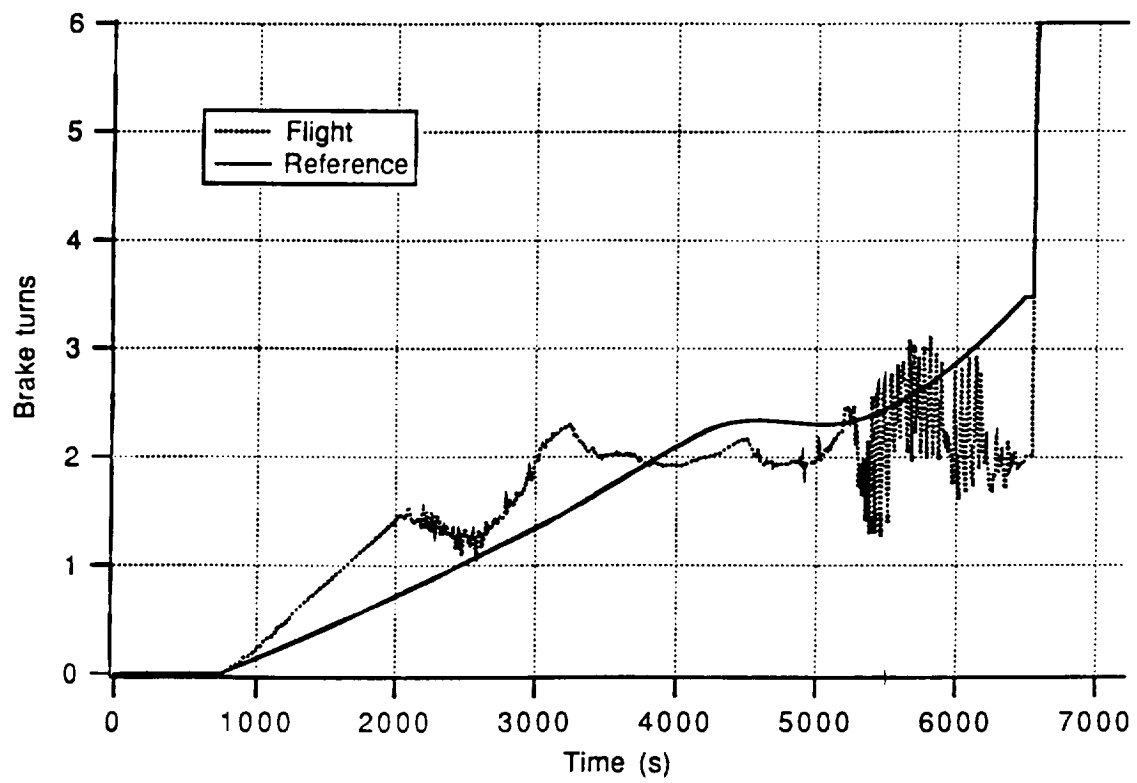
### **11.3 Conclusions on SEDS-2 control law**

The (closed-loop) control law of SEDS-2 was developed for reducing the final libration amplitude to less than  $10^\circ$  as opposed to the  $57^\circ$  libration amplitude exhibited by SEDS-1 during its flight.

The control law was designed for robustness with respect to variations or uncertainties of the tension model parameters and of the brake response. Specifically, a variation of the most influential parameter, the minimum tension, between 10 mN and 45 mN was estimated to cause a final libration amplitude ranging from 2 deg to 10 deg, respectively. Consequently, the best performance had to be expected for low values of the minimum tension. The control law was also robust with respect to uncertainties of the friction coefficient, which affects the brake response, of  $\pm 50\%$  and almost immune to random tensional noise.

During the flight, the control law of SEDS-2 performed as expected notwithstanding the detected failure of one turn counter at about  $t = 2200$  s and a tether length of 3.3 km. A final deployment length of 19,745 m was reached at  $t = 6560$  s with a final deployment speed of 0.018 m/s.

The maximum libration amplitude at the end of deployment is presently estimated at about 3 deg with respect to the local vertical. A value which is also consistent with the expected performance for a minimum tension of 10-20 mN. All the success criteria established before the flight were met with ample margin. The control law performed at the very top of the pre-flight expectations.



Figures 11.23

#### 11.4 References

- [1] E.C. Lorenzini et al., "Analytical Investigation of the Dynamics of Tethered Constellation in Earth Orbit (Phase II)." SAO Quarterly Report #32, NASA/MSFC Contract NAS8-36606, November 1993.
- [2] S.B. Bortolami, E.C. Lorenzini, C.C. Rupp and F. Angrilli "Control Law for the Deployment of SEDS-II." Proceedings of the AAS/AIAA Astrodynamics Specialist Conference, Victoria, Canada, August 16-19, 1993.
- [3] E.C. Lorenzini et al., "Analytical Investigation of the Dynamics of Tethered Constellation in Earth Orbit (Phase II)." SAO Quarterly Report #33, NASA/MSFC Contract NAS8-36606, March 1994.
- [4] J-J.E. Slotine and W. Li, "Applied Nonlinear Control", Prentice Hall, 1991.
- [5] W.J. Palm III, "Modeling, Analysis and Control of Dynamic Systems", John Wiley & Sons, 1983.
- [6] J. Glaese and R. Issa, "SEDS DRM Preliminary Presentation". Logicon Control Dynamics Inc., Huntsville, Alabama, June 1992.
- [7] S. Carroll and J. Powers, *Output files of comparison simulations carried out at NASA/MSFC*, 1993.
- [8] J. Glaese and P. Lakshamanan, "SEDS-2 Design Reference Mission". Release 1, Logicon Control Dynamics Inc., Huntsville, Alabama, August 1993.

## **Acknowledgments**

We would like to thank Charles Rupp and James Harrison of NASA Marshall Space Flight Center for their continuous support and invaluable advice provided during the entire duration of this research project. We would like to thank all the members of the Small Expendable Deployment System (SEDS) team who directly and indirectly helped us in the study of this exciting and successful project. We would also like to acknowledge the contributions from the graduate students who visited the Smithsonian Astrophysical Observatory during the course of this project and worked on many important research issues. Their names are: Marco Quadrelli and Simone Bortolami from the University of Padova, Italy; Monica Pasca from the University of Rome, Italy; Manfred Krischke, Johannes Klein, and Thomas Hahn from the Technische Universität München, Munich, Germany; and Michele Grassi from the University of Naples, Italy. Finally, a special thank to Dieter Sabath from the Technische Universität München for carrying out the friction coefficient tests on the flight tether of SEDS-II.

